Transactions of the ASME

The Journal of Engineering for Gas Turbines and Power (ISSN 0022-0825) is published quarterly for $100 per year by The American Society of Mechanical Engineers, 345 East 47th Street, New York, NY 10017. Second class postage paid at New York, NY and additional mailing offices. POSTMASTER: Send address change to The Journal of Engineering for Gas Turbines and Power, c/o The AMERICAN SOCIETY OF MECHANICAL ENGINEERS, 22 Law Drive, Box 2300, Fairfield, NJ 07007-2300.

CHANGES OF ADDRESS must be received at Society headquarters seven weeks before they are to be effective. Please send old label and new address.

PRICES: To members, $24.00, annually; to nonmembers, $100.00.
Add $8.00 for postage to countries outside the United States and Canada.

INDEXED by Engineering Information

Journal of Engineering for Gas Turbines and Power

Published Quarterly by The American Society of Mechanical Engineers

VOLUME 108 • NUMBER 2 • APRIL 1986

TECHNICAL PAPERS

(Continued on P. 230)

(Contents Continued)

Journal of Engineering for Gas Turbines and Power

Editorial

Starting with the July 1986 issue, a new ASME journal will come into existence called the *Journal of Turbomachinery*. The *Journal of Turbomachinery* is a spinoff from the JOURNAL OF ENGINEERING FOR GAS TURBINES AND POWER. It was created to provide the increased publishing capacity necessary to accommodate the increasing number of papers appearing in the field of power generation. This journal will concentrate on compressor and turbine component technology. Judging from the present backlog, the heaviest concentration of papers will be in the area of compressor and turbine aerodynamics, followed by turbine cooling and heat transfer.

The JOURNAL OF ENGINEERING FOR GAS TURBINES AND POWER will continue to publish all papers dealing with research, development, and operating experience with complete systems including gas turbines, fossil fuel and nuclear-fired steam power plants, and internal combustion engines. It will also retain all papers on combustion, on system dynamics, most papers on structures and materials topics, and those on control systems and all types of auxiliaries such as fuel systems, pollution control systems, inlet and exhaust systems, etc.

Papers dealing with the fluid mechanics of hydraulic turbines and pumps will continue to appear in the *Journal of Fluids Engineering*.

ARTHUR J. WENNERSTROM
Technical Editor

A Theory of Post-Stall Transients in Axial Compression Systems: Part II—Application

E. M. Greitzer
Massachusetts Institute of Technology, Cambridge, MA

F. K. Moore
Cornell University, Ithaca, NY

Using the theory developed in Part I, calculations have been carried out to show the evolution of the mass flow, pressure rise, and rotating-stall cell amplitude during compression system post-stall transients. In particular, it is shown that the unsteady growth or decay of the stall cell can have a significant effect on the instantaneous compressor pumping characteristic and hence on the overall system behavior. A limited parametric study is carried out to illustrate the impact of different system features on transient behavior. It is shown, for example, that the ultimate mode of system response, surge or stable rotating stall, depends not only on the B *parameter, but also on the compressor length-to-radius ratio. Small values of the latter quantity tend to favor the occurrence of surge, as do large values of* B. *Based on the analytical and numerical results, some specific topics are suggested for future research on post-stall transients.*

Introduction

In a companion paper, presented as Part I [1], a new theoretical approach was described for analysis of the types of post-stall transients that occur in multistage axial compression systems. An approximate solution procedure was developed, using a Galerkin technique, which led to a system of coupled, nonlinear, ordinary differential equations for the annulus averaged mass flow, the plenum pressure, and the rotating-stall cell amplitude, respectively.

In the present paper, we consider the application of these equations. We first examine their overall qualitative features. Following this, quantitative numerical results are presented for a representative low-speed compression system. These serve to illustrate not only the effects of various system parameters, but also some of the basic fluid dynamic phenomena that occur in the transients of interest. Finally, some recommendations are given concerning specific topics for research in the general area of stall recovery in aircraft gas turbine engines.

Qualitative Features of the Transient System Behavior

Before considering specific cases of interest, it is useful to examine the general features of the simplified equation set developed in Part I (equations I.59, 60, 61).[1] As mentioned there, these equations can be reduced to those describing either pure surgelike (i.e., purely one-dimensional) transients, or pure rotating stall, and permit the existence of pure modes, that is, either surge or rotating stall without the other.

A physically relevant question, however, is whether such modes could evolve from initial small disturbances. This question was touched on in Part I, and it was suggested that finite amplitude rotating stall cannot evolve without producing a finite disturbance in Φ or Ψ, although for small values of B, the disturbance can be a noncyclic transient. Equations (I.59–61), in fact, suggest that if B is small and the throttle is steep, Φ may remain essentially constant while J and Ψ vary with time. In this limiting case, the solution of equation (I.61) is:

$$\frac{J}{J_e} = \frac{1}{1+\left(\frac{J_e}{J_0}-1\right)\exp\left(-\frac{3aJ_eH/W}{4(1+ma)}\xi\right)} \tag{1}$$

where J_0 is an assumed initial disturbance. J thus grows steadily from J_0 to a final, fully developed pure rotating-stall value of J_e, defined in equation (I.62).

Figure 1 shows this behavior for the compressor geometry

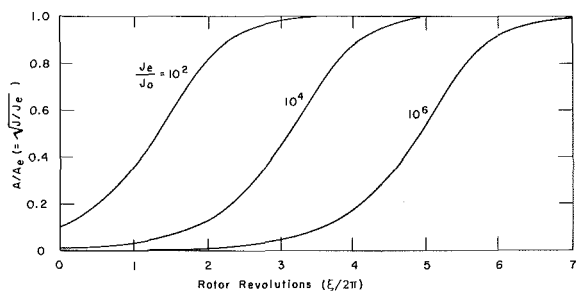

Fig. 1 Growth of (normalized) stall-cell amplitude at constant mass flow (m = 1.75, H/W = 0.72, $1/a$ = 3.5); curves from equation (1)

[1] Equations given in Part I will be denoted by roman numeral prefixes.

Contributed by the Gas Turbine Division of THE AMERICAN SOCIETY OF MECHANICAL ENGINEERS and presented at the 30th International Gas Turbine Conference and Exhibit, Houston, Texas, March 18–21, 1985. Manuscript received at ASME Headquarters, January 10, 1985. Paper No. 85-GT-172.

discussed in Part I. For reference, the relevant parameters are: $m = 1.75$, $H = 0.18$, $W = 0.25$, $1/a = 3.5$. The calculations have been done for $\Phi = 0.25$ and three different values of J_e/J_0: 10^2, 10^4, and 10^6.

The graph shows the normalized rotating stall amplitude, A/A_e $(= \sqrt{J/J_e})$, versus time, with time being plotted in rotor revolutions. It is clear from the figure that the growth is dependent on the initial conditions. This can be seen from equation (1) which, if $J_0 \ll J_e$, can be written for small times as:

$$J - J_0 = J_0 \left(\frac{3aJ_eH/W}{4a(1+ma)} \right) \xi + \ldots \tag{2}$$

i.e., the increment of J is proportional to the initial value. However, once the value of J has grown enough that the nonlinear aspects of the process become important, the approach to the final amplitude becomes independent of the initial conditions. This type of behavior, which is typical of nonlinear systems, will also be encountered later, when we discuss the results for the combined rotating stall and surge transients.

Small Axisymmetric Disturbance to Finite Amplitude Rotating Stall. We know that our equations permit both pure surge and pure rotating stall. We can also inquire whether those "pure" motions are stable to disturbances of the other family. First, consider the case of fully developed rotating stall subject to weak axisymmetric, (i.e., surgelike) disturbances. For the limiting case of an infinitely steep throttle line, we obtain a harmonic-oscillator equation for $\Phi(\xi)$, with the coefficient of the damping term given by

$$\text{damping coefficient: } -\frac{3}{2}\left[1 - \frac{1}{2}J - \left(\frac{\Phi}{W} - 1\right)^2\right]\frac{1}{W} \tag{3}$$

The damping would be negative if J were zero. If the stall is fully developed, however, J is $J_e = 4\{1 - [(\Phi/W) - 1]^2\}$, and the damping coefficient becomes

$$\text{damping coefficient: } \frac{3}{2}\left[1 - \left(\frac{\Phi}{W} - 1\right)^2\right]\frac{1}{W} \tag{4}$$

which is positive. We thus conclude that small-disturbance surge-type oscillations tend to be damped in the presence of equilibrium rotating stall. This might also be inferred from the fact that the relevant compressor curve is now the negatively sloped fully developed rotating-stall curve.

Small Angular Disturbance of Surge. The converse situation is that of a finite amplitude axisymmetric (surge) oscillation subjected to a small rotating-stall-like disturbance. Equation (I.61) governs the growth or decay of J. During the surge oscillation, Φ is varying so that the bracket in equation (I.61) may be either positive or negative, and it is therefore not obvious whether J will have a net growth.

To examine this in the limiting case of an infinitely steep throttle, one may show that the pure surge equation in this case takes the same form as equation (I.48) for rotating stall, with the time variable $\xi/(2Bl_c)$ playing the role of θ^*. We may thus infer from equations (I.53, 62) that the corresponding Galerkin solution is:

$$\Phi - \bar{\Phi} = W J_e(\bar{\Phi}) \sin\left(\frac{\xi}{2Bl_c}\right) \tag{5}$$

Using this in (I.61), and neglecting terms of order J^2, gives a linearized equation for J:

$$\frac{1}{J}\frac{dJ}{d\xi} = \frac{3aH/W}{1+ma}\left[-\frac{J_e}{4} - 2\sqrt{J_e\left(1 - \frac{J_e}{4}\right)}\sin\left(\frac{\xi}{2Bl_c}\right) + \frac{1}{2}J_e\cos 2\left(\frac{\xi}{2Bl_c}\right)\right] \tag{6}$$

The solution is:

$$\frac{J}{J_0} = \exp\frac{3aH/W}{1+ma}2Bl_c\left[-\frac{J_e}{4}\frac{(\xi - \xi_A)}{2Bl_c} + 2\sqrt{J_e\left(1 - \frac{J_e}{4}\right)}\cos\left(\frac{\xi}{2Bl_c}\right) + \frac{J_e}{4}\sin 2\left(\frac{\xi}{2Bl_c}\right)\right] \tag{7}$$

where a constant of integration ξ_A is included. The question is whether J is greater or less than its initial value J_0.

If the square bracketed term in equation (7) is positive, $J > J_0$, while if it is negative, $J < J_0$. The first term in the square bracket, being negative and increasing, represents a tendency for J to be progressively smaller than J_0 for large time; however, the oscillatory harmonic terms could reverse that tendency for early or moderate times.

Figure 2 illustrates the possibilities for the special case of $\bar{\Phi}/W = 1$ $(J_e = 4)$. In this case the square bracket takes the form:

$$\text{overall growth factor: } \left[-\frac{\xi - \xi_A}{2Bl_c} + \sin 2\left(\frac{\xi}{2Bl_c}\right)\right] \tag{8}$$

Nomenclature

A_e = amplitude of first-harmonic angular disturbance in pure rotating stall, $\sqrt{J_e}$
A_c = compressor duct area
a = reciprocal time-lag parameter of blade passage
a_s = sound speed
B = $(U/2a_s)\sqrt{V_p/A_cL_c}$
f_0 = nondimensional propagation speed of rotating-stall-like disturbances
H = semi-height of cubic characteristic
J = square of amplitude of angular disturbance of axial-flow coefficient
J_0 = initial value of J
J_e = value of J for fully developed rotating stall at the existing average axial-flow coefficient
K_T = parabolic throttle coefficient
L_c = total effective length of compressor and ducts
l_c = total length of compressor and ducts, in wheel radii
m = downstream duct-flow parameter
U = wheel speed at mean diameter
V_p = volume of plenum
W = semi-width of cubic characteristic
ξ = time, referred to time for wheel to rotate one radian
ξ_e = dimensionless time for development of equilibrium rotating stall
ξ_A = defines time of start of angular disturbance
Φ = axial flow coefficient, averaged over angle (axial velocity divided by wheel speed)
$\bar{\Phi}$ = flow coefficient averaged over both angle and time
Φ_T = flow coefficient of throttle duct, referred to entrance-duct area
ϕ = local axial velocity coefficient (local axial velocity divided by wheel speed)
Ψ = total-to-static pressure-rise coefficient (inlet to plenum)
ψ = pressure-rise coefficient, $\Delta P/\rho U^2$
ψ_c = axisymmetric pressure-rise coefficient
ψ_{c_0} = shut-off head coefficient

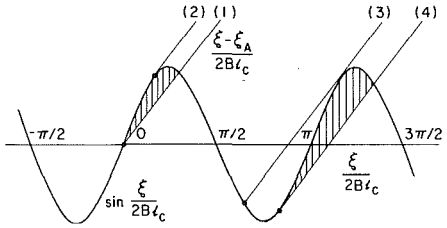

Fig. 2 Amplitude of rotating stall during a surge cycle, as indicated by terms in equation (8), with $\Phi = W$; different choices of ξ_A provide different starting points; net amplification occurs in shaded zone

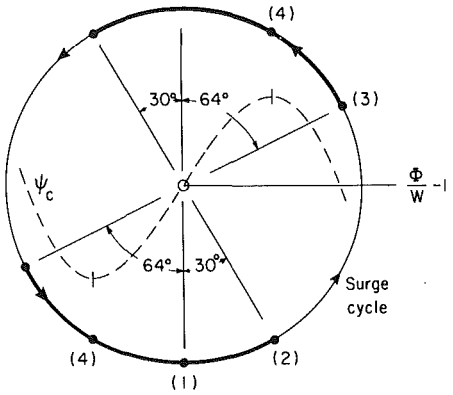

Fig. 3 Sketch of surge cycle showing regions in which net growth of rotating stall can occur; numbered points correspond to lines of Fig. 2

The first and second terms of this expression are plotted separately on Fig. 2. A series of lines are shown to represent the first term, because ξ_A is arbitrary. Where any one of these lines cross the sine wave is a possible starting time for the disturbance. What happens after the starting time clearly depends on the phase of the sine wave (surge oscillation) when the angular variation starts. If the start is at $\xi = 0$, then the shaded area above line (1) shows the duration and intensity of the excursion of J, although whether the amplification is sufficient for rotating stall to develop cannot be found from this small-perturbation solution.

If the intersection point is moved along the sine wave, the time available for amplification shortens, until line (2) is reached for which there can be no growth at all. Not until line (3) is reached does amplification again become positive. The greatest overall growth of the rotating stall is found for line (4).

To visualize these results in a different manner, we sketch on Fig. 3 the axisymmetric compressor characteristic, and overlay a surge cycle sketched as a counterclockwise circle centered at $\beta = 0$. The heavy lines indicate phase zones in which initial angular disturbances will at least briefly amplify.[2] Outside those zones, overall growth of a weak angular disturbance cannot occur. Points are labeled on Fig. 3 to show correspondence with the lines of Fig. 2.

The foregoing discussion indicates that it is important to know the character of an initial disturbance and the timing of its introduction, whether it is velocitylike or pressurelike, and its magnitude. All those factors can have an effect on the ultimate trajectory of the disturbance.

Summary of Qualitative System Behavior. Before presenting the numerical results for the trajectories in Φ, Ψ, and A space, we can summarize certain expectations about the system behavior:

1 Pure modes of either surge or rotating stall are permitted as permanent oscillations.

[2] Note that the growth we are describing is the overall value; the local growth rate is just dependent on the slope of the compressor characteristic and is positive at all points where the compressor has a positive slope.

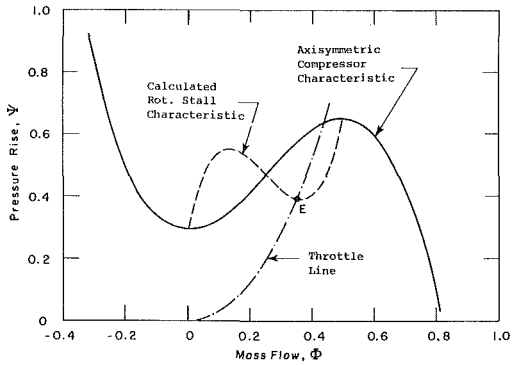

Fig. 4 Compressor and throttle characteristics ($H/W = 0.72$ and $\psi_c/H = 1.67$)

2 Pure surge can evolve from an initial weak axisymmetric disturbance.

3 In general, a weak angular disturbance will not produce pure rotating stall, but will produce some degree of axisymmetric disturbance.

4 The initial growth rate of an angular disturbance (toward a limit cycle value) depends on the strength of the initial disturbance, but becomes independent of this when the nonlinear aspects of the process become important.

5 Angular disturbances will grow toward an equilibrium value depending on the instantaneous flow coefficient; if the latter is also changing with time, angular-disturbance amplitude "chases a moving target."

6 Excursions of flow coefficient will tend to suppress angular variations, and the presence of angular variations will tend to suppress surge.

7 For the compressor characteristic examined, any small surgelike disturbances in the presence of fully developed rotating stall will tend to decay.

8 In the presence of fully developed surge, a small angular disturbance may decay or may grow (but only during a fraction of one surge cycle), depending on the phase of the surge cycle in which the disturbance originates.

Numerical Results for General Post-Stall Transients

The set of coupled ordinary differential equations given as equations (I.59), (I.60), and (I.61) have been solved numerically for a representative set of parameters to show some of the basic features of the phenomena. Specifically, calculations have been carried out to illustrate the effects of the nondimensional parameters B and l_c as well as of the initial conditions. In view of the approximate nature of the approach taken, however, it is to be emphasized that no extensive parametric study has been performed.

In the calculations, the axisymmetric compressor characteristic has been taken to be the same cubic curve described in Part I, with the parameters used in Chue's calculations [1]; this is shown for reference as the solid line in Fig. 4. The throttle curves are taken as parabolas. The one shown as the dash-dot line in the figure corresponds to $K_T = 6.5$, for which most of the calculations were carried out; other throttle settings used are noted in the text. As mentioned in Part I, these curves are representative of a three-stage, low-speed compressor, somewhat similar to that used in [2].

Unless specified, the initial values of nondimensional pressure rise and flow coefficient are taken to be the values at the peak of the curve, i.e., $\Phi = 0.5$ and $\Psi = 0.66$, for the particular characteristic chosen. At that condition, we shall impose a level of circumferential nonuniformity defined by $A(0)$ at time $\xi = 0$ (recalling that the nondimensional amplitude of the θ dependent velocity nonuniformity is AW, and $A \equiv \sqrt{J}$). The system of equations (I.59-61) governs the

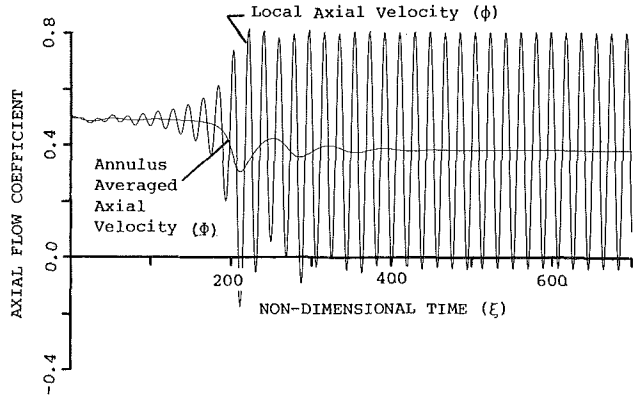

Fig. 5(*a*) Time history of local and annulus-averaged axial velocity coefficient during transient to rotating stall

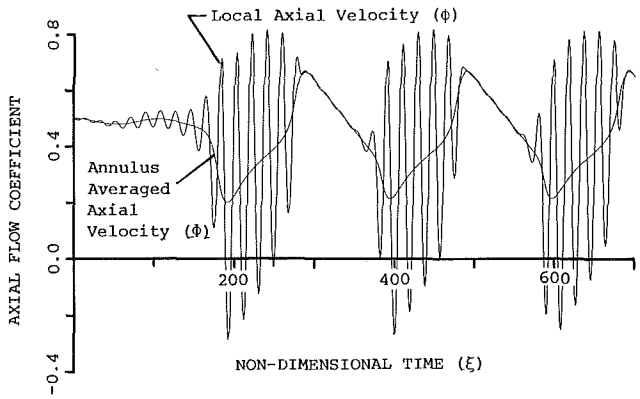

Fig. 5(*b*) Time history of local and annulus-averaged axial velocity coefficient during transient to surge

ensuing transient which, due to the coupling, shows either temporal (surgelike) or circumferential (rotating-stall-like) variations.

Compressor and Compression System Transient Behavior in Surge and Rotating Stall. To introduce the quantitative results, we show the transient behavior for two situations: one in which the outcome is rotating stall and one in which it is surge. These are illustrated in Figs. 5(*a*) and 5(*b*). The figures show the nondimensional annulus averaged and local axial velocity (i.e., the axial velocity that would be measured by a hot-wire probe at the compressor inlet) versus nondimensional time in rotor revolutions. The local velocity is given by the following expression obtained by combining equations (I.52, 53, 57):

$$\phi = \Phi(\xi) + WA(\xi)\sin(\theta - f_0\xi) \tag{9}$$

The two calculations correspond to a throttle setting of K_T = 5.5, and to values of B of 0.5 and 1.0, respectively. In the calculations, the value of l_c was 8.0 and the initial rotating stall amplitude $WA(0)$ was 1% of the average velocity (nondimensional amplitudes of axial velocity perturbation of 0.005). In addition, the minimum value of axial velocity nonuniformity occurring at any subsequent time during the transient was set equal to the initial value; this seems more physically realistic than letting this quantity decrease to zero.

It can be seen that the resulting instantaneous velocities are very similar to those seen in the time traces than one obtains during compressor transients (e.g., [2]). In particular, the growth and decay of the stall cell as the compressor mass flow goes in and out of the stalled flow regime is very evident. What may be less evident from this time-domain representation, but will be shown in the subsequent figures, is that this growth and decay of the stall cell does not occur in a quasi-steady manner, and that the instantaneous compressor

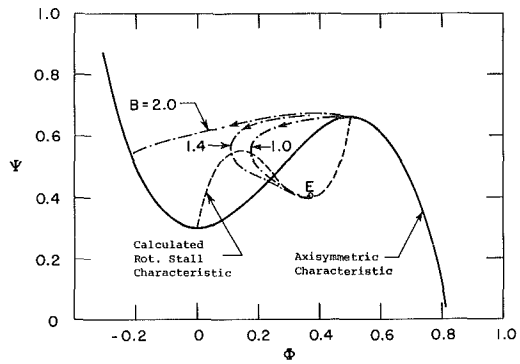

Fig. 6 Transient compression system response (Ψ versus Φ) for different values of B (l_c = 8.0, $A(0)W$ = 0.005)

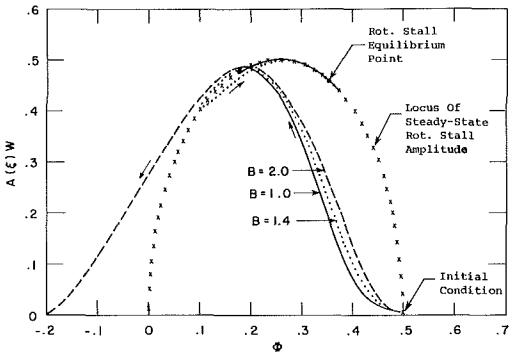

Fig. 7 Evolution of rotating-stall amplitude during system transient; effect of B parameter (l_c = 8.0, $A(0)W$ = 0.005)

performance does not therefore correspond to the steady-state rotating-stall characteristic.

Effect of B Parameter. Although Fig. 5 gives one illustration of the (familiar) effect of the B parameter, Fig. 6 shows this in more detail. In the figure, the transient system response is presented in terms of the overall pressure rise (atmosphere to plenum) and annulus-averaged flow coefficient for three different values of B: 1.0, 1.4, and 2.0. Also indicated is the axisymmetric curve (the solid line) and the calculated rotating stall curve (dashed). The values of l_c and $WA(0)$ are the same as for Fig. 5. The throttle setting is that illustrated in Fig. 4, K_T = 6.5. Note that, at this throttle setting, the surge included an appreciable portion of reversed flow contrary to the situation shown in Fig. 5 (deep surge versus classic surge, in the terminology of [2] and [3]).

As expected, higher values of B cause larger excursions in axial velocity. At the highest value, this would lead to surge cycles, whereas for the lower values, the eventual result of the initial transient is operation at a new equilibrium point on the rotating-stall curve.

The picture shown in Fig. 6 is a somewhat familiar one. However, Fig. 7 presents a new, more detailed view of these same transients. This figure shows the rotating-stall amplitude, $A(\xi)W$ ($= \sqrt{J}W$), versus annulus-averaged flow coefficient (Φ) for the same conditions. Also indicated in the figure is the locus of steady-state rotating-stall amplitudes for different values of Φ, i.e., the amplitude for steady-state operation at that mass flow. This is just the value calculated from equation (I.62), which has a maximum at Φ = 0.25 and goes to zero (i.e., steady-state rotating stall ceases) at Φ = 0.5 and Φ = 0.0. This curve represents the locus of equilibrium states toward which rotating-stall-like disturbances must tend.

An obvious feature of the transients is that over the first part (for Φ greater than roughly 0.25) the amplitude is substantially less than that during steady-state operation. For lower flows, however, the amplitude can actually exceed the

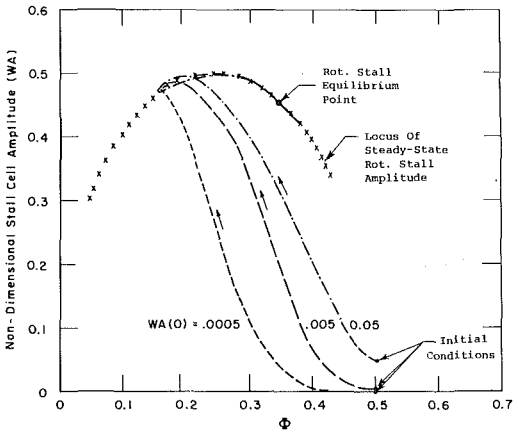

Fig. 8 Evolution of rotating-stall amplitude during system transient; effect of initial conditions (l_c = 8.0, B = 1.0)

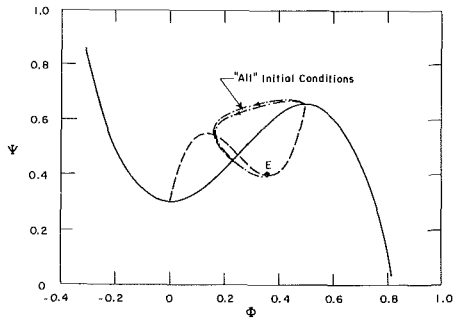

Fig. 9 Transient compression system response; effect of initial conditions (l_c = 8.0, B = 1.0)

steady-state value. Further, as seen in the curve for $B = 2.0$, the rotating stall persists into the reverse-flow regime during the transient. This can be contrasted with steady-state operation in which (for this compressor) rotating stall cannot exist when flow is reversed.

It should be noted that when the transient leads to surge cycles, calculations have only been carried out for part of the initial cycle. The reason is that the calculated stall-cell amplitude decays to a very low value during the extended operation at reverse flow. Thus the "initial condition" for the part of the transient when the flow through the compressor accelerates (from zero) back to unstalled operation is essentially that of zero stall-cell amplitude. Under these conditions, as discussed above, there will be no subsequent growth of rotating stall, and the transient will proceed as pure surge.

It does not seem physically realistic, however, that there would be a lower level of flow asymmetry during a surge cycle than during operation prior to stall, and thus this part of the calculation does not appear to be a valid description. As done in the calculations leading to Fig. 5, it might be more correct to say that there is always some minimum disturbance amplitude present, able to provide an "initial disturbance" at any time. In view of the lack of information about this point, however, we have not elected to do this, but rather to restrict computations to the first part of each transient. We will return to a discussion of this point in the next section.

A basic feature shown in Figs. 5 and 7 is the growth and decay of the rotating stall as the mass flow varies, an effect anticipated in Figs. 2 and 3 and the related discussion. That this process must actually occur has been known qualitatively for some time. As far as the authors know, however, this is the first time that it has been calculated, in even an approximate manner, using the equations of motion for nonaxisymmetric flow in a compressor.

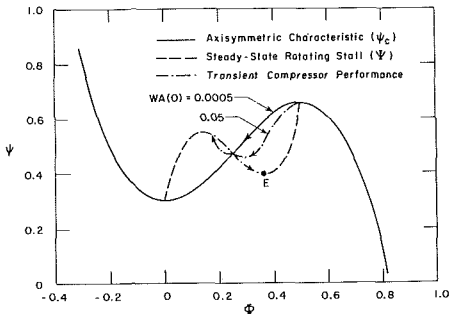

Fig. 10 Instantaneous compressor pumping characteristic during system transient; effect of initial conditions (l_c = 8.0, B = 1.0)

Effect of Initial Conditions. Effects of initial level of disturbance, $A(0)W$, have also been examined. The results are given in Fig. 8, which show the compressor treatment in an AW, Φ (rotating-stall amplitude, flow coefficient) plane. The calculations shown are for $B = 1.0$, $l_c = 8.0$, and for three different initial values of axial velocity nonuniformity: 0.05, 0.005, 0.0005; these correspond to initial perturbations of 10%, 1%, and 0.01% of the mean axial velocity. The last of these is roughly the size that would be expected in a good wind-tunnel test section, and the first appears to be larger than the (long-wavelength) velocity disturbances generally seen prior to rotating stall. Thus, the range of initial disturbance amplitude conditions encompasses essentially all physically plausible situations. The value regarded as the "base case," the 1% level, might be a reasonable estimate for the magnitude of velocity nonuniformities to be expected prior to rotating stall, but there seem to be few data on this point. In the figure, the locus of steady-state rotating stall amplitude is again indicated (by the crosses) as is the eventual equilibrium point in rotating stall, at $\Phi = 0.35$, $\Psi = 0.455$.

The effect of the initial conditions is strong early in the transient, since the growth rate is proportional to the amplitude of the perturbation. After the stall amplitude has reached a certain size, however, on the order of 0.1-0.2, nonlinear effects become important, and the slope of the trajectory is no longer set primarily by initial conditions. Although there are some differences in the extent of the excursion in axial velocity between the three cases, the behavior once the trajectory approaches the vicinity of the steady-state locus is fairly similar for the three cases. As stated earlier, this relative independence from the initial conditions during the approach to the equilibrium state is typical of nonlinear systems of the type which we are examining.

The effect of initial conditions can also be shown in a Φ, Ψ representation, as in Fig. 9, where curves for initial amplitudes 0.05 and 0.0005 are shown. Even though there are two orders of magnitude difference between the initial values, the trajectories of the plenum pressure versus flow coefficient are not at all dissimilar; they both show roughly the same excursion in mass flow before ending up at the eventual equilibrium point in rotating stall, denoted on the graph by E.

The influence of initial conditions on the compressor pumping characteristic, i.e., the instantaneous compressor output, can also be examined. The instantaneous output can be found by subtracting the momentum changes in the compressor duct from the overall (atmosphere to plenum) pressure rise. The result is presented in Fig. 10, which gives instantaneous compressor pressure rise versus instantaneous annulus-averaged axial velocity parameter, for the same conditions as in Fig. 9, namely $B = 1.0$, $l_c = 8.0$, and initial amplitudes $WA(0) = 0.0005$ and 0.05.

The trajectory for the former can be seen to follow the axisymmetric characteristic until near $\Phi \sim 0.25$ (the point of maximum steady-state rotating stall amplitude), then depart and verge towards the steady-state rotating-stall curve. The trajectory for 0.05 departs from the axisymmetric curve

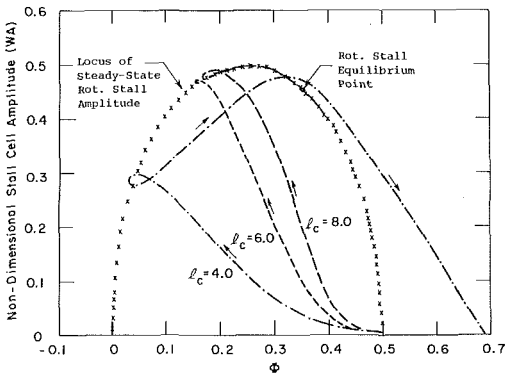

Fig. 11 Evolution of rotating stall amplitude during system transient; effect of length-to-radius ratio ($A(0)W = 0.005, B \simeq 1.0$)

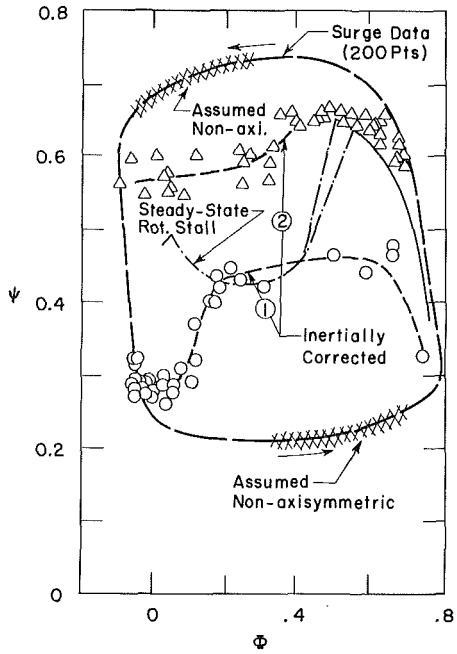

Fig. 12 Instantaneous compressor pumping characteristic derived from surge cycle data (from [4]); measured steady-state rotating stall curve also shown for reference ($B = 1.58, l_c = 8, A(0)W = 0.005$)

virtually from its initial point and tracks essentially along the steady-state rotating-stall curve after it first passes through $\Phi = 0.25$. The eventual equilibrium point is again indicated in the figure as E.

Calculations have also been carried out for other values of B to examine the effect of initial conditions. These confirm, in general, the trends shown in the preceding figures, namely that over a fairly wide range of initial conditions, the results do not depend strongly on the precise values used. There are, however, situations in which the initial condition can make a great deal of difference in the eventual outcome. For example, if one is on the "borderline" with regard to encountering surge or rotating stall, a change in the initial amplitude can alter the system behavior, from tending to an equilibrium point to undergoing a surge cycle. The range of situations in which the initial condition had a significant effect on the ultimate result was not investigted in any detail. From the few studies that were done, it appears that if B differs by more than about 10% from the transition value, the influence of the initial condition is substantially diminished. As suggested above, the possible influence of initial conditions, and thus the question of how to specify initial conditions properly (as well as the details of the nature of disturbances at different stages of the surge cycle), is a topic that must be investigated further.

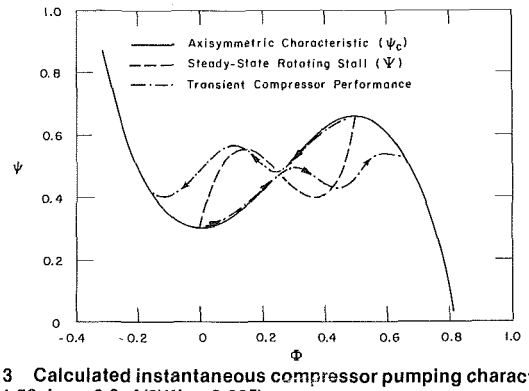

Fig. 13 Calculated instantaneous compressor pumping characteristic ($B = 1.58, l_c = 8.0, A(0)W = 0.005$)

Note that one *can* produce changes in computed system behavior by making sufficient changes of initial conditions. For example, if the initial amplitude is decreased to 0.00005 (0.01% of mean velocity), the growth of the rotating-stall cell is so slow during the transient that the compressor behavior is virtually on the axisymmetric curve throughout, and surge occurs. As discussed previously, however, it is felt that this represents an unrealistically weak initial disturbance, and it thus appears that the calculations may not be very sensitive to the initial conditions, although the matter clearly deserves more study.

Effect of Compressor Length to Radius Ratio. The other parameter investigated was l_c, the compressor length-to-radius ratio, and Fig. 11 shows trajectories for values of l_c of 4.0, 6.0, and 8.0. The value of B is 1.0 and the initial amplitude is $A(0)W = 0.005$ As in previous figures, the steady-state and equilibrium values of rotating stall amplitude are also indicated.

The curves for $l_c = 8.0$ and 6.0, while quantitatively different, have the same qualitative features, namely an initial rapid rise in amplitude and then a nearly quasi-steady motion along the steady-state amplitude curve until the equilibrium value is reached. A different situation exists for $l_c = 4.0$, however. There is a large difference between the unsteady trajectory and the steady-state curve and the system does not settle down to a new equilibrium point. Starting from initial conditions, the mass flow decreases then increases again and the stall-cell amplitude decays to a low value as the compressor returns to the unstalled portion of the compressor characteristic. This would thus indicate surge cycles, rather than an approach to equilibrium in rotating stall.

These calculations show that, in addition to the B parameter, the length-to-diameter ratio, l_c, can also affect whether a given system will exhibit surge or rotating stall. The physical reason is that, for the same value of B, a decrease in length-to-radius ratio means that the time for the formation of a rotating stall cell becomes relatively longer in proportion to the time for a mass flow excursion so that the instantaneous characteristic is more like the axisymmetric characteristic.

It is also relevant to briefly relate these calculations to previous studies. In [2], the only effect investigated was the influence of the B parameter. In the published results, the "time constant" that characterized the rotating-stall formation time was kept constant at two rotor revolutions, since the available data was insufficient to determine it more precisely. (It was, however, stated that some calculations had been carried out using different values of that time constant and the results for the critical value of B were somewhat different, although over the range examined the difference was not great.) In the present study, there is no need to assume such a time constant, because the manner in which the compressor output transitions from axisymmetric to fully developed rotating stall is not calculated.

Comparison with Data on Instantaneous Compressor Performance. In addition to examining the impact of B parameter, initial conditions, and compressor length-to-radius ratio, the present calculation procedure has also been used to help interpret transient compressor data. Specifically, data from a surge cycle, in the form of overall atmospheric to plenum pressure rise versus mass flow, has been used to form an estimate of the instantaneous compressor pumping characteristic.

The procedure originally followed [4, 5] was to subtract from this overall pressure rise a one-dimensional (i.e., axisymmetric) correction for the inertial forces due to fluid accelerations during the surge cycle. The explicit expression for the correction is:

$$\psi_c = \Psi + l_c \frac{d\Phi}{d\xi} \tag{10}$$

The terms given by the data are Ψ and $l_c\ d\Phi/d\xi$, ψ_c being calculated; details of the procedure are given in [4, 5].

In applying this procedure, it is necessary to examine the (compressor inlet) time-resolved data to determine whether the flow is indeed axisymmetric. It was found that the data showed rotating stall, not fully developed, toward the end of each period of rapid flow change. Although the information is not sufficient to resolve all the details of the flow, the conclusion is that axisymmetric flow cannot be assumed for the entire surge transient that the data represents. The present theory, however, provides a means to calculate the effect of this departure from axisymmetry (perhaps most dramatically illustrated in Fig. 5(*b*), and thus to aid in extracting the axisymmetric characteristic from this type of transient.

A sample of the data is shown in Fig. 12, with the inertially corrected characteristics determined by equation (10). The triangles and the circles denote the values obtained for the decelerating and accelerating portions of the surge cycle; curves 1 and 2 have been fitted through these points. The dot-dash line is measured data for steady-state rotating stall operation. It can be seen that even though there is some scatter in the calculated ψ_c, due presumably to the differentiation of the experimental data, the points fall into two categories: For decelerations, the corrected curve lies substantially above the steady-state rotating-stall curve, whereas for accelerations (at least for $\Phi > 0.4$), the derived pumping characteristic is considerably below the steady-state curve. In view of this behavior, the question arises whether a single-valued axisymmetric curve is indeed a valid representation, or whether a more complex axisymmetric behavior must be invoked.

To examine this matter from the point of view of the present theory, calculations have been carried out using the system parameters that characterize the transient data: $B = 1.58$, $l_c = 8.0$, and throttle curve C (see Fig. 3). The calculations were done for both accelerating and decelerating flows. For the decelerations, initial conditions were $\Phi = 0.5$, $\psi = 0.66$, and $A(0)W = 0.005$. For the accelerating part of the cycle initial conditions were $\Phi = 0.0$, $\Psi = 0.3$, and $A(0)W = 0.005$.

The results are shown in Fig. 13. The solid line is the axisymmetric characteristic and the dashed line is the steady-state rotating stall curve. The computed instantaneous compressor performance (which corresponds to the quantity shown dashed in Fig. 12) is indicated by the heavy dash-dot lines. The arrows showing the direction of motion of the operating point should be carefully observed.

It can be seen that the computed and the experimental curves have strong similarities, at least qualitatively. In particular, the tendency for the compressor pumping characteristic to be above the axisymmetric performance in the reverse flow region and below it at high forward flows is clearly manifested.

The reason for this is found from consideration of the growth and decay of the rotating stall. During the latter part of the deceleration, the instantaneous rotating-stall amplitude is much larger than the steady-state value (which is zero for negative values of Φ) and the compressor output is thus increased, compared to the axisymmetric value. During the acceleration, for the flows greater than $\Phi = 0.4$, say, the rotating stall amplitude is again much larger than that in steady-state operation, so the performance (i.e., pressure rise) is decreased compared to the axisymmetric value.

The main points in the foregoing comparison of experimental data with the present computations are thus:

1 The behaviors of the two are qualitatively similar, and
2 The departure of the compressor pumping characteristic from both axisymmetric and steady-state performance arises because the instantaneous rotating stall amplitude differs considerably from the steady-state value. In particular, in the latter part of both deceleration and acceleration processes, the stall cell is much larger than one would presume from steady-state considerations.

Discussion of the Present Model and Suggestions for Future Work

Although the analysis and numerical calculations have pointed out certain features of the general transient which appear to be important, it is clear that the present treatment has only made a start on this very complex problem. It is thus appropriate to give some discussion about the aspects of the actual flow that are included in the theory, the aspects that are potentially important but have not been included, and the areas that have been mentioned as needing further investigation.

We can start by listing those aspects of the unsteady compressor and compression system behavior that are accounted for:

1 System dynamic characteristics: These are analyzed in a lumped parameter fashion. For the situations considered in the present report (low Mach number and low frequency) this is a very good approximation. As either frequency or Mach number is increased, one may have to adopt a more complex description of these components. In particular, there is, for high-pressure ratio compressors, the possibility of mass storage within the compressor itself so that a simple representation of the inertance of the flow in the compressor duct may not suffice. In this regard, however, it is of interest to note that Mani [6] has achieved some quite reasonable comparisons with experiments using very simple representations of the system parameters.

2 Inlet flow field: A description of the upstream flow is included in the theory. The flow upstream of the compressor is modeled as two-dimensional and unsteady, but irrotational. The upstream annulus is taken as having constant area, although this assumption can be relaxed, if necessary. It is not clear how valid the irrotationality assumption is, and this is a subject for investigation. Data are scarce on this point, although the results of Day [7] give some credence to this assumption.

Perhaps more serious is the assumption that axial and circumferential disturbances are related as they would be if they were harmonic. This assumption requires evaluation, as does that regarding entrance to the inlet guide vane as accomplished without head loss.

3 Exit flow field: A linearized description of the exit flow field is included in the theory. It is clear that the assumption of linearity in the exit static pressure perturbations cannot be correct in general, although the degree to which it is in error and, more importantly, its effect on the predictions of the theory is not obvious. Previous theories of steady-state

rotating stall, in particular [8] and [9] which have used this assumption, have had good success with predicting at least some of the features of the stall cell flow field.

4 The model of the throttle characteristic that is included is quite adequate for low-pressure ratios. For higher-pressure-ratio systems, there should be no problem with introducing a compressible version of this, as was done by Wenzel [10].

5 Throttle transients have not been included in the present calculations, but are within the scope of theory. There should be no difficulty in applying the theory to account for these. This is of interest since it has been found that throttle transients can have a significant effect on system behavior.

6 System hysteresis appears naturally in the theory since it is set by the stability of the system at the various intersection points of throttle and compressor curves. When closing the throttle (into stall) the compressor curve is the axisymmetric one. When opening the throttle from operation in fully developed rotating stall, the compressor curve is the rotating-stall one. There can thus be a difference in the throttle settings at which transition from unstall to stall and from stall to unstall occur.

7 Compressor geometry is represented by the axisymmetric characteristic.

8 Unsteady blade row response (internal aerodynamic lag of the compressor) is included in the theory. It is done in a rudimentary manner, because at present one does not know how much detail is needed to provide a satisfactory description.

From the above, it does appear that the basic elements that one might think necessary for an analytical description of general post-stall transients have been included. Having said this, however, it should be emphasized that their inclusion has, in some instances, been done in a quite approximate manner, with an impact on the overall prediction which is not well understood. In this connection, we can refer back to the analytical framework [8] on which this study is based. The equations developed there will always result in axial velocity profiles that are like those shown in Figs. 5(*a*, *b*) of Part I, rather than the "top-hat" type of profile that seems to be more characteristic of compressors that operate in rotating stall. At present, the reason for this discrepancy is unclear, but the fact that it exists suggests that there are aspects of the theory which should be improved, even for low-speed, low-pressure-ratio situations.

We have described those features that are included, and we now turn to others which we think will be important to include for problems of practical interest.

1 Effects of compressibility on compressor performance and inlet and exit flow fields.
2 Front-to-rear mismatching effects due to off-design operation in the compressor.
3 Heat addition in the burner.
4 Effects of inlet flow distortion.
5 Engine matching effects (nonconstant speed, for example).
6 Other compression system components.
7 Steady-state hysteresis in the axisymmetric compressor characteristic, if such exists.

Research is necessary to elucidate the influence of the effects named above. In addition to these, however, there are other topics that must be explored if one is to improve the quantitative capabilities of the theory. The first of these is the development of more exact methods for the calculations. The numerical results given in the present report are based on a one-term Galerkin procedure (equations (I.59–61)); as mentioned, this was all that could be carried out in the limited time available. However, the types of phenomena that are being investigated would appear to be very well suited for spectral or pseudospectral calculation methods [11], which might be applied, for example, to equations (I.42–44).

Another matter of concern is the rotating stall performance. The question of the behavior of the compressor at or near the point of instability is by no means settled. The present theoretical analysis predicts that the flow in the compressor will become unstable at the peak of the steady-state pressure rise curve. In practice, compressors are observed to become unstable on the negatively sloped part of the curve. While interstage (one-dimensional), volume effects have been invoked as a possible cause for this in high-pressure-ratio compressors, the behavior is observed at low pressure ratios also, and here the interstage effects are very small. Both experimental and theoretical research is needed on this topic.

The effect of inlet conditions has been mentioned before, and the point will not be belabored here. We will merely note that this is a new aspect of the problem, and one on which there is little data.

Effects of the features of the initial disturbance have received only cursory attention in this report. Only a rotating-stall-like disturbance was considered. Other possibilities also need study; disturbances which are statistically defined fluctuations, which arise from inlet distortions, asymmetric burner pulses, etc. are all possibilities for transient initiation, perhaps in combination with symmetric (surgelike) pulses arising either naturally or from control actions. Research on these questions of disturbance initiation should be helpful to guide experimental tests.

Summary and Conclusions

1 An approximate theory has been developed for general post-stall transients in axial compression systems.

2 The analysis includes a two-dimensional, unsteady representation of the compressor flow field in the compressor annulus, together with a description of the overall dynamic response of the system. The resulting set of equations is thus capable of describing the strong coupling which can exist between surgelike and rotating-stall-like oscillations.

3 Examination of the coupled equations shows that surge and rotating stall can each exist in "pure" or equilibrium form; however, rotating stall cannot evolve without inducing some surgelike unsteadiness in the process. During either equilibrium surge or rotating stall, small amplitude disturbances of the other family will tend to die out.

4 Calculations have been carried out for general post-stall transients, which involve the growth or decay of rotating stall in the compressor. This growth or decay is calculated, along with the instantaneous system operating point. To the authors' knowledge, this is the first time that this has been done.

5 The instantaneous rotating stall-cell amplitude is found to have a significant effect on the instantaneous compressor pumping characteristic, and hence on the overall system response.

6 The theory extends previous analyses concerning the effect of the B parameter ($B = (U/2a_s)\sqrt{V_p/A_cL_c}$) on post-stall transients, and adds details of the transient process: how rotating stall decays for large B and how it evolves to a fixed level when B is less than the critical value.

7 Other parameters besides B, in particular the compressor length to radius ratio $l_c = L_c/R$, can also have a strong effect on the system response. A limited parametric study shows that, for a given value of B, compressors of shorter length-to-radius ratio are more likely to exhibit surge than rotating stall. Initial conditions concerning stall-cell amplitude at the start of the transient may also be of importance, and should be studied.

8 The rotating-stall cell amplitude during unsteady flow is

different from that during steady-state operation in rotating stall. Consequently, the instantaneous compressor performance during a system transient can differ considerably from the characteristic measured during steady-state rotating stall.

9 The numerical results that are presented show qualitative agreement with the existing (but scarce) experimental data concerning the nature of the flow field during this type of transient.

10 Based on the results of the analysis, recommendations are made concerning future work on nonrecoverable stall.

Acknowledgments

Most of the work described in the paper was carried out while the authors were in residence at NASA Lewis Research Center during the summer of 1983. The assistance of Mr. C. L. Ball in arranging this stay, as well as in providing a very conducive atmosphere for the research, is gratefully acknowledged. Additional support has also been provided by NASA under grant NSG-3208.

References

1 Moore, F. K., and Greitzer, E. M., "A Theory of Post-Stall Transients in Axial Compressor Systems: Part I – Development of Equations," ASME Paper No. 85-GT-172.

2 Greitzer, E. M., "Surge and Rotating Stall in Axial Flow Compressors, Parts I, II," ASME JOURNAL OF ENGINEERING FOR POWER, Vol. 98, No. 2, Apr. 1976, pp. 190–217.

3 Greitzer, E. M., "The Stability of Pumping Systems—The 1980 Freeman Scholar Lecture," *ASME J. Fluids Eng.*, Vol. 103, June 1981, pp. 193–243.

4 Koff, S. G., and Greitzer, E. M., "Stalled Flow Performance for Axial Compressors–I: Axisymmetric Characteristics," ASME Paper No. 84-GT-93, 1984.

5 Koff, S. G., "Stalled Flow Characteristics for Axial Compressors," S. M. Thesis, Massachusetts Institute of Technology, Department of Mechanical Engineering, 1983.

6 Mani, R., "Compressor Post Stall Operation," *Lecture Notes from AIAA Professional Study Seminar on Airbreathing Propulsion*, G. C. Oates, course director, June 1982.

7 Day, I. J., "Axial Compressor Stall," Ph.D. Thesis, Cambridge University, Engineering Department, 1976.

8 Moore, F. K., "A Theory of Rotating Stall of Multistage Compressors, Parts I, II, III," ASME JOURNAL OF ENGINEERING FOR POWER, Vol. 106, No. 2, Apr. 1984, pp. 313–336.

9 Cumpsty, N. A., and Greitzer, E. M., "A Simple Model for Compressor Stall Cell Propagation," ASME JOURNAL OF ENGINEERING FOR POWER, Vol. 104, No. 2, Jan. 1982, pp. 170–176.

10 Wenzel, L., and Bruton, W. M., "Analytical Investigation of Non-Recoverable Stall," NASA TM-82792, 1982.

11 Peyret, R., and Taylor, T. D., *Computational Methods for Fluid Flow*, Springer-Verlag, New York, 1983.

The Importance of Circumferential Non-uniformities in a Passage-Averaged Quasi-Three-Dimensional Turbomachinery Design System

I. K. Jennions
Engineer,
Aero Design Methods,
General Electric Company,
Cincinnati, OH 45215

P. Stow
Chief Aerodynamic Scientist,
Theoretical Science Group,
Rolls-Royce Limited,
Derby DE2 8BJ, England

The purpose of this paper is to show, for both rotating and non-rotating blade rows, the importance of including circumferential non-uniform flow effects in a quasi-three-dimensional blade design system. The paper follows from previous publications on the system in which the mathematical analysis and computerized system are detailed. Results are presented for a different stack of the nozzle guide vane presented previously and for a turbine rotor. In the former case it is again found that the blade force represents a major contribution to the radial pressure gradient, while for the rotor the radial pressure gradient is dominated by centrifugal effects. In both examples the effects of circumferential non-uniformities are detailed and discussed.

Introduction

In [1, 2] a quasi-three-dimensional turbomachinery blade design system was presented. This was composed of linked through-flow, blade-to-blade, and blade section stacking programs. Communication was through a database, allowing a number of blade-to-blade programs to be incorporated and making the system very versatile. A consistent passage-averaging technique, discussed in [1], was used in which the only assumption adopted was that the blade-to-blade streamsurfaces for blade design were surfaces of revolution. The through-flow radial equilibrium equation derived using the technique contains the effects of the blade turning, the blade stack (axial and radial leans), loss, and circumferential nonuniformities. These latter terms are integrals of differences from passage mean quantities. Their calculation from a blade-to-blade analysis is straightforward and their inclusion in the system adds little in terms of complexity.

In [2] results from the system were given for a particular stack of a turbine HP nozzle guide vane. Comparison with experimental results showed good agreement and indicated a significant improvement over a nonlinked duct flow approach. It was shown how the individual terms composing the radial pressure gradient in the radial equilibrium equation could be considered and their influence and importance studied. In the example shown particular attention was given to the importance of the blade force. It was seen that such a system gave valuable information at an early stage in the design prior to a full three-dimensional flow analysis.

In this paper further results from the systems are presented and additional aspects discussed. In one example a restack of the nozzle guide vane presented in [2] is shown illustrating the effects of changing the blade force on the resulting flow. Again good agreement between the results from the linked system and experiment are found indicating that the effects of the blade force can be modeled accurately. The individual components of the radial pressure gradient are presented in the same way as in [2] but the contributions of the perturbation terms are included here in order that their importance may be realized.

A further example shown is that of a turbine rotor, where the breakdown of the terms illustrates the effects of rotation and perturbation terms on the radial pressure gradient.

In both examples the contribution from the perturbation terms is found to be significant and, as their inclusion in a quasi-three-dimensional system does not add significantly to the computing time, their inclusion is viewed as mandatory.

The first two sections of the paper describe the passage-averaged through-flow equations and solution procedure. Convergence of the solution and consistency between the through-flow and blade-to-blade programs are then discussed followed by results of applying the system to both a stationary and rotating blade.

Through-Flow Equations

The radial equilibrium equation (REE) used in the streamline curvature through-flow method is

$$\underbrace{\frac{I}{\bar{\rho}}\frac{\partial \bar{p}}{\partial R}}_{\text{Radial pressure gradient}} = \underbrace{-\widetilde{W}_x^2 \cos^2\lambda \left.\frac{\partial \tan\lambda}{\partial x}\right|_{\psi}}_{\text{Streamline curvature in } (R, x)}$$

Contributed by the Gas Turbine Division and presented at the 1985 Beijing International Gas Turbine Symposium and Exposition, Beijing, People's Republic of China, September 1–7, 1985. Manuscript received at ASME Headquarters May 31, 1985. Paper No. 85-IGT-63.

$$+\underbrace{\frac{(\tilde{W}_x \tan\beta+\Omega R)^2}{R}\cos^2\lambda}_{\text{Centrifugal effect}}+\underbrace{\frac{\sin\lambda\cos\lambda}{\bar{\rho}}\frac{\partial\bar{p}}{\partial x}}_{\text{Axial pressure gradient}}\Bigg|_\psi$$

$$+\underbrace{F_{B\theta}(\tan\lambda\tan\sigma-\tan\delta)\cos^2\lambda}_{\text{Blade force effect}}+\underbrace{P\cos^2\lambda}_{\text{REE perturbation terms}} \quad (1)$$

in which:

$$P=\underbrace{-\widetilde{W_x''^2}\frac{\partial\tan\lambda}{\partial x}\Big|_\psi}_{\text{Curvature perturbation}}+\underbrace{\frac{\widetilde{W_\theta''^2}}{R}}_{\text{Centrifugal perturbation}}$$

$$+\underbrace{\frac{(p_s'+p_p')}{2\bar{\rho}B}\left(\sec^2\lambda\frac{\partial B}{\partial R}-\tan\lambda\frac{\partial B}{\partial x}\Big|_\psi\right)}_{\text{Blade force perturbation}} \quad (2)$$

see [1] for more details. For simplicity this is given for a radial calculating station inside a blade row whereas in practice a curved station may well be used. The terms composing the radial pressure gradient are labeled appropriately. The tilde represents density-weighted passage mean quantities and the double-primed quantities are "perturbations" from these means although they are not assumed small. It is these terms that are the main concern of this paper. The blade force $F_{B\theta}$ is determined from the circumferential momentum equation.

$$\underbrace{F_{B\theta}}_{\text{Blade force}}=\underbrace{\frac{\widetilde{W}_x}{R}\frac{\partial}{\partial x}[(\tilde{W}_x\tan\beta+\Omega R)R]}_{\text{Mean change in angular momentum}}-\underbrace{\tilde{F}_{\tau\theta}}_{\text{Loss}}+\underbrace{P_\theta}_{\text{Angular momentum perturbation}} \quad (3)$$

where

$$P_\theta=\frac{1}{BR\bar{\rho}}\frac{\partial}{\partial x}(BR\,\overline{\rho W_\theta'' W_x''})\Big|_\psi+\widetilde{W_\theta''W_x''}\frac{\partial\tan\lambda}{\partial R}+\frac{\widetilde{W_\theta''W_x''}}{R}\tan\lambda \quad (4)$$

and where $\tilde{F}_{\tau\theta}$ represents a loss term, although in the results presented later only inviscid flow is considered.

In the REE the perturbation term is composed of three parts: a curvature perturbation, a centrifugal perturbation, and a blade force perturbation. The first two arise naturally in the analysis from the use of density-weighted means. The latter arises from the choice of how to decompose the blade force. In the approach adopted the blade mean cambersurface is taken as the datum in defining the blade stacking angles and the perturbation term follows naturally from this. It should be emphasized that no approximation is adopted in this approach.

The energy equation is used in the form

$$I_{\text{inlet}}=C_p\tilde{t}+\underbrace{\tfrac{1}{2}\widetilde{W}_x^2(1+\tan^2\lambda+\tan^2\beta)}_{\text{Mean flow kinetic energy }(\frac{1}{2}\tilde{q}^2)}-\frac{\Omega^2R^2}{2}+\underbrace{\tfrac{1}{2}\widetilde{W_x''^2}(1+\tan^2\lambda)+\tfrac{1}{2}\widetilde{W_\theta''^2}}_{\text{Kinetic energy of the non-uniform flow }(\frac{1}{2}\widetilde{q''^2})} \quad (5)$$

In addition the continuity equation is used in the form

$$\dot{m}=2\pi\int_{R_H}^{R_T}BR\bar{\rho}\tilde{W}_x dR \quad (6)$$

where, because of the use of density-weighted quantities, no perturbation terms occur.

The perturbation terms that occur in the above equations are easily determined from a blade-to-blade analysis as described in [1], and in the linked system can be included with little overhead. In determining the terms only velocity perturbations in the blade-to-blade streamsurfaces are considered in line with the quasi-three-dimensional approach adopted.

Solution Procedure

The solution procedure is described in detail in [2] but is given here for completeness. If we take the case of analysis of a single blade row then the blade and annulus geometry are known as well as the inlet flow conditions. The through-flow program is run to produce the streamline geometry through the blade row as well as the inlet conditions on the streamsurfaces. Streamline blade sections can be interpolated from the stacked blade geometry onto the through-flow streamlines. These can then be analyzed in an appropriate blade-to-blade program using the through-flow inlet conditions and the Kutta closure condition at the blade trailing edge. It should be noted that the resulting exit whirl angle and Mach number will not in general agree with those from the through-flow program until the system has reached convergence. From the blade-to-blade program the mean whirl angle, blockage, loss, and perturbation terms are calculated for each analyzed section and passed back to the through-flow program for the next cycle of the iteration. This process is continued until convergence is achieved (see below).

Communication between the programs through a database means that often after a first cycle through the system the

Nomenclature

B = blade blockage term
C_P = specific heat at constant pressure
F_B = blade force
F_τ = dissipative body force
I = rothalpy
$\dot{m}$ = mass flow rate
p = static pressure
P = perturbation term
R = radius from machine axis
t = static temperature
$\mathbf{W}$ = relative flow vector
x = distance along machine axis
β = relative whirl angle
δ = radial blade lean
λ = hade angle (Rolls-Royce terminology)
ρ = density
σ = axial blade lean
Ω = angular velocity of the blade row

Superscripts

$\bar{}$ = passage average
$\tilde{}$ = density-weighted average
$'$ = perturbation about a passage average
$''$ = perturbation about a density-weighted average

Subscripts

H = hub
p = pressure surface
s = suction surface
T = tip
x = axial component
θ = circumferential component
ψ = along a streamline

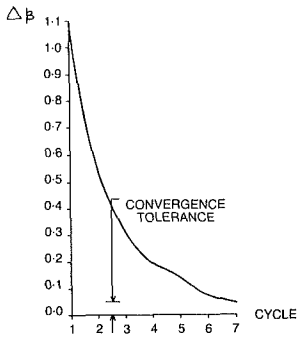

Fig. 1 Change in rotor exit angle with cycles

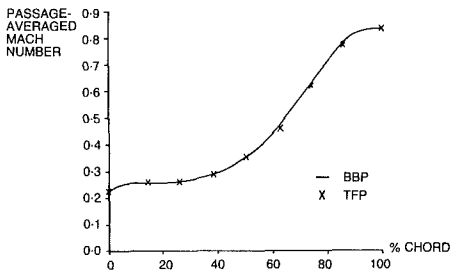

Fig. 2 Rotor midheight section Mach numbers

procedure can be continued using a "monitor" program, avoiding the need for further manual intervention. Such a monitor program also enables convergence between the through-flow and blade-to-blade programs to be easily examined. These topics are discussed more fully in the next section.

Convergence and Consistency

With all iterative schemes one has the problem of how to define, and then check, convergence of the scheme. Running the quasi-three-dimensional system in the analysis mode, outlined in the previous section, it has been found convenient to define convergence in terms of the change in exit angle imposed by the blade-to-blade calculation. Specifically, the quantity $\Delta\beta$ is formed which is the difference between the maximum and minimum changes in relative outlet angle between consecutive cycles. This quantity is shown for the rotor case presented in the next section in Fig. 1. An arbitrary convergence limit of $\Delta\beta < 0.05$ deg has been imposed on this solution, which has converged to this limit in seven cycles. It should be noted that this limit is set very low, and in normal use would be linked to the design tolerance of the component being examined.

Once convergence has been obtained and there is no change (or very little) from one cycle to the next, the solution can then be examined for consistency. There are at least two sources of possible inconsistency with a scheme such as this, if we discount computer roundoff favoring one particular program. They are: (*i*) the mathematical expression of the governing equations in the blade-to-blade and through-flow programs not being compatible; and (*ii*) the evaluation and repeated interpolation of the interaction terms.

Apart from careful formulation of the governing equations, little can be done on the first point. It has not been found to be a problem but as more blade-to-blade programs are used with the system one has to be aware of the potential problem. The second source of inconsistency can never really be eliminated, but it can relatively easily be kept below the

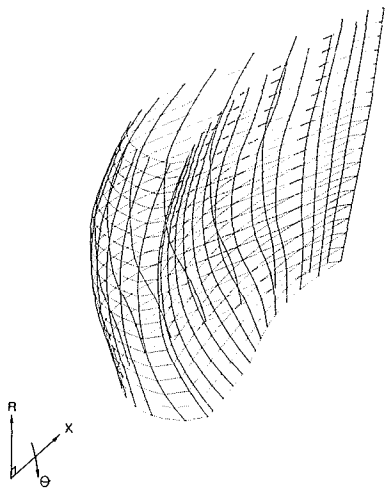

Fig. 3 Stack 2 vane

level needed for design purposes. Figure 2 shows a comparison of the rotor midheight Mach numbers from the through-flow (TFP) and blade-to-blade program (BBP) showing that a good level of consistency has been achieved. The maximum value of $|(M_{BBP} - M_{TFP})/M_{BBP}|$, a quantity used by Wang et al. [3], is 0.016, or a difference of 1.6 percent locally between solutions. When one considers that values have to be interpolated off the blade-to-blade grid onto pitchwise lines, then averaged to give the perturbation terms, which are passed to the through-flow and interpolated onto the internal stations for use, this value appears acceptable.

Results and Discussion

Example 1 Restacked Vane. In [2] the flow through a high-pressure nozzle guide vane was examined using the present quasi-three-dimensional system. The results were compared against test data and showed good agreement. In the same paper the component terms of the REE were presented and it was argued that the blade stack, via the blade force term, played an important role in forming the radial pressure gradient. The sections forming this vane (stack 1) have also been stacked on the trailing edge with 12 deg of radial lean to produce the vane shown in Fig. 3, which we will call the stack 2 vane. This stack 2 vane has been rig tested in the same annulus configuration as stack 1 and therefore allows a direct comparison.

Axial and radial blade lean angles for the stack 2 vane are shown in Fig. 4. The radial blade leans show the 12 deg lean at the trailing edge, along with the general concave shape of the vane toward the leading edge, which can clearly be seen from Fig. 3. The system was run to convergence using five equally spaced internal stations, analyzing the flow on 11 blade-to-blade surfaces, all other conditions being as described in [2]. The convergence and consistency obtained are shown in Fig. 5. The computed results against the test data at 20 percent (hub), 50 percent (midspan), and 80 percent (tip) heights are shown in Fig. 6 and are seen to be in good agreement.

We have again broken down the component terms of the REE for this vane, presenting the results on the internal stations at 1/6, 1/2, and 5/6 axial chord in Fig. 7. The meaningful names shown under the REE (equation (1)) have been used to isolate the physical effects. Upon examination of Fig. 7 it can be seen that the blade force is responsible for the final form of the radial pressure gradient. Briefly, the streamline curvature and axial pressure gradient balance each other while the centrifuging term grows toward the rear of the

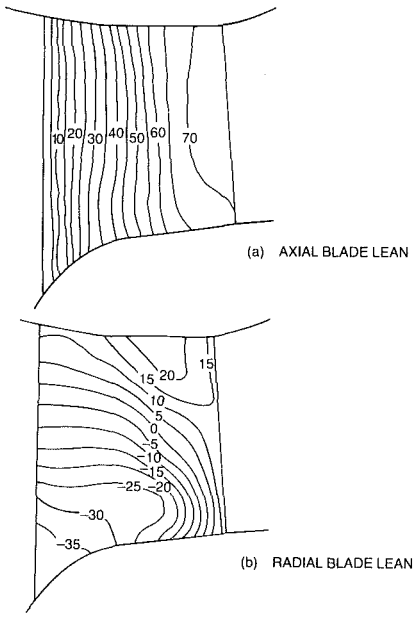

Fig. 4 Stack 2 lean angles

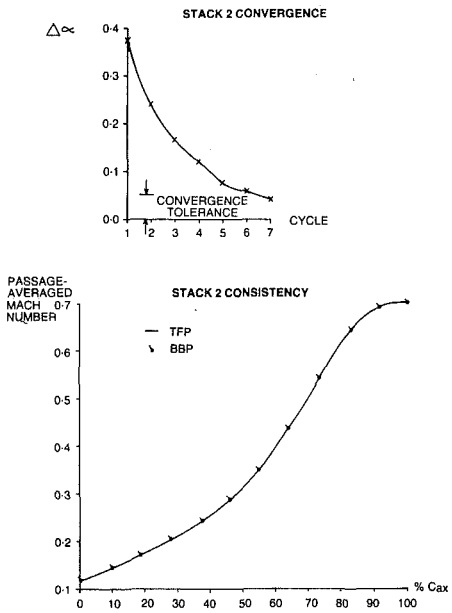

Fig. 5 Stack 2 convergence and consistency

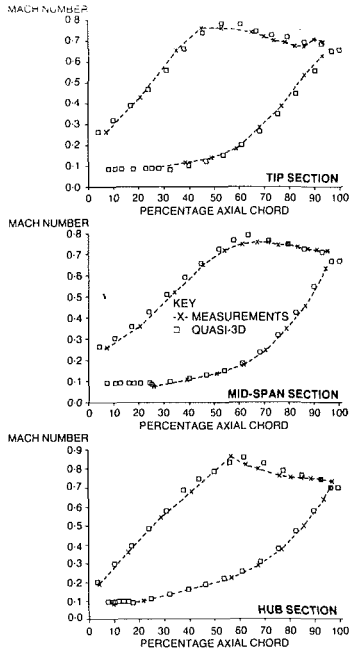

Fig. 6 Surface Mach number comparison for the stack 2 vane

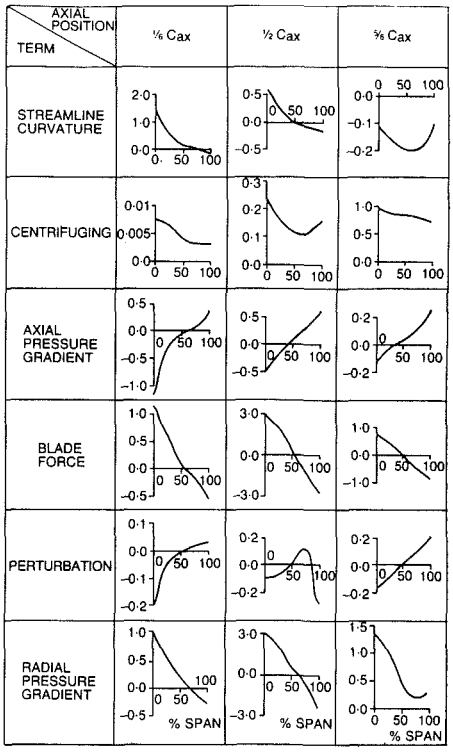

Fig. 7 Balance of REE terms for stack 2

vane only significantly contributing on the 5/6 C_{ax} station. This leaves the blade force term under the action of a much smaller perturbation term to set the radial pressure gradient. It should be noted that the REE perturbation term is as important as some of the other effects included. The situation is similar, but clearer, than that found for stack 1 of this vane.

There are five groups of perturbation terms that are important to the through-flow solution. In order to explore their importance they are given in Fig. 8 as they appear in equations (2) to (5) with their associated names. It is worth noting that while the term "perturbation" has been used in describing these terms there is no assumption that any of them are small; the word has only been used to describe the difference between the actual and the averaged flow. The angular momentum perturbation is of the order of 10–20 percent of the circumferential blade force and is therefore a significant term in determining the radial pressure gradient. While velocity perturbations will, in general, increase toward the midchord position in a blade row and then decrease as the flow becomes more uniform toward exit this term is larger at 5/6 C_{ax} than it is at 1/2 C_{ax}. This is directly attributable to the dominance of the gradient term (first term on RHS of equation (4)) in forming P_θ.

The three REE perturbation terms are shown in the next three rows of Fig. 8, and if summed produce the REE perturbation row of Fig. 7. The centrifuging perturbation follows what has just been stated regarding velocity perturbations,

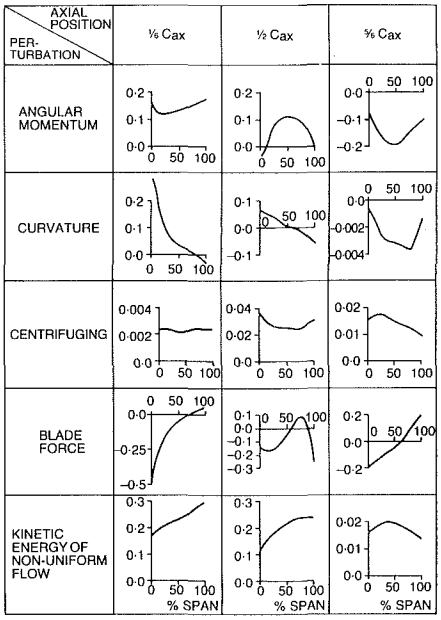

Fig. 8 Perturbation terms for stack 2 vane

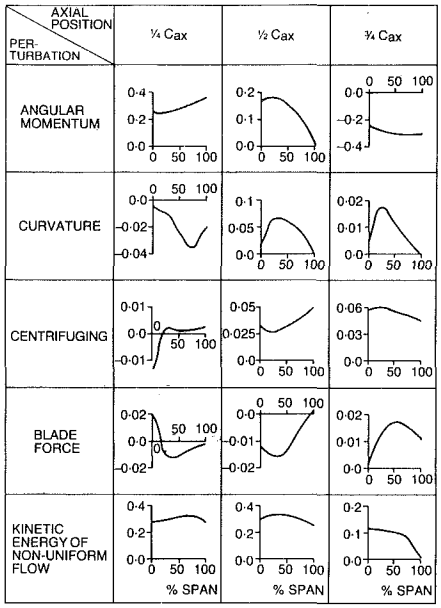

Fig. 10 Perturbation terms for rotor

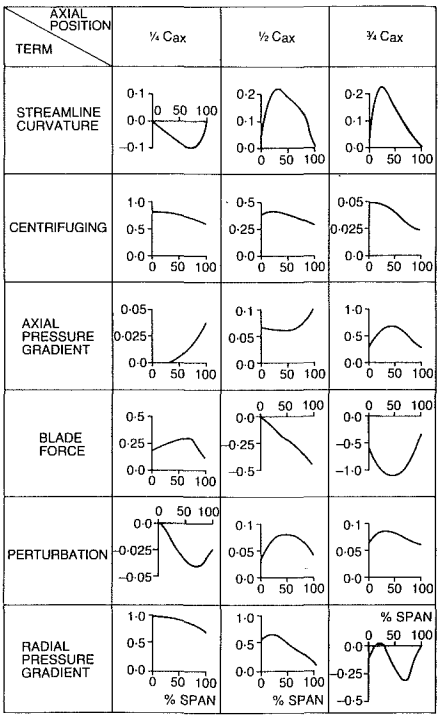

Fig. 9 Balance of REE terms for rotor

making its maximum effect at midchord. Its overall effect though is weak with the blade force perturbation being the dominant term except near the highly contracting entrance to the vane where the curvature perturbation contributes. This latter term suffers from the combined effect of a falling perturbation velocity and reducing streamline curvature as percentage chord increases.

Finally, the last row in Fig. 8 shows the perturbation kinetic energy which contributes to the energy equation. This term is as high as 30 percent of the mean flow kinetic energy and is therefore a significant term in equation (5). In formulating their energy equation Sehra and Kerrebrock [4] postulated that this perturbation kinetic energy was unavailable to the mean flow and was lost, rather like the velocity fluctuations in a turbulent flow. Moore and Adhye [5] have shown that in the mixing process downstream of a cascade the flow develops as if the primary flow was reversible and only the secondary flow kinetic energy decays irreversibly. The truth therefore seems to be that some of the perturbation kinetic energy could be unavailable to the mean flow but more experimental information would be needed to understand the mechanism. Meanwhile we have to keep our energy equation as given by equation (5) in order to be consistent with our blade-to-blade programs which assume that if the rothalpy is constant at inlet then it is constant throughout the blade-to-blade streamsurface.

In broad terms, all the above discussion applies equally to the stack 1 vane and the vane presented here.

Example 2 Turbine Rotor. This example has been selected to show the balance of the REE terms for a rotating component, and hence bring out the differences between this and the previous example. Figure 9 shows the breakdown of the REE, all plots being nondimensionalized against the maximum radial pressure gradient at 1/4 C_{ax}. The centrifuging term starts off large and reduces considerably through the rotor, in agreement with the low absolute whirl angle at the trailing edge. The axial pressure gradient however starts off small and rises through the rotor in line with falling static pressure and small negative hade[1] angles, the blade force exhibiting a similar trend.

At 1/4 C_{ax} the centrifugal term dominates, with the blade force contributing to a small extent. By midchord the streamline curvature is large enough to be felt, while at exit all terms except for the now low centrifugal term produce an erratic radial pressure gradient.

The relative sizes of the perturbation terms are shown in Fig. 10. For this case the angular momentum perturbation reaches a maximum of 36 percent of the circumferential blade force, and is consistently large throughout the rotor. The three terms forming the perturbation term for the REE appear to be more equal than on example 1, the centrifugal perturbation making such a contribution that it dominates at 3/4 C_{ax}. Finally the perturbation kinetic energy is seen to be around 30 percent of the mean flow kinetic energy reducing to 10 percent on the last station presented.

[1] Rolls-Royce terminology: the angle between the streamline and the axial direction in the meridional plane.

Comparing results from the rotor with those from the vane, it appears that the blade force is not as dominant an effect on the rotor as on the vane because of the stack being much less severe. Further, the overall level of pressure gradients encountered in the rotor appears to be lower, and the centrifuging term more dominant. As for the perturbation terms, the overall levels are very similar with the exception of a stronger contribution from the centrifugal perturbation on the rotor. The levels of perturbation kinetic energy are seen to be quite high and have to be accounted for in terms of consistency between the BBP and the TFP.

Conclusions

Further results have been shown from a quasi-three-dimensional system linking through-flow, blade-to-blade and section stacking programs. The case of a radically different stack of a previously published HP nozzle guide vane is presented and, like its predecessor, shows good agreement with experimental data. The blade force is very different for the two blade stacks and its importance in determining the radial pressure gradient is clearly seen with the system adopted.

A further example of a turbine rotor illustrates the relative magnitude of the physical effects in determining the radial pressure gradient and the dominance of the centrifugal term in certain parts of the flow.

In both examples perturbation terms arising in the analysis, from the use of density-weighted passage means and the blade force datum, are seen to be important in ensuring consistency between the through-flow and blade-to-blade programs and in determining the overall radial pressure gradient. In the linked system described these terms are easily included with little computational overhead.

Acknowledgments

The authors wish to thank Rolls-Royce Limited for permission to publish this paper.

References

1 Jennions, I. K., and Stow, P., "A Quasi-Three-Dimensional Turbomachinery Blade Design System: Part I—Through-Flow Analysis," ASME JOURNAL OF ENGINEERING FOR GAS TURBINES AND POWER, Vol. 107, No. 2, Apr. 1985, pp. 301–307.

2 Jennions, I. K., and Stow, P., "A Quasi-Three-Dimensional Turbomachinery Blade Design System: Part II—Computerized System," ASME JOURNAL OF ENGINEERING FOR GAS TURBINES AND POWER, Vol. 107, No. 2, Apr. 1985, pp. 308–316.

3 Wang, Q., Zhu, G., and Wu, C. H., "Quasi-Three-Dimensional and Full Three-Dimensional Rotational Flow Calculations in Turbomachines," ASME JOURNAL OF ENGINEERING FOR GAS TURBINES AND POWER, Vol. 107, No. 2, Apr. 1985, pp. 277–285.

4 Sehra, A. K., and Kerrebrock, J. L., "The Effect of Blade-to-Blade Flow Variations on the Mean Flow-Field of a Transonic Compressor," AIAA Paper No. 79-1515, July 1979.

5 Moore, J., and Adhye, R. Y., "Secondary Flows and Losses Downstream of a Turbine Cascade," ASME JOURNAL OF ENGINEERING FOR GAS TURBINES AND POWER, Vol. 107, No. 4, Oct. 1985, pp. 961–968.

Through-Flow Modeling of Axial Turbomachinery

R. P. Dring

H. D. Joslyn

United Technologies Research Center,
East Hartford, CT 06108

Through-flow analysis, which is at the heart of the aerodynamic design of turbomachinery, requires as aerodynamic input a row-by-row description of the airfoil loss, deviation, and blockage. Loss and deviation have been investigated extensively in both cascades and rotating rigs as well as in numerous two- and three-dimensional analytical studies. Blockage, however, has received far less attention. As defined herein, blockage is a measure of the departure of the flow field from the condition of axisymmetry which is assumed in the through-flow analysis. The full-span blockage distributions calculated from measured single-stage rotor wake data were used to provide the input to the through-flow analysis, along with the measured full-span distributions of loss and deviation. Measured and computed results are compared for the single-stage rotor operating with both thick and thin inlet hub and tip boundary layers. It is demonstrated that both the level and the spanwise and streamwise distributions of blockage have a strong impact on the computed rotor exit flow field.

Introduction

The aerodynamic mechanisms playing important roles in turbomachinery include: compressibility, unsteadiness, three dimensionality, and viscous effects such as boundary layer transition and separation. Although highly sophisticated full Navier–Stokes solution algorithms are beginning to appear which have the potential to attack these flows in full generality, the basis of many contemporary compressor aerodynamic design systems is a series of calculations which treat the flow as a sequence of two-dimensional calculations. Because of their speed and efficiency these two-dimensional calculations will continue to play a significant role in multistage compressor and turbine aerodynamic design. For this reason there is great incentive to conduct an assessment of these analyses in order to guide the analyst as to the interpretation of the results of these calculations and as to how these calculations can be employed most reliably in the design of new configurations and in the analysis of rotating rig data.

Following the approach of Wu [1] the aerodynamic analysis of turbomachinery is composed of a two-dimensional calculation on the axial–radial plane, the through-flow analysis, and a second two-dimensional analysis on the axial (or meridional)–tangential plane, the blade-to-blade or cascade potential flow analysis. The through-flow analysis is an axisymmetric calculation of the inviscid compressible flow in the annulus. The calculation determines the spanwise distributions of the velocity triangles at each of the streamwise calculation planes along the annulus. The effects of viscosity and three dimensionality are included through various correlations for the spanwise distributions of airfoil total pressure loss, exit flow angle (or deviation), and blockage. Loss and deviation are usually based on an extensive background of cascade and/or rotating rig data. Blockage, however, is treated differently. Blockage is the parameter that bridges the gap between the assumption of axisymmetry in the analysis and the fact that the flow in an actual compressor is nonaxisymmetric [2].

The objective of the present paper is to provide an assessment of through-flow analysis by comparing the results of such an analysis with the flow measured on a single-stage compressor rotor tested at its nominal design flow coefficient ($\Phi = 0.85$) with both thick and thin inlet endwall boundary layers [2–9]. This benchmark data base consists of detailed measurements in both the rotating and stationary frames of reference. Sufficient data are available to provide all of the required aerodynamic input for the calculation. In addition, sufficient data are also available to provide an in-depth and detailed assessment of the computed results.

The through-flow analysis of Habashi and Youngson [10, 11] has been selected for the assessment. This is a practical finite element procedure which is well documented in the literature. It is a fast calculation with great geometric flexibility. It has been demonstrated [10] to be in excellent agreement with the more historical streamline curvature method. For this reason the present comparison should be considered an assessment of through-flow analysis in general and not an assessment of this solution algorithm in particular.

It will be shown that when blockage is accounted for through-flow theory describes many aspects of the flow with reasonable accuracy. However, there are features which are not well predicted and this indicates the need for a more precise formulation of the equation and possibly the inclusion of effects which are frequently neglected, for example, radial components of the blade force and/or the fluctuation terms due to nonaxisymmetry in the flow.

Contributed by the Gas Turbine Division and presented at the 1985 Beijing International Gas Turbine Symposium and Exhibition, Beijing, People's Republic of China, September 1–7, 1985. Manuscript received at ASME Headquarters May 13, 1985. Paper No. 85-IGT-42.

Discussion

Background. The "through-flow" analysis in compressor design is a two-dimensional axisymmetric calculation describing the spanwise variation of the flow at various streamwise locations both within and between the airfoil rows from the inlet of the compressor to its discharge. The actual flow is only axisymmetric in a circumferentially averaged sense and to ensure thermodynamic consistency this average is usually considered to be a mass average (as opposed to an area average). Formal derivations of the radial equilibrium equation in terms of circumferentially area- and density-averaged quantities are presented in [12–17]. These derivations result in terms containing circumferentially averaged quantities, e.g., $\bar{C}$, $\bar{T}$, $\bar{I}$, $\bar{s}$, as well as terms involving averages of products of circumferentially varying (or fluctuating) quantities, e.g., $\overline{C_r'^2}$, $\overline{C_r'C_x'}$, $\overline{C_\theta'^2}$. It has been demonstrated [13–16] that although these fluctuation terms are generally small they can be significant in the endwall regions. The explanation for this can be seen in the traverse data shown in Fig. 1. These data illustrate the circumferential variations of the total and static pressures in the flow in the rotating frame of reference downstream of the single-stage compressor rotor. These profiles have been extracted from the full-span contour plots of the data as presented in [5–7]. For reference, the inlet relative total pressure at each span location has also been indicated. At midspan (50 percent span) the airfoil wakes are narrow and relatively shallow and the relative total pressure between the airfoil wakes is very close to the inlet value at this radius. The fact that the relative total pressure between wakes is slightly greater than the inlet value may be due to a small radial shift in the stream surface or due to experimental error. Near the hub (12.5 percent span) and near the tip (87.5 percent span) the flow is far more complicated. Near the hub the corner stall on the rotor suction surface has greatly increased the width and depth of the wakes relative to the midspan profiles. Near the tip there is a large region of low total pressure between the airfoil wakes due to tip leakage. The fact that the exit total pressure is locally above the inlet values at these near-hub and near-tip spanwise locations is due to the strong radial gradient in inlet relative total pressure and the radial transport that occurs in the flow between the rotor inlet and the measurement plane 30 percent chord downstream of the rotor trailing edge. Although the overall nature of the flow may be more clearly seen in the full-span contour plots in [5–7], these data were included here to indicate the nature of the departures from axisymmetry that are present in a typical compressor flow field.

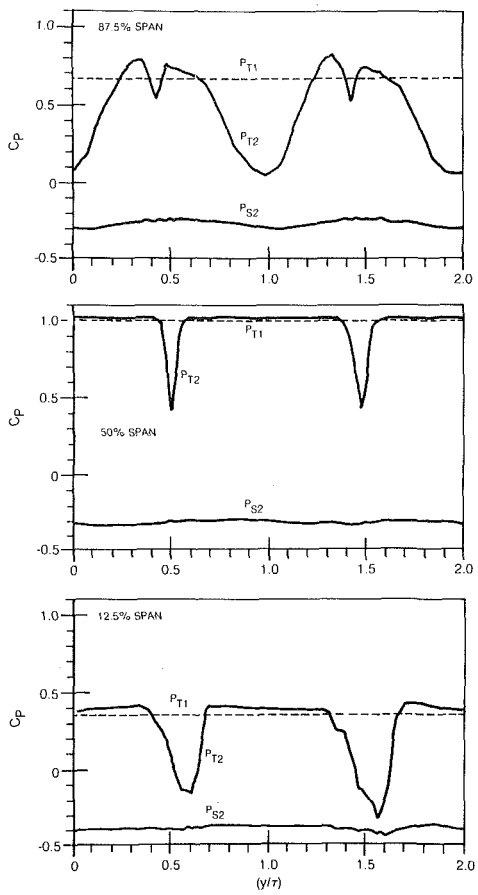

Fig. 1 Single-stage rotor wake profiles, thick inlet boundary layers, Φ = 0.85, 30 percent aft

Analytical Background. If the continuity and radial momentum equations are circumferentially density averaged, as in [16], the basic equation of through-flow analysis results

$$\tilde{C}_x\left[\frac{\partial \tilde{C}_r}{\partial x}-\frac{\partial \tilde{C}_x}{\partial r}\right]-\frac{\tilde{W}_\theta}{r}\frac{\partial (r\tilde{C}_\theta)}{\partial r} = \tilde{T}\frac{\partial \tilde{s}}{\partial r}-\frac{\partial \tilde{I}}{\partial r}+F_{b,r}/\tilde{\rho}+F_{f,r}/\tilde{\rho}-\sum_{i=1}^{5}N_i^{(r)}/\tilde{\rho} \quad (1)$$

The interaction terms are as follows [16]

$$N_1^{(r)}=\frac{1}{\bar{K}r}\frac{\partial}{\partial r}(\bar{K}r\,\overline{\rho W_r' W_r'}) \quad (2)$$

Nomenclature

B_x = airfoil axial chord
C = absolute flow speed
C_P = pressure coefficient = $(P-P_{TOA})/Q_{U_m}$
C_x = axial component of velocity
F_b = blade force
F_f = friction force
I = rothalpy
$\bar{K}$ = blockage factor
$\dot{m}$ = mass flow
$N_i^{(r)}$ = interaction terms
P = pressure
Q = local dynamic pressure
Q_{U_m} = dynamic pressure based on midspan wheel speed = $1/2\,\rho U_m^2$
r = radial distance
s = entropy
T = temperature
U_m = wheel speed at midspan
W = relative flow speed
x = axial distance
y = tangential distance
θ = circumferential coordinate
Θ = flow yaw angle (from axial)
Φ = flow coefficient = C_x/U_m
ϕ = flow pitch angle (from axial)
ψ = stream function
δ^* = displacement thickness
ρ = fluid density
τ = cascade pitch

Subscripts

m = midspan
p = pressure surface
s = suction surface
S = static
T = total
x = axial
r = radial
θ = tangential

Superscripts

$\tilde{}$ = pitchwise density average
$-a$, (A) = pitchwise area average
$-m$, (M) = pitchwise mass average
$'$ = deviation from density-averaged value

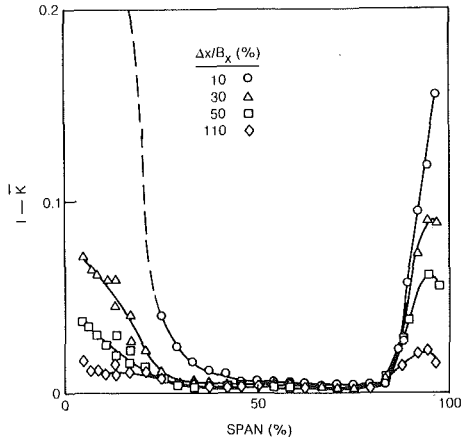

Fig. 2 Spanwise distribution of blockage, single-stage rotor, thin inlet boundary layers, $\Phi = 0.85$

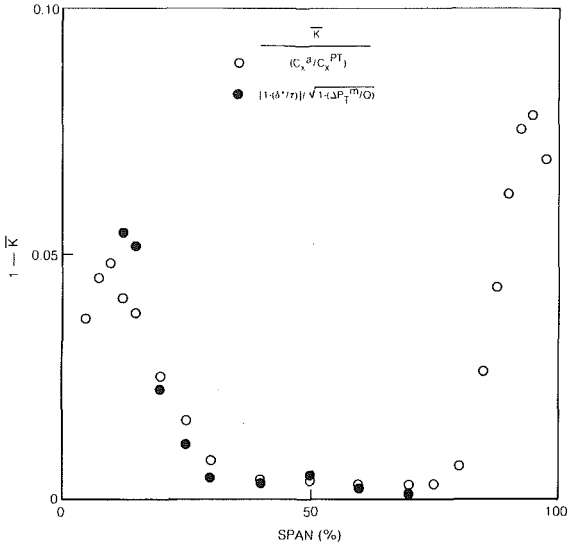

Fig. 3 Spanwise distribution of blockage, single-stage rotor, thick inlet boundary layers, $\Phi = 0.85$, 30 percent aft

$$N_2^{(r)} = \frac{1}{\bar{K}r}\frac{\partial}{\partial x}\left(\bar{K}r\,\overline{\rho W_r' W_z'}\right) \tag{3}$$

$$N_3^{(r)} = \frac{1}{r}\left(\overline{\rho W_\theta' W_\theta'}\right) \tag{4}$$

$$N_4^{(r)} = \frac{1}{2\bar{K}}\frac{\partial \bar{K}}{\partial r}\left\{\left(h_s' - \tilde{T}s_s'\right)\rho_s + \left(h_p' - \tilde{T}s_p'\right)\rho_p\right\} \tag{5}$$

$$N_5^{(r)} = \overline{\left(\tilde{T}s' - h'\right)\frac{\partial(\bar{\rho}+\rho')}{\partial r}} - \overline{\rho T'\left(\frac{\partial s}{\partial r}\right)'} \tag{6}$$

By defining:

$$\tilde{C}_x = \frac{\dot{m}}{2\pi\bar{\rho}r\bar{K}}\frac{\partial\psi}{\partial r} \tag{7}$$

$$\tilde{C}_r = \frac{-\dot{m}}{2\pi\bar{\rho}r\bar{K}}\frac{\partial\psi}{\partial x} \tag{8}$$

equation (1) can be written as

$$\frac{\partial}{\partial r}\left(\frac{1}{\bar{\rho}r\bar{K}}\frac{\partial\psi}{\partial r}\right) + \frac{\partial}{\partial x}\left(\frac{1}{\bar{\rho}r\bar{K}}\frac{\partial\psi}{\partial x}\right) = \frac{-1}{\tilde{C}_x}\left[\frac{\tilde{W}_\theta}{r}\frac{\partial(r\tilde{C}_\theta)}{\partial r} + \tilde{T}\frac{\partial\tilde{s}}{\partial r} - \frac{\partial\tilde{I}}{\partial r} + F_{b,r}/\bar{\rho} + F_{f,r}/\bar{\rho} - \sum_{i=1}^{5} N_i(r)/\bar{\rho}\right]\frac{2\pi}{\dot{m}} \tag{9}$$

The boundary conditions are:

$$\begin{aligned} &\text{on the hub,} && \psi = 0\\ &\text{on the shroud,} && \psi = 1\\ &\text{at the inlet,} && \frac{\partial\psi}{\partial n} = 0\\ &\text{at the exit,} && \frac{\partial\psi}{\partial n} = 0, \text{ where } n \text{ is the outward normal} \end{aligned} \tag{10}$$

At present, however, few (if any) practical design calculations include all of the terms in equation (9). Specifically, the radial components of the blade and friction forces ($F_{b,r}$ and $F_{f,r}$) are frequently neglected. In the present assessment these terms will be neglected but the magnitude of the radial blade force will be discussed based on the measured rotor airfoil fullspan pressure distribution. The five fluctuation terms $N_i^{(r)}$ are also usually neglected. These terms arise from the nonaxisymmetry in the flow and, except in the endwall regions, they are relatively small. The primary reason for omitting the fluctuation terms, however, is that their magnitudes and distributions are not generally known. In the present assessment these terms will also be neglected but their magnitude will be discussed based on the fullspan wake data obtained downstream of the single-stage rotor [3].

After these approximations the only terms remaining on the right hand side of equation (9) are those related to the radial gradients of angular momentum rC_θ, entropy s, and rothalpy I. This is the form of the equation as it is used in most practical design and analysis calculations [10, 11]. Recall, however, as mentioned above for thermodynamic consistency the equation is considered to describe the spanwise distributions of circumferentially *mass*-averaged quantities whereas equation (9) was formally derived on the basis of a circumferential density average [16]. Although a formally mass-averaged formulation is, to the best of the authors' knowledge, not currently available in the literature, it is to be expected that it will be similar in many respects to equation (9) but with a different set of fluctuation terms.

Before equation (9) (without the radial force and fluctuation terms) can be utilized to provide a description of the mass-averaged flow quantities, it is necessary to provide additional information in order to obtain closure. This is achieved through the introduction of aerodynamic blockage. The tangential blockage factor $\bar{K}$ in equation (9) formally only accounts for mechanical blockage, i.e., airfoil tangential thickness. Since equation (9) is going to be used to determine the mass-averaged total and static pressures and the mass-averaged flow angles, the axial mass flux calculated based on these quantities when integrated from hub to tip will not give the correct mass flow. Mass flow must be based on an integration from hub to tip of the circumferentially area-averaged mass flux. The ratio of these two different mass fluxes is taken to be equal to the tangential aerodynamic blockage. The reasoning behind this definition of blockage is described more completely in [2]. The spanwise distributions of aerodynamic blockage in the flow downstream of the single-stage compressor rotor being used in the present assessment are given in [2, 6, 8]. For the sake of clarity Fig. 2 (from [2]) is included here. This figure illustrates how the spanwise distribution of aerodynamic blockage decays with distance downstream of the rotor. The method of calculating aerodynamic blockage from the measured data will be discussed below.

The objective of the present assessment (and also that of [18]) of through-flow theory is to determine how well the

approximate form of equation (9), when coupled with this definition of aerodynamic blockage, can represent the flow in a single-state compressor rotor where the flow is highly three dimensional and the departures from axisymmetry are significant (Fig. 1).

In addition to geometric input describing the annulus, the location of airfoil rows, and mechanical blockage, the through-flow calculation requires certain aerodynamic input. This input information includes spanwise descriptions of the total pressure loss and the exit flow angle (deviation) for each airfoil row (or their equivalents: stage pressure ratio, reaction, efficiency, and so on). Blockage, like loss and deviation, must be specified as a function of span, but unlike loss and deviation which must be specified within blade rows, blockage must be specified at all streamwise locations, both within and between blade rows.

The spanwise distribution of relative total pressure loss across the airfoil row was determined by taking the difference between the mass-averaged measured relative total pressures at the rotor inlet and exit [3–8]. This difference was taken at a fixed radius and it was used in the analysis in a consistent manner, i.e., as the difference at a fixed radius. Loss was not taken along stream lines since their location is not known a priori. Although the loss was based on measurements some distance upstream of the airfoil leading edge and some distance downstream of the trailing edge, in the present assessment the loss was assumed to increase linearly from zero at the airfoil leading edge to the measured value at its trailing edge.

The spanwise distributions of airfoil exit flow angle were taken from the mass-averaged measured relative yaw angles [3–8]. These flow angles were measured some distance downstream of the trailing edge, yet they were input to the analysis at the rotor trailing edge plane. For this reason small adjustments were made to the exit flow angle distributions in order to obtain more precise agreement between the measured and computed results at the downstream measurement plane. Turning within each airfoil row was distributed linearly from the leading edge to the trailing edge.

Blockage Modeling. The spanwise distributions of blockage were calculated directly from the measured data [2, 5–8]. As described in [2], at each streamwise station and at each radius the circumferentially area-averaged axial velocity $\bar{C}_x{}^a$ may be related to the axial velocity computed by the through-flow analysis from mass-averaged quantities $\bar{C}_x{}^{PT}$ by the blockage factor $\bar{K}$ as follows (for incompressible flow).

$$\bar{K} = (\bar{C}_x{}^a / \bar{C}_x{}^{PT}) = f(r) \tag{11}$$

where (for flow in the absolute frame)

$$\bar{C}_x{}^{PT} = \sqrt{2(\bar{P}_T{}^m - \bar{P}_S{}^m)/\rho}\ \cos\ \bar{\Theta}^m\ \cos\ \bar{\phi}^m \tag{12}$$

or, based purely on velocity

$$\bar{C}_x{}^{PT} = \sqrt{\overline{C^2}^m}\ \cos\ \bar{\Theta}^m\ \cos\ \bar{\phi}^m \tag{13}$$

Applying this definition of aerodynamic blockage (equations (11) and (12)) to the measured data taken at the four planes downstream of the rotor (for the case with the thin inlet boundary layer) resulted in the spanwise distributions of blockage shown in Fig. 2 (from [2]).

Where a well-defined core flow region exists between the wakes of adjacent airfoils, as in Fig. 1 at 50 percent span, blockage may also be determined from the following expression

$$\bar{K} = [1 - (\delta^*/\tau)]/\sqrt{1 - (\Delta\bar{P}_T{}^m/Q)} \tag{14}$$

In this expression $\Delta\bar{P}_T{}^m$ is the mass-averaged total pressure loss in the wake and Q is the dynamic pressure between wakes. It is important to realize that the total pressure loss $(\Delta\bar{P}_T{}^m/Q)$ is present in equation (14) only as a measure of the wake shape and not as a measure of airfoil performance. Blockage is a measure of the departure from axisymmetry at a particular spanwise location in a plane and is unrelated to the nature of the flow at other planes or at other spanwise locations. As an example of a blockage profile based on equation (14), Fig. 3 (for the case with thick inlet boundary layers) illustrates the spanwise distribution of $(1 - \bar{K})$ based on both the general formulation (equations (11) and (12)) and also on the approximate formulation for isolated wakes (equation (14)). The approximate expression has only been plotted over the portion of the flow around midspan where it is in close agreement with the general formulation. Because of the lack of a well-defined core flow region between the wakes in the flow near the hub and tip (Fig. 1 at 87.5 percent span) the approximate formulation (equation (14)) is highly inaccurate in these regions. The approximate formulation has been discussed here only in an attempt to relate aerodynamic blockage to more familiar wake parameters. In the through-flow assessment, however, only blockage profiles from the general formulation (equations (11) and (12)) have been employed.

In the limit of very shallow and widely spaced wakes, where the velocity defect is proportional to $X^{-1/2}$ and the wake width is proportional to $X^{1/2}$, it can be shown that the blockage decays according to $X^{-1/2}$. This type of decay is to be expected in the core flow region where the wakes of adjacent airfoils in a row do not interact (e.g., Fig. 1 at 50 percent span). Near the endwalls, however, where the wakes do interact, it might be expected that the velocity defect is proportional to X^{-1} [19, equation (24.41)]. In this case the blockage would decay according to X^{-2}. In the present study the decay of blockage with downstream distance was based on the single-stage rotor data which were acquired at four axial locations from 10 to 110 percent of axial chord aft of the rotor (Fig. 2).

A number of rather subjective judgments were required in order to fully define the aerodynamic input to the through-flow analysis. For example, both the blockage and loss input at the airfoil trailing edge plane were measured a short distance downstream of the trailing edge. The local loss does not change dramatically with axial distance and hence the impact of applying the measured value at the trailing edge plane is expected to be slight. The same can not be said for blockage. It is reasonable to expect large variations in blockage immediately downstream of the airfoil trailing edge. The data presented in Fig. 2 clearly demonstrate this. For lack of data directly on the airfoil training edge plane, the blockage distribution there was made the same as that at the nearest downstream traverse plane (10 percent aft).

Some aerodynamic blockage was added to the airfoil mechanical blockage from the 75 percent chord location to the trailing edge near the hub and the tip in order to simulate the effects within the airfoil row of hub corner stall and rotor tip leakage. This was found to be necessary in order to suppress static pressure excursions within the airfoil row. These excursions occurred due to the high mechanical blockage at the 50 percent chord location (varying from 9.2 percent at the hub to 5.7 percent at the tip) and the high aerodynamic blockage at the trailing edge plane (39 percent at the hub). This excursion could be eliminated by fairing in aerodynamic blockage near the hub and tip to produce a smoother increase from the mechanical blockage profile to the aerodynamic blockage profile at the trailing edge. As will be discussed below, this added aerodynamic blockage had a negligible effect on the flow outside of the blade row.

The single-stage rotor was initially tested with very thin inlet annulus boundary layers ($\delta \approx 5$ to 10 percent span) [2–4]. It was subsequently retested with very thick inlet hub and tip boundary layers ($\delta \approx 37$ percent span) [6–8]. For the

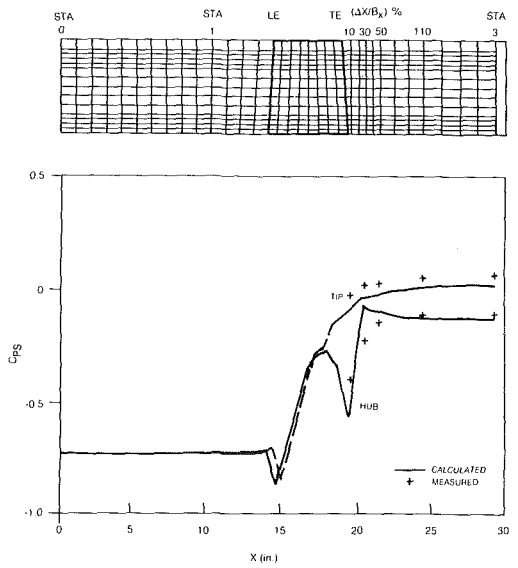

Fig. 4 Hub and tip static pressures with aerodynamic and mechanical blockage, single-stage rotor, thin inlet boundary layers, $\Phi = 0.85$

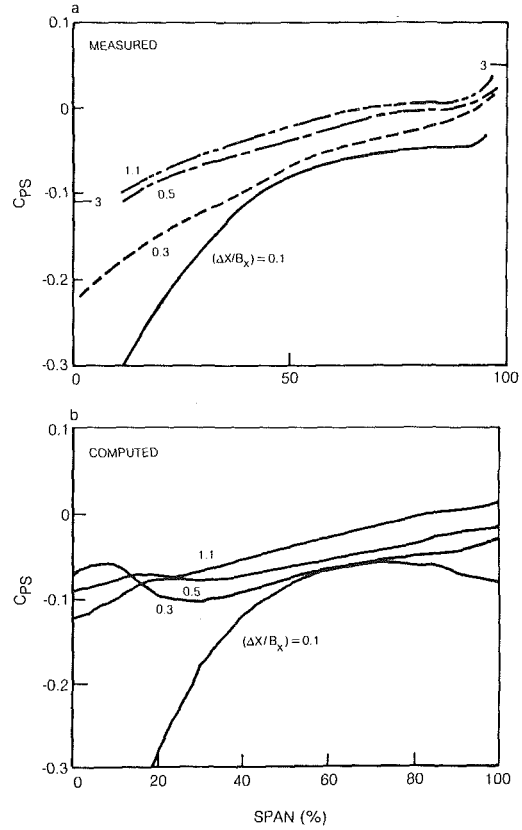

Fig. 5 Spanwise distributions of static pressure, single-stage rotor, thin inlet boundary layers, $\Phi = 0.85$

thin inlet boundary layer case traverse data were available from 10 to 110 percent of axial chord axially downstream of the rotor trailing edge. The loss, deviation, and blockage at the trailing edge plane were based on the profiles measured 10 percent aft. Since the rotor hub corner stall penetrated downstream to the traverse plane 10 percent aft, the locally very large pitch angles and back-flow made it impossible to acquire data in this region (see [4], Fig. 12). It was assumed that over the circumferential increments where data could not be acquired that the relative flow velocity was zero. Thus, these increments did not contribute to the mass-averaged quantities. This assumption was only required for the data out to 17 percent span. The dashed line in Fig. 2 indicates the region over which this assumption was made. The assumption produced spanwise distributions of the flow quantities which were very similar to those obtained at the traverse planes further downstream. The blockage profiles calculated (using equations (11) and (12)) from the measured data at the downstream planes (10, 30, 50 and 110 percent aft) as shown in Fig. 2 were used to provide the blockage profiles for all calculation planes aft of the rotor.

For the thick inlet boundary layer case traverse data were only acquired at the plane 30 percent aft of the rotor trailing edge. Since the blockage profiles for the thin and thick cases (Figs. 2 and 3, respectively) were very similar at this plane, the trailing edge blockage profile for the thick case was taken to be the same as for the thin case. The trailing edge deviation profile was adjusted until the measured and computed flow angles at the traverse plane (30 percent aft) were identical.

The thin inlet boundary layer profile ($\delta^* \approx 1$ percent of span) could not be accurately described with a reasonable number of radial elements in the through-flow analysis. For this reason it was neglected in the calculation and the upstream axial velocity was taken as constant from hub to tip. For the thick case the measured upstream profile was closely matched in the analysis.

Experimental-Analytical Comparisons. The computational grid used for both the thin and thick inlet boundary layer cases is shown at the top of Fig. 4. The increased grid density near the hub and tip was required in order to capture the abrupt variations in the input data in these regions. Note that the airfoil has been broken up into eight elements axially and that the region from the trailing edge aft to 50 percent of axial chord downstream has been broken up into five elements axially. The motivation for utilizing this fine structure grid is discussed below.

The measured and computed distributions of the flow path static pressure on the hub and tip for the thin inlet boundary layer case are shown in Fig. 4. The measured data 10, 30, 50 and 110 percent aft were extrapolated from the traverse results (Fig. 5*a*). The measured and computed results downstream of the rotor at the tip are in relatively good agreement as to level and trend. At the hub, however, the monotonic diffusion from the trailing edge aft that occurs in the measured results is not matched by the computed results. The very high aerodynamic blockage at the plane 10 percent aft (and at the trailing edge) has caused a very low static pressure. However, the computed results have a maximum in the hub static pressure at the plane 30 percent aft which is not present in the data. It should be pointed out that the blockage $(1 - \bar{K})$ profiles are decaying monotonically with downstream distance (Fig. 2).

The spanwise distributions of measured and computed static pressures at the planes 10, 30, 50 and 110 percent aft are shown in Figs. 5(*a*) and 5(*b*). The far downstream (Sta. 3) flowpath hub and tip measured static pressures are also shown in Fig. 5(*a*). The high hub static pressures predicted at the planes 30 and 50 percent aft are evident in the computed profiles (Fig. 5*b*).

It is noteworthy that the very low static pressure 10 percent aft is predicted by the analysis. This is a result of the 39 percent blockage at this location ($\bar{K} = 0.61$). As mentioned above, the rotor hub corner stall penetrated downstream to this plane and some approximation was required in order to evaluate the spanwise distribution of blockage out to 17 percent span. A comparison of Figs. 5(*a*) and 5(*b*) indicated that the blockage in the hub region 10 percent aft may be too high since the predicted static pressures were somewhat below the measured values out to 40 percent span. At the planes 30

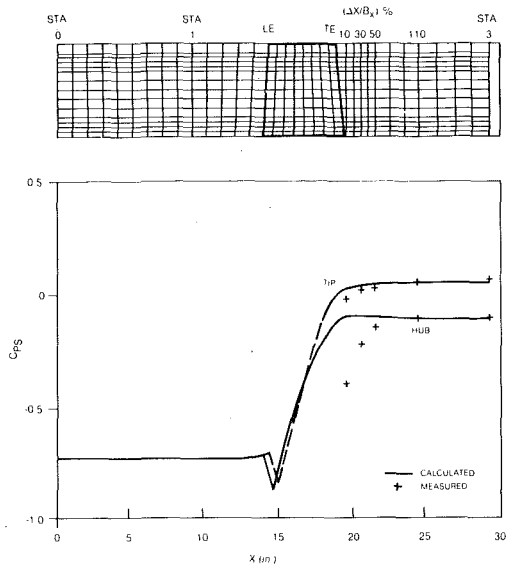

Fig. 6 Hub and tip static pressure without aerodynamic blockage, single-stage rotor, thin inlet boundary layers, $\Phi = 0.85$

and 50 percent aft the predicted static pressure is locally too high near the hub (as also seen in Fig. 4). It would have been possible to match the measured static pressure profiles by adjusting the blockage distributions locally at these planes. Such adjustment, however, can not be justified based on the blockage distributions calculated from the measured wake profiles at these locations using equations (11) and (12).

In light of the approximation involved in determining the blockage profile near the hub 10 percent aft, the impact of lowering the blockage at this plane on the high hub static pressure 30 percent aft was evaluated. Reducing the maximum hub blockage from 39 percent ($\bar{K} = 0.61$) to 20 percent ($\bar{K} = 0.80$) and smoothing this modified blockage distribution into the measured distribution at 20 percent span did have a significant impact on the computed results. In addition to eliminating the maximum in hub static pressure at the 30 percent aft location, reducing the maximum blockage drove up the pressure at the rotor trailing edge and at the 10 percent aft location. The result was a monotonically increasing hub static pressure from the rotor trailing edge to far downstream. At most of the measurement planes (10, 30, and 50 percent aft), however, the predicted hub static pressures were above the measured values. The difference between the computed pressure coefficients and the measured values was 0.14 at the plane 10 percent aft, 0.10 at 30 percent aft, and 0.04 at 50 percent aft. All that can be said for the present is that an inconsistency exists between the measured data and the results calculated based on the present through-flow formulation.

Mesh refinement was shown to have no significant impact on the high and low hub static pressure regions. A case was run with only four stations within the airfoil and without the planes 20 and 40 percent aft of the rotor. The changes in the computed hub static pressure distribution were negligible. Another case was run with only leading and trailing edge planes (i.e., no calculation planes within the rotor) and this also had no significant impact on the maximum in static pressure predicted at the hub 30 percent aft.

The effects of aerodynamic blockage can be seen in Fig. 6 where it has been eliminated from the calculation ($\bar{K} = 1$). It had been demonstrated in a separate calculation that the impact of eliminating the mechanical blockage alone on the flow downstream of the airfoil was extremely small. The elimination of the aerodynamic blockage has caused the static pressure rise to occur almost entirely within the rotor. The diffusion seen in the measured data downstream of the

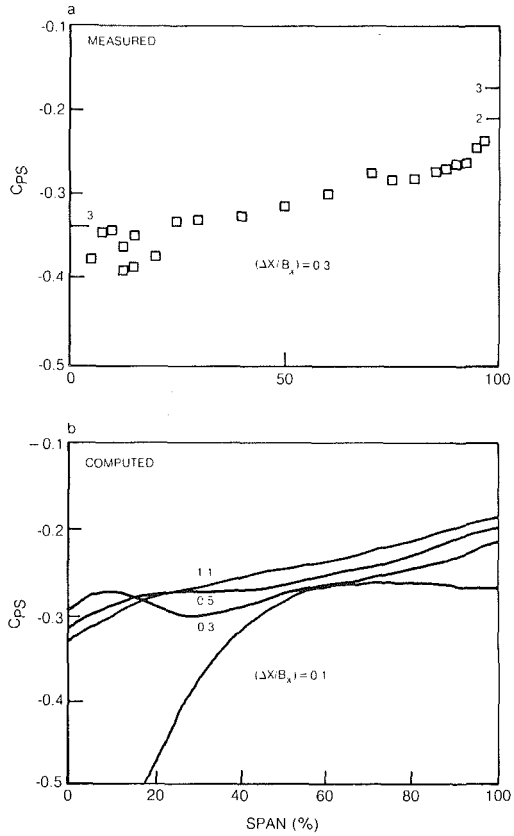

Fig. 7 Spanwise distributions of static pressure, single-stage rotor, thick inlet boundary layers, $\Phi = 0.85$

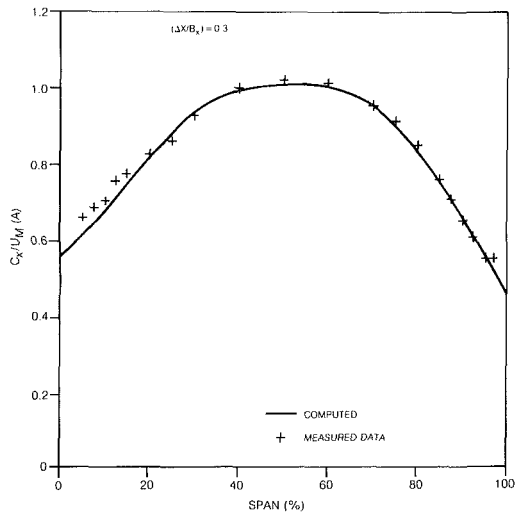

Fig. 8 Spanwise distributions of axial velocity, single-stage rotor, thick inlet boundary layers, $\Phi = 0.85$

trailing edge is not predicted by the calculation. The comparison makes it clear why some accounting for aerodynamic blockage must be included in the calculation if reasonable results are to be obtained in the region immediately downstream of airfoil rows.

Although the computed results presented in Fig. 4 are for the thin inlet boundary layer case, they are very similar to the case with thick inlet boundary layers in that the same static pressure maxima and minima occurred at the hub. This can be seen in the measured and computed results presented in Fig. 7(*a*) and 7(*b*). For this case, as mentioned above, traverse data were only acquired at the plane 30 percent aft. In spite of the fact that the predicted static pressure near the hub 30

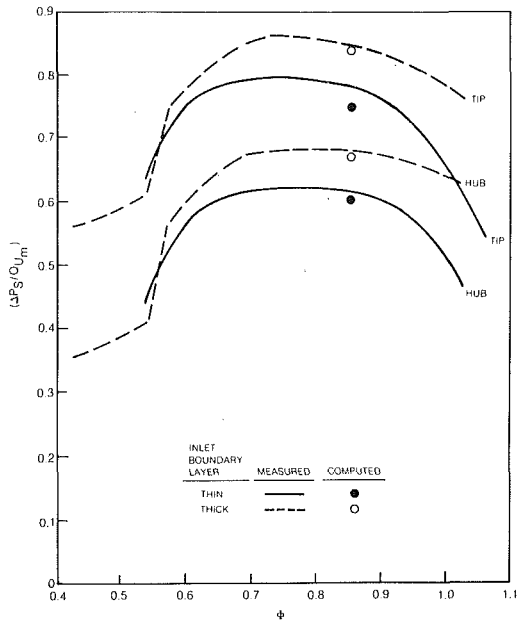

Fig. 9 Single-stage rotor static pressure rise

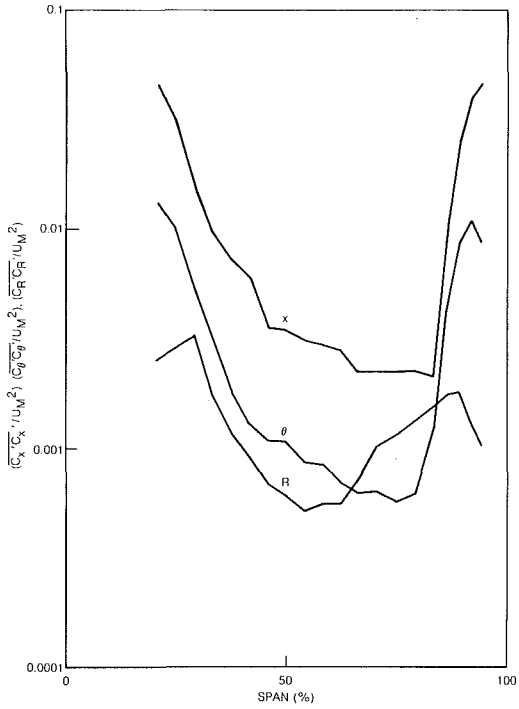

Fig. 10 Fluctuating velocity components, single-stage rotor, thin inlet boundary layers, Φ = 0.85, 10 percent aft

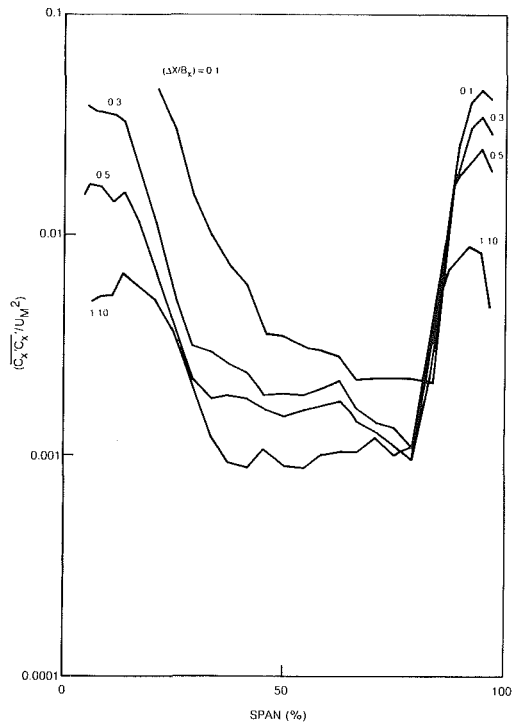

Fig. 11 Fluctuating axial velocity component, single-stage rotor, thin inlet boundary layers, Φ = 0.85

percent aft is too high, the impact on the axial velocity profile is relatively small. This can be seen in the measured and computed axial velocity profiles presented in Fig. 8. The measured results have been circumferentially area averaged and the computed result plotted is the product of the axial velocity computed in the analysis (from mass-averaged quantities) and the blockage factor ($\bar{K}$). The agreement is in general excellent but near the hub the computed results are slightly low due to the high static pressure predicted in this region.

The measured and computed static pressure rise for the thin and thick inlet boundary layer cases are presented in Fig. 9. The blockage has decayed to zero at the far downstream location at which the static pressure rise was measured (Sta. 3) and hence the details of the blockage profiles immediately downstream of the airfoil have little impact on the computed results. This can also be seen in the excellent prediction of the far downstream static pressure rise that was obtained without any accounting for blockage (Fig. 6). It is significant that both the measured and computed results are in agreement as to the increase in static pressure rise across the rotor as the inlet boundary layer thickness was increased.

Fluctuation and Radial Force Effects. This assessment of through-flow theory has been focused on the form of the through-flow equation (equation (9)) most commonly used in turbomachinery design and analysis, that is, with the fluctuation terms $N_i^{(r)}$ and the radial force terms $F_{b,r}$ and $F_{f,r}$ neglected. The benchmark data set, however, does permit one to estimate the magnitudes of these terms.

The spanwise distributions of the axial, tangential, and radial fluctuation velocities are shown in Fig. 10 for the thin inlet boundary layer case at the plane 10 percent aft. The data in Fig. 10 begin at 20 percent span since, as mentioned above, the hub corner stall prevented data from being acquired in the wake region this close to the trailing edge. The fluctuations are large near the endwalls due to the hub corner stall and the rotor tip leakage and the large departures from axisymmetry produced by these complex three-dimensional flow mechanisms. For comparison, the square of the average axial velocity is: $(C_x^2/U_m^2) = 0.85^2 = 0.72$. The fluctuation terms for the density-averaged formulation ($N_i^{(r)}$, equations (2–6)) depend primarily on the tangential and radial fluctuation velocities and these are in general much smaller than the axial velocity fluctuations. The decay of the axial fluctuation velocity with downstream distance is shown in Fig. 11. This rapid decay, especially near the hub, suggests that the impact of the fluctuation terms will be limited to regions very close to the airfoil trailing edge.

In order to judge their impact on through-flow analysis, the magnitude of the fluctuation terms must be judged with respect to the terms on the right-hand side of equation (9) resulting from the radial gradients of absolute angular

momentum, entropy, and rothalpy. When consistently nondimensionalized, the sum of these terms varies between 1 and 5 in the endwall regions and between 0.1 and 1 in the core flow region. The fluctuation terms $N_1^{(r)}$, $N_2^{(r)}$, and $N_3^{(r)}$ (equations (2–4)) were evaluated based on the fluctuation velocities and over most of the flow they did not exceed 0.01. The maximum value occurred at 30 percent span, 10 percent aft where $N_1^{(r)}$ reached 0.16. It is difficult to see how these relatively small fluctuation terms can have an impact comparable in magnitude to blockage distributions which locally can reach 40 percent ($1 - \bar{K} = 0.6$). One must keep in mind, however, that equation (9) is not the result of a formal circumferential mass averaging of the equations of motion and hence it is premature to comment with any confidence about the magnitude of the fluctuation terms that might be present in such a formulation.

Finally, let us consider the radial blade force term which was also neglected in this assessment. If the airfoil was defined by purely radial lines passing through a reference contour, at midspan for example, then it would exert no radial pressure force on the flow. The present airfoil was not generated in such a way and hence it is capable of generating a radial component of pressure force. The measured fullspan airfoil pressure distributions [4, 7] were used to make an estimate of the magnitude of this radial force for the thin inlet boundary layer case. In the region near the hub, especially near the trailing edge, the radial pressure force on the flow is outward, toward the tip. The region of radially inward pressure force on the flow is distributed primarily over the forward half of the airfoil. When the radial force is averaged over the tangential projection of the airfoil the positive and negative contributions to the nondimensionalized radial pressure force are both equal to approximately 0.02 and the net value is a radially inward force of magnitude 0.004. This corresponds to approximately 0.2 percent of the tangential airfoil pressure force. It is also small relative to the other terms on the right hand side of equation (9). It seems unlikely, for the present comparisons, that neglecting the radial blade force could be of any significant consequence.

Conclusions

An assessment of through-flow theory has been carried out by comparing the prediction of a modern finite element through-flow analysis with a benchmark data base acquired for an isolated single-stage rotor operating with both thin and thick inlet endwall boundary layers. The benchmark data base was used to supply the aerodynamic input required by the analysis including loss, deviation, and blockage. Although the spanwise velocity profile in the flow downstream of the rotor and the far field static pressure rise were predicted with reasonable accuracy, the details of the static pressure field close to the rotor trailing edge were not predicted accurately. Although a proposed model for aerodynamic blockage (equations (11) and (12)) did reproduce the low static pressure region close to the rotor trailing edge, it did not duplicate the details of the diffusion process downstream of the rotor trailing edge. It was demonstrated, however, that the absence of aerodynamic blockage produces an even poorer result.

It was shown that the two groups of terms commonly neglected in through-flow analysis, namely those involving the nonaxisymmetric fluctuation velocities and the radial blade force, were indeed small for the test case being considered.

In light of the typically close coupling of blade rows in a compressor, with axial gaps ranging from 20 to 50 percent chord, the inability of through-flow theory to accurately predict the measured static pressure field in the region close to the rotor trailing edge is a serious matter. A more precise formulation of the equations may be required to improve this situation. Such a formulation must include a more formal treatment of the differences between area (or density)-averaged quantities and mass-averaged quantities, that is, a more formal treatment of blockage.

Acknowledgments

The authors are indebted to Mr. Gordon Youngson for his assistance with the through-flow analysis. The thin boundary layer isolated rotor data were acquired under Air Force contract funding under the direction of C. Herbert Law (AFWAL/POTX), project engineer, Contract No. F33615-77-C-2083. The thick boundary layer isolated rotor data were acquired under funding from NASA Lewis Research Center under the direction of Mr. Michael Pierzga, project manager, Contract No. NAS3-23157. The assessment of through-flow theory was carried out under Navy funding under the direction of Dr. Raymond Shreeve, Contract No. N00014-84-C-0354. Finally, the software required to make the various codes compatible with the present applications and the software required to produce the various graphic outputs presented in this paper were all developed under UTC Corporate funding.

References

1 Wu, C. H., "A General Theory of Three-Dimensional Flow in Subsonic and Supersonic Turbomachines of Axial-Radial- and Mixed Flow Type," NACA TN 2604, 1952.

2 Dring, R. P., "Blockage in Axial Compressors," ASME JOURNAL OF ENGINEERING FOR GAS TURBINES AND POWER, Vol. 106, July 1984, pp. 712–714.

3 Dring, R. P., Joslyn, H. D., and Hardin, L. W., "Experimental Investigation of Compressor Rotor Wakes," AFAPL-TR-79-2107, Air Force Aero Propulsion Laboratory, Technology Branch, Turbine Engine Division (TBX), Wright-Patterson AFB, OH.

4 Dring, R. P., Joslyn, H. D., and Hardin, L. W., "An Investigation of Compressor Rotor Aerodynamics," ASME JOURNAL OF ENGINEERING FOR POWER, Vol. 104, Jan. 1982, pp. 84–96.

5 Dring, R. P., Joslyn, H. D., and Wagner, J. H., "Compressor Rotor Aerodynamics," AGARD-CP-351, *Viscous Effects in Turbomachines*, Copenhagen, Denmark, June 1–3, 1983, Paper No. 24.

6 Wagner, J. H., Dring, R. P., and Joslyn, H. D., "Axial Compressor Middle Stage Secondary Flow Study," NASA CR-3701, July 1983.

7 Wagner, J. H., Dring, R. P., and Joslyn, H. D., "Inlet Boundary Layer Effects in an Axial Compressor Rotor, Part I: Blade-to-Blade Effects," ASME JOURNAL OF ENGINEERING FOR GAS TURBINES AND POWER, Vol. 107, No. 2, Apr. 1985, pp. 374–380.

8 Wagner, J. H., Dring, R. P., and Joslyn, H. D., "Inlet Boundary Layer Effects in an Axial Compressor Rotor, Part II: Through-Flow Effects," ASME JOURNAL OF ENGINEERING FOR GAS TURBINES AND POWER, Vol. 107, No. 2, Apr. 1985, pp. 381–386.

9 Dring, R. P., "Boundary Layer Transition and Separation on a Compressor Rotor Airfoil," ASME JOURNAL OF ENGINEERING FOR POWER, Vol. 104, Jan. 1982, pp. 251–253.

10 Habashi, W. G., and Youngson, G. C., "A Transonic Quasi 3-D Analysis for Gas Turbine Engines Including Split-Flow Capability for Turbofans," *Int. Jour. for Num. Meth. in Fluids*, Vol. 3, 1983, pp. 1–21.

11 Habashi, W. G., "Numerical Methods for Turbomachinery," in: *Recent Advances in Numerical Methods in Fluids*, C. Taylor and K. Morgan, eds., Pineridge Press, 1980, Chap. 8.

12 Ruden, P., "Investigation of Single-Stage Axial Fans," NACA TM 1062, 1944.

13 Smith, L. H., "The Radial Equilibrium Equation of Turbomachinery," ASME JOURNAL OF ENGINEERING FOR POWER, Vol. 88, No. 1, 1966.

14 Hirsch, C., "Unsteady Contributions to Steady Radial Equilibrium Flow Equations," AGARD Conference on Unsteady Phenomena in Turbomachinery, CP-177, No. 13, 1975.

15 Hirsch, C., and Warzee, G., "A Finite Element Method for Through Flow Calculations in Turbomachines," ASME *Journal of Fluids Engineering*, Sept. 1976, pp. 403–421.

16 Hirsch, C., and Warzee, G., "An Integrated Quasi-3D Finite Element Calculation Program for Turbomachinery Flows," ASME JOURNAL OF ENGINEERING FOR POWER, Jan. 1979, pp. 141–148.

17 Sehra, A. K., and Kerrebrock, J. L., "The Effect of Blade-to-Blade Flow Variations on the Mean Flow-Field of a Transonic Compressor," AIAA 12th Fluid and Plasma Dynamic Conf., July 1979, Paper No. 79-1515.

18 Dring, R. P., and Joslyn, H. D., "An Assessment of Single- and Multi-Stage Compressor Flow Modeling, Part I, Design Conditions," ONR/NASC, Contract No. N00014-84-C-0354, Final Report, July 1985.

19 Schlichting, H., *Boundary Layer Theory*, McGraw-Hill, 6th edn., 1968.

A Unified Theory of Hybrid Problems for Fully Three-Dimensional Incompressible Rotor Flow Based on Variational Principles With Variable Domain

Liu Gao-lian
Associate Research Professor.
Shanghai Institute of Mechanical Engineering,
Shanghai, People's Republic of China

Making use of functional variations with variable domain and natural boundary conditions, this paper presents a unified theory of various hybrid problems (being a unification as well as a generalization of direct and inverse problems) for three-dimensional incompressible potential flow in a rotor blading. Three families of variational principles (VPs) have been established and provide a series of new rational ways for blade design and a sound theoretical basis for the finite element method (FEM). This theory can be extended to compressible and rotational flows and also constitutes an important part of the optimum design theory of bladings [8].

1 Introduction

Traditionally, there are two kinds of aerodynamic problems: the direct and inverse problems. In blade design practice, however, the inverse method is seldom employed, because it may lead to blade configurations unfeasible from material-strength, vibration, cooling, or technological considerations, e.g., unclosed or too thin profiles or even profiles with negative thickness. Therefore, up to now, almost all practical bladings have been designed by solving the direct problem iteratively. Such a procedure is, of course, rather inconvenient, time consuming, and cannot keep up with the requirements of the modern turbomachine development. To overcome these disadvantages, it is natural and appropriate to pose a new problem category: the hybrid problem, which is a unification as well as a generalization of the direct and inverse problems. Various hybrid problem types have been dealt with by variational principles (VPs) and FEM [1-3, 14], image-plane (-space) methods [4, 12, 13] or time-marching methods [16, 17].

The great success achieved by FEM in applied mechanics has renewed the interest of scientists in VPs and stimulated this author to start working on this subject about ten years ago. At that time VPs in fluid mechanics, compared with solid mechanics, were underdeveloped and all restricted to the direct problem, subsonic flow, and stationary system [10, 11]. A systematic search for VPs for sub- and transonic flows in a rotating system was undertaken [7], taking full advantage of three powerful means: the natural boundary condition, the functional variation with variable domain, and the artificial interface. For the direct problem, for instance, Bateman's and Giese's VPs have been extended to three-dimensional shocked transonic rotor flow [5]. Our major effort, however, is placed on hybrid problems. Thus, in the context of quasi-three-dimensional flow, based on an image-plane concept, VP families for various hybrid problems of blade-to-blade flow and S_2-flow have been established in [1, 14], and the corresponding FE solutions are given in [2]. A unified theory of hybrid problems based on VPs with variable domain is suggested in [3], capable of handling blunt nose cascades accurately and extending to fully three-dimensional flow. As for fully three-dimensional flow, as early as 1952 a series expansion method for solving inverse problem was proposed in [6] and improved in [15]; and recently a general theory of three-dimensional hybrid problems based on an image-space concept was suggested in [4]. The present paper, based on [3-5], is intended to develop a unified variational theory of various hybrid problems for fully three-dimensional incompressible potential flow past axial-, radial-, and mixed-flow turbo-rotors via variations with variable domain.

2 Basic Equations for Fully Three-Dimensional Incompressible Flow

The three-dimensional potential, steady relative flow of an inviscid incompressible fluid past a blading rotating with constant angular speed ω (Fig. 1) is governed by the following equations [4-6]:

Continuity equation

$$\nabla \cdot \mathbf{W} = \frac{1}{r}\frac{\partial (rW_r)}{\partial r} + \frac{1}{r}\frac{\partial W_\varphi}{\partial \varphi} + \frac{\partial W_z}{\partial z} = 0 \qquad (1)$$

Contributed by the Gas Turbine Division and presented at the 1985 Beijing International Gas Turbine Symposium and Exposition, Beijing, People's Republic of China, September 1-7, 1985. Manuscript received at ASME Headquarters June 14, 1985. Paper No. 85-IGT-119.

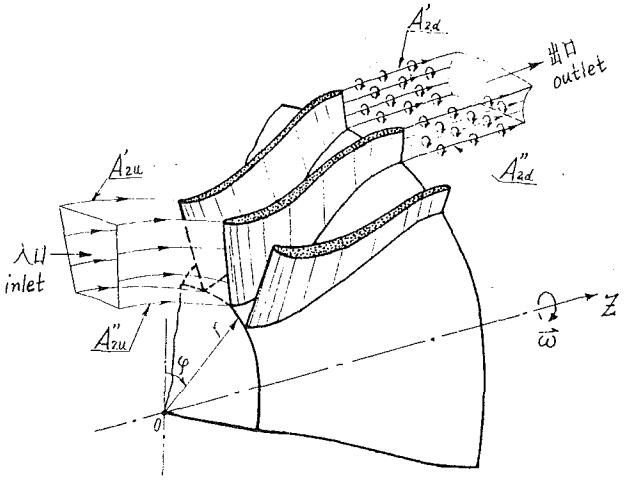

Fig. 1 Three-dimensional flow field in rotor

Irrotationality of the absolute flow

$$\nabla \times (\mathbf{W} + \mathbf{U}) = 0 \tag{2}$$

Bernoulli's equation

$$p/\rho + \frac{1}{2}(W^2 - U^2) = B \tag{3}$$

From equation (2) a potential function $\Phi(r, \varphi, z)$ can be defined

$$\nabla \Phi = \mathbf{W} + \mathbf{U} = \mathbf{C}$$

or

$$\left.\begin{aligned} \frac{\partial \Phi}{\partial r} &= W_r \\ \frac{\partial \Phi}{\partial \varphi} &= (W_\varphi + U)r \\ \frac{\partial \Phi}{\partial z} &= W_z \end{aligned}\right\} \tag{2'}$$

Substituting in equation (1) yields the following potential equation

$$\nabla^2 \Phi = \frac{1}{r}\left\{\frac{\partial}{\partial r}\left(r\frac{\partial \Phi}{\partial r}\right) + \frac{\partial}{\partial \varphi}\left(\frac{1}{r}\frac{\partial \Phi}{\partial \varphi}\right) + r\frac{\partial^2 \Phi}{\partial z^2}\right\} = 0 \tag{4}$$

3 Classification of Three-Dimensional Hybrid Problems

The hybrid problems for fully three-dimensional flow can be posed in a great many ways and have been discussed in [4] in detail. In brief, all three-dimensional hybrid problems are characterized by the fact that some of the wall boundary conditions (BC) are geometric, while the others are aerodynamic in nature. Thus, they are a unification as well as a generalization of the direct and inverse problems. According to [4], the following definitions and symbols are adopted:

Direct Problem (D-Problem) [5]. All blading geometry is given.

Inverse Problem (I-Problem) [1–4, 12, 13]. The pressure (or velocity) distribution along walls is specified, but wall geometry is unknown.

Hybrid Problems (H-Problems) [1–4, 12, 13]. They may have various types, e.g.:

Type A (H_A-Problem) [1–4, 12, 13]. The shape of some part of wall and the pressure distribution on the remaining wall are given.

Type B (H_B-Problem) [1–4]. The pressure-difference distribution on two opposite walls (e.g., the blade loading on blades) and the distance distribution between them (e.g., the blade thickness distribution or the blade height distribution) are specified.

Type C (H_C-Problem) [3–4, 12]. The distance distribution between two opposite walls and the pressure distribution along one of these walls are given.

Obviously, to characterize the hybrid problem in fully three-dimensional flow some compound symbols must be adopted. Such compound symbols have already been rendered by [4], e.g., $(I \times H_A)$ designates that hybrid problem in which an inverse- and a H_A-problem are posed on the blade surface and on the annular walls respectively, etc. Moreover, it is also possible to have different problem types on different portions

Nomenclature

A = area of boundary surfaces
A_1 = inlet and outlet surfaces (Fig. 1)
A_2 = periodic boundary surfaces (Fig. 1): $A_2 = A_{2u} U A_{2d}$, $A_{2u} = A'_{2u} U A''_{2u}$, $A_{2d} = A'_{2d} U A''_{2d}$
A_3 = all boundary walls: $A_3 = A_a U A_b = A_3^* U A_3^{**}$
A_a = hub and casing annular walls: $A_a = A_a^* U A_a^{**}$
A_b = blade surfaces: $A_b = A_b^* U A_b^{**}$
A_3^* = portion of A_3 with wall shape known
A_3^{**} = unknown portion of A_3
A_a^*, A_b^* = portions of A_a and A_b with wall shape known, respectively
A_a^{**}, A_b^{**} = unknown portions of A_a and A_b respectively
$dA_{r,\varphi,z}$ = components of an elementary area $d\mathbf{A}$ in r, φ, z directions, respectively
B = Bernoulli's constant in equation (3)
$\mathbf{C}$ = absolute velocity
$\mathbf{i}_r, \mathbf{i}_\varphi, \mathbf{i}_z$ = unit vectors along the coordinate directions
l = arc length along the generatrices of the annular walls
p = pressure
r, φ, z = cylindric coordinates fixed on rotor
$\delta \mathbf{s}$ = variation of boundary position vector
$\mathbf{U}$ = $\omega \times \mathbf{r}$
dV = elementary volume: $dV = r \cdot d\varphi \cdot dr \cdot dz$
$\mathbf{W}$ = relative velocity
$r_a(z)$ = in the equation of annular walls in axial-flow region, $r = r_a(z)$
$z_a(r)$ = in the equation of annular walls in radial-flow region, $z = z_a(r)$
$\varphi_b(r, z)$ = $\varphi = \varphi_b(r, z)$ is the equation of blade surface
Φ = potential function
ω = angular speed of the rotor
ρ = density
Σ = artificial interface [9]

Subscripts

pr = prescribed
m = circumferentially averaged value
a = annular walls
b = blade surface
d = downstream
u = upstream
t = tangential component
s = suction blade surface
p = pressure blade surface

of the blade (or annular) wall. Therefore it becomes quite clear that a great variety of hybrid problem types is possible for fully three-dimensional flow. It is just for this reason that the three-dimensional hybrid problems have provided the design engineers with a series of novel design tools, which enable them to choose the most appropriate hybrid problem type to meet various design conditions and requirements (e.g. cooling, material strength, vibration, technology, etc.).

Different problem types will have also different BC on the walls. For the convenience of discussion and without much loss of generality, we shall take only the three hybrid problems $(H_A \times H_A)$, $(H_B \times H_A)$, and $(H_C \times H_A)$ for example and establish the corresponding VP families for them. Evidently, they embrace very comprehensive special cases which, to a large extent, are capable of fulfilling various practical requirements of blade design. For instance, the $(H_A \times H_A)$-problem includes $(D \times D)$, $(I \times D)$, $(D \times I')$, $(I \times I')$, $(H_A \times D)$, $(H_A \times I')$, $(D \times H_A)$, and $(I \times H_A)$, etc. as special cases. It is worth noting that for the annular walls there cannot be a pure inverse problem, because there must be some surfaces of revolution (a boundary constraint of geometric character), so that the symbol I' designates a "semi-inverse" problem: the hub and casing walls must be some surfaces of revolution with specified distributions of pressure averaged in the circumferential direction $p_m(l)$.

4 VP Family for $(H_A \times H_A)$-Problem

The VP families for the $(D \times D)$-problem of three-dimensional incompressible potential flow can be derived in two ways: (*i*) as a special case from [5]; (*ii*) applying the inverse-deduction method and the constraint-removing transformation [7] to equations (1) and (2′) directly. Then, upon handling them via functional variations with variable domain, the VP families for hybrid problems can be established. Without going into details, the final results are given below.

VP I. The solution to the $(H_A \times H_A)$-problem of three-dimensional incompressible potential flow in rotor blading makes the following functional J_I stationary, i.e., $\delta J_I = 0$, where Φ, A_3^{**}, and A_{2d} should be varied independently.

$$J_I(\Phi, A_3^{**}, A_{2d}) = I_I + L + L^{AA} \tag{5}$$

where

$$2I_I = \iiint_{(V)} \left\{ \left(\frac{\partial \Phi}{\partial r}\right)^2 + \left(\frac{1}{r}\frac{\partial \Phi}{\partial \varphi} - U\right)^2 + \left(\frac{\partial \Phi}{\partial z}\right)^2 \right\} dV$$

$$L = -\iint_{(A_1 + A_3)} (W_n)_{pr} \cdot \Phi \cdot dA + \iint_{(A_{2u}')} (\Phi'' - \Phi' - \Delta\Phi_u) W_n' \cdot dA + \iint_{(\Sigma)} (\Phi_+ - \Phi_-) W_{n-} \cdot dA$$

$$2L^{AA} = -\iint_{(A_a^{**})} (W_m^2)_{pr} \mathbf{s}_a \cdot d\mathbf{A} - \iint_{(A_b^{**})} (W^2)_{pr} \mathbf{s}_b \cdot d\mathbf{A}$$

Proof. For this purpose, the following general formula for the variation of functional $J(\phi)$ with variable domain derived in [5, 7] via a new analogy to Reynolds' transport theorem should be used

$$\delta J(\phi) = \iiint_{(V)} \sum_{j=1}^{I} \left[\left(\frac{\partial F}{\partial \phi^j} - \nabla \cdot \mathbf{G}^j \right) \delta\phi^j \right] dV + \oiint_{(A)} \sum_{j=1}^{I} \left\{ \mathbf{G}^j \cdot \delta\phi^j + \left(F - G_n^j \cdot \frac{\partial \phi^j}{\partial n} \right) \delta\mathbf{s} \right\} \cdot d\mathbf{A} \tag{5a}$$

where

$$J(\phi) = \iiint_{(V)} F\left(\phi, \frac{\partial \phi}{\partial x}\right) dV \qquad \phi = \{\phi^1, \phi^2, \ldots, \phi^I\}$$

$$\mathbf{G}^j = (\partial F/\partial \phi^j_{,x_1})\mathbf{i}_1 + (\partial F/\partial \phi^j_{,x_2})\mathbf{i}_2 + (\partial F/\partial \phi^j_{,x_3})\mathbf{i}_3$$

$$\phi_{,x} = \frac{\partial \phi}{\partial x} = \left\{ \frac{\partial \phi^1}{\partial x}, \frac{\partial \phi^2}{\partial x}, \ldots, \frac{\partial \phi^I}{\partial x} \right\}, \qquad x = \{x_1, x_2, x_3\},$$

$\delta\mathbf{s}$ = the variation of boundary position

Therefore we have

on A_a^{**}: $s = s_a = r_a(z)$ for axial-flow rotor,
$s = s_a = z_a(z)$ for radial-flow rotor;

on A_b^{**}: $s = s_b = r \cdot \varphi_b(r, z)$.

Taking the first variation with variable domain of equation (5) by means of equation (5*a*), we obtain:

$$\delta J_I = -\iiint_{(V)} (\nabla \cdot \mathbf{W}) \delta\Phi \cdot dV + \iint_{(A_1)} (W_n - W_{n,pr}) \delta\Phi \cdot dA + \iint_{(A_3 + A_{2d})} W_n \cdot \delta\Phi \cdot dA + \iint_{(A_{2u}')} \{(\Phi'' - \Phi' - \Delta\Phi_u)\delta W_n' - (W_n'' - W_n')\delta\Phi''\} dA + \iint_{(\Sigma)} \{(\Phi_+ - \Phi_-)\delta W_{n-} - [(W_n)_+ - (W_n)_-]\delta\Phi_+\} dA + \iint_{(A_3^{**})} \left\{ (W^2 - W_{pr}^2)/2 - W_n \frac{\partial \Phi}{\partial n} \right\} \delta\mathbf{s} \cdot d\mathbf{A} + \iint_{(A_{2d}')} \left\{ \left(\frac{W^2}{2} - W_n \frac{\partial \Phi}{\partial n} \right)' - \left(\frac{W^2}{2} - W_n \frac{\partial \Phi}{\partial n} \right)'' \right\} \delta\mathbf{s} \cdot d\mathbf{A}$$

Here, it must be stressed that a rational choice of the variation of the position vector $\delta\mathbf{s}$ of the unknown boundary surface A_3^{**} is crucial for making the practical computation of $\delta\mathbf{s}$ and δJ_I simple and convenient. To this end, we take, without any loss of generality, the variation $\delta\mathbf{s}$ on A_3^{**} in the following special way:

on A_a^{**}: $\delta\mathbf{s} = \delta r_a \cdot \mathbf{i}_r$, $\therefore\ \delta\mathbf{s} \cdot d\mathbf{A} = \delta r_a \cdot dA_r$, for axial-flow region,

$\delta\mathbf{s} = \delta z_a \cdot \mathbf{i}_z$, $\therefore\ \delta\mathbf{s} \cdot d\mathbf{A} = \delta z_a \cdot dA_z$, for radial-flow region,

on A_b^{**}: $\delta\mathbf{s} = r \cdot \delta\varphi_b \cdot \mathbf{i}_\varphi$, $\therefore\ \delta\mathbf{s} \cdot d\mathbf{A} = r \cdot \delta\varphi_b \cdot dA_\varphi$.

With these in mind, and since all variations on the right-hand side of the foregoing δJ_I-expression are independent, we can obtain from $\delta J_I = 0$ the following set of natural stationary conditions:

Euler's equation:

$$\nabla^2\Phi = 0,$$

Natural BC:

on A_1: $W_n = (W_n)_{pr}$

on A_{2u}: $W_n' = W_n''$, and $\Phi'' = \Phi' + \Delta\Phi_u$ (i.e., $W_t' = W_t''$) which lead to the periodicity of all flow parameters in the circumferential direction.

on A_{2d}: $W_n' = W_n'' = 0$, and $(W^2)' = (W^2)''$ (i.e., $p' = p''$).

These are just the interface conditions on free trailing vortex sheets.

on A_3^{**}: $W_n = 0$

on A_a^{**}: $W_n = 0$, and $W_m^2 = (W_m^2)_{pr}$ [i.e., $p_m = (p_m)_{pr}$]

on A_b^{**}: $W_n = 0$, and $W^2 = W_{pr}^2$

on Σ: $(W_n)_- = (W_n)_+$ and $\Phi_- = \Phi_+$ [i.e., $(W_t)_- = (W_t)_+$], which result in the continuity of all flow parameters on Σ.

Therefore it has been shown that from this VP I actually the flow equation (4) and all BC for $(H_A \times H_A)$-problem can be derived automatically.

If, alternatively, BC on the upstream periodic boundary A_{2u} ($\Phi'' = \Phi' + \Delta\Phi_u$) and on the artificial interface Σ[9]($\Phi_- = \Phi_+$) are used as enforced (essential) BC, the boundary integral terms on A_{2u}' and Σ involved in L of equation (5) should be deleted. This is also true for all VPs given in this paper.

By using a constraint-removing transformation via Lagrange's multipliers [7] to J_I, the following generalized VP (GVP) can be derived.

GVP II. The solution to the above $(H_A \times H_A)$-problem makes the following functional J_{II} stationary, i.e., $\delta J_{II} = 0$, where Φ, W_r, W_φ, W_z, A_3^{**}, and A_{2d} are varied independently.

$$J_{II}(\Phi, \mathbf{W}, A_3^{**}, A_{2d}) = I_{II} + L + L^{AA} \tag{6}$$

where

$$I_{II} = \iiint_{(V)} \left\{ W_r \frac{\partial\Phi}{\partial r} + W_\varphi \left(\frac{1}{r}\frac{\partial\Phi}{\partial\varphi} - U \right) + W_z \frac{\partial\Phi}{\partial z} - \frac{W^2}{2} \right\} dV$$

In a way similar to that used above we can show that from δJ_{II} the following set of natural conditions results:

Euler's equations: $\nabla \cdot \mathbf{W} = 0$,

$$\nabla\Phi = \mathbf{W} + \mathbf{U}$$

Natural BC: the same as in VP I.

Subgeneralized VPs (SGVPs). By means of a constraint-recovering transformation [7] a family of subgeneralized VPs can be derived, of which one is the above VP I.

5 VP Family for $(H_B \times H_A)$-Problem

In this case the given BC on blade walls are:

(*i*) blade thickness distribution

$$\varphi_p - \varphi_s = g_\varphi(r, z) \tag{7a}$$

and (*ii*) distribution of blade loading

$$p_p - p_s = (W_s^2 - W_p^2)/2 = q_p(r, z) \tag{7b}$$

where g_φ and g_p are given functions.

Using the same method as in the foregoing section, we can establish the following VP family for $(H_B \times H_A)$-problem, which differs from that for $(H_A \times H_A)$-problem only in that the boundary integral term L^{AA} should be replaced by the following L^{BA}

$$L^{BA} = -\iint_{(A_a^{**})} (W_m^2/2)_{pr}\mathbf{s}_a \cdot d\mathbf{A} + \iint_{(A_b)_s} g_p \mathbf{s}_b \cdot d\mathbf{A} \tag{8}$$

treating blade thickness equation (7*a*) as an enforced BC. In equation (8) the symbol $(A_b)_s$ stands for the suction blade surface.

VP III. The solution to the $(H_B \times H_A)$-problem of three-dimensional incompressible potential rotor flow makes the following functional J_{III} stationary, i.e., $\delta J_{III} = 0$; thereby Φ, A_a^{**}, A_b, A_{2d} are varied independently.

$$J_{III}(\Phi, A_a^{**}, A_b, A_{2d}) = I_I + L + L^{BA} \tag{9}$$

From $\delta J_{III} = 0$ the same Euler's equation and natural BC set as in VP I can be obtained with the only exception that the natural BC on the blade surface A_b has now become equation (7*b*).

GVP IV. The solution to the above $(H_B \times H_A)$-problem makes the following functional J_{IV} stationary, i.e. $\Delta J_{IV} = 0$ with independent variations of Φ, $\mathbf{W}$, A_a^{**}, A_b, and A_{2d}

$$J_{IV}(\Phi, \mathbf{W}, A_a^{**}, A_b, A_{2d}) = I_{II} + L + L^{BA} \tag{10}$$

From $\delta J_{IV} = 0$ the same Euler's equations and natural BC set as in GVP II can be derived except that the natural BC on A_b has become equation (7*b*).

SGVP Family. Via the constraint-recovering transformation [7] a family of SGVPs can be derived, including also the VP III.

6 VP Family for $(H_C \times H_A)$-Problem

Here the following blade surface BC are given:

(*i*) blade thickness distribution, equation (7*a*); (*ii*) velocity (or pressure) distribution on the suction blade surface:

$$\left.\begin{aligned} W_s &= [W_s(r, z)]_{pr} \\ \text{or} \quad p_s &= [p_s(r, z)]_{pr} \end{aligned}\right\} \tag{11}$$

Now, we are going to establish VP family for $(H_C \times H_A)$-problem, which differs from that for $(H_A \times H_A)$-problem only in that the boundary integral term L^{AA} should be replaced by the following L^{CA}

$$L^{CA} = -\iint_{(A_a^{**})} (W_m^2/2)_{pr}\mathbf{s}_a \cdot d\mathbf{A} + \iint_{(A_b)_s} [\overset{0}{p}_p - (p_s)_{pr}]\mathbf{s}_b \cdot d\mathbf{A} \tag{12}$$

Thereby the blade thickness equation (7*a*) should be treated as an enforced BC. The superscript '0' denotes that the "restricted variations" [7, 11] should be taken, namely, $\overset{0}{p}$ is treated as if it were a given function during the variation, but once the variation has been completed, $\overset{0}{p}$ should be treated entirely the same as p.

VP V. For the $(H_C \times H_A)$-problem $\delta J_V = 0$ holds

$$J_V(\Phi, A_a^{**}, A_b, A_{2d}) = I_I + L + L^{CA} \tag{13}$$

GVP VI. $\delta J_{VI} = 0$,

$$J_{VI}(\Phi, \mathbf{W}, A_a^{**}, A_b, A_{2d}) = I_{II} + L + L^{CA} \tag{14}$$

SGVP Family. Applying the constraint-recovering

transformation [7], we can derive a family of SGVPs for $(H_C \times H_A)$-problem from GVP VI, of which one is VP V.

It can be easily shown that the Euler's equations and natural BC sets of the VP V, GVP VI, and its SGVP family are the same as those of the VP I, GVP II, and its SGVP family respectively, except that the natural BC on blade surface now has become equation (11).

7 Concluding Remarks

We have succeeded in extending the unified theory of hybrid problems for cascades on an arbitrary stream-sheet of revolution developed in [3] to fully three-dimensional incompressible flow. Clearly, the conventional direct problem $(D \times D)$ [5] is only the simplest special case of the $(H_A \times H_A)$-problem, taking $A_a^{**} = A_b^{**} = 0$.

We have suggested two different unified theories of hybrid problems for fully three-dimensional flow: One is based on an image space concept [4], while the other (in the present paper) is based on the functional variations with variable domain. They both provide a theoretical foundation for FEM and wide new possible ways for new blade design and modification of old blades and also constitute an important part of the optimization theory of three-dimensional rotor-bladings [8].

The present theory can be generalized further to fully three-dimensional compressible as well as rotational flows.

Acknowledgments

This research is supported by the Science Foundation of Academia Sinica.

References

1 Liu, G. L., "Variational Principles (VPs) and Generalized VPs for Hybrid Aerodynamic Problem of Airfoil Cascades on an Arbitrary Streamsheet of Revolution," Part I, *Scientia Sinica*, Vol. 23, No. 10, 1980, pp. 1339–1347; Part II, *Chinese J. Engng. Thermophysics*, Vol. 2, No. 4, 1981, pp. 335–342.

2 Yao, Z., Chen, Y. L., and Shi, D. Q., "Variational FE Calculation for Hybrid Aerodynamic Problem of Turbomachine Cascade on an Arbitrary Streamsheet of Revolution," IMechE Paper C 69/84, Conf. on Comput. Methods in Turbomachinery, 1984.

3 Liu, G. L., "A Unified Variational Theory of Hybrid Problems for Cascades on an Arbitrary Streamsheet of Revolution via Variations With Variable Domain," *Acta Aerodynamica Sinica*, No. 3, 1985, pp. 24–33.

4 Liu, G. L., "A General Theory of Hybrid Problems for Fully 3-D Compressible Potential Flow in a Turbo-Rotor I," *Chinese J. Engng. Thermophysics*, Vol. 6, No. 1, 1985, pp. 40–45.

5 Liu, G. L., "Variational Principles (VPs) and Generalized VPs for 3-D Transonic Flow With Shock Waves in a Rotating Turboimpeller," Part I, *Acta Mechanica Sinica*, Vol. 13, No. 5, 1981, pp. 421–429; Part II, to appear in *J. Engng. Thermophysics*.

6 Wu, C. H., "A General Theory of 3-D Flow in Sub- and Supersonic Turbomachines of Axial-, Radial- and Mixed-Flow Types," NACA TN 2604, 1952.

7 Liu, G. L., *Variational Principles for 3-D Compressible Flow in Turbomachines*, Lecture notes, Shanghai Society of Engineering Thermophysics and Shanghai Institute of Mechanical Engineering, 1981.

8 Liu, G. L., "Aerodynamic Optimization Theory of a 3-D Axial-Flow Rotor-Blading via Optimal Control," *Symposium Papers of the 6th Int. Symp. on Air-Breathing Engines*, Paris, June 1983, AIAA Paper No. 83-7037.

9 Peng, H. W., "An Approximate Method Based on a Variational Principle That Includes All Boundary Conditions," *Kexue Tongbao*, Vol. 20, No. 9, 1975, pp. 416–418.

10 Serrin, J., *Mathematical Principles of Classical Fluid Mechanics*, Handbuch der Physik, Vol. VIII/1, Springer-Verlag, 1959.

11 Finlayson, B. A., *The Method of Weighted Residuals and Variational Principles*, Academic Press, 1972, pp. 336–337.

12 Liu, G. L., "A New Approach to Some Hybrid Aerodynamic Problems of Cascades on a General Streamsheet of Revolution (I)," *Chinese J. Engng. Thermophysics*, Vol. 5, No. 1, 1984, pp. 27–32.

13 Liu, G. L., "The Moment Function and Its Application to Inverse and Hybrid Problems of Cascades on a General Streamsheet of Revolution," *Chinese J. Engng. Thermophysics*, Vol. 3, No. 2, 1982, pp. 138–144.

14 Cai, R. Q., and Liu, G. L., "Families of VPs for the Semi-inverse and Type-A Hybrid Problems on a S_2-Streamsheet in Mixed-Flow Turbomachines," *Chinese J. Engng. Thermophysics*, Vol. 6, No. 1, 1985, pp. 37–39.

15 Zhao, X. L., and Wu, C. H., "A Simple Approximate Method for Solving Inverse Problems of 3-D Flow in Turbomachines," *Scientia Sinica (A)*, Vol. 26, No. 12, 1983.

16 Meauze, G., "An Inverse Time Marching Method for the Definition of Cascade Geometry," ASME JOURNAL OF ENGINEERING FOR POWER, Vol. 104, No. 3, 1982, pp. 650–656.

17 Thompkins, W. T., Jr., and Siu Shing Tong, "Inverse or Design Calculations for Non-potential Flow in Turbomachinery Blade Passages," ASME JOURNAL OF ENGINEERING FOR POWER, Vol. 104, No. 2, 1982, pp. 281–285.

A New Theory for Solving Turbulent Vortices in Flowing Fluids

Ge Gao

Huang Ning

Department of Jet Propulsion,
Institute of Aeronautics & Astronautics,
Beijing, People's Republic of China

Turbulent vortices occur everywhere in flowing fluids and possess the properties of dissipation and dispersion. A set of new control equations is presented featuring the interaction between dissipation and dispersion of turbulence. By analysis of instability the rate of turbulent energy production is established. Two third-order derivative momentum equations are derived, one for weak and the other for strong vorticity. By this new theory various turbulent flow problems can be solved, such as: energy inversion in the vortex tail behind a bluff body, the coherent horseshoe vortices in a turbulent boundary layer, the delay in cascading down of turbulent energy through the spectrum, anisotropy of turbulence intensities, etc. Two computational examples are presented.

Introduction

Turbulent vortices appear everywhere in flowing fluids. It is well known that the Reynolds averaging of Navier–Stokes equations for turbulent flow resulted in unclosed problems. Turbulence models for closing the Reynolds equations so far are not quite satisfactory. Discovery of the coherent horseshoe vortices in a turbulent boundary layer revealed that turbulence is not absolutely a stochastic process. Miles [1] showed that in continuous stratified shear flow there exists a swarm of innumerable discretized solitons. Zhang Xueh-Ming [2] formulated the relation of soliton, pseudo-potential, and energy spectrum. Lin [3] suggested that turbulence possesses the duality of wave and particle which is closely related to energy inversion. These imply that turbulence as described by energy spectrum should possess somehow the dispersive nature as in optics. Turbulent energy inversion reveals the presence of dispersion. Since dissipation means entropy rise it forbids inversion. However, possessing the duality of wave and particle, dispersion allows energy to be either focused or resolved. Therefore new equations of motion are required to include the interaction between dissipation and dispersion of turbulence. The canonical equation of turbulence should be a mixture of Burgers and K–dV equation.

$$\bar{U}_t + \bar{U}\bar{U}_x - \nu_T \bar{U}_{xx} + \xi_T \bar{U}_{xxx} = 0$$

Control Equations for Turbulence

In energy balance the dissipation function is always positive. ϕ describes the random motions of turbulent eddies which irreversibly transform some mechanical energy into heat. Whatever form the second partial derivative may take in the momentum equation, its corresponding term in the energy equation must always be positive.

In a region of turbulent flow select a point 0 on a streamline as the origin. Assign the tangent and the outward normal at 0 as the x and y axes (Fig. 1). This flow and spin coordinate system is radically different from either the Euler or the Lagrange system. Loss of stability does not mean destruction of the streamline but means eddies bursting off from the turbulent region.

Neglecting molecular viscosity for two-dimensional incompressible flow, the control equations are

$$\frac{\partial U}{\partial X} + \frac{\partial V}{\partial y} + KV = 0 \tag{1}$$

$$\frac{\partial \Omega}{\partial t} + U\frac{\partial \Omega}{\partial x} + V\frac{\partial \Omega}{\partial y} = 0 \tag{2}$$

$$\frac{\partial U}{\partial t} + U\frac{\partial U}{\partial x} + V\frac{\partial U}{\partial y} + KUV = \frac{-1}{\rho}\frac{\partial p}{\partial x} \tag{3}$$

$$\frac{\partial V}{\partial t} + U\frac{\partial V}{\partial x} + V\frac{\partial V}{\partial y} - KU^2 = \frac{-1}{\rho}\frac{\partial p}{\partial y} \tag{4}$$

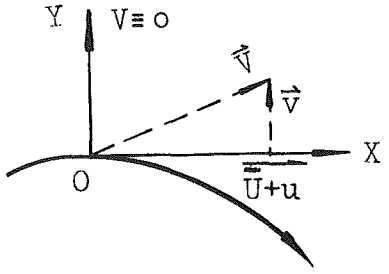

Fig. 1 The flow and spin coordinates

Contributed by the Gas Turbine Division and presented at the 1985 Beijing International Gas Turbine Symposium and Exposition, Beijing, People's Republic of China, September 1–7, 1985. Manuscript received at ASME Headquarters June 14, 1985. Paper No. 85-IGT-120.

Using the moving coordinates the velocity component normal to a streamline $V \equiv 0$.

$$\left.\begin{array}{l}\text{The fluctuating velocity vector } \mathbf{V} = (\bar{\mathbf{U}} + \mathbf{u}) + \mathbf{v} \\ \\ \text{The instantaneous vorticity } \Omega = \Omega_0 - \Omega_0' \eta\end{array}\right\} \quad (5)$$

For incompressible flow the disturbing vorticity waves propagate as transverse waves along the flow direction. The wave equation

$$\eta(x, y, t) = F(y) \exp im(x - Ct) \quad (6)$$

Substituting equations (5) and (6) into equations (1) to (4), neglecting higher order infinitesimals, and adopting the derivations in [4], we finally obtain the condition of stability for turbulence

$$\underbrace{\frac{4}{p_0}\frac{\partial p_0}{\partial y}\left(K\bar{U}^2 - \bar{U}\frac{\partial \bar{U}}{\partial x}\right)}_{\text{I}} - \underbrace{\left\{\left[\left(\frac{\partial \bar{U}}{\partial y}\right)^2 + 2\bar{\Omega}\frac{\partial \bar{U}}{\partial y}\right]}_{\text{II}} - \underbrace{\omega\frac{\partial \bar{U}}{\partial y}}_{\text{III}}\right\} \geq 0 \quad (7)$$

In condition (7) group I exerts a stabilizing effect upon the eddies due to interactions among the pressure gradient, the centrifugal force, and vortex stretching along the streamline direction.

Group II is the destabilizing factor with dissipation. Its corresponding terms in the energy equation and the turbulent energy production rate are always positive.

Group III is the unstable factor caused by the disturbing eddy particles.

By analogy with Maxwell's supposition group I represents the stable attractive centers while groups II and III represent the unstable attractive centers. Depending upon the "critical scale" of the eddies or the "cutoff frequency" of the disturbing wavelets, the change from stable to unstable flow occurs abruptly.

For $I < 0$, the flow is absolutely unstable; for $I > 0$ and (7) is satisfied, flow is stable; for $I > 0$ but (7) is not satisfied, the flow is neutrally stable. In this case momentum and energy are continuously fed into and accumulated within the eddies without increasing amplitudes. After a lapse of time when the accumulated energy has reached a critical amount energy is emitted abruptly in catastrophe.

For convenience's sake henceforth, the overbars are eliminated and all variables in the following formulae are time-averaged values.

In fixed Cartesian coordinates group II of (7) may be expressed as:

$$\text{II} = \left[\left(\frac{\partial u_i}{\partial x_j} + \frac{\partial u_j}{\partial x_i}\right) + 2\Omega_{ij}\right]\frac{\partial u_i}{\partial x_j} \quad (8)$$

The circular frequency of the disturbing wave is proportional to the scale of turbulence l and the gradient of vorticity along the normal to a streamline

$$\omega = l\frac{\partial |\Omega_{ij}|}{\partial x_j}$$

$$\text{Group III} = -\text{sign}(u_i) l \frac{\partial |\Omega_{ij}|}{\partial x_j}\frac{\partial u_i}{\partial x_j} \quad (9)$$

Quoting the k-ϵ model from [5], the rate of turbulent kinetic energy production is

$$G_k = \mu_T\left(\frac{\partial u_i}{\partial x_j} + \frac{\partial u_j}{\partial x_i}\right)\frac{\partial u_i}{\partial x_j}$$

In this model Reynolds stress is simulated as viscous stress in laminar flow without rigorous proof. In this paper by analysis of turbulence instability, the relation between the destabilizing factors and turbulent energy production is established. Instability means that the disturbed eddies are unable to continue the journey along a streamline. They burst off and disperse. The energy emitted by the bursting eddies is

Nomenclature

ADC = artificial damping and compressibility [7]
C = complex velocity of disturbance wave
C_0, C_1, C_2, C_μ = empirical constants
$F(y)$ = amplitude of the disturbance wave
F = Coriolis force per unit mass
G_k = rate of kinetic energy production
h = enthalpy per unit mass
k = turbulent kinetic energy per unit mass
K = local curvature of a streamline
l = scale of eddies or mixing length
m = wave number $= 2\pi/l$
p = instantaneous pressure
p_0 = pressure prior to the disturbance
r = radius of a circular vortex
r_0 = core radius of a circular vortex
Re = Reynolds number
U = instantaneous velocity along streamline or tangential to a circular vortex
V = instantaneous velocity along the normal to a streamline
$\mathbf{V}$ = resultant fluctuating velocity vector
$\bar{U}$ = time-averaged velocity along x axis
$\bar{V}$ = time-averaged velocity along y axis
u = fluctuating velocity along x axis
v = fluctuating velocity along y axis
ϵ = dissipation rate of turbulent kinetic energy per unit mass
η = displacement of a fluid particle from its original position
λ = coefficient of heat conduction, or wavelength
μ_L = molecular viscosity
μ_T = turbulent viscosity
ν_L = kinematic viscosity of laminar flow
ν_T = kinematic viscosity of turbulent flow
ξ = relaxation coefficient of disintegration for turbulent eddies
ξ_T = dispersion coefficient of turbulence
ρ = instantaneous density
ρ_0 = original density prior to the disturbance
σ_k = Prandtl number for turbulent kinetic energy
σ_ϵ = Schmidt number for dissipation of turbulent kinetic energy
ϕ = dissipation function
ψ = dispersion function
Ω = instantaneous vorticity
Ω_0 = original vorticity prior to disturbance
$\bar{\Omega}$ = time-averaged vorticity
ω = circular frequency of the disturbance wave
ω_0 = angular velocity of the vortex core
$' = \frac{\partial}{\partial y}$ = differentiation with respect to y

equal to the critical amount stored in the eddies previously by turbulent energy production. This is actually the energy exchange between the oriented collective flow and the discretized eddies. Therefore, the stronger the destabilizing factors, the greater is the turbulent kinetic energy production. We arrange II and III together:

$$G_k = \mu_T \left\{ \left| \left[\left(\frac{\partial u_i}{\partial x_j} + \frac{\partial u_j}{\partial x_i} \right) + 2\Omega_{ij} \right] \frac{\partial u_i}{\partial x_j} \right| - \text{sign}(u_i) l \frac{\partial |\Omega_{ij}|}{\partial x_j} \frac{\partial u_i}{x_j} \right\} \tag{10}$$

Group II corresponds to the viscous dissipation in the momentum equation and must use the absolute value in equation (10). If $\text{II} < 0$, the corresponding terms in the momentum equation should take the negative sign. Group III corresponding to the third-order partial derivative of velocity in the momentum equation represents the eddy dispersion effect. When the negative dispersion force is great and stratification effect is strong the soliton character of eddies predominates and vortex disintegration is delayed. Condition (7) gives the quantitative relation of the effects on turbulent flow stability. From this expression the relaxation coefficient of eddy disintegration ξ is defined as follows:

In disintegration and dissipation mode

$$\text{III} \geq 0,\ \xi = 1 - \frac{\text{I}}{|\text{II}| + \text{III}},\ \text{I} \leq 0,\ \xi = 1,\ \xi_{\min} = 0;$$

In negative dispersion mode

$$\text{III} < 0,\ G_k > 0,\ \xi = 0;$$

In mixed dissipation and negative dispersion mode

$$\text{III} < 0,\ G_k > 0,\ \xi = 1 - \frac{\text{I} - \text{III}}{|\text{II}|};\ (\text{I} - \text{III}) < 0,$$

$$\xi = 1,\ \xi_{\min} = 0.$$

From these modes the control equations for various turbulence patterns of incompressible flow may be formulated.

$\text{II} < 0$, the momentum equation for strong vorticity is:

$$\frac{\partial u_i}{\partial t} + u_j \frac{\partial u_i}{\partial x_j} = \frac{-1}{\rho} \frac{\partial p}{\partial x_i} + \frac{\partial}{\partial x_j} (\nu_L - \nu_T) \left(\frac{\partial u_i}{\partial x_j} + \frac{\partial u_j}{\partial x_i} \right) - \frac{\partial}{\partial x_j} \nu_T \left[2\Omega_{ij} + \text{sign}(u_i) C_0 \frac{k^{3/2}}{\epsilon} \frac{\partial |\Omega_{ij}|}{\partial x_j} \right] \tag{11}$$

$\text{II} > 0$, the momentum equation for weak vorticity is:

$$\frac{\partial u_i}{\partial t} + u_j \frac{\partial u_i}{\partial x_j} = \frac{-1}{\rho} \frac{\partial P}{\partial x_i} + \frac{\partial}{\partial x_j} (\nu_L + \nu_T) \left(\frac{\partial u_i}{\partial x_j} + \frac{\partial u_j}{\partial x_i} \right) + \frac{\partial}{\partial x_j} \nu_T \left[2\Omega_{ij} - \text{sign}(u_i) C_0 \frac{k^{3/2}}{\epsilon} \frac{\partial |\Omega_{ij}|}{\partial x_j} \right] \tag{12}$$

The turbulent kinetic energy k and dissipation rate ϵ equations are

$$\frac{\partial k}{\partial t} + u_j \frac{\partial k}{\partial x_j} = \frac{1}{\rho} \frac{\partial}{\partial x_j} \left(\frac{\mu_T}{\sigma_k} \frac{\partial k}{\partial x_j} \right) + \frac{G_k}{\rho} - \xi\epsilon \tag{13}$$

$$\frac{\partial \epsilon}{\partial t} + u_j \frac{\partial \epsilon}{\partial x_j} = \frac{1}{\rho} \frac{\partial}{\partial x_j} \left(\frac{\mu_T}{\sigma_\epsilon} \frac{\partial \epsilon}{\partial x_j} \right) + C_1 \frac{\epsilon}{\rho k} G_k - C_2 \frac{\epsilon^2}{k} \tag{14}$$

where in the above expressions $\Omega_{ij} = \partial u_j/\partial x_i - \partial u_i/\partial x_j$, $\mu_T = C_\mu \rho k^2/\epsilon$, $l = C_0 k^{3/2}/\epsilon$, $C_0 = 0.38 - 0.41$, $C_\mu = 0.09$, $C_1 = 1.44$, $C_2 = 1.92$, $\sigma_k = 1.0$, $\sigma_\epsilon = 1.3$, for G_k see equation (10). In other conditions the above equations may be simplified.

(*a*) For $\text{II} > 0$, when the vorticity is very weak, or the stratification is very slight or there is strong stretching of the vortex, $\xi = 1$; then equations (12), (13), and (14) degenerate to the k–ϵ equations of [5]. These equations can obtain satisfactory results for pure stretching turbulent flow but for homogeneous shearing flow the computational result is disappointing [6].

(*b*) For $\text{II} < 0$, considering the effects of vorticity and stratification after simplification by the continuity equation, the two-dimensional momentum equations are

$$\frac{\partial u}{\partial t} + u \frac{\partial u}{\partial x} + v \frac{\partial u}{\partial y} = \frac{-1}{\rho} \frac{\partial p}{\partial x} + \nu_L \left(\frac{\partial^2 u}{\partial x^2} + \frac{\partial^2 u}{\partial y^2} \right) - \frac{\partial}{\partial y} \nu_T \Omega - \text{sign}(u) C_0 \nu_T \frac{k^{3/2}}{\epsilon} \frac{\partial^2 |\Omega|}{\partial y^2} \tag{15}$$

$$\frac{\partial v}{\partial t} + u \frac{\partial v}{\partial x} + v \frac{\partial v}{\partial y} = \frac{-1}{\rho} \frac{\partial p}{\partial y} + \nu_L \left(\frac{\partial^2 v}{\partial x^2} + \frac{\partial^2 v}{\partial y^2} \right) + \frac{\partial}{\partial x} \nu_T \Omega - \text{sign}(v) C_0 \nu_T \frac{k^{3/2}}{\epsilon} \frac{\partial^2 |\Omega|}{\partial x^2} \tag{16}$$

$$G_k = C_\mu \frac{\rho k^2}{\epsilon} \left\{ \left| 2 \left(\frac{\partial u}{\partial x} \right)^2 + 2 \left(\frac{\partial v}{\partial y} \right)^2 - \Omega^2 + 4 \frac{\partial u}{\partial y} \frac{\partial v}{\partial x} \right| - C_0 \frac{k^{3/2}}{\epsilon} \left[\text{sign}(u) \frac{\partial |\Omega|}{\partial y} \frac{\partial u}{\partial y} - \text{sign}(v) \frac{\partial |\Omega|}{\partial x} \frac{\partial v}{\partial x} \right] \right\} \tag{17}$$

The vorticity is $\Omega = \dfrac{\partial v}{\partial x} - \dfrac{\partial u}{\partial y}$; $\dfrac{\partial^2 |\Omega|}{\partial x^2}$ and $\dfrac{\partial^2 |\Omega|}{\partial y^2}$ are the third-order spatial derivatives of the velocity components. The last term on the right of both equations (15) and (16) is the dispersive force per unit mass. The term $-(\partial/\partial y)\nu_T \Omega$ in (15) and $+(\partial/\partial x)\nu_T \Omega$ in (16) is the orientation force per unit mass.

Numerical computations showed that the curling directions of the horseshoe vortices were determined mainly by the orientation force, while turbulent energy inversion was by the dispersive force. For $\text{II} < 0$, equation (11) is the most important result of research of interaction between dissipation and dispersion. Many perplexing turbulence problems are related with this equation. Most previous models for turbulence may be included in equation (12) for the case $\text{II} > 0$. These two equations coexist. In previous works equations like (11) were absent.

Negative Dispersion and Energy Inversion

Negative dispersive force has special significance. It rectifies the random motion of micro-eddies into the directed collective flow. This is energy inversion or feedback. The following is an example.

Superimpose a field of fluctuating eddies on the background of a plane circular vortex field. This composite vortex field is composed of many concentric layers containing in each a population of arbitrary shaped micro-eddies (Fig. 2*a*). Concentric circles *b*–*b*, *a*–*a*, and *c*–*c* are streamlines of the background vortex. The tangential velocity distribution along r is shown in Fig. 2(*b*). Observe two adjacent micro-eddies sandwiched between streamlines *b*–*b*, *a*–*a*, and *c*–*c*. In relative motion each eddy retains its vorticity Ω due to shear between the layers. Select $0'$ on *b*–*b* and $0''$ on *c*–*c*, respectively, as the instantaneous centers of rotation for the inner and outer eddy. On $a-a$, the contacting pair of eddies imparts an upstream disturbing velocity $u = \frac{1}{2}\Omega l + \frac{1}{2}\Omega l = \Omega l$, reducing the maximum tangential velocity to $U - u$. The velocity distribution along r across the vortex core boundary $a-a$ is smoothed into the curve *bHc* instead of *bac* (Fig. 2*b*). This is the result of vorticity diffusion due to turbulent viscosity.

Assume the inner eddy is propagating radially outward with

disturbing velocity $+v$, and the outer eddy is propagating inward with disturbing velocity $-v$. Each eddy with its angular velocity $\frac{1}{2}\Omega$ about the instantaneous center of rotation will generate the Coriolis force per unit mass $F=\Omega v$ acting in the same direction as U(Fig. 2*a*). The Coriolis force in this way converts the kinetic energy of fluctuating eddies into the directed collective flow. This is negative dispersion or energy inversion. Lin [3] stated a similar proposition. On streamline $a-a$ the gradient of vorticity with respect to radius $\partial^2\Omega/\partial r^2$ has the maximum value which produces strong negative dispersion in such region. The excited micro-eddies possess the duality of wave and particle. Their behavior follows the Schrödinger equation. The fluid layers on both sides of $a-a$ containing micro-eddies of scale l may be considered as a "wave guide." Only eddies with scale or wavelength less than or equal to a critical value (the cutoff) wavelength), can be rectified into directed collective flow. Longer wavelength than l or small wave number than m can not be rectified.

When the strength of eddy vorticities on opposite sides of the dividing streamline a–a are different, the amounts of rectified kinetic energy are different. For example, in a passive wake vortex, due to pressure stratification the vorticity is stronger in the internal side causing greater drop of stagnation temperature after rectification.

In a wall boundary layer disturbances come only from the main external flow. Fluctuating eddies in the unstable layer are rectified to unidirectional flow by Coriolis force F (Fig. 3) forming the 1/7 power velocity profile of the turbulent boundary layer. It is worthwhile to mention that negative dispersion occurs only when the negative dispersive energy is greater than the dissipative energy.

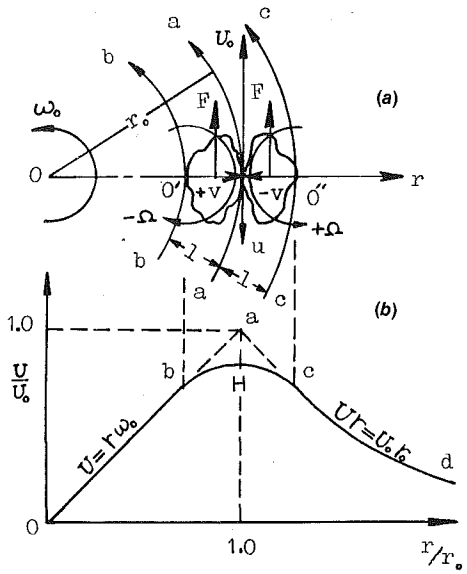

Fig. 2 Composite vortex field

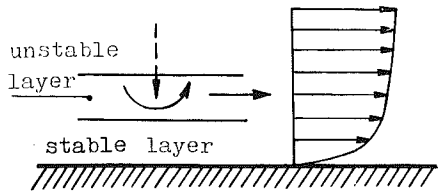

Fig. 3 Rectification of eddies in turbulent boundary layer to maintain the 1/7 power velocity profile

Energy Equation of Turbulent Flow

In the energy equation of turbulent flow the dissipation function ϕ and dispersion function ψ coexist

$$\frac{\partial h}{\partial t}+v_j\frac{\partial h}{\partial x_j}=\frac{1}{\rho}\frac{\partial p}{\partial t}+\frac{1}{\rho}v_j\frac{\partial p}{\partial x_j}+\frac{1}{\rho}\frac{\partial}{\partial x_j}\left(\lambda\frac{\partial T}{\partial x_j}\right)+\frac{\phi}{\rho}+\frac{\psi}{\rho} \tag{18}$$

$$\phi=\mu_T\left|\left[\left(\frac{\partial u_i}{\partial x_j}+\frac{\partial u_j}{\partial x_i}\right)+2\Omega_{ij}\right]\frac{\partial u_i}{\partial x_j}\right|+\mu_L\left(\frac{\partial u_i}{\partial x_j}+\frac{\partial u_j}{\partial x_i}\right)\frac{\partial u_i}{\partial x_j} \tag{19}$$

$$\psi=-\xi_T\,\mathrm{sign}(u_i)\frac{\partial|\Omega_{ij}|}{\partial x_j}\frac{\partial u_i}{\partial x_j} \tag{20}$$

In any case $\phi\geq 0$. For negative dispersion $\psi<0$. For positive dispersion $\psi>0$ which contributes to disintegration of eddies by frequency "scattering" of the disturbance waves. The negative dispersion region with maximum vorticity gradient is a nonlinear, unstable thermodynamic subsystem transferring mass and energy with the surroundings by means of the disturbing waves. Negative dispersion follows the "dissipative structure" theory proposed by Prigogine. This theory stated that when a nonlinear system deviates far away from equilibrium a new orderly dissipative structure is generated. The "wave guide" effect in Fig. 2 is a typical dissipative structure.

Interactions of disturbing waves and solitons enable a nonlinear system to jump from an unstable to a stable mode. Many interesting phenomena are produced in this way, such as energy inversion in the vortex tail behind a bluffbody, coherent horseshoe vortices in a turbulent boundary layer, temperature separation in the Ranque–Hilsch tube, tornados, typhoons, oceanic vortex, vortex in the galaxy, and the autoregulatory microcirculation of blood flow.

Selection of Empirical Coefficients

Turbulent eddies in different stages of evolution and disturbing waves at different frequencies possess different rates of decay in different regions. Diffusion of gradients of some property was used in the control equations. In order to obtain the temporal mean parameters, at least one empirical coefficient C_0 is required in equations (11)–(17). This is due to the lack of knowledge about the mean frequency of the propagating disturbing vorticity waves. Regretfully, this frequency is indirectly expressed by the gradient of vorticity, the turbulent mixing length, and C_0. From experiments the calculated value is $C_0=0.38$–0.41.

The empirical coefficients of the k–ϵ model fit the experimental data of isotropic turbulence. Using these coefficients we may obtain satisfactory calculation results for pure stretching flows [6], but very poor results for pure shearing flows. When the vorticity is very weak, equations (12)–(14) degenerate to the k–ϵ model equations. So we just need a set of coefficients suitable for pure stretching. From G_k(equation (10)), the term related to vorticity is arranged bilaterally with the deformation rate tensor. This means that in either extreme case of pure stretching or pure shear, the same empirical coefficient may be used. Our computations have shown that adopting the coefficients from the k–ϵ model equations, the results are satisfactory for both pure shear and pure stretching flows.

Computational Procedure

1 Solve the nondimensionalized Navier–Stokes equations for the flow field using the "equivalent Reynolds number"

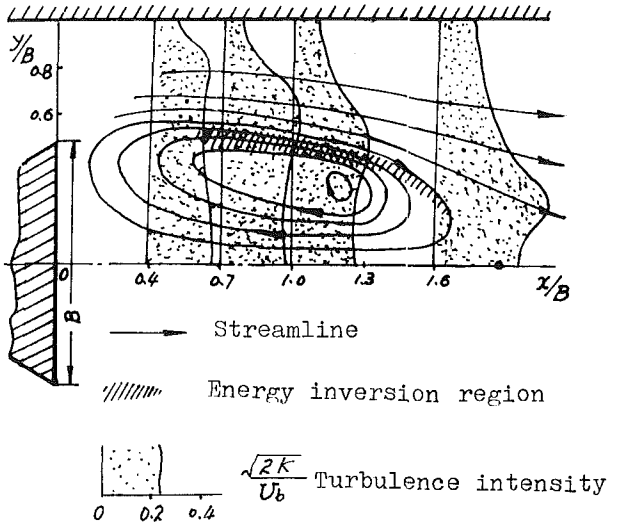

Fig. 4 Computational result of the wake vortex field behind a bluff-body

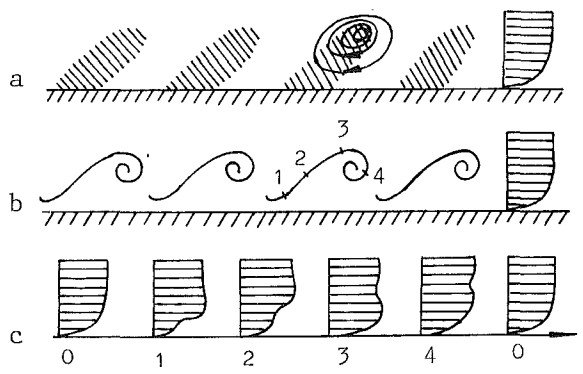

Fig. 5 The coherent vortex pattern in a two-dimensional turbulent boundary layer: (*a*) vortex speckles in fixed coordinates; (*b*) vortex curls in moving coordinates; (*c*) periodic change of velocity profiles

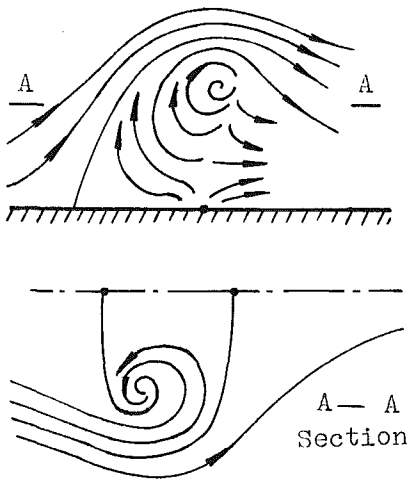

Fig. 6 The horseshoe vortex in moving coordinates transformed from calculated data in fixed coordinates: (*a*) side view, (*b*) top view

which is several hundred times smaller than the inlet Reynolds number.

2 Use the above solution and the inlet Reynolds number as input to the computation of the discretized equations (10)–(14) by the ADC method from [7].

3 Both equations (11) and (12) are stored in the computer. At each grid point and each iterative step, equation (8) is checked for proper sign; let the computer choose the suitable equation from (11) and (12).

4 Estimate the relaxation coefficient ξ prior to finding the turbulent kinetic energy k at each grid point.

5 To show the significance of each term in the control equations, the following tests are made:

Deliberately omit a certain term at first, then retain all the terms in the control equations. Compare the two calculated flow patterns with available experimental results.

6 Repeat the numerical experiments to ratify the selected constants C_0, C_μ, C_1, C_2, σ_k, σ_ϵ.

Calculation of a Wake Vortex

To simulate a turbojet afterburner as in [8], the wake vortex behind a 60 deg wedge in a rectangular duct with blockage ratio 0.5 and inlet Re of 6.9×10^4 was calculated by equations (10)–(14). The streamlines of recirculating flow, the distribution of turbulence intensities, and the energy inversion region are shown in Fig. 4. These agree very well with the experimental results of [9]. By equation (11) with $C_0 = 0.38$ to 0.41, the sum of orientation and dispersion forces in the energy inversion region is greater than zero. This corresponds to "negative viscosity." If the third-order derivative term is omitted then negative viscosity also disappears. This example supports our theory that negative dispersion results in turbulent energy inversion. In a highly compressed, high pressure gradient, and high centrifugal force region, the dissipation of turbulent kinetic energy does not follow the Kolmogoroff law. Disintegration of eddies stops in such regions.

Calculation of Turbulent Boundary Layer

Using equations (10)–(14) the periodic coherent vortex patterns within a two-dimensional turbulent boundary layer have been calculated and are shown in Fig. 5.

The boundary conditions were: The velocity along the wall and the pressure gradients and vorticity gradients normal to the wall were all equal to zero. The time-averaged velocity profile of the turbulent boundary layer conformed to the 1/7 power law. The value of C_0 must be kept in the range 0.38–0.41. Reducing C_0 to 0, the velocity profile changed to that of laminar flow. Increasing C_0 greater than 0.41, the computation diverged. These explain that the 1/7 power law is determined mainly by the negative dispersion force. Only with a suitable value of C_0, the periodic coherent vortex pattern is then generated. In fixed coordinates the oblique vortex speckles appear as in Fig. 5(*a*). Maximum vorticity is located at the vortex eye. In moving coordinates those speckles appear as periodic curls in Fig. 5(*b*). The velocity profiles corresponding to different points 1, 2, 3, . . . on a certain curl are plotted in Fig. 5(*c*). It may be seen that initially the profile is indented at the location of maximum $\partial^2\Omega/\partial y^2$. Then the indentation gradually moves upward until the profile recovers to its 1/7 power shape again in a full period. According to equations (15) and (16) the curling directions are dictated by the orientation forces. Numerical experiments obtained the following facts:

If the negative dispersion term in equation (11) is omitted, due to the input of 1/7 power velocity profile at the inlet, a single incomplete curl appears only once but never again.

If the negative dispersion term is retained but the orientation term is omitted, then in spite of the 1/7 power input profile no coherent curls are generated.

These indicate that orientation forces generate the coherent curls and negative dispersion forces maintain the periodicity of velocity profiles.

The same computational technique and boundary conditions were applied to a three-dimensional turbulent

boundary layer. An array of three-dimensional horseshoe vortices was obtained, one of which is shown in Fig. 6.

There exist fast and slow speckles in the sublayer. The center line of the horseshoe vortex coincides with that of the slow speckles. Such vortex structure conforms with that reported in [10]. Computation also discovered that in a diffuser duct adverse pressure gradient excited the coherent flow pattern in the boundary layer. Periodicity of the flow pattern is directly proportional to the external flow velocity and inversely to the boundary layer thickness. By assessing the sum of orientation and dispersion forces, the "equivalent Reynolds stresses" may be evaluated. Thus, the anisotropic turbulent viscosities can be found.

Conclusions

1 Turbulence is a physical process of interaction between dissipation and dispersion of turbulent eddies.

2 There exist two momentum equations for turbulent flow: equation (11) for strong and equation (12) for weak vorticity.

3 The momentum equation for strong vorticity describes the nature of coherent flow patterns, energy inversion, and the delay of eddy disintegration through the energy spectrum.

4 Turbulent energy equation (18) contains both dissipation and dispersion functions. Dispersion functions may be positive or negative depending upon the "dissipative structure" of turbulence.

References

1 Miles, J. W., "Solitary Waves," *Ann. Rev. Fl. Mech.*, Vol. 12, 1980, pp. 11-43.

2 Zhang, Xueh-Ming, "Theory of Pseudo-Potential and Solitons in Modern Physics," *J. Mathematical Physics*, Vol. 1, No. 1, 1981, p. 59 (in Chinese).

3 Lin, C. C., "Galaxy, Turbulence and Plasmas," *Symposium of the 2nd Asian Con. Fl. Mech.*, p. 1.

4 Gao, G., "On the Localized Stability of Vortices," 6th ISABE Symposium Paris, 1983.

5 Launder, D. E., and Spalding, D. B., "The Numerical Computation of Turbulent Flow," *Comp. Method in App. Mech. and Eng.*, Vol. 3, 1974, pp. 269-288.

6 Reynolds, W. C., "Computation of Turbulent Flows," *Ann. Rev. Fl. Mech.*, Vol. 8, 1976, p. 183.

7 Gao, G., "The ADC Method; A Rapid Numerical Method for Solving Three Dimensional Navier-Stokes Equation," ASME Paper No. 82-GT-76.

8 Gao, G., "Analysis of the Bluffbody Wake Vortex Calculated by the k-ϵ Turbulence Model," *J. Eng. Thermophysics*, Vol. 5, No. 2, 1984, p. 210.

9 Fujii, S., et al., "Cold Flow Tests on a Bluff Body Flame Stabilizer," *J. Fl. Eng.*, Vol. 100, Sept. 1978, p. 323.

10 Head, M. R., and Bandyopadhyay, P., "New Aspects of Turbulent Boundary Layer Structure," *J. of Fluid Mech.*, Vol. 107, 1981, pp. 297-337.

Shi Jing

Han Jianyuan

Nanhwa Powerplant Research Institute

Zhou Shiying

Zhu Mingfu

Shengyang Aero-Engine Research Institute

Zhang Yaoko

The Academy of Science of China

She Mengyu

Tsinghua University

An Investigation of a Highly Loaded Transonic Turbine Stage With Compound Leaned Vanes

An investigation was made to compare the performance of a highly loaded transonic turbine stage with and without compound leaned vanes. In both cases, velocity distribution along the vane surfaces was calculated from a full three-dimensional time-marching finite volume method. Nozzles were tested in a wind tunnel. Through rig tests, velocity profile at the stage exit was measured and the stage overall performance obtained. Performance in both tip and hub regions was improved by using the compound leaned vanes so that the stage efficiency increased by approximately 1 percent. The improvement is particularly remarkable at off-design points.

Introduction

Generally speaking, the aspect ratio of a high-pressure turbine in high-flow engines and small engines is comparatively low, and secondary loss shares 60-70 percent in total loss occurred in such a turbine. High potential of increasing efficiency lies in minimizing secondary losses. A simple and effective way to do that is to use compound leaned vanes. On the topic, subsonic long vanes [1, 2] and transonic short vanes [3, 4] were investigated. In order to demonstrate the effects of compound leaned vanes on a transonic turbine stage with low aspect ratio, an investigation has been carried out at NPRI. Firstly, a highly loaded transonic turbine model with conventional vanes was tested [5]. That stage was used as a basic stage. Secondly, the same stage, with compound leaned vanes instead of conventional vanes, was tested. Both vanes were examined in a wind tunnel to set up their aerodynamic behavior. Furthermore, a full three-dimensional flow field has also been calculated for the two kinds of vane. This paper is to analyze and evaluate the results obtained from the work mentioned above.

Basic Stage Design

As pointed out, the basic stage is a highly loaded transonic stage. The flow path and parameters are shown in Fig. 1, and velocity diagram at mean diameter in Fig. 2. Vane height $H = 48.75$ mm. Relative height of vane $H/R_{mid} = 1/3.77$, vane aspect ratio $H/B = 0.97$. The radial stacking line of vane sections is positioned near the throat.

The basic stage design was of a controlled vortex type. The work varied as parabolic distribution along blade height so as to reduce the loss at both ends and all sections can be operated at a favorable condition, especially sections near two walls. As a result of using such a work distribution, the following advantages can be obtained: decreasing the flow deflection at both ends of the vane and the Mach number at the outlet, increasing the difference of flow angle of the blades between inlet and outlet, decreasing the turning angle, therefore decreasing the transverse pressure gradient across the passage at both ends of vanes and blades.

To obtain profiles with good performance that are suited to

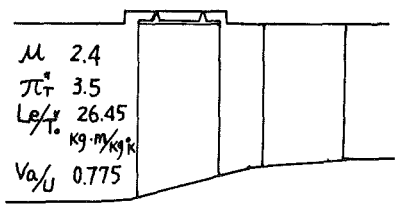

Fig. 1 Flow path

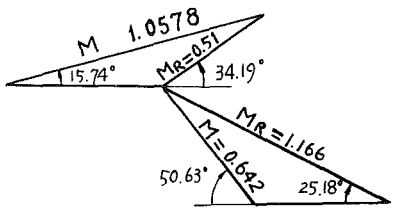

Fig. 2 Velocity diagram at mean diameter

Contributed by the Gas Turbine Division and presented at the 1985 Beijing International Gas Turbine Symposium and Exposition, Beijing, People's Republic of China, September 1-7, 1985. Manuscript received at ASME Headquarters May 6, 1985. Paper No. 85-IGT-8.

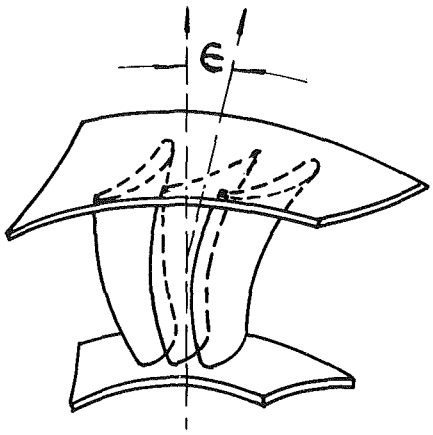

Fig. 3 Scheme of compound leaned vanes

transonic conditions, contours of the vanes and the blades, in particular the contour of suction surface, have been designed with great care. Some typical sections were tested in linear cascades. Results showed their performance was very satisfactory not only at design point but also at off-design point [5].

Design of Compound Leaned Vanes and the Flow Field Calculation

It is well known that secondary flow in a turbomachine resulted from interaction of boundary layers on end walls and pressure gradient in transverse and radial direction caused by main flow. Needless to say, the situation of the boundary layers and the pressure gradient in such directions are two important factors. Boundary layers can be controlled, thus loss can be reduced, by sucking the layers away or injecting flow with higher energy. However, they are more costly. Transmitting fluid particles with lower energy from the boundary layer on the end walls to the suction surface, the transverse pressure gradient across the passage serves as the dynamic source that causes the secondary flow. The transmission of lower energy particles accumulating near the two end walls in the radial direction depends on the radial pressure gradient. Therefore, the intensity and extension of the secondary flow would be affected by the magnitude and the direction of the radial pressure gradient.

As we know, the equation of motion in the radial direction on stream surface S_2 is

$$\frac{1}{\rho}\frac{\bar{\partial}P}{\partial r} = \frac{V_\theta^2}{r} + \frac{V_m^2}{r_m}\cos\phi - V_m \sin\phi \frac{\bar{\partial}V_m}{\partial m} + \mathrm{Fr}$$

where

$$\mathrm{Fr} = -\frac{1}{\rho r\partial\theta}\frac{N_r}{N_\theta} = -\frac{1\partial P}{\rho r\partial\theta}\tan\epsilon$$

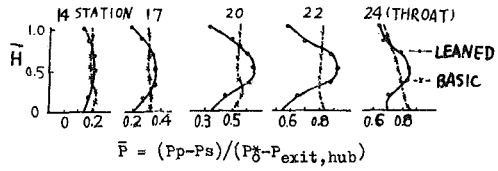

Fig. 4 Pressure difference between pressure and suction surface in a cascade passage

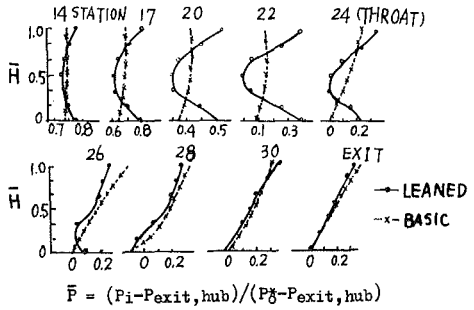

Fig. 5 Distribution of relative pressure on suction surface

It is obvious that the radial pressure gradient can be changed by making use of the radial component of flow surface force Fr. Correspondingly, the pressure gradient on stream surface S_1 will also be altered. When the manner that the sections of a vane or blade are stacked changes in such a way that can cause a radial component of stream surface force producing an advantageous pressure distribution, "leaned vanes" are obtained. At the hub, the lean that causes pressure surface to incline toward the inner wall of flow path is referred to positive, but at the tip, the lean that causes it to incline toward the outer wall is negative (Fig. 3). The inclined angle at each end is about 25 deg.

As pointed out earlier, different flow field exists in compound leaned vanes and ordinary vanes. A full three-dimensional calculation of the flow field for both vanes is carried out by using the time-marching finite volume method [6]. The computational results showed that the pressure difference between pressure and suction surface in a cascade passage somewhat increases at midspan, but decreases somewhat at both ends (Fig. 4). That is to say, the transverse pressure gradient is decreased at two ends of vane so that the transmittal of lower-energy fluid particles from the boundary layer near the end walls to suction surface is suppressed, which results in substantially minimizing losses at tip and hub. In addition, the radial pressure gradient existing at both ends can be changed by compound leaned vanes as it was to be desired. Circumferential component of the absolute velocity increases with the increasing of flow expansion from entrance to geometric throat (Station 24 in Fig. 5) of the passage on suction surface; the radial component of the stream surface

Nomenclature

B = chord of the airfoil
F = stream surface force
H = vane height
Le = effective work
M = Mach number
N = stream surface vector
$\bar{n}$ = relative value of rotational speed
r = radius
r_m = curvature radius
T = temperature
u = blade wheel speed
V = velocity
α = outlet flow angle of vanes
ϵ = leaned angle of vanes in circumferential direction
η = efficiency
μ = load coefficient
π = pressure drop ratio
ρ = density
ρV_a = density flow
ρ_t = reaction
ϕ = angle of stream line

Subscripts

a = axial
D = design
i = local
m = meridional
mid = midradius
r = radial
t = theoretical
θ = circumferential

Superscripts

$*$ = stagnation
$-$ = stream surface or relative value

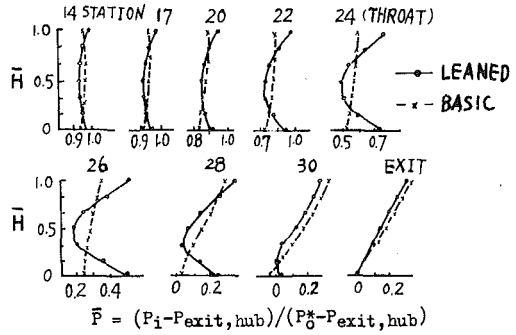

Fig. 6 Distribution of relative pressure on mean line of a passage

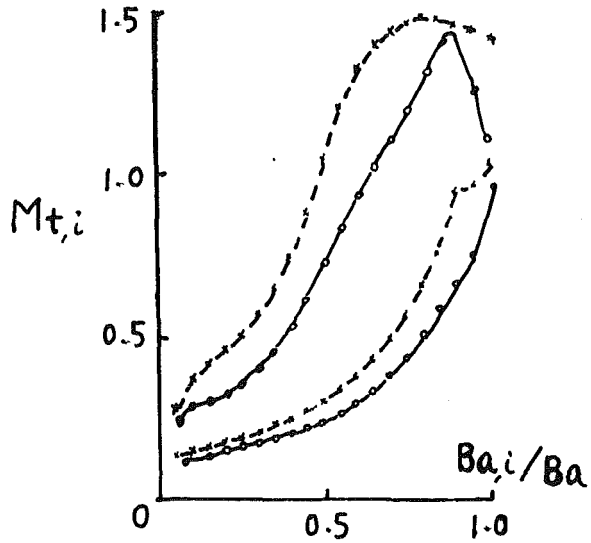

Fig. 7 Computational distribution of surface velocity: hub section

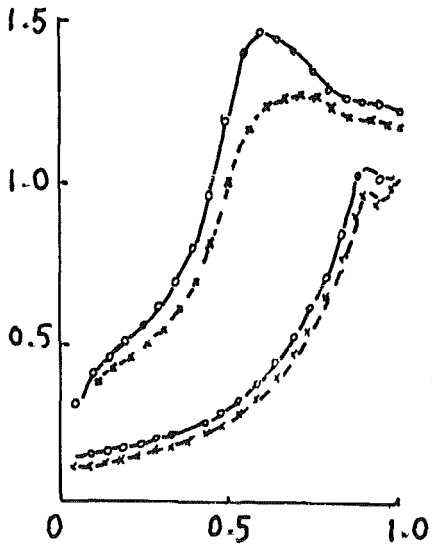

Fig. 8 Computational distribution of surface velocity: midspan section

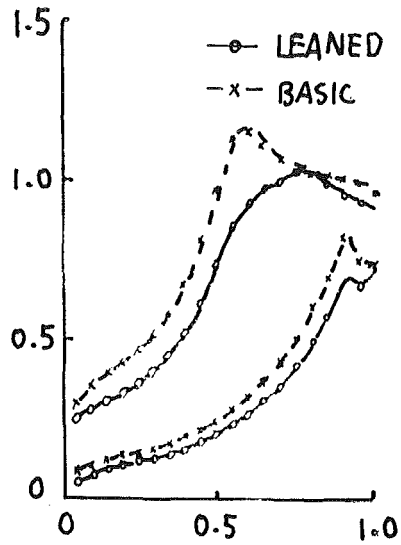

Fig. 9 Computational distribution of surface velocity: tip section

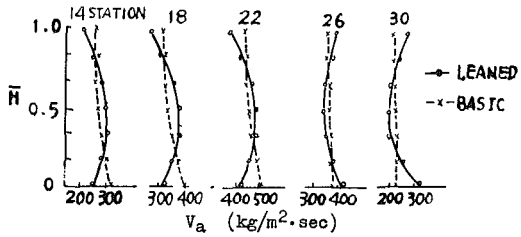

Fig. 10 Density flow distribution

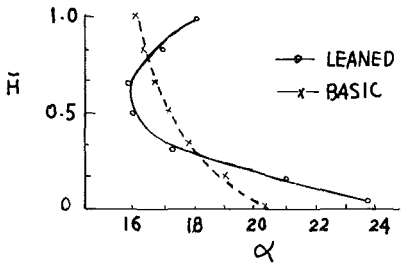

Fig. 11 Computational distribution of flow angle at vane exit

force, however, increases seriously. Therefore, the difference of pressure gradient between both vanes would reach to its maximum value at stations near the geometric throat and would be reduced downstream of the throat, since the more supersonic expansion, the larger circumferential component and the weaker action of the stream surface force there. This difference would even become less at gap stations (Fig. 5). The development of secondary flow is greatly suppressed by the significant alteration of the radial pressure gradient at both ends of vanes before the throat. The difference appears to be diminished after the throat, but its effects on losses seem to weaken as well, because the separate point is located in the rear of the suction side if separation occurs. The difference of relative pressure gradient at the mean line of passage varies with the same tendency as that on suction surface except that the value is smaller (Fig. 6). The difference on the pressure side is very small. The pressure gradient at the tip and hub of compound leaned vanes directs in the opposite direction due to the action of Fr. Static pressure rises toward two end walls and decreases at midspan. Correspondingly, the Mach number on the suction surface at both ends decreases, with a greater reduction value and a more rearward peak position at hub (Fig. 7 and Fig. 9), having a favorable effect on minimizing losses near the path walls. The Mach number rises slightly at midspan sections (Fig. 8). As for the outlet Mach number, it reduces at hub sections, rises at tip, and closes to that at midspan.

The density flow distribution of the compound leaned vane is shown in Fig. 10. At both ends, it is less than that of the basic vane at stations upstream of the throat and larger at stations downstream of it. This assures more uniform flow distribution at tip and hub of the turbine blade inlet and results in less losses there.

In addition, flow angles near two walls at the vane outlet

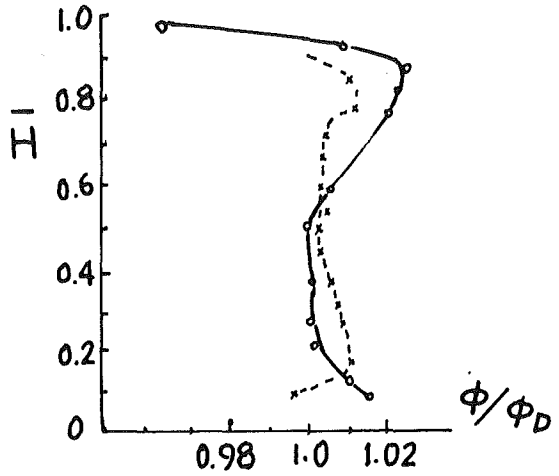

Fig. 12 Radial distribution of nozzle vane velocity coefficient

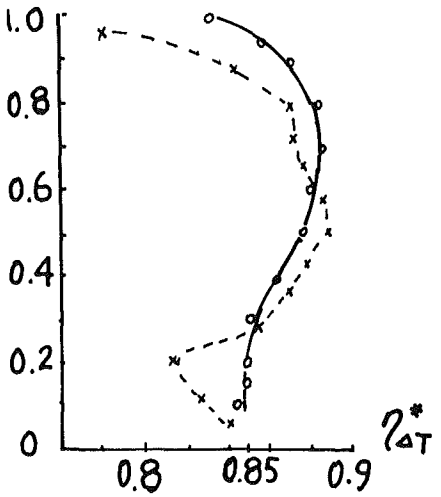

Fig. 13 Radial distribution of stage efficiency

would increase in the case of using compound leaned vanes (Fig. 11). This will cause the turbine blade to operate at negative incidences at both ends and improve aerodynamic behavior in those places.

The full three-dimensional calculation has indicated that the flow field of compound leaned vane reflects the design features to a large extent and fulfills the design concept satisfactorily.

Basic Results of Experiment

The nozzles with compound leaned vane and basic vane were tested individually in a wind tunnel. Radial and circumferential measurements were taken within an annular cascade window continuously and automatically, by using wedge-shaped total-pressure direction probes downstream of the cascade, at a total of 15 sections along the vane height. Shock-wave correction was made under supersonic conditions. In the meantime, static pressures on both outer and inner walls were also recorded. Mean values of such parameters were arithmetically averaged along the corresponding constant radius. The stagnation efficiencies are based on arithmetic mean values measured by five multipoint total-pressure probes located at 71 cm downstream from the blade trailing edge, and on torque measured by a hydraulic dynamometer. Since the measurement position is far enough from the exit so that all the loss can be taken, the efficiency obtained is convincing.

Compared with the basic vane, losses have been reduced

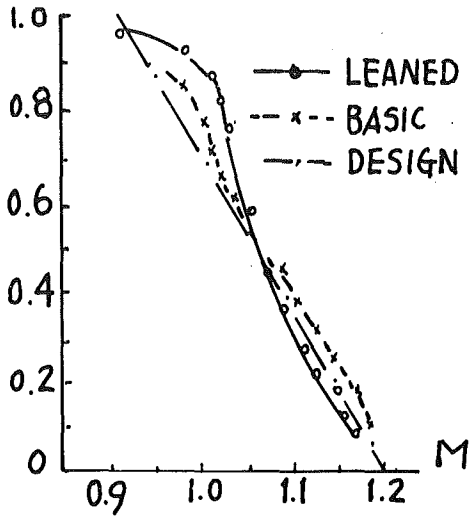

Fig. 14 Radial distribution of Mach number at vane exit

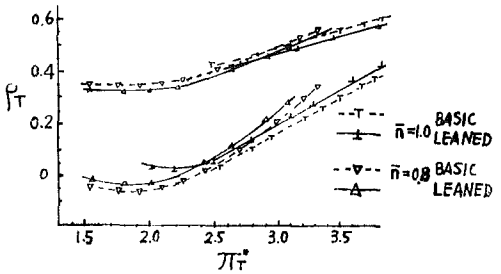

Fig. 15 Variation of reaction at hub and tip with pressure drip ratio

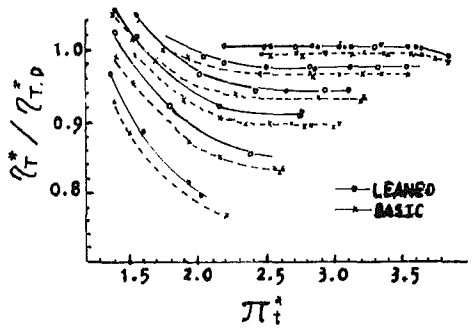

Fig. 16 Comparison of stage relative efficiency

significantly in the upper part and in the region approximately 20 percent of vane height at hub in the case of compound leaned vane. Velocity coefficient, however, was somewhat reduced in the region of about 20-45 percent of the height (Fig. 12). The active effects of the compound leaned vane can be seen obviously. The temperature difference efficiency distribution measured at stations downstream of the stage shows similar results to those of the nozzle tested in wind tunnel (Fig. 13).

The comparison of experimental results between the basic stage and the stage with compound leaned vanes has completely verified the design intention and conclusion from theoretical analysis. The pressure drop ratio obtained from static pressure on both outer and inner walls has indicated that the ratio in the stage with compound leaned vanes increases at hub and decreases at tip, and the absolute increment of the former is greater than the latter. The Mach number distribution along the vane height downstream of the cascade obtained from wind tests has also shown that the distribution varies toward a more uniform one when the leaned vanes are used (Fig. 14). As a result, the reaction of the stage increases

at the hub and decreases at the tip (Fig. 15). The reduction of losses at both ends of the nozzle vanes, the increase in the density flow at the tip and hub of the vane exit, and the equalization of outlet Mach numbers all cause the flow that enters turbine blades at both ends to be more uniform; thus, the boundary layer becomes thinner. The alteration of stage reaction, the tendency for the incidence at blade tip and hub to vary toward a negative value, and the ability of flow acceleration at both ends decrease the losses. In Fig. 16, the stagnation efficiency value of two stages divided by the design efficiency value of the basic stage is used to indicate the efficiency improvement. It is 0.8 percent at design speed and 1.6-2.0 percent at lower speeds for the leaned vane stage. For the same speed, the improvement is slightly greater in the case of lower pressure drop ratio. At off-design; turbine stages generally operate at lower reactions or larger incidence. Compound leaned vanes, however, can play a role of changing flow field at various working conditions, increasing the reaction level at the hub from a lower, even negative, value or decreasing the positive incidence, thus giving rise to a greater advantage.

Conclusions

1 By using compound leaned vanes, the transverse pressure gradient across flow passage at both ends is decreased, and the transmission of lower energy particles to suction surface is diminished. Furthermore, a positive radial pressure gradient at the tip is increased and a negative pressure gradient at the hub is obtained. These will not only control the development of secondary flow occurring within the nozzle vane passages but also cause the flow that enters the next blade row to vary toward a uniform field.

2 The tests have shown a substantial improvement in performance at both end walls from using compound leaned vanes. Secondary losses are appreciably reduced with only slightly reduced performance at midspan.

3 The reaction can be raised at the hub and reduced at the tip by compound leaned vanes. For a highly loaded transonic turbine stage with vane aspect ratio of 0.97 and design pressure drop ratio of 3.5, the stage with compound leaned vanes has a stagnation efficiency 0.8 percent higher than that of the basic stage with ordinary vanes at design speed and 2 percent higher at lower operating speeds. It has been shown that the compound leaned vanes are useful and effective even in a transonic stage.

Acknowledgments

The authors wish to express their thanks to associate Prof. Wang Zhong-chi of Harbine Industrial University and Prof. Cui Ji-ya of the Beijing Institute of Aeronautics and Astronautics for their kind support during this investigation.

References

1 Deich, M. E., Gubalev, A. B., Filoppov, G. A., and Wang Zhong-chi, "A New Method of Profiling the Guide Vane Cascades of Stages With Small Rations of Diameter to Length," *Teploenergetika*, No. 8, 1962.

2 Wang Zhong-chi et al., "Aerodynamic Calculation of Turbine Stator Cascades With Curvilinear Leaned Blades and Some Experimental Results," Fifth International Symposium on Airbreathing Engines, 1981.

3 Patel, K. V., "Research on a High Work Axial Gas Generator Turbine," SAE 800618, 1980.

4 Liu, H. C., et al., "Application of 3-D Viscous Flow Analysis to the Design of Low-Aspect-Ratio Turbine," ASME Paper No. 79-GT-53.

5 Shi Jing et al., "Design and Experimental Investigation of a High-Loaded Transonic Axial Model Turbine," *Acta Aeronautica and Astronautica Sinica*, Vol. 5, No. 3, Sept. 1984, pp. 280-287.

6 Zhang Yaoko, Gong Zengjin, and Shen Mengyu, "Numerical Tests of Three-Dimensional Flow in a Transonic Turbine," *Acta Aeronautica and Astronautica Sinica*, Vol. 2, No. 3, 1981, pp. 57-75.

Growth of Secondary Flow Losses Downstream of a Turbine Blade Cascade

L. D. Chen
Design Institution,
Chengdu, Sichuan, China

S. L. Dixon
Department of Mechanical Engineering,
The University of Liverpool,
Liverpool, England

Endwall total pressure losses downstream of a low-speed turbine cascade have been measured at several planes in order to determine the changes in secondary flow loss coefficients and the growth of the mixing loss with distance downstream. The results obtained are compared with various published secondary flow loss correlations in an attempt to explain some of the anomalies which presently exist. The paper includes some new correlations including one for the important gross secondary loss coefficient Y_{SG} *with loading and aspect ratio parameters as well as the upstream boundary layer parameters.*

Introduction

The secondary flow losses, which are associated with the streamwise vorticity in the exit flow from turbine blades, are often a very significant fraction of the total losses. Control or minimization of these losses is, therefore, very important in the design of turbines. It is obviously necessary to obtain a quantitative understanding of the influencing parameters for a given turbine geometry and flow condition.

Experiments by Came [1] in 1973 described a series of measurements of secondary loss with varying inlet-wall boundary layer thickness and varying air inlet angle. The averaged secondary loss was correlated with blade loading, aspect ratio and inlet boundary layer parameters.

Morris and Hoare [2] made detailed measurements of several forms of meridional endwall profile and in which the blade aspect ratio and inlet-wall boundary layer thickness were varied. The experimental facility appeared to be the same in every respect to that of Came, except for the addition of a movable "false" wall within the wind tunnel. Two of Came's measurement points are shown corrected in this paper.

The values of Y_{SG} of Dixon and Cooke [3] as determined by experiment showed differences from those determined by the correlation given by Morris and Hoare [2]. However, these correlations were obtained from data measured at 1.35 c in the stream direction from the trailing edge plane whereas Dixon and Cooke [3] obtained their data at 0.18 c in the same direction.

This paper concerns a program of experimental work carried out to determine the effect of flow mixing processes and varying inlet boundary layer thickness on the total pressure losses developed by a low-speed flow through a high-deflection turbine blade cascade.

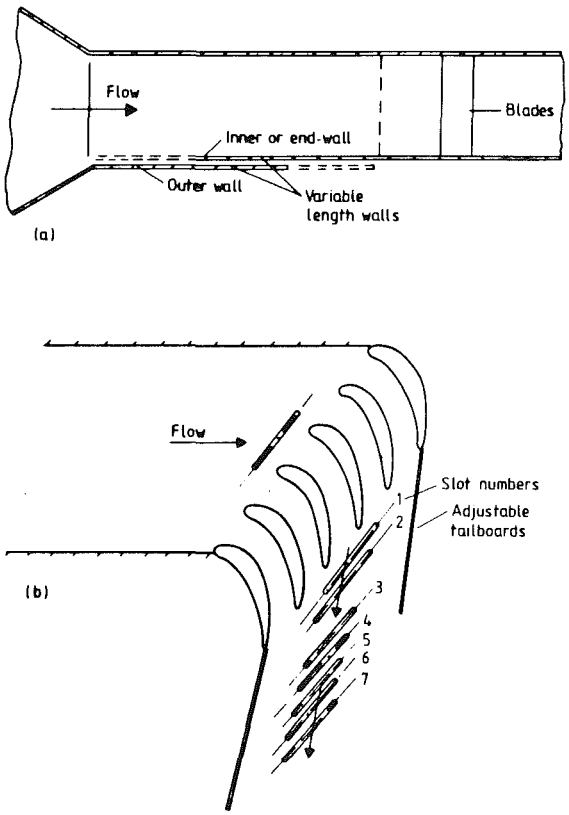

Fig. 1 The tunnel working section (*a*) showing variable length scheme for endwall; (*b*) the blade cascade and position of measurement slots

Experimental Facility

Testing the blade cascade was conducted by means of a low-speed wind tunnel exhausting directly to atmosphere at the cascade exit. The experimental facility was the same in every respect as that of [3], except for the addition of a movable outer wall (Fig. 1*a*) and a pair of adjustable tailboards (Fig. 1*b*) 60 cm long. The thickness of the cascade end wall boundary layer was varied by making alterations to the length of an inner wall or an outer wall.

Contributed by the Gas Turbine Division and presented at the 1985 Beijing International Gas Turbine Symposium and Exposition, Beijing, People's Republic of China, September 1-7, 1985. Manuscript received at ASME Headquarters May 13, 1985. Paper No. 85-IGT-35.

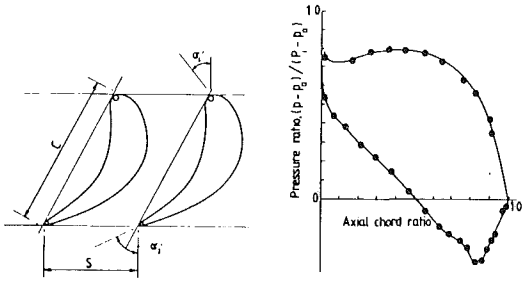

Fig. 2 T113 turbine blades and measured midspan surface pressure distribution

The cascade consisted of six turbine blades with a nominal camber of 100 deg (Fig. 2) made from cast epoxy resin reinforced with glass fiber matting. The main geometric details of the cascade are given in Table 1. The blading section used was based on a parabolic arc camber line with a thickness distribution designated T113 developed by Smith and Johnson [4]. Pressure tappings set into the pressure and suction surfaces on either side of the central blade passage enabled the pressure distributions to be determined. Figure 2 shows the blade surface pressure distributions measured at midspan. Measurements of pressure were also made at 7.5 cm and 2.5 cm from the endwall but as these were little different from the readings obtained at midspan they have been omitted. Testing was conducted at an air speed such that the blade chord Reynolds number was approximately 3.5×10^5 based on the average outlet velocity.

Instrumentation and Measurements

The upstream total pressure in the mainstream was measured with a simple pitot probe, whereas the downstream total pressure traverse was measured with a miniature cranked Kiel probe, 3 mm o.d., and the inlet wall boundary layer was measured with the same Kiel probe. The Kiel probe, or shrouded total-pressure probe, has the important characteristic of being insensitive to large changes in flow direction (i.e., ±40 deg approximately). This characteristic was exploited in this flow investigation by simply setting the probe against the average flow direction. Total pressure readings

Table 1

Blade chord c	27.5 cm
Blade aspect ratio h/c	2.36
Pitch/chord ratio s/c	0.651
Maximum thickness/chord t/c	0.272
Blade inlet angle α_1'	34.8 deg
Blade outlet angle α_2'	−66.05 deg

were transmitted by a short length of plastic tube to a small sensitive pressure transducer (Gaeltec Type 8T). The electrical analogues of total pressure and probe position were input to the A to D converter (AI13) and the numerical values input to the Apple II computer. Probe motion across the blade pitch and along the blade span was implemented by an L.C. Smith traverse gear under computer control. A full area traverse over the range $z = 0.2$ to 32.4 cm (50 percent span) from the endwall was made with about 20 pitchwise sweeps. Close to the end wall about 70 pressure readings were recorded and about 25 toward midspan, the full area traverse taking about 45 min, but less than 30 min without the detailed printout of every measurement point of the traverses. In all the flow traverses a whole blade wake was covered with the readings closely incremented.

The "gross" secondary loss coefficient Y_{SG} was obtained by subtracting the profile loss coefficient Y_P from the mass-averaged total loss coefficient Y_T. It is recognized that Y_P is not equal to the two-dimensional profile loss coefficient. Sharma and Graziani [5] concluded that existing two-dimensional boundary layer calculation methods can substantially underestimate the midspan boundary layer losses in low aspect ratio cascades. One of the main sources quoted by Sharma and Graziani is the well-known work of Langston et al. [6] in which the span/chord ratio was the relatively low value of 0.8077. The present work had a span/chord ratio of 2.36 and the values of Y_P measured over the central part of the span are probably not much different from the two-dimensional value.

It was assumed that the static pressure downstream of the blade was equal to the atmospheric pressure. Subsequent measurements showed this assumption was approximately true. Static pressure measurements were made on the end wall downstream of the trailing edge plane along a line midway between and extending just beyond the tailboards. Values of

Nomenclature

c = blade chord
C_p = static pressure coefficient = $(p - p_a)/\frac{1}{2}\rho V_{2fs}^2$
C_{pr} = diffuser pressure recovery factor = $(\Delta p)/\frac{1}{2}\rho V_{2fs}^2$
h = blade height (or span)
H = shape factor of boundary layer
l = distance from exit plane in flow direction
m = index in power law
p = static pressure
P = total pressure
q = dynamic pressure
Re = Reynolds number
s = blade pitch
V = velocity
x, y, z = axial, pitchwise, and spanwise directions
X = gross secondary loss parameter

$$= \frac{h}{c}\frac{Y_{SG}}{Z}\frac{\cos\alpha_1}{\cos\alpha_2}$$

Y_1 = mass-averaged inlet loss coefficient, relative to exit q
Y_1^* = mass-averaged inlet loss coefficient, relative to inlet q
Y_{2b} = mass-averaged exit boundary layer loss coefficient
Y_p = profile loss coefficient mass averaged in pitch and span directions
Y_{SG} = "gross" secondary loss coefficient
Y_S = "net" secondary loss coefficient = $Y_{SG} - Y_1 - Y_{2b}$
Y_y = pitchwise mass-averaged blade loss coefficient
Z = blade loading coefficient = $[2(\tan\alpha_1 - \tan\alpha_2)]^2\cos^2\alpha_2/\cos\alpha_m$
α = air angle
α_2^* = midpitch midspan exit flow angle
α' = blade angle
δ = boundary layer thickness
δ^* = boundary layer displacement thickness
ΔP = total pressure loss (relative to P_1)
θ = momentum thickness
ρ = air density

Subscripts

1 = cascade inlet measuring station
2 = cascade exit measuring station
a = atmosphere
fs = free-stream conditions
m = mean
T = total

Table 2

l/c	0.42	0.82	1.28	1.82	2.18	2.55
C_p	−0.025	−0.009	0.036	0.036	0.030	0.029

Table 3 Inlet boundary layer properties

Test	δ_1*, cm	δ_1*/C	δ_1*/h	θ_1, cm	H_1	δ_1, cm	m	Y_1*
1	1.58	0.0575	0.0244	1.262	1.25	14.2	0.1252	0.0761
2	1.53	0.0556	0.0236	1.22	1.252	13.67	0.126	0.0746
3	1.16	0.0422	0.0179	0.94	1.241	10.76	0.1208	0.0519
4	1.13	0.0411	0.0174	0.89	1.28	9.25	0.1404	0.0506
5	1.11	0.0404	0.0171	0.89	1.25	10.0	0.125	0.0519
6	0.77	0.0280	0.0119	0.58	1.32	5.6	0.1594	0.033
7	0.39	0.0142	0.0060	0.28	1.375	2.47	0.1875	0.0159

the static pressure coefficient C_p for various distances l along this line are given in Table 2.

The tailboards were set at the reference exit flow angle (α_2* = −64 deg). On completing the test program careful checking revealed a small discrepancy, one board having been set at −63.7 deg, giving 0.3 deg of divergence of the passage. However, if the flow is considered to be uniform the pressure recovery coefficient C_{pr} for this diverging passage would be only 0.003. The larger variation in C_{pr} (corresponding to the overall change of C_p in Table 2) must be associated with the flow mixing of the wakes with the free-stream flow. Mixing would reduce the free-stream velocity and this would be reflected in the initially rising value of C_p seen in Table 2.

Results and Discussion

The inlet wall boundary layer thickness was varied by using different lengths of the inner and outer walls (Fig. 1*a*). Measurements of the velocity profiles were made at a streamwise distance of 0.436 c upstream of the cascade inlet plane by making a series of pitchwise traverses across one full pitch. At this distance upstream only minor pitchwise variations in velocity were discernible. The pitchwise averages of seven velocity traverses of the inlet boundary layer are shown in Fig. 3 and Table 3 presents values of properties determined from these measurements.

It is convenient to assume that the inlet boundary layer velocity profile can be represented by a simple power-law expression, i.e.

$$\frac{V_1}{V_{fs}} = \left(\frac{z}{\delta_1}\right)^m$$

where m is not necessarily equal to 1/7 as is sometimes assumed.

No satisfactory explanation can be given for the variation in the values of H for the different boundary layers. The proximity of the blades produces only slight pitchwise variations in the measurements made to derive pitchwise average velocity profiles. The use of a Kiel probe for these measurements was not ideal but the probe outside diameter (3 mm) to boundary layer thickness ratio was still small enough to give realistic results.

The present tests were conducted to establish the influence of the position of the exit measuring station on the measured values of the secondary losses. These experiments covered the range $0.15 \le l/C \le 2.4$. Both profile and total cascade loss coefficients showed a rising trend up to $l/C \approx 2.4$. These loss increases are due to flow mixing together with an additional loss due to the skin friction on the endwalls. This additional loss may be significant because of the effect of the large velocity gradients produced near the endwall by the action of the secondary flows near cascade exit. Earlier tests, i.e., Dixon and Cooke [3], reported that in turbine cascades of large flow deflection the original boundary layer entering the cascade

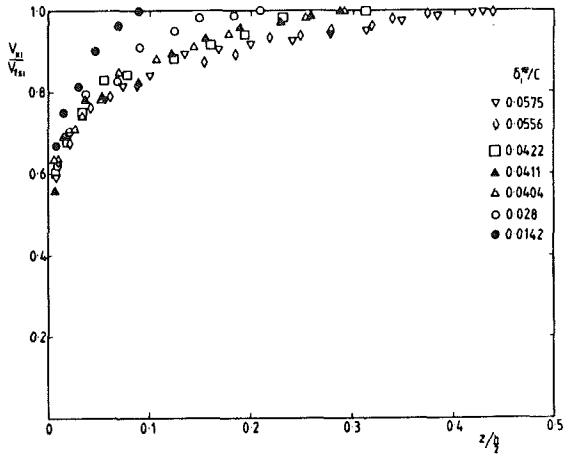

Fig. 3 Inlet boundary layer velocity profiles

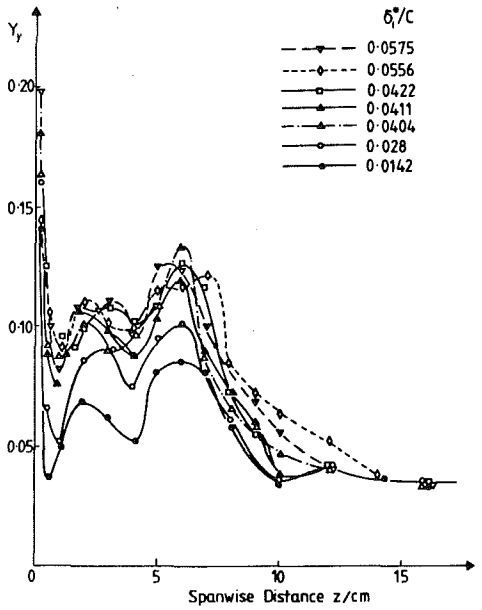

Fig. 4 Variation of pitchwise mass-averaged total pressure loss coefficient with distance along span at $l = 0.15c$

was swept across the blade passage and away from the end wall as the flow progressed through the cascade. At $l/C = 0.15$ the new boundary layer was found by them to be very thin and the secondary flow velocities close to the end-wall to be of nearly the same magnitude as the main stream velocity at cascade exit.

The spanwise variations of the pitchwise mass-averaged loss coefficients were measured at $l/C = 0.15$, 0.5, 1.05, 1.35, 1.58, 1.9, and 2.4 for all seven inlet boundary layers. A selection only of these results are presented in Figs. 4 to 7 for $l/C = 0.15$, 1.05, 1.58, and 2.4 to show the development of the loss coefficient profiles. Figure 8 shows the typical evolution of the loss profile with distance downstream (for $l/C = 0.15$, 0.5, 1.05, 1.58, and 2.4) for one value of δ_1*/C of 0.0411.

Endwall losses continue to rise with increasing distance downstream. Figure 8, for δ_1*/C = 0.0411, shows that close to the endwall the pitchwise averaged losses increase continuously from $l/C = 0.15$ to 2.4 which would be the effect to be expected from wall skin friction. The double peak loss distribution changes with a marked shift outward of the outer peak from $Z = 5.9$ cm at $l/C = 0.15$, to $Z = 6.9$ cm at $l/C = 0.5$ and to $Z = 8.2$ cm at $l/C = 1.05$, whereafter it appears to remain at the same position up to $l/C = 2.4$. The magnitude of the second loss peak initially reduces and then continues to

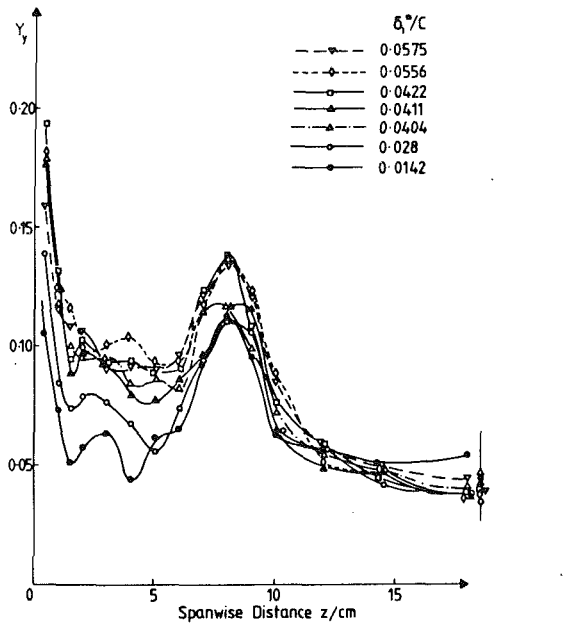

Fig. 5 Variation of pitchwise mass-averaged total pressure loss coefficient with distance along span at $l = 1.05c$

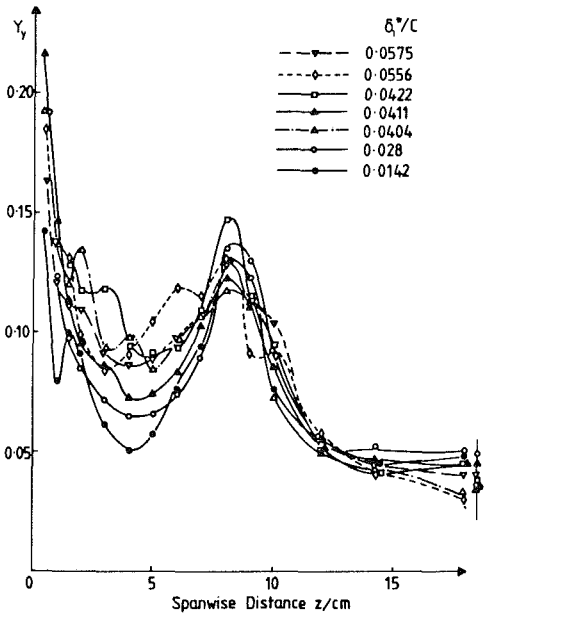

Fig. 6 Variation of pitchwise mass-averaged total pressure loss coefficient with distance along span at $l = 1.58c$

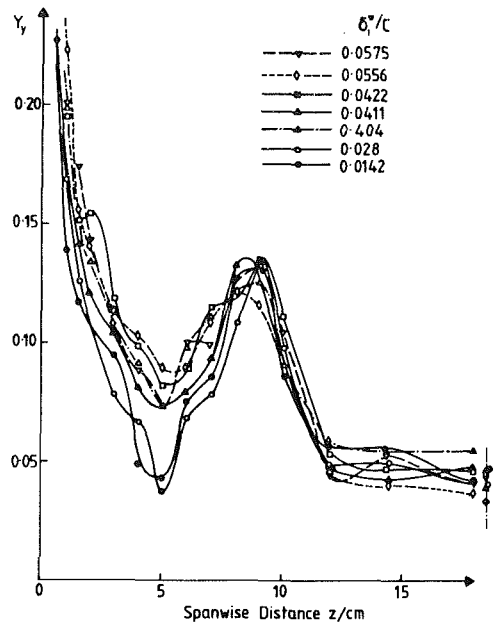

Fig. 7 Variation of pitchwise mass-averaged total pressure loss coefficient with distance along span at $l = 2.4c$

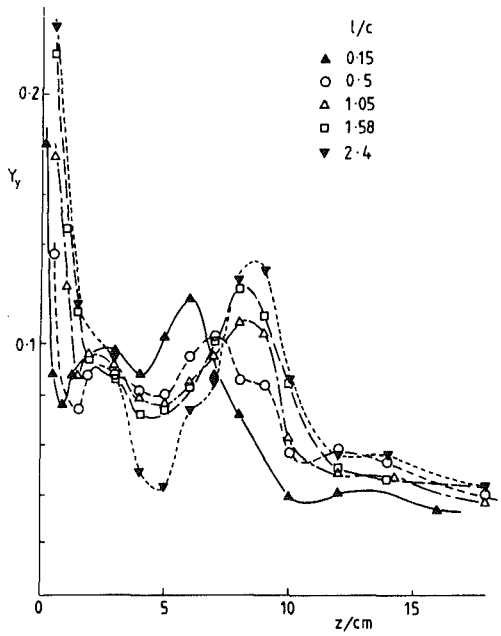

Fig. 8 Variation of pitchwise mass-averaged total pressure loss coefficient with spanwise distance for $\delta_1^*/C = 0.0411$

grow for $0.5 < l/C < 2.4$. It can also be seen that the first peak diminishes with downstream distance and by $l/C = 1.58$ has disappeared, partly as a result of the growth in losses close to the endwall which swallow it up.

Figures 4 to 7 show that the double peak loss distributions and the gradual disappearance of the first peak occur at about the same distances from the endwall *irrespective of the value of* δ_1^*/C. However the magnitudes of the loss peaks differ markedly close to the cascade but at $l/C = 2.4$ these differences become less pronounced.

The subject of secondary flow losses in turbine blades has now received a large amount of attention since the publication by Ainley [7] in 1948 of an empirical secondary loss coefficient for assisting attempts at performance prediction. Sieverding [8] has comprehensively reviewed the results of experimental secondary flow research in turbine blade passages, mainly for the period 1974–1983. Some of the facts to emerge which are considered relevant to the discussion of losses are as follows.

There are two main features of a turbine cascade secondary flow, the passage vortex and the loss core associated with the inlet boundary layer. As discovered by Langston et al. [6], the vorticity of the inlet boundary rolls up and wraps itself around both sides of the blades forming the aptly named "horseshoe" vortex. This vortex gives rise to two separation lines, one sloping outward from the endwall on the blade suction surfaces and the other crossing the endwall to the suction surface of the adjacent blade. As discussed by Gregory-Smith and Graves [9], this becomes associated with a counterrotating vortex in the corner formed by the endwall and the blade suction surface. These surface separation lines enable the losses caused by fluid shear close to the suction surface to feed into the mainstream. It is the passage vortex

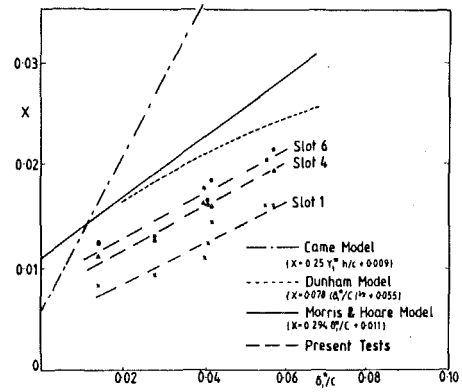

Fig. 9 Variation of gross secondary loss parameter with displacement thickness ratio

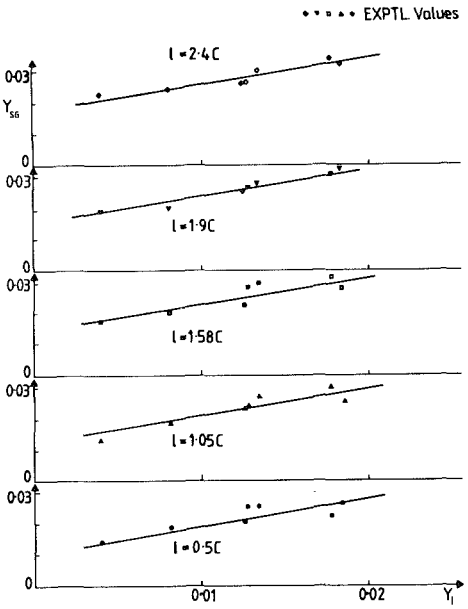

Fig. 10 Variation of Y_{SG} with Y_1 at various distances downstream of trailing edge plane

which convects the loss core across the passage to the suction surface where it is then displaced outward to the separation line mentioned above.

There are three types of loss that may be encountered in the trailing edge plane, i.e., (*i*) the corner loss; (*ii*) the loss core associated with the passage vortex; and (*iii*) a loss core along the passage vortex separation line. These loss cores may be more or less superimposed, according to Sieverding [8].

Loss Correlations

Dunham [10] in 1970 demonstrated the variation of gross secondary loss coefficient as a function of the inlet wall boundary layer displacement thickness. Came [1] in 1973 and Morris and Hoare [2] in 1975 suggested that the secondary loss can be represented as a function of the straight line of $\delta_1{}^*/C$. The correlation deduced by Came [1] for the gross secondary loss coefficient Y_{SG} is

$$Y_{SG} = Z\frac{\cos\alpha_2}{\cos\alpha_1}\left(K_3 Y_1{}^* + K_4\frac{C}{h}\right)$$

Unfortunately, the results obtained for high deflection turbine blade cascades for secondary losses are in obvious disagreement, especially using the formula given by Came.

Figure 9 shows the gross secondary loss parameter X, i.e., Y_{SG} corrected for the effects of aspect ratio and aerodynamic loading, plotted against $\delta_1{}^*/C$. The experimental results are

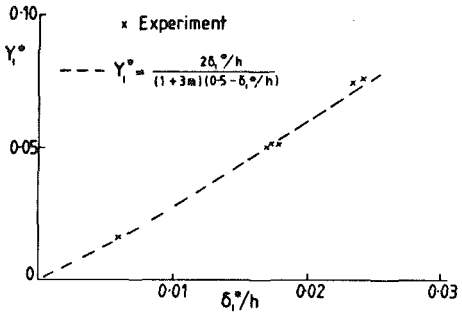

Fig. 11 Variation of inlet boundary layer loss coefficient with inlet boundary layer displacement thickness

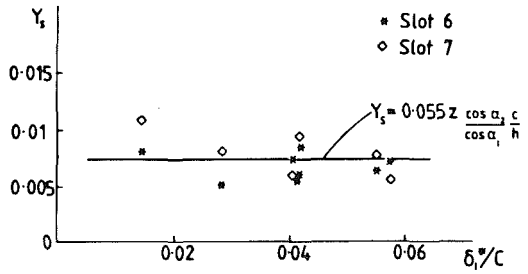

Fig. 12 Variation of secondary loss coefficient with inlet boundary layer displacement thickness

less than the values determined by the correlations. They are in substantial disagreement with all the experimental points.

As pointed out by Came [1], in many cases Y_{SG} had to be calculated from Y_S and $\delta_1{}^*/C$, assuming a 1/7 power law inlet boundary layer. This assumption may have introduced some error. In order to discount the assumption of the 1/7 power law, it is more rational to arrange the Y_{SG} correlation in terms of Y_1 instead of $\delta_1{}^*/C$ or $Y_1{}^*$. Y_1 is a pressure loss coefficient relative to the exit dynamic head, i.e.,

$$Y_1 = Y_1{}^*\cos^2\alpha_2/\cos^2\alpha_1$$

Using Y_1 leads to a more convenient and useful means of expressing Y_{SG} in terms of other blade deflections.

In Fig. 10, the variation of the gross secondary loss coefficient Y_{SG} was plotted against inlet boundary layer loss coefficient Y_1 at different distances downstream. These experiments covered the range $0.5 < l/C < 2.4$. The gross secondary loss coefficient shows a uniform increase of constant slope up to $l/C = 2.4$. A simple correlation applicable to this particular cascade geometry but for all of the inlet boundary layer thicknesses tested can be derived from Fig. 10 immediately. The correlation is

$$Y_{SG} = 0.0085(1 + 0.43l/C) + 0.825\,Y_1$$

and this accurately represents the curves drawn in Fig. 10. Although some wall friction measurements were taken no satisfactory way of isolating this loss in the correlation was determined.

In a more general analysis of losses it is suggested that the following secondary loss correlation could be used in turbine blade loss predictions

$$Y_{SG} = Y_1 + Y_S + Y_{2b}$$

where $Y_S = K_1 Z\dfrac{\cos\alpha_2}{\cos\alpha_1}\left(\dfrac{C}{h}\right)$, $K_1 = 0.0055$,

$$Y_{2b} = \frac{2\delta_2/h}{(3m+1)\left(\dfrac{1}{2m}+\dfrac{1}{2}-\dfrac{\delta_2}{h}\right)}$$ (it is assumed that $m = \frac{1}{7}$, if m is unknown), $\dfrac{\delta_2}{l} = 0.379\ (\mathrm{Re})_l^{-0.2}$ as found by Dixon and Cooke [3].

It would be expected that the difference in Y_{SG} between any two downstream locations A and B (i.e., Y_{2b} (slot A) $- Y_{2b}$ (slot B)) is the combined result of flow mixing and the extra wall friction. It should be emphasized that the values of inlet wall boundary layer displacement thickness and momentum thickness were obtained by a reasonably satisfactory measurement method.

The mathematical modeling of a power-law velocity profile for the inlet flow is

$$\frac{V_1}{V_{1fs}} = \left(\frac{z}{\delta_1}\right)^m$$

δ^*, θ, H, and m may be represented by

$$\delta^* = \delta/\left(1+\frac{1}{m}\right),\ \theta = \delta^*\frac{1}{2m+1},\ H = \frac{\delta^*}{\theta},\ \text{and}\ m = \frac{H-1}{2}$$

so that δ^*, θ, δ, H, and m can be found from V_1 obtained by experiment.

Figure 11 shows the variation of inlet boundary layer loss coefficient $Y_1{}^*$ against inlet boundary layer displacement thickness $\delta_1{}^*$. The experimental points agree considerably with the correlation

$$Y_1{}^* = \frac{2\dfrac{\delta_1{}^*}{h}}{(1+3m)\left(0.5-\dfrac{\delta_1{}^*}{h}\right)}$$

which is deduced from

$$Y_1{}^* = \frac{\displaystyle\int_0^{h/2} V_{X1}\,\Delta P dz}{\displaystyle\int_0^{h/2} V_{X1}\,dz} \Big/ (P_{1fs} - p_1)$$

where $\dfrac{V_1}{V_{1fs}} = \left(\dfrac{z}{\delta_1}\right)^m$ and $\delta_1 = \delta_1{}^*\left(1+\dfrac{1}{m}\right)$.

As has been discussed above, in the secondary loss coefficient Y_S against $\delta_1{}^*/C$ no obvious variation of Y_S is observed over the entire range of $\delta_1{}^*/C$ covered except a reasonable scatter band (Fig. 12).

Conclusions

1 A simple correlation of the gross secondary loss coefficient with distance downstream and with Y_1 is determined for the cascade tested, i.e.,

$$Y_{SG} = 0.0085(1+0.43l/C) + 0.825\,Y_1$$

This growth in Y_{SG} results from flow mixing processes and the wall friction loss.

2 A new correlation of Y_{SG} including loading, aspect ratio, and inlet boundary layer velocity profile parameters is proposed, i.e.,

$$Y_{SG} = Y_1 + K_1 Z\frac{\cos\alpha_2}{\cos\alpha_1}\left(\frac{C}{h}\right) + \frac{2\delta_2/h}{(3m+1)\left(\dfrac{1}{2m}+\dfrac{1}{2}-\dfrac{\delta_2}{h}\right)}$$

where $K_1 = 0.0055$ and $\delta_2/h = 0.379\,(l/h)\,\mathrm{Re}_l{}^{-0.2}$.

3 A correlation relating inlet boundary layer loss coefficient and inlet-wall boundary layer displacement thickness is deduced for prediction of $Y_1{}^*$

$$Y_1{}^* = \frac{2(\delta_1{}^*/h)}{(1+3m)(0.5-\delta_1{}^*/h)}$$

4 The secondary loss coefficient Y_S, excluding the inlet boundary layer loss, does not vary obviously with inlet boundary layer displacement thickness over the entire range of $\delta_1{}^*/C$ covered, except for a reasonable scatter band. The results disagree with the experiments of Came [1], but agree with those of other investigators.

5 The existence of two areas of peak loss some distance away from the end wall as well as a thin boundary layer type of loss is verified near the cascade exit. As the flow progresses downstream the boundary layer type loss thickens rapidly, the first peak declines in magnitude and appears to be swallowed by boundary layer loss, and the second peak grows in magnitude after an initial decrease.

6 The positions of low-energy fluid, double peak or single peak, away from the endwall are not influenced by the relative change in inlet boundary layer. However, the magnitudes of the peak losses close to the turbine exit are significantly affected by the initial boundary layer thickness. As a general rule, the larger the value of $\delta_1{}^*$ is, the bigger the loss peaks become.

Acknowledgments

The authors wish to express their sincere thanks for the assistance rendered by members of the Electronics Workshop, Metal Workshop, Wood Workshop, Drawing Office, and secretaries of the Department of Mechanical Engineering of the University of Liverpool and the University of Liverpool generally for the support and use of the facilities during the period of this research.

References

1 Came, P. M., "Secondary Loss Measurements in a Cascade of Turbine Blades," Institution of Mechanical Engineers, Conference Publication 3, 1973, pp. 75–83.

2 Morris, A. W. H., and Hoare, R. G., "Secondary Loss Measurements in a Cascade of Turbine Blades With Meridional Wall Profiling," ASME Paper No. 75-WA/GT.

3 Dixon, S. L., and Cooke, J. A., "Secondary Flow Development in High Deflection Turbine Blade Cascades," *Proceedings of 11th National Conference on Fluid Mechanics and Fluid Power*, Hyderabad, India, 1982.

4 Smith, D. J., and Johnston, I. H., "Investigation on an Experimental Single Stage Turbine of Advanced Design," Aeronautical Research Council, R and M, No. 3541, 1967.

5 Sharma, O. P., and Graziani, R. A., "Influence of End Wall Flow on Airfoil Suction Surface Midheight Boundary Layer Development in a Turbine Cascade," ASME JOURNAL OF ENGINEERING FOR POWER, Vol. 105, 1983, pp. 147–155.

6 Langston, L. S., Nice, M. L., and Hooper, R. M., "Three-Dimensional Flow Within a Turbine Cascade Passage," ASME JOURNAL OF ENGINEERING FOR POWER, Vol. 99, 1977, pp. 21–28.

7 Ainley, D. G., "The Performance of Axial Flow Turbines," *Proc. Institution of Mechanical Engineers*, Vol. 159, 1948.

8 Sieverding, C. H., "Recent Progress in the Understanding of Basic Aspects of Secondary Flows in Turbine Blade Passages," ASME JOURNAL OF ENGINEERING FOR GAS TURBINES AND POWER, Vol. 107, No. 2, Apr. 1985, pp. 248–257; Paper No. 84-GT-78.

9 Gregory-Smith, D. G., and Graves, C. P., "Secondary Flows and Losses in a Turbine Cascade," *Viscous Effects in Turbomachines*, AGARD CP351, 1983.

10 Dunham, J., "A Review of Cascade Data on Secondary Losses in Turbines," *J. Mechanical Engineering Science*, Vol. 12, 1970, pp. 48–59.

APPENDIX

As a Kiel probe is the main pressure probe for flow traversing, only simple approximations for flow averages can be obtained.

The pitch-mass-averaged loss coefficient is

$$Y_y = \frac{(P_1 - \bar{P}_2)}{P_{1fs} - p_2} = 1 - \frac{\bar{P}_2 - p_a}{P_{1fs} - p_a}$$

where it is assumed that $p_2 = p_a$.

The mass flow weighted total pressure averaged across the pitch is

$$\bar{P}_2 - p_a = \frac{\int_0^s V_{x2}(P_2 - p_a)dy}{\int_0^s V_{X2}dy} = \frac{\int_0^s (P_2 - p_a)^{3/2}dy}{\int_0^s (P_2 - p_a)^{1/2}dy}$$

where $V_{X2} = V_2 \cos \alpha_2{}^* = \cos \alpha_2{}^* \left\{ \frac{2}{\rho}(P_2 - p_a) \right\}^{1/2}$.

The total pressure loss coefficient mass averaged in pitch and span directions is

$$Y_T = \frac{\Delta P_T}{P_{2m} - p_2}$$

where $\Delta P_T = \dfrac{\int_0^{h/2} \int_0^S V_{X2}(P_{1fs} - P_2)dydz}{\int_0^{h/2} \int_0^s V_{X2}dydz}$

and $P_{2m} = P_{1fs} - \Delta P_T$.

Profile loss coefficient mass averaged in pitch and span directions is

$$Y_P = \frac{\Delta P_P}{P_{2m} - p_2}$$

where $\Delta P_P = \dfrac{\int_{2D} \int_0^s V_{X2}(P_{1fs} - P_2)dydz}{\int_{2D} \int_0^s V_{X2}dydz}$

The mass-averaged inlet boundary layer loss coefficient is

$$Y_1{}^* = \frac{\int_0^{h/2} V_1(P_{1fs} - P_1)dz}{\int_0^{h/2} V_1 dz} / (P_{1fs} - P_1)$$

R. Kiock
Institute for Design Aerodynamics,
DFVLR, Flughafen,
D-3300 Braunschweig, West Germany

F. Lehthaus
Institute for Experimental Fluid Mechanics,
DFVLR,
D-3400 Göttingen, West Germany

N. C. Baines
Imperial College,
Department of Mechanical Engineering,
London SW7 2BX,
United Kingdom

C. H. Sieverding
Von Karman Institute for Fluid Dynamics,
B-1640 Rhode-St.-Genèse, Belgium

The Transonic Flow Through a Plane Turbine Cascade as Measured in Four European Wind Tunnels

Reliable cascade data are esssential to the development of high-speed turbomachinery, but it has long been suspected that the tunnel environment influences the test results. This has now been investigated by testing one plane gas turbine rotor blade section in four European wind tunnels of different test sections and instrumentation. The Reynolds number of the transonic flow tests was $Re_2 = 8 \times 10^5$ *based on exit flow conditions. The turbulence was not increased artificially. A comparison of results from blade pressure distributions and wake traverse measurements reveals the order of magnitude of tunnel effects.*

Introduction

The specific fuel consumption of jet engines has been halved during the last thirty years thanks in part to more effective turbine and compressor blade design methods. These methods were proved and improved by experimental verification. The experience shows that experiments are indispensable especially in the region of transonic flow in which there is great interest today. The quasi-two-dimensional flow through compressor or turbine blading can be simulated by the flow through a plane cascade, i.e., by a row of blades having identical shape and constant spacing along the blade height. In order to be able to compare theory and experiment, the flow must be physically similar in both cases. The following similarity parameters and flow conditions have to be considered:

- Mach number
- Reynolds number
- Turbulence
- Axial velocity density ratio
- Aspect ratio in the case of non-two-dimensional flow, i.e., $\Omega \neq 1$
- Periodicity from one blade channel to the next one
- Relative inlet boundary layer thickness

Some of these parameters are difficult to handle. The turbulence, for example, which can be defined by the components of the fluctuations, by its spectrum, by microscale and macroscale, is far from understood in a multistage engine and can only be approximated in theory and experiment.

Cascade testing has been carried out for many years and will be required in the future, too. The estimate of the accuracy of a cascade test is seen to be extremely difficult and partly dubious because it is impossible to consider all possibilities of error. It is also known that the cascade environment, which includes factors such as the development of the inlet flow, blockage due to measuring probes, etc., can significantly influence the cascade performance, particularly in the transonic regime. Therefore, an attempt has been made to compare the aerodynamic data obtained on a turbine cascade of given geometry in four different wind tunnels at sub/transonic flow conditions in order to gain some insight into the magnitude of such "tunnel effects," and the mechanisms by which they influence the cascade. Some of the individual cascades were of different sizes due to the special test conditions. The probes used were different in size and shape. The operating conditions were steady as well as intermittent. Flow properties were measured in an upstream plane, along the blade surface, and in a downstream plane of the cascade. Because of space limitations, only a selection of Mach number distributions on the blade and wake traverse data are compared here to illustrate the principal findings. A complete set of data is to be published subsequently [10].

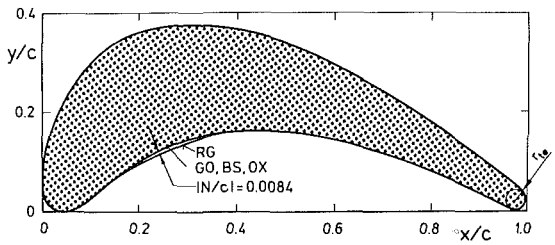

Fig. 1 Blade shape

Test Model

A turbine cascade was chosen as the test model because the

Contributed by the Gas Turbine Division and presented at the 1985 Beijing International Gas Turbine Symposium and Exposition, Beijing, People's Republic of China, September 1-7, 1985. Manuscript received at ASME Headquarters May 13, 1985. Paper No. 85-IGT-44.

Table 1 Blade coordinates

x/c	$(y/c)_P$	$(y/c)_S$	x/c	$(y/c)_P$	$(y/c)_S$
0.0000	0.0638	0.0638	0.5215	0.1601	0.3301
0.0061	0.0255	0.1135	0.5368	0.1583	0.3239
0.0153	0.0120	0.1586	0.5522	0.1561	0.3175
0.0307	0.0031	0.1979	0.5675	0.1537	0.3107
0.0460	0.0000	0.2276	0.5828	0.1506	0.3037
0.0614	0.0031	0.2525	0.5982	0.1469	0.2966
0.0767	0.0114	0.2730	0.6135	0.1429	0.2893
0.0920	0.0227	0.2902	0.6288	0.1390	0.2816
0.1074	0.0356	0.3043	0.6442	0.1347	0.2736
0.1227	0.0470	0.3166	0.6595	0.1304	0.2653
0.1380	0.0587	0.3276	0.6749	0.1258	0.2568
0.1534	0.0702	0.3374	0.6902	0.1209	0.2479
0.1687	0.0811	0.3457	0.7055	0.1156	0.2387
0.1841	0.0915	0.3528	0.7209	0.1104	0.2295
0.1994	0.1008	0.3583	0.7362	0.1049	0.2199
0.2147	0.1092	0.3629	0.7515	0.0991	0.2104
0.2301	0.1180	0.3666	0.7669	0.0933	0.2006
0.2454	0.1257	0.3693	0.7822	0.0871	0.1908
0.2607	0.1325	0.3712	0.7976	0.0801	0.1807
0.2761	0.1382	0.3724	0.8129	0.0745	0.1706
0.2914	0.1439	0.3733	0.8282	0.0681	0.1601
0.3068	0.1484	0.3736	0.8436	0.0614	0.1497
0.3221	0.1525	0.3736	0.8589	0.0546	0.1390
0.3374	0.1559	0.3730	0.8742	0.0476	0.1282
0.3528	0.1586	0.3721	0.8896	0.0405	0.1175
0.3681	0.1605	0.3709	0.9049	0.0331	0.1064
0.3834	0.1620	0.3690	0.9203	0.0258	0.0954
0.3988	0.1632	0.3666	0.9356	0.0181	0.0844
0.4141	0.1638	0.3635	0.9509	0.0104	0.0733
0.4295	0.1641	0.3599	0.9601	0.0058	0.0666
0.4448	0.1644	0.3558	0.9693	0.0015	0.0601
0.4601	0.1644	0.3515	0.9755	0.0000	0.0537
0.4755	0.1638	0.3466	0.9816	0.0015	0.0500
0.4908	0.1629	0.3414	0.9877	0.0040	0.0454
0.5061	0.1617	0.3359	0.9939	0.0089	0.0411
			1.0000	0.0245	

end wall effects are less severe than in the case of a compressor cascade. A nearly two-dimensional flow can be established easily and the influence of the aspect ratio is small. The cascade is typical for a coolable gas turbine rotor blade section. It was designed following Dejc's method [1]. The suction side is derived from one basic lemniscate, while the pressure side is composed of both a circular arc and a lemniscate. The blade is shown in Fig. 1. The blade, designated "RG," served as a test case for calculation [2] at the occasion of a VKI lecture series in 1973. Since then it has been used by various authors to check their numerical codes, e.g., [3]. Many of these methods are now capable of very good predictions, and it is therefore important to the development of these methods, as much as to experimental techniques, that the current limitations of experimental data be understood.

Table 2 Cascade data (nominal)

s/c	=	0.71
arc cos(o/s)	=	67.8°
β_S	=	33.3°
β_1	=	30°

This blade profile was thus considered to be very suitable for the present work.

Later it turned out that the manufactured blade of [2] actually did have an undesirable flat part on the front pressure side. The coordinates were modified and all subsequent blades, i.e., the blades tested at GO, BS, and OX, were made according to the modified blade coordinates presented in Table 1.

The cascade parameters are summarized in Table 2. The GO blades were equipped with a trip wire of 0.05 mm diameter on the suction side at $x/c = 0.60$.

The comparison here is restricted to investigations at the design inlet flow angle, $\beta_1 = 30$ deg.

Experimental Arrangements

The experiments which will be compared here were carried out in four European wind tunnels at VKI Rhode-St.-Genèse, Belgium; DFVLR Goettingen, West Germany; DFVLR Braunschweig, West Germany; and Oxford University, UK. The individual conditions concerning test sections and instrumentation will be described below.

Test Sections. There are many differences in the types and dimensions of the facilities used (see Fig. 2 and Table 3). The width of the test section ranged from $h = 50$ to 300 mm, and the chord from $c = 32.6$ to 100 mm. The number of blades was seven or ten. All blade surfaces were ground and can be described as hydraulically smooth. The test sections of BS and OX had the same size so that physically the same cascade could be investigated in these two wind tunnels. The ratio of upstream length to tunnel width covered a large range from 3 to 20. The ratio of downstream length to tunnel width ranged from 0.8 to 5. All facilities were equipped with solid parallel end walls. No tailboards were used.

The deviations of the true values of the geometric cascade

Nomenclature

c = chord
$c_{p,te}$ = base pressure coefficient $= (p_{te} - p_2)/0.5\rho_2 w_2^2$
h = blade height = span = width of flow channel
H = height of flow channel perpendicular to flow direction
M = Mach number $= f(p/p_{01})$; $M_1 = f(p_1/p_{01})$, $M_2 = f(p_2/p_{02})$, $M_{2,is} = f(p_2/p_{01})$
o = throat
p = static pressure
p_0 = total pressure
r = radius
Re = Reynolds number $= w\rho c/\mu$
s = spacing
Tu = degree of turbulence in mainstrain direction $= 100\sqrt{\overline{w'^2}}/w$
w = velocity
x, y = blade coordinates, bitangential
β, β_s = flow angle and blade angle relative to cascade axis, see Fig. 2
κ = ratio of specific heats
μ = dynamic viscosity
ξ = loss coefficient $= 1 - w_2^2/w_{2,is}^2$
ρ = density
Ω = axial velocity density ratio $= \rho_2 w_2 \cos\beta_2/\rho_1 w_1 \cdot \cos\beta_1$

Subscripts

1 = measurement plane upstream of cascade
2 = transferred to homogeneous exit flow from cascade
ch = choked flow
cr = critical
is = isentropic flow
P = pressure side
S = suction side
te = trailing edge

Abbreviations

AVDR = axial velocity density ratio
BS = Braunschweig
GO = Goettingen
OX = Oxford
RG = Rhode-St.-Genèse

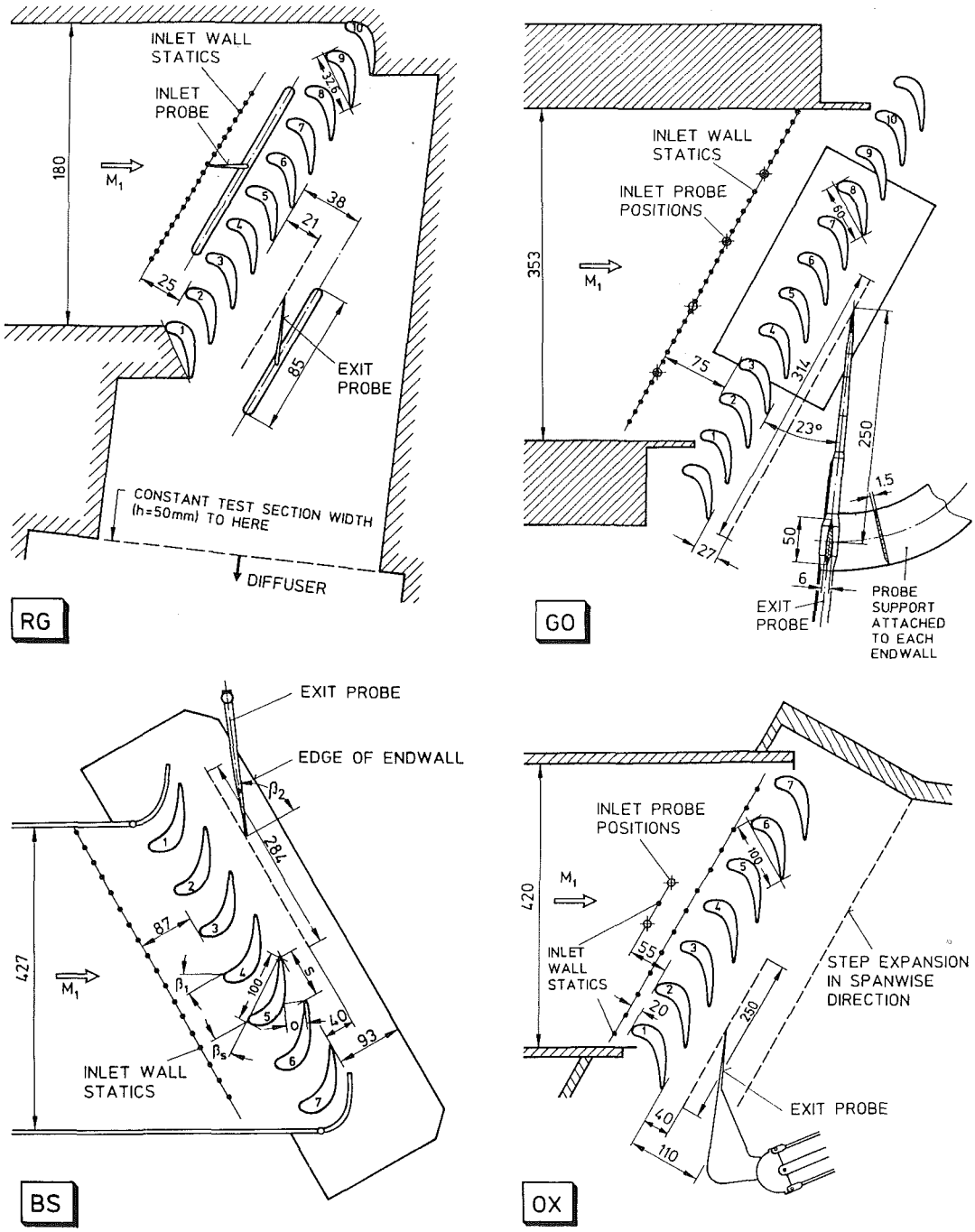

Fig. 2 Comparison of test sections

parameters from the nominal ones were small, and the deviations from blade to blade within one cascade were also low (Table 3).

Instrumentation. The flow properties such as static pressure T, total pressure and flow angle were measured in planes upstream and downstream of the cascade in order to adjust the flow for given M/Re conditions and in order to carry out the wake traverse (see Table 4).

Figure 3 shows the probes for the wake traverse measurements. Finger probes were used at RG, BS, and OX so that each finger (single tube or tube combination) measured one flow quantity except the RG probe where one finger was sensitive to total pressure and yaw angle. A wedge probe was used at GO. This probe was originally developed for use in supersonic flows.

All these probes were calibrated carefully. The calibration of such probes for measuring high subsonic and transonic flows is discussed extensively in [7]. The probes were moved stepwise or continuously with very different velocities so that a wake traverse over one pitch took a duration from 1 to 180 s. Because of the short measuring time of 1 s at OX the transducers were installed in the probe holder (see Fig. 2), giving a length of approximately 0.15 m for the pneumatic tubes. This length ranged from 1.5 m to 6 m in the other cases. The accuracy of the transducers amounted to 0.1 percent of full scale. These local wake data were transferred to a hypothetical plane of homogeneous flow using the laws of conservation [8]. The results are shown versus the mixed-out value of the exit Mach number M_2.

The surface pressure was measured by tappings on two

Table 3 Geometric parameters of test sections and cascades

Parameter \ Tunnel	RG	GO	BS	OX
Name of facility	High speed cascade wind tunnel (C-2)	Plane cascade wind tunnel (EGG)	High speed cascade wind tunnel (HGB)	O.U.E.L. blowdown tunnel
Reference	[2]	[4]	[5]	[6]
Type of facility	Blowdown	Suckdown	Closed loop	Blowdown
Test section h x H_1	50 mm x 180 mm	125 mm x 353 mm	300 mm x 427 mm	300 mm x 420 mm
Length of upstream straight end wall[1)]	1000 mm	2550 mm	1550 mm	800 mm
Length of downstream guided flow[2)]	200 mm	650 mm	250 mm	290 mm
Number of blades	10	10	7	Identical with BS cascade
Blade shape	see fig. 1			
Difference nominal and real shape[3)]	±0.031 mm ±0.031 mm	±0.025 mm ±0.040 mm	±0.055 mm ±0.083 mm	
Chord c	32.6 mm	60 mm	100 mm	
Aspect ratio h/c	1.534	2.083	3.000	
True gauging angle arc cos (o/s)[4)]	$67.74^{\circ}\pm0.10^{\circ}$	$67.92^{\circ}\pm0.11^{\circ}$	$67.96^{\circ}\pm0.03^{\circ}$	
True pitch[4)]	(23.15±0.04)mm	(42.58±0.19)mm	(70.88±0.10)mm	
True stagger angle[4)]	$33.14^{\circ}\pm0.09^{\circ}$	$33.56^{\circ}\pm0.12^{\circ}$	$33.29^{\circ}\pm0.03^{\circ}$	

1) Upstream of cascade center
2) Downstream of cascade center in isentropic exit flow direction, $\beta_{2,is} = 67.8^{\circ}$, range with channel width being equal to blade height
3) Average value and standard deviation around blade with respect to table 1, normal to contour, positive sign means real blade is too thick, front part of pressure side not considered
4) Average value and standard deviation over four central pitches

Table 4 Measurement of flow quantities

Parameter \ Tunnel	RG	GO	BS	OX
Flow quantities at cascade inlet: Static pressure: Total pressure: Flow angle:	Side wall tappings } Probe	Side wall tappings } Probe	Side wall tappings } Probe	Side wall tappings } Probe
Flow quantities at cascade exit: Static pressure: Total pressure: Flow angle:	} Two-finger probe	} Wedge probe	} Three-finger probe	} Three-finger probe
Wake traverse on blade no.[1)]	5	5	4	4
Axial distance[2)]	21 mm	27 mm	40 mm	40 mm
Probe motion	Continuous	Continuous	Step wise	Continuous
Time required for one wake traverse[3)]	45 s	70 s	180 s	1 s
Pressure tappings on blade no.	5 and 6	4 and 5	3 and 5	3 and 5

1) Smooth blade with no tapping in each case
2) Between trailing edge plane and probe tapping for total pressure measurement
3) Without flow adjustment

central blades. One blade was equipped with tappings on the suction side and the other with tappings on the pressure side. The tappings were distributed over two blades in order to allow the installation of as many pressure tubes as possible. The trailing edge tappings were aligned in the direction of the camber line at the trailing edge. In the case of the GO cascade, tappings were overlapping in the region of leading and trailing edge so that the pressure could be measured on two neighbored blades within these regions. In the case of the OX cascade, each tapping was connected to an individual transducer. Scanivalves were used at GO and BS and a mercury multimanometer was applied at RG.

For the wake traverses, the instrumented blades were replaced by blank blades at RG and GO.

The degree of turbulence *Tu* was measured by a single hot wire in order to obtain the fluctuations in mainstream direction.

Overall Flow Conditions

Except for BS all facilities allow testing at supersonic exit Mach numbers, but only GO extended the tests into this range (see Table 5). The exit Reynolds number Re_2 could be varied independently of the exit Mach number M_2 in the wind tunnels of BS and OX. The relation of Re_2 with M_2 is shown in Fig. 4. The tests in the transonic flow region, $M_2 = 0.8$ to 1.1, were carried out in all wind tunnels around $Re_2 = 8 \times 10^5$ while $Re_2 \approx 3.5 \times 10^5$ at RG and GO for the lowest value of M_2. To have a better comparison for low M_2, Re_2 was decreased at BS to the values of GO.

The degree of turbulence was not increased artificially, i.e., it was of the order of 1 percent. The total temperature was close to ambient.

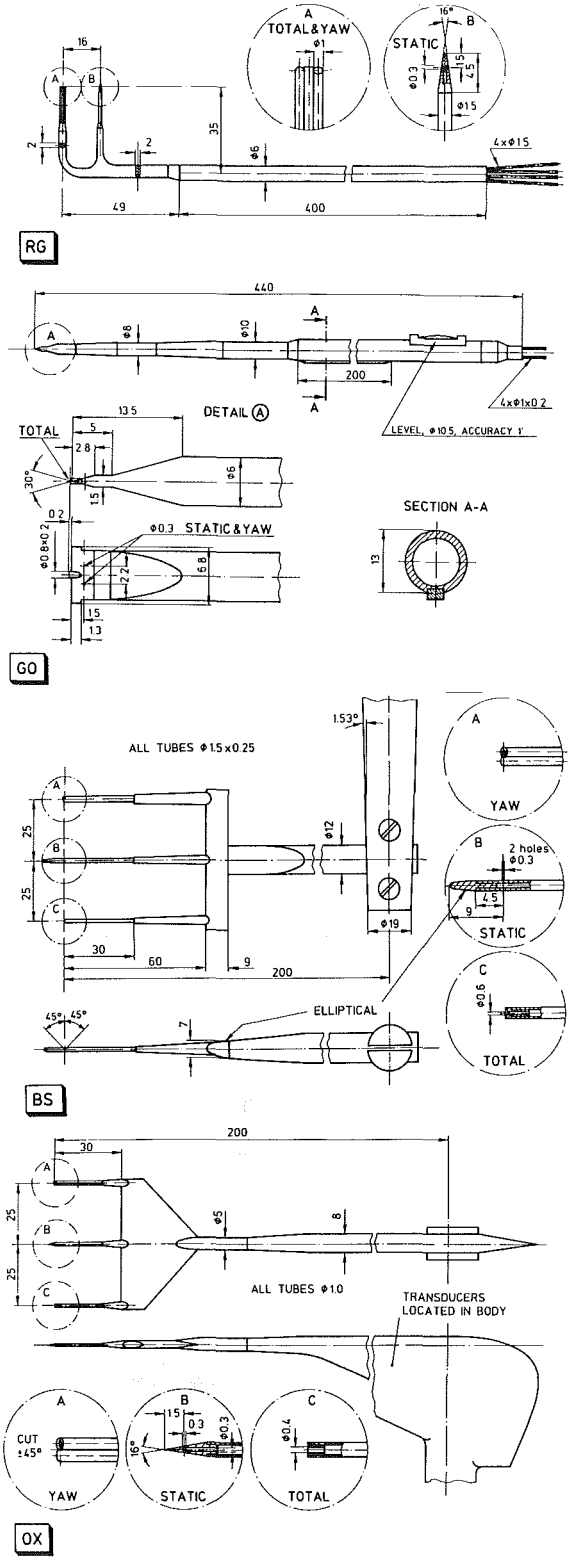

Fig. 3 Comparison of wake traverse probes

Comparison of Results

The results from these cascade measurements in four facilities are described in the order of inlet flow, blade channel, and exit flow. The losses and outlet flow angles quoted for RG are not those reported in [2] but data taken in 1980 with a slightly different probe from that used before. These data are believed to be more accurate and present mixed-out values which was not the case for the first data set.

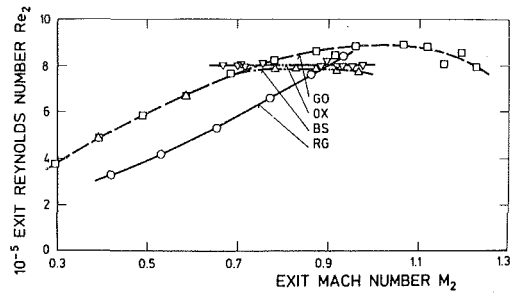

Fig. 4 Exit Reynolds number, $\beta_1 = 30$ deg

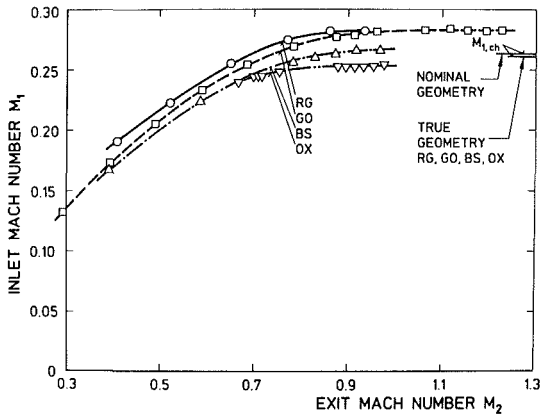

Fig. 5 Inlet Mach number, $\beta_1 = 30$ deg

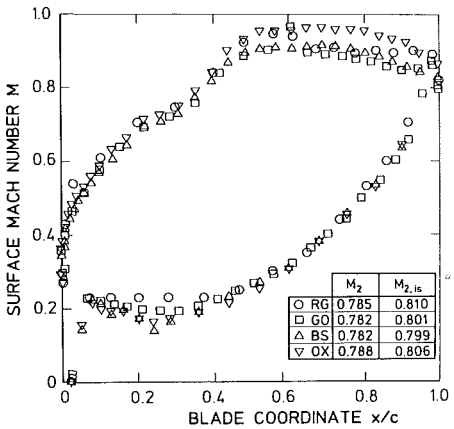

Fig. 6 Surface Mach number, $\beta_1 = 30$ deg, $M_2 = 0.78$, $Re_2 = 6.8$ to 8.2×10^5

The results of GO reported in this paper are evaluated from measurements conducted at the end of 1983. Contrary to the earlier experimental investigations [3] the probe stem and holder were changed in order to decrease blockage, which mainly affected the exit flow angle. Additionally a new and more accurate probe calibration was used.

Inlet Flow Field. The inclination of the cascade and the gaps between end blades and top/bottom wall were chosen in such a way that the inlet flow angle amounts closely to $\beta_1 = 30$ deg and that the flow is periodic in the measurement plane upstream and downstream of the cascade. Table 6 shows some checks of those flow parameters taken over several pitches and given by the terms of average value and standard deviation. The inlet flow angle was close to 30 deg. The variation of the total pressure over time was small with a relative standard deviation of less than ± 0.1 percent.

The inlet Mach number M_1 generally reaches its maximum when the local Mach number across the blade channel exceeds unity. This choking condition results in an exit Mach number

Table 5 Operating conditions

Parameter \ Tunnel	RG	GO	BS	OX
Cascade exit velocity	Sub/transonic	Sub/supersonic	Sub/transonic	Sub/transonic
Reynolds number Re_2	Varying with exit velocity		Independent of exit velocity	
Degree of turbulence Tu_1	1%	1%	0.3 to 0.6%	<1%
Total temperature	278 K	290 K	313 K	287 K

Table 6 Pitchwise variations of flow quantities in the inlet and exit plane, average value, and standard deviation

Parameter \ Tunnel		RG	GO	BS	OX
Inlet	Flow angle β_1	$28.95^\circ \pm 0.47^\circ$ 4)	$29.92^\circ \pm 0.13^\circ$ 6)		$30.04^\circ \pm 0.13^\circ$ 1)
	Mach number M_1	0.282 ±0.003 4)	0.282± 0.001 4)	0.260 ±0.000 3)	0.252 ± 0.005 3)
Exit	Flow angle β_2	$67.03^\circ \pm 0.15^\circ$ 3)	$67.02^\circ \pm 0.22^\circ$ 4)	$67.33^\circ \pm 0.06^\circ$ 3)	$67.76^\circ \pm 0.1^\circ$ 2)
	Mach number M_2	0.933 ±0.006 3)	0.957 ± 0.003 4)	0.828 ±0.003 3)	0.932 ± 0.004 2)
Overall	Loss coefficient ζ	0.046 ±0.007 3)	0.049 ± 0.001 4)	0.039 ±0.003 3)	0.040 ± 0.003 2)
	AVDR Ω	0.929 ± 0.011 3)	0.937 ± 0.008 4)	0.984 ±0.006 3)	1.012 ± 0.01 2)

1) 2) 3) 4) 6) Over 1, 2, 3, 4 or 6 pitches

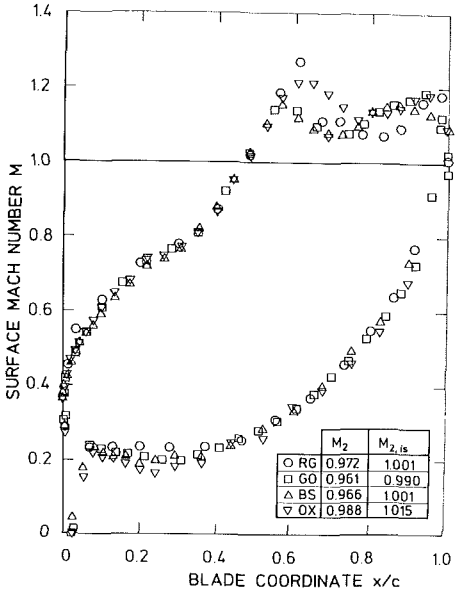

Fig. 7 Surface Mach number, $\beta_1 = 30$ deg, $M_2 = 0.97$, $Re_2 = 7.6$ to 8.9×10^5

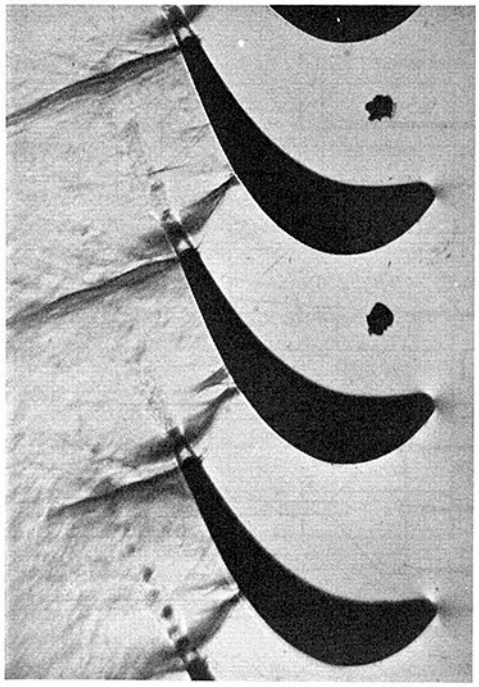

Fig. 8 Schlieren picture, $\beta_1 = 30$ deg, $M_2 = 0.96$, $Re_2 = 8.8 \times 10^5$

of roughly unity. Figure 5 shows different levels for M_1 in the four facilities. For comparison, the theoretical values for choked two-dimensional flow and for a straight sonic line are indicated for the nominal and for the true geometry of all four cascades, i.e., o/c and β_1. These two values are very close to each other. The standard deviation of M_1 given in Table 6 lies between 0 and ± 0.005 and does not explain the spread of the data.

In the absence of endwall boundary layers the choking Mach number will be lower than the theoretical value because of the blade boundary layers and curvature of the sonic line. In the presence of endwall boundary layers the flow acceleration between the inlet and throat planes produces an effective increase of channel width and hence higher inlet Mach numbers, as can be seen for all tunnels but OX in Fig. 5. This effect is proportionally bigger for longer inlet duct lengths and smaller channel widths, and in fact in the case of RG and GO, where this ratio is approximately 20, inlet Mach numbers are significantly higher than for BS and OX, where the ratios are 5 and 3, respectively.

Surface Mach Number Distributions. The Mach number distributions from two flow conditions are shown here: one example for pure subsonic flow and one in the transonic flow region (see Figs. 6 and 7). The flow is characterized by acceleration along the suction side up to $x/c = 0.6$ and by moderate deceleration downstream.

Although the exit Mach numbers in the four facilities lie close together in the subsonic flow case forming a band of $\Delta M_2 = 0.006$, the surface Mach number distributions differ

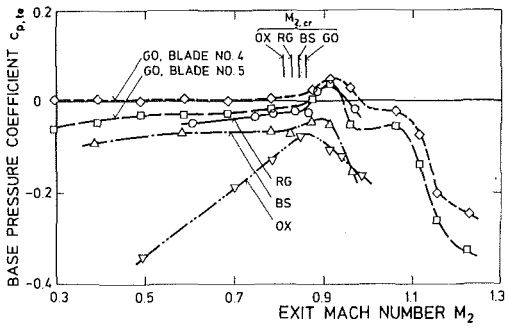

Fig. 9 Base pressure coefficient, $\beta_1 = 30$ deg

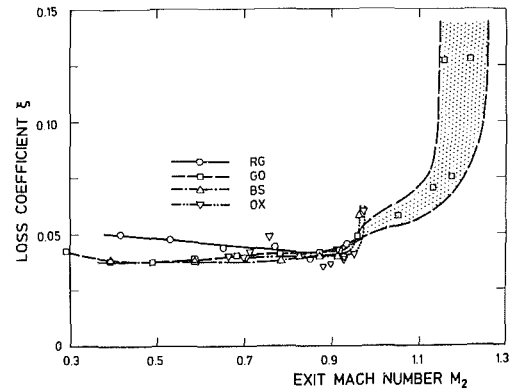

Fig. 10 Loss coefficient, $\beta_1 = 30$ deg

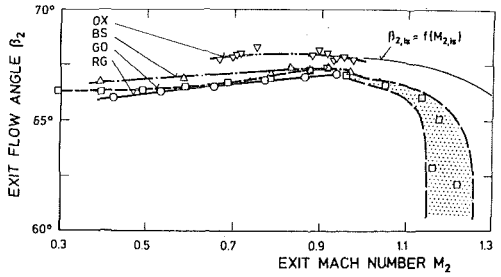

Fig. 11 Exit flow angle, $\beta_1 = 30$ deg

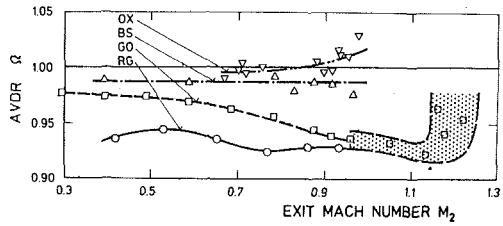

Fig. 12 Axial velocity density ratio, $\beta_1 = 30$ deg

considerably in the rear half of the suction side. Experience in BS [10] showed that Reynolds number variations between $Re_2 = 7$ to 9×10^5 do not affect the aerodynamic characteristics. In particular, the higher Mach number values of OX compared with those of BS on the same hardware are surprising although the inlet Mach number of OX is lower than that of BS. These differences were also observed at other exit Mach numbers [10], and are believed to be due to a discrepancy in the measurement of exit static pressure. Whereas the BS cascade exhausts into a plenum, the OX cascade exhausts through a duct containing the probe traversing mechanism and then to the exhaust system. The practice at OX has been to calibrate a static pressure tapping in the sidewall of this duct behind a sudden expansion step against the mixed-out static pressure measured with the probe in order to be able to set up for predetermined Mach and Reynolds numbers when the probe is removed. This would be done for measuring blade surface velocities, which it is known that the probe can influence. It is apparent from Figs. 6 and 7 that there is a significant loss in pressure due to the presence of the probe and its traverse mechanism while calibrating, despite every effort to minimize their dimensions. It is likely that a more representative downstream static pressure can be based on the average of several sidewall tappings covering one or more pitches in the plane of the probe tip, where the effects of probe blockage should be much reduced.

The results of GO and BS agree fairly well. The slightly higher Mach numbers for the RG blade on the front part of the pressure and suction side and on the rear part of the suction side are related to a different blade contour as checked on a ZEISS profile measuring machine and as computationally proved by a time marching method [3].

The local peak at $x/c = 0.61$ on the suction side of the GO cascade is caused by the trip wire which is positioned just upstream of this tapping. A comparison with recent GO tests without trip wire showed no further difference in the local or overall characteristics.

In the transonic flow case (Fig. 7), sonic conditions are obtained at $x/c \approx 0.47$ on the suction side and $x/c \approx 0.99$ on the pressure side resulting in a fairly straight sonic line across the blade passage. A comparison of the four Mach number distributions leads to similar conclusions as in the subsonic case. In particular, the Mach number distribution for the RG blade indicates a turbulent shock boundary layer interaction. The surface roughness, due to very dense instrumentation of a very small blade, or a different structure of the flow turbulence might be responsible for transition of the boundary layer near the throat. However, the band of exit Mach numbers is wider with $\Delta M_2 = 0.027$. This may influence the location of compression shocks. Heavy decelerations occur on the suction side at $x/c \approx 0.65$ and 0.98. The Schlieren picture from GO in Fig. 8 shows compression shocks at these two locations.

Base Pressure. The pressure at the blade trailing edge is important for the calculation of the trailing edge losses and the mass flow rate of cooling air in the case of trailing edge ejection as well as for the determination of the trailing edge shock system in supersonic exit flow [9].

This pressure is also called the base pressure and shown as a dimensionless coefficient in Fig. 9. Two results are given from the GO cascade showing the spread of data from one blade to the next one. Except the OX results, the base pressure coefficient does not change remarkably with M_2 in the subsonic range, $M_2 \leq M_{2,cr}$. The critical exit Mach number $M_{2,cr}$ was determined by available sets of surface Mach number distributions: $M_{2,cr}$ is that value of M_2 at which M becomes unity at one location of the blade surface. It is $M_{2,cr} = 0.81$ to 0.86 as indicated. The highest $c_{p,te}$ is obtained at a slightly higher exit Mach number, $M_2 - M_{2,cr} \approx 0.06$. In that case, the normal trailing edge shock causes some pressure increase. With further increase of M_2, the normal shock develops in an oblique shock which entails a rapid drop of the base pressure. The lower base pressures at OX are consistent with the blade surface pressure distributions, and indicate that the downstream pressure p_2 is too high (or equivalently, that the sidewall reference pressure is too low), in reality.

Wake Traverse Results. Wake traverses were carried out over three to four pitches at RG and GO and their average values are shown in Figs. 10–12. At BS and OX only one pitch was considered except for one example with several pitches. Concerning the GO results at high exit Mach numbers, $M_2 > 0.95$, the band of the standard deviation is also indicated. This band is small up to $M_2 = 0.95$ but widened with increasing M_2 in both M_2 and wake parameters. The cascade was not designed for supersonic exit flow, and the boundary

layer separates on the convex curved suction surface downstream of the throat which causes very high losses.

Typical values of the standard deviations are given in Table 6 for $M_2 < 0.96$.

The loss coefficient is nearly constant at $M_2 < 0.95$ T (see Fig. 10). The somewhat higher loss at the lowest values of M_2 at RG and GO could be due to the lower Re_2 in these cases. This tendency was also seen in additional tests at BS with varying Reynolds number [10]. However, this explanation does not hold any more for M_2, between 0.80 and 0.95 where the Reynolds numbers are nearly the same in all cases. The RG, GO, and BS data differ by only $\Delta\xi = 0.003$ which is tolerable in view of the standard deviation given in Table 6 for these tunnels.

The scatter of the OX losses looks to be somewhat higher despite $Re_2 = \text{const}$. This might be caused by insufficient pressure adjustment in that short running time. However, there are only three points ($M_2 = 0.756$, 0.880, and 0.895) which fall out of the band of the RG-GO-BS results.

The loss increases at $M_2 > 0.92$ for GO and BS due to the occurrence of stronger compression shocks. This M_2 agrees with the peak in base pressure in Fig. 9.

The exit flow angle increases slightly as usual with increasing exit Mach number up to $M_2 = 0.95$ which corresponds to the low loss region (see Fig. 11). At transonic flow, the results of RG, GO, and BS form a very narrow band of $\beta_2 = 67.2 \pm 0.2$ deg which corresponds to the standard deviation in Table 6. The β_2 level is believed with respect to the theoretical value of $\beta_{2,is} = 67.8$ deg at $M_2 = 1.0$ allowing a few tenths of a degree for frictional effects. $\beta_{2,is}$ was calculated assuming again choked two-dimensional flow and a straight sonic line. The level of β_2 decreases with increasing M_2 at $M_2 > 1.0$ due to the increase in loss mentioned above. This is also the reason for the increasing difference in the exit flow angles of isentropic and real flow.

A check of the flow conditions in the inlet and exit measurement planes can be made by consideration of the axial velocity density ratio Ω (see Fig. 12), which is based on midspan measurements. A deviation of Ω from 1 may be the result of either a non-two-dimensional flow or of a measurement error, in particular of an error in the flow angles. Obviously an error in β_1 or β_2 makes the flow look more or less two-dimensional. A measurement error of ± 0.5 T deg results in a $\Delta\Omega$ of ± 0.005 for an error in β_1 and of ± 0.02 for an error in β_2. For both OX and BS the measured Ω is within $\Omega = 1.000 \pm 0.025$, which indicates that the flow in both tunnels is fairly two-dimensional. This is not the case for the RG and GO tunnels, where maximum deviations of $\Delta\Omega = 0.08$ are recorded. These deviations point clearly to non-two-dimensional flow conditions, which is confirmed by measured inlet Mach numbers greater than the theoretical choked value (Fig. 5). A difference of $\Delta M_1 = +0.02$ for both tunnels is equivalent to a decrease of Ω of 0.08. Since the inlet Mach numbers are related directly to the inlet area to throat area ratio, it follows that the flow downstream of the throat is essentially two-dimensional. If this were not the case, it would be difficult to explain the good agreement in β_2 between RG and GO on one side and BS on the other side. It appears therefore that contrary to compressor cascades $\Omega \neq 1$ does not necessarily affect the outlet flow angle measurements or the loss measurements, as shown before.

Conclusions

A plane turbine cascade was investigated in four European wind tunnels at sub/transonic exit velocities. Due to the different size of the individual test sections, the chord length of the blades ranged from $c = 32.6$ to 100 mm. Two facilities are characterized by two particular features: First, they have test sections of the same size so that identical cascades could be investigated, and second, the exit Mach number could be varied at constant Reynolds number. All tests were carried out at normal wind tunnel turbulence.

The comparison of the main results from these four facilities leads to the following conclusions:

1 The inlet Mach number evaluated from static and total pressure measured upstream of the cascade is in three facilities slightly too high for choked flow, i.e., it is higher than the theoretical value due to inlet flow displacement by side wall boundary layers. This may be correlated, at least qualitatively, with the different tunnel inlet geometries.

2 The surface Mach number distributions show small differences due to small deviations of the contours and due to the fact that the comparison could not be made at the identical exit Mach number. The exit Mach number has to be evaluated carefully when the surface pressure is measured independent of the wake traverse, i.e., with removed exit probe. The critical Mach number amounts to $M_{2,cr} = 0.81$ to 0.86.

3 The losses of the individual tunnels lie within a band which corresponds to the standard deviations of each tunnel over several pitches. They are with $\xi \approx 0.04$ relatively high due to the thick trailing edge. At higher Mach numbers, $M_2 > 0.92$, ξ increases because of compression shock losses.

4 The exit flow angles of three facilities agree fairly well with $\beta_2 = 67.2 \pm 0.2$ within $M_2 = 0.8$ to 1.0 and lie slightly below the value $\beta_{2,is} = 67.8$ deg for isentropic flow as it should be.

5 The axial velocity density ratio indicates nearly two-dimensional flow only in two facilities. The other two tunnels give lower values due to the inlet geometry. It appears that Ω does not necessarily affect the loss and the exit flow angle in the range of $\Omega = 0.9$ to 1, unlike compressor cascades.

Acknowledgments

Part of this investigation was carried out by M.L.G. Oldfield and P. King from Oxford University and by H. Hoheisel and G. Ramm from DFVLR Braunschweig. Their cooperation is gratefully acknowledged.

References

1 Dejc, H. E., Filippov, G. A., and Lazarev, L. A., "Atlas of Axial Turbine Blade Characteristics. Part I: Method of Profiling and the Aerodynamic Characteristics of Cascades," Mashinostroenie, Moscow, 1965 (C.E. Trans. 4563).

2 Sieverding, C. H., "Experimental Data on Two Transonic Turbine Blade Sections and Comparison With Various Theoretical Methods," in: *Transonic Flows in Turbomachinery*, VKI LS 59, 1973.

3 Lehthaus, F., "Berechnung der transsonischen Strömung durch ebene Turbinengitter nach dem Zeit-Schritt-Verfahren," VDI-Forschungsheft 586, 1978, pp. 5-24.

4 Heinemann, H.-J., "The Test-Facility for Rectilinear Cascades (EGG) of the DFVLR," DFVLR IB 222-83 A 14, 1983.

5 Hoheisel, H., and Kiock, R., "Zwanzig Jahre Hochgeschwindigkeits-Gitterwindkanal des Instituts für Aerodynamik der DFVLR in Braunschweig," *Zeitschrift fur Flugwissenschaften und Weltraumforschung*, Vol. 1, No. 1, 1977, pp. 17-29.

6 Baines, N. C., Oldfield, M. L. G., Jones, T. V., Schultz, D. L., King, P. I., and Daniels, L. C., "A Short Duration Blowdown Tunnel for Aerodynamic Studies on Gas Turbine Blading," ASME Paper No. 82-GT-312.

7 Sieverding, C. H., "Pressure Probe Measurements in Cascades," in: *Modern Methods of Testing Rotating Components of Turbomachines (instrumentation)*, M. Pianko, ed., AGARDograph No. 207, 1975.

8 Amecke, J., "Anwendung der transsonischen Ähnlichkeitsregel auf die Strömung durch ebene Schaufelgitter," in: *Probleme der transsonischen Stromung durch Turbinen-Schaufelgitter*, VDI-Forschungsheft No. 540, VDI-Verlag Dusseldorf, 1970, pp. 16-28.

9 Sieverding, C. H., Stanislas, M., and Snoek, J., "The Base Pressure Problem in Transonic Turbine Cascades," Trans. ASME JOURNAL OF ENGINEERING FOR POWER, Vol. 102, No. 3, July 1980, pp. 711-718.

10 Baines, N. C., King, P., Oldfield, M. L. G., Kiock, R., Hoheisel, H., Ramm, G., Lehthaus, F., Kost, F., and Sieverding, C. H., Symposium on "Measuring Techniques in Transonic and Supersonic Flows in Cascades and Turbomachines," Genoa, 1985, to be published.

Investigations of the Effect of Annulus Taper on Transonic Turbine Cascade Flow

W. Bräunling

F. Lehthaus

DFVLR—Institute for Experimental Fluid Mechanics,
D-3400 Göttingen, West Germany

In a test facility for rotating annular cascades with three conical test sections of different taper angles (0, 30, 45 deg), experiments are conducted for two geometrically different turbine cascade configurations, a hub section cascade with high deflection and a tip section cascade with low deflection. The evaluation of time-averaged data derived from conventional probe measurements upstream and downstream of the test wheel in the machine-fixed absolute system is based on the assumption of axisymmetric stream surfaces. The cascade characteristics, i.e., mass flow, deflection, and losses, for a wide range of inlet flow angles and outlet Mach numbers are provided in the blade-fixed relative system with respect to the influence of annulus taper. Some of the results are compared with simple theoretical calculations. To obtain some information about the spatial structure of the flow within the cascade passages, surface pressure distributions on the profiles of the rotating test wheels are measured at three different radial blade sections. For some examples those distributions are compared with numerical results on plane cascades of the same sweep and dihedral angles and the same aspect ratios. The computer code used is based on a three-dimensional time-marching finite-volume method solving the Euler equations. Both experimental and numerical results show a fairly good qualitative agreement in the three-dimensional blade surface pressure distributions. This work will be continued with detailed investigations on the spatial flow structure.

Introduction

Calculation and design methods used by industry for analyzing subsonic flows through axial turbomachines are often based on the assumption of coaxial cylindrical stream surfaces. Experimental and theoretical approaches based on this simplified model have been quite successful in the past. Such stream surfaces may exist exactly in incompressible flow machines of free vortex design, but this flow model has also turned out to be useful when the flow does not meet these conditions exactly, as for example when the compressibility effects of the flow are no longer negligible but are of a moderate magnitude.

The development of modern high-power axial turbines has led to transonic flow regimes. Consequently, the corresponding high expansion of the flow medium and the resulting increase of its volume often requires an increase of the annulus cross section in flow direction. Therefore, especially in the rear stages of low-pressure steam turbines and in high-pressure turbines of jet engines, the annulus walls may be tapered with cone half-angles up to 30 deg or even up to 45 deg in some cases resulting in a more or less conical flow. Thus, significant amounts of sweep and dihedral occur where blades intersect a tapered annulus wall or a hypothetical conical stream surface, even when the staggered blades themselves are radial [1] (Fig. 1).

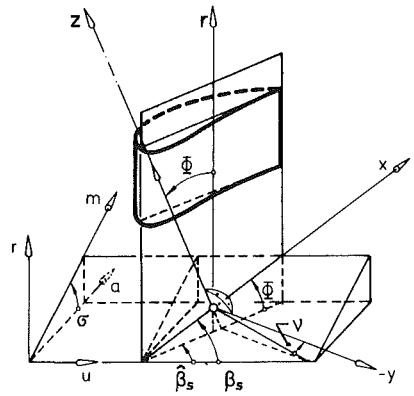

Fig. 1 Geometric definitions

It is well known from single airfoils of finite aspect ratio with sweep and dihedral that, even neglecting secondary flow effects induced by viscous boundary layers, a complicated three-dimensional flow exists. On the suction and pressure sides of such a profile significant differences in flow pattern appear, resulting in a considerable shift of the streamlines. In a turbine wheel where a number of blades are present these characteristics yield a flow model with periodically warped

Contributed by the Gas Turbine Division and presented at the 1985 Beijing International Gas Turbine Symposium and Exposition, Beijing, People's Republic of China, September 1-7, 1985. Manuscript received at ASME Headquarters May 31, 1985. Paper No. 85-IGT-64.

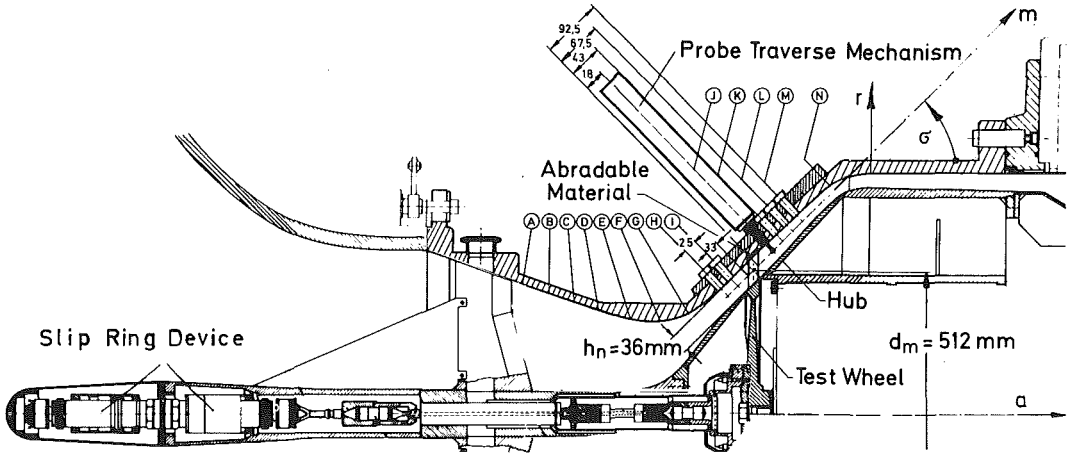

Fig. 2 $\sigma = 45$ deg test section of test facility for rotating annular cascades

stream surfaces. However, from the theoretical aerodynamics of single airfoils, it is well known that the influence of sweep decreases with decreasing aspect ratios. Analogously it may be concluded that a three-dimensional flow model is necessary for turbine cascades with large annulus taper angles and high aspect ratios. Whereas in cases of small or moderate aspect ratios an inviscid flow model with conical stream surfaces may be an appropriate simplifying assumption, even when considerable taper angles occur.

For flows of such or similar kind only a few theoretical and experimental results are available in the open literature which are listed in [2]. All this literature is exclusively confined to subsonic flows. Therefore, the aim of the present investigations is to provide some knowledge about the influence of annulus taper when transonic flow regimes exist. As a first step, the experimental work presented here does not include sophisticated investigations of the complete three-dimensional flow structure in a tapered flow annulus. Rather, the tests, conducted mainly as contract work for industry, should be regarded as a simplified work useful to design engineers to describe conical flows at different taper angles with respect to the basic aerodynamic characteristic quantities of a turbine cascade. Some preliminary information about the spatial flow structure in the test cases is provided by blade surface pressure measurements and some numerical calculations. Detailed investigations of the spatial flow structure by means of laser anemometry will be conducted in the near future.

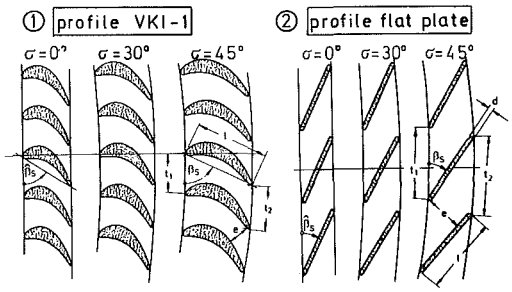

Fig. 3 Development of the conical midsections at the mean diameter of test wheel bladings into a plane

Experimental Techniques and Data Evaluation

Test Facility and Test Configurations. The measurements reported here have been carried out in a test facility for rotating annular cascades. A complete description of the test facility, the measurement and evaluation methods used, are reported in detail in [2, 3].

Nomenclature

c_p = specific heat at constant pressure
c^*_{p1} = critical pressure coefficient, equation (6)
d = trailing edge thickness
d_m = mean diameter of the test wheels = 512 mm
e = throat of a cascade passage
$h, (h_n)$ = stream channel height perpendicular to a hypothetical conical stream surface (within the wheel region = 36 mm)
l = profile chord length
M, Ma = Mach number
p = pressure
p_m = measured blade surface pressure
p_{01} = total pressure of the homogeneous inlet flow at the time-marching finite-volume method
t = cascade pitch
u = circumferential velocity
v, w = absolute, relative velocity
x, y, z = blade fixed coordinates, Fig. 1
α, β = absolute, relative flow angle
γ = ratio of specific heats
ζ_w = total pressure loss coefficient, equation (5)
ν = dihedral angle
σ = taper angle or cone half-angle
Φ = sweep angle
ω, ω_{max} = rotor angular velocity, maximum at choked flow

Subscripts

1, 2 = inlet, outlet plane of a cascade
a, m, r = axial, meridional and radial direction
c = choked
e = throat
is = isentropic
R = blade root
rot = rothalpy
s = staggered
t = total flow conditions
th = theoretical
T = blade tip
u = circumferential direction
v, w = absolute, and relative system

Superscripts

* = critical flow conditions
$\hat{}$ = projected from a conical onto a cylindrical reference surface

Table 1 Geometric data of hub section cascade (1) and tip section cascade (2)

	σ	Φ	ν	β_S	e	e/t_1	t_2/t_1	t_1/l
	[°]	[°]	[°]	[°]	[mm]	[1]	[1]	[1]
(1)	0	00.00	00.00	56.70	7.573	0.3766	1.000	0.710
	30	25.76	15.93	60.37	8.564	0.4376	1.055	0.622
	45	39.89	22.84	65.09	9.823	0.5123	1.097	0.520
(2)	0	00.00	00.00	25.00	13.274	0.3713	1.000	1.000
	30	13.71	26.95	28.30	14.875	0.4238	1.037	0.954
	45	22.91	39.86	33.40	17.166	0.4959	1.065	0.892

The investigations were performed for cone half-angles $\sigma = 0$, 30, and 45 deg. Figure 2 shows for example a sketch of the $\sigma = 45$ deg test section. Within the wheel region the contours of hub and casing are parallel to each other and inclined to the axis at the cone half-angle. Downstream of the test wheel, where probe measurements were performed, the area of annulus cross section is constant. By combination of the $\sigma = 45$ deg housing with a $\sigma = 40$ deg hub an additional test configuration was assembled with a stream channel diverging in the meridional direction within the wheel region.

The two cascades tested were a high turning hub section, built with VKI-1 profiles, and a low turning tip section, built with flat plate profiles, $d/l = 0.05$. The coordinates of the VKI-1 profile are given in [4]. The significant changes in the geometric data of the conical midsections at the mean diameter of the bladings, $d_m = 512$ mm (Fig. 2) due to changing taper angles may be seen from Fig. 3 and Table 1. For example, with increasing taper angle the thickness of the trailing edge increases; the ratio of the smallest distance e to the inlet pitch t_1 between two adjacent profiles also increases while the deflection decreases. The hub section cascade retains its type as a cascade with convergent flow passages when cut conically, despite the resulting geometric distortions whereas the tip section cascade yields geometric conditions with an increasing divergence of the flow passages in flow direction due to an increasing taper angle.

Like the cascade geometry, the flow conditions in the cascade-fixed relative system are defined on a hypothetical conical stream surface at midheight of the annulus. The spatial velocity triangle in Fig. 4 yields the definitions of the absolute and relative velocity vectors. Inlet guide vanes are not used. Therefore, the circumferential velocity u_1 of the test wheel has to be adjusted to the absolute inlet velocity v_1, which is axial and has to be measured, and to the desired flow angle β_1. To simulate the relative inlet flow correctly for the hub section turbine cascade, the test wheel has to be driven at low circumferential speeds and for the tip section cascade the rotor is braked at high circumferential velocities.

Probe Measurements. The leading feature of the measurement and evaluation method used is the determination of aerodynamic characteristic cascade data in the inlet and outlet plane of the cascade calculated from time-averaged absolute flow quantities. With conventional total pressure and total temperature probes fixed upstream and downstream of the test wheels, measurements were performed. The reduction of data from the measurement planes to the respective inlet and outlet plane is done by means of the flow model of conical stream surfaces and using the conservation laws of mass, momentum, and energy. The essential results of the investigations are the relative inlet Mach number M_{w1}, the relative outlet flow angle β_2, and the loss coefficient for relative total pressure ζ_w, which in turn depend on the relative inlet flow angle β_1, and the relative downstream Mach number M_{w2}. Such a measurement and evaluation method was developed earlier for cylindrical rotating annular cascades [3], and has now been extended and modified to deal with the current investigations of conical flows [2]. The fundamental assumptions are: axisymmetric conical stream surfaces, homogeneous steady inlet flow, ideal gas, negligible end-wall boundary layers and secondary flow effects in the midsection of the stream channel, and finally no heat exchange from the flow medium to the blades or vice versa. By traversing the downstream probes at different axial distances from the blading it is checked whether the absolute total pressure and absolute total temperature are sufficiently constant in the core flow at midheight [2]. At this station measurements were taken.

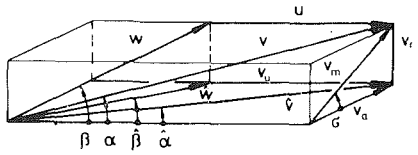

Fig. 4 Spatial velocity triangle

Blade Surface Pressure Distribution Measurements. For a better understanding of the physical behavior of conical flows within the blade passages, measurements of blade surface pressure distributions from the rotating test wheels were performed. The device used (Fig. 2) operates trouble free up to 10,000 rpm and is described in detail in [2, 5] together with its calibration procedures and the respective evaluation method including the correction for centrifugal forces. Forty-eight blades of each test wheel are instrumented, each with only one static pressure tapping. Altogether, the tappings are in sequence such that for one of the blade sections, which are at 25, 50, and 75 percent of the blade height, measurements at 16 locations in chord direction can be obtained. The tappings are connected by pressure tubes to a disk. In the counterpart of this disk the transducers are mounted at a radius of 60 mm such that the diaphragms are perpendicular to the axis of the test facility. They are of KULITE type XTH-1-190-10A; their range is from zero to ten psi absolute pressure. In this way the pressure distribution in one of the three blade sections may be measured during one test run. Then, by turning the housing of the transducers against the disk the connections are provided for the measurements in the next blade section. The electrical signals from the rotating system are led via slip rings to the machine-fixed system.

Effect of Annulus Taper on Experimental Results

In the following sections, results of both the probe and the pressure distribution measurements will be discussed with regard to the effect of annulus taper. To provide for a convenient comparison of the results inlet flow angles have to be defined consistently with the different profile and cascade geometries at different taper angles (Fig. 3). This means, instead of the inlet flow angle β_1 on the conical stream surface, its projection onto a cylindrical reference surface β_1, which is identical to the inlet flow angle of the cylindrical cascade, is kept constant for the comparison.

$$\hat{\beta}_1 = \left(\frac{\pi}{2}\right) - \arctan\left(\frac{\tan\left(\frac{\pi}{2} - \beta_1\right)}{\cos\sigma}\right) \qquad (1)$$

In order to get an estimate of the effect of annulus taper, two simple theoretical relations can be derived. The first relation gives a theoretical maximum choking Mach number,

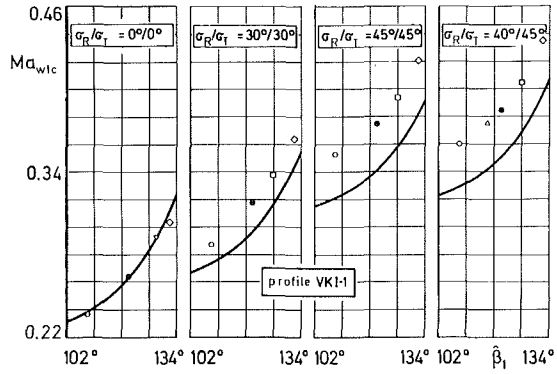

Fig. 5(*a*) Effect of relative inlet flow angle and of annulus taper on relative choking Mach number

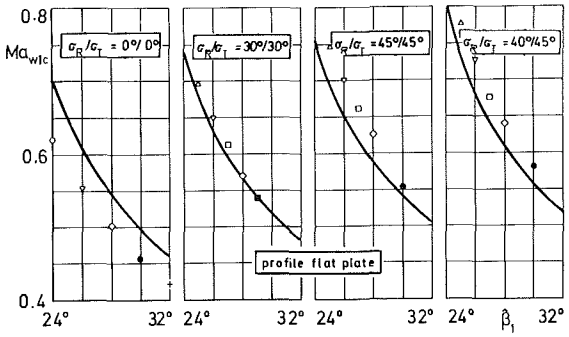

Fig. 5(*b*) Effect of relative inlet flow angle and of annulus taper on relative choking Mach number

M_{w1c}. This calculation is possible by developing the axisymmetric conical stream surface into a plane and then by assuming isentropic flow and a straight sonic line between two adjacent blades with perpendicular through-flow. At midheight of the blades the equation of continuity is applied to a control surface between the inlet plane and the throat *e* (see Fig. 3) to obtain

$$M_{w1c} = \left(\left(1 + \frac{\gamma-1}{2} M_{w1c}^2\right)\left(\frac{2}{\gamma+1}\right)\left(\frac{T_{twe}}{T_{tw1}}\right)\right)^{\frac{\gamma+1}{2(\gamma-1)}} \cdot \frac{h_e}{h_1} \frac{e}{t_1} \frac{1}{\sin \beta_1} \tag{2}$$

This equation can be solved iteratively. Using the same assumptions as before and establishing a control surface between the throat and the outlet plane an analogous equation for the relative outlet flow angle β_{2c} is derived

$$\sin \beta_{2c} = \left(\left(1 + \frac{\gamma-1}{2} M_{w2}^2\right)\left(\frac{2}{\gamma+1}\right)\left(\frac{T_{twe}}{T_{tw2}}\right)\right)^{\frac{\gamma+1}{2(\gamma-1)}} \cdot \frac{1}{M_{w2}} \frac{h_e}{h_2} \frac{e}{t_2} \frac{1}{1-\zeta_w} \tag{3}$$

The equations (2) and (3) contain a quotient of relative total temperatures in each case, which may be expressed as follows

$$\frac{T_{twe}}{T_{tw1(2)}} = \frac{1 + \frac{(r_e\omega)^2}{2c_p T_{\text{rot}}}}{1 + \frac{(r_{1(2)}\omega)^2}{2c_p T_{\text{rot}}}} \tag{4}$$

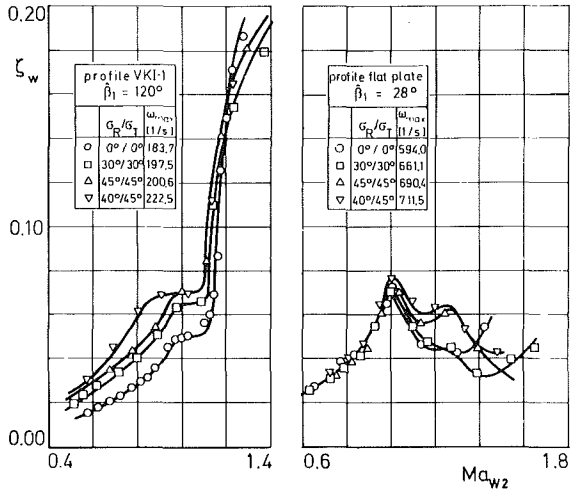

Fig. 6 Effect of relative outlet Mach number and of annulus taper on relative total pressure loss coefficient

They are unity in cases of stator flows ($\omega = 0$), or flows on cylindrical stream surfaces ($r_1 = r_2 = r_e$). In these two equations the product $c_p T_{\text{rot}}$ is the rothalpy. For axial absolute inlet flow, the temperature T_{rot} is identical to the absolute total temperature T_{tw1} measured upstream of the test wheel [2].

Inlet Mach Number. In Fig. 5 the experimental choking Mach numbers and the predicted ones are plotted versus the whole range of projected relative inlet flow angles $\hat{\beta}_1$ where measurements were carried out. The measured values are marked by symbols and the corresponding solutions from equation (2) by lines. For calculation purposes radius r_e in the middle of the throat was used and the stream surface thickness h_e/h_1 was assumed to be a constant and equal to unity. The theoretical results agree with the measurements in their trend. The differences between the calculated and the measured choking Mach numbers lie within a range of the same order of magnitude as that from corresponding comparisons for straight cascades. Obviously, the greater part of the experimental results lie above the theoretical ones, which means that the experimental mass flux is larger than the theoretically predicted one. This is contrary to the physical assumptions used in the theoretical relations. Therefore, the sensitivity of the method was checked by enlarging the ratio e/t_1 by only 1 percent. The discrepancies were reduced considerably. Such a small modification can occur, for example, by a small difference between the taper angle of the actual flow and the hypothetical one. The effect is the same as when changes in stream surface thickness along the current control volume occur. Therefore slight increase in mass flux occurs at the 40/45 deg configurations when compared to the 45/45 deg configuration due to the additional increase in cross-sectional area.

Total Pressure Loss. One way to describe cascade performance is to make use of the coefficient of total pressure loss, which generally for conical flow conditions can be defined as follows

$$\zeta_w = 1 - \left(\frac{p_{tw2}}{p_{tw1}}\right)\left(\frac{T_{tw1}}{T_{tw2}}\right)^{\frac{\gamma}{\gamma-1}} \tag{5}$$

The ratio of the relative total pressures in the cascade outlet plane for nonisentropic and for isentropic flow respectively is the basis for this loss definition. The quotient of the relative total temperatures is unity in the case of cylindrical rotating annular cascade flows.

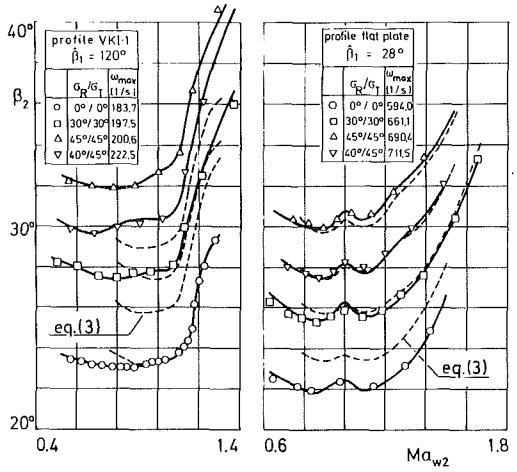

Fig. 7 Effect of relative outlet Mach number and of annulus taper on relative outlet flow angle

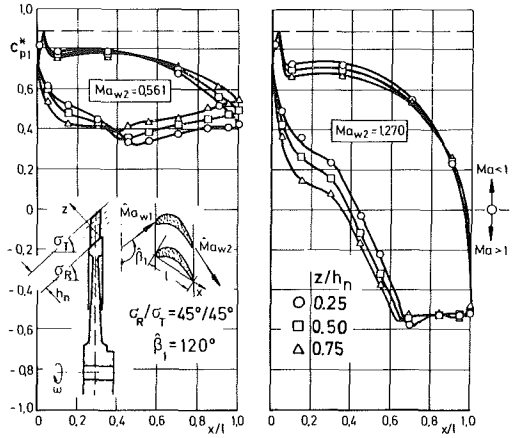

Fig. 8 Blade surface pressure distribution at the $\sigma = 45$ deg hub section cascade

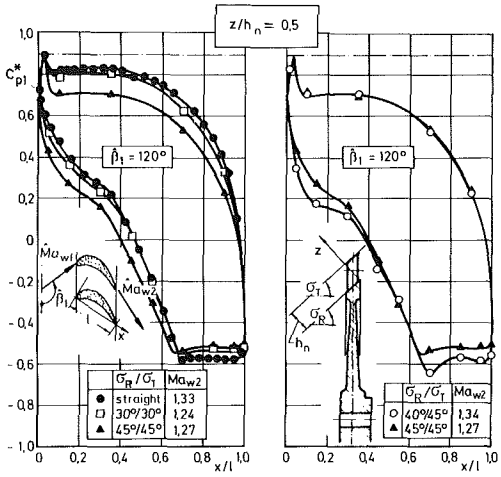

Fig. 9 Effect of annulus taper on the pressure distribution at mid-section of the blading

The change in total pressure loss versus the relative outlet Mach number due to different taper angles is shown in Fig. 6 for the two investigated cascade types, each at one specified inlet flow angle. In the whole investigated outlet Mach number range for the hub section cascades up to the point of steep growth of the losses, which lies for all configurations near $M_{w2} = 1.1$, an increase of losses with increasing taper angles is seen and an additional increase is evident when the annulus walls are divergent. However, the curves of the losses coincide for all tip section cascade configurations in the subsonic Mach number range. Only in the supersonic range differences occur. In principle, the same interdependences between losses and taper angles are evident in the Mach number range $1.0 < M_{w2} < 1.2$, as was the case for the hub section cascade in the subsonic range. At still higher Mach numbers intersections of the curves occur, and in such a way that the loss minima shift to higher Mach numbers with increasing taper angles. Then it may be concluded that this is a consequence of the increasing divergence of the cascade passages in flow direction suitable for higher supersonic Mach numbers. Although in the downstream measurement planes test data still could be evaluated in the range of the highest investigated Mach numbers, especially in the case of the tip section cascade, it was not possible to reduce these data from the downstream measurement plane to the outlet plane by using the flow model of conical stream surfaces. In this case the flow model does not represent the real flow conditions sufficiently well to satisfy the equation of continuity. Therefore, the loss minima of both 45/45 deg and 40/45 deg configurations are not drawn in Fig. 6, although they can be proved in the measurement planes [2].

Flow Outlet Angle. Figure 7 shows the measured and predicted relative outlet flow angles versus the relative outlet Mach number. The flow angles predicted from equation (3) are marked with broken lines. The parameter is the cone half-angle again. The different levels of the curves indicate the differences in mass fluxes along the hypothetical conical stream surfaces, as was the case for the inlet Mach number. The curves of the divergent 40/45 deg configurations lie below those of the 45/45 deg configurations with the parallel walls. Using the equation of continuity it is easy to verify that this is a consequence of the increasing flow cross sections in meridional direction.

For predicting the outlet flow angles, the total pressure losses according to Fig. 6 and the rotational speed of the test wheels were used in equation (3). The differences between the measured angles and the predicted ones here are also due to the differences between the measured and predicted mass fluxes, as was the case for the predicted and measured choking inlet Mach numbers. The trends observed in the experiments are verified quite well by the theoretical calculations. The good agreement for the results of the tip section cascade can not be generalized, especially when compared with the results of the hub section cascade where some considerable level shifts are evident.

Blade Surface Pressure Distribution. In order to present blade surface pressure distributions in transonic flows, it is appropriate to use the critical pressure coefficient

$$c_{p1}^* = \frac{p_m - p_1^*}{p_1^*} = \frac{p_m}{p_{tw1}} \left(\frac{\gamma+1}{2} \right)^{\frac{\gamma}{\gamma-1}} \tag{6}$$

c_{p1}^* will have positive and negative values for subsonic and supersonic flows respectively, with sonic conditions corresponding to $c_{p1}^* = 0$.

The pressure distributions from the rotating test wheels were measured in three radial locations at 25, 50, and 75 percent of blade height from the hub. Figure 8 shows a comparison of the pressure distributions at these three radial locations for two different Mach numbers for the $\sigma = 45$ deg hub section cascade at one projected inlet flow angle of $\hat{\beta}_1 = 120$ deg. Considerable change in pressure distributions along the blade height is evident. Near the leading edges of the blades the profile loading is lower near the hub than near the

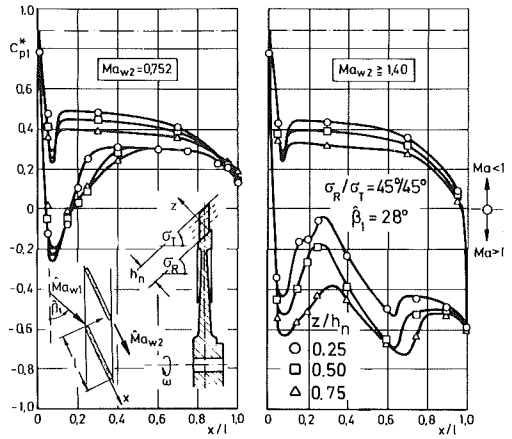

Fig. 10 Blade surface pressure distribution at the $\sigma = 45$ deg tip section cascade

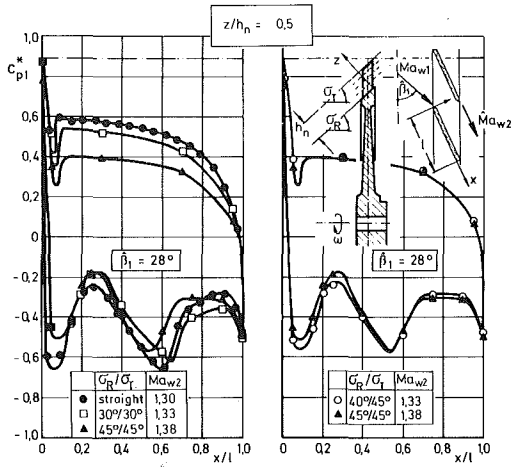

Fig. 11 Effect of annulus taper on the pressure distribution at the midsection of the blading

casing. Then, farther downstream, a region follows where the pressure distribution curves intersect each other in such a way that the local loading conditions are reversed. The points of intersection shift toward the trailing edge with increasing expansion of the flow medium; but at the highest investigated Mach numbers flow separation from hub to tip is observed on the rear part of the suction side. From other pressure distributions it can be concluded that on the rear part of the suction side, the flow separates earlier near the hub than near the casing as is well known from stator flows, where low-energy material in the profile boundary layer is transported into the hub region due to the radial static pressure gradients, thus encouraging a premature flow separation in this region. In the case of a rotating wheel the centrifugal forces are opposite in direction to this radial pressure gradient. Due to the low rotation speeds at the investigated hub section cascade test wheels, one can assume that the influence of the centrifugal forces is so small that the radial pressure gradient dominates. The increase in inlet flow angle of about 2 deg [2] from hub to tip is not a sufficient reason for the different blade loadings near the leading edges. Therefore one can conclude that this blade loading behavior is essentially due to tapering. Away from the leading edges a similar conclusion can be drawn even though an effect of the radial pressure gradient due to the outlet swirl of the test wheel is present.

Figure 9 shows the variation of the pressure distributions at the middle of the blade height, due to both increasing taper angle and annulus divergence. As regards the dependence on taper angle this figure shows the same trends for both suction side and pressure side. This means that the local Mach numbers at the profile contour increase progressively in each case with increasing cone half-angle. The additional annulus divergence merely gives local changes in the pressure distribution curves of the suction side, which are confined to the vicinity of the leading edge of the profile.

Figure 10 shows some results of the pressure distribution measurements from the $\sigma = 45$ deg tip section cascade. Using Schlieren pictures from a geometrically similar straight cascade, but without sweep and dihedral, the general physical background of the curves is explained in [2]. At the leading edge of the profiles a considerable overexpansion with steep gradients is evident in each case. Especially on the suction side a considerable increase of the surface pressures, with compression shock development depending on Mach number follows. By this recompression the attached boundary layer is caused to undergo transition to turbulence, mostly combined with a small separation bubble. For a higher outlet Mach number a Prandtl-Meyer expansion, originating from the trailing edge of the adjacent profile, influences the suction side from approximately $x/l = 0.3$ onward in such a way that the flow on the suction side is now accelerated again. Behind the second pressure minimum a recompression follows due to the reflection of an oblique shock, coming from the wake confluence at the trailing edge of the adjacent profile. This shock becomes more oblique with increasing Mach numbers. Therefore, the location of the shock reflection is shifted in a direction toward the trailing edge, whereby the second minimum of the pressure distribution curves is shifted in an analogous manner.

Compared to the pressure distributions of the hub section cascade no appreciable differences in trend occur. However, it should be noted that the radial changes of the pressure distributions on the pressure side of the tip section cascade profiles due to increasing taper angles are more distinct than those of the hub section cascade profiles.

From Fig. 11 relating to the influence of taper angle on pressure distribution at midheight of the blades, a progressively increasing local Mach number on the pressure side of the profile contours is evident, just as was the case for the hub section cascade. Whereas on the suction side, in contrast to the hub section cascade, no definite correlations are recognizable. The additional annulus divergence results in a slight increase of the loading near the leading edge of the profiles due to a small increase of the Mach numbers on the corresponding suction side contours.

Some Numerical Results

Time-Marching Finite-Volume Calculation Method. Starting from the isentropic time-marching finite-volume method in [6], a computational method and a corresponding computer code [7] were developed earlier in order to calculate the two-dimensional inviscid transonic turbine cascade flow. The basic equations, i.e., the time-dependent conservation laws in integral form for mass, momentum, and energy, were discretized, elaborating and using an extended version of the damping surface technique, which was suggested in [8]. Starting from an assumed distribution of local flow values at the nodes of the computational grid, the solution for stationary flow is found by iteration with respect to time. Using this iteration, prescribed values of total temperature, total pressure, and flow angle are kept constant in the inlet plane, as well as the static pressure in the outlet plane. To improve the solution obtained in this coarse computational grid, this grid is refined up to three times successively always using the solution of the coarser grid as the starting conditions for the next grid. For some cases it was shown in [7] that the computed pressure distributions on the blade contours agree

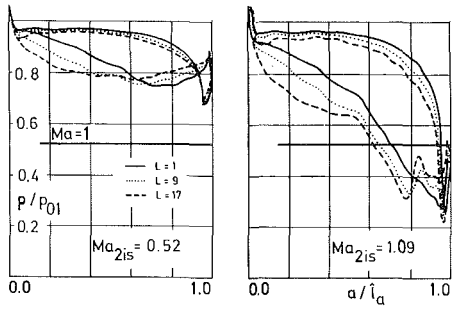

Fig. 12 Calculated pressure distributions at the $\sigma = 30$ deg plane hub section cascade for $h_r/\hat{l}_a = 1.76$ and $\hat{\beta}_1 = 120$ deg

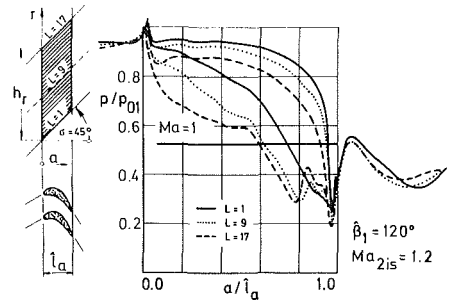

Fig. 13 Calculated pressure distribution at the $\sigma = 45$ deg plane hub section cascade for $h_r/\hat{l}_a = 2.15$ and $\hat{\beta}_1 = 120.0$ deg

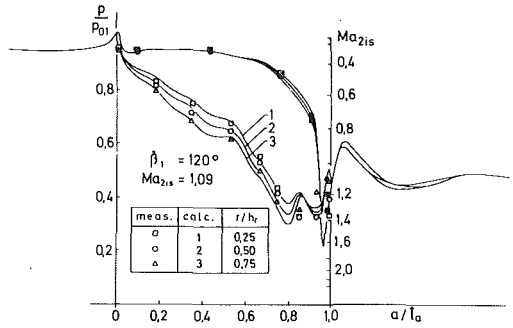

Fig. 14 Comparison of computed and measured pressure distributions for the $\sigma = 30$ deg hub section cascade

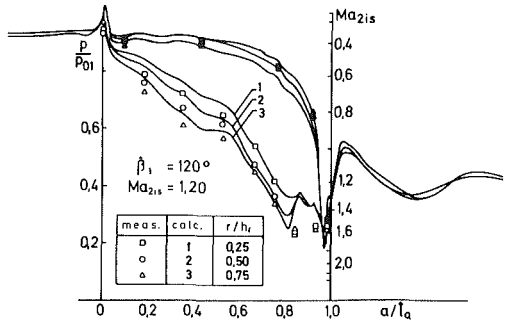

Fig. 15 Comparison of computed and measured pressure distributions for the $\sigma = 45$ deg hub section cascade

quite well with the corresponding experimental results provided that the real flow does not separate from the profile before reaching the trailing edge. The comparison between calculated and measured homogeneous upstream Mach numbers is quite perfect. The homogeneous downstream flow conditions are calculated from the nonhomogeneous distributions of the computed flow values in the outlet plane of the computational domain by integration, using the conservation laws of mass, momentum, and energy. The deviation between computed and experimentally derived downstream flow angles is found to be less than 1 deg. The total pressure losses versus outlet Mach number show good agreement at least in their behavior. A detailed discussion of the method as well as of the important advances in time-marching finite-volume techniques during the last few years, e.g., [9, 10], is beyond the scope of this paper.

Calculations for a Plane Cascade With Sweep and Dihedral. In order to calculate the three-dimensional inviscid transonic flow past plane turbine cascade configurations of finite aspect ratio with sweep and dihedral the above two-dimensional method was extended straightforwardly to the third dimension of the Cartesian coordinate system retaining the boundary conditions as mentioned above. Sample calculations were conducted using two successive refinements of the computational grid, thus resulting in $69 \times 17 \times 17$ nodal points [11].

In Fig. 12 the profile pressure distributions on the lower end wall, the midsection, and the upper end wall are shown for the plane hub section cascade with $\sigma = 30$ deg taper angle, at two different outlet Mach numbers. In both cases the pressure level on the pressure side is higher for the lower wall than for the upper wall. The same result is found for the suction side in the subsonic case up to 60 percent and in the transonic case up to 80 percent of the axial width of the cascade, after which the curves intersect. From the lower wall to the upper wall the loading strongly increases at the profile leading edge and decreases at the trailing edge. In the transonic regime, the flow on the lower surface follows the limit loading condition while on the upper surface the flow is characterized by shock reflection in the rear part of the suction side. Therefore, a curved shock surface is formed in part of the blading passage.

The differences between the pressure distributions on the lower and the upper walls increase with increasing taper angles, as is evident from Fig. 13 for the $\sigma = 45$ deg configuration.

Comparison of Experimental and Numerical Results. A comparison of the three-dimensional pressure distributions, computed for this plane turbine cascade and measured for the corresponding rotating annular cascade with tapered side walls, is shown in Fig. 14. Both cascades have the same sweep and dihedral angle, as well as the same aspect ratio, but only at the mean diameter d_m of the annular cascade is the pitch identical to the constant pitch of the plane cascade. Therefore, in addition to viscous effects in the real flow and to the rotation of the test wheel, some geometric features due to the fan-shaped blade assembly are neglected in the computations. For these reasons the comparisons can only show a qualitative agreement. Nevertheless, the agreement is astonishingly good.

Figure 15 shows the corresponding comparison of the computed and the measured pressure distributions for the $\sigma = 45$ deg hub section cascade with analogous but bigger geometric differences, between the plane and the annular case. Obviously, the agreement is reduced markedly, especially at the suction side near the leading edge. It can be concluded that the differences are mainly due to the increase of the annulus cross section in meridional direction contrary to the constant cross section of the plane cascade. Moreover, the calculations show a considerable radial change for the pressure distributions at the pressure side, which is not so clearly seen in the measurement results.

Much more considerable differences between the measurements and the calculations occur for the corresponding comparisons at the tip section cascade. Although some similarities are evident even now, the high overexpansion measured on the suction side near the leading edge was not verified sufficiently by the calculation. Ac-

cording to two-dimensional comparative calculations it was concluded that the computational grid used has to be improved to solve for local overexpansions with such steep gradients.

The above results may be summarized as follows: The dominating features of the spatial flow structure are described fairly well by the three-dimensional computer code used, which should be changed to conditions appropriate to turbomachinery bladings with rotation to improve the comparison with the above measurements.

Conclusion

Within the scope of the present paper, the essential results of systematic investigations of the effect of annulus taper with regard to the aerodynamic characteristic cascade data are given for the first time at transonic flow conditions. The results do not allow the derivation of a general correlation between the losses and the flow outlet angles with the annulus taper. But they give some essential clues about the different effects of annulus taper at different geometry and flow conditions. The results for the hub section cascade are a good addition to the relatively few available in literature [12]. Although in [12] some considerable differences in cascade geometries exist in comparison to those presented here, an agreement in trend is evident, i.e., especially a continuous increase of losses with increasing taper angle.

Moreover, some typical results from blade surface pressure distribution measurements in the rotating system are presented which show a considerable spatial flow structure within the blade passages, even when low aspect ratios and moderate taper angles are specified.

Finally, some results of three-dimensional calculations of blade surface pressure distributions on plane turbine cascades with sweep and dihedral are presented, as well as their comparison with the corresponding measurements on the annular configurations. The agreement is quite good.

Acknowledgments

The investigations presented were conducted mainly as contract work for FVV-Frankfurt, FRG and sponsored partly by AIF-Frankfurt, FRG. The authors wish to thank the above institutions for permission to publish this paper.

References

1 Smith, L. H., and Yeh, H., "Sweep and Dihedral Effects in Axial-Flow Turbomachinery," ASME *Journal of Basic Engineering*, Vol. 85, No. 3, 1969, pp. 401–416.

2 Bräunling, W., "Untersuchungen zum Einfluss der Konizität auf die Kennwerte rotierender Turbinen-Ringgitter im transsonischen Geschwindigkeitsbereich," VDI-Forschungsheft 627, VDI-Verlag, Düsseldorf, 1985.

3 Heinemann, H.-J., "The Test Facility for Rotating Annular Cascades of the DFVLR and Its Measurement and Evaluation Method," ICIASF 79 Record, IEEE publication, New York, 1979.

4 Kiock, R., Lehthaus, F., Baines, N. C., and Sieverding, C. H., "The Transonic Flow Through a Plane Turbine Cascade as Measured in Four European Wind Tunnels," ASME Paper No. 85-IGT-44.

5 Heinemann, H.-J., and Bräunling, W., "Measurement Methods for Evaluating Static Pressures From Rotating Annular Cascades," *Proceedings of the 7th Symposium of Measuring Techniques for Transonic and Supersonic Flow in Cascades and Turbomachines,* Aachen FRG, 1983.

6 McDonald, P. W., "The Computation of Transonic Flow Through Two-Dimensional Gas Turbine Cascades," ASME Paper No. 71-GT-89.

7 Lehthaus, F., "Berechnung der transsonischen Strömung durch ebene Turbinengitter nach dem Zeit-Schritt-Verfahren," VDI-Forschungsheft 586, VDI-Verlag, Düsseldorf, 1978.

8 Couston, M., McDonald, P. W., and Smolderen, J. J., "The Damping Surface Technique for Time-Dependent Solutions to Fluid Dynamics Problems," VKI-Technical Note 109, Von Karman Institute, Rhode-Saint-Genèse, Belgium, 1975.

9 Denton, J. D., and Singh, U. K., "Time Marching Methods for Turbomachinery Flow Calculation," VKI-Lecture Series "Transonic Flows for Turbomachinery," Von Karman Institute, Rhode-Saint-Genèse, Belgium, 1979.

10 Denton, J. D., "An Improved Time Marching Method for Turbomachinery Flow Calculation," ASME Paper No. 82-GT-239.

11 Lehthaus, F., "Transonic Inviscid Flow Calculations for Flow Past Swept-Back Plane Turbine Cascades," *Proceedings of the 7th Conference on Fluid Machinery*, Hungarian Academy of Sciences, Budapest, Vol. 2, 1983, pp. 494–504.

12 Dejc, M. E., Filippov, G. A., and Lazarev, L. Ya., "Atlas of Axial Turbine Characteristics," Mashinostroenie, Moscow, 1965.

Vibration Characteristics of Mistuned Shrouded Blade Assemblies

N. A. Valero
Graduate Student.
Mem. ASME

O. O. Bendiksen
Assistant Professor.

Department of Mechanical and Aerospace Engineering,
Princeton University,
Princeton, N.J. 08544

An investigation of the mode localization phenomenon associated with mistuning is presented for shrouded blade assemblies. The calculations are based on a generic finite element model, which permits modeling of arbitrary mistuning and both slipping and nonslipping shroud interfaces. The results presented indicate that interactions occur between mistuning and slip effects, with maximum mode localization occurring when the shrouds slip freely. Certain modes are found to be very sensitive to shroud slip, and in some cases completely change character when slip occurs. Mode localization is most pronounced in the predominantly bending modes, and varies considerably from mode to mode. As the ratio of interblade coupling strength to mistuning strength is increased, the effect of mistuning is observed to decrease significantly. This result has important implications for the flutter problem, since it suggests that the stabilization effect available from mistuning is significantly less for a shrouded rotor as compared to an unshrouded rotor.

Introduction

Common design practice often requires the blades of jet engine rotors to be stiffened by part-span shrouds. These shrouds are intended to lock up and form a segmented ring as the blades untwist when the rotors approach the design speed. However, frictional forces at the shroud interfaces may be insufficient to counteract the shear forces and slip may occur.

Another complexity in the analysis of shrouded-blade assemblies is due to the mistuning resulting from variations in the individual blade properties. Although mistuning complicates the analysis, it often provides a stabilizing effect on the rotor from a flutter standpoint and should therefore be included. Thus an understanding of the dependence of the natural modes upon slip and mistuning is of extreme importance if more accurate flutter prediction is to be obtained [1]. Furthermore, since the mistuning will have a significant effect on the aggregate slip, it will have a significant influence on the system damping, and hence also on the forced response of the rotor.

Previous investigations have concentrated on mistuned blade assemblies [2–9] and shrouded-blade assemblies [1, 10–14]. While several of these studies have considered slip at the shroud interfaces, the interaction between slip and mistuning effects has not been studied in a systematic manner. The objective of this paper is to develop a model for such an analysis which keeps the required computational effort to a minimum. The dependence of the system response on certain parameters will be investigated.

The two parameters that have the most significant contributions to the slip and mistuning effects are the shroud interface angle and the type and magnitude of the mistuning in the system. This paper will study the dependence of the vibrational response on these two factors and will present a model suitable for use in this type of analysis. Also, the phenomenon involving mode localization due to mistuning and its relationship to shroud interface angle and degree of mistuning will be examined.

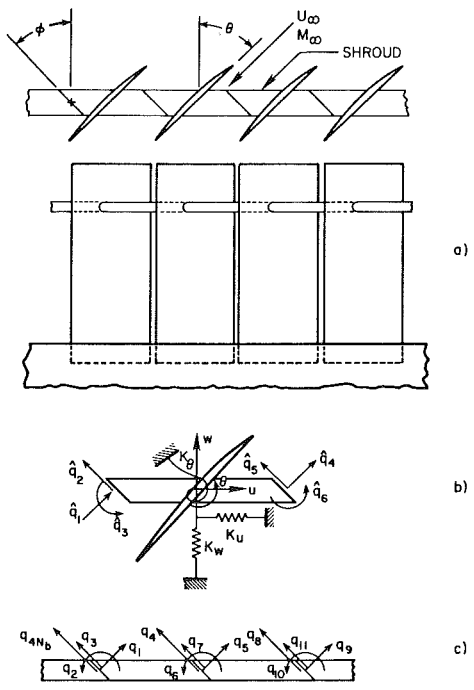

Fig. 1 Structural model of shrouded rotor: (a) infinite shrouded cascade; (b) blade-shroud element; (c) shroud coordinates

Contributed by the Gas Turbine Division of THE AMERICAN SOCIETY OF MECHANICAL ENGINEERS and presented at the 30th International Gas Turbine Conference and Exhibit, Houston, Texas, March 18–21, 1985. Manuscript received at ASME Headquarters, December 27, 1984. Paper No. 85-GT-115.

Formulation

An exact treatment of the dynamics of a shrouded blade assembly is complicated by the nonlinear boundary conditions caused by friction at the shroud interfaces. The resulting contact problem presents considerable mathematical difficulties within the framework of the theory of elasticity. The analytical approaches for this problem can be grouped into two broad classifications. The first is the microslip approach, which requires a detailed analysis of the stress distribution at each shroud interface and is typically carried out via a finite element procedure. The magnitude of the numerical computation involved proves to be quite cumbersome for most practical applications. The second is the macroslip approach, which will be used in this paper. This approach assumes that the entire interface is either slipping or stuck at any given instant and remains planar during slip [14]. This assumption alleviates some of the complications mentioned previously, although the equations of motion remain nonlinear. In this paper, the macroslip approach will be used to formulate a *linearized* eigenvalue problem based upon a generic finite element model of a shrouded N-bladed rotor.

The macroslip approach has some limitations inherent in the model. For example, the local stresses and the magnitude of the dry friction damping at the shroud interfaces cannot be accurately predicted by a macroslip model. Another limitation arises when the interface is subjected to a nonuniform load distribution.

Equations of Motion

The structural model used in this study is illustrated in Fig. 1. The shroud is modeled as a segmented infinite beam, Fig. 1(c), while the blades are modeled as typical sections, Fig. 1(b). This is an extension of the infinite two-dimensional cascade, an aeroelastic model often used for rotors. Periodic boundary conditions are then imposed on the model to define an N-bladed rotor.

Structural Model. Equations of motion for assemblies with either slipping or stuck interfaces have been derived based on the segmented beam model of Fig. 1(a), and finite element codes have been developed for both cases. Each blade-shroud element, Fig. 1(b), is modeled with six nondimensionalized displacement coordinates $\hat{q}_i$. The translational coordinates are nondimensionalized with respect to the segment shroud length l. Assembly of the elements results in four generalized coordinates per element for the slipping case, and in three generalized coordinates per element for the stuck case, Fig. 1(c). The additional degree of freedom is attributed to the fact that, in the slipping case, the adjacent element interfaces are allowed to move relative to one another in a direction parallel to the interface plane. The element interfaces have been constrained to prevent separation. The codes allow up to 48 blade-shroud elements.

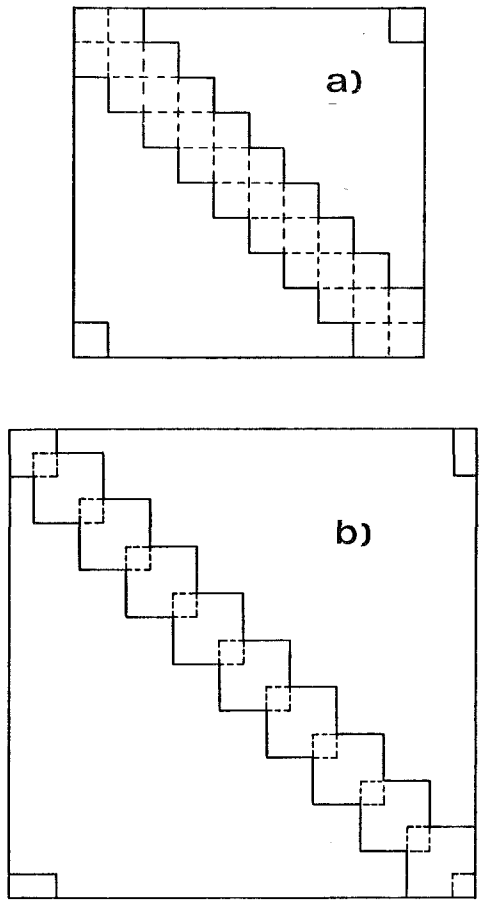

Fig. 2 Form of assembled mass and stiffness matrices: (a) nonslipping or stuck system; (b) slipping system

Corresponding to the coordinates

$$\{\tilde{q}\}^T = \{u_1 \; w_1 \; \hat{q}_3 \; u_2 \; w_2 \; \hat{q}_6\} \tag{1}$$

the mass and stiffness matrices for the shroud-only elements are

$$[k]_s = \frac{EI}{l}\begin{bmatrix} \rho^2 & 0 & 0 & -\rho^2 & 0 & 0 \\ & 12 & 6 & 0 & -12 & 6 \\ & & 4 & 0 & -6 & 2 \\ & & & \rho^2 & 0 & 0 \\ & & & & 12 & -6 \\ & & & & & 4 \end{bmatrix} \tag{2}$$

Nomenclature

EI = shroud flexural rigidity
I_b = effective blade mass moment of inertia
$\bar{I}$ = blade/shroud element inertia ratio, I_b/ml^3
K_u = effective blade lag stiffness
K_w = effective blade flap stiffness
K_θ = effective blade torsional stiffness
$\bar{k}_l$ = blade/shroud element lag stiffness ratio, $(K_u/EI)\,l^3$
$\bar{k}_f$ = blade/shroud element flap stiffness ratio, $(K_w/EI)\,l^3$
$\bar{k}_t$ = blade/shroud element torsional stiffness ratio, $(K_\theta/EI)\,l$
l = shroud segment length
L = total shroud length
m = shroud mass per unit length
Δm_i = mistuning factor
M_b = effective blade mass
$\bar{M}$ = blade/shroud element mass ratio, $M_b/(ml)$
N = number of blade-shroud elements
q_i = nondimensional shroud generalized coordinates
u = displacement in plane of rotation
u_b = blade displacement in plane of rotation
w = displacement out of plane of rotation
w_b = blade displacement out of plane of rotation
β_n = mode characteristic number
θ_b = blade twist at shroud
ρ = shroud slenderness ratio $\equiv (Al^2/I)^{1/2}$
ϕ = shroud interface angle

$$[m]_s = \frac{ml^3}{420}\begin{bmatrix} 140 & 0 & 0 & 70 & 0 & 0 \\ & 156 & 22 & 0 & 54 & -13 \\ & & 4 & 0 & 13 & -3 \\ & & & 140 & 0 & 0 \\ & & & & 156 & -22 \\ & & & & & 4 \end{bmatrix} \tag{3}$$

These are symmetric, standard beam element matrices derived from Bernoulli-Euler beam theory, using Hermite cubic polynomials for $w(x)$ and linear functions for $u(x)$

$$u(x) = N_1(x)u_1 + N_2(x)u_2 \tag{4}$$

$$w(x) = N_3(x)w_1 + N_4(x)w_2 + N_5(x)\hat{q}_3 + N_6(x)\hat{q}_6 \tag{5}$$

where u_i and w_i are the shroud end displacements and the $N_i(x)$ are

$$\begin{aligned} N_1(x) &= 1 - x/l \\ N_2(x) &= x/l \\ N_3(x) &= 1 - 3(x/l)^2 + 2(x/l)^3 \\ N_4(x) &= 3(x/l)^2 - 2(x/l)^3 \\ N_5(x) &= (x/l)(1 - x/l)^2 \\ N_6(x) &= -(1 - x/l)(x/l)^2 \end{aligned} \tag{6}$$

Note the inclusion of the axial displacements that are typically neglected in many finite element beam problems. Due to the importance of flap-lag coupling in the model's vibrational response, the axial components are included.

The blades are represented as typical sections, with u, w, and θ displacements uniquely determined from the shroud coordinates $\hat{q}_i$, using

$$u_b = u(l/2),\ w_b = w(l/2),\ \theta_b = w_x(l/2) \tag{7}$$

The blade flexural stiffness and torsional rigidity are represented by the springs K_u, K_w, and K_θ, as in Fig. 1(*b*). The blade elastic axis is taken to be coincident with the intersection of the shroud centerline and the airfoil chord. In order to minimize the total number of degrees of freedom, the blade properties are lumped at the shroud endpoints $\hat{q}_i$, rather than adding degrees of freedom at the shroud midpoints. The blade mass and stiffness matrices are

$$\begin{aligned} [m]_b &= M_b l^2 [m]_f + I_b [I]_\theta + M_b l^2 [m]_l \\ [k]_b &= K_w l^2 [k]_f + K_\theta [k]_l + K_u l^2 [k]_l \end{aligned} \tag{8}$$

where $[m]_f$, $[k]_f$, $[k]_l$, $[m]_l$, $[k]_t$, and $[I]_\theta$ are derived in the Appendix. The element matrices become

$$[m]_i = [m]_s + [m]_b \quad \text{and} \quad [k]_i = [k]_s + [k]_b \tag{9}$$

with the blade matrices rewritten as

$$\begin{aligned} [m]_b &= (ml^3/420)\{420\,\bar{M}[m]_f + \bar{I}\,[I]_\theta \\ &\quad + 420\,\bar{M}[m]_l\} \\ [k]_b &= (EI/l)\{\bar{k}_f[k]_f + \bar{k}_t[k]_t + \bar{k}_l[k]_l\} \end{aligned} \tag{10}$$

to be compatible with the form of the shroud matrices.

Mistuning. Mistuning in the shroud-blade assembly is introduced by mistuning factors Δm_i into the individual element's mass and stiffness matrices. The mistuning appears as a deviation from the "standard" element, $(1 + \Delta m_l)[-]_i$. This procedure allows for arbitrary mistuning in the stiffness and/or mass of the blade and/or the shroud for each element.

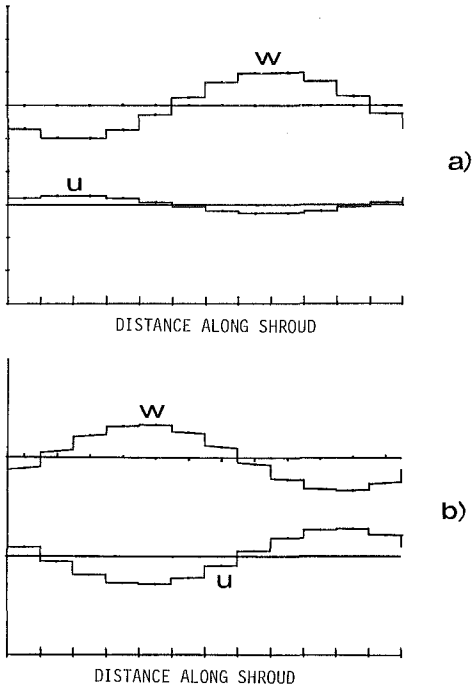

Fig. 3 First predominately blade bending mode: (*a*) ϕ = 15 deg, (*b*) ϕ = 45 deg

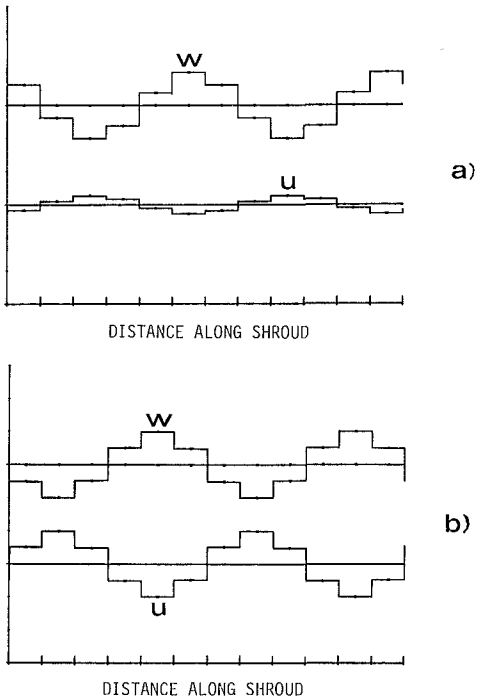

Fig. 4 Second predominately blade bending mode: (*a*) ϕ = 15 deg, (*b*) ϕ = 45 deg

Interblade Coupling. The interblade coupling is comprised of the element flap-lag coupling and the mode-dependent coupling. The amount of flap-lag coupling varies directly with the interface angle ϕ, Fig. 1(*a*). This coupling is a direct consequence of the slip that occurs parallel to the interface. Hence a nonzero interface angle introduces $u-w$ coupling in the generalized coordinates $\hat{q}_i$ with the coupling strength increasing with increasing angle. The transformation of the element matrices is discussed further in the Appendix.

The interblade coupling is mode shape dependent as well. The amount of participation of the nodal displacements in a particular slipping mode affects the interblade coupling, with

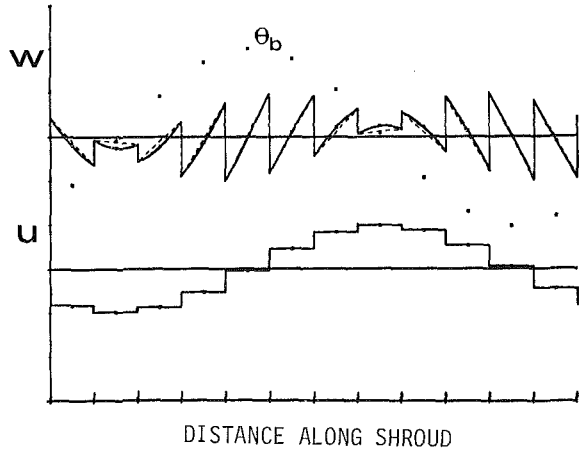

Fig. 5(a) First predominantly blade torsional mode with $\phi = 15$ deg

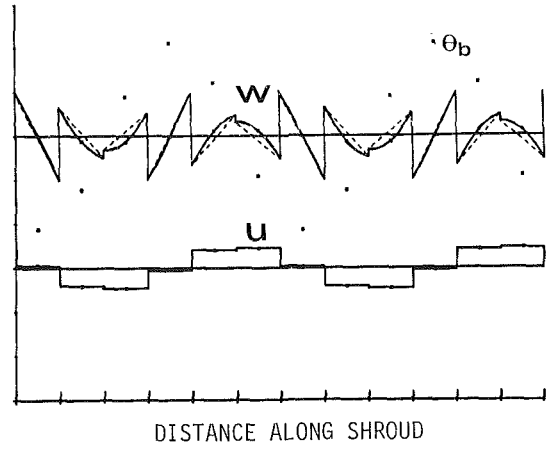

Fig. 6(a) Second predominantly blade torsional mode with $\phi = 15$ deg

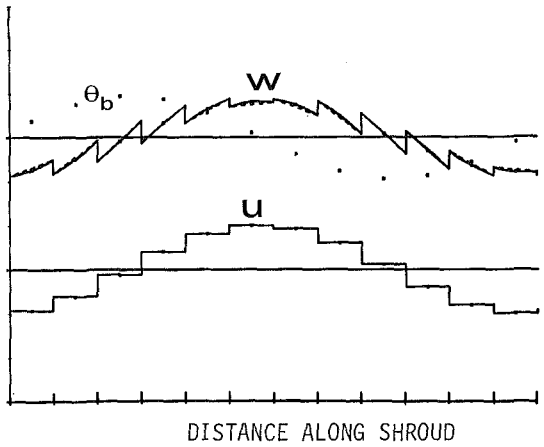

Fig. 5(b) Mode corresponding to Fig. 5(a) with $\phi = 45$ deg. Note strong bending-torsion coupling.

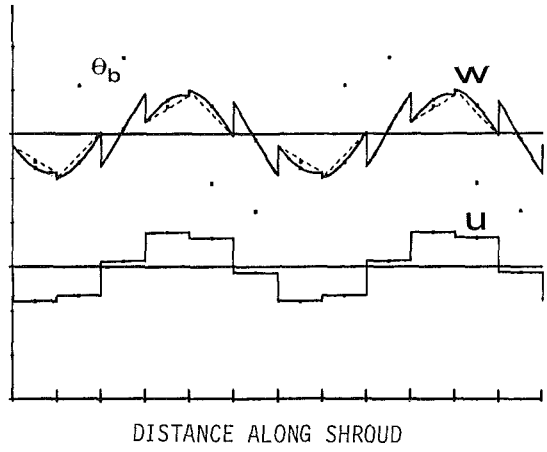

Fig. 6(b) Mode corresponding to Fig. 6(a) with $\phi = 45$ deg, which has now become a coupled bending-torsion mode

the most influence coming from modes with significant torsional displacements.

The Eigenvalue Problem. The undamped, free vibration equations of motion in matrix form are

$$[M]\{\ddot{q}\} + [K]\{q\} = 0 \tag{11}$$

where $[K]$ and $[M]$ are the assembled stiffness and mass matrices, respectively. The assembly of the respective matrices varies between the slipping and stuck cases, since the periodicity of the structure defines $q_i = q_i + 4N$ for the slipping case and $q = q_i + 3N$ for the stuck case. The form of the assembled matrices for a 10-element system is shown in Fig. 2. The (2×4) and (3×3) off-diagonal submatrices are characteristic of the periodic boundary conditions. Bandwidth minimization techniques can be applied to eliminate the off-diagonal submatrices and transform the matrices into banded, symmetric matrices. This allows for the use of optimized eigensolution routines to minimize the computational effort required for large assemblies.

The modal frequencies and mode shapes are then determined by solving an eigenvalue problem of order $3N \times 3N$, or $4N \times 4N$ in the presence of slip. The eigenvalue problem in matrix form is

$$[K]\{q\} = \omega^2[M]\{q\} \quad \text{where} \quad \omega^2 = (\beta_n L)^4 EI/mL^4 \tag{12}$$

Results and Discussion

A computer program has been developed for the proposed model, and it has been run for a number of 12-blade and 48-blade rotor configurations with varying types and degree of

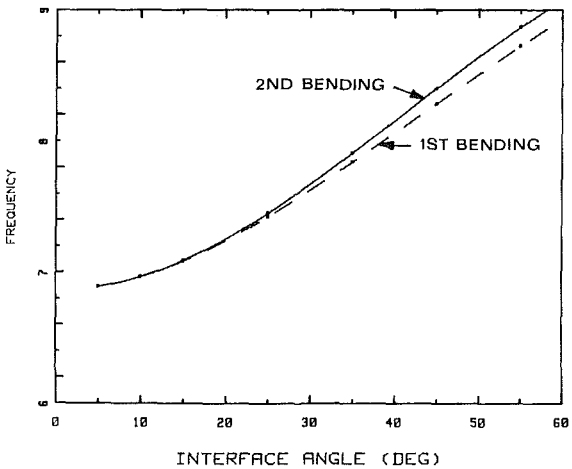

Fig. 7 Plot of βL versus interface angle for the first two predominantly blade bending modes of a tuned rotor with freely slipping shrouds

mistuning. The cases presented have the following parameters: $\bar{k}_f = .025$, $\bar{k}_l = .050$, $\bar{k}_t = .00025$, $\bar{M}_l = 10$, and $\bar{I}_l = 5$. Numerical results as well as some representative mode shapes for a number of these cases are presented in Figs. 3-14. For the mode shapes, the shroud displacements u and w are plotted versus distance along the shroud, using $l = 1$ as the length of each shroud element. The blade displacements are represented by the value at the midpoint of each shroud element.

Tuned Rotor. In the case of tuned nonslipping shrouds,

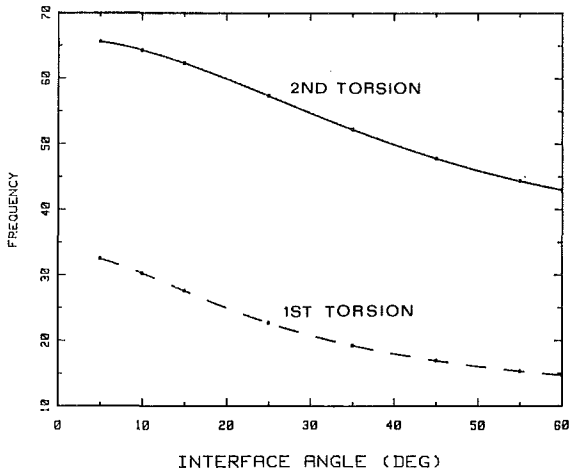

Fig. 8 Same as Fig. 7, for the first two predominantly torsional modes (low ϕ) and coupled bending-torsion modes (high ϕ). As ϕ is increased, the modes change gradually from torsional to strongly coupled bending-torsion modes.

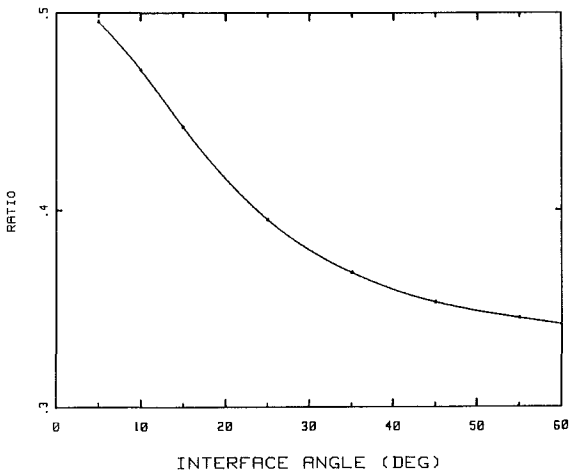

Fig. 9 Plot of ratio of frequency between first and second torsional or coupled bending-torsion modes shown in Fig. 8

the corresponding mode shapes are very similar to pure sinusoids. When the shrouds slip, a number of nonslipping modes are preserved and the additional degrees of freedom give rise to additional predominantly bending modes with little or no participation of the torsional displacements. The slipping interfaces also result in modes that are drastically different from the nonslipping modes. However, these modes retain their sinusoidal qualities.

The mode shapes for the tuned slipping cases can be categorized by the dominant displacements. For the tuned, slipping, 12-blade cases, there are 8 simple natural frequencies and 20 with a multiplicity of two. These 20, in turn, can be grouped according to their dominant blade displacements, either predominantly bending, predominantly torsional or strongly coupled bending-torsion. It should also be mentioned that a group of predominantly shroud modes exists at higher frequencies, but that these are unimportant from an aeroelastic standpoint. The pairs of identical frequencies have identical mode shapes except for a phase difference of 90 deg, and may be combined to form travelling waves.

The first predominantly bending mode shape for a slipping shroud with $\phi = 15$ deg is presented in Fig. 3(a) and the corresponding mode for $\phi = 45$ deg is illustrated in Fig. 3(b). There is no torsional participation in the former while a small amount of torsional displacements is evident in the latter. The increase in interface angle is accompanied by an increase in displacement interaction resulting in the predominantly

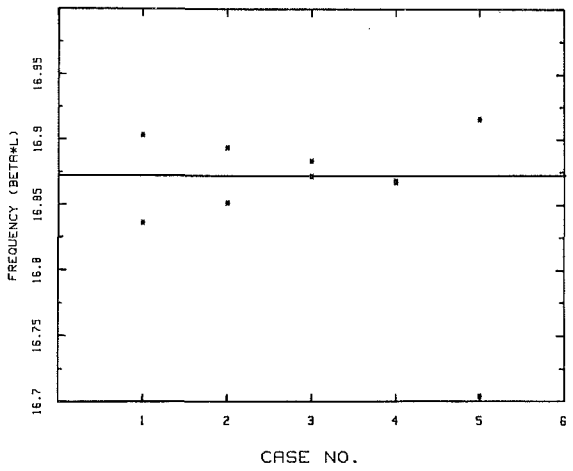

Fig. 10 Mistuned frequencies of first predominantly torsional mode for a 12-bladed system with freely slipping shrouds

bending mode's metamorphosis toward a coupled bending-torsion mode. Figure 4 illustrates the behavior of the corresponding two-nodal-diameter mode.

The first predominantly torsional mode for $\phi = 15$ deg, Fig. 5(a), shows a preponderance of blade torsion while the corresponding mode with $\phi = 45$ deg, Fig. 5(b), shows the torsional and flexural displacements to have approximately the same magnitude, i.e., a strongly coupled mode. A similar behavior is observed in the corresponding two-nodal-diameter mode, Fig. 6. Also Figs. 6(a) and 6(b) show an increase in the u/w displacement ratio as the interface angle is increased. It is evident that displacement interaction increases with the flap-lag coupling strength as the interface angle is increased. The natural frequencies of the predominantly bending modes tend to increase with flap-lag coupling strength while those of the predominantly torsional modes decrease, Figs. 7 and 8.

Another indication of the importance of the shroud interface angle ϕ is shown in Fig. 9. Here the frequency ratio between the first and second nodal diameter modes is observed to decrease as the mode frequencies tend toward each other with increasing interface angle. Clearly, the interface angle is an important parameter in the aeroelastic problem, as pointed out in [1], and it should be possible to improve the flutter margin of a given rotor by optimizing ϕ.

Mistuned Rotor. The following cases of mistuning for 12-bladed rotors were considered:

1 ± 5 percent mistuning of two adjacent element stiffnesses

2 ± 5 percent mistuning of two adjacent element masses

3 5 percent sinusoidal (along shroud) mistuning of element masses

4 5 percent sinusoidal (along shroud) mistuning of element stiffnesses

5 ± 5 percent random mistuning of blade and shroud matrices

6 ± 5 percent alternate blade mass mistuning

In addition, the results for case No. 4 with a 48-bladed rotor are presented.

The effects of mistuning depend considerably on the type of mistuning as well as on the class of mode shape. As in Fig. 10, the paired frequencies separate, typically one below and one above the original frequency. This phenomenon has been observed previously in unshrouded mistuned assemblies [2]. The degree of "splitting" is dependent upon the type of mistuning and is much more pronounced when the mistuning strength is increased. However, when the interface angle is increased while the mistuning level is held fixed, there is only a

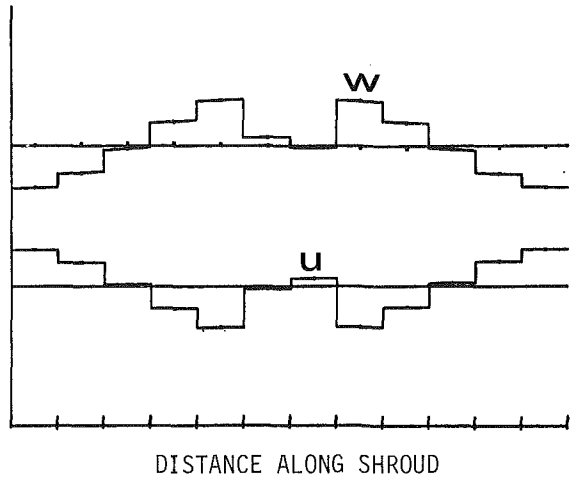

Fig. 11 First predominantly bending mode with ±20 percent adjacent blade mistuning. The tuned mode is shown in Fig. 3(*b*).

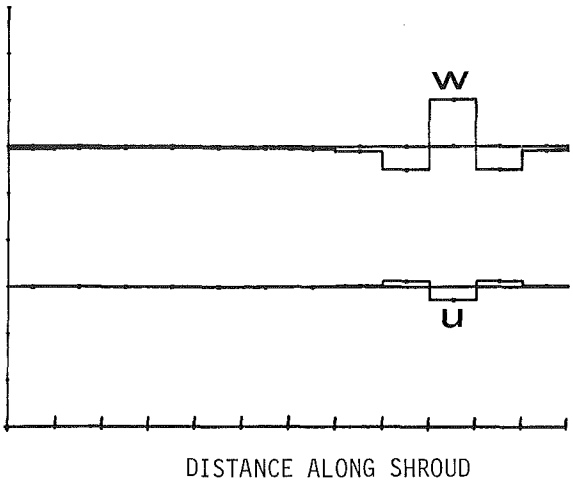

Fig. 13 Example of mode localization caused by a one-wave sinusoidal stiffness mistuning with 5 percent amplitude: ϕ = 15 deg

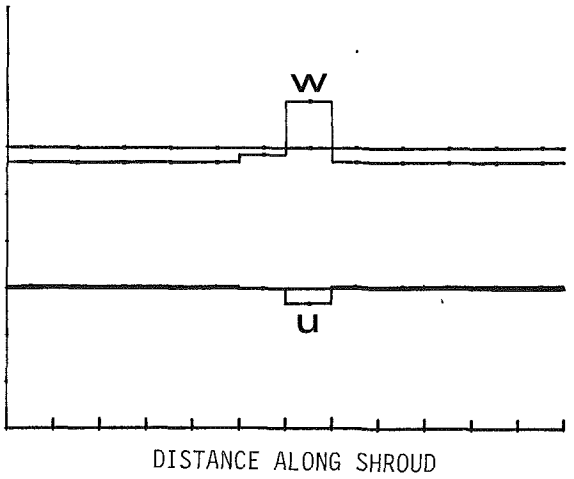

Fig. 12 Example of mode localization caused by ±5 percent adjacent blade mistuning: ϕ = 15 deg

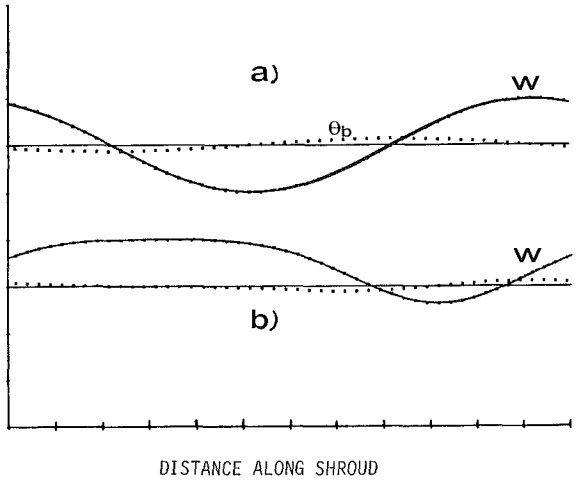

Fig. 14 First one-nodal diameter coupled bending-torsion mode for a 48-bladed rotor with freely slipping shrouds: (*a*) tuned; (*b*) 5 percent sinusoidal mistuning

slight change in the mistuning effects. The influence of mistuning is observed to be greater at the lower frequency modes which are typically predominantly bending modes with relatively weak interblade coupling, Figs. 11–14. For these modes, mode localization is frequently observed to occur. This behavior is consistent with mode localization theory, which predicts mode localization in modes with relatively weak interblade coupling [15].

For mistuned cases with $2N$ elements, the Nth predominantly bending mode, which corresponds to one of the simple modes for the tuned case, disappears completely. It is replaced by a mode with highly localized behavior or one with strongly coupled flap-lag displacements.

For alternate blade mistuning, the "splitting" of paired frequencies is not observed to occur. This is in agreement with observations made in [3] for the corresponding unshrouded mistuned assembly. The most significant effects of mistuning occur when the mistuning is highly localized and the interblade coupling is relatively weak, as in Cases 1 and 2 for the first nodal diameter bending mode. The vibratory amplitude of the two mistuned elements is considerably greater than that of the other elements, Figs. 11 and 12. For cases where the mistuning is more distributed and the interblade coupling is stronger, Figs. 13 and 14(*b*), extreme localization of the modal amplitude is not observed.

From an aeroelastic standpoint, the potentially unstable modes are those which have torsional displacements of the same order or larger than the bending displacements [1]. Unfortunately, these modes have relatively strong interblade coupling and should therefore be less affected by mistuning from a theoretical standpoint. Results from a recent study [15] clearly support this conclusion; in fact, no perceivable stabilization by mistuning was observed in any of the shrouded rotors studied.

Conclusions

The following conclusions can be drawn as a result of this study:

1 A change in the shroud interface angle alters the natural frequencies and affects the ratio of bending to torsional displacements. The magnitude of the slip and hence the dry friction damping is also dependent on the shroud interface angle.

2 For the cases studied, the magnitude of the mistuning effects was found to be essentially independent of the interface angle.

3 As the ratio of mistuning strength to interblade coupling strength (which is a function of the mode shape as well as the interface angle) is decreased, the mistuning effects decrease. This suggests that stabilizing effects from mistuning are significantly less for a shrouded rotor than for an unshrouded rotor.

4 The mistuning effects are most evident in the lower frequency predominantly bending modes where the interblade

coupling strength is relatively weak. For these modes, localization is most likely to occur.

5 Highly localized response is most likely to occur in systems where mistuning is highly concentrated in relatively few elements.

Acknowledgment

This research was supported by NASA Lewis Research Center, Grant NAG 3-308, with Dr. G. V. Brown as technical monitor. The authors gratefully acknowledge this support.

References

1 Bendiksen, O. O., "Effect of Structural and Damping Nonlinearities on Flutter of Shrouded Fans," AIAA Paper No. 84-0990, presented at the 25th AIAA/ASME/ASCE/AHS Structures, Structural Dynamics, and Material Conference, Palm Springs, Calif., May 14-16, 1984.

2 El-Bayoumy, L. E., and Srinivasan, A. V., "Influence of Mistuning on Rotor Blade Vibrations," *AIAA Journal*, Vol. 13, No. 4, Apr. 1975, pp. 460-464.

3 Whitehead, D. S., "Effect of Mistuning on the Vibration of Turbomachine Blades Induced by Wakes," *Journal of Mechanical Engineering Science*, Vol. 8, No. 1, Mar. 1966, pp. 15-21.

4 Dye, R. C. F., and Henry, T. A., "Vibration Amplitudes of Compressor Blades Resulting from Scatter in Blade Natural Frequencies," ASME JOURNAL OF ENGINEERING FOR POWER, Vol. 91, July 1969.

5 Ewins, D. J., "Vibration Modes of Mistuned Bladed Disks," ASME JOURNAL OF ENGINEERING FOR POWER, July 1976, pp. 349-355.

6 Fabuni, J. A., "Forced Vibrations of a Single Stage Axial Compressor Rotor," ASME Paper No. 79-GT-108, Mar. 1979.

7 MacBain, J., "An Investigation of Dual Mode Phenomena in a Mistuned Bladed-Disk," ASME Paper No. 81-DET-133, Sept. 1981.

8 Kaza, K. R., and Kielb, R. E., "Flutter and Response of a Mistuned Cascade in Incompressible Fow," *AIAA Journal*, Vol. 20, No. 8, Aug. 1982, pp. 1120-1127.

9 Bendiksen, O. O., "Flutter of Mistuned Turbomachinery Rotors," ASME JOURNAL OF ENGINEERING FOR GAS TURBINES AND POWER, Vol. 106, Jan. 1984, pp. 25-33.

10 Williams, E. J., and Earles, S. W. E., "Optimization of the Response of Frictionally Damped Beam Type Structures with Reference to Gas Turbine Compressor Blading," ASME *Journal of Engineering for Industry*, May 1974, pp. 471-476.

11 Cottney, D. J., and Ewins, D. J., "On Predicting the Natural Frequencies of Shrouded Bladed Disks," ASME Paper No. 75-DET-113, Sept. 1975.

12 Bielawa, R. L., "An Analytic Study of the Energy Dissipation of Turbomachinery Bladed Disk Assemblies Due to Inter-Shroud Segment Rubbing," ASME *Journal of Mechanical Design*, Vol. 100, Apr. 1978, pp. 222-228.

13 Srinivasan, A. V., Lionberger, S. R., and Brown, K. W., "Dynamic Analysis of an Assembly of Shrouded Blades Using Component Modes," ASME *Journal of Mechanical Design*, Vol. 100, July 1978, pp. 520-526.

14 Srinivasan, A. V., and Cutts, D. G., "Dry Friction Damping Mechanisms in Engine Blades," ASME Paper No. 82-GT-162, 1982.

15 Bendiksen, O. O., "Aeroelastic Stabilization by Disorder and Imperfections," presented at the XVIth International Congress of Theoretical and Applied Mechanics, Lyngby, Denmark, August 19-25, 1984.

APPENDIX

Blade Element Matrices

The blade displacements are:

$$\begin{aligned} w_b &= w(l/2) \\ &= N_3(l/2)w_1 + N_4(l/2)w_2 \\ &\quad + N_5(l/2)\hat{q}_3 + N_6(l/2)\hat{q}_6 \end{aligned} \tag{13}$$

$$\begin{aligned} \theta_b &= w'(l/2) \\ &= N_3'(l/2)w_1 + N_4'(l/2)w_2 \\ &\quad + N_5'(l/2)\hat{q}_3 + N_6'(l/2)\hat{q}_6 \end{aligned} \tag{14}$$

$$\begin{aligned} u_b &= u(l/2) \\ &= N_1(l/2)u_1 + N_2(l/2)u_2 \end{aligned} \tag{15}$$

Let $\{w_i\}^T = \{w_1\ \hat{q}_3\ w_2\ \hat{q}_6\}$ and $\{u_i\}^T = \{u_1\ u_2\}$, then the blade potential energy can be written as,

$$\begin{aligned} U &= 1/2\ K_w l^2 \{w_i\}^T \{N_i(l/2)\}\{N_i(l/2)\}^T \{w_i\} \\ &\quad + 1/2\ K_\theta \{w_i\}^T \{N_i'(l/2)\}\{N_i'(l/2)\}^T \{w_i\} \\ &\quad + 1/2\ K_u l^2 \{u_i\}^T \{N_i(l/2)\}\{N_i(l/2)\}^T \{u_i\} \end{aligned} \tag{16}$$

where the column vectors involving N_i are understood to contain the appropriate entries consistent with equations (13-15). Performing the matrix multplications involving the $\{N_i\}$ vectors, one can write

$$\begin{aligned} U &= 1/2\ K_w l^2 \{w_i\}^T [\tilde{k}]_f \{w_i\} \\ &\quad + 1/2\ K_\theta \{w_i\}^T [\tilde{k}]_t \{w_i\} \\ &\quad + 1/2\ K_u l^2 \{u_i\}^T [\tilde{k}]_l \{u_i\} \\ &= 1/2 \{\tilde{q}\}^T (K_w l^2 [k]_f + K_u l^2 [k]_l \\ &\quad + K_\theta [k]_t) \{\tilde{q}\} \end{aligned} \tag{17}$$

where $\{\tilde{q}\}$ is given by equation (1), and

$$[m]_f = \begin{bmatrix} 0 & 0 & 0 & 0 & 0 & 0 \\ & 1/4 & 1/16 & 0 & 1/4 & -1/16 \\ & & 1/64 & 0 & 1/16 & -1/64 \\ & & & 0 & 0 & 0 \\ & & & & 1/4 & -1/16 \\ & & & & & 1/64 \end{bmatrix} \tag{18}$$

$$[k]_t = \begin{bmatrix} 0 & 0 & 0 & 0 & 0 & 0 \\ & 9/4 & 3/8 & 0 & -9/4 & 3/8 \\ & & 1/16 & 0 & -3/8 & 1/16 \\ & & & 0 & 0 & 0 \\ & & & & 9/4 & -3/8 \\ & & & & & 1/16 \end{bmatrix} \tag{19}$$

$$[k]_l = \begin{bmatrix} 1/4 & 0 & 0 & 1/4 & 0 & 0 \\ & 0 & 0 & 0 & 0 & 0 \\ & & 0 & 0 & 0 & 0 \\ & & & 1/4 & 0 & 0 \\ & & & & 0 & 0 \\ & & & & & 0 \end{bmatrix} \tag{20}$$

By constructing the kinetic energy, the matrices $[m]_f$, $[m]_l$, and $[I]_\theta$ can be shown to be

$$\begin{aligned} [m]_f &= [k]_f \\ [m]_l &= [k]_l \\ [I]_\theta &= [k]_t \end{aligned} \tag{21}$$

The mass and stiffness matrices $[\hat{m}]$ and $[\hat{k}]$ for the blade shroud element are 6×6 matrices given by

$$[\hat{m}]_i = [T]^T [m]_i [T] \tag{22}$$

$$[\hat{k}]_i = [T]^T [k]_i [T] \tag{23}$$

where $[T]$ is the matrix that transforms the u_i and w_i to the coordinates $\hat{q}_i$ and $[m]_i$ and $[k]_i$ are the mistuned blade-shroud element matrices.

The Influence of a Variable Normal Load on the Forced Vibration of a Frictionally Damped Structure

C.-H. Menq[1]

J. H. Griffin

J. Bielak

Carnegie Institute of Technology,
Carnegie-Mellon University,
Pittsburgh, PA 15213

An approximate procedure is developed for calculating the steady-state response of frictionally damped structures for which the normal load across the friction interface consists of a constant force and a force that varies linearly with the vibratory displacement. Such situations occur quite frequently in practice, as, for example, in the case of shrouded fan blades or in certain types of turbine-blade friction dampers. Depending on the magnitudes of the constant and the variable normal loads, the friction element will either stick, slip, or lift off at various intervals during a cycle of oscillation. The various possibilities are considered in the present study. Results from the approximate method are compared with "long-time" solutions obtained from a conventional transient analysis of the problem in order to assess the accuracy of the proposed procedure. As an application, the new method is then used to study the influence of the dynamic coupling on the optimization of the friction force in turbine blade dampers. Results show that the optimum friction force and the maximum amplitude of the response increase with dynamic coupling.

1 Introduction

Studies of the vibration of systems with coulomb damping usually assume that the magnitude of the normal load at the friction interface remains constant throughout the motion; for typical examples see the recent references [1–13]. This paper considers a more complex slip mechanism in which the normal load and the associated friction slip load can vary dynamically during the cycle. This type of slip load variation is important physically when the direction of the vibratory displacement is not parallel to the friction interface, since under these conditions the oscillation will tend to alter the normal load across the friction interface as well as cause the joint to slip. In extreme circumstances this effect can lead to a separation of the surfaces that form the interface producing liftoff and dynamic chatter. In gas turbine engine components this type of situation can occur at fan-blade shroud interfaces, in blade attachments, and in certain types of blade friction dampers which rest on damper pads (on the inboard sides of the blade platforms) which are angled to improve damper seating during engine startup [1].

The main features of the problem can be examined by considering the motion of the simple system shown in Fig. 1, where a mass, m, attached to a rigid base through a spring with stiffness k is acted upon by a harmonic force $f_0 \cos\omega t$. The motion is damped by a viscous dashpot with constant c, and by a coulomb friction element in which the force depends on the normal pressure at the contact interface and on the stiffness, k_d, of the friction damper element. In this study the normal load is taken as the sum of the initial contact pressure at equilibrium, N_0, plus a term which is proportional to the mass's displacement.

The simple system shown in Fig. 1 may be viewed either as a model of an actual single-degree-of-freedom oscillator, or, more generally, as a one-mode approximation of a multidegree system near resonance, provided the system contains a single friction interface. In addition, the mathematical approach that is presented in the following section for handling the nonlinear friction damper is independent of the particular linear subsystem to which the element is attached. Thus, the procedure used for solving the simple spring-mass system shown in Fig. 1 will work equally well with more general lumped parameter systems and, in fact, can be used to evaluate the steady-state response of finite-element-based structural models if an approach analogous to that of [11] is employed.

The organization of the paper is as follows. In Section 2 the

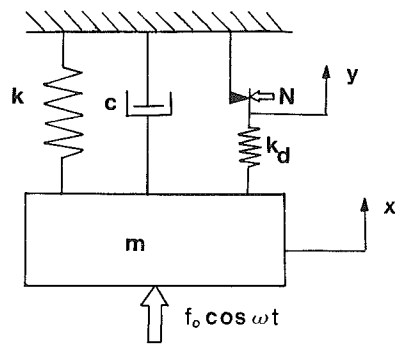

Fig. 1 Single-degree-of-freedom system with friction damper

[1] Presently with the Department of Mechanical Engineering, The Ohio State University, Columbus, OH.

Contributed by the Gas Turbine Division of THE AMERICAN SOCIETY OF MECHANICAL ENGINEERS and presented at the 30th International Gas Turbine Conference and Exhibit, Houston, Texas, March 18–21, 1985. Manuscript received at ASME Headquarters, December 21, 1984. Paper No. 85-GT-63.

equations which govern the dynamic response of the system are stated and then an approximate solution is developed based on the method of harmonic balance. Results from the method are compared with highly accurate, numerically generated, "long-time" solutions in Section 3. In Section 4, the new method is used to study the effect of dynamic coupling on the optimal friction force in turbine blade dampers. Lastly, some concluding remarks are listed in Section 5.

2 Analysis of the System

2.1 Problem Formulation. The equation of motion for the system depicted in Fig. 1 is

$$m\ddot{x}(t)+c\dot{x}(t)+kx(t)=f_0\cos\omega t-f_n(t) \tag{1}$$

where f_n is the nonlinear force in the friction joint. The contact pressure on the joint, N, is assumed to be a linear function of the displacement

$$N(x)=N_0+\gamma k_d x(t) \text{ if } x\geq -N_0/(\gamma k_d) \tag{2}$$

and equal to zero when liftoff occurs ($x<-N_0/\gamma k_d$). The parameter N_0 is the initial contact pressure, k_d is the stiffness of the friction damper element, and γ is a "coupling ratio" which determines how strongly the motion affects the contact pressure. The joint will slide when the magnitude of f_n equals N multiplied by μ, the coefficient of friction for the materials in contact.

In order to complete the formulation of the problem it only remains to specify the behavior of the nonlinear force, f_n. It is assumed that the inertia of the friction element is negligible and, consequently, f_n is constant throughout its length. As a result, f_n is always equal to $k_d(x-y)$, the force in the damper spring. In addition when the damper is stuck y is a constant (to be determined) and when the damper slips, f_n opposes the relative motion and has a magnitude equal to μN. Clearly, f_n vanishes for liftoff.

It should be noted that the governing equations could be written in dimensionless form in several ways, two of which involve using either N_0, the joint preload, or f_0, the magnitude of the excitation as the characteristic force. The key result of such an exercise is that if f_0/N_0 is held constant then the amplitude of the vibratory response is directly proportional to f_0. Consequently, the results presented in this paper, which were computed for f_0 equal to unity, are equally applicable to other levels of excitation provided the displacement amplitude and N_0 are also scaled by the same amount as the excitation.

The main objective of this study is to evaluate the steady-state response of the system shown in Fig. 1. This could be accomplished by solving numerically the equation of motion (1) over a sufficiently long time period so that a steady-state condition is attained. This, however, is an inefficient procedure that will be used here only for purposes of verification. Instead, an alternate, more efficient, approximate method is developed.

2.2 Approximate Solution Method. Since the excitation is periodic it is probable that x and, therefore, f_n are also periodic and have the same fundamental period, $2\pi/\omega$. If it is assumed that this is true then x and f_n can be represented exactly by infinite Fourier series. The method of harmonic balance develops an approximate solution by truncating these series after the fundamental terms. In earlier papers on friction damping of structures the first, time-invariant terms in the series were assumed to be zero since the friction force was a symmetric function of displacement and could not induce a permanent offset. In this instance, however, because of the dynamic coupling the friction element slips differently in one direction than in the other; consequently, the time invariant terms must be included in the formulation to accommodate a permanent, mean offset of the mass. This new aspect of the technique used in this paper is similar to the use of dual describing functions in control theory [14]. It follows then that the first two terms in a Fourier series representation for x can be expressed as

$$x(t)=A\cos\theta+B \tag{3}$$

where

$$\theta=\omega t-\psi$$

Then from (2), for N positive

$$N=(N_0+\gamma k_d B)+\gamma k_d A\cos\theta \tag{4}$$

Using this expression for N, the coefficients of the truncated Fourier-series expansion of f_n can be calculated in terms of the steady-state response variables, A and B, and the system parameters, γ, k_d, and N_0 (see Appendix). That is,

$$f_n=f_b+f_c\cos\theta+f_s\sin\theta \tag{5}$$

where

$$\begin{aligned} f_b &= \mu N_0^* F_b(k_d A/\mu N_0^*;\gamma) \\ f_c &= \mu N_0^* F_c(k_d A/\mu N_0^*;\gamma) \\ f_s &= \mu N_0^* F_s(k_d A/\mu N_0^*;\gamma) \end{aligned} \tag{6}$$

and where $N_0^* = N_0 + \gamma k_d B$ and F_b, F_c, and F_s are the dimensionless Fourier coefficients established in the Appendix in the usual manner. Note that since the dynamic displacement is proportional to $\cos\theta$ it is apparent from (5) that f_c contributes to the dynamic stiffness of the system while f_s provides damping. Consequently, friction dampers can significantly change the resonant frequency of the system, as well as dampen the vibratory response.

Formally (3) and (6) are substituted into (1), linearly independent terms are equated, and ψ eliminated by using the elementary trigonometric identity, $\sin^2\psi + \cos^2\psi = 1$. This results in the two nonlinear, algebraic equations

$$kB+f_b\equiv g_1(A,B,\omega)=0 \tag{7}$$

and

$$[(k-\omega^2 m)A+f_c]^2+[\omega cA-f_s]^2-{f_0}^2\equiv g_2(A,B,\omega)=0 \tag{8}$$

Once the frequency and magnitude of excitation, ω and f_0, are specified equations (7) and (8) may be solved iteratively to establish the amplitude of vibration, A, and the permanent offset, B. Notice that the left-hand side of (7) has formally been defined as a function of ω, even through $\partial g_1/\partial\omega$ is clearly zero. This notation will prove useful in the next section which seeks to establish a direct method for calculating the frequency, ω_m, and amplitude, A_m, of maximum response.

2.3 Equations for Peak Response. Equations (7) and (8) can be used to calculate the vibratory amplitude, A, at any excitation frequency, ω. In this section a method is developed for calculating the maximum value of $A(\omega)$ that occurs at any frequency (provided f_0, N_0, and the values of the other system parameters are held constant during the frequency sweep). Formally, A will equal its maximum value, A_m, if

$$\frac{\partial A}{\partial\omega}=0,\ \omega=\omega_m \tag{9}$$

Since (9) cannot be expressed explicitly it is necessary to proceed in an indirect fashion. First note that if f_0 is considered fixed then (7) and (8) establish A and B as functions of ω. Consequently, (7) and (8) imply that g_1 and g_2 are only functions of ω and that

$$\frac{dg_1}{d\omega}=\frac{\partial g_1}{\partial A}\frac{\partial A}{\partial\omega}+\frac{\partial g_1}{\partial B}\frac{\partial B}{\partial\omega}+\frac{\partial g_1}{\partial\omega}=0 \tag{10}$$

and

$$\frac{dg_2}{d\omega}=\frac{\partial g_2}{\partial A}\frac{\partial A}{\partial\omega}+\frac{\partial g_2}{\partial B}\frac{\partial B}{\partial\omega}+\frac{\partial g_2}{\partial\omega}=0 \tag{11}$$

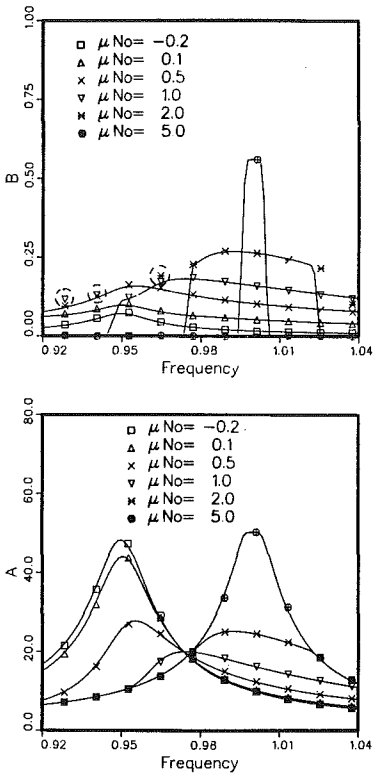

Fig. 2 Response for weak dynamic coupling, $\mu\gamma = 0.1$; $k = 0.9$, $c = 0.01$, $m = 1.0$, $k_d = 0.1$

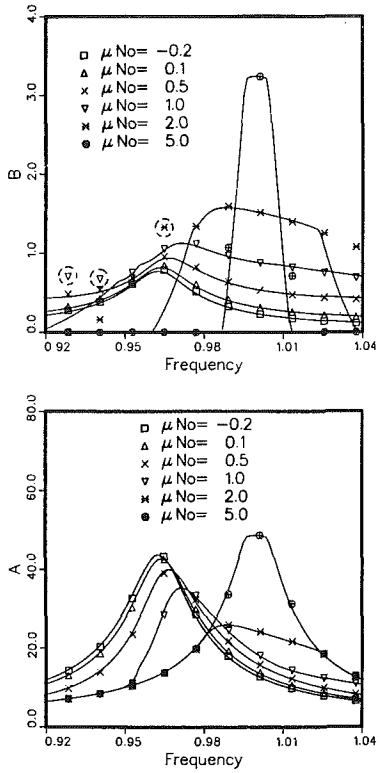

Fig. 3 Response for strong dynamic coupling, $\mu\gamma = 0.6$; $k = 0.9$, $c = 0.01$, $m = 1.0$, $k_d = 0.1$

From (7) and the expressions given in the Appendix it can be shown that

$$\frac{\partial g_1}{\partial \omega} = 0 \text{ and } \frac{\partial g_1}{\partial B} \neq 0 \tag{12}$$

Substituting (9) and (12) into (10) implies that B also attains an extremum value at the same frequency as A since

$$\frac{\partial B}{\partial \omega} = 0, \ \omega = \omega_m$$

and consequently from (11)

$$\frac{\partial g_2}{\partial \omega} = 0, \ \omega = \omega_m \tag{14}$$

Furthermore, an explicit expression for (14) may be calculated from (8). Thus, the three equations that determine the peak values of A and B, and the corresponding frequency of excitation are

$$\begin{aligned} g_1(A_m, B_m, \omega_m) &= 0 \\ g_2(A_m, B_m, \omega_m) &= 0 \\ \frac{\partial g_2}{\partial \omega}(A_m, B_m, \omega_m) &= 0 \end{aligned} \tag{15}$$

3 Results

3.1 Approximate Method Versus Long-Time Solutions. Before analyzing in detail the effects of the various parameters on the system's response the validity of the approximate procedure is examined by comparing results from (7) and (8) with those obtained from a direct numerical solution of the equation of motion (1). Equations (7) and (8) are solved iteratively by means of the standard IMSL subroutine ZSCNT [15].

Values of the vibratory amplitude, A, and offset, B, are shown by the continuous lines in Figs. 2 and 3 as functions of the frequency of excitation, ω, for a sequence of static preloads, N_0, and for typical combinations of the system parameters. In these simulations N_0 was varied over its entire possible range including values less than zero. Physically, negative values of N_0 correspond to gaps between the initial position of the mass and the friction interface since from (2) the normal load is zero until the amplitude of vibration is greater than $-N_0/\gamma k_d$, the effective gap distance. Also shown in Figs. 2 and 3 by discrete data points are the transient numerical solutions computed by approximating the derivatives in (1) by central differences and by updating N and the nonlinear frictional force, f_n, on a step-by-step basis. In these examples the long-time, steady-state behavior was typically attained in 50 to 60 cycles.

From Figs. 2 and 3 it is seen that the solutions for A from the two procedures are in close agreement. While this is also true, in general, for the offset B, there is one situation (denoted by circled data points on Figs. 2(a) and 3(a)) for which the values of B computed by the two procedures differ significantly. Further study indicated that in these instances the steady offset was not unique but depended on the initial displacement and velocity of the mass. However, the corresponding vibratory amplitude was unaffected by this uncertainty in B, since the damper remained stuck for this particular frequency and consequently A was determined uniquely from linear theory.

From this limited comparison it appears that the truncated Fourier-series solution (3) and the associated method of harmonic balance leading to (7) and (8) provide an accurate means for estimating the steady-state dynamic response of the system shown for arbitrary values of N_0.

3.2 Calculation of Peak Response. In applications, system components are designed so that the friction loads have a specified static preload, N_0. For example, in shrouded fan stages this is accomplished by selecting an appropriate shroud tightness parameter, and in the case of turbine blades the value of N_0 is established by choosing the damper's mass since the device is held in place by centrifugal acceleration.

In order to maximize the effectiveness of the friction element it is necessary to determine the value of N_0 that will minimize the peak response for a prescribed level of excitation

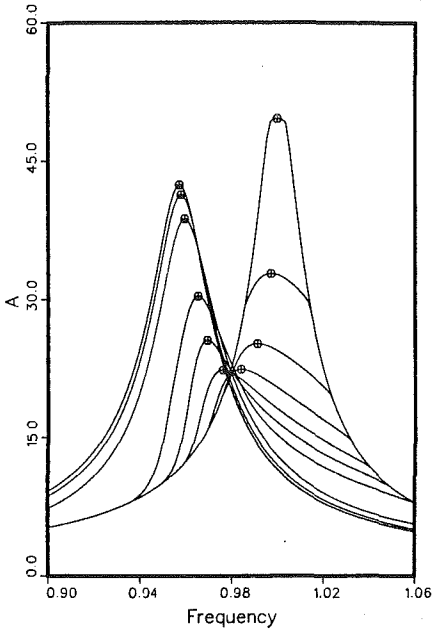

Fig. 4 Verification of peak response calculation

and for all frequencies of excitation of interest. To illustrate this point consider again the typical frequency response curves shown in Figs. 2 and 3. The energy dissipated per cycle by friction is proportional to an average slip load multiplied by the distance, d, that the joint slips. If N_0 is small the average slip load also is small, little energy is dissipated by friction, and consequently the peak amplitude is large. As N_0 is increased the average slip load increases while d decreases since the slip joint is restricted more by the larger normal loads. The amount of energy dissipated per cycle initially increases with the increase in average slip load but then diminishes as the joint approaches a pinned condition and d goes to zero. That there exists an optimum value of N_0 that maximizes the amount of energy dissipated by friction and that minimizes the peak response, A_m, may be seen from Figs. 2(b) and 3(b).

In addition to modifying the maximum response, friction coupling also has the effect of increasing the resonant frequency, ω_m, as N_0 increases. It is important to be able to calculate this frequency change since in practice the range of excitation frequencies is limited and it may be possible to select a value of static preload so that the resonant frequency is outside the range of excitation.

From the preceding discussions, it is clear that for design purposes the key response quantities that must be computed accurately as functions of the static preload, N_0, are the peak response, A_m, and the resonant frequency, ω_m. The procedure developed in Section 2.3 may be used to calculate these quantities directly. Naturally, the values of A_m and ω_m thus calculated should coincide with those obtained by selecting the peak values and the corresponding frequencies directly from the frequency response curves. This has been checked for the particular case shown in Fig. 4, where the discrete points were obtained from the solution to (15).

3.3 Influence of Variable Normal Load on Damper Optimization. The direct procedure for calculating peak response is used next to study the influence of variable normal load on damper optimization. This will be done by constructing curves for A_m and ω_m as functions of N_0 for different values of γ, the coupling factor appearing in (2). If γ is zero there is no dynamic interaction and the slip load is established entirely by the static preload, N_0. The opposite extreme occurs if $\mu\gamma$ equals unity in which case the force required for slip increases at the same rate as f_n and, hence, no steady-state slip or energy dissipation is possible. Results

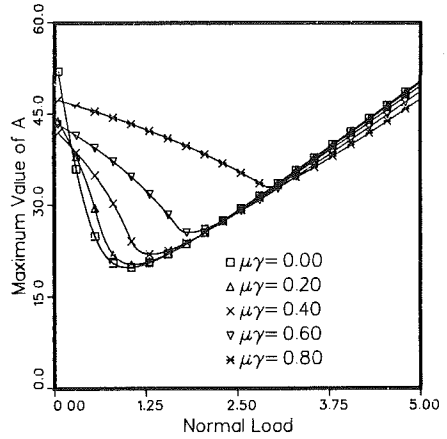

Fig. 5 Influence of $\mu\gamma$ on peak amplitude

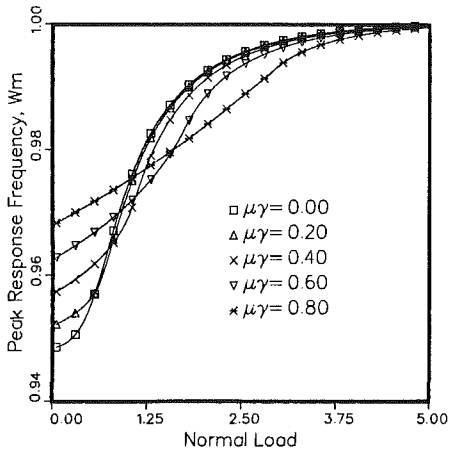

Fig. 6 Influence of $\mu\gamma$ on frequency of peak response

for several values of $\gamma < \mu^{-1}$ are depicted in Figs. 5 and 6, for A_m and ω_m, respectively. These results show that the effect of γ on both the peak response and the corresponding resonant frequency depends strongly on the value of the preload, N_0. Whereas for small values of this parameter A_m decreases with increasing γ, the opposite occurs beyond a certain value of N_0. This is because γ has the effect of increasing the effective normal load which for small values tends to reduce the response; as the effective normal load increases the trend is decreased. Notice also that the optimal value of N_0 increases with γ and so does the peak response. These effects may also be discerned by comparing Figs. 2(b) and 3(b). Similar comments apply to the resonant frequency ω_m.

4 Concluding Remarks

1 A new method has been developed for calculating the steady-state response of frictionally damped systems in which the contact pressure on the friction joint varies dynamically with the vibratory motion. In the examples considered the procedure proved to be efficient and accurate.

2 The mathematical approach used here was somewhat more general than that used for systems in which the contact pressure is constant. Specifically, the form of the solution, a truncated Fourier series, had to include an additional constant term that corresponded to a permanent offset displacement. This is a requirement when the nonlinear force is not symmetric, as was the case here.

3 For the system analyzed, increasing the amount of dynamic coupling had the effect of increasing the optimum preload, N_0, as well as making the damper element less efficient. In practice, these effects could prove significant and

should be taken into account in systems having significant amounts of dynamic coupling.

5 Acknowledgments

This work was supported by the Air Force Office of Scientific Research, Grant AFOSDR-0134, under the direction of Dr. Anthony K. Amos, and by the Air Force Aero Propulsion Laboratory, Contract No. F33615-83-K-2316, under the direction of Mr. William A. Stange. The authors also wish to thank Dr. Enrique Bazan for useful discussions.

6 References

1 Griffin, J. H., and Sinha, A., "The Interaction Between Mistuning and Friction in the Forced Response of Bladed Disk Assemblies," to be published in ASME JOURNAL OF ENGINEERING FOR GAS TURBINES AND POWER.

2 Griffin, J. H., "Friction Damping of Resonant Stresses in Gas Turbine Engine Airfoils," ASME JOURNAL OF ENGINEERING FOR POWER, Vol. 102, Apr. 1980, pp. 329–333.

3 Plunkett, R., "Friction Damping," in: *Damping Applications for Vibration Control*, AMD Vol. 38, edited by P. J. Torvik, ASME, New York, 1980.

4 Earles, S. W. E., and Williams, E. J., "A Linearized Analysis for Frictionally Damped Systems," *Journal of Sound and Vibration*, Vol. 24, No. 4, 1972, pp. 445–458.

5 Muszynska, A., and Jones, D. I. G., "A Parametric Study of Dynamic Response of a Discrete Model of Turbomachinery Bladed Disk," ASME *Journal of Vibration, Acoustics, Stress, and Reliability in Design*, Vol. 105, No. 4, Oct. 1983, pp. 434–443.

6 Muszynska, A., Jones, D. I. G., Lagnese, T., and Whitford, L., "On Nonlinear Response of Multiple Blade Systems," *Shock and Vibration Bulletin*, Vol. 51, Part 3, May 1981, pp. 88–110.

7 Dowell, E. H., "The Behavior of a Linear, Damped Modal System with a Nonlinear Spring-Mass-Dry Friction Damper Attached," to be published in *Journal of Sound and Vibration*.

8 Dowell, E. H ., and Schwartz, H. B., "Forced Response of a Cantilever Beam with a Dry Friction Damper Attached," submitted to *Journal of Sound and Vibration*.

9 Dominic, R. J., "The Analysis by the Lumped Parameter Method of Blade Platform Friction Dampers Used in the High Pressure Fuel Turbopump of the Space Shuttle Main Engine," paper presented at the 54th Shock and Vibration Symposium, Pasadena, California, Oct. 1983; *Shock and Vibration Bulletin*, Vol. 54, May 1984.

10 Soni, M. L., and Bogner, F. K., "Finite Element Vibration Analysis of Damped Structures," *AIAA Journal*, Vol. 20, No. 5, May 1982, pp. 700–707.

11 Menq, C.-H., and Griffin, J. H., "A Comparison of Transient and Steady State Finite Element Analyses of the Forced Response of a Frictionally Damped Beam," *ASME Journal of Vibration, Acoustics, Stress, and Reliability in Design*, Vol. 107, No. 1, Jan. 1985, pp. 19–25.

12 Sinha, A., and Griffin, J. H ., "Effects of Static Friction on the Forced Response of Frictionally Damped Turbine Blades," ASME JOURNAL OF ENGINEERING FOR GAS TURBINES AND POWER, Vol. 106, Jan. 1984, pp. 65–69.

13 Sinha, A., and Griffin, J. H., "Friction Damping of Flutter in Gas Turbine Engine Airfoils," *Journal of Aircraft*, Vol. 20, No. 4, Apr. 1983, p. 372.

14 Gelb, A., and Vander Velde, W. E., *Multiple-Input Describing Functions and System Design*, McGraw-Hill, New York, 1968, pp. 297–357.

15 *IMSL Library Reference Manual*, 9th edition, Vol. 4, INSL, Inc.

APPENDIX

Fourier Coefficients of Nonlinear Friction Force, F_n

Because a spring of stiffness k_d is in series with the friction contact (Fig. 1) the nonlinear force, f_n, is always proportional to the displacement across the spring, i.e., $f_n = k_d(x-y)$. Its magnitude is limited by the curves $\pm \mu N$ where the normal load, N, is equal to $N_0 + \gamma k_d x$ when $x \geq -N_0/\gamma k_d$ and equal to zero when $x \leq -N_0/\gamma k_d$. When $f_n = \pm \mu N$ the friction contact can slip and y may change in such a way as to keep f_n equal to $\pm \mu N$ until x achieves an extremum. When the mass reverses direction the friction contact again sticks and the process is repeated in the opposite direction. Given this behavior the nonlinear force can be expressed as a function of the mass's displacement during a cycle of oscillation and its Fourier coefficients calculated in terms of the amplitude of vibration.

If the displacement of the lumped mass is assumed to be sinusoidal, i.e., $x = A\cos\theta$, where $\theta = \omega t - \psi$, then the configuration of the slip and stick can be broken into three cases:

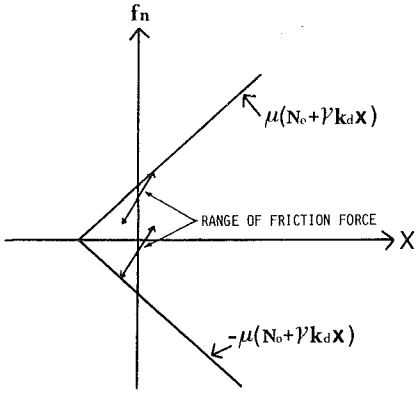

Fig. 7 Nonlinear force: no steady-state slip

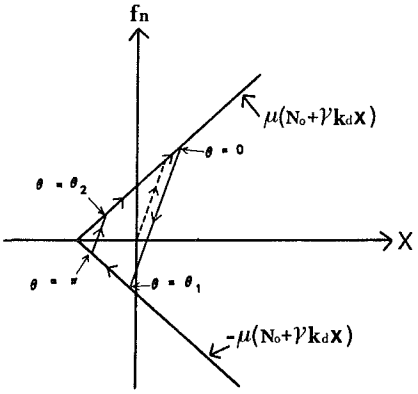

Fig. 8 Nonlinear force: steady-state slip but no liftoff

no slip, slip but no liftoff, and liftoff. The key results are summarized in the following sections.

1 No Slip: $0 \leq A \leq \mu N_0/k_d$. For this case, an unknown amount of slip may occur during the transient response which results in a permanent offset in the steady-state solution. This displacement causes an equally unknown mean value of the friction force, f_b. However, from Fig. 7, it is apparent that f_b lies between the values:

$$-\mu N_0 + (1-\mu\gamma)k_d A \leq f_b \leq \mu N_0 + (\mu\gamma - 1)k_d A$$

and

$$f_c = k_d A \qquad (A.1)$$
$$f_s = 0$$

2 Slip but No Liftoff: $\mu N_0/k_d \leq A \leq N_0/\gamma k_d$. From Fig. 8, the friction force can be separated into four sections during a cycle of vibratory motion.

$$f_n = \begin{cases} \mu N_0 + (\mu\gamma - 1)k_d A + k_d A\cos\theta & 0 \leq \theta \leq \theta_1 \\ -\mu N_0 - \mu\gamma k_d A\cos\theta & \theta_1 \leq \theta \leq \pi \\ -\mu N_0 + (\mu\gamma + 1)k_d A + k_d A\cos\theta & \pi \leq \theta \leq \theta \\ \mu N_0 + \mu\gamma k_d A\cos\theta & \theta_2 \leq \theta \leq 2\pi \end{cases} \qquad (A.2)$$

where

$$\theta_1 = \cos^{-1}\left\{\frac{-[2\mu N_0/k_d A + (\mu\gamma - 1)]}{\mu\gamma + 1}\right\}$$

$$\theta_2 = 2\pi - \cos^{-1}\left\{\frac{2\mu N_0/k_d A - (\mu\gamma + 1)}{1 - \mu\gamma}\right\} \qquad (A.3)$$

Using (*A*.2) and (*A*.3), the standard integral formula for the Fourier coefficients of a periodic function implies

$$f_n = f_b + f_c\cos\theta + f_s\sin\theta \qquad (A.4)$$

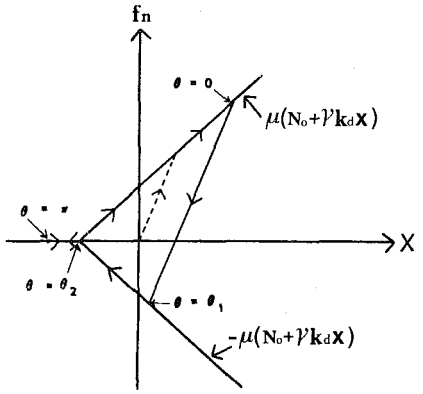

Fig. 9 Nonlinear force: liftoff

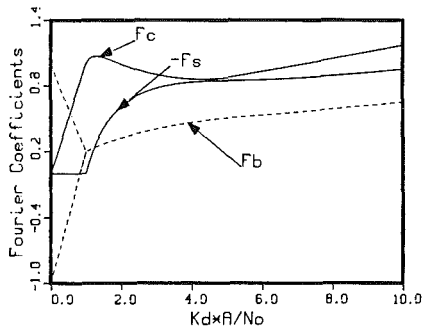

Fig. 10 Nondimensionalized Fourier coefficients: $N_0 > 0$, $\mu\gamma = 0.2$

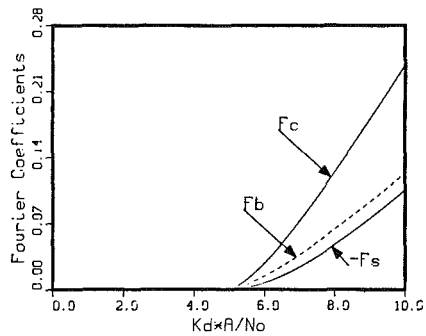

Fig. 11 Nondimensionalized Fourier coefficients: $N_0 < 0$, $\mu\gamma = 0.2$

where

$$
\begin{aligned}
f_b &= \frac{1}{2\pi}\{(\pi-\theta_2)[2\mu N_0-(\mu\gamma+1)k_dA] \\
&+ \theta_1[2\mu N_0+(\mu\gamma-1)k_dA]+(\mu\gamma+1)k_dA\sin\theta_1 \\
&+ (1-\mu\gamma)k_dA\sin\theta_2\} \\
f_c &= \frac{1}{\pi}\left\{(\pi-\theta_2)\left(\frac{\mu\gamma-1}{2}\right)k_dA+\theta_1\left(\frac{\mu\gamma+1}{2}\right)k_dA\right. \\
&+ \frac{1}{2}[2\mu N_0+(\mu\gamma-1)k_dA]\sin\theta_1 \\
&+ \left.\frac{1}{2}[-2\mu N_0+(1+\mu\gamma)k_dA]\sin\theta_2\right\} \\
f_s &= \frac{1}{\pi}\left\{-k_dA+\frac{1}{2}[-2\mu N_0+(1-\mu\gamma)k_dA]\cos\theta_1\right. \\
&+ \left.\frac{1}{2}[2\mu N_0-(1+\mu\gamma)k_dA]\cos\theta_2\right\} \qquad (A.5)
\end{aligned}
$$

3 Liftoff: $N_0/\gamma k_d \le A$. From Fig. 9, the friction force can again be separated into four sections for a cycle of vibratory motion

$$
f_n = \begin{cases} \mu N_0+(\mu\gamma-1)k_dA+k_dA\cos\theta & 0\le\theta\le\theta_1 \\ -\mu N_0-\mu\gamma k_dA\cos\theta & \theta_1\le\theta\le\theta_2 \\ 0 & \theta_2\le\theta\le 2\pi-\theta_2 \\ \mu N_0+\mu\gamma k_dA\cos\theta & 2\pi-\theta_2\le\theta\le 2\pi \end{cases} \qquad (A.6)
$$

where

$$
\theta_1 = \cos^{-1}\left\{\frac{-[2\mu N_0/k_gA+(\mu\gamma-1)]}{\mu\gamma+1}\right\}
$$

$$
\theta_2 = \cos^{-1}\left\{-\frac{N_0}{\gamma k_dA}\right\} \qquad (A.7)
$$

Using (*A*.6) and (*A*.7), the same procedure as in the case of slip but no liftoff yields

$$
\begin{aligned}
f_b &= \frac{1}{2\pi}\{\theta_1[2\mu N_0 \\
&+ (\mu\gamma-1)k_dA]+(\mu\gamma+1)k_dA\sin\theta_1\} \\
f_c &\doteq \frac{1}{\pi}\left\{\theta_1\left(\frac{\mu\gamma+1}{2}\right)k_dA\right. \qquad (A.8) \\
&+ \left.\frac{1}{2}[2\mu N_0+(\mu\gamma-1)k_dA]\sin\theta_1\right\} \\
f_s &= \frac{1}{\pi}\left\{\frac{1}{2}[2\mu N_0+(\mu\gamma-1)k_dA]\right. \\
&- \frac{1}{2}[2\mu N_0+(\mu\gamma-1)k_dA]\cos\theta_1 \\
&+ \left.(\mu N_0+\mu\gamma k_dA)\cos\theta_2\right\}
\end{aligned}
$$

The results obtained are valid when the value of N_0 is positive. For the case of negative N_0, the same procedure can be applied as for liftoff and one finds that the same formulas are obtained. Finally, it is noted that the friction force always can be written as

$$
f_n = f_b(A,N_0;\gamma,k_d)+f_c(A,N_0;\gamma,k_d)\cos\theta+f_s(A,N_0;\gamma,k_d)\sin\theta \qquad (A.9)
$$

Furthermore, these three coefficients can be nondimensionalized as follows:

$$
\begin{aligned}
f_b(A,N_0,\gamma,k_d) &= \mu N_0F_b\left(\frac{k_dA}{\mu N_0},\gamma\right) \\
f_c(A,N_0,\gamma,k_d) &= \mu N_0F_c\left(\frac{k_dA}{\mu N_0},\gamma\right) \qquad (A.10) \\
f_s(A,N_0,\gamma,k_d) &= \mu N_0F_s\left(\frac{k_dA}{\mu N_0},\gamma\right)
\end{aligned}
$$

Typical results depicting these nondimensional functions are shown in Figs. 10 and 11. As shown in Fig. 10, the dynamic coupling component F_b of the nonlinear friction force is not unique for the case of no sustained slip. However, the dynamic component of the forced response is not affected since there is no energy dissipation in this case. Note for application in Section 2.2 that N_0 is replaced by its effective value, $N_0+\gamma k_dB$, as indicated in (4).

A. V. Srinivasan
United Technologies Research Center,
East Hartford, CT

R. E. Kielb

C. Lawrence

NASA Lewis Research Center,
Cleveland, OH

Dynamic Characteristics of an Assembly of Prop-Fan Blades

Introduction

The renewed interest in propeller propulsion is based on large reductions expected in fuel burned and direct operating costs compared to advanced turbofan propulsion. Current predictions [1] indicate that a prop-fan (Advanced Propeller) powered 120-passenger aircraft will burn 20% less fuel than a similar turbofan powered aircraft. Potentially greater benefits are predicted with counter-rotating prop fans.

In contrast to conventional propellers, prop-fan blades are thin and highly swept back giving rise to large bending and twisting deformations and complex vibratory characteristics. Aerodynamic performance depends on the extent of steady-state deformation and the aeroelastic response depends upon the vibratory frequency and mode shape. Therefore, the steady-state and vibratory characteristics need to be calculated in order to predict accurately the performance and stability characteristics of the blade assembly. The reliability of the calculation procedures needs to be established on the basis of comparison with data generated under carefully controlled test conditions. The object of this paper is to present and discuss the principal results of structural analyses of a five-bladed prop-fan assembly and compare the results with corresponding test data.

The test results reported here include both steady deformations and vibratory frequencies and mode shapes of the prop-fan in a vacuum centrifugal environment. Several unique measurement techniques were used during the program including determination of the steady-state deformations by measuring the angular deflections of a laser beam reflected from mirrors bonded to the blades. In addition, direct tip deflection measurements were made with high-speed strobe photography. Use of a piezoelectric crystal excitation system provided smooth sinusoidal blade excitation of the assembly at arbitrary amplitude and interblade phase angle.

Experimental Program

The experimental program was generally directed toward developing a structural data base from which the steady-state blade motions as well as vibratory characteristics of the prop-fan assembly could be determined.

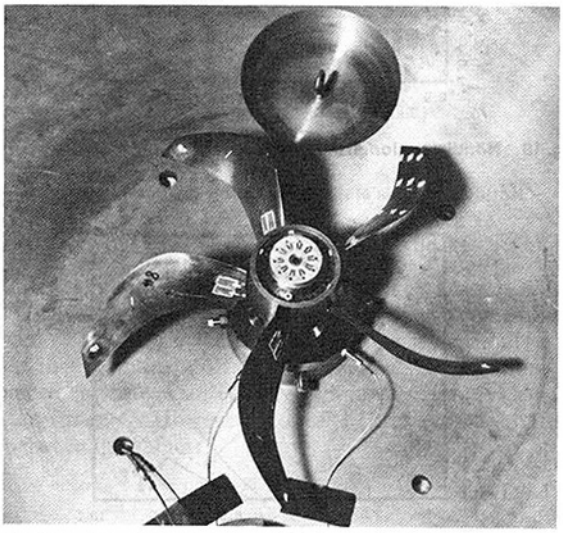

Fig. 1 Photograph of instrumented SR5 assembly in UTRC spin rig

The overall goals of the program were to (*a*) assess the extent of correlation between finite element analysis and corresponding test results, and (*b*) determine the extent of mechanical coupling among the blades through an examination of the response of the assembly in its system modes.

The specific objectives were to:

1 Measure the centrifugally induced steady blade deflections up to the mechanical design speed of 9000 rpm.
2 Measure the frequency and mode shape of the first five normal modes of vibration at selected speeds.
3 Determine the character and extent of blade-to-blade mechanical coupling through the hub during vibration.
4 Compare the experimental results with corresponding analytical predictions from NASTRAN.

Test Rotor and Blade Geometry

The test rotor, designated as SR-5, consisted of five Ti 6-4 prop-fan blades mounted on a steel hub which retains the

Contributed by the Gas Turbine Division of THE AMERICAN SOCIETY OF MECHANICAL ENGINEERS and presented at the 30th International Gas Turbine Conference and Exhibit, Houston, Texas, March 18–21, 1985. Manuscript received at ASME Headquarters, January 7, 1985. Paper No. 85-GT-134.

Table 1

Number of blades in rotor:	5 (10 in prototype)
R_{Tip}	12.1 in. (31 cm)
R_{Hub}	2.83 in. (7.19 cm)
t/b_{Root}	0.105
t/b_{Tip}	0.018
Mechancal design rpm	9000
Tip speed at design	950 ft/s (290 m/s)
Material	Ti 6-4
Reference angle at 3/4 radius	58.5 deg relative to tangential plane
Max sweep back angle at tip	63 deg
LE radius tip (nominal)	0.003 in. (0.0076 cm)
LE radius root (nominal)	0.0614 in. (0.156 cm)

blades in a centrifugal field and has provision for varying the pitch angle of the blades. The SR-5 rotor, designed as a ten-bladed rotor, had undergone extensive wind-tunnel testing under a variety of conditions to measure both its aerodynamic and structural characteristics. The tests reported here were cnducted on a five-bladed version of the SR-5 rotor (Fig. 1), with blades set at the nominal cruise flight pitch angle of 58.5 deg at a reference radius of 3/4 span. Table 1 is a summary of the significant airfoil geometric parameters which are more completely described in [2]. After the instrumentation was installed, the individual blades were moment weighed and mounted in the hub in a sequence to minimize initial imbalance.

The blade/rotor coordinate system is shown in Fig. 2; the X-axis is coincident with the rotor axis (positive aft), Y is radial and coincident with center of the blade pitch change axis (positive outward), and Z is perpendicular to the XY plane. For purposes of surface identification, the pressure or face surface is the surface facing in the positive Z direction, and the suction or camber surface faces the negative direction.

Instrumentation

(*a*) Steady Centrifugal Blade Deformation. The technique of measuring deflections by means of reflection from mirrors bonded to the blade surface requires an intense narrow beam light source and adhesives strong enough so that the mirrors remain attached to the blade in a centrifugal field. Readily available and inexpensive lasers and epoxy adhesives have led to the development and refinement of this technique reported in [3, 4]. The method of using reflection of a laser beam from mirrors bonded to the blade was thus a logical choice to determine the complex deformation patterns of the prop fan.

The location of the mirrors mounted on the blades is shown in Fig. 3 and the schematic arrangement of the laser/mirror system is shown in Fig. 4. One blade (S/N 10) has the full array of 11 mirrors; each of the other four blades in the rotor have a single mirror at the A-2 location. Alignment and bonding of the mirrors were carried out with the blades mounted in the hub at the specified pitch angle, and the hub mounted in the spin-rig. The intense narrow beam light source is provided by a Hughes, Series 4000 HeNe laser.

Direct photographs of the blade tips were made by using a high-intensity short-duration spark gap flash unit and a specially designed and fabricated digital phase shifter which operated from the 1 per rev and 60 per rev signals available from the spin-rig drive shaft. A simple calculation shows that at maximum speed of 9000 rpm, the blade tip will move approximately 0.003 inches during the 1/4 μs flash duration resulting in sharp, well-defined photographs. The camera, a 35 mm SLR, was mounted outside the vacuum chamber.

(*b*) Dynamic Instrumentation. The blade-mounted dynamic instrumentation consisted of piezoelectric crystals used to induce vibration in a desired mode, and resistance strain gages to define blade response. Figure 5 shows the strain gage and crystal locations. Crystals were located on the basis of bench test experiments to give good vibratory response of the blade

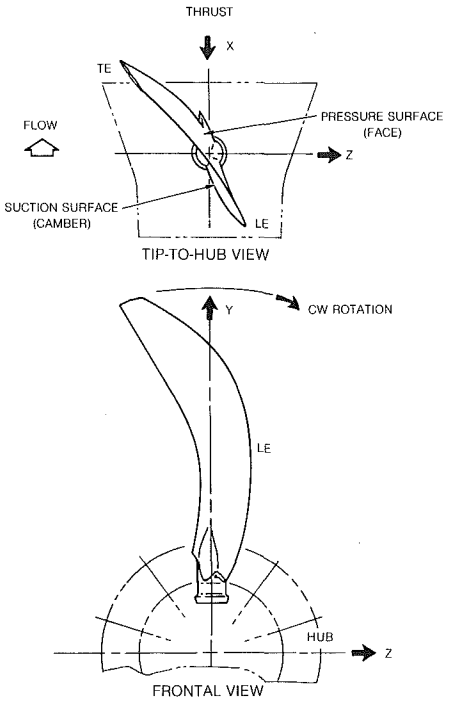

Fig. 2 Blade coordinate system

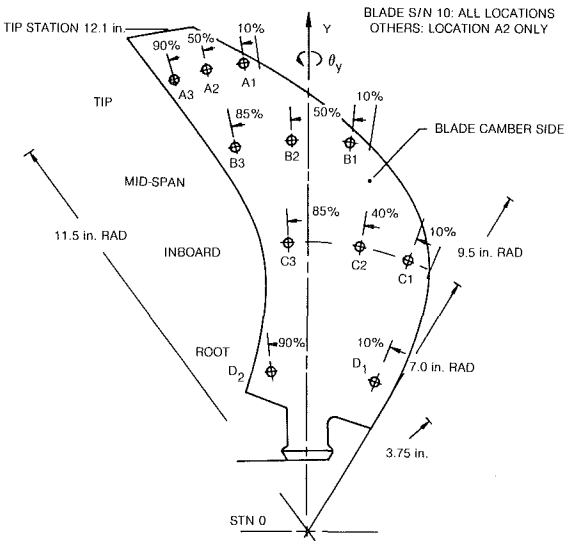

Fig. 3 SR-5 model prop-fan blade mirror locations

in the first five normal modes. Two lead zirconate-titanate crystals, electrically paralleled to increase force input, were used to excite each blade. The crystals, Type G1356 (1.00 × 0.5 1× 0.010 in.) were supplied by Piezo Electric Products. Development of the crystal excitation technique is described in [5]. Strain gage locations were chosen on the basis of analytical stress distributions derived from NASTRAN [6] for the first five vibratory modes. The two blades chosen to have the extensive instrumentation (blade S/N 2 with 15 strain gages, and blade S/N 10 with 11 mirrors) were selected on the basis of their having average frequencies as measured on the bench.

The tests were carried out in the UTRC high-speed spin facility, a 10 ft diameter by 3 ft high vacuum chamber which is mounted on a platform 4 ft above the floor with the vertical axis drive system mounted on the bottom plate. This arrangement allows unobstructed visual access to the test component from the top.

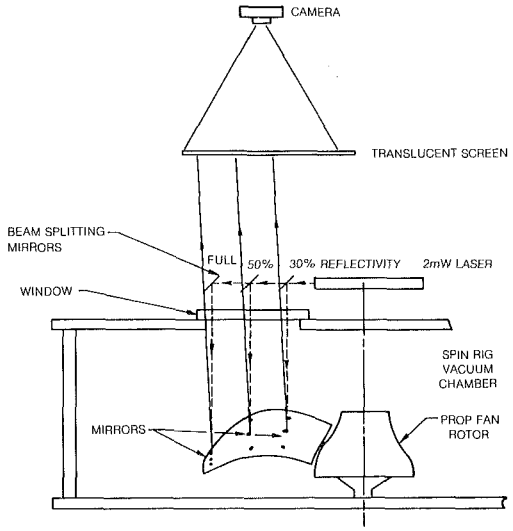

Fig. 4 Schematic of laser mirror setup for blade-deflection measurement

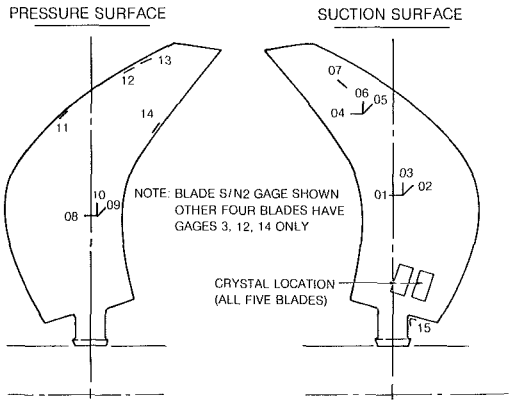

Fig. 5 SR5 prop fan strain gage and crystal locations

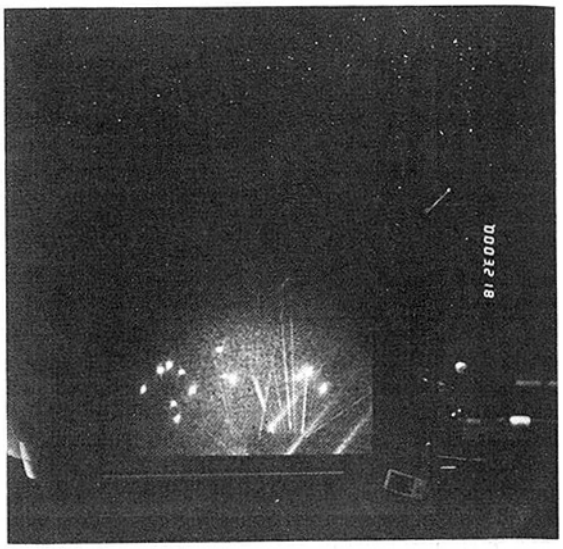

Fig. 6 Photograph of spots reflected from blade-mounted mirrors

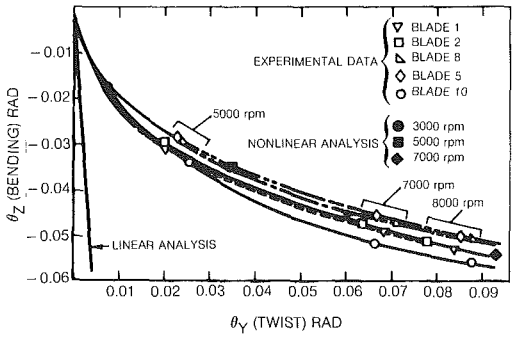

Fig. 7 SR5 steady-state bending (Θ_Z) and twist (Θ_Y) at midchord tip

Test Procedure

(a) **Steady-State Deflections.** Prior to recording data from the surface-mounted mirrors, the initial positions of the spots on the screen were recorded by turning the rotor by hand with the chamber evacuated and marking the reflections from each mirror on the screen. A photograph of the marked-up screen was made and served as the zero speed reference location for each mirror. The rotor was then accelerated, allowed to stabilize at each required speed, and a photograph of the reflections was made. The exposure duration was chosen to give 10 to 20 repetitions of each reflection. Figure 6 shows a typical photograph of the screen which also shows the scales needed for length calibration and a repeating tachometer for measuring the speed. This procedure served well up to a certain speed beyond which most of the reflections had passed outside the field of the window and thus could not be recorded. Several attempts were made to rebond the mirrors to the blades to permit greater range of travel but the combination of blade bending, twisting angles, and the plane of the rotor relative to the window resulted in spot deflections at 9000 rpm which exceeded the 12 in. diameter of the viewing window. To provide positive spot identification and eliminate ambiguity from spot crossings on the still photographs at increasing speeds, a real-time video recording was made of a slow acceleration, and from this a continuous tracing of each spot (Fig. 7) as a function of speed was prepared. Figure 7 shows the trajectories of the midchord tip mirror reflections from all five blades which represent a measure of how well the blades match each other. The components of rotation Θ_y and Θ_Z, for blade S/N 10 are generally larger than for the other four blades because of the extra mass of the 11 mirrors and epoxy adhesive on that blade. The curvature apparent in these trajectories shows that significant nonlinear displacements are occurring. This feature is discussed later.

To obtain photographs of the blade tips, the rotor was brought up to a given speed and stroboscopically illuminated with a multiple flash strobotach triggered by the 1 per rev signal from the drive shaft. A digital phase shifter was used to adjust the time of flash relative to the 1 per rev pulse; thus, the rotor could be "stopped" at any angular location. Each blade was lined up visually using the hub reference mark relative to the hub pointer. When the correct alignment had been achieved, the strobotach was removed from the circuit and replaced with the single pulse high intensity Microflash 599-11 light source and driver. Recording was achieved by opening the camera shutter, pulsing the flash unit and closing the shutter. In this manner, two independent photographs of each of the five blades were taken at each of six speeds.

Data reduction was accomplished by projecting the negatives onto vellum at an overall magnification of approximately 4×. The position of the blade leading and trailing edges was marked as were the position of the horizontal and vertical fixed reference lines. Blade deflections were determined by the variations in position from the reference marks.

(b) **Dynamic Testing.** Prior to the determination of vibratory characteristics of the assembly at speed, the blades were individually characterized through experimental modal analysis. For tests at speed, the rotor was mounted in the vacuum spin rig and strain gages and crystals were connected through the slip ring to the data system and excitation control respectively. The decay of free vibration data was reduced by

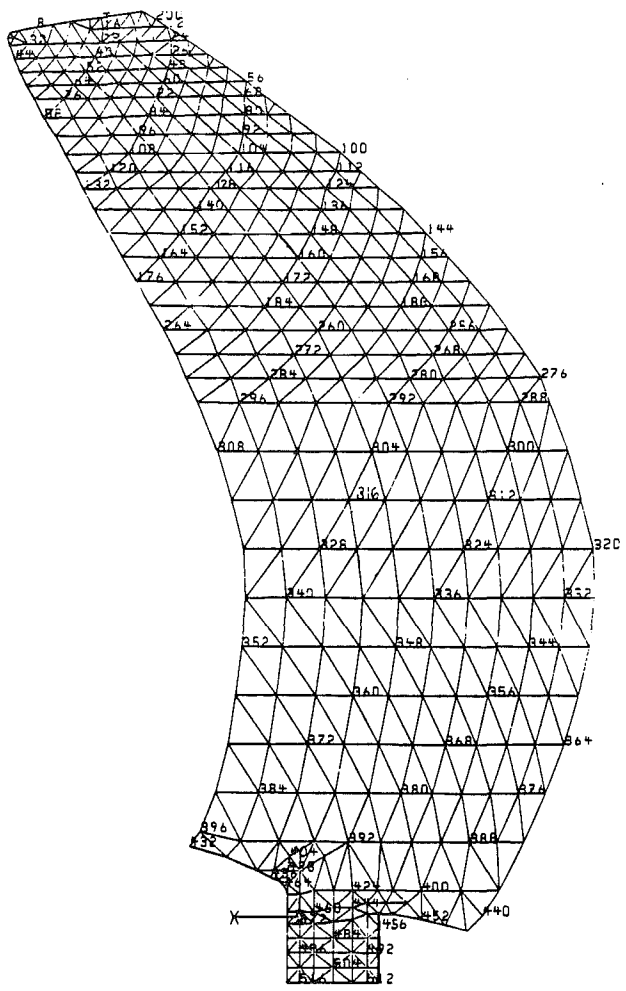

Fig. 8 NASTRAN grid breakup of SR5 blade

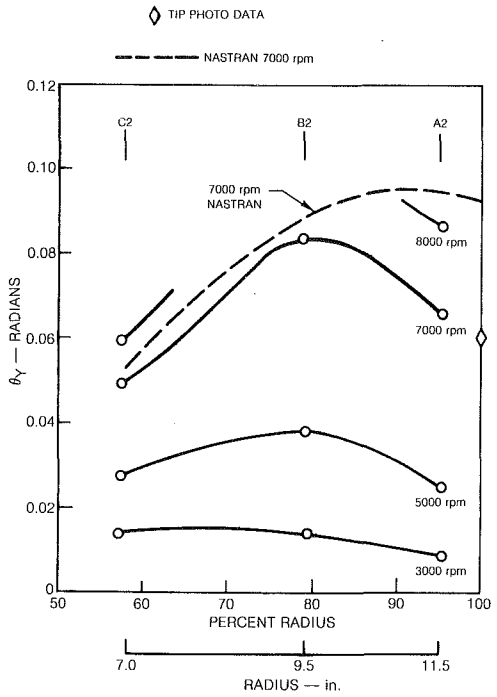

Fig. 9 Blade midchord twist Θ_Y versus % radius

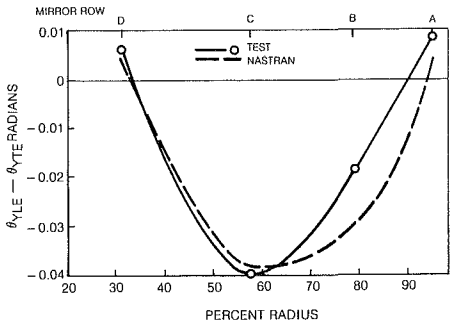

Fig. 10 Blade uncamber versus span at 7000 rpm

a time domain analysis as outlined in [7]. To obtain a data record with the rig stabilized at a specified speed, the crystals were energized at a specified amplitude and interblade phase angle. To find the system frequency, a responsive strain gage channel was monitored visually on an oscilloscope as the excitation oscillator was swept slowly around the frequency of interest. When it was determined that the blade response was at a maximum, the excitation was switched off and data recording started simultaneously. This method proved satisfactory for data records in modes 1, 2, 4, and 5, but the 3rd mode proved to be very difficult to excite. Vibratory testing was limited to speeds under 7000 rpm because earlier calculations had indicated a potentially large steady stress at the airfoil trailing edge. The combination of this high steady stress and vibratory stress suggested the risk of failure to be unacceptably high.

NASTRAN Analysis

The model used for the finite element analysis (MSC/NASTRAN version 62A) is shown in Fig. 8. This model consists of 882 triangular plate elements (CTRIA3) and 517 node points. The plate element isoparametric formulation includes both membrane and bending action. Isotropic material properties and lumped nodal masses were used for the element. The base of the blade root is modeled as fully constrained and therefore does not allow for any coupling that may exist among blades.

Since the turboprop blade is relatively flexible, it responds to loading with relatively large deflections. The computation of these deflections requires a geometrically nonlinear analysis. NASTRAN, which is capable of performing this type of analysis, was used to compute the blade's steady-state displacements produced by the centrifugal loading.

NASTRAN utilizes a modified Newton–Raphson algorithm to solve the geometrically nonlinear problem [6]. This algorithm required nine iterations to adequately converge. After convergence the structural mass and stiffness matrices are used for the subsequent frequency analysis. The centrifugal softening terms associated with in-plane displacements are included in the final stiffness matrix. The large displacement and frequency analyses were repeated at several rotational speeds.

Discussion

***(a)* Steady-State Deflections.** Both the measured and predicted steady-state rotations are shown in Fig. 7. In addition to the nonlinear analysis described above, NASTRAN was used to predict the linear behavior. The deviation of the "Linear analysis" line from the curves representing the experimental data and nonlinear analysis shows that significant nonlinear behavior is present even at moderate rotational speeds. Figure 7 also shows that the experimental data and the nonlinear analysis agree on the dependency of the bending (Θ_Z) and twisting (Θ_Y) rotations. However, at 5000 and 7000

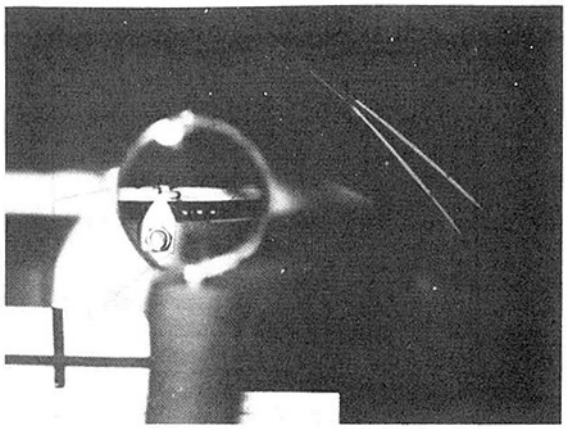

Fig. 11 Tip photos—9000 rpm (upper) and 1680 rpm (lower)

rpm the analysis predicts significantly larger rotations (especially twist) than were measured.

The influence of the centrifugal field on the steady-state blade twist for the SR-5 is summarized in Fig. 9 which shows the spanwise distribution of airfoil twist about the Y (radial) axis obtained from measurements at the midchord row of mirrors at three spanwise locations ($A2$, $B2$, $C2$). It is seen that the twist angle increases uniformly with span up to about 80% from which point it decreases out to the tip. The interruption in the 8000 rpm curve is caused by the fact that the spots reflected from the B row of mirrors were outside the range of viewing. Also shown in Fig. 9 are the results of NASTRAN calculations at 7000 rpm. NASTRAN results are in agreement to within 5% of the mirror data up to this spanwise position of maximum twist angle beyond which NASTRAN does not predict the decrease in twist clearly indicated by these data. The reasons for the disagreement between results from NASTRAN analysis and corresponding results from test data cannot be fully explained. However, considering the extent of agreement evident in the results up to 80% of the span (i.e., where the deflections are smaller than those in the other 20% of the blade span), it is likely that the nonlinear analysis in NASTRAN is not adequate to model the large motion of such components.

Figure 10 compares the difference in twist angle from leading to trailing edge along the span at 7000 rpm. NASTRAN results at similar blade locations are also shown. It is seen that over most of the span the trailing edge twists much more than the leading edge resulting in the significant decrease in airfoil camber shown. Near the root and tip the sense of the camber change is reversed leading to a small camber increase particularly at the tip. NASTRAN results show a similar uncambering characteristic with span which agrees closely with the measured values up to about 60% span above which NASTRAN indicates larger uncamber than was measured. For the transonic Mach numbers at which the blade operates, it may be anticipated that (*a*) similar changes in airfoil camber will have a significant effect on overall rotor performance and (*b*) a precise knowledge of the blade twist and uncamber will be required to predict the aerodynamics.

Figure 11 is a superposition of two photographs of the tip of blade number 5 taken at 1600 and 9000 rpm and shows clearly the large centrifugal twists and displacements that can occur. In the figure, the lower image of the tip (painted white to enhance visibility) was taken at 1600 rpm and the upper image taken at 9000 rpm.

A careful review of the data indicated that a single photographic image of the tip does not contain adequate information for twist angle to be compared directly with corresponding laser/mirror twist data. The tip chord has projections on the X, Y, and Z axes; consequently, centrifugal

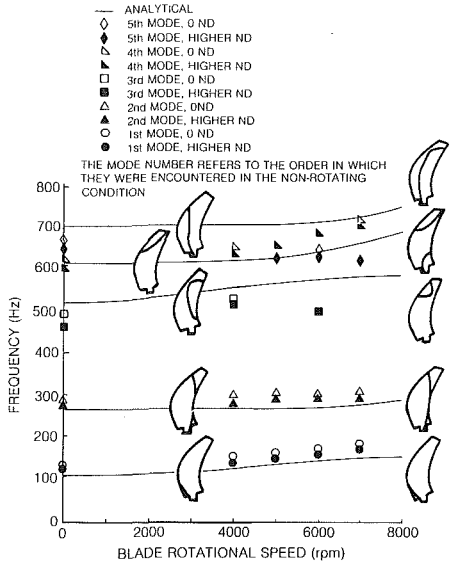

Fig. 12 Comparison between calculated and measured frequencies for several blade modes

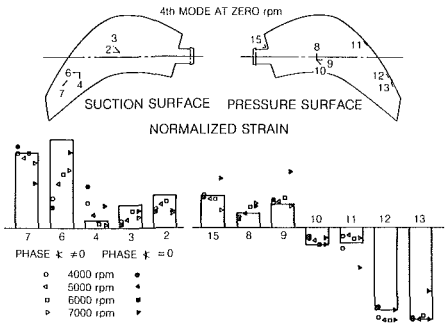

Fig. 13 Blade 2 strain mode shape variation with speed—fourth bench mode versus fifth mode at speed

deformation of the blade results in projection of rotation on all the axes. The camera records only one of these projections which is related to Θ_Y and therefore will not admit to quantitative comparison because the other components of rotation which couple with Θ_Y cannot be recorded on a single photographic plane.

(*b*) Vibratory Tests. The specific rotor characteristics which were evaluated include:

1 natural frequency versus speed for the first five blade modes;
2 extent and characteristics of mechanical coupling among the blades and the resulting coupled modes;
3 blade strain mode shape response with speed for the first five blade modes.

Results obtained from reducing the vibratory tests are presented and discussed below.

Natural Frequencies of the Rotor. The variation of the vibratory natural frequencies of the assembly with speed is shown in Fig. 12. Although excitation was imposed on all the blades at a variety of prescribed interblade phase angles in both forward and backward traveling waves, amplitude decay signatures generally contained a mixture of waves.

At several speeds and modes, pairs of frequencies very close together were observed as shown in Fig. 12. In these data, the upper frequency represents a mode in which all the blades are exactly in phase in an "umbrella" mode, and the lower frequency exhibits a mixed nodal diameter pattern. While strong response was noted in modes one, two, four, and five,

Table 2 Nodal diameter response pattern during decay versus type of excitation

6000 rpm
First mode
Strain gage No. 12 on all blades

	Excitation pattern					
Strength of response during decay	Single blade excitation	0 nodal dia. (umbrella)	1 nodal dia. forward	2 nodal dia. forward	2 nodal dia. backward	1 nodal dia. backward
0 nodal dia. (umbrella)	100%	100%	40%	15%		15%
1 nodal dia. forward	0	0	65%	30%		40%
2 nodal dia. forward	10%	10%	25%	90%		100%
2 nodal dia. backward	5%	5%	30%	100%		95%
1 nodal dia. backward	5%	5%	100%	45%		35%
System response frequency	173.99 Hz	174.43 Hz	158.8 Hz	157.18 Hz		157.71 Hz

the third mode proved to be difficult to excite at speeds above 4000 rpm. Therefore, few data could be obtained close to the third mode frequency. This characteristic was also observed in the bench tests, in which the third mode response was always significantly less than that in the other four modes. Examination of the mode shapes in the fourth and fifth modes shows that there is an apparent crossover of modal frequencies.

Figure 12 also shows results from NASTRAN, a blade-alone frequency calculation, for the frequency of the first five modes as a function of speed. The predicted mode shapes are also included in Figure 12. It is emphasized that the test data shown in Fig. 12 represent system modes and therefore are not directly comparable with the blade-alone calculations shown. The frequency of the system modes shown are approximately 10% higher than the individual blade-alone frequencies for the first two modes. This is possibly due to the predominance of inertial effects in the coupling mechanism [8]. As can be seen there is poor agreement between the analytical and experimental results for the third and higher modes.

All of the experimental modes shown in Fig. 12 represent rotor coupled modes; i.e., the response frequency of each blade in the rotor is the same, and there is a fixed interblade phase angle between them. Whether one blade of the assembly or the complete assembly was subjected to forced vibration, the entire assembly responded indicating a significant level of mechanical coupling among the blades. Attempts to relate the nodal diameter patterns of the response with the nodal pattern of the excitation show that they are not simply related because the response modes contain contributions from many harmonics.

The excitation of the assembly included both single blade as well as all blades at 0, 1, and 2 nodal diameters in forward and backward traveling waves. Decay patterns were characterized by either strong umbrella-mode response and/or a mixture of the other patterns. Table 2 compares the relative response amplitude of the waves for different patterns of excitation including the excitation where only a single blade was driven. As observed earlier, no consistent relationship is evident between the pattern of excitation and correspondent patterns of response. A possible explanation for this lack of traveling wave correlation is that the transient force induced by switching off the excitation induces a mixture of traveling waves. The specific mixture is related to the timing of the transient during the cycle. The detailed characteristics shown for the first mode are typical of the higher modes also. It is interesting to note, however, that when the umbrella mode is the major constituent of the rotor response, the decay frequency was observed to be about 10% higher than those cases where the response contains other nodal diameter patterns.

(c) Blade Strain Mode Shape. In order to clarify individual blade strain mode shapes, the variation in strain distribution for each mode and speed are evaluated. As an example, Fig. 13 displays the output from the twelve active gages on blade #2. Additional data of this type are presented and discussed in [9]. In Fig. 13, an outline of the pressure and suction surface of the blade is shown along with the location and orientation of each of the strain gages. Strain gage numbers 1 and 5 were not included in the data recording because their output during the bench test characterization was less than 5% of the maximum reading strain gage for all five modes of vibration, so it was felt that they would contribute little to mode identification. Below the blade outline is a bar chart where each bar represents the strains at zero speed obtained from the corresponding numbered gage on the blade. The height of the bar represents strain amplitude normalized to the maximum (which varies for different modes) and the position above or below the axis shows whether the phase angle relative to gage number 2 is 0 or 180 deg.

Two groups of four symbols have been superimposed on each bar to show blade mode response for the two characteristic system modes with zero interblade phase angle (umbrella mode) having solid symbols, and the nonzero interblade phase (mixed nodal diameters) angle having open symbols. The speed at which the data were recorded is shown by the shape of the symbols.

Examination of the change of the mode shapes with respect to speed leads to the following observations.

(*a*) The system mode with a predominant zero interblade phase angle (umbrella mode) and modes with nonzero interblade phase angle (mixed nodal diameters) show virtually no difference in blade strain mode shape despite the frequency difference on the order of 9%.

(*b*) The modal distribution of strain from the zero rpm measurements is only an initial screen for modal identification because the data at speed may show a substantial difference and may reflect changes in blade root constraint.

(*c*) The highest frequency mode measured at speeds above 4000 rpm shows a strain distribution resembling that of the fourth mode at zero rpm.

(*d*) The fourth mode at speeds above 4000 rpm shows a strain distribution resembling that of the fifth mode at zero rpm.

(*e*) The third mode was difficult to excite at speeds above 4000 rpm; consequently changes in strain distribution with speed could not be recorded.

The vibratory stresses at the strain gage positions calculated from NASTRAN, were used for comparison with the corresponding experimental blade measurements. With the computed values of σ_x, σ_y, τ_{xy} for each finite element, the stress component oriented in the strain gage direction were calculated and averaged arithmetically for the elements immediately adjacent to the nodal point identified with a particular strain gage.

The first two modes showed satisfactory correspondence between experimental bench test mode shapes and the NASTRAN predictions at both zero and 7000 rpm. The third NASTRAN mode, in contrast, showed no relationship to any of the three higher bench modes. The fourth bench test mode showed significant similarity to the fifth mode of the NASTRAN predictions. The fifth bench test mode and the fourth NASTRAN modes showed a limited similarity to each other.

Principal Conclusions

Based on (*a*) the test data obtained by testing the five blade configuration of the SR-5 assembly, and (*b*) the NASTRAN analytical results, the following major conclusions can be drawn.

1 Centrifugal loads acting on the assembly cause large reductions in airfoil camber over most of the blade surface.
2 Maximum twist due to centrifugal loads occurs inboard of the tip at approximately 80% span.
3 For the first five modes of vibration, the rotor responds as a system with all blades vibrating at the same frequency.
4 Blade strain mode shapes exhibit small changes between 4000 and 7000 rpm for the first five modes of vibration.
5 NASTRAN blade alone frequencies for the first two modes are within 10% of the measured system mode frequencies. The agreement for the hgher modes is generally poor.
6 Significant differences were noted between calculated vibratory stress distributions and corresponding measurements at both zero and 7000 rpm for the 3rd, 4th, and 5th modes of vibration. Modes 1 and 2 show satisfactory agreement.
7 NASTRAN calculation of blade tip axial deflection in the centrifugal field agrees with the measured values.
8 Significant differences exist between results calculated from NASTRAN and corresponding measurements for twist and uncamber distribution.
9 Mechanical coupling among the blades can arise due to either the inertia of the hub and/or the elasticity of the hub and pitch change mechanism.
10 The added mass of the blade mounted mirrors is apparent in the centrifugal deflection measurements.

References

1 Dugan, J. F., Miller, B. A., Grabear, J. J., and Sagerser, D. A., "The NASA High Speed Turboprop Program," National Aeronautics and Space Administration, NASA TM 81561, Oct. 1980.

2 Mehmed, O., Kaza, K. R. V., Lubomski, J. F., and Kielb, R. E., "Bending Torsion Flutter of a Highly Swept Advanced Turboprop," NASA TM 82975, Oct. 1982.

3 Stargardter, H., "Optical Determination of Rotating Fan Blade Deflections," ASME JOURNAL OF ENGINEERING FOR POWER, Apr. 1977, pp. 204–209.

4 Stargardter, H., U.S. Patent 4,080,823: Vibration Measurement.

5 Srinivasan, A. V., and Cutts, D. G., *Basic Study of Bladed Disk Structural Response*, United Technologies Research Center, AFWAL TR-83-2075, Nov. 1983.

6 Lawrence, C., and Kielb, R. E., "Nonlinear Displacement Analysis of Advanced Propeller Structures Using NASTRAN," NASA TM 83737, Aug. 1984.

7 Ibraham, S. R., and Mikulcik, E. C., "A Method for the Direct Identification of Vibration Parameters from the Free Response," *Shock and Vibration Bulletin*, Vol. 47, Part 4, Sept. 1977, pp. 183–198.

8 Crawley, E. F., and Mokadam, D. R., "Stagger Angle Dependence of Inertial and Elastic Coupling in Bladed Disks," *Journal of Vibration, Acoustics, Stress and Reliability in Design*, April 1984, pp. 181–188.

9 Srinivasan, A. V., and Fulton, G. B., "Advanced Turboprop Vibratory Characteristics," NASA CR 174708, April 1984.

A. Sinha
Assistant Professor of Mechanical Engineering.
The Pennsylvania State University,
University Park, PA 16802

J. H. Griffin
Associate Professor
of Mechanical Engineering.
Carnegie-Mellon University,
Pittsburgh, PA 15213

R. E. Kielb
Aerospace Engineer.
National Aeronautics
and Space Administration,
Lewis Research Center,
Cleveland, OH 44135

Influence of Friction Dampers on Torsional Blade Flutter

This paper deals with the stabilizing effects of dry friction on torsional blade flutter. A lumped parameter model with single degree of freedom per blade has been used to represent the rotor stage. The well-known cascade theories for incompressible and supersonic flows have been used to determine the allowable increase in fluid velocity relative to the blade. It has been found that the effectiveness of friction dampers in controlling flutter can be substantial.

Introduction

This paper is concerned with the stabilizing effects of dry friction on torsional blade flutter which is an important problem in the development of modern gas-turbine engines. The feasibility of incorporating additional friction devices to increase the amount of mechanical damping in the gas-turbine rotor stages to stabilize flutter was first investigated by Sinha and Griffin [1, 2, 3]. The aerodynamic instability in the earlier papers was simulated by taking the viscous damping associated with each blade to be negative. This simple representation of aerodynamic forces provided a good basis for the development of the physical concepts and mathematical techniques which are required to analyze the stabilizing effects of friction dampers. However, this model does not consider certain essential features of cascade aerodynamics, e.g., aerodynamic coupling between blades and the dependence of aerodynamic damping on interblade phase angle, frequency of blade oscillation, Mach number, and various cascade parameters. Consequently, the results obtained in the previous papers [1, 2, 3] do not provide a quantitative method for assessing how effective friction may be in an actual application. Therefore, it is not known to what extent the use of friction dampers can lead to an advancement in gas turbine technology, e.g., an increase in engine rpm. Often, a higher value of engine rpm is desirable since the increase in performance would lead to a higher thrust-to-weight ratio. However, higher engine speeds can cause aeroelastic instability since the fluid velocity relative to the blade is also increased. The objective of this paper is to determine if the use of additional friction devices can allow the engine to operate at a significantly higher fluid velocity relative to the blade while still maintaining stable vibratory response.

Two types of friction dampers, blade-to-blade (*B-B*) and blade-to-ground (*B-G*), are considered in this paper. Both types are currently used in turbine stages to limit resonant stresses [4, 5, 6, 7]. As indicated in Fig. 1, these dampers are modeled as massless springs [1, 2, 3] located either between the blades or between the blades and a relatively rigid structure such as the coverplate. These devices provide links between points experiencing relative motion caused by vibration. They transmit shear loads, μR, through friction contacts which dissipate energy when slip occurs.

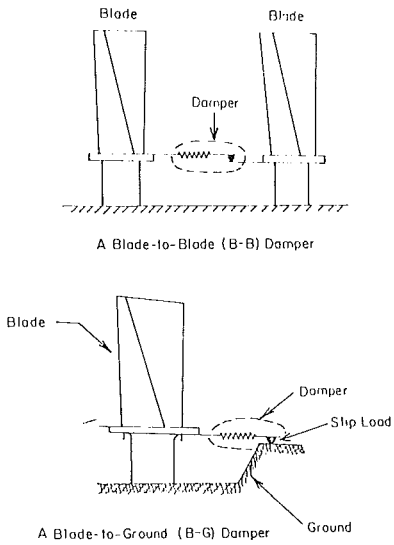

Fig. 1 Types of friction dampers

Contributed by the Gas Turbine Division of THE AMERICAN SOCIETY OF MECHANICAL ENGINEERS and presented at the 30th International Gas Turbine Conference and Exhibit, Houston, Texas, March 18–21, 1985. Manuscript received at ASME Headquarters, January 10, 1985. Paper No. 85-GT-170.

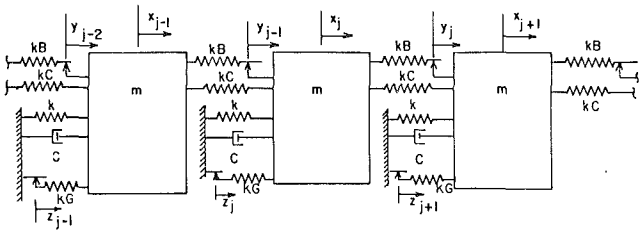

Fig. 2 Tuned model of a rotor stage

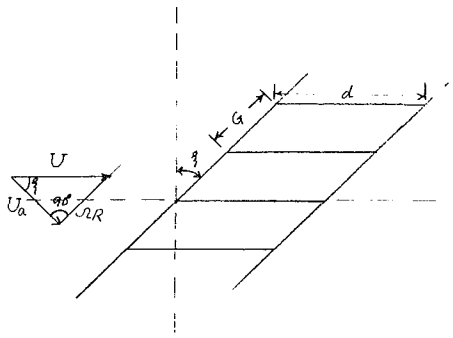

Fig. 3 Cascade of blades

The spring/mass model, shown in Fig. 2, is used in this paper to represent a rotor stage. This model considers only a torsional mode of vibration for each blade and is the same as that used in the previous studies [2, 3] except that the viscous damping associated with each blade is taken to be positive to represent any structural damping. In Fig. 2, m and k are the mass-moment of inertia and torsional stiffness, respectively, of the blade. The variation in modal properties of blades, known as mistuning, has a beneficial effect on aeroelastic instability [8, 9] and, therefore, has been ignored in the present study. The mechanical coupling between the adjacent blades due to disk flexibility has been simulated by a spring with stiffness kC. The stiffness of the B-B dampers is represented by kB and that of the B-G dampers by kG.

The unsteady aerodynamic moment due to the motion of blades in a rotor stage has been calculated by using the well-known linear cascade theories for unstalled incompressible [10] and supersonic flows [11]. In the development of these theories, the rotor stage is modeled as a cascade of blades (Fig. 3). Also, the blade is represented by a "typical section" model which is assumed to vibrate in torsion about an axis located at a distance ηd from the leading edge (Fig. 4). It is also assumed that the motion of each blade is sinusoidal with identical amplitude and constant interblade phase angle. The aerodynamic moment on each blade in incompressible flow depends on reduced velocity (U_1), stagger angle (ξ) gap-to-chord ratio (G/d), interblade phase angle (β_r) and the location of the torsion-axis (η). For supersonic flow, the Mach number (M) is an additional parameter.

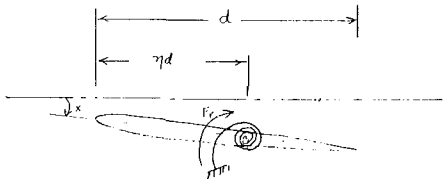

Fig. 4 Equivalent section of a blade

Specifically, this paper is concerned with the dynamic behavior of the system, depicted in Fig. 2, at reduced velocities greater than its critical value, $(U_1)_{cr}$. At $U_1 > (U_1)_{cr}$, the aerodynamic damping is negative in at least one mode of vibration. Consequently, a perturbation in the quiescent initial condition of displacement and velocity will result in the growth of amplitudes even in the absence of any external excitation. If the motion of blades is such that the maximum force in the damper exceeds the slip load, the damper slips and there is a dissipation of energy. Hence, the system may attain a steady state (limit cycle), provided the work done due to the unstable aerodynamic forces equals the energy dissipated by friction.

The steady-state response, also described as limit cycles, is obtained using the technique established in the earlier paper [2]. It is assumed that steady-state solutions are harmonic and correspond to one of the tuned modes, i.e., those having identical amplitude for each blade and constant interblade phase angle. Similar to the results obtained with constant negative damping, a pair of steady-state solutions is found in a tuned mode. The solution with the lower amplitude is described as a stable limit cycle, whereas the other solution corresponds to a stability limit which if exceeded would result in unbounded response. If the initial conditions are below the stability limit, the system settles down in a steady-state oscillation with the lower amplitude. It has also been found that there exists a maximum value of reduced velocity, $(U_1)_{\max}$, beyond which a steady-state solution is not found in all the tuned modes. Since the system settles down in one of the stable steady-state oscillations for all perturbations in quiescent initial conditions only if a pair of solutions are obtained in all the tuned modes [2], $(U_1)_{\max}$ is taken to be the maximum value of reduced velocity beyond which friction dampers are unable to stabilize the system. Using the values of $(U_1)_{\max}$ and $(U_1)_{cr}$, a method has been developed in this paper to estimate the increase in relative fluid velocity as a fraction of critical fluid velocity.

First, the impact of friction dampers (B-B and B-G) on torsional blade flutter is studied for three, six, nine, and twelve-bladed disks. The aerodynamic moment on each blade

Nomenclature

a = Fourier coefficient
A = amplitude
b = Fourier coefficient
C = structural damping
d = chord length
F_r = aerodynamic moment in the r-th tuned mode
i = $(-1)^{1/2}$
k = torsional stiffness of the blade
kB = B-B damper stiffness
kC = coupling due to the disk
kD = B-B or B-G damper stiffness
k_e = equivalent modal stiffness
kD_e = equivalent damper stiffness
kG = B-G damper stiffness
m = mass-moment of inertia
N = number of blades
R = normal load at the friction joint
U = fluid velocity relative to the blade
U_1 = reduced velocity ($U/\omega d$)
U_a = axial fluid velocity
x = displacement
y = displacement of the damper spring at the friction contact
β_r = interblade phase angle in the r-th tuned mode ($2\pi(r-1)/N$)
ϵ = nondimensionalized damper stiffness
η = location of the torsion axis
μ = coefficient of friction
ξ = stagger angle
ρ = fluid density
χ = mass ratio
ω = frequency
Ω = engine rpm

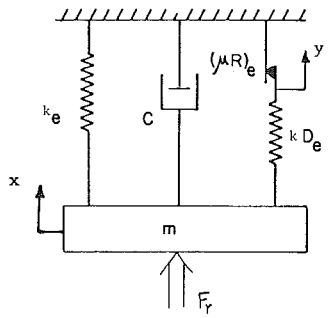

Fig. 5 Equivalent SDOF model with *B-G* dampers

is calculated using Whitehead's theory for incompressible flow [10]. The choice of a small number of blades and incompressible flow field keeps the computation effort to a minimum while still illustrating the role of each parameter, e.g., interblade phase angle, dependence of aerodynamic damping on reduced velocity, etc., that governs the damper's performance. Next, a 28-bladed NASA rotor stage is considered to evaluate the effects of friction on flutter in a more realistic situation. The flow is assumed to be supersonic with a subsonic leading edge and the theory developed by Adamczyk and Goldstein [11] is used to calculate the unsteady aerodynamic moment on each blade. The results from extensive computer simulations indicate that in this instance the use of *B-G* dampers can allow the engine to operate at a significantly higher value of relative Mach number.

Steady-State Analysis

For the response in a tuned mode, the multi-degree-of-freedom (MDOF) model of the rotor stage with either *B-B* or *B-G* dampers is equivalent [2] to the single-degree-of-freedom (SDOF) model with *B-G* dampers (Fig. 5). In this figure, F_r is the aerodynamic moment due to the motion of blades in the r-th tuned mode with β_r as the constant interblade phase angle. The value of β_r is equal to $2\pi(r-1)/N$, where N is the number of blades and r varies from 1 to N. The expressions for equivalent stiffness (K_e), equivalent damper stiffness (kD_e) and the slip load ($(\mu R)_e$) are presented in Appendix I.

The dynamics of the equivalent SDOF model, depicted in Fig. 5, is governed by the following differential equation:

$$mx'' + Cx' + (k_e + kD_e)x - kD_e y = F_r \tag{1}$$

It is assumed that the flow conditions are such that flutter occurs and that the steady-state response induced by friction dampers is harmonic, i.e.,

$$x = Ae^{i\omega t} \tag{2}$$

Under this assumption, the aerodynamic moment, F_r, is calculated as follows [8, 9]:

$$F_r = \pi\rho d^4 \omega^2 l_r x \tag{3}$$

where ρ is the fluid density and

$$l_r = U_1^2 (C_{M\alpha})\eta \tag{4}$$

The coefficient $(C_{M\alpha})\eta$, which is a complex number, is obtained from the existing codes [10, 11]. Now, introducing the following notations

$$\omega_{nr}^2 = \frac{k_e}{m}, \frac{C}{m} = 2\zeta\omega_{nr},$$

$$t_d = \frac{kD_e}{k_e}, \tag{5}$$

$$\chi = \frac{\pi\rho d^4}{m} \text{ and } l_r = l_{rR} + il_{rI}$$

Table 1 Rotor stage parameters

	Incompressible flow	Supersonic flow
G/d	1.0	0.8
η	0.429	0.5
ξ	45 deg	64.86 deg

the governing differential equation (1) can be written as follows:

$$x'' + 2\zeta\omega_{nr}x' + (1+t_d)\omega_{nr}^2 x - t_d\omega_{nr}^2 y = \chi(\omega^2 l_{rR}x + \omega l_{rI}x') \tag{6}$$

Using the expressions for k_e and kD_e (Appendix I),

$$\omega_{nr}^2 = \omega_0^2(1 + 4(kC/k)\sin^2(\beta_r/2)) \tag{7}$$

and

$$t_d = \begin{cases} \dfrac{(kG/k)}{1+4(kC/k)\sin^2(\beta_r/2)}, & B\text{-}G \text{ dampers} \\ \dfrac{4(kB/k)\sin^2(\beta_r/2)}{1+4(kC/k)\sin^2(\beta_r/2)}, & B\text{-}B \text{ dampers} \end{cases} \tag{8}$$

where

$$\omega_0{}^2 = k/m \tag{9}$$

From (6), it can be seen in the absence of any mechanical damping ($\zeta = y = 0$) that flutter occurs when

$$l_{rI} > 0 \tag{10}$$

In order to obtain the amplitude, A, and the frequency, ω, associated with the steady-state solution, the nonlinear term, y, in (6) is expanded in a Fourier series and only the fundamental terms are considered, i.e.,

$$y = ae^{i\omega t} - ibe^{i\omega t} \tag{11}$$

where the expressions for a and b are given in Appendix I. Substituting (2) and (11) into (6),

$$-\sigma^2 + 2i\zeta\sigma + (1+t_d) - t_d(a - ib)/A = \chi\sigma^2(l_{rR} + il_{rI}) \tag{12}$$

where

$$\sigma = \omega/\omega_{nr} \tag{13}$$

Separating real and imaginary parts in (12),

$$2\zeta\sigma + t_d b/A = \chi\sigma^2 l_{rI} \tag{14}$$

and

$$1 - \sigma^2 + t_d(1 - a/A) = \chi\sigma^2 l_{rR} \tag{15}$$

Substituting the expressions for a and b into (14) and (15),

$$\frac{A}{(\mu R)_e/kD_e} = \frac{-4t_d/\pi \pm ((4t_d/\pi)^2 + 16t_d/\pi(2\zeta\sigma - \chi\sigma^2 l_{rI}))^{1/2}}{(4\zeta\sigma - 2\chi\sigma^2 l_{rI})} \tag{16}$$

and

$$\sigma^2 = \frac{1 + t_d(\theta_c - 0.5\sin 2\theta_c)/\pi}{1 + \chi l_{rR}} \tag{17}$$

Equations (16) and (17) are solved simultaneously to determine A and σ in a tuned mode for various reduced velocities.

Results for Incompressible Flow

The rotor stage parameters required for the calculation of aerodynamic moments have been obtained from [12] and are listed in Table 1. The values of kC/k and kD/k, where kD is defined in Appendix I, are chosen to be 0.1 and 0.2, respectively, and are typical of those found in modern gas-turbine engines. The slip distance, $\mu R/kD$, which is a scale factor for the amplitude [1], is arbitrarily selected to be 0.5. The structural damping, ζ, has been set to zero and, therefore,

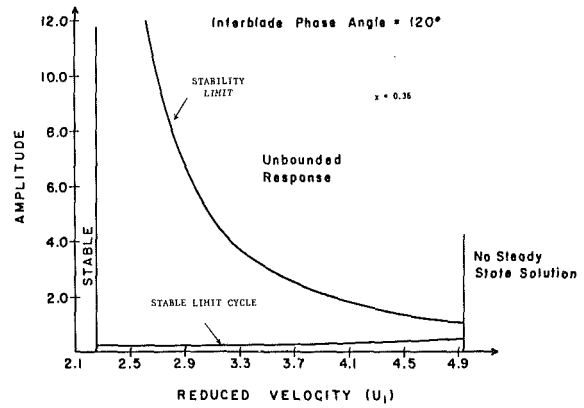

Fig. 6 Amplitudes of steady-state solutions for a three-bladed disk with *B-B* dampers

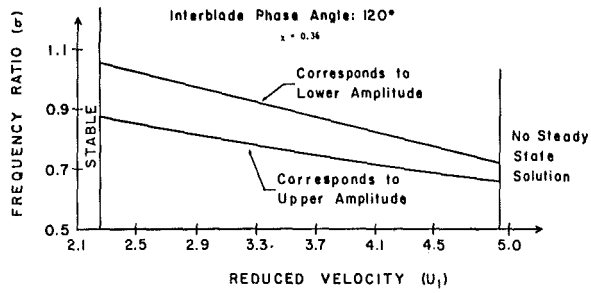

Fig. 7 Frequencies of steady-state solutions for a three-bladed disk with *B-B* dampers

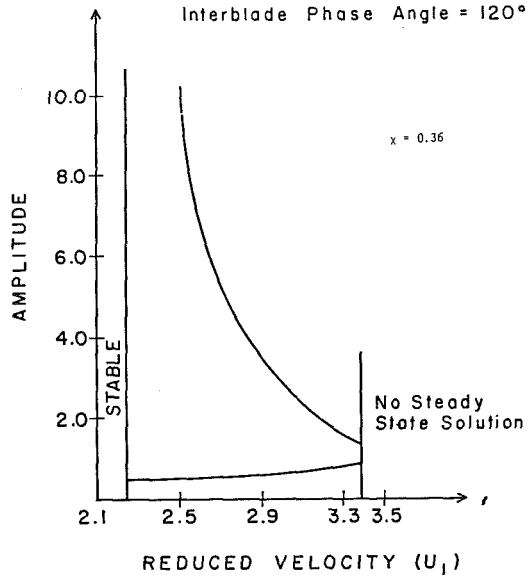

Fig. 8 Amplitudes of steady-state solutions for a three-bladed disk with *B-G* dampers

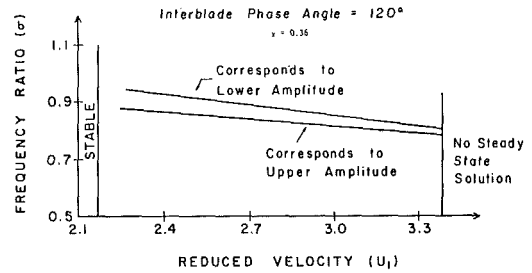

Fig. 9 Frequencies of steady-state solutions for a three-bladed disk with *B-G* dampers

the mechanical damping in the rotor stage is assumed to be due to friction only.

Steady-State Solutions. First, a three-bladed system is considered. The critical reduced velocity, $(U_1)_{cr}$, which has been defined in Section 1, is found for the $\beta_r = 120$ deg. The steady-state solutions due to friction dampers are obtained at reduced velocities greater than $(U_1)_{cr}$. For *B-B* dampers, amplitudes and frequencies of steady-state solutions have been plotted against reduced velocity in Figs. 6 and 7, respectively. It can be seen that there is a maximum value of reduced velocity beyond which a steady-state solution does not exist in 120 deg tuned mode. At a reduced velocity less than $(U_1)_{\max}$, the tuned modes with 0 deg and 240 deg interblade phase angles are found to be stable and there are two solutions in the unstable 120 deg tuned mode. The results from the analysis with constant negative damping [1, 2] show that the solution with lower amplitude is a stable limit cycle as long as the initial displacement is lower than the amplitude associated with the upper solution. The results for *B-G* dampers are similar to those for *B-B* dampers (Figs. 8 and 9). However, $(U_1)_{\max}$ is lower for the system with *B-G* dampers because of the smaller value of ϵ, defined in Appendix I, in the 120 deg tuned mode. The higher the value of ϵ, the greater the value of negative damping that can be stabilized [1].

It is observed that $(U_1)_{cr}$ and $(U_1)_{\max}$ may correspond to modes having different interblade phase angles; for example, consider the results for the nine-bladed system with *B-B* dampers. The reduced velocity at which flutter occurs is the lowest for $\beta_r = 80$ deg, (Fig. 10). However, $(U_1)_{\max}$ is found for the response in a 40 deg tuned mode because of the lower value of ϵ.

Lastly, note that upper and lower solutions occur at different frequencies for a specified reduced velocity. Therefore, they do not correspond to the same fluid velocity, U. For a fixed reduced velocity, the higher the frequency of oscillation, the greater the fluid velocity.

Increase in Fluid Velocity. In order to estimate this increase in fluid velocity, the following two quantities must be evaluated: (*a*) the maximum fluid velocity, $U_{\max}$, for which a stable limit cycle exists, and (*b*) the critical velocity, U_{cr}, at which flutter occurs in the absence of friction dampers.

The determination of $U_{\max}$ requires that $(U_1)_{\max}$ be multiplied by a frequency. The value of this frequency is to be chosen such that

$$U_1 < (U_1)_{\max} \text{ if } U \leq U_{\max} \tag{18}$$

Condition (18) may be satisfied if the least possible value of frequency is chosen for $U_1 < (U_1)_{max}$. At a given reduced velocity, the natural frequency, ω_f, of the aeromechanical system with fully slipping (slip load = 0) dampers is a lower bound for the frequency of oscillation. From (6),

$$\omega_f \equiv \omega_f(U_1, \beta_r) = \frac{\omega_{nr}}{(1 + \chi l_{rR})^{1/2}} \tag{19}$$

The values of U_1 and β_r are chosen such that ω_f is minimized and $U_{\max}$ is calculated as follows:

$$U_{\max} = (U_1)_{\max} \omega_e d \tag{20}$$

where

$$\omega_e = \min \omega_f(U_1, \beta_r) \tag{21}$$

The critical fluid velocity, U_{cr}, is obtained as follows:

$$U_{cr} = (U_1)_{cr} \omega_s d \tag{22}$$

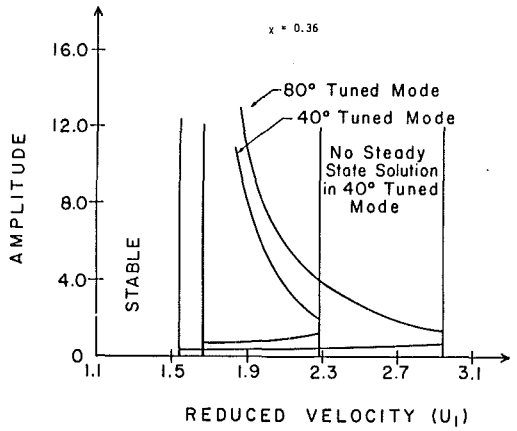

Fig. 10 Steady-state solutions for a nine-bladed disk with *B-B* dampers

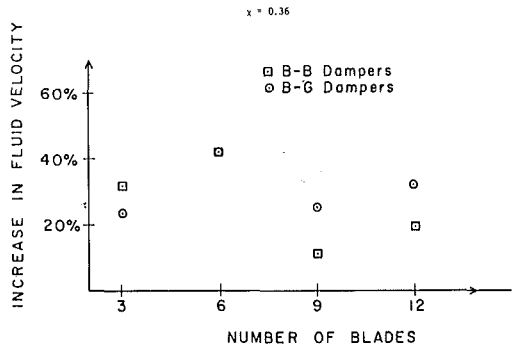

Fig. 11 Increase in incompressible fluid velocity as a percentage of critical velocity

where ω_s is the natural frequency of the aeromechanical system with fully stuck (slip load = ∞) dampers at $U_I = (U_I)_{cr}$. Since ω_s is the upper bound on the frequency of oscillation, a conservative estimate is obtained for the increase in fluid velocity, $U_{\max} - U_{cr}$.

From (20) and (22), a conservative estimate for the increase in fluid velocity as a percentage of critical velocity is

$$= \left(\frac{(U_1)_{\max}\omega_e}{(U_1)_{cr}\omega_s} - 1 \right) * 100 \tag{23}$$

The increase in fluid velocity due to both types of dampers has been estimated for three, six, nine, and twelve-bladed systems (Fig. 11). The lowest values of this increase in fluid velocity are 11% and 23% for *B-B* and *B-G* dampers, respectively. The interblade phase angles corresponding to $(U_1)_{cr}$ and $(U_1)_{\max}$ are presented in Table 2. For three-bladed systems, the increase in fluid velocity is higher for the *B-B* dampers due to the higher value of ϵ in the 120 deg tuned mode (Table 2). For six-bladed systems, the fluid velocity can be increased by the same amount for both the dampers because $\epsilon_{B\text{-}B}/\epsilon_{B\text{-}G}$ is equal to one in the 60 deg tuned mode. For nine and twelve blades, *B-G* dampers are more effective due to the higher value of ϵ in the tuned mode corresponding to $(U_1)_{\max}$.

Also, the effectiveness of dampers in terms of the percentage increase in fluid velocity depends on the rate of change of effective negative damping, l_{rI}, as a function of reduced velocity. For example, the effectiveness of *B-B* dampers for the six-bladed disk is greater than that for the three-bladed system in spite of the fact that ϵ is lower for the 60 deg tuned mode.

Results for Supersonic Flow

In practice, flow conditions are frequently supersonic and the number of blades is often much larger than twelve. To explore this type of application, the influence of friction dampers on supersonic flutter is evaluated in the context of a 28-bladed NASA rotor stage. As mentioned earlier, the aerodynamic moment on each blade is calculated using the code developed by Adamczyk and Goldstein [11]. The structural parameters for the rotor stage are listed in Table 1. The values of kC/k, kD/k and $\mu R/kD$ are the same as those used for incompressible flow.

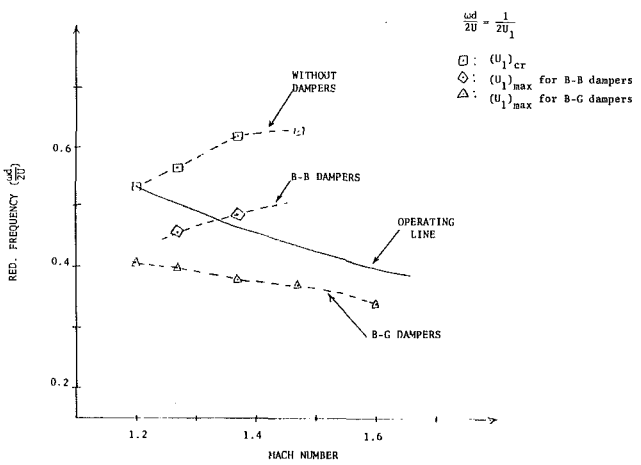

Fig. 12 Results for supersonic flow

Table 2 Interblade phase angles corresponding to $(U_1)_{cr}$ and $(U_1)_{\max}$

No. of blades	Critical interblade Phase angle	Interblade phase angles corresponding to $(U_1)_{\max}$ For B-G dampers	For B-B dampers	$\epsilon_{B\text{-}B}/\epsilon_{B\text{-}G}$
3	120 deg	120 deg	120 deg	0.42
6	60 deg	60 deg	60 deg	1.0
9	80 deg	80 deg	40 deg	1.78
12	60 deg	60 deg	30 deg	3.18

Three different regimes of flutter have been classified for supersonic flow depending on whether the acoustic disturbance decays or propagates [9]. This classification of flutter regimes is governed by the values of β_{r1} and β_{r2} which are calculated as follows:

$$\beta_{r1,2} + 2\pi n = 2\frac{G}{d} \cdot \frac{1}{U_1}\left[-\frac{M^2}{M^2-1}\sin\xi \pm \sqrt{\frac{M^4}{(M^2-1)^2}\sin^2\xi - \frac{M^2}{M^2-1}} \right] \tag{24}$$

The value of the integer, n, is chosen such that $0 \le \beta_{r1,2} < 2\pi$. Flutter is called supercritical if the flutter interblade phase angle, β_r, lies inside β_{r1} and β_{r2}. If $\beta_r < \beta_{r1}$ or $\beta_r > \beta_{r2}$, the flutter is called subcritical.

At different values of Mach number, $(U_1)_{cr}$ and $(U_1)_{\max}$ are evaluated for both types of friction dampers in a manner described in Section 3, Fig. 12. The interblade phase angles associated with $(U_1)_{cr}$ and $(U_1)_{\max}$ are found to be less than $3\pi/14$ in each case. Since *B-G* dampers are more effective for such small values of flutter interblade phase angle, $(U_1)_{\max}$ for *B-G* dampers is greater than that for *B-B* dampers. The interblade phase angles for $(U_1)_{\max}$ and $(U_1)_{cr}$ are also found to be less than β_{r1} in all the cases. Therefore, they correspond to subcritical flutter. For $(U_1)_{cr} < U_1 < (U_1)_{\max}$, various occurrences of supercritical flutter are encountered. *B-G* dampers are able to stabilize the system in all such cases of flutter. The impact of *B-B* dampers on supercritical flutter is not specifically investigated because of its greater effectiveness in the higher interblade phase angle mode, i.e., the

fact that *B-G* dampers can stabilize the supercritical flutter implies that *B-B* dampers would also be able to do so.

Lastly, the effectiveness of friction dampers in controlling flutter is evaluated in terms of possible increase in relative Mach number. First, an operating line which defines the lowest value of reduced frequency $(1/U_1)$ for aeroelastic stability at any given Mach number is constructed by fixing the speed of sound and the blade's uncoupled torsional frequency [9] (Fig. 11). On the basis of numerical simulations presented in this paper, the flutter Mach number for the rotor stage is 1.2. With the introduction of *B-B* dampers, the Mach number can be increased only up to 1.34. On the other hand, the use of *B-G* friction dampers can allow the engine to operate at least up to M = 1.6. Thus, *B-G* dampers are significantly more effective in controlling supersonic torsional flutter in this 28-bladed disk.

Conclusions

At a reduced velocity greater than its critical value, there are two steady-state solutions in an unstable tuned mode (Fig. 6). The lower solution is described as the stable limit cycle whereas the upper solution corresponds to a stability limit which if exceeded would result in an unbounded response. Also, there exists a maximum value of reduced velocity beyond which a friction damper is unable to stabilize the rotor stage. Using this maximum value of reduced velocity, a method has been developed to estimate the increase in the relative fluid velocity. The increase in the incompressible fluid velocity, presented in Fig. 11 as a percentage of critical velocity for three, six, nine, and twelve-bladed systems, is found to be greater than 11% and 23% for *B-B* and *B-G* dampers, respectively. The *B-G* dampers are more effective than *B-B* dampers if the aerodynamic instability occurs in tuned modes with interblade phase angle less than 60 deg. In addition to the interblade phase angles associated with aerodynamic instability the effectiveness of dampers also depends on the rate of change of negative damping as a function of reduced velocity.

For the NASA rotor stage with 28 blades, the effectiveness of *B-G* dampers in controlling supersonic flutter is much higher than that of *B-B* dampers. It has been calculated that the use of *B-G* dampers can allow the engine to operate at Mach numbers up to 1.6 whereas without dampers the rotor stage would flutter at 1.2.

References

1 Sinha, A., and Griffin, J. H., "Friction Damping of Flutter in Gas Turbine Engine Airfoils," *AIAA Journal of Aircraft*, Vol. 20, No. 4, Apr. 1983.

2 Sinha, A., and Griffin, J. H., "Effects of Friction Dampers on Aerodynamically Unstable Rotor Stages," *AIAA Journal*, Vol. 23, No. 2, Feb. 1985, pp. 262–270.

3 Sinha, A., and Griffin, J. H., "Stability of Limit Cycles in the Multi-Degree-of-Freedom Model of an Aerodynamically Unstable Rotor Stage with Friction Dampers," *Journal of Sound and Vibration*, Vol. 103, No. 3, 1985, pp. 341–356.

4 Griffin, J. H., "Friction Damping of Resonant Stresses in Gas Turbine Engine Airfoils," ASME JOURNAL OF ENGINEERING FOR POWER, Vol. 102, April 1980.

5 Srinivasan, A. V., and Cutts, D. J ., "Dry Friction Damping Mechanisms in Engine Blades," ASME JOURNAL OF ENGINEERING FOR POWER, Vol. 105, No. 2, Apr. 1983; Paper No. 82-GT-162.

6 Muszynska, A., and Jones, D. I. G., "On Tuned Bladed Disk Dynamics, Some Aspects of Friction Related Mistuning," *Journal of Sound and Vibration*, Vol. 86, No. 1, 1983.

7 Griffin, J. H., and Sinha, A., "The Interaction Between Mistuning and Friction in the Forced Response of Bladed Disk Assemblies," ASME JOURNAL OF ENGINEERING FOR GAS TURBINES AND POWER, Vol. 107, No. 1, Jan. 1985; Paper No. 84-GT-139.

8 Kaza, K. R. V., and Kielb, R. E., "Effects of Mistuning on Bending-Torsion Flutter and Response of a Cascade in Incompressible Flow," *AIAA Journal*, Vol. 20, No. 8, Aug. 1982.

9 Kielb, R. E., and Kaza, K. R. V., "Aeroelastic Characteristics of a Cascade of Mistuned Blades in Subsonic and Supersonic Flows," ASME Paper No. 81-DET-122, Sept. 1981.

10 Whitehead, D. S., "Force and Moment Coefficients for Vibrating Airfoils in Cascade," R&M 3254, British Aeronautical Research Council, London, Feb. 1960.

11 Adamczyk, J. J., and Goldstein, M. E., "Unsteady Flow in Supersonic Cascade with Subsonic Leading-Edge Locus," *AIAA Journal*, Vol. 16, No. 12, Dec. 1978.

12 Srinivasan, A. V., "Influence of Mistuning on Blade Torsional Flutter," NASA-CR-165137, Aug. 1980.

APPENDIX I

(*a*) Expressions for parameters of Equivalent Single-Degree-of-Freedom Model [2].

$$k_e = k + 4kC\sin^2(\beta_r/2) \tag{A-1}$$

$$kD_e = \begin{cases} 4kB\sin^2(\beta_r/2), & \text{for } B\text{-}B \text{ dampers} \\ kG, & \text{for } B\text{-}G \text{ dampers} \end{cases} \tag{A-2}$$

$$(\mu R)_e = \begin{cases} 2\mu R\sin(\beta_r/2), & \text{for } B\text{-}B \text{ dampers} \\ \mu R, & \text{for } B\text{-}G \text{ dampers} \end{cases} \tag{A-3}$$

$$kD = \begin{cases} kB, & \text{for } B\text{-}B \text{ dampers} \\ kG, & \text{for } B\text{-}G \text{ dampers} \end{cases} \tag{A-4}$$

(*b*) Definition of ϵ

$$\epsilon = \frac{kD_e}{k_e + kD_e}$$

(*c*) Expressions for Fourier coefficients in the expansion of the nonlinear term [1]

$$a = A[\pi - \theta_c + 0.5\sin 2\theta_c]/\pi \tag{A-5}$$

$$b = 4(1 - 1/A)/\pi \tag{A-6}$$

where

$$\theta_c = \cos^{-1}\left(1 - \frac{2(\mu R)_e}{kD_e A}\right) \tag{A-7}$$

On the Importance of Shear Deformation, Rotatory Inertia, and Coriolis Forces in Turbine Blade Vibrations

K. A. Ansari[1]
Professor of Mechanical Engineering,
School of Engineering,
Gonzaga University,
Spokane, WA 99258

This paper is concerned with the significance of the effects of shear deformation, rotatory inertia, and Coriolis forces in the analysis of turbine blade vibrations. Since these are quite pronounced at the high frequency ranges encountered in turbine blade vibration problems, they should not be overlooked although their inclusion paves the way for a complicated nonlinear analysis. An approximate analysis technique is presented which involves an application of the stationary functional method using the normal modes of a discretized model. Numerical results for a typical blade are obtained and discussed. An advantage of this analysis as applied to a lumped parameter model is that nonlinear modes higher than the fundamental can also be easily computed and assessed.

Introduction

Failure of turbine blades often occurs as a result of sustained blade vibration at or near their natural frequencies. To prevent such failures, it is therefore necessary to be able to compute the natural frequencies theoretically during the process of design so that a suitable blade configuration can be achieved having resonant frequencies which are outside the frequency range of the exciting forces. However, because of the presence of such features as cross-sectional asymmetry, pretwist, taper, camber, and blade stagger, the analysis of turbine blade vibration which involves coupled bending-bending-torsional motions becomes quite a complex undertaking. In addition, the high speeds of rotation pertinent to gas turbine blades generate sizable centrifugal forces which should not be overlooked. These complications are further enhanced when the Coriolis effect, which is a nonlinearity arising from blade rotation, is also included.

Krupka and Baumanis [1] have shown that shear deformation and rotatory inertia terms tend to decrease the natural frequencies of vibration, their significance increasing with increase in frequency as well as rotational speed. They have found that at the high frequency ranges encountered in turbine blade design, the inclusion of these effects is quite important as it leads to changes of the order of 4 and 8 percent in the first and second natural frequencies, respectively. According to Bogdanoff [2], the exclusion of gyroscopic effects in problems dealing with the lower modes of propellers and helicopter rotor blades leads to satisfactory results, since these are long and slender. However, this is questionable for turbine and compressor blades which are blades of low aspect ratio rotating at high speeds. Lo and Renbarger [3] have shown that the effect of the nonlinear coupling terms arising from Coriolis acceleration is negligible, but their discussion is restricted to small motions. Lo [4] arrived at the same conclusion, but his analysis is limited to a beam that is rigid in bending everywhere except at the root where a spiral spring is used to connect the beam to the rotating disk. The plate analysis of Dokainish and Rawtani [5] is indeed useful for turbine blades, but it does not include the Coriolis effect. Lalanne et al. [6] and Trompette and Lalanne [7] have used finite element models to obtain stresses as well as natural frequencies and mode shapes of rotating turbine blades, but here again, the Coriolis effect has not been taken into account. Carnegie [8] used a variational approach to derive the partial differential equations of motion of a pretwisted blade of uniform cross section mounted on the periphery of a rotating disk. His equations do include the effects of rotatory inertia, coupled bending-bending-torsion, and Coriolis forces but are complicated and, in general, unsolvable. Rao and Carnegie [9] considered a uniform, untwisted, rotating cantilevered blade of symmetric cross section vibrating in the plane of rotation, and after simplifying the problem considerably by ignoring the shear deformation and rotatory inertia effects, obtained the fundamental nonlinear mode shape by a continuous system approach. Using a lumped parameter model, Fu [10] transformed the Carnegie formulation into a set of recursion formulae suitable for digital computation and obtained the blade natural frequencies under various end conditions. However, his analysis considers neither the shear deformation nor the Coriolis effect. Swaminathan and Rao [11] obtained the first three natural frequencies of a rotating, pretwisted and tapered cantilevered blade but only after idealizing it as a beam of rectangular cross section and ignoring the effects of shear deformation and Coriolis forces. In this paper, the nonlinear problem of a

[1]Formerly Associate Professor of Mechanical Engineering, University of Petroleum and Minerals, Dhahran, Saudia Arabia.

Contributed by the Gas Turbine Division for publication in the JOURNAL OF ENGINEERING FOR GAS TURBINES AND POWER. Manuscript received at ASME Headquarters June 14, 1985.

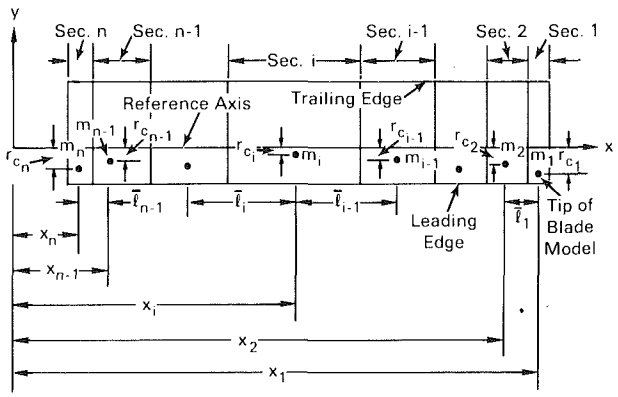

Fig. 1 Plan view of turbine blade

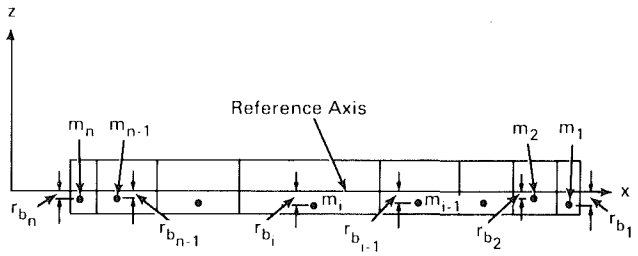

Fig. 2 Side view of turbine blade

rotating, tapered-twisted, nonuniform turbine blade of asymmetric airfoil cross section is treated and nonlinear vibration modes are derived by an application of the stationary functional method with the Coriolis force, shear deformation, and rotatory inertia contributions included in the analysis. Because the continuous system formulation of this problem [8] has proven to be intractable, a discrete system representation has been employed which, besides being convenient and practical, also leads to a reasonably accurate prediction of vibration frequencies for blades having substantial pretwist even with a modest number of degrees of freedom [12].

Mathematical Model

Figures 1 and 2 show two views of a nonuniform cantilevered turbine blade rotating with a constant angular velocity Ω about the z axis. The blade is divided into a suitable number of sections not necessarily of equal length and the x axis shown which intersects the axis of rotation is selected as the reference axis. Each section has a mass center and principal axes of inertia to account for its mass properties. The projection of the mass center m_i on to the reference axis locates the ith mass station. The field between two adjacent mass stations is massless but has bending, shear, and torsional flexibilities. The tip of the mathematical model is at station 1, which is not actually the tip of the real blade. However, by making section 1 very short, one could bring the mathematical tip and the physical tip close together. Since turbine blades are quite stiff longitudinally, the axis of mass centers is assumed to be inextensional. Figure 3 shows a

Nomenclature

$A_i^{(j)}$ = ith component of the jth normal mode vector for the linearized rotating turbine blade
b, c = axes parallel to the principal axes of blade section
A_i, B_i, C_i = principal moments of inertia of the ith section at its mass center
B_i^* = undetermined parameters in the "stationary functional" method
B_1^* = fundamental amplitude
B_2^* = second harmonic amplitude
$B_{1_{st}}^*$ = blade static deflection
F_y, F_z = amplitudes of exciting forces
J_R = Reissner functional
$\bar{l}_i$ = distance between station i and station $i+1$
L = the Lagrangian function
L_R = dynamic Reissner functional
m_i = mass of ith section, mass center of ith section
$M_{(j)}$ = generalized mass for the jth normal mode of the linear rotating turbine blade
M_x, M_y, M_z = amplitudes of exciting moments
n_s = number of mass stations on turbine blade
$\bar{P}$ = average power over a cycle
$\bar{Q}_i$ = average nonconservative generalized force associated with B_i^*
r_f = frequency ratio
r_{a_1}, r_{a_2} = amplitude ratios
r_{b_i}, r_{c_i} = distances of mass center m_i from the reference axis in beamwise and chordwise directions
t = time
T = kinetic energy of the rotating turbine blade
V = potential energy of the rotating turbine blade
W_{nc} = work done on system by nonconservative forces
x_i = distance of ith mass station from the z axis
x, y, z = coordinate axes, coordinates of mass center m_i
y_i, z_i = displacements of ith mass station in y and z directions
$Y_i^{(j)}, Z_i^{(j)}$ = ith components of jth chordwise and jth beamwise deflection vectors
Ω = blade angular velocity
ω_f = frequency of the exciting forces and moments
$\omega_{(i)}$ = ith natural frequency of the linearized rotating turbine blade
ω = nonlinear natural frequency of the linearized rotating turbine blade
θ_i = angle of pretwist at the ith mass station
ϕ_i, β_i, ψ_i = angular displacements of the ith section in the directions of the negative x, negative y, and positive z axes
$\Phi_{x_i}^{(j)}, \Phi_{y_i}^{(j)}, \Phi_{z_i}^{(j)}$ = ith components of the jth torsional displacement vector, the jth beamwise slope vector, and the jth chordwise slope vector
$\tilde{\phi}$ = stationary functional

Subscripts and Superscripts

$\bar{}$ = average value taken over a cycle
$\dot{}$ = differentiation with respect to time
t = tip of blade model

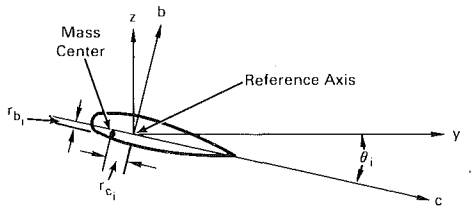

Fig. 3 Blade cross section at *i*th mass station

typical blade cross section in which the b and c axes are parallel to the section principal axes.

An important consideration relative to modeling of turbine blades is the number of segments to be taken for a particular application. This depends upon the number of natural modes needed. Calculations indicate that a total of six stations for the first natural mode and four more for each additional mode are adequate from the standpoint of accurate mathematical representation. However, even with a large number of segments, accuracy cannot be guaranteed in situations where the effects of shear deformation and rotatory inertia are ignored. This is especially true when natural modes of vibration higher than the fundamental are desired.

Method of Analysis

The nonuniform rotating turbine blade mathematically modeled as above is a nonlinear n-degree of freedom discrete system whose behavior is governed by differential equations of the form

$$F_i[D;\, x_1(t),\, x_2(t),\, \ldots\, x_n(t);\, t] = 0 \qquad (i = 1,\, 2,\, \ldots\, ,n) \tag{1}$$

where $D = d/dt$, t is the independent variable and the x are system coordinates such as blade displacements and slopes. Under the assumption that blade displacement amplitudes are only moderately large and any deviation from the vibratory modes of the linearized blade is therefore small, the technique of analysis used involves considering an approximate harmonic solution to equation (1) in the form

$$x_i(t) = \sum_{j=1}^{n} A_i^{(j)} B_j^* \sin j\omega t \qquad (i = 1,\, 2,\, \ldots\, ,n) \tag{2}$$

where $A_i^{(j)}$ represents the ith component of the jth normal mode corresponding to the linearized system and the B_j^* are arbitrary parameters to be determined as functions of the nonlinear natural frequency ω. The assumed solution is then substituted into a functional $\bar{\phi}$ and a system of n algebraic equations in $B_i{}^*$ is obtained by setting

$$\partial\bar{\phi}/\partial B_i^* = 0 \qquad (i = 1,\, 2,\, \ldots\, ,n) \tag{3}$$

This system of equations is solved for $B_i{}^*$, determining the assumed approximate solution completely. An advantage with this approach is that the functions selected need not satisfy all the boundary conditions of the problem.

Consider the functional

$$\bar{\mathrm{L}}_E = \int_{t_1}^{t_2} \mathrm{L}_E\, dt = \int_{t_1}^{t_2} (\mathrm{L} + W_{nc})\, dt \tag{4}$$

where L is the Lagrangian function and W_{nc} denotes the work done by the nonconservative forces acting on the blade such as time-dependent exciting forces, damping/friction forces, etc. By the extended Hamilton's principle, $\bar{\mathrm{L}}_E$ is stationary for a motion satisfying Newton's laws, assuming that the system is holonomic. Thus,

$$\delta \int_{t_1}^{t_2} \mathrm{L}_E\, dt = 0 \tag{5}$$

The stationary value is actually a minimum and can be used as the stationary functional $\bar{\phi}$. Equation (3) now yields

$$\partial\bar{\mathrm{L}}/\partial B_i{}^* = -\bar{Q}_i \qquad (i = 1,2,\, \ldots\, ,n) \tag{6}$$

where $\bar{Q}_i$ is the average nonconservative generalized force corresponding to the generalized coordinate $B_i{}^*$ and $\bar{\mathrm{L}}$ is the average Lagrangian.

Another functional, among others, satisfying equation (6) is the "dynamic" Reissner functional

$$\mathrm{L}_R = T - J_R \tag{7}$$

where J_R is the Reissner functional as defined in [13, 14]. For a discrete turbine blade such as the one employed in this work however, the system potential energy V would be much easier to obtain than the Reissner functional J_R since the former can be readily generated in terms of the linear system natural frequencies and mode shapes which can be easily determined with the help of the many sophisticated linear blade vibration computer programs available in most organizations that must deal with rotating blades. In any event, whether V is used or J_R, this approach presents a significant attraction in that good results can be achieved even with a small number of terms in the series of equation (2).

Problem Formulation and Analysis

Including the contribution due to the centrifugal force field, the total potential energy of the rotating turbine blade is

$$V = \frac{1}{2} \sum_{j=1}^{N=5n_s} \omega_{(j)}^2 M_{(j)} B_j{}^{*2} \sin^2 j\omega t \tag{8}$$

where $\omega_{(j)}$ represents the jth natural frequency of the linear rotating blade, and

$$\begin{aligned} M_{(j)} = \sum_{i=1}^{n_s} & [m_i Y_i^{(j)2} + m_i Z_i^{(j)2} + (m_i (r_{y_i}^2 + r_{z_i}^2) + A_i)\Phi_{x_i}^{(j)2} \\ & + (B_i \sin^2\theta_i + C_i \cos^2\theta_i)\Phi_{z_i}^{(j)2} \\ & + (B_i \cos^2\theta_i + C_i \sin^2\theta_i)\Phi_{y_i}^{(j)2} \\ & + 2m_i r_{z_i} Y_i^{(j)} \Phi_{x_i}^{(j)} + 2m_i r_{y_i} Z_i^{(j)} \Phi_{x_i}^{(j)} \\ & + 2(B_i - C_i) \sin\theta_i \cos\theta_i \Phi_{z_i}^{(j)} \Phi_{y_i}^{(j)}] \end{aligned} \tag{9}$$

is the associated generalized mass. Here, $Y_i^{(j)}$ is the ith component of the jth chordwise deflection vector $\{Y\}^{(j)}$ for the linear rotating blade, $Z_i^{(j)}$ is the ith component of the jth beamwise deflection vector $\{Z\}^{(j)}$, $\Phi_{x_i}^{(j)}$ is the ith component of the jth torsional displacement vector $\{\Phi_x\}^{(j)}$, $\Phi_{y_i}^{(j)}$ is the ith component of the jth beamwise slope vector $\{\Phi_y\}^{(j)}$, and $\Phi_{z_i}^{(j)}$ is the ith component of the jth chordwise slope vector $\{\Phi_z\}^{(j)}$.

Since the potential energy of equation (8) is computed using the normal modes of the linear system, the contribution of the centrifugal force field acting on the blade is included in it. Therefore, this effect must be removed from the total kinetic energy of the turbine blade if a Lagrangian formulation is to be employed. However, all the nonlinear coupling terms due to rotation must be retained since the effect of these nonlinearities is to be investigated. The resulting expression for the turbine blade kinetic energy can be shown to be

$$T = \frac{1}{2} \sum_{i=1}^{n_s} \Big[m_i \Big\{ 2\Omega y_i \sum_{j=i+1}^{n_s} \bar{l}_j (\psi_j \dot{\psi}_j + \beta_j \dot{\beta}_j) - 2\Omega r_{y_i} \sum_{j=i+1}^{n_s}$$

$$\bar{l}_j (\psi_j \dot{\psi}_j + \beta_j \dot{\beta}_j) + 2\Omega r_{z_i} \phi_i \sum_{j=i+1}^{n_s} \bar{l}_j (\psi_j \dot{\psi}_j + \beta_j \dot{\beta}_j)$$

$$+\dot{y}_i^2+r_{z_i}^2\dot{\phi}_i^2+2\dot{y}_i r_{z_i}\dot{\phi}_i+2\Omega r_{z_i}x_i\dot{\phi}_i-\Omega r_{z_i}\dot{\phi}_i\sum_{j=i+1}^{n_s}\bar{l}_j(\psi_j^2+\beta_j^2)+2\Omega x_i\dot{y}_i-\Omega\dot{y}_i\sum_{j=i+1}^{n_s}\bar{l}_j(\psi_j^2+\beta_j^2)+\dot{z}_i^2+2r_{y_i}\dot{\phi}_i\dot{z}_i+r_{y_i}^2\dot{\phi}_i^2\Big\}+A_i(\dot{\phi}_i^2-2\Omega\beta_i\dot{\phi}_i)+B_i(\dot{\psi}_i^2\sin^2\theta_i+\dot{\beta}_i^2\cos^2\theta_i+2\Omega\dot{\psi}_i\sin^2\theta_i+2\Omega\phi_i\dot{\psi}_i\sin\theta_i\cos\theta_i+2\dot{\psi}_i\dot{\beta}_i\sin\theta_i\cos\theta_i+2\Omega\dot{\beta}_i\sin\theta_i\cos\theta_i+2\Omega\dot{\beta}_i\phi_i\cos^2\theta_i)+C_i(\dot{\psi}_i^2\cos^2\theta_i+\dot{\beta}_i^2\sin^2\theta_i+2\Omega\dot{\psi}_i\cos^2\theta_i-2\Omega\phi_i\dot{\psi}_i\sin\theta_i\cos\theta_i-2\dot{\beta}_i\dot{\psi}_i\cos\theta_i\sin\theta_i-2\Omega\dot{\beta}_i\sin\theta_i\cos\theta_i+2\Omega\dot{\beta}_i\phi_i\sin^2\theta_i)\Big] \tag{10}$$

where ϕ_i, β_i, and ψ_i are the angular displacements of the ith blade section in the directions of the negative x, negative y, and positive z axes at the ith mass station, A_i, B_i, and C_i are its principal moments of inertia about orthogonal axes at its mass center, n_s denotes the total number of mass stations on the blade, and r_{y_i} and r_{z_i} are defined by

$$\left.\begin{aligned} r_{y_i}&=r_{c_i}\cos\theta_i+r_{b_i}\sin\theta_i\\ r_{z_i}&=r_{c_i}\sin\theta_i-r_{b_i}\cos\theta_i\end{aligned}\right\} \tag{11}$$

Free Vibrations. Using only two terms for algebraic simplicity, turbine blade displacements can now be written down in terms of the arbitrary parameters B_j^* and the linear normal modes as follows

$$y_i=\sum_{j=1}^{2}Y_i^{(j)}B_j^*\sin j\omega t,\qquad z_i=\sum_{j=1}^{2}Z_i^{(j)}B_j^*\sin j\omega t,$$

$$\phi_i=\sum_{j=1}^{2}\Phi_{x_i}^{(j)}B_j^*\sin j\omega t,\qquad \psi_i=\sum_{j=1}^{2}\Phi_{z_i}^{(j)}B_j^*\sin j\omega t, \tag{12}$$

$$\beta_i=\sum_{j=1}^{2}\Phi_{y_i}^{(j)}B_j^*\sin j\omega t$$

With the averaging done over one period, equation (6) will yield algebraic relationships for the first and second harmonics B_1^* and B_2^* in terms of the nonlinear frequency ω, the rotational speed Ω, and other blade parameters in the fundamental nonlinear mode.

Forced Vibrations. There are various forms [15] of blade excitation in a turbojet engine such as transmission of vibration through the fixings, fixed wake excitation, rotating stall cell excitation, and random type of excitation. Since any excitation $F(t)$ can, in general, be broken up into a Fourier series of sine and cosine functions with fundamental period 2Π as follows

$$F(t)=F_0+\sum_{n=1}^{\infty}F_{nc}\cos\omega_f t+\sum_{n=1}^{\infty}F_{ns}\sin n\omega_f t \tag{13}$$

where the coefficients F_{nc} and F_{ns} can be determined from

$$F_{nc}=\frac{\omega_f}{\Pi}\int_{-\Pi/\omega_f}^{\Pi/\omega_f}F(t)\cos n\omega_f t\,dt$$

$$F_{ns}=\frac{\omega_f}{\Pi}\int_{-\Pi/\omega_f}^{\Pi/\omega_f}F(t)\sin n\omega_f t\,dt \tag{14}$$

a simple, yet representative, forced vibration problem will be formulated that is not too cumbersome algebraically with the following force and moment combination acting at the tip of the mathematical model: a force $F_y\sin\omega_f t$ in the positive y direction, a force $F_z\sin\omega_f t$ in the positive z direction, a twisting moment $M_x\sin\omega_f t$ in the negative x direction, a bending moment $M_y\sin\omega_f t$ in the negative y direction, and a bending moment $M_z\sin\omega_f t$ in the positive z direction.

A steady-state solution can be considered in the form of equations (12) in which ω is now replaced by the frequency ω_f of the exciting forces and moments. With the assumed excitation, the average power taken over a cycle would be

$$\bar{P}=\int_0^{2\Pi/\omega_f}\{F_y\delta\dot{y}_t+F_z\delta\dot{z}_t+M_x\delta\dot{\phi}_t+M_y\delta\dot{\beta}_t+M_z\delta\dot{\psi}_t\}\sin\omega_f t\,dt \tag{15}$$

where subscript t refers to the blade tip. Equating the expression resulting from this to $\sum_{i=1}^{2}\bar{Q}_i\,\delta\,\dot{B}_i^*$, the average nonconservative generalized forces $\bar{Q}_1$ and $\bar{Q}_2$ associated with B_1^* and B_2^*, respectively, can be derived. Substitution of these generalized forces into equation (6) will lead to two nonlinear algebraic relationships between the frequency ratio $r_f\ (=\omega_f/\omega_{(1)})$ and the amplitude ratios $r_{a1}=[B_1^*/B_{1st}^*]$ and $r_{a2}=[B_2^*/B_{1st}^*]$. These will provide the nonlinear response of the turbine blade in its fundamental nonlinear mode. Here, B_{1st}^* is the blade static deflection obtained by setting $\omega_f=0$ in equation (6) for $i=1$.

Assessment of Higher Nonlinear Modes

Since, according to Rosenberg's theory [16], an infinite number of vibration modes are possible in nonlinear problems, it should be useful to investigate modes higher than the fundamental. If the first and second normal modes are replaced by the pth and $(p+1)$th normal modes respectively, the pth nonlinear mode is obtained. Thus, by a mere interchange of linear normal modes, nonlinear modes higher than the fundamental can be readily generated and assessed. With this advantage made available with blade discretization, turbine blade dynamic behavior in the vicinity of the linear resonant frequencies can be predicted and evaluated quite elaborately.

Numerical Results and Discussion

The numerical example attempted is that of a short and stubby turbine blade 9 cm long mounted on a disk of radius 26 cm. The blade is made of steel and its mean cross-sectional area and cross-sectional moment of inertia are 0.8 cm^2 and 0.06 cm^4 respectively. The blade is represented by seven mass stations and six sections and vibration is restricted to the plane of rotation with 2000N as the amplitude of the harmonic exciting force. The mathematical model data used to generate

Table 1 Mathematical model data for blade

Field	Masses (kg)	Rotatory inertias (10^6 kg-m^2)	Field length (cm)	x_i (cm)
1	0.009842	0.0714284	1.52	34.80
2	0.009842	0.0714284	1.52	33.27
3	0.009842	0.0714284	1.52	31.75
4	0.009842	0.0714284	1.52	30.23
5	0.009842	0.0714284	1.55	28.70
6	0.0101574	0.0728380	0.79	27.15
7	0	0.0371240	–	26.37

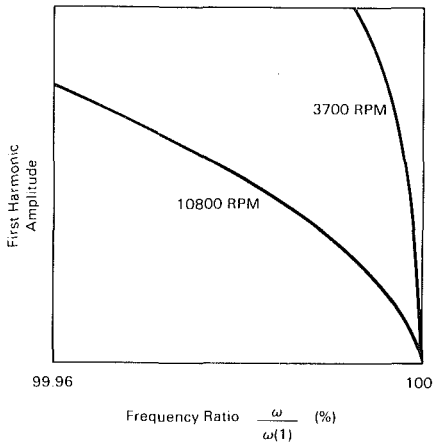

Fig. 4 Variation of natural frequency with first harmonic amplitude in fundamental nonlinear mode

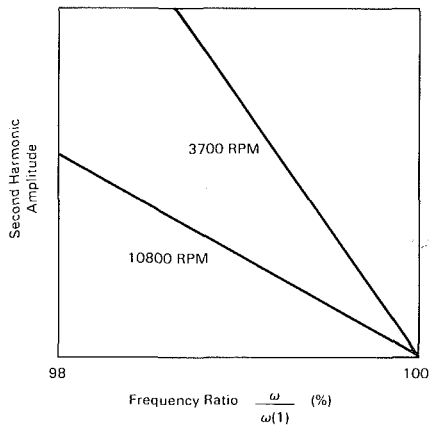

Fig. 5 Variation of natural frequency with second harmonic amplitude in fundamental nonlinear mode

the numerical results are given in Table 1. Nonlinear vibration modes are obtained for two speeds of rotation, namely 3700 rpm and 10,800 rpm, by the technique presented, utilizing normal modes and linear natural frequencies computed by the Myklestad method [17–20]. The results generated are shown in Figs. 4–7.

The nonlinear frequency versus amplitude curves for this problem are shown in Figs. 4 and 5. While the free vibration curve for the linearized blade will be a straight line, the curves sketched indicate that the amplitudes B_1^* and B_2^* become rather large when the nonlinear frequency is different from the fundamental natural frequency of the linearized system. Also, since the amplitudes decrease with the frequency, the nonlinearities have the same effect as that of a soft spring in free vibration.

The response curves plotted in Figs. 6 and 7 show linear system response and first and second harmonics in the fundamental and second nonlinear modes. Regions of instability are marked. From these curves, the following effects are noted: (1) The form of the first-harmonic curves in both modes is essentially similar to that of the linearized system with small damping. However, the curves bend over to the right as in the case of a hard-spring Duffing system in which the spring becomes stiffer with increasing amplitudes. (2) Amplitudes at resonance which are infinitely large in the case of the linearized system with no damping have been curtailed by the presence of the nonlinearities. The rounding off of the resonance peaks is due to the velocity-dependent terms in the differential equations of motion of the problem. In the vicinity of the linear natural frequency, the effect of these terms has been the same as that of the presence of damping on

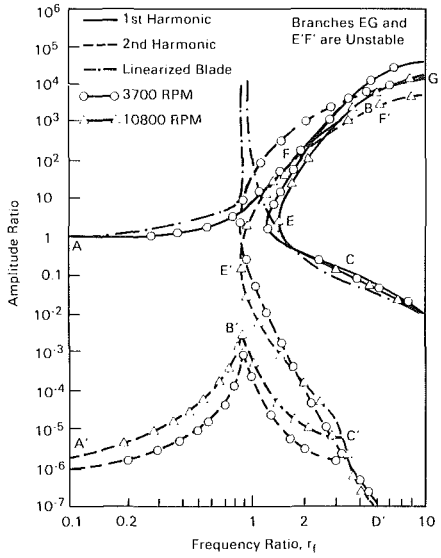

Fig. 6 Blade response in first nonlinear mode

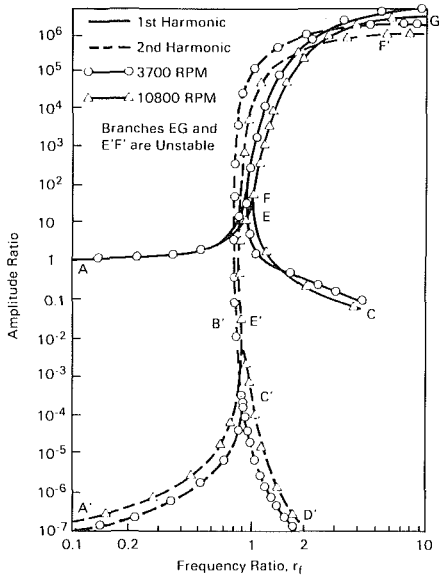

Fig. 7 Blade response in second nonlinear mode

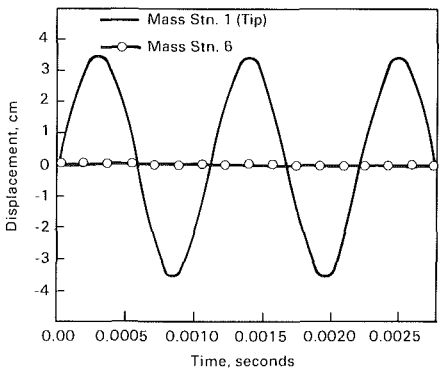

Fig. 8 Time history of blade displacements

linear system response. This is to be expected and only reasonable since some damping will always be present in any physical system. (3) The first harmonic becomes more nonlinear with increase in rotational speed. (4) The small amplitudes of the second harmonic for $r_f < 1$ may be attributed to the nonlinear terms which have had an effect

similar to that of small damping on the amplitudes of superharmonic vibration of a nonlinear system.

A blade displacement time history is presented in Fig. 8 for the case where the driving frequncy is equal to the fundamental natural frequency of the linearized system. The extremum blade tip displacements, which, for the linearized system, would normally be very large in real life and infinite in theory, are, in this case, only a fraction of the blade length. It is known that in a nonlinear system, a response is possible at a frequency other than the driving frequency. In general, a component of considerable magnitude will occur at a frequency near the linear resonant frequency although other additional components at multiples as well as submultiples of the linear resonant frequency may also be present. However, when the driving frequency is the same as the linear fundamental frequency, the first harmonic normally tends to dominate. This is confirmed by Fig. 8.

Concluding Remarks

The nonlinear problem of a rotating, tapered-twisted turbine blade of asymmetric airfoil cross section undergoing coupled bending-bending-torsion-type vibrations has been attempted. Numerical results for a short and stubby steel blade have been generated which include the effects of Coriolis forces as well as shear deformation and rotatory inertia. Advantages afforded with discretization are: (1) Accurate modeling of real blades can be obtained. (2) Shear deformation and rotatory inertia effects can be included with ease. (3) Nonlinear modes other than the fundamental can be generated and evaluated. The analysis results indicate that the nonlinearity due to Coriolis forces in combination with the shear deformation and rotatory inertia terms is significant at the high rotational speeds that turbine blades are subjected to and should not therefore be ignored. The analysis presented suggests a viable means of handling the problem.

Recommendations for Further Study

The following ideas may constitute additional contributions to the general problem of turbine blade vibration: (1) Relax the restriction of an inextensional motion of the mass center axis. (2) Consider end conditions other than cantilevered. (3) Investigate the effect of a nonlinear stress-strain curve for the material of the blade. (4) Since turbine blades have a low aspect ratio, it should be interesting to solve the nonlinear problem by modeling the blade as a rotating cantilevered plate using finite elements. Comparisons with present work should be of use.

Acknowledgments

The author wishes to acknowledge the support provided by the University of Petroleum and Minerals, Dhahran, Saudi Arabia. Thanks are due to Mr. Najeeb Ullah Khan for his help with the computations, to Mr. Syed I. Jameel for his accurate typing of the original manuscript, and to Judy Jech for putting the revised version on the word processor. Finally, the support provided by Battelle Pacific Northwest Laboratories, Richland, Washington for completion of the revision of this paper is also gratefully acknowledged.

References

1 Krupka, R. M., and Baumanis, A. M., "Bending-Bending Mode of a Rotating Tapered-Twisted Turbomachine Blade Including Rotatory Inertia and Shear Deformation," ASME Paper No. 69-Vibr-50.

2 Bogdanoff, J. L., "Influence of Secondary Inertia Terms on Natural Frequencies of Rotating Beams," *Journal of Applied Mechanics*, Vol. 22, Dec. 1955, pp. 587–591.

3 Lo, H., and Renbarger, J. L., "Bending Vibrations of a Rotating Beam," *First U.S. National Congress of Applied Mechanics*, pp. 75–79.

4 Lo, H., "A Nonlinear Problem in the Bending Vibration of a Rotating Beam," *Journal of Applied Mechanics*, Vol. 19, Dec. 1952, pp. 461–464.

5 Dokainish, M. A., and Rawtani, S., "Vibration Analysis of Rotating Cantilever Plates," *International Journal for Numerical Methods in Engineering*, Vol. 3, 1971, pp. 233–248.

6 Lalanne, M., et al., "Rotating Blade Analysis by the Finite Element Method," *Proceedings of the Symposium of International Union of Theoretical and Applied Mechanics*, Lyngby, Denmark, Aug. 1974, pp. 299–318.

7 Trompette, P., and Lalanne, M., "Vibration Analysis of Rotating Turbine Blades," ASME Paper No. 74-WA/DE-23.

8 Carnegie, W., "The Application of the Variational Method to Derive the Equations of Motion of Vibrating Cantilever Blading Under Rotation," *Bulletin of Mechanical Engineering Education*, Vol. 6, 1967, pp. 29–38.

9 Rao, J. S., and Carnegie, W., "Nonlinear Vibrations of Rotating Cantilever Beams," *Aeronautical Journal*, Vol. 74, Feb. 1970, pp. 161–165.

10 Fu, C. C., "Computer Analysis of a Rotating Axial Turbomachine Blade in Coupled Bending-Bending-Torsion Vibrations," *International Journal for Numerical Methods in Engineering*, Vol. 8, 1974, pp. 569–588.

11 Swaminathan, M., and Rao, J. S., "Vibrations of Rotating, Pretwisted and Tapered Blades," *Mechanism and Machine Theory*, Vol. 12, 1977, pp. 331–337.

12 Downs, B., "Vibration Analysis of Turbomachinery Blades Using Dedicated Discretization and Twisted Beam Theory," ASME *Journal of Mechanical Design*, Vol. 102, July 1980, pp. 574–578.

13 Fung, Y. C., *Foundations of Solid Mechanics*, Prentice-Hall, NJ, 1965, Chap. 10, pp. 299–300.

14 Zienciewicz, O. C., *The Finite Element Method*, McGraw-Hill, United Kingdom, 1977, Chap. 12, pp. 304–312.

15 Dokainish, M. A., and Jagannath, D. V., "Experimental Investigation of Gas Turbine Blade Vibrations—A Review," ASME Paper No. 69-Vibr-59.

16 Rosenberg, R. M., "The Normal Modes of Nonlinear *n*-Degree of Freedom Systems," *Journal of Applied Mechanics*, Vol. 7, 1962, pp. 7–14.

17 Myklestad, N. O., "Vibrations Involving Bending," unpublished class notes, University of Texas, Arlington, TX, Chap. 10.

18 Meirovitch, L., *Analytical Methods in Vibrations*, Macmillan, New York, 1967, Chap. 6, pp. 257–262.

19 Myklestad, N. O., *Vibration Analysis*, McGraw-Hill, New York, 1956, Chap. 8, pp. 239–247.

20 Thomson, W. T., *Theory of Vibration With Applications*, 2nd ed., Prentice-Hall, Englewood Cliffs, NJ, 1981, Chap. 10, pp. 304–316.

An Iwatsubo-Based Solution for Labyrinth Seals: Comparison to Experimental Results[1]

D. W. Childs
Professor of Mechanical Engineering.

J. K. Scharrer
AFRAPT Graduate Research Trainee.

Texas A&M University,
College Station, TX 77843

The basic equations are derived for compressible flow in a labyrinth seal. The flow is assumed to be completely turbulent in the circumferential direction where the friction factor is determined by the Blasius relation. Linearized zeroth and first-order perturbation equations are developed for small motion about a centered position by an expansion in the eccentricity ratio. The zeroth-order pressure distribution is found by satisfying the leakage equation while the circumferential velocity distribution is determined by satisfying the momentum equation. The first-order equations are solved by a separation of variable solution. Integration of the resultant pressure distribution along and around the seal defines the reaction force developed by the seal and the corresponding dynamic coefficients. The results of this analysis are compared to published test results.

Introduction

The problem of self-excited vibration in turbomachinery due to labyrinth seals has led to the development of many analyses which attempt to model the physical phenomenon so that the problem can be better understood and therefore solved. The shortcoming with the analyses which have been presented to date is that they are difficult to understand and require limiting assumptions such as ignoring the area derivative in the circumferential direction, assuming that the friction factor is the same for all surfaces, and assuming that the flow coefficient is constant along the seal. These assumptions may be of some use mathematically, but do very little for the understanding of the physical occurrence. The first steps toward analysis of this problem were taken by Alford [1], who neglected circumferential flow, and Spürk et al. [2], who neglected rotation of the shaft. Vance and Murphy [3] extended the Alford analysis by introducing a more realistic assumption of choked flow. Kostyuk [4] performed the first comprehensive analysis, but failed to include the change in area due to eccentricity which is responsible for the relationship between cross-coupled forces and parallel rotor displacements. Iwatsubo [5, 6] refined the Kostyuk model by including the time dependency of area change, but he neglected the area derivative in the circumferential direction. Kurohashi [7] incorporated dependency of the flow coefficient on eccentricity into his analysis, but assumed that the circumferential velocity in each cavity was the same.

The analysis presented here includes the variation of the area in the circumferential direction due to eccentricity and incorporates as many of the physical phenomena in the flow field as was thought necessary to produce an adequate result.

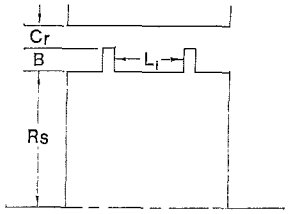

Fig. 1 A typical cavity

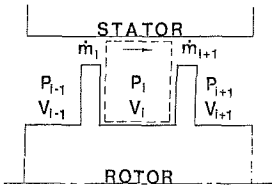

Fig. 2 Cavity control volume

The main purpose of this paper is to present a unified and comprehensive derivation of a reduced set of equations and a new solution format for those equations. The results of this analysis are compared with the published test results of Wachter and Benckert [8, 9, 10].

Procedure

The analysis presented here is developed for the see-through type of labyrinth seal shown in Fig. 1. The continuity and momentum equations will be derived for a single cavity control volume as shown in Figs. 2, 3, 4, and 5. A leakage model will be employed to account for the axial leakage. The governing equations will be linearized using perturbation analysis for small motion about a centered position. The zero-th-order continuity and momentum equations will be solved to determine the steady-state pressure and velocity for each cavity. The first-order continuity and momentum equations will be reduced to linearly independent algebraic

[1] The results reported herein were partially supported by AFOSR Contract F49620-82-K-0033 from Bolling Air Force Base.

Contributed by the Gas Turbine Division of THE AMERICAN SOCIETY OF MECHANICAL ENGINEERS and presented at the 30th International Gas Turbine Conference and Exhibit, Houston, Texas, March 18-21, 1985. Manuscript received at ASME Headquarters, January 7, 1985. Paper No. 85-GT-136.

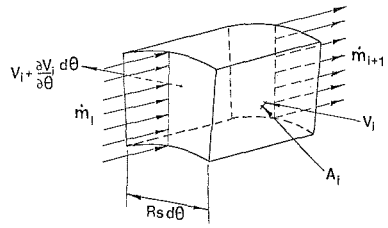

Fig. 3 Cavity control volume

equations by assuming an elliptical orbit for the shaft and a corresponding harmonic response for the pressure and velocity perturbations. The force and force coefficients for the seal are found by integration of the first-order pressure perturbation along and around the shaft.

Assumptions

1 Fluid is considered to be an ideal gas.

2 Pressure variations within a chamber are small compared to the pressure difference across a seal strip.

3 The frequency of acoustic resonance in the cavity is much higher than that of the rotor speed.

4 Added mass terms are neglected.

5 The eccentricity of the rotor is small compared to the radial seal clearance.

6 In the determination of the shear stresses in the circumferential direction, the axial component of velocity is neglected.

7 The contribution of shear stress to the stiffness and damping coefficients is neglected.

8 Constant temperature.

Governing Equations

Continuity Equation. Referring to the control volume in Figs. 2 and 3, the continuity equation for the control volume shown is:

$$\frac{\partial}{\partial t}(\rho_i A_i) + \frac{\partial}{\partial \theta}\left(\frac{\rho_i V_i A_i}{Rs}\right) + \dot{m}_{i+1} - \dot{m}_i = 0 \qquad (1)$$

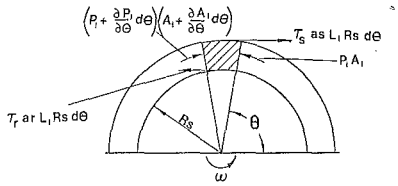

Fig. 4 Forces on control volume

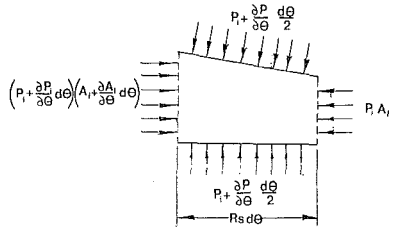

Fig. 5 Forces on control volume

where the transverse surface area A_i is defined by;

$$A_i = (B_i + H_i + B_{i+1} + H_{i+1}) L_i / 2 \qquad (1.a)$$

Momentum Equation. The momentum equation (2) is derived using Figs. 4 and 5 which show the pressure forces and shear stresses acting on the control volume. This equation includes the area derivative in the circumferential direction, which was neglected by Iwatsubo [5, 6].

$$\frac{\partial \rho V_i A_i}{\partial t} + \frac{2\rho V_i A_i}{Rs}\frac{\partial V_i}{\partial \theta} + \frac{\rho V_i^2}{Rs}\frac{\partial A_i}{\partial \theta} + \frac{V_i A_i}{Rs}\frac{\partial \rho}{\partial \theta}$$

$$+ \dot{m}_{i+1} V_i - \dot{m}_i V_{i-1} = -\frac{A_i}{Rs}\frac{\partial P_i}{\partial \theta} + \tau_{ri} ar_i L_i - \tau_{si} as_i L_i \qquad (2)$$

where ar and as are the dimensionless length upon which the shear stresses act and are defined for teeth on rotor by

$$as_i = 1 \quad ar_i = (2B_i + L_i)/L_i,$$

and for teeth on the stator by

Nomenclature

A_i = cross-sectional area of the cavity ($L^{**}2$); defined in equation (1.a)
B_i = height of labyrinth seal strip (L); defined in Fig. 1
C = direct damping coefficient (Ft/L)
Cr = nominal radial clearance (L); defined in Fig. 1
D_h = hydraulic diameter of cavity (L); introduced in equation (3)
H = local radial clearance (L)
K = direct stiffness coefficient (F/L)
L = pitch of seal strips (L); defined in Fig. 1
NT = number of seal strips
$NC = NT - 1$ = number of cavities
P = pressure ($F/L^{**}2$)
R = gas constant
Rs = radius of seal (L); defined in Fig. 1
T = temperature (T)
$Rs\omega$ = surface velocity of rotor (L/t)
V_i = average velocity of flow in circumferential direction (L/t)
a,b = radial seal displacement components due to elliptical whirl (L); defined in equation (13)
ar = dimensionless length upon which shear stress acts on rotor
as = dimensionless length upon which shear stress acts on stator
c = cross-coupled damping coefficient (Ft/L); in equation (18)
k = cross-coupled stiffness coefficient (F/L); in equation (18)
$\dot{m}$ = leakage mass flow rate per circumferential length (M/Lt)
mr, nr, ms, ns = coefficients for Blasius relation for friction factor; defined in equation (3)
t = time (t)
ω = shaft angular velocity ($1/t$)
ρ = density of fluid ($M/L^{**}3$)
ν = kinematic viscosity ($L^{**}2/t$)
ϵ = e/Cr = eccentricity ratio
γ = ratio of specific heats
π = 3.141592
K_Q^* = dimensionless cross-coupled stiffness parameter; defined in equations (27)
E_0^* = dimensionless entry swirl parameter; defined in equations (27)

Subscripts

0 = zeroth-order component
i = i-th chamber value
1 = first-order component
x = X-direction
y = Y-direction
r = reservoir value
s = sump value

$$as_i = (2B_i + L_i)/L_i \quad ar_i = 1$$

Blasius [11] determined that the shear stresses for turbulent flow in a smooth pipe could be written as

$$\tau = \frac{1}{2}\rho U_m^2 \, no \left(\frac{UmDh}{\nu}\right)^{mo}$$

where Um is the mean flow velocity relative to the surface upon which the shear stress is acting. The constants mo and no can be empiricallly determined for a given surface from pressure flow experiments. However, for smooth surfaces the coefficients given by Yamada [12] for turbulent flow between annular surfaces are:

$$mo = -0.25 \quad no = 0.079$$

Applying Blasius' equation to the labyrinth rotor and stator surfaces yields the following definitions for the rotor and stator shear stresses

$$\tau_{ri} = \frac{\rho_i}{2}(R\omega - V_i)^2 \, nr \left[\frac{|R\omega - V_i| Dh_i}{\nu}\right]^{mr} sgn(R\omega - V_i)$$

$$\tau_{si} = \rho_i \frac{V_i^2}{2} ns \left[\frac{|V_i| Dh_i}{\nu}\right]^{ms} sgn(V_i) \tag{3}$$

where Dh_i is the hydraulic diameter defined by

$$Dh_i = \frac{2(H_i + B_i)L_i}{(H_i + B_i + L_i)} \tag{4}$$

Separate parameters (ms, ns), (mr, nr) for the stator and rotor, respectively, account for different rotor and stator roughnesses.

If equation (1) times the circumferential velocity is now subtracted from equation (2), the following reduced form of the momentum equation is obtained:

$$\rho_i A_i \frac{\partial V_i}{\partial t} + \rho_i V_i A_i \frac{\partial V_i}{Rs\partial\theta} + \dot{m}_i (V_i - V_{i-1})$$

$$= \frac{-A_i}{Rs}\frac{\partial P_i}{\partial\theta} - \tau_{si}\, as_i L_i + \tau_{ri} ar_i L_i \tag{5}$$

In order to reduce the numbers of variables, all of the density terms are replaced with pressure terms using the ideal gas law.

$$P_i = \rho_i RT \tag{6}$$

Furthermore, in order to make the perturbation analysis easier, the following substitution is made in the continuity equation:

$$\dot{m}_{i+1} - \dot{m}_i = \frac{\dot{m}_{i+1}^2 - \dot{m}_i^2}{2\dot{m}_0}$$

where $\dot{m}_0$ is the steady-state mass flow rate.

Leakage Equation. To account for the leakage mass flow rate in the continuity and momentum equations, the leakage model of Neumann [13] was chosen. This model predicts leakage and pressures fairly accurately and has a term to account for kinetic-energy carryover. However, the empirical flow coefficient relations given by Neumann were discarded in favor of the equations of Chaplygin [14] for flow through an orifice. This was done to produce a different flow coefficient for succeeding contractions along the seal as has been shown to be the case by Egli [15]. The form of the model is:

$$\dot{m}_i = \mu_{1i}\mu_2 H_i \sqrt{\frac{P_{i-1}^2 - P_i^2}{RT}} \tag{7}$$

where the kinetic-energy carryover coefficient μ_2 is defined for straight through seals as:

$$\mu_2 = \sqrt{\frac{NT}{(1-j)NT + j}}$$

where

$$j = 1 - (1 + 16.6Cr/L)^{-2}$$

and is unity, by definition, for interlocking and combination groove seals. The flow coefficient is defined as:

$$\mu_{li} = \frac{\pi}{\pi + 2 - 5s_i + 2s_i^2} \quad \text{where } s_i = \left(\frac{P_{i-1}}{P_i}\right)^{\frac{\gamma-1}{\gamma}} - 1$$

For choked flow, Fliegner's formula [16] will be used for the last seal strip. It is of the form:

$$\dot{m}_{NC} = \frac{0.510\mu_2}{\sqrt{RT}} P_{NC} H_{NT} \tag{8}$$

Perturbation Analysis

For cavity i, the continuity equation (1), momentum equation (5), and leakage equation (7) are the governing equations for the variables V_i, P_i, m_i. A perturbation analysis of these equations is to be developed with the eccentricity ratio, $\epsilon = e/Cr$, selected to be the perturbation parameter. The governing equations are expanded in the perturbation variables

$$P_i = P_{0i} + \epsilon P_{1i} \qquad H_i = Cr_i + \epsilon H_1$$

$$V_i = V_{0i} + \epsilon V_{1i} \qquad A_i = A_0 + \epsilon K H_i$$

where $\epsilon = e/Cr$ is the eccentricity ratio. The zeroth-order equations define the leakage mass flow rate and the circumferential velocity distribution for a centered position. The first-order equations define the perturbations in pressure and circumferential velocity due to a radial position perturbation of the rotor. Strictly speaking, the results are only valid for small motion about a centered position.

Zeroth-Order Solution. The zeroth-order leakage equation is

$$\dot{m}_{i+1} = \dot{m}_i = \dot{m}_0 \tag{9}$$

and is used to determine both the leakage rate m_0 and pressure distribution for a centered position. The leakage rate is determined using either equation (7) or equation (8), depending on the operating conditions. To determine whether the flow is choked or not, assume that the pressure in the last cavity is equal to the critical pressure for choking. Using this pressure, find the leakage from equation (8) and then use equation (7) to determine the reservoir pressure necessary to produce this condition. Based on this pressure, a determination can be made whether the flow is choked or not. The associated pressure distribution is determined by employing the calculated leakage, along with a known boundary pressure, and solving equation (7) sequentially for each cavity pressure P_{0i}.

The zeroth-order circumferential-momentum equation is

$$m_0 (V_{0i} - V_{0i-1}) = (\tau_{ri0} ar_i - \tau_{si0} as_i) L_i;$$
$$i = 1, 2, \ldots NC, \tag{10}$$

From calculated pressures, the densities can be calculated at each cavity from equation (6), and the only unknowns remaining in equation (10) are the circumferential velocities V_{0i}. Given an inlet tangential velocity, a Newton-root-finding approach can be used to solve equation (10) for the i-th velocity, one cavity at a time. This is done starting at the first cavity and working downstream.

First-Order Solution. The governing first-order equations (11, 12) define the pressure and velocity fluctuations resulting from the seal clearance function. The continuity equation (11) and momentum equation (12) follow:

$$G_{1i}\frac{\partial P_{1i}}{\partial t} + G_{1i}\frac{V_{0i}}{Rs}\frac{\partial P_{1i}}{\partial\theta} + G_{1i}\frac{P_{0i}}{Rs}\frac{\partial V_{1i}}{\partial\theta} + G_{3i}P_{1i}$$

$$+ G_{4i}P_{1i-1} + G_{5i}P_{1i+1} = -G_{6i}H_i - G_{2i}\frac{\partial H_i}{\partial t}$$

$$-G_{2i}\frac{V_{0i}}{Rs}\frac{\partial H_1}{\partial\theta} \tag{11}$$

$$X_{1i}\frac{\partial V_{1i}}{\partial t}+\frac{X_{1i}V_{0i}}{Rs}\frac{\partial V_{1i}}{\partial\theta}+\frac{A_{0i}}{Rs}\frac{\partial P_{1i}}{\partial\theta}+X_{2i}V_{1i}-\dot{m}_0$$

$$V_{1i-1}+X_{3i}P_{1i}+X_{4i}P_{1i-1}=X_{5i}H_1 \tag{12}$$

where the X_i's and G_i's are defined in Appendix A. If the shaft center moves in an elliptical orbit, then the seal clearance function can be defined as:

$$\epsilon H_1=-a\cos\omega t\cos\theta-b\sin\omega t\sin\theta \tag{13}$$

$$=-\frac{a}{2}[\cos(\theta-\omega t)+\cos(\theta+\omega t)]-\frac{b}{2}[\cos(\theta-\omega t)-\cos(\theta+\omega t)]$$

The pressure and velocity fluctuations can now be stated in the associated solution format:

$$P_{1i}=P_{ci}^{+}\cos(\theta+\omega t)+P_{si}^{+}\sin(\theta+\omega t)+P_{ci}^{-}\cos(\theta-\omega t)+P_{si}^{-}\sin(\theta-\omega t) \tag{14}$$

$$V_{1i}=V_{ci}^{+}\cos(\theta+\omega t)+V_{si}^{+}\sin(\theta+\omega t)+V_{ci}^{-}\cos(\theta-\omega t)+V_{si}^{-}\sin(\theta-\omega t) \tag{15}$$

Substituting equations (13), (14), and (15) into equations (11) and (12) and grouping like terms of sines and cosines (as shown in Appendix B) eliminates the time and theta dependency and yields eight linear algebraic equations per cavity. The resulting system of equations of the i-th cavity is of the form:

$$[A_{i-1}](X_{i-1})+[A_i](X_i)+[A_i+1](X_i+1)=\frac{a}{\epsilon.}(B_i)+\frac{b}{\epsilon.}(C_i) \tag{16}$$

where

$$(X_{i-1})=(P_{si-1}^{+},P_{ci-1}^{+},P_{si-1}^{-},P_{ci-1}^{-},V_{si-1}^{+},V_{ci-1}^{+},V_{si-1}^{-},V_{ci-1}^{-})^T$$

$$(X_i)=(P_{si}^{+},P_{ci}^{+},P_{si}^{-},P_{ci}^{-},V_{si}^{+},V_{ci}^{+},V_{si}^{-},V_{ci}^{-})^T$$

$$(X_{i+1})=(P_{si+1}^{+},P_{ci+1}^{+},P_{si+1}^{-},P_{ci+1}^{-},V_{si+1}^{+},V_{ci+1}^{+},V_{si+1}^{-},V_{ci+1}^{-})^T$$

The A matrices and column vectors B and C are given in Appendix B. To use equation (16) for the entire seal solution, a system matrix must be formed which is block tridiagonal in the A matrices. The size of this resultant matrix is ($8NC \times 8NC$) since pressure and velocity perturbations at the inlet and the exit are assumed to be zero. This system is easily solved by various linear equation algorithms, and yields a solution of the form:

$$P_{si}^{+}=\frac{a}{\epsilon}F_{asi}^{+}+\frac{b}{\epsilon}F_{bsi}^{+}$$

$$P_{si}^{-}=\frac{a}{\epsilon}F_{asi}^{-}+\frac{b}{\epsilon}F_{bsi}^{-}$$

$$P_{ci}^{+}=\frac{a}{\epsilon}F_{aci}^{+}+\frac{b}{\epsilon}F_{bci}^{+}$$

$$P_{ci}^{-}=\frac{a}{\epsilon}F_{aci}^{-}+\frac{b}{\epsilon}F_{bci}^{-} \tag{17}$$

Determination of Dynamic Coefficient

The force-motion equations for a labyrinth seal are assumed to be of the form:

$$-\begin{Bmatrix}F_x\\F_y\end{Bmatrix}=\begin{bmatrix}K & k\\-k & K\end{bmatrix}\begin{Bmatrix}X\\Y\end{Bmatrix}+\begin{bmatrix}C & c\\-c & C\end{bmatrix}\begin{Bmatrix}\dot{X}\\\dot{Y}\end{Bmatrix} \tag{18}$$

The solution of equation (18) for the stiffness and damping coefficients is the objective of the current analysis. For the assumed elliptical orbit of equation (13), the X and Y components of displacement and velocity are defined as:

$$X=a\cos\omega t \qquad \dot{X}=-a\omega\sin\omega t$$

$$Y=b\sin\omega t \qquad \dot{Y}=b\omega\cos\omega t$$

Substituting these relations into (18) yields:

$$+F_x=-Ka\cos\omega t-kb\sin\omega t+Ca\omega\sin\omega t-cb\omega\cos\omega t$$

$$+F_y=-ka\cos\omega t-Kb\sin\omega t-ca\omega\sin\omega t-Cb\omega\cos\omega t \tag{19}$$

Redefining the forces, F_x and F_y, as the following:

$$F_x=F_{xc}\cos\omega t+F_{xs}\sin\omega t$$

$$F_y=F_{yc}\cos\omega t+F_{ys}\sin\omega t \tag{20}$$

and substituting back into (19) yields the following relations:

$$-F_xc=Ka+cb\omega \qquad -F_xs=-Ca\omega+kb$$

$$-F_yc=ka+Cb\omega \qquad -F_ys=Kb+ca\omega \tag{21}$$

The X and Y components of force can be found by integrating the pressure around the seal as follows:

$$F_x=-Rs\epsilon\sum_{i=1}^{NC}\int_0^{2\pi}P_{1i}L_i\cos\theta\,d\theta \tag{22}$$

$$F_y=Rs\epsilon\sum_{i=1}^{NC}\int_0^{2\pi}P_{1i}L_i\sin\theta\,d\theta \tag{23}$$

Only one of these components needs to be expanded in order to determine the dynamic coefficients. For this analysis, the X component was chosen. Substituting equation (14) into (22) and integrating yields:

$$F_x=-\epsilon\pi Rs\sum_{i=1}^{NC}L_i[(P_{si}^{+}-P_{si}^{-})\sin\omega t+(P_{ci}^{+}+P_{ci}^{-})\cos\omega t] \tag{24}$$

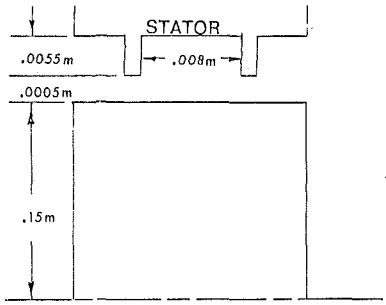

Fig. 6 Configuration used for experiment

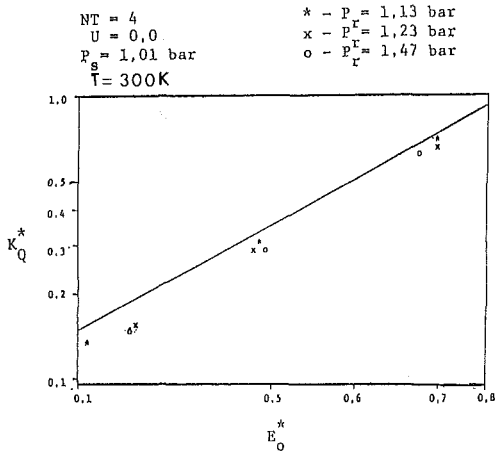

Fig. 7 Comparison to data of [8] for seal in Fig. 6

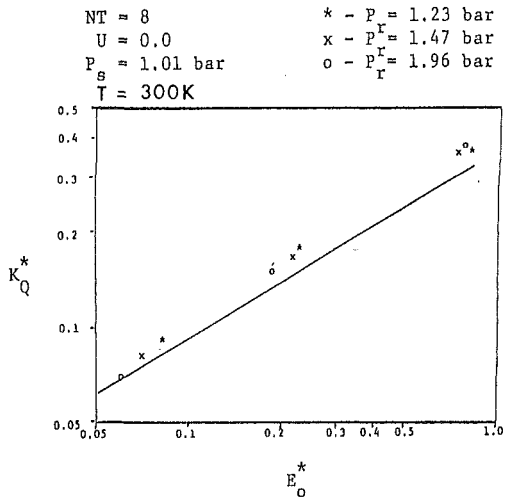

Fig. 8 Comparison to data of [8] for seal in Fig. 6

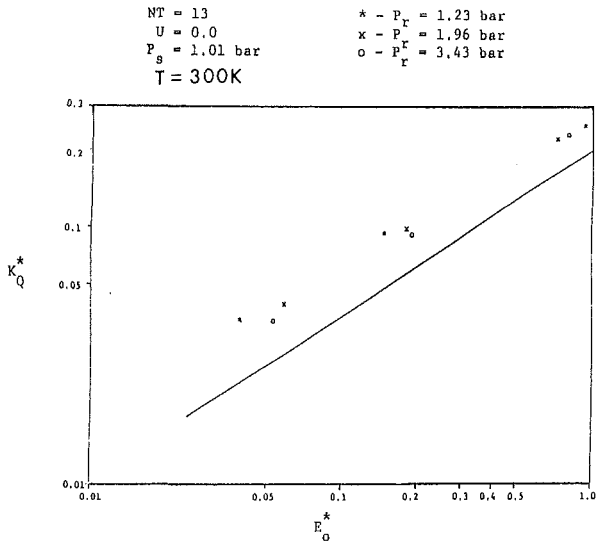

Fig. 9 Comparison to data of [8] for seal in Fig. 6

Substituting from equation (17) and (19) into equation (24) and equating coefficients of $\sin\omega t$ and $\cos\omega t$ yields:

$$F_{xs} = -\pi RS \sum_{i=1}^{NC} L_i[a(F_{asi}^+ - F_{asi}^-) + b(F_{bsi}^+ - F_{bsi}^-)]$$

$$F_{xc} = -\pi RS \sum_{i=1}^{NC} L_i[a(F_{aci}^+ + F_{aci}^-) + b(F_{bci}^+ + F_{bci}^-)] \quad (25)$$

Equating the definitions for F_{xs} and F_{xc} provided by equations (21) and (25) and grouping like terms of the linearly independent coefficients a and b yields the final solutions to the stiffness and damping coefficients:

$$K = \pi R \sum_{i=1}^{NC} (F_{aci}^+ + F_{aci}^-) L_i$$

$$k = \pi R \sum_{i=1}^{NC} (F_{bsi}^+ - F_{bsi}^-) L_i$$

$$C = \frac{-\pi RS}{\omega} \sum_{i=1}^{NC} (F_{asi}^+ - F_{asi}^-) L_i$$

$$c = \frac{\pi RS}{\omega} \sum_{i=1}^{NC} (F_{bci}^+ + F_{bci}^-) L_i \quad (26)$$

Solution Procedure Summary

In review, the solution procedure uses the following sequential steps:

(*a*) Leakage is determined from equation (7) or (8).
(*b*) Pressure distribution is found using equation (7).
(*c*) Velocity distribution is determined using equation (10).
(*d*) A system equation is formed and solved using the cavity equation (16).
(*e*) Results of this solution, as defined in equations (17), are inserted into equation (26).

Results

To compare the present analytic solution with the experimental results of Wachter and Benckert [8, 9, 10], the following dimensionless parameters are introduced. The dimensionless cross-coupled stiffness and entry-swirl parameters are defined by Wachter and Benckert as:

$$K_Q^* = \frac{Cr\,Kxy}{RsLNC(Pr-Ps)} \qquad E_0^* = \frac{0.5\rho_0 V_0^2}{(Pr-Ps)+0.5\rho_0 V_x^2} \quad (27)$$

All of the results presented for comparison in this paper are for a seal with teeth on the stator, with entry swirl, and no shaft rotation. Although Wachter and Benckert published results for shaft rotation, the data for the operating conditions and seal geometry were insufficient for use in this study. The results in Figs. 7, 8, and 9 are from [8] and show the relationship between cross-coupled stiffness and the entry swirl, for a seal with strips on the stator and the geometry shown in Fig. 6. The line shown is the experimental result and the symbols are the results from this analytical model. These figures show that the model compares favorably to the experimental results in magnitude and the overall trend for various operating conditions. The figures also show that the model does not yield a consistently high or low result. Instead, the model tends to overpredict the value of the stiffness for a large number of strips and underpredict stiffness for a small number of seals. This trend is probably due to errors in calculating the zeroth-order pressure distribution using the leakage model.

The results in Table 1 are from [9, 10] for a seal with strips on the stator. The results show the effect of change in seal parameters such as pitch, number of teeth, radius, strip height, and clearance on the cross-coupled stiffness. The model accurately shows the increase in cross-coupled stiffness due to decrease in clearance and decrease in strip height, but it fails to remain constant for change of pitch and consistently overestimates the cross-coupled stiffness for the larger radius cases by about 26%. The data in Table 2 are also from [9, 10] and show the results for full labyrinths. The comparison is very poor.

Conclusion

A clear and understandable analysis utilizing reduced equations has been presented for the problem of calculating rotordynamic coefficients for labyrinth seals. This paper was developed to provide a less restrictive analysis and a better explanation of the current analyses. The model developed gives results that are within 25% of the experimental results which are available. However, this error must be balanced against the known uncertainties in the experimental data. This is especially important since all of the data used are for a nonrotating shaft and the only influence on the cross-coupled stiffness was the entry swirl. Although Wachter and Benckert published data for a rotating shaft, the data were not sufficient to calculate a result. Also, the only data available for see-through labyrinths is for the type with strips on the stator. For a more rigorous test of this and other models, more complete data are required over a wider range of parameters

Table 1 Comparison of data for various geometries operating conditions for a seal with teeth on the stator and no shaft rotation [9, 10]

E_0*	U	NT	C_r(m)	L(m)	B(m)	Rs(m)	P_r(bar)	P_s(bar)	EXP. K_{xy}(N/mm)	CALC. K_{xy}(N/mm)	% Error
0.023	0.0	18	.00025	.005	.0025	0.15	2.947	0.943	257	233	+9
0.024	0.0	18	.00025	.005	.0025	0.15	1.43	0.943	75	69	+8
0.038	0.0	18	.00025	.005	.006	0.15	2.947	0.943	157	142	+10
0.018	0.0	18	.00025	.005	.006	0.15	1.43	0.943	27	26	−4
0.04	0.0	18	.00058	.005	.006	0.075	1.925	0.943	29	20	−31
0.04	0.0	18	.00058	.005	.006	0.075	2.418	0.943	41	28	−32
0.04	0.0	9	.00058	.010	.006	0.075	1.925	0.943	29	16	−45
0.04	0.0	9	.00058	.010	.006	0.075	2.418	0.943	41	23	−44

Table 2 Comparison of data for full labyrinth [9, 10]

Rs mm	B mm	L mm	Cr mm	NT	W rpm	V_0 m/s	Pr/Ps	k(meas.) N/n	k(calc.) N/m	%Err
150	5.50	4.00	.500	18	9550	43.2	1.51	1.97 E5	0.19 E5	942
150	5.50	4.00	.500	24	9550	40.0	1.51	2.89 E5	0.38 E5	660
150	5.50	4.00	.500	24	9485	66.1	0.79	2.63 E5	0.31 E5	756
150	5.50	4.00	.500	24	9550	47.1	1.51	2.95 E5	0.44 E5	570

for different seal geometries. Finally, this analysis is only considered valid for the see-through type of labyrinth seal since the model fared very poorly in comparison with experimental results for interlocking seal data.

References

1 Alford, J. S., "Protecting Turbomachinery From Self-Excited Rotor Whirl," ASME JOURNAL OF ENGINEERING FOR POWER, Vol. 87, No. 4, Oct. 1965, pp. 333-344.

2 Spürk, J. H., and Keiper, R., "Selbsterregte Schwingungen bei Turbomaschinen infolge der Labyrinthstromung," *Ingerieur-Archive 43*, 1974, pp. 127-135.

3 Vance, J. M., and Murphy, B. T., "Labyrinth Seal Effects on Rotor Whirl Stability," *Inst. of Mechancial Engineer*, 1980, pp. 369-373.

4 Kostyuk, A. G., "A Theoretical Analysis of the Aerodynamic Forces in the Labyrinth Glands of Turbomachines," *Teploenergetica*, 19 (11)0, 1972, pp. 39-44.

5 Iwatsubo, T., "Evaluation of Instability Forces of Labyrinth Seals in Turbines or Compressors," NASA CP 2133 Proceedings of a workshop at Texas A&M University 12-14 May 1980, entitled Rotordynamic Instability Problems in High Performance Turbomachinery, pp. 139-167.

6 Iwatsubo, T., Matooka, N., and Kawai, R., "Flow Induced Force and Flow Pattern of Labyrinth Seal," NASA CP 2250 Proceedings of a workshop at Texas A&M University 10-12 May 1982, entitled Rotordynamic Instability Problems in High Performance Turbomachinery, pp. 205-222.

7 Kurohashi, M., Inoue, Y., Abe, T., and Fujikawa, T., "Spring and Damping Coefficients of the Labyrinth Seal," Paper No. C283/80 delivered at the Second International Conference on Vibrations in Rotating Machinery, The Inst. of Mech. Engineering.

8 Wachter, J., and Benckert, H., "Querkrafte aus Spaltdichtungen-Eine mogliche Ursache fur die Laufunruhe von Turbomaschinen," *Atomkernenergie*, Vol. 32, 1978, Lfg. 4, pp. 239-246.

9 Wachter, J., and Benckert, H., "Flow Induced Spring Coefficients of Labyrinth Seals for Applications in Rotordynamic," NACA CP 2133 Proceedings of a workshop held at Texas A&M University 12-14 May 1980, entitled Rotordynamic Instability Problems of High Performance Turbomachinery, pp. 189-212.

10 Benckert, H., "Stromungsbedinte Federkennwerte in Labyrinthdichtungen," Doctoral dissertation, University of Stuttgart, 1980.

11 Blasius, H., "Forschungoarb," *Ing.-Wes.*, No. 131, 1913.

12 Yamada, Y., *Trans. Japan Soc. Mechanical Engineers*, Vol. 27, No. 180, 1961, p. 1267.

13 Neumann, K., "Zur Frage der Verwendung von Durchblickdichtungen im Dampfturbinenbau," *Maschinentechnik*, Vol. 13, 1964, No. 4.

14 Gurevich, M. I., *The Theory of Jets in An Ideal Fluid*, Pergamon Press, 1966, pp. 319-323.

15 Egli, A., "The Leakage of Steam Through Labyrinth Glands," *Trans. ASME*, Vol. 57, 1935, pp. 115-122.

16 John, E. A. J., *Gas Dynamics*, Wiley, 1979.

APPENDIX A

Definition of the First-Order Continuity and Momentum Equation Coefficients

$$G_1 = \frac{A_{0i}}{RT} \qquad G_2 = \frac{P_{0i}L}{RT}$$

$$G_3 = \frac{\dot{m}_0 P_i}{P_i^2 - P_{i-1}^2} + \frac{\dot{m}_0 \mu_{1i+1}}{\pi}(5-4S_{1i+1})\frac{\gamma-1}{\gamma P_{0i+1}}$$

$$\left(\frac{P_{0i}}{P_{0i+1}}\right)^{\frac{1}{\gamma}} + \frac{\dot{m}_0 \mu_{1i}}{\pi}(5-4S_{1i})\left(\frac{\gamma-1}{\gamma P_{0i}}\right)\left(\frac{P_{0i}}{P_{0i+1}}\right)^{\frac{\gamma-1}{\gamma}}$$

$$G_4 = \frac{-\dot{m}_0 P_{0i-1}}{P_{0i-1}^2 - P_{0i}^2} + \frac{\dot{m}_0}{\pi}\mu_{1i}(4s_i - 5)$$

$$\left[\frac{1}{P_{0i}}\left(\frac{\gamma-1}{\gamma}\right)\left(\frac{P_{0i-1}}{P_{0i}}\right)^{-\frac{1}{\gamma}}\right]$$

$$G_5 = \frac{-\dot{m}_0 P_{0i+1}}{P_{0i}^2 - P_{0i+1}^2} + \frac{\dot{m}_0}{\pi}\mu_{1+i}(4s_i - 5)$$

$$\left[\frac{1}{P_{0i+1}}\left(\frac{\gamma-1}{\gamma}\right)\left(\frac{P_{0i}}{P_{0i+1}}\right)^{\frac{\gamma-1}{\gamma}}\right]$$

$$G_6 = \dot{m}_0\left(\frac{Cr_i - Cr_{i+1}}{C_{ri+1}C_{ri}}\right)$$

$$X_1 = \frac{P_{0i}A_{0i}}{RT} \qquad X_2 = \dot{m}_0 + \frac{\tau_{si}as_iL_i(2+ms)}{V_{0i}}$$

$$+ \frac{\tau_{ri}ar_iL_i(2+mr)}{(R\omega - V_{0i})}$$

$$X_3 = \frac{\tau_{si}as_iL_i}{P_{0i}} - \frac{\tau_{ri}ar_iL_i}{P_{0i}} - \frac{\dot{m}_0 P_{0i}}{P_{0i-1}^2 - P_{0i}^2}$$

$$(V_{0i} - V_{0i-1})P_{0i} + \frac{\dot{m}_0}{\pi}\mu_{1i}(4s_i - 5)$$

$$\left[\frac{1}{P_{0i}}\left(\frac{\gamma-1}{\gamma}\right)\left(\frac{P_{0i-1}}{P_{0i}}\right)^{\frac{\gamma-1}{\gamma}}\right](V_{0i} - V_{0i-1})$$

$$X_4 = \frac{\dot{m}_0 P_{0i-1}}{P_{0i-1}^2 - P_{0i}^2}(V_{0i} - V_{0i-1})$$

$$- \frac{\dot{m}_0}{\pi}(V_{0i} - V_{0i-1})\mu_{1i}(4s_i - 5)$$

$$\left[\frac{1}{P_{0i}}\left(\frac{\gamma-1}{\gamma}\right)\left(\frac{P_{0i-1}}{P_{0i}}\right)^{-\frac{1}{\gamma}}\right]$$

$$X_5 = \frac{-\dot{m}_0}{Cr_i}(V_{0i} - V_{0i-1}) - \frac{ms\tau_{si}as_iL_iD_i}{2(Cr_i + B_i)^2} + \frac{\tau_{ri}armr_iL_iD_i}{2(Cr_i + B_i)^2}$$

A_{i-1} *Matrix*

$a_{1,2} = a_{2,1} = a_{3,4} = a_{4,3} = G_4$

$a_{5,2} = a_{6,1} = a_{7,4} = a_{8,3} = X_4$

$a_{5,6} = a_{6,5} = a_{7,8} = a_{8,7} = -\dot{m}_0$

The remaining elements are zero.

A_i *Matrix*

$$a_{1,1} = G_1\left(\omega + \frac{V_{0i}}{Rs}\right) \quad a_{2,2} = -G_1\left(\omega + \frac{V_{0i}}{Rs}\right)$$

$$a_{3,3} = G_1\left(\frac{V_{0i}}{Rs} - \omega\right) \quad A_{4,4} = -G_1\left(\frac{V_{0i}}{Rs} - \omega\right)$$

$a_{1,2} = a_{2,1} = a_{3,4} = a_{4,3} = G_3$

$a_{5,2} = a_{6,1} = a_{7,4} = a_{8,3} = X_3$

$$a_{5,1} = a_{7,3} = \frac{A_{0i}}{Rs} \quad a_{6,2} = a_{8,4} = \frac{-A_{0i}}{Rs}$$

$$a_{5,5} = X_1\left(\omega + \frac{V_{0i}}{Rs}\right) \quad a_{6,6} = -X_1\left(\omega + \frac{V_{0i}}{Rs}\right)$$

$$a_{7,7} = X_1\left(\frac{V_{0i}}{Rs} - \omega\right) \quad a_{8,8} = X_1\left(\omega - \frac{V_{0i}}{Rs}\right)$$

$a_{5,6} = a_{6,5} = a_{7,8} = a_{8,7} = X_2$

$$a_{1,5} = a_{3,7} = G_1\frac{P_{0i}}{Rs}$$

$$a_{2,6} = a_{4,8} = -G_1\frac{P_{0i}}{Rs}$$

The remaining elements are zero.

A_{i+1} *Matrix*

$a_{1,2} = a_{2,1} = a_{3,4} = a_{4,3} = G_5$

APPENDIX B

Separation of the Continuity and Momentum Equations and Definition of the System Matrix Elements

Continuity

$$\cos(\theta+\omega t): G_{1i}P_{si}^{+}\left(\omega + \frac{V_{0i}}{Rs}\right) + G_{1i}\frac{P_{0i}}{Rs}V_{si}^{+} + G_{3i}P_{ci}^{+} + G_{4i}P_{ci-1}^{+} + G_5P_{ci+1}^{+} = \frac{G_{6i}}{2}(a-b)$$

$$\sin(\theta+\omega t): -G_{1i}P_{ci}^{+}\left(\frac{V_{0i}}{Rs} + \omega\right) - G_{1i}\frac{P_{0i}}{Rs}V_{ci}^{+} + G_{3i}P_{si}^{+} + G_{4i}P_{si-1}^{+} + G_{5i}P_{si+1}^{+} = \frac{G_{6i}}{2}\left(\frac{V_{0i}}{Rs} + \omega\right) \quad (b-a)$$

$$\cos(\theta-\omega t): G_{1i}\left(\frac{V_{0i}}{Rs} - \omega\right)P_{si}^{-} + G_{1i}\frac{P_{0i}}{Rs}V_{si}^{-} + G_{3i}P_{ci}^{-} + G_{4i}P_{ci-1}^{-} + G_{5i}P_{ci+1}^{-} = \frac{G_{6i}}{2}(a+b)$$

$$\sin(\theta-\omega t): G_{1i}\left(\omega - \frac{V_{0i}}{Rs}\right)P_{ci}^{-} - \frac{G_{1i}P_{0i}}{Rs}V_{ci}^{-} + G_{3i}P_{si}^{-} + G_{4i}P_{si-1}^{-} + G_{5i}P_{si-1}^{-} = \frac{G_{6i}}{2}\left(\omega - \frac{V_{0i}}{Rs}\right)(a+b)$$

Momentum

$$\cos(\theta+\omega t): X_{1i}\left(\omega + \frac{V_{0i}}{Rs}\right)V_{si}^{+} + \frac{A_{0i}}{Rs}P_{si}^{+} + X_{2i}V_{ci}^{+} - \dot{m}_0V_{ci-1}^{+} + X_{3i}P_{ci}^{+} + X_{4i}P_{ci-1}^{+} = \frac{X_{5i}}{2} \quad (b-a)$$

$$\sin(\theta+\omega t): -X_{1i}\left(\omega + \frac{V_{0i}}{Rs}\right)V_{ci}^{+} - \frac{A_{0i}}{Rs}P_{ci}^{+} + X_{2i}V_{si} - \dot{m}_0V_{si-1}^{+} + X_{3i}P_{si}^{+} + X_{4i}P_{si-1}^{+} = 0$$

$$\cos(\theta+\omega t): X_{1i}\left(\frac{V_{0i}}{Rs} - \omega\right)V_{si}^{-} + \frac{A_{0i}}{Rs}P_{si}^{-} + X_{2i}V_{ci}^{-} - \dot{m}_0V_{ci-1}^{-} + X_{3i}P_{ci}^{-} + X_{4i}P_{ci-1}^{-} = \frac{-X_{5i}}{2} \quad (a+b)$$

$$\sin(\theta-\omega t): X_{1i}\left(\omega - \frac{V_{0i}}{Rs}\right)V_{ci}^{-} - \frac{A_{0i}}{Rs}P_{ci}^{-} + X_{2i}V_{si}^{-} - \dot{m}_0V_{si-1}^{-} + X_{3i}P_{si}^{-} + X_{4i}P_{si-1}^{-} = 0$$

The remaining elements are zero.

B and C column vectors:

$$B = \begin{bmatrix} \frac{G_6}{2} \\ \frac{-G_2}{2}\left(\frac{V_{0i}}{Rs} + \omega\right) \\ \frac{G_6}{2} \\ \frac{G_2}{2}\left(\omega - \frac{V_{0i}}{Rs}\right) \\ \frac{-X_5}{2} \\ 0 \\ \frac{-X_5}{2} \\ 0 \end{bmatrix} \quad C = \begin{bmatrix} \frac{-G_6}{2} \\ \frac{G_2}{2}\left(\frac{V_{0i}}{Rs} + \omega\right) \\ \frac{G_6}{2} \\ \frac{G_2}{2}\left(\omega - \frac{V_{0i}}{Rs}\right) \\ \frac{X_5}{2} \\ 0 \\ \frac{-X_5}{2} \\ 0 \end{bmatrix}$$

Effects of Fluid Inertia and Turbulence on the Force Coefficients for Squeeze Film Dampers

L. San Andrés

J. M. Vance

Texas A&M University,
College Station, TX 77843

The effects of fluid inertia and turbulence on the force coefficients of squeeze film dampers are investigated analytically. Both the convective and the temporal terms are included in the analysis of inertia effects. The analysis of turbulence is based on friction coefficients currently found in the literature for Poiseuille flow. The effect of fluid inertia on the magnitude of the radial direct inertia coefficient (i.e., to produce an apparent "added mass" at small eccentricity ratios, due to the temporal terms) is found to be completely reversed at large eccentricity ratios. The reversal is due entirely to the inclusion of the convective inertia terms in the analysis. Turbulence is found to produce a large effect on the direct damping coefficient at high eccentricity ratios. For the long or sealed squeeze film damper at high eccentricity ratios, the damping prediction with turbulence included is an order of magnitude higher than the laminar solution.

Introduction

Squeeze film dampers (SFD) are designed to have a stabilizing effect on the rotordynamics of turbomachinery. This has generally been accomplished by using the Reynolds effect in a thin oil film around a bearing to produce a predictable damping coefficient. The increase in size and speed of modern turbomachinery using light-viscosity oils has brought the need to include fluid inertia effects in the design analysis. Sparked by the recent pioneering work of Tichy [1-4], researchers are now extending the lubrication theory into the range where the Reynolds (slow flow) assumption is no longer applicable.

At least for some simple geometries and motions, the fluid inertia effects have been shown to be quite significant.

To the rotordynamicist fluid film forces and dynamic coefficients are more important than velocity or pressure fields. Analytical [2-7] and numerical [5, 6] approaches have been developed for calculating the damping and inertia coefficients, assuming motions of small amplitude α about an equilibrium point. In this case, it can be shown that the convective inertial terms may be neglected in the equations of motion, since they are of order α^2 while the temporal terms are of order α. In all these analyses, the trend of the damping and inertia coefficients is to increase as the static eccentricity ratio increases, a fact that has been shown to be true in practice.

However, for large excursions of the journal center about its centered position the full inertial term should be retained in the momentum equations. The temptation to neglect convective terms in order to simplify and linearize the problem is no longer justifiable even for very simple cases such as the long or short bearing solutions. For example, [9] recently presented numerical calculations for the dynamic coefficients of an SFD performing circular orbits (CCO) about the center of the bearing housing. Using the same approach as in [5], the convective inertia effects were neglected, so the coefficients have the characteristic form described above. This behavior of the fluid film forces will be shown to be in error even for moderate eccentricities and totally incorrect at large orbit amplitudes. Furthermore, in [9] the direct damping and inertia coefficients for the cavitated SFD were found to be 1/2 the value of the full film case and independent of the inertia parameters of the fluid. This appears unreasonable since if cavitation is allowed, the extent of the region where the film is broken will be influenced by the magnitude of the inertial forces. Our purpose in the present analysis will be to determine the dynamic coefficients taking into account the full inertial terms for simple geometries in order to understand better the action of viscous and inertial forces in an SFD.

The inclusion of inertia complicates the problem in a SFD, and turbulence effects make the problem even more involved. Unlike the journal bearing case where a considerable amount of analytical and experimental work has been done, turbulence in squeeze film dampers remains rather obscure due to the lack of experimental data or a good understanding of the mechanics of squeezing flows. Nelson [11] used the empirical friction coefficient for pure Poiseuille flows in an attempt to include turbulent effects for the long SFD case. No satisfactory results were obtained since the fluid apparent viscosity was used to calculate the empirical friction factor for the flow.

Contributed by the Gas Turbine Division of THE AMERICAN SOCIETY OF MECHANICAL ENGINEERS and presented at the 30th International Gas Turbine Conference and Exhibit, Houston, Texas, March 18-21, 1985. Manuscript received at ASME Headquarters, January 16, 1985. Paper No. 85-GT-191.

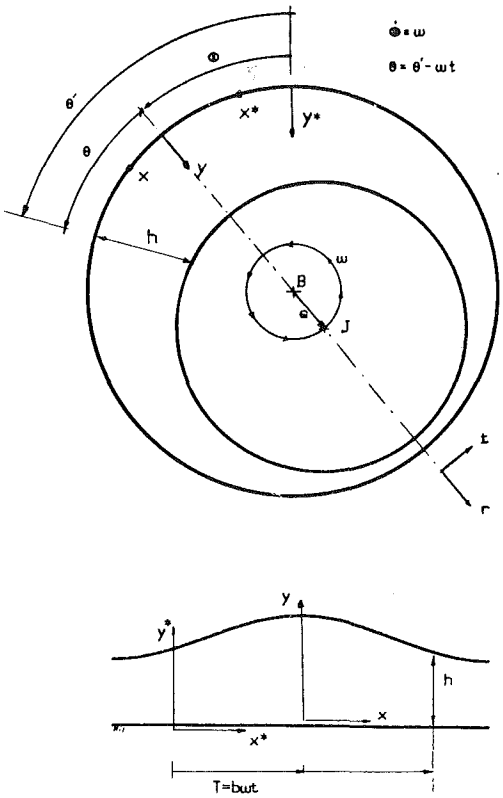

Fig. 1 Squeeze film damper geometry and coordinate systems

Tichy [4] suggests that turbulent flow in SFD's will occur at higher Reynolds numbers than for Poiseuille flows, i.e., Rep > 2000. This assertion seems reasonable since the velocity field in a SFD is constantly changing and adjusts itself to the normal motion of the boundary, thus making the flow more stable. It also seems reasonable that transition from laminar to turbulent regions should be smooth in order to satisfy continuity of the flow. All these considerations make the problem more untractable and point out the urgent need of experimental data. In the meantime, it will prove helpful to use the empirical correlations currently found in the literature and thus obtain upper bounds for the forces and dynamic coefficients when turbulence is present in the flow.

Statement of the Problem

Figure 1 shows the geometry of the SFD system. The equations of motion for the flow in the annular region between a whirling nonrotating inner cylinder and its bearing housing are stated in a moving coordinate frame. Appendix A contains the details of the integration of the motion equations across the lubricant film, to finally obtain in dimensionless form:

$$\mathrm{Re}\left\{\frac{\partial}{\partial\theta}I_{\theta\theta}+\frac{\partial}{\partial\xi}I_{\theta\xi}\right\}=-Hk\frac{\partial\bar{p}}{\partial\theta}+\Delta\tau_{\theta\eta} \tag{1}$$

$$\mathrm{Re}\left\{\frac{\partial}{\partial\theta}I_{\theta\xi}+\frac{\partial}{\partial\xi}I_{\xi\xi}\right\}=-Hk(b/L)^2\frac{\partial\bar{p}}{\partial\xi}+\Delta\tau_{\xi\eta} \tag{2}$$

$$\frac{\partial}{\partial\theta}q_\theta+\frac{\partial}{\partial\xi}q_\xi=0 \tag{3}$$

Nomenclature

a = inner cylinder radius
$\bar{a}_r=-\epsilon$ = dimensionless journal center radial acceleration
b = outer cylinder radius
$\bar{C}_{rt},\bar{C}_{tt}$ = dimensionless damping coefficients in (r, t) directions due to tangential velocity $\bar{V}_t$
C_{rt},C_{tt} = damping coefficients $= (\bar{C}_{rt}, \bar{C}_{tt})\ ^*\mu kL/\delta^3$
$\bar{D}_{rr},\bar{D}_{tr}$ = dimensionless inertia coefficients in (r, t) direction due to normal acceleration $\bar{a}_r$
D_{rr},D_{tr} = inertia coefficients $= (D_{rr}, D_{tr})\ ^*\ \mu kL/\delta^3\omega$
e = circular centered orbit radius
f_r,f_t = dimensionless fluid film force in (r, t) direction
f_θ,f_ξ = inertial wall shear stress functions
H = $1+\epsilon\cos\theta$ = dimensionless film thickness
h = $b\delta H$ = film thickness
$I_{\theta\theta},I_{\theta\xi},I_{\xi\xi}$ = momentum integrals over the film thickness
k = geometry parameter $= (L/b)^2$ for short SFD assumption, 1 for others
k_θ,k_ξ = parameters depending on the nature of the flow
L = squeeze film damper length
p = pressure
$\bar{p}$ = $p\delta^2/(k\omega\mu)$ = dimensionless pressure
q_θ,q_ξ = dimensionless local flow rates in (θ, ξ) direction
Re = $\omega\delta^2b^2/\nu$ = squeeze Reynolds number
Rep = $\frac{\mathrm{Re}}{\delta}[(q_\theta+H)^2+(L/b\ q_\xi)^2]^{1/2}$ = Poiseuille flow Reynolds number
u = fluid relative velocity along lubricant film
u^* = absolute fluid velocity along lubricant film = $u+b\omega$
$\bar{u}$ = $u/b\omega$ = dimensionless fluid velocity
$\bar{u}_m$ = $\int_0^1\bar{u}d\eta$ = mean fluid velocity along lubricant film
v = fluid velocity across lubricant film
$\bar{v}$ = $v/b\delta\omega$ = dimensionless fluid velocity
$\bar{V}_t$ = ϵ = dimensionless journal center tangential velocity
w = fluid velocity in the axial direction
$\bar{w}$ = $w/L\omega$ = dimensionless axial velocity
$\bar{w}_m$ = $\int_0^1\bar{w}d\eta$ = mean fluid velocity in axial direction
ω = frequency of damper motion
t = time
(x,y,z) = moving coordinate system
$(x,y,z)^*$ = fixed coordinate system
$\alpha_1,\alpha_2,\alpha_3$ = coefficients eventually depending on Re for turbulent motion
γ = $\partial H/\partial\theta$ = film thickness gradient along circumferential direction
Γ = $\Gamma(\bar{u}_m^2)$ = dimensionless inertia function for long SFD assumption
δ = $(b-a)/b$ = clearance ratio
ϵ = $e/b\delta$ = dimensionless circular orbit radius, eccentricity radius
(θ,η,ξ) = dimensionless coordinates = $(x/b, y/h, z/L)$
$\Delta\tau_{\theta\eta},\Delta\tau_{\xi\eta}$ = wall shear stress difference in (θ, ξ) direction
ρ = fluid density
μ = fluid viscosity
ν = μ/ρ = kinematic viscosity
τ = $t\omega$ = dimensionless time

Subscripts

0 = inertialess or purely viscous
i = inertial

This system of equations must be solved with appropriate boundary conditions for the flow rates (q_θ, q_ξ) and the pressure $\bar{p}$. Analytical solutions to the problem are extremely difficult since the exact form of the wall shear stress difference ($\Delta\tau_{\theta\eta}$, $\Delta\tau_{\xi\eta}$) is unknown and some assumption regarding their functional form becomes necessary. Presumably, the problem may be solved numerically on a computer with its full tridimensional complexity, but such an effort may prove to be unnecessarily costly or even impractical.

As a first approximation to a practical solution of the problem, we assume that for the laminar region, and even in the presence of turbulent effects, the shear stresses at the walls may be written as:

$$\Delta\tau_{\theta\eta} = -k_\theta \frac{(q_\theta + H)}{H^2} + \mathrm{Re}\, f_\theta \tag{4a}$$

$$\Delta\tau_{\xi\eta} = -k_\xi \frac{q_\xi}{H^2} + \mathrm{Re}\, f_\xi \tag{4b}$$

The approximate form of the functions k_θ, k_ξ, f_θ, and f_ξ will be discussed later in the analysis. Note also that in equations (4) we have included an explicit contribution of inertia to the wall shear stresses.

Once a solution to the system of equations (1) to (3) has been obtained the fluid film forces acting on the inner cylinder are calculated by integration of the pressure distribution over the flow region. For rotordynamics applications, the forces are expressed in terms of damping and inertia coefficients. Let (f_r, f_t) be the radial (along the centerline of both cylinders) and tangential dimensionless fluid film forces, and given by:

$$f_r = \int_R \bar{p} \cos\theta \, dR = -\bar{C}_{rt}\bar{V}_t - \bar{D}_{rr}\bar{a}_r \tag{5a}$$

$$f_t = \int_R p \sin\theta \, dR = -\bar{C}_{tt}\bar{V}_t - \bar{D}_{tr}\bar{a}_r \tag{5b}$$

$$R = \{0 \le \theta \le 2\pi,\ 0 \le \xi \le 1\}$$

In equations (5), $\bar{V}_t$, $\bar{a}_r$ are the dimensionless journal center tangential velocity and radial acceleration, respectively; and ($\bar{C}_{rt}$, $\bar{C}_{tt}$), ($\bar{D}_{rr}$, $\bar{D}_{tr}$) are the dimensionless damping and inertia coefficients. The dimensional counterparts of these coefficients are given by the relations:

$$C_{ij} = \frac{\mu k L}{\delta^3}\bar{C}_{ij},\quad D_{ij} = \frac{\mu k L}{\delta^3 \omega}\bar{D}_{ij} \tag{6}$$

Our interest is to obtain approximate solutions to the uncavitated case, and present the dynamic coefficients with inertia and turbulence effects accounted for in the flow. This is a necessary step preliminary to any more refined analysis, since it will contribute to a better understanding of the problem. We will treat the laminar and turbulent solutions for the long and short SFD's separately. No cavitation is considered in the flow region. This last assumption is unrealistic for some cases, but permits us to do a first treatment of the fluid film forces with inertia and turbulence included, and will be accurate for high supply pressures. Furthermore, the direct effects of fluid inertia and turbulence will be isolated from the indirect effect caused by changes in the region of cavitation.

Laminar Flow Solutions

Long Bearing Assumption. In this section we assume that the cylinders are infinite in extent, or that very tight end seals are placed at the ends of the SFD, or that the axial flow q_ξ is negligible. We are left with the equation:

$$q_\theta = \bar{u}_m H \tag{7}$$

$$\frac{\partial \bar{p}_0}{\partial\theta} = \frac{-k_\theta}{H^3}(q_\theta + H) \tag{8}$$

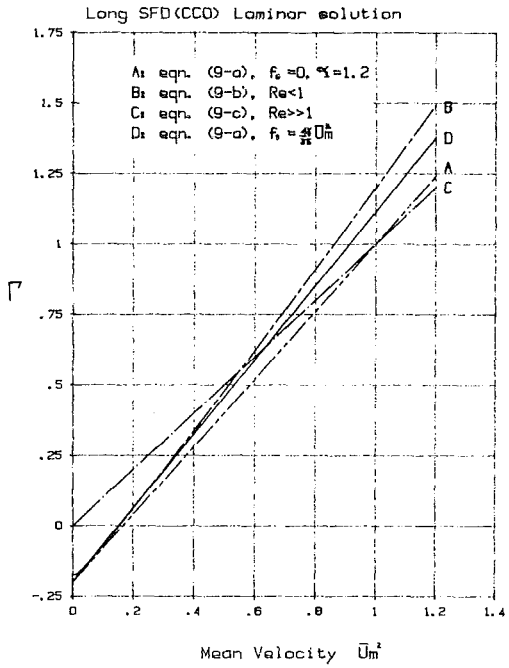

Fig. 2 Function Γ ($\bar{U}m^2$) indicating magnitude of inertia term in pressure equation for infinitely long SFD

$$\frac{\partial \bar{p}_i}{\partial\theta} = \frac{\gamma}{35\,H}[-7 + 35\alpha_1 \bar{u}_m^2] + \frac{f_\theta}{H} \tag{9a}$$

$$\bar{p} = \bar{p}_0 + \mathrm{Re}\, \bar{p}_i$$

Here we have divided the pressure into two parts so that $\bar{p}_i$ contains explicitly the influence of inertia. The purpose here is not to claim universality of the assumption employed and which is questionable to all lights for Re > 1, but rather to show for asymptotic values of the Reynolds number the pressure field and force coefficients due solely to the effect of fluid inertia.

In analyzing the effects of fluid inertia for the long and short SFD's, we have applied a perturbation technique to solve the velocity field as well as the pressure distribution by expanding the solution in powers of the Reynolds number Re. The solutions so obtained have shown consistently that the term associated with Re^1 is of $0(10^{-1}, 10^{-2})$ and that of Re^2 is of $0(\mathrm{Re}^{-2}, \mathrm{Re}^{-4})$ while the zero-th order term (inertialess solution) is of 0(1) for small to moderate and large orbit radii respectively. This fortunate behavior of the inertial corrections makes it valid for large Re of order (10^1). It is not unusual to find that equations have been successful beyond the limits of their original derivation.

For small Reynolds numbers, Re $\le$ 1, Brindley [7] and the first author [10] have found that k_θ = 12 as in the usual lubrication approximation, and that the inertial pressure gradient is given by:

$$\frac{\partial \bar{p}_i}{\partial\theta} = \frac{\gamma}{35H}[-6 + 6\,\bar{u}_m + 54\,\bar{u}_m^2] \tag{9b}$$

For large Reynolds numbers, assuming that the flow remains stable and laminar, the inviscid pressure gradient is given as:

$$\frac{\partial \bar{p}_i}{\partial\theta} = \frac{\gamma}{H}\bar{u}_m^2 \tag{9c}$$

It should be remarked that for inviscid flow, the viscous pressure field vanishes and the pressure should be redefined as $\bar{p} = \mathrm{Re}\,\bar{p}^*$.

Equation (9c) is different from the result presented by Tichy in [4], apparently due to an error in the boundary conditions used for the inviscid flow region.

Table 1 Direct inertia coefficient $\bar{D}_{rr}$ for the long squeeze film damper

Definitions: $\beta=(1-\epsilon^2)^{1/2}$, $b=(2+\epsilon^2)$

$\Gamma_1=2\beta/b^2$, $\Gamma_2=(\beta-1)/\epsilon^2$ (1.1)

Re	$\bar{D}_{rr}$/Re	
small Re $\ll 1$	$\frac{12\pi}{35}[\Gamma_2(1+2\beta/b)+9\Gamma_1]$	(1.2)
large Re $\to \infty$	$2\pi\,\Gamma_1$	(1.3)
moderate $f_\theta=0$	$\frac{14\pi}{35}[\Gamma_2+6\Gamma_1]$	(1.4)
moderate f_θ from equation (12)	$\frac{14\pi}{35}[\Gamma_2+6.5714285\,\Gamma_1]$	(1.5)
temporal effects only, Re $\ll 1$	$\frac{-6\pi}{5}\Gamma_2[4+\Gamma_1 b]$	(1.6)

For both extreme values of the inertial parameter Re, the dimensionless flow rate q_θ is unaffected by inertia and is equal to

$$q_\theta=\frac{2(\epsilon^2-1)}{(2+\epsilon^2)} \tag{10}$$

In order to make a quantitative comparison of equations (9*a–c*) we let

$$\Gamma=\frac{H}{\gamma}\frac{\partial\bar{p}_i}{\partial\theta}=\Gamma(\bar{u}_m{}^2) \tag{11}$$

be a function that indicates the magnitude of the inertia term in the pressure equation.

Figure 2 shows equations (9*a–c*); curves *A* represents (9*a*) with $f_\theta = 0$, $\alpha_1 = 1.2$, curves *B* and *C*, equations (9*b–c*), respectively.

A brief look at Fig. 2 shows the surprisingly similar behavior of the flow for the large range of Re considered. The actual value of Γ for moderate Reynolds numbers will lie between curves *A* and *B*; and curve *D* shows the best fitting line between the *A* and *B* curves from which we select the inertial contribution to the wall shear stress difference as:

$$f_\theta=\frac{4}{35}\gamma\frac{q_\theta{}^2}{H^2} \tag{12}$$

Thus we assume that for moderate Reynolds numbers, the wall shear stress difference is approximately given by:

$$\Delta\tau_{\theta\eta}=-12\frac{(q_\theta+H)}{H^2}+\mathrm{Re}\frac{4}{35}\gamma\frac{q_\theta{}^2}{H^2} \tag{13}$$

With these considerations, the pressure field for the flow can be determined, and from this, the dynamic coefficients. As previously stated, only the uncavitated SFD is treated here so that the effect of inertia on the fluid film forces can be clearly isolated. Otherwise, the extent of the cavitated region depends on the Reynolds number and the dynamic coefficients must be determined numerically for each change in the inertia parameter.

Integration of equations (8) and (9), subject to the continuity condition for the pressure field, is relatively easy and is given in [8]. The dynamic coefficients for the long SFD with laminar flow come to be:

$$\bar{C}_{rt}=\bar{D}_{tr}=0,\ \bar{C}_{tt}=\frac{24\pi}{(2+\epsilon^2)(1-\epsilon^2)^{1/2}} \tag{14}$$

Note that the direct damping coefficient $\bar{C}_{tt}$ is the same as in the inertialess solution. Analytical expressions for the direct inertia coefficient $\bar{D}_{rr}$ are given in Table 1. Figure 3 shows a comparison of this coefficient for the different cases considered. The behavior of the inertia coefficient $\bar{D}_{rr}$ divided by Re is surprisingly similar for the large range of Reynolds number considered. The largest difference occurs at small and large eccentricities but is never more than 20% (between Re = 0 and Re = ∞). The rapid decrease of the inertia coefficient as the eccentricity ratio grows larger appears to contradict the recent results presented in [9]. The reason for the discrepancy is that in the MTI study only temporal effects were accounted for in the equation of motion while here both the convective and temporal inertia terms are retained. The upper dashed curve in Fig. 3 shows the inertia coefficient when only the temporal effects are included.

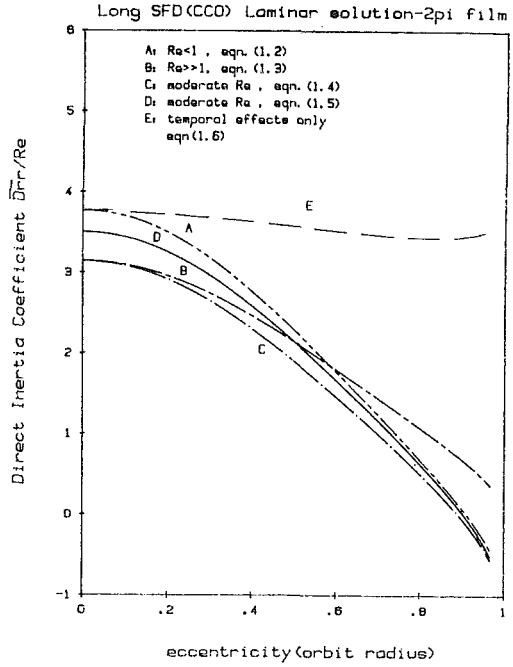

Fig. 3 Direct inertia coefficient $\bar{D}_{rr}$/Re for circular centered orbits: laminar flow; long SFD assumption

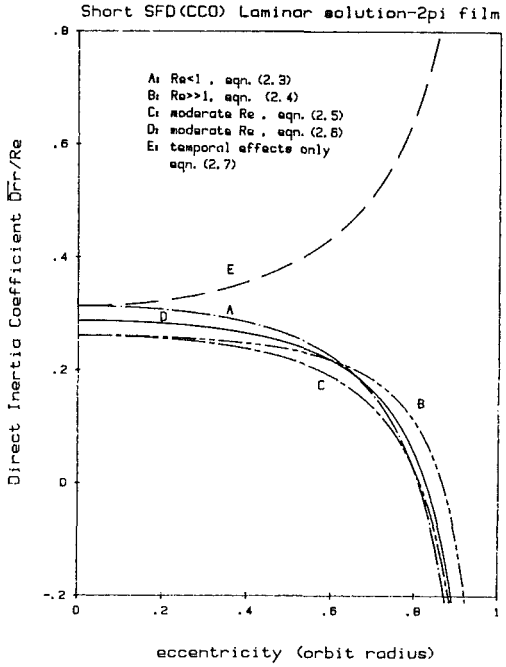

Fig. 4 Direct inertia coefficient $\bar{D}_{rr}$/Re for circular centered orbits: laminar flow; short SFD assumption

Short Bearing Assumption. In this section we assume that the SFD has small L/D ratios, the ends are open to the at-

Table 2 Direct inertia coefficient $\bar{D}_{rr}$ for the short squeeze film damper

$\bar{D}_{rr}/\mathrm{Re} = -\Gamma[C_1 + C_2(\beta - 1)]$

Definitions: $\beta = (1-\epsilon^2)^{1/2}$

$$\Gamma = \frac{\pi(\beta-1)}{6\beta\epsilon^2}$$

Re	C_1	C_2	
small Re $\ll 1$	1.2	102/35	(2.3)
large Re $\gg 1$	1.0	2.0	(2.4)
moderate $f_\xi = 0$	1.0	2.4	(2.5)
moderate f_ξ from equation (19)	1.1	2(1.2+4/35)	(2.6)
temporal effects only, Re $\ll 1$	1.2	0	(2.7)

mosphere, and for simplicity we also assume that no high externally induced axial flow is present in the damper. The reason for the latter assumption is to avoid pressure boundary conditions which would require the explicit presence of the inertial parameter Re. As is current practice for the short journal bearing analysis, the circumferential flow is assumed to be negligible. We set $k = (L/b)^2$ in equations (1) to (3) and get the following set of equations:

$$q_\theta = -H \tag{15}$$

$$\frac{\partial q_\xi}{\partial \xi} = \gamma \tag{16}$$

$$H\frac{\partial \bar{p}_0}{\partial \xi} = -k_\xi \frac{q_\xi}{H^2} \tag{17}$$

$$H\frac{\partial p_i}{\partial \xi} = f_\xi + \frac{\partial q_\xi}{\partial \theta} - \frac{\alpha_3}{H}\frac{\partial}{\partial \xi}(q_\xi^2) \tag{18a}$$

The axial inertial pressure gradient obtained for small Re using a regular perturbation solution in Re is given by Tichy [3] as:

$$H\frac{\partial \bar{p}_i}{\partial \xi} = 1.2\frac{\partial q_\xi}{\partial \theta} - \frac{51}{35H}\frac{\partial}{\partial \xi}(q_\xi^2) \tag{18b}$$

Assuming the flow remains stable and laminar, for large Re the inviscid pressure gradient is given by:

$$H\frac{\partial \bar{p}_i}{\partial \xi} = \frac{\partial q_\xi}{\partial \theta} - \frac{1}{H}\frac{\partial}{\partial \xi}(q_\xi^2) \tag{18c}$$

From a quantitative comparison of equation (18*a-c*), for moderate Reynolds numbers we select the inertial contribution to the wall shear stress difference to be:

$$f_\xi = -\frac{2}{35H}\frac{\partial}{\partial \xi}(q_\xi^2) + \frac{1}{10}\frac{\partial q_\xi}{\partial \theta} \tag{19}$$

Thus, we assume that the wall shear stress difference for the short SFD approximation is given by:

$$\Delta\tau_{\xi\eta} = -k_\xi \frac{q_\xi}{H^2} - \frac{2}{35H}\frac{\partial}{\partial \xi}(q_\xi^2) + \frac{1}{10}\frac{\partial q_\xi}{\partial \theta} \tag{20}$$

With these considerations, equations (17) and (18*a-c*) are integrated to obtain the pressure field. For the full film assumption, the dynamic coefficients come to be:

$$\bar{C}_{rt} = \bar{D}_{tr} = 0,\ \bar{C}_{tt} = \frac{\pi}{(1-\epsilon^2)^{3/2}} \tag{21}$$

Note that the direct damping coefficient $\bar{C}_{tt}$ is the same as in the inertialess solution. Analytical expressions for the direct inertia coefficient $\bar{D}_{rr}$ are given in Table 2. For the different cases considered, Fig. 4 shows the inertia coefficient $\bar{D}_{rr}$ divided by Re as a function of the eccentricity. As in the long SFD case, the form of the inertia coefficient is surprisingly

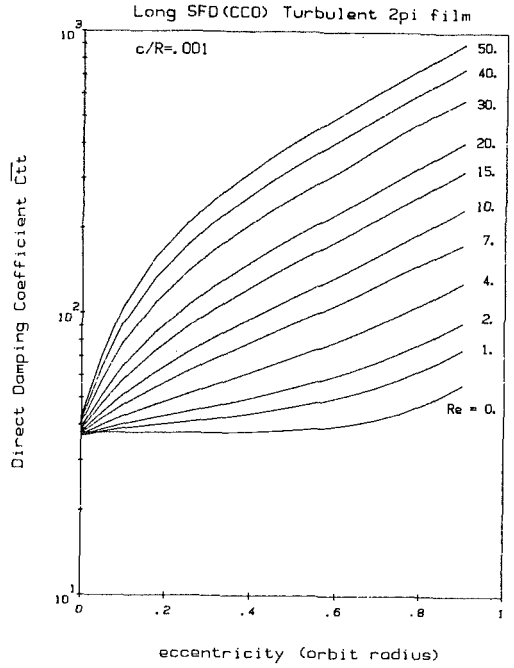

Fig. 5 Direct damping coefficient $\bar{C}_{tt}$ for circular centered orbits: long SFD assumption; turbulent flow solution

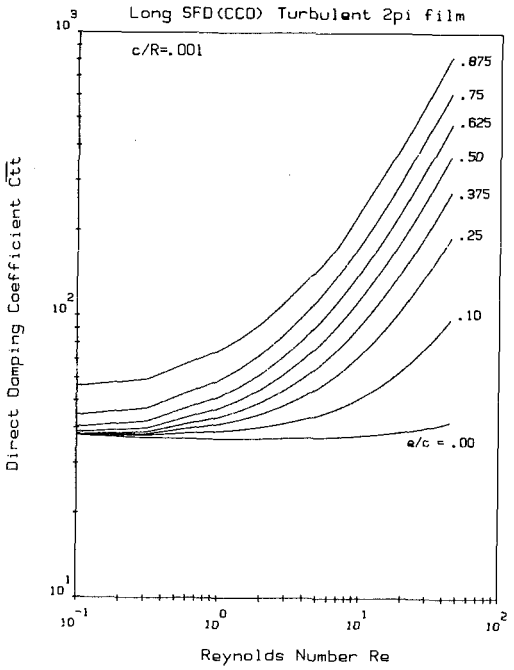

Fig. 6 Direct damping coefficient $\bar{C}_{tt}$ for circular centered orbits: long SFD assumption; turbulent flow solution

similar for the large range of squeeze Reynolds numbers considered. Note the tremendous influence that the convective inertial terms have on the coefficient when compared to the dashed curve which is based only in the inclusion of temporal effects on the equation of motion. Thus, analyses based on small perturbation about an equilibrium point are in large error compared to the exact solution, if the orbit radius is large.

Turbulent Flow Solutions

The inclusion of turbulence effects into the flow complicates the problem enormously. Although the mechanism of turbulence for fully developed Couette and Poiseuille flows has been studied extensively, both analytically and ex-

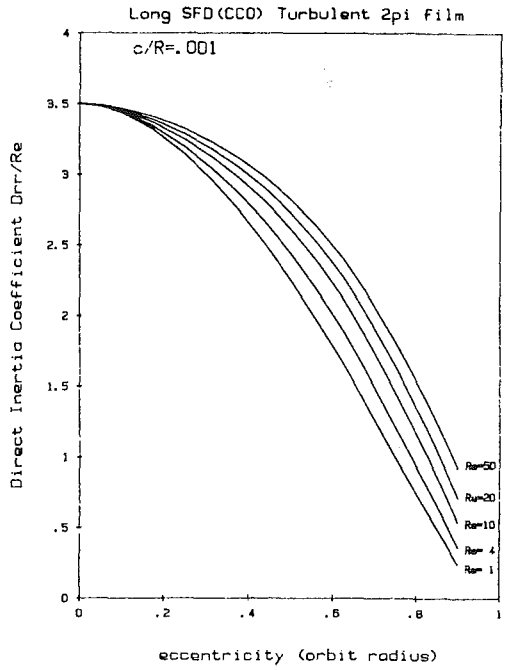

Fig. 7 Direct inertia coefficient D_{rr}/Re for circular centered orbits: long SFD assumption; turbulent flow solution

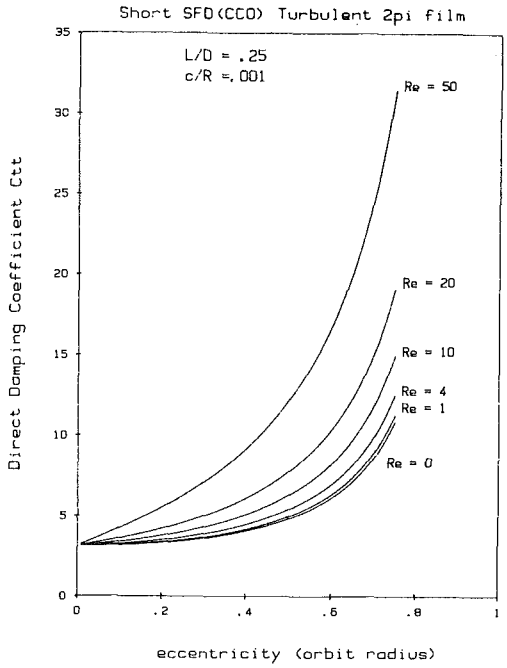

Fig. 8 Direct damping coefficient C_{tt} for circular centered orbits: short SFD assumption; turbulent flow solution

perimentally, and many contributions to the analysis of flow in narrow channels have been given in the past years; the mechanics of squeezing flows are far more complicated. The subject still remains obscure due to the complete absence of theoretical-empirical formulation and the lack of experimental results.

Undaunted, we assume that the coefficients k_θ and k_ξ to be used in turbulent flow in a SFD are given by:

$$k_\xi = k_\theta = 12 + 0.005\ \mathrm{Rep} \tag{22}$$

where

$$\mathrm{Rep} = \frac{\mathrm{Re}}{\delta} * [(q_\theta + H^2) + (L/b)^2 q_\xi^2]^{1/2} \tag{23}$$

is the Poiseuille Reynolds number currently found in the literature.

Relation (22) was obtained as the best fitting curve between the experimental correlation given by Hirs [12] and the analytical results based on the mixing length theory given by Elrod and Ng [13]. Here we have assumed that the transition from the laminar to turbulent regions in a SFD must be smooth in order to insure continuity of the flow.

The assumed expressions may be far away from the actual expressions which should be obtained from experimental results. However, we have chosen them in the absence of better empirical formulations, and the results obtained will prove to be upper bounds of the actual forces and dynamic coefficients.

Long Journal-Bearing Assumption. As in the section on long bearing assumption, the axial flow is neglected and the pressure gradient field is given by:

$$\frac{\partial \bar{p}}{\partial \theta} = -\left(12 + 0.005 \frac{\mathrm{Re}}{\delta} |H + q_\theta|\right) \frac{(H + q_\theta)}{H^3} \tag{24}$$

$$+ \frac{\mathrm{Re}}{35} \frac{\gamma}{H} \left[-7 + 46 \frac{q_\theta^2}{H^2}\right]$$

$$q_\theta = q_\theta(\epsilon, \mathrm{Re}, \delta) \tag{25}$$

Note that we have assumed that f_θ given in (12) prevails even in the turbulent regime. A very simple computer code was written to obtain the pressure field. Using numerical integration, the dynamic coefficients were calculated for an uncavitated SFD with a clearance ratio $\delta = 0.001$.

Figure 5 shows the direct damping coefficient $\bar{C}_{tt}$ as a function of the eccentricity ratio for different Re, and Fig. 6 depicts the same coefficient as a function of the Reynolds number for different orbit radius ϵ. From the figures it is evident that turbulence has a large effect on the damping coefficient, and consequently on the tangential force. This is due to the increase in the apparent viscosity of the fluid as the inertia parameter grows.

Figure 7 shows the direct inertia coefficient $\bar{D}_{rr}$/Re for various orbit radius; the pattern of the curves is the same as in Fig. 3 for moderate Reynolds numbers. It is clearly seen that the effect of turbulence is to increase the coefficient, especially at large whirling orbits, which is due to the increase in flow rate q_θ as ϵ grows in order to satisfy continuity of the pressure field.

A comparison of the results given in Figs. 5 and 7 shows that the ratio $\bar{D}_{rr}/\bar{C}_{tt}$ is less than 1/10 for all eccentricities and Reynolds numbers considered; this may be an important result since it implies that the tangential force will be larger than the purely inertial radial force.

Short Journal-Bearing Assumption. For the short SFD assumption, the axial pressure gradient equation comes to be:

$$\frac{\partial \bar{p}}{\partial \xi} = -\left(12 + 0.005 \frac{\mathrm{Re}}{\delta} (L/b) |q_\xi|\right) \frac{q_\xi}{H^3} \tag{26}$$

$$+ \frac{\mathrm{Re}}{H} \left[\frac{11}{10} \frac{\partial q_\xi}{\partial \theta} - \frac{44}{35H} \frac{\partial}{\partial \xi} q_\xi^2\right]$$

$$\frac{\partial q_\xi}{\partial \xi} = -\gamma \tag{27}$$

Assuming that there is no high axial flow externally induced into the SFD, the flow q_ξ remains unchanged from the inertialess solution. Equations (26) and (27) are amenable to closed form integration, the details of the same are omitted for brevity; it is found that the direct inertia coefficient $\bar{D}_{rr}$ is the same as given in equation (2) of Table 2.

Figure 8 shows the direct damping coefficient $\bar{C}_{tt}$ as a function of the eccentricity ratio for different values of the

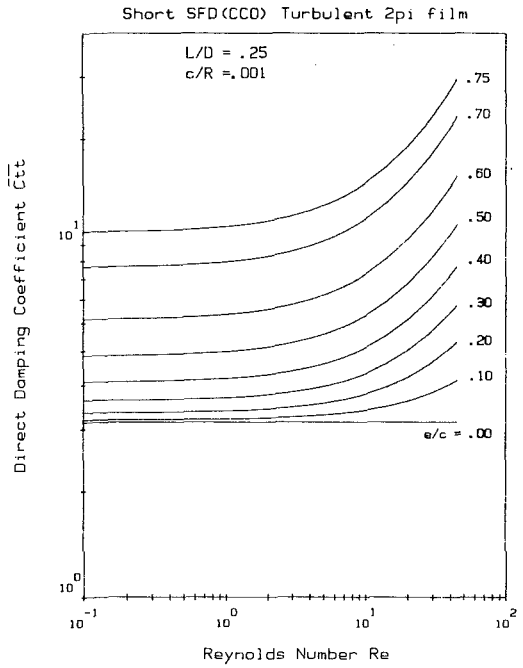

Fig. 9 Direct damping coefficient $\overline{C_{tt}}$ for circular centered orbits: short SFD assumption; turbulent flow solution

squeeze Reynolds number Re, and Fig. 9 shows the same coefficient as a function of Re for various values of the orbit radius ϵ. All calculations were made for an uncavitated SFD with a clearance ratio of $\delta = 0.001$, and an L/D ratio equal to 0.25. From the figures a significant influence of turbulence on the damping coefficient is seen. As expected, the larger the Reynolds number, the larger the dynamic coefficient and consequently the tangential force increases proportionally. Once again, this effect is due to the increase in the apparent viscosity of the fluid as the inertia parameter grows.

Summary

The present paper has considered the influence of inertia and turbulence on the flow in the annular region between a whirling damper journal, describing circular centered orbits, and its bearing. After an analysis of the fluid-flow equation for the problem, the usual assumptions considering the length of the SFD are made to obtain the classical long and short journal-bearing approximations.

The region of flow was assumed to be continuous, i.e., no cavitation was allowed in the fluid. This allowed a clear analysis of the effect of inertia and turbulence on the fluid film forces and the dynamic coefficients. The laminar solution showed the importance of the inclusion of convective inertia terms in the equations of motion. The resulting reversal of the "added mass effect" makes it clear that numerical or analytical approaches that calculate the dynamic coefficients for large motion amplitudes in base to small perturbations about an equilibrium point may be largely in error.

In the absence of empirical coefficients for the turbulent motion in squeezing flows, a friction coefficient based on the Poiseuille analysis of Hirs and Elrod and Ng was used. This may be modified by experimental results in the future, since the transition from laminar to turbulent motion may turn out to appear at larger Reynolds numbers than here considered. As suggested in [4], the values here presented should be considered as upper bounds for the actual dynamic coefficients and as qualitative indicators of the influence of turbulence on the flow. If these bounds are even approached by the real case, turbulence will be found to have a large effect on the direct damping coefficient for squeeze film dampers.

The present analysis should prove to be a stepping stone for future developments that will consider SFD's of finite extent and also the influence of inertia in the boundary conditions of the flow.

Acknowledgments

This research was supported by the Turbomachinery Research Consortium at Texas A&M University.

References

1 Modest, M. F., and Tichy, J. A., "Squeeze Film Flow in Arbitrarily Shaped Journal Bearings Subject to Oscillations," *Journal of Lubrication Technology*, July 1978, pp. 323-329.

2 Tichy, J. A., "Effects of Fluid Inertia and Viscoelasticity on Squeeze Film Bearing Forces," *ASLE Transactions*, Vol. 25, Jan. 1982, pp. 125-132.

3 Tichy, J. A., "A Simple Low Deborah Number Model for Unsteady Hydrodynamic Lubrication, Including Fluid Inertia," *Journal of Rheology*, Vol. 24, 1980, pp. 829-845.

4 Tichy, J. A., "The Effect of Fluid Inertia in Squeeze Film Damper Bearings: A Heuristic and Physical Description," ASME Paper No. 83-GT-177.

5 Reinhardt, E., and Lund, J. W., "The Influence of Fluid Inertia on the Dynamic Properties of Journal Bearings," *Journal of Lubrication Technology*, Apr. 1975, pp. 159-175.

6 Szeri, A. Z., Raimondi, A. A., and Giron-Duarte, A., "Linear Force Coefficients for Squeeze Film Dampers," *Journal of Lubrication Technology*, July 1983, pp. 326-334.

7 Brindley, J., Elliott, L., and McKay, J. T., "Flow in a Whirling Rotor Bearing," *Journal of Applied Mechanics*, Dec. 1979, Vol. 46, pp. 767-771.

8 Szeri, A. Z., "Tribology: Friction, Lubrication and Wear," McGraw-Hill, New York, 1980, p. 40.

9 Lund, J. W., Smalley, A. J., Tecza, J. A., and Walton, J. F., "Squeeze Film Damper Technology: Part 1—Prediction of Finite Length Damper Performance," ASME Paper No. 83-GT-247.

10 San Andres, A., "Flow in a Journal Bearing Subject to Arbitrary Motions," Internal Report, Turbomachinery Labs, Mechanical Engineering Dept., Texas A&M University, Dec. 1983.

11 Nelson, C., "The Effect of Turbulence and Fluid Inertia on a Squeeze Film Damper," AIAA/SAE/ASME, 16th Joint Propulsion Conference, June 30-July 2, 1980.

12 Hirs, G. G., "A Bulk Flow Theory for Turbulence in Lubricant Films," *ASME Journal of Lubrication Technology*, Apr. 1973, pp. 137-146.

13 Elrod, H. G., and Ng, C. W., "A Theory for Turbulent Fluid Films and Its Applications to Bearings," *ASME Journal of Lubrication Technology*, July 1967, pp. 346-362.

APPENDIX A

Coordinate System and Equations of Motion

Consider two circular cylinders of radii a and b ($> a$) and assume that the center of the smaller cylinder rotates with constant angular velocity ω in a circle of radius e about the center of the larger one. The condition that the cylinders do not touch is:

$$0 \le \epsilon < 1 \tag{A.1}$$

$$\text{where} \quad \delta = \frac{b-a}{b} \ll 1, \; \epsilon = \frac{e}{(b-a)} \tag{A.2}$$

Here δ and ϵ are the clearance and eccentricity ratios, respectively.

The first characteristic of the geometry of lubricant films that permits simplification of the problem is that the thickness of the lubricant film, h, is very small compared to its length or to its radius of curvature. As consequences of this the following assumptions are made [8]:

1 The effects of the curvature of the film are negligible.
2 The variation of the pressure across the film is small and may be neglected.
3 The rate of change of any velocity component along the film is small when compared to the rate of change of this same velocity component across the film and can be neglected.

In accordance with assumption (1), we can prescribe a fixed orthogonal cartesian coordinate frame $\{x_i^*\}^3_{i=1}$ in the plane of the lubricant film. See Fig. 1, where the y^* axis is in the

direction of the minimum film dimension. A moving orthogonal coordinate frame $\{x_i\}^3_{i=1}$ translating with velocity $T = b\omega$ with respect to $\{x_i^*\}^3_{i=1}$ and its x axis perpendicular to the line joining the centers of both cylinders is introduced, and it can be shown that the flow will be steady to an observer moving with the $\{x_i\}^3_{i=1}$ frame.

The following dimensionless coordinates are introduced:

$$\theta = \frac{x}{b}, \quad \xi = \frac{z}{L}, \quad \eta = \frac{y}{h}, \quad \tau = t\omega, \quad \theta^* = \frac{x^*}{b} = \theta + \tau \tag{A.3}$$

where $h = b\delta H(\theta), H(\theta) = 1 + \epsilon\cos\theta$ (A.4)

is the lubricant film thickness at location θ.

Dimensionless velocity components in the two coordinate frames are defined as:

$$\bar{u}^* = \frac{u^*}{b\omega}, \quad \bar{v}^* = \frac{v}{\delta b\omega} = \bar{v}, \quad \bar{w}^* = \frac{w^*}{L\omega} = \bar{w}, \quad \bar{u} = \frac{u}{b\omega} \tag{A.5}$$

$$\bar{u}^* = \bar{u} + 1$$

The pressure and the shear stresses are made dimensionless according to

$$\bar{p} = \frac{(p - pa)\delta^2}{\omega\mu} k^{-1}, \quad \tau_{\theta\eta} = \frac{\tau_{xy}}{\omega\mu/\delta}, \quad \tau_{\xi\eta} = \frac{\tau_{zy}}{\omega\mu/\delta}(b/L) \tag{A.6}$$

and $k = 1$ for long-bearing assumption

$$k = (L/b)^2 \text{ for short-bearing assumption} \tag{A.7}$$

With these considerations, the momentum and continuity equations for the tridimensional flow expressed in the moving coordinate system are:

$$\mathrm{Re}\left\{\frac{\partial\bar{u}^2}{\partial\theta} + \frac{1}{H}\frac{\partial}{\partial\eta}[\bar{u}\bar{v} - \eta\gamma\bar{u}^2] + \frac{\gamma\bar{u}^2}{H} + \frac{\partial}{\partial\xi}(\bar{u}\bar{w})\right\} = -k\frac{\partial\bar{p}}{\partial\theta} + \frac{1}{H}\frac{\partial}{\partial\eta}\tau_{\theta\eta} \tag{A.8}$$

$$\mathrm{Re}\left\{\frac{\partial\bar{w}^2}{\partial\xi} + \frac{1}{H}\frac{\partial}{\partial\eta}[\bar{w}\bar{v} - \eta\gamma\bar{w}\bar{u}] + \frac{\bar{u}\bar{w}}{H} + \frac{\partial}{\partial\theta}(\bar{u}\bar{w})\right\} = -k\left(\frac{b}{L}\right)^2\frac{\partial\bar{p}}{\partial\xi} + \frac{1}{H}\frac{\partial}{\partial\eta}\tau_{\xi\eta} \tag{A.9}$$

$$\frac{\partial\bar{u}}{\partial\theta} + \frac{1}{H}\frac{\partial}{\partial\eta}[\bar{v} - \eta\gamma\bar{u}] + \frac{\gamma\bar{u}}{H} + \frac{\partial\bar{w}}{\partial\xi} = 0 \tag{A.10}$$

where $\gamma = \partial H/\partial\theta$ and

$$\mathrm{Re} = \frac{\omega\delta^2}{\nu}b^2 \tag{A.11}$$

is the squeeze Reynolds number.

The boundary conditions appropriate for the flow are:

$$\text{at} \quad \eta = 0 \qquad \bar{u} = -1, \ \bar{v} = \bar{w} = 0$$
$$\eta = 1 \qquad \bar{u} = -1, \ \bar{v} = -\gamma, \ \bar{w} = 0 \tag{A.12}$$

(note that we have neglected the velocity comonent due to the motion of the surface $\eta = 1$ in the θ direction since it is of order δ).

The pressure must satisfy appropriate conditions at the ends of the SFD and must be single valued and periodic in the circumferential direction, i.e.

$$\oint \frac{\partial\bar{p}}{\partial\theta}d\theta = 0 \tag{A.13}$$

Equations (A.8) to (A.10) are integrated across the film to obtain:

$$\mathrm{Re}\left\{\frac{\partial}{\partial\theta}I_{\theta\theta} + \frac{\partial}{\partial\xi}I_{\theta\xi}\right\} = -kH\frac{\partial\bar{p}}{\partial\theta} + \Delta\tau_{\theta\eta} \tag{A.14}$$

$$\mathrm{Re}\left\{\frac{\partial}{\partial\theta}I_{\theta\xi} + \frac{\partial}{\partial\xi}I_{\xi\xi}\right\} = -kH(b/L)^2\frac{\partial\bar{p}}{\partial\xi} + \Delta\tau_{\xi\eta} \tag{A.15}$$

$$\frac{\partial}{\partial\theta}q_\theta + \frac{\partial}{\partial\xi}q_\xi = 0 \tag{A.16}$$

where q_θ and q_ξ are the dimensionless local flow rates in the θ and ξ directions,

$$q_\theta = H\int_0^1 \bar{u}d\eta = H\,\bar{u}_m \tag{A.17a}$$

$$q_\xi = H\int_0^1 \bar{w}d\eta = H\,\bar{w}_m \tag{A.17b}$$

and the I_{ij}'s are defined as:

$$I_{ij} = H\int_0^1 \bar{u}_i\bar{u}_j d\eta \tag{A.18}$$

To proceed, further assumptions about the velocity distribution should be made. To this end we assume that the shape of the velocity field is not greatly affected by inertia, and we let the velocity momentum integrals in (A.18) be given by

$$I_{\theta\theta} = \alpha_1 q_\theta^2/H + 0.4\,q_\theta + 0.2\,H$$
$$I_{\theta\xi} = \alpha_2 q_\theta q_\xi/H + 0.2\,q_\xi \tag{A.19}$$
$$I_{\xi\xi} = \alpha_3 q_\xi^2/H$$

For the type of flow considered, the range of variation of the coefficients $\{\alpha_i\}^3_{i=1}$ is between 1.2 and 1.0 for small Reynolds numbers and large Reynolds numbers, respectively; thus it may be assumed that averaged values will suffice to obtain meaningful results.

A Model for the Prediction of Thermal, Prompt, and Fuel NO_x Emissions From Combustion Turbines

J. L. Toof[1]
Senior Engineer.
Westinghouse Electric Corporation,
Concordville, Pa. 19331

A model has been developed for the prediction of NO_x emissions from combustion turbines. Thermal, prompt, and fuel NO are all treated and are all assumed to be formed at a stoichiometric equivalence ratio. Prompt and fuel NO are assumed to be fast with respect to thermal NO and establish a finite concentration of NO at the beginning of the thermal NO formation process. Thermal NO is calculated via the extended Zeldovich mechanism; a thermal NO formation time is determined from the ratio of flame length to convective velocity within the combustor. Prompt NO is assumed to be formed from the hydrocarbon chemistry and is related to the equilibrium concentration of NO rather than to O-atom overshoot. Fuel NO is calculated assuming an indispensible intermediate in the formation mechanism and a constant Fenimore α parameter for combustion turbine flames. The model employs equilibrium hydrocarbon chemistry; the flame temperature and concentrations of key species are determined in an equilibrium subroutine. The effects of water or steam injection and ambient humidity are included through their impact on the flame temperature and species concentrations. The model has been applied to can-type combustors and its accuracy has been verified by data on high and low nitrogen fuels with and without water injection, and on combustors of different geometry. The treatment of all three mechanisms of NO formation is unique to this model and permits prediction of emissions for the range of conventional and alternative fuels encountered in industrial combustion turbines.

Introduction

The oxides of nitrogen (NO_x) have been recognized as important atmospheric pollutants for the past fifteen years. During this period, emissions limits have been legislated and much effort has been devoted to understanding the mechanisms of NO_x formation and developing technology for emissions abatement. Three important formation mechanisms have been identified (thermal, prompt, and fuel NO) and each has its own characteristics.

The chemical and physical processes determining the rate of NO_x formation in combustors are: (*i*) atomization and vaporization of liquid fuel, (*ii*) turbulent mixing of fuel, air and combustion products, (*iii*) chemical kinetics of fuel oxidation, and (*iv*) chemical kinetics of NO formation [1]. These complex processes and their interactions are not yet fully understood.

When the fuel is gaseous, atomization and vaporization are not involved. However, when the fuel is liquid, spray dynamics and evaporation can influence NO_x emissions. If the droplets are far apart, they burn as individuals, each surrounded by its own envelope flame. If they are close together, which is commonly the case in combustors, they form a vapor cloud with combustion taking place at the edges of the cloud. A wide distribution of droplet sizes occurs in practical sprays with droplet trajectories varying with size. Rates of vaporization depend on whether drops are traversing regions of air, fuel vapor, or combustion products [2].

In large industrial combustors, turbulent mixing rates typically have a much greater influence on NO_x emissions than do spray characteristics. The mixing process, which is induced by air jets penetrating into the combustor, can be divided into two stages: macromixing and micromixing. Macromixing occurs on a large scale in shear layers via coalescence of adjacent vortices and simultaneous engulfment of the surrounding fluid [3]. Micromixing occurs on a smaller scale as concentration nonuniformities within the coalesced vortices are dissipated by turbulence. Mixing rates are very important in thermal NO formation since they determine time at temperature.

Because of the relative rates of reaction, chemical kinetics of fuel oxidation are not important in thermal NO formation but can be important in prompt and fuel NO formation. Combustion, prompt NO, and fuel NO all occur on about the same time scale; thermal NO is much slower. Details of

[1] Current address: Senior Project Engineer, Allison Gas Turbine Division, General Motors Corporation, Indianapolis, IN 46206-0420.

Contributed by the Gas Turbine Division of THE AMERICAN SOCIETY OF MECHANICAL ENGINEERS and presented at the 30th International Gas Turbine Conference and Exhibit, Houston, Texas, March 18–21, 1985. Manuscript received at ASME Headquarters December 18, 1984. Paper No. 85-GT-29.

Table 1 Level of treatment in previous combustor NO_x models

		THERMAL NO	PROMPT* NO	FUEL NO	HYDROCARBON KINETICS	FUEL INJECTION	FLUID MECHANICS
Empirical Correlations	[5]	X					
Flame Temperature Models	[6,7,8]	X					
Constant Residence Time	[9,10]	X	X				
Characteristic Time	[11,12,13]	X				X	
MIT Mixedness Model	[14]	X		X			X
Northern Research Mixedness Model	[15]	X					X
Westinghouse Limited Mixing Model	[16]	X		X		X	
Purdue Chemical Reactor	[17]	X			X		
Pratt & Whitney Streamtube	[18]	X			X	X	X
Coalescence/Dispersion	[19]	X			X		X
General Applied Science Modular Model	[20]	X			X	X	X
Finite Difference	[21,22]	X			X	X	X

*Via hydrocarbon fragments

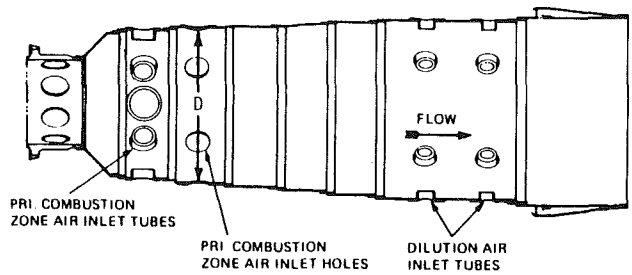

Fig. 1 Example of conventional combustor to which model is applicable

combustion reaction mechanisms are only known for simple fuels.

All the details of the kinetic mechanisms of prompt and fuel NO are not known. The mechanism of thermal NO formation is known, but there has been disagreement on the rate of the controlling reaction [4].

Due to the complexity and incomplete understanding of the processes involved, prediction of NO_x emissions based on first principles is difficult. In most cases, predictions have been based on simplifying assumptions and/or empiricism. A number of models for predicting NO_x emissions from combustors have been described in the literature. These have varied widely in their complexity, applicability, and accuracy. The length of this paper does not permit a review of these models; however, the general level of treatment for some of them is listed in Table 1. As shown, none of the models treats all three mechanisms of NO formation.

In this work the modeling of thermal, prompt, and fuel NO was considered necessary for the range of conventional and alternative fuels encountered in industrial combustion turbines. These may be liquid or gaseous, may contain nitrogen, and may require water injection for NO_x control. The modeling approach described in this paper is relatively simple, yet provided good agreement with laboratory and field NO_x data. It is applicable to conventional combustors such as that pictured in Fig. 1, but is not applicable to advanced low NO_x designs such as rich/lean, lean premixed, and catalytic.

Table 2 Rate constants for extended Zeldovich mechanism

$O + N_2 \rightarrow NO + N$	$k_1 = 1.439 \times 10^{14} * \exp(-75{,}000/RT)$	[26]
$NO + N \rightarrow O + N_2$	$k_{-1} = 3.09 \times 10^{13} * \exp(-330/RT)$	[26]
$N + O_2 \rightarrow NO + O$	$k_2 = 6.427 \times 10^{9} * T * \exp(-6250/RT)$	[26]
$NO + O \rightarrow N + O_2$	$k_{-2} = 1.45 \times 10^{9} * T * \exp(-38{,}340/RT)$	[26]
$N + OH \rightarrow NO + H$	$k_3 = 4.2 \times 10^{13}$	[27]

Units: k(cc/gm mole sec),
E(cal/gm mole),
R(cal/gm mole °K),
T(°K)

Model Formulation

A number of similarities and differences exist among the three mechanisms of nitric oxide formation. Thermal and prompt NO are formed from N_2 in air; fuel NO is formed from N atoms chemically bound in fuel. Prompt and fuel NO are weakly temperature dependent; thermal NO is strongly temperature dependent. Prompt and fuel NO reactions are rapid—about the same rate as hydrocarbon combustion and much faster than fluid mechanical mixing. Thermal NO reactions are slower.

Most fundamental research on prompt and fuel NO has been conducted in premixed flames. The reactions take place at a single equivalence ratio—prompt and fuel NO are formed in the flame front, and thermal NO is formed in the post flame region.

The situation is far more complicated in a combustor. Fuel and air are initially unmixed and react in a diffusion flame; the flow is turbulent and recirculating; if the fuel is liquid, then spray dynamics and combustion can have an influence. To simplify matters a number of assumptions were made in the formulation of the model described in this paper. These are:

1 Thermal, prompt, and fuel NO are all formed at a stoichiometric equivalence ratio. Any further addition of air dilutes the NO that has been formed. Prompt and fuel NO

Nomenclature

D = combustor diameter, cm
k = kinetic rate constant, cc/gm mole s
L = flame length, cm
P = pressure, atm
t = effective residence time, s
V = air jet velocity, cm/s
X = mole fraction, dimensionless
Y = yield of NO from fuel nitrogen, dimensionless
α = fuel nitrogen kinetic parameter, dimensionless
θ = recirculation factor, dimensionless
λ = excess air factor, dimensionless
ϕ = fuel/air equivalence ratio, dimensionless
[ ] = concentration, gm mole/cc

Subscripts

CH = hydrocarbon
eq = equilibrium
N = nitrogen
Ox = oxidant
prompt = prompt NO

reactions are assumed to be infinitely fast with respect to mixing rates and in the classical diffusion limited sense take place at $\phi = 1$. In the case of fuel NO, this assumption requires that any tendency for the fuel nitrogen kinetics to proceed on the rich side of the flame front in laminar diffusion flames is washed out at the onset of turbulence [23]. Thermal NO reactions can be as fast as, or slower than, mixing rates [1], but these reactions are strongly temperature dependent, so most thermal NO is formed at or near $\phi = 1$ with thermal NO correlating with stoichiometric flame temperature.

2 Prompt NO is formed from hydrocarbon fragments rather than superequilibrium concentrations of O atoms.

3 Fuel NO is formed through one or more indispensible nitrogen containing intermediates.

4 Prompt and fuel NO are additive.

5 Prompt and fuel NO are fast with respect to thermal NO and establish an initial NO concentration at the beginning of the thermal process.

6 Thermal NO is formed via the extended Zeldovich mechanism.

7 Large-scale mixing processes control thermal NO formation. This implies that thermal NO will scale with the combustor diameter and precludes the penetration of droplets beyond the main body of the flame [12].

8 Fuel injection characteristics are not modeled.

9 Hydrocarbon kinetics are at equilibrium during thermal NO formation.

10 The calculation of NO (nitric oxide) is sufficient for determining NO_x. NO_2 (nitrogen dioxide) is also formed in combustors; however, the route to NO_2 is through NO. Therefore, the total NO_x ($NO + NO_2$) is not affected by the amount of NO_2 formed.

Thermal NO. Thermal NO is calculated via the extended Zeldovich mechanism [24]

$$O + N_2 = NO + N \tag{1}$$

$$N + O_2 = NO + O \tag{2}$$

$$N + OH \rightarrow NO + H \tag{3}$$

Additional reactions involving NO formation from N_2O are sometimes considered but usually account for less than 1 percent of the NO formed and are not included here.

Assuming a steady-state concentration of N and H atoms, the rate of NO formation becomes [25]

$$\frac{d[NO]}{dt} = 2k_1[O]\left(\frac{[N_2] - k_{-1}k_{-2}[NO]^2/k_1k_2[O_2]}{1 + k_{-1}[NO]/(k_2[O_2] + k_3[OH])}\right) \tag{4}$$

The applicable rate constants are listed in Table 2. Equation (4) is integrated by Euler's method to determine the amount of thermal NO formed. Inputs required for the integration are the pressure, temperature, residence time, and initial concentrations of N_2, O_2, O, OH and NO. The pressure is known. The stoichiometric flame temperature and concentrations of all species other than NO are calculated in an equilibrium subroutine. The initial concentration of NO is the sum of prompt and fuel NO. The interference of this initial concentration on thermal NO formation is manifested through the reverse of equations (1) and (2).

The effective residence time for thermal NO formation in a flowing system is determined from the ratio of a characteristic length to a characteristic velocity in the combustor.

$$t \propto \frac{L}{V} \tag{5}$$

This approach is similar to that taken in [11, 12, 13]; however, the length and velocity scales are determined differently here. The characteristic length is taken to be the flame length. In a classical free turbulent diffusion flame, it is proportional to the diameter of the fuel jet. However, Lenze [28] has shown that the length of an enclosed turbulent diffusion flame is also a function of recirculation and excess air. The characteristic flame length can then be expressed as

$$L \propto D * f(\lambda) * f(\theta) \tag{6}$$

where D is the diameter of the combustor, and $f(\lambda)$ and $f(\theta)$ are functions of excess air and recirculation, respectively.

The recirculation factor was removed from the model after it was found to produce negligible change in the flame length over the range of recirculation normally encountered in combustors.

When Lenze's expression for the excess air factor is substituted, the flame length becomes

$$L \propto \frac{D}{0.5 + 0.22(\lambda - 1)} \tag{7}$$

where λ is the percent theoretical air divided by 100 and is limited to a maximum value of 3.5.

Likely candidates for the characteristic velocity are the bulk velocity in the combustor or the air jet velocity entering the combustor. Both were tried and better correlation with NO_x data was obtained using the jet velocity which was incorporated into the model. This implies that thermal NO formation in combustors is primarily controlled by eddy lifetimes rather than bulk residence times. This should hold as long as enough air is introduced into the primary zone for all the fuel to mix through stoichiometric without subsequent dwell near a stoichiometric mixture. Other models [14, 19] have used the power of the air jets to determine mixing rates and, consequently, the time available for NO formation.

When equations (5) and (7) are combined, the effective residence time becomes

$$t \propto \frac{D}{V(0.5 + 0.22[\lambda - 1])} \tag{8}$$

When the model was calibrated against clean fuel data, the proportionality constant was found to be 0.161. Therefore

$$t = \frac{0.161\,D}{V(0.5 + 0.22[\lambda - 1])} \tag{9}$$

As λ approaches its maximum value of 3.5 for lean flames, the excess air factor, $1/(0.5 + 0.22\,[\lambda - 1])$, approaches unity. In addition, since the real physical time in the flame is represented by D/V, the proportionality constant in equation (9) can somewhat loosely be considered as the fraction of time that each parcel of fuel spends at or near a stoichiometric equivalence ratio as it passes through the flame.

The thermal NO residence time is a function of combustor diameter, air jet velocity, and stoichiometry in the primary zone. As shown in Fig. 1, the diameter is taken at the second row of primary zone air admission holes, and the primary zone stoichiometry is determined by all air (swirler, cooling and jet) entering up to and including the second row of holes.

"British" style combustors, like that pictured in Fig. 1, are typically quite fuel lean before the dilution zone. For that reason, the influence of the dilution jets has not been modeled here. "American" style combustors with several rows of closely spaced holes have not as yet been modeled and might require the inclusion of more than two rows as primary air. Annular combustors have not been modeled but could be treated by replacing the combustor diameter with the annular height between the liner walls. A change in the proportionality constant in equation (9) might also be required. For the combustors and operating conditions modeled so far, equation (9) yields an effective thermal NO residence time in the range of 0.4 to 0.8 ms.

Prompt NO. The existence of prompt NO was first reported by Fenimore [29]. He measured the buildup of NO in premixed ethylene–air flames as a function of time (distance) from the flame front. Extrapolation of the data to time equals

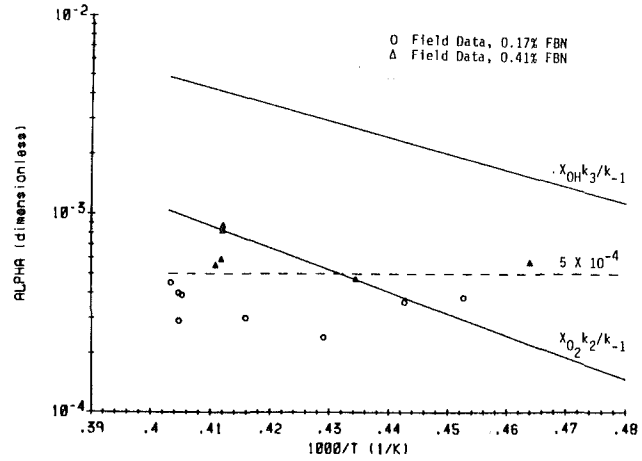

Fig. 2 Alpha parameter calculated from field data and from equation (18)

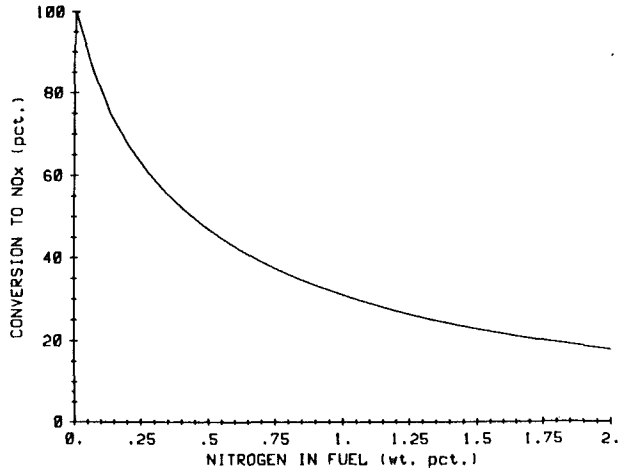

Fig. 3 Calculated yield of NO from fuel nitrogen with $\phi = 1$ and $\alpha = 5 \times 10^{-4}$

zero revealed positive intercepts on the NO axis. This was attributed to some rapid non-Zeldovich mechanism ocurring in the flame front. Reactions involving hydrocarbon fragments and atmospheric nitrogen are believed to be a source of nitrogen-containing radicals, which are subsequently oxidized to form NO. These include the following

$$CH + N_2 \rightarrow HCN + N \tag{10}$$

$$CH_2 + N_2 \rightarrow HCN + NH \tag{11}$$

Others [30, 31, 32] suggested that prompt NO could be explained by the Zeldovich mechanism and superequilibrium concentrations of O and OH in the flame front. However, it has been shown that superequilibrium concentrations cannot account for all the NO formed [33]. The time available in the flame front is too short for the slow Zeldovich mechanism. In addition, prompt NO has only been observed in hydrocarbon flames (never in CO or H_2 flames), which provides additional support for the hydrocarbon mechanism.

By assuming that prompt NO was formed at a stoichiometric equivalence ratio in the turbulent diffusion flames of combustors, Fenimore estimated that prompt NO was responsible for 30 percent of the NO_x emissions from combustion turbines [29]. Based on Fenimore's results, prompt NO formation was correlated as [34]

$$[NO]_{prompt} = f(\phi) P^{1/2} [NO]_{eq} \tag{12}$$

In this equation, $f(\phi)$ is an empirical function of equivalence ratio with a value of 0.016 for stoichiometric mixtures, P is the pressure in atmospheres, and $[NO]_{eq}$ is the equilibrium concentration of nitric oxide. Shaw [9] used this correlation plus a thermal NO calculation to successfully predict NO_x emissions from water-injected combustion turbines.

A slight modification is made to equation (12) for use in the model reported here. The right side of the equation is multiplied by the mole fraction of hydrocarbon in the fuel to approximate prompt NO when mixtures of hydrocarbon and non-hydrocarbon gaseous fuels are burned. Equation (12) then becomes:

$$[NO]_{prompt} = X_{CH} f(\phi) P^{1/2} [NO]_{eq} \tag{13}$$

X_{CH} is equal to 1 for gaseous and liquid hydrocarbon fuels.

Fuel NO. When fuels are doped with compounds containing elemental nitrogen, the concentration of NO in flames increases. A fraction of the fuel nitrogen is converted to NO in the flame front. Tests in premixed flames have shown that this conversion fraction decreases with increasing amounts of fuel nitrogen and with increasing equivalence ratio.

The gross characteristics of the reaction mechanism for fuel NO_x formation can be repesented as [35]

$$\text{fuel-N} \longrightarrow \text{HCN} \longrightarrow \text{NH}_i \begin{cases} \xrightarrow{+\text{Oxidant}} \text{NO} \\ \xrightarrow{+\text{NO}} \text{N}_2 \end{cases} \tag{14}$$

The mechanism begins with the pyrolysis of nitrogen-containing fuel to form hydrogen cyanide. Amine species are subsequently formed and are in turn oxidized to NO. Once some NO has been created it can react directly with the amine pool to form molecular nitrogen. The fraction of fuel nitrogen converted to NO depends on the relative rates of the two parallel paths at the end of the reaction scheme

$$NH_i + Ox \xrightarrow{k_{15}} NO + \ldots \tag{15}$$

$$NH_i + NO \xrightarrow{k_{16}} N_2 + \ldots \tag{16}$$

By assuming that the NH_i species is a necessary intermediate in the mechanism, Fenimore derived an expression for the conversion fraction or yield of NO from the fuel nitrogen [36]

$$Y = \frac{1 - \exp\left(\dfrac{-X_N}{2\alpha}(Y+1)\right)}{X_N/\alpha} \tag{17}$$

where X_N is the mole fraction of NO in the burnt gas if all of the fuel-N were converted and

$$\alpha = \frac{k_{15}}{k_{16}} X_{Ox} \tag{18}$$

X_N and X_{Ox} are expressed here as mole fractions so that α is dimensionless. The yield defined by equation (17) pertains to the flame front before the formation of thermal NO and is not the more commonly used definition that is applied to the exhaust. The significance of this will be discussed later.

Various species have been proposed as the nitrogen intermediate and oxidant in equations (15) and (16), for example [35, 37]. Two combinations that were investigated during the formulation of this model are N, O_2 and N, OH. In the first case, α becomes $X_{O_2} k_2/k_{-1}$, and in the second case $X_{OH}\, k_3/k_{-1}$, where the rate constants are those of equations (1-3). These two expressions are plotted as the two solid lines in Fig. 2 and are for stoichiometric mixtures of a typical distillate fuel and air at equilibrium. The temperature was varied by varying the water injection rate. Also plotted in Fig. 2 are symbols representing values of α determined from a

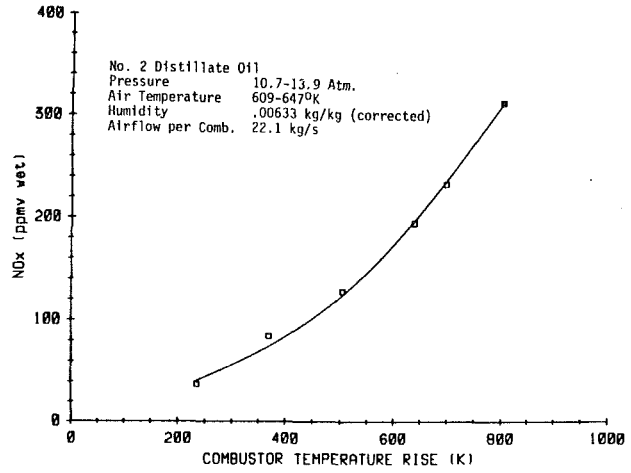

Fig. 4 Comparison of predicted and measured NO_x for a laboratory test of a 31.1-cm-dia combustor

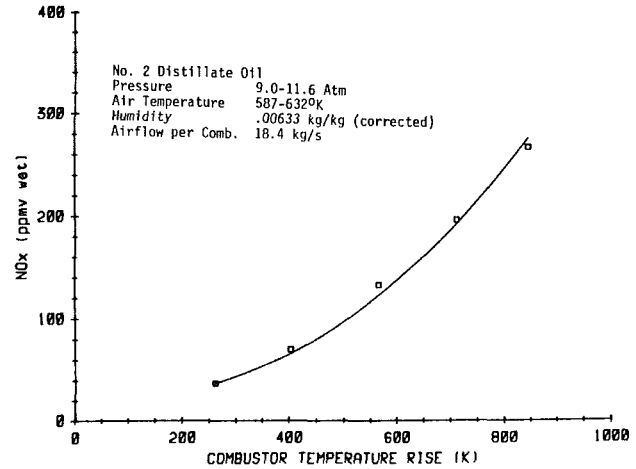

Fig. 5 Comparison of predicted and measured NO_x for a laboratory test of a 25.2-cm-dia combustor

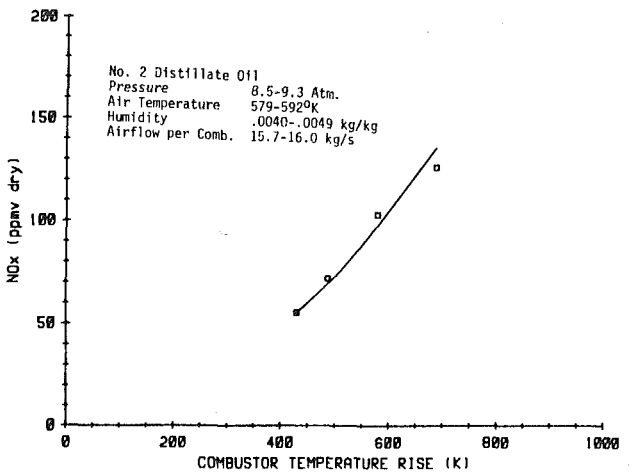

Fig. 6 Comparison of predicted and measured NO_x for a field test of a 25-MW engine burning No. 2 distillate oil

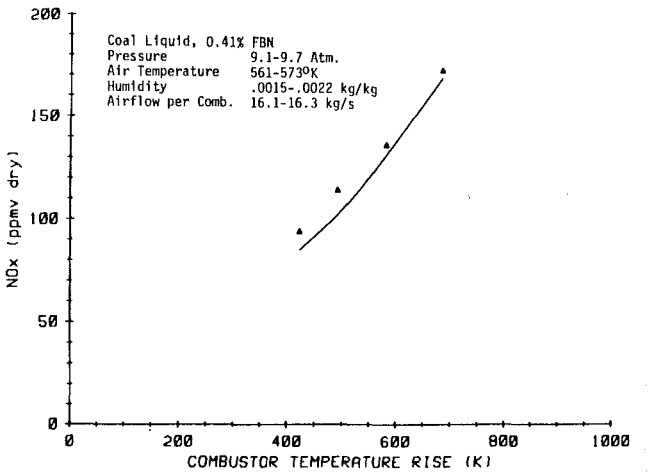

Fig. 7 Comparison of predicted and measured NO_x for a field test of a 25-MW engine burning a coal liquid with 0.41 weight percent nitrogen

field test of two coal liquids in a 25-MW combustion turbine. The two fuels had 0.41 and 0.17 percent by weight bound nitrogen. To calculate these values of α, the model was first calibrated for thermal NO formation on clean fuels as described earlier. This permitted a determination of the amount of fuel NO in the total measured NO_x and, therefore, the yield. Then α was calculated using equation (17) and the assumption that fuel NO is formed at a stoichiometric equivalence ratio.

Figure 2 shows that agreement between the field values and the N, O_2 combination was fair, while agreement with the N, OH combination was relatively poor. However, it also shows that the field values are scattered about a constant value of 5×10^{-4}. This perhaps indicates that a single nitrogen intermediate and a single oxidizing species are not sufficient to describe the fuel-N conversion process. Whatever the reason, based on the field data and until the fuel NO mechanism is better understood, a constant value of 5×10^{-4} for α has been incorporated into the model rather than equation (18). The resulting NO_x predictions and the field NO_x data are compared in the next section.

If a constant value is used in the model for α, the stoichiometry becomes relatively unimportant. This means that another equivalence ratio, such as 1.25, could have been adopted along with a constant α of 6.5×10^{-4} with nearly the same results. The larger value for α is needed to offset the larger value of X_N in richer products. In addition, oxidant concentrations are lower in rich gases, which would move the solid lines in Fig. 2 downward, resulting in better agreement of the field data with the N, OH combination rather than N, O_2. However, based on data showing equivalent fuel-N yields in stoichiometric premixed flames and overventilated turbulent diffusion flames [38], the $\phi = 1$ assumption for fuel-N conversion was maintained in the model. Calculated yields for $\phi = 1$ and $\alpha = 5 \times 10^{-4}$ are plotted in Fig. 3 as a function of nitrogen content in the fuel.

Model Verification

During formulation of the model, NO_x predictions were compared to various laboratory and field test data. The results are presented in this section. On all graphs the model predictions are indicated by solid lines and the data by symbols. Combustor geometries and fuel properties are listed in Tables 3 and 4. NO_x data were measured with a Thermo Electron (TECO) Model 10AR chemiluminescence meter with an accuracy of ± 1 percent of full scale. Depending on the magnitude of individual measurements, full scale was 100, 250 or 1000 ppmv. The accuracy of the calibration gas was ± 2 percent.

Figure 4 shows predicted and measured NO_x for a laboratory test of a 31.1-cm-dia combustor. The fuel was No. 2 distillate oil and the nominal base load pressure ratio was 14:1. These data were used to calibrate the thermal NO residence time constant (as described earlier), and good agreement can be expected between predicted and measured values. It is interesting to note that the characteristic upward concavity of the curve could not entirely be accounted for by the increases in pressure and inlet air temperature as load (combustor temperature rise) is increased. Modification of the flame length, and consequently the effective thermal NO

Table 3 Combustor diameter and flow areas for laboratory and field tests

	Figures 2,6,7,8,9	Figure 4	Figure 5
Diameter (cm)	24.9	31.1	25.2
Effective Flow Area (cm^2)	267.7	255.7	276.9
Primary Air (%)	45.0	56.9	51.7

Table 4 Fuel properties

	No. 2 Oil	Coal Liquid 0.17% N	Coal Liquid 0.41% N
Composition (Wt.%)			
Carbon	87.25	88.66	86.35
Hydrogen	12.74	10.03	10.48
Oxygen	---	1.11	2.75
Nitrogen	.01	.17	.41
Sulfur	---	.03	.06
Lower Heating Value (kJ/kg)	42,565	40,405	38,695

residence time, by Lenze's excess air factor was also necessary.

Without making any changes in the model, predictions were made for the laboratory test of a different combustor. The diameter of this combustor was 25.2 cm and its airflow distribution was slightly different. The fuel was the same but the nominal base load pressure ratio was 12:1 in this case. Figure 5 shows that agreement was again good.

Figures 6–9 plot predicted and measured NO_x for a field test of a 25-MW combustion turbine, performed with the support of the Electric Power Research Institute [39]. Three fuels were burned: No. 2 oil and two coal liquids with 0.41 and 0.17 percent (by weight) nitrogen. The nominal pressure ratio was 10:1, the burner outlet temperature at base load was approximately 1260 K, and the combustors had a somewhat smaller percentage of primary air than the previous combustors modeled.

Figure 6 shows that No. 2 oil predictions are still good with this combustor and the lower pressure ratio. The absolute NO_x level is lower here than in Figs. 4 and 5 due to the difference in pressure ratio.

Figures 7 and 8 demonstrate the agreement obtained between predicted and measured NO_x with the constant value of 5×10^{-4} for the α parameter in the fuel NO calculation. The absolute NO_x levels of the two coal liquids are about the same because the stoichiometric flame temperature of the fuel with less nitrogen is higher and more thermal NO is formed.

The datum point at the highest load in Fig. 8 looks suspiciously low. This was carried over into Fig. 9, which shows the effect of water injection at base load for all three fuels. Agreement is good except for the 0.17 weight percent nitrogen fuel at low injection rates. At high injection rates the bulk of the NO_x with the coal liquids is fuel NO and a separation in the absolute levels occurs after reduction of the thermal NO. With the oil fuel, agreement is good between predictions and data at water injection rates from 0.0 to 1.2 kg per kg of fuel. Although no measurements were made in the flame, it appears that the model is accurately predicting both thermal and prompt NO, since most of the NO is thermal at zero injection while most is prompt at the high injection rates. Thermal NO is much more sensitive to water injection than is prompt NO, a point that will be discussed further in the next section.

Discussion

In this section, model predictions are used to illustrate some

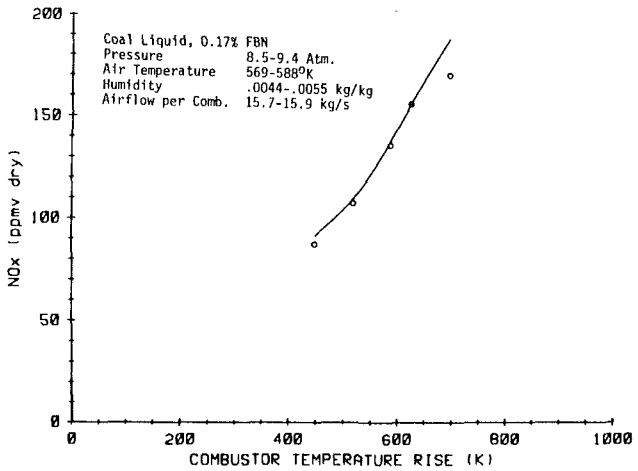

Fig. 8 Comparison of predicted and measured NO_x for a field test of a 25-MW engine burning coal liquid with 0.17 weight percent nitrogen

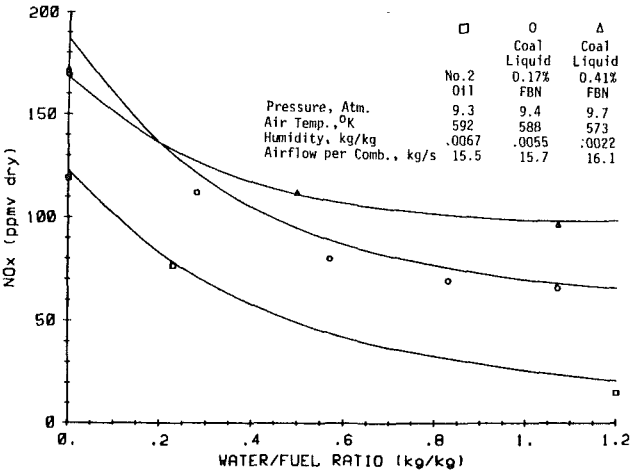

Fig. 9 Comparison of predicted and measured NO_x for a field test of a 25-MW engine with water injection, base load

of the relationships among thermal, prompt, and fuel NO and to discuss the implications of these relationships. In all cases the fuel is No. 2 distillate oil with varying amounts of water injection or added nitrogen. Burner outlet temperature is 1450 K in Figs. 10–13, and 1255 K in Fig. 14. In the figures, the vertical distance between lines represents the individual contributions of thermal, prompt, and fuel NO to the total NO_x level.

Figure 10 indicates what happens to thermal and prompt NO when water is injected with a nitrogen free fuel. At zero water injection, most of the NO is thermal. The situation is reversed at high injection rates where most of the NO is prompt. Thermal NO is a strong function of flame temperature and is greatly reduced with water injection. Prompt NO varies with the stoichiometric equilibrium concentration of NO which displays much less reduction with water injection. Figure 10 illustrates the rapidly diminishing returns of injecting more than 1 kg of water per kg of fuel because most of the remaining NO is prompt. To accurately model the effects of water injection, a prompt NO calculation must be included; a thermal NO calculation based on the Zeldovich mechanism and equilibrium hydrocarbon chemistry would predict about a 95 percent reduction rather than the 80 percent reduction shown here.

Figure 11 shows the absolute amounts of thermal, prompt, and fuel NO as the fuel nitrogen content is increased from 0 to 1 percent. Prompt NO remains constant because the equilibrium concentration of NO does not change in this case. However, thermal NO is seen to decrease as more nitrogen is

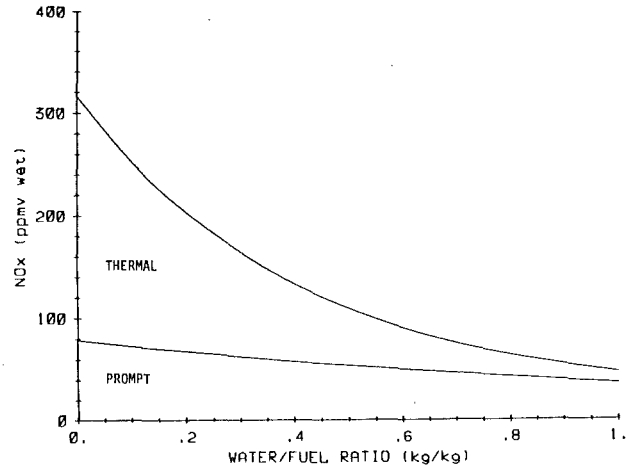

Fig. 10 Effect of water injection on thermal and prompt NO_x for a distillate fuel with zero nitrogen, pressure ratio 14:1

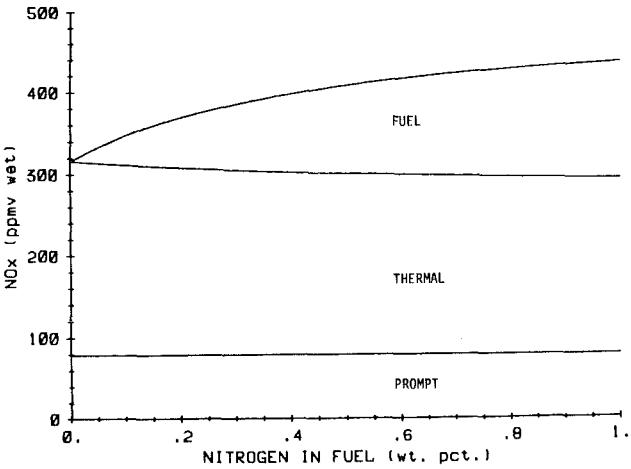

Fig. 11 Thermal, prompt, and fuel NO_x for a distillate fuel with varying amounts of added nitrogen, pressure ratio 14:1

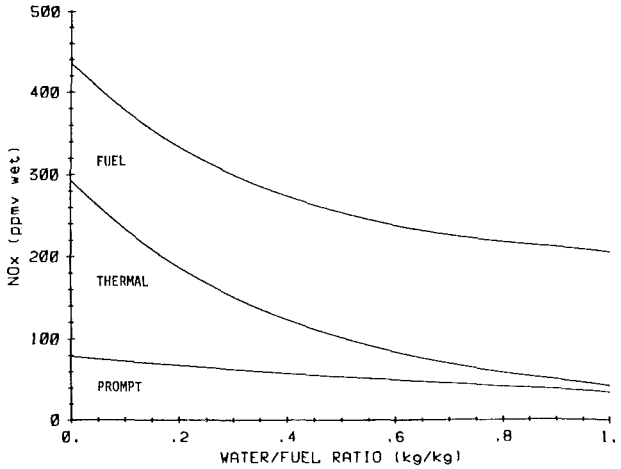

Fig. 12 Effect of water injection on thermal, prompt, and fuel NO_x for a distillate fuel with 1.0 weight percent added nitrogen, pressure ratio 14:1

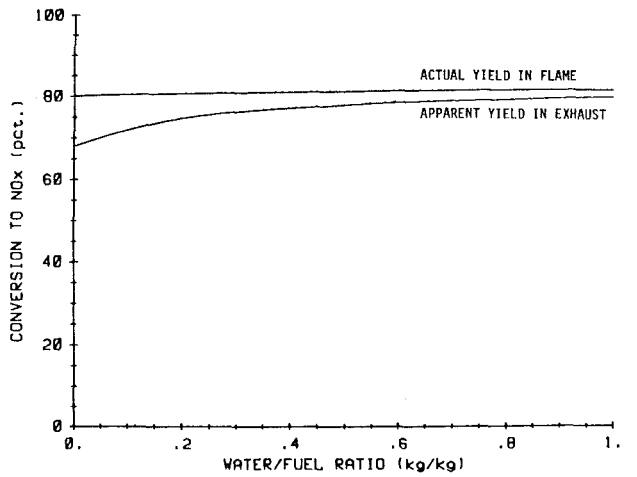

Fig. 13 Difference between the actual fuel nitrogen yield in the flame and the apparent yield in the exhaust, distillate fuel with 0.1 weight percent added nitrogen, pressure ratio 14:1

added to the fuel. This is because prompt and fuel NO are assumed to be formed before thermal NO. As fuel NO increases, thermal NO formation begins with a larger initial NO concentration and the overall rate of thermal formation is slower. This interference of fuel NO on thermal NO can be significant and should be considered when modeling.

In this model, the yield from fuel nitrogen is defined in the flame front before the formation of thermal NO. However, in most practical combustion hardware, measurements of NO in the flame front are not available and the yield is calculated from measurements made in the exhaust. The NO_x measured with a nitrogen-free baseline fuel is subtracted from that measured with a nitrogen-containing fuel to determine fuel NO. The yield is then calculated by dividing the fuel NO by the amount expected if all fuel nitrogen had converted to NO. Yields calculated in this manner will only be correct if the thermal NO formed when burning the baseline and nitrogen-containing fuels is equal. This is not the case in Fig. 11 where thermal NO is 237 ppmv at zero fuel nitrogen and 214 ppmv at 1 percent nitrogen. This difference of 23 ppmv makes the fuel NO in the exhaust appear to be 119 ppmv rather than the 142 ppmv predicted by the model. This in turn leads to an apparent 26 percent yield in the exhaust rather than the actual 31 percent yield in the flame front.

Yields calculated from measurements made in the exhaust will always be less than or equal to the actual yields in the flame. This is acceptable if the only concern is how the total exhaust NO_x emissions will change with varying fuel nitrogen content. However, if the split between fuel and thermal NO (and the processes involved) is a matter of concern, then fuel NO calculated from exhaust measurements can obscure the trends.

Figure 12 shows the effect of water injection on NO_x emissions from a fuel containing 1 percent nitrogen. As in the clean fuel case, a large reduction in thermal NO is obtained with water injection while the reduction in prompt NO is relatively small. Fuel NO is seen to increase slightly with water injection for two reasons: More fuel is required to maintain turbine inlet temperature when water is injected, and there is a slight increase in the yield of fuel nitrogen. The increase in yield is due to the diluting effect of the water in the flame, which reduces X_N in equation (17).

The discrepancy between fuel nitrogen yields calculated in the flame front and those calculated from exhaust measurements is reduced as water is injected. This effect is illustrated in Fig. 13 where yields are shown for a fuel containing 0.1 percent nitrogen. The difference is 12 percentage points with zero injection but only 2 percentage points at an injection ratio of 1. The reason is that at high injection rates, most of the thermal NO has been eliminated and the absolute magnitude of the interference of fuel NO on thermal NO formation is relatively small. Any change that reduces thermal NO (water injection, lower air temperature, a fuel with lower flame temperature) will reduce the discrepancy between the two methods of calculating yield.

Figure 13 also shows that the actual yield in the flame front increases only slightly (from 80.1 to 81.5 percent) as the in-

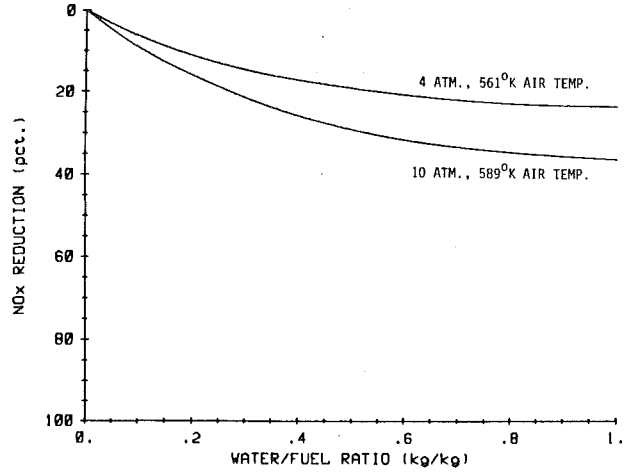

Fig. 14 Different percentage NO_x reductions obtained with water injection at different operating conditions, distillate fuel with 1.0 weight percent added nitrogen

jection ratio is increased from 0 to 1. The apparent yield based on exhaust concentrations exhibits a much larger increase (from 68.1 to 79.9 percent) and overestimates the effect of water injection on the actual yield.

Another example where care should be taken in interpreting NO_x data is shown in Fig. 14. The predicted percentage NO_x reduction with water injection is plotted for a fuel containing 1 percent nitrogen. The two lines correspond to two different hypothetical laboratory tests—one at 10 atmospheres and 589 K inlet temperature, the other at 4 atmospheres and 561 K inlet temperature. More thermal NO is formed in the higher pressure, higher temperature case. As a result, a greater percentage reduction in NO_x is obtained at higher pressure and temperature even though the fuel is the same in both cases. The point to be made is that percentage reductions in NO_x with water injection are a function of the operating conditions as well as the fuel composition. Such reductions reported for a given fuel should not be considered universal at all conditions.

Conclusions

The model described in this paper predicts thermal, prompt, and fuel NO emissions from combustion turbines. The relative contributions of the three forms of NO to total emissions levels have been shown for a variety of operating conditions. The model has been applied to can-type combustors and its accuracy has been verified by data on high- and low-nitrogen fuels with and without water injection, and on combustors of different geometry. Based on the work reported here the following conclusions are drawn:

1 A model incorporating thermal, prompt and fuel NO has been developed to predict the effects of water injection and nitrogen-containing fuels on NO_x emissions.

2 The assumption that thermal, prompt, and fuel NO are all formed at a stoichiometric equivalence ratio is sufficient for modeling purposes.

3 The effective thermal NO residence time in a can-type combustor is proportional to the combustor diameter, inversely proportional to the combustor air jet velocity and is also a function of primary zone stoichiometry.

4 The Fenimore α parameter used for calculating the yield of NO from fuel nitrogen appears to be constant in combustion turbine flames.

5 For hydrocarbon fuels the injection of more than 1 kg of water per kg of fuel for NO_x control yields rapidly diminishing returns because most of the thermal NO has already been eliminated. The remaining NO is prompt and it is only weakly temperature sensitive.

6 Prompt and fuel NO establish an initial concentration of NO for the Zeldovich mechanism and therefore interfere with thermal NO formation. This effect can be significant at combustion turbine operating conditions.

7 Due to the interference mentioned in item 6, the apparent yield of NO from fuel nitrogen as calculated by measurements in the exhaust is lower than the actual yield in the flame. Any change in operating conditions that reduces flame temperature, and therefore thermal NO, will also reduce the discrepancy between the actual and apparent yields.

8 Water injection greatly reduces thermal NO, slightly reduces prompt NO, and slightly increases the yield of NO from fuel nitrogen.

9 The percentage reduction in NO_x emissions with water injection is not a specific curve for a given fuel but rather a family of curves varying with operating conditions.

Acknowledgment

Appreciation is extended to Charles Hussey, Géza Vermes, and Dr. Egon DeZubay for their helpful discussions during the formulation of this model.

References

1 Vranos, A., *Combustion and Flame*, Vol. 22, 1974, pp. 253–258.
2 Chigier, N. A., *Energy, Combustion and Environment*, McGraw-Hill, New York, 1981.
3 Roshko, A., *AIAA Journal*, Vol. 24, No. 10, Oct. 1976.
4 Monat, J. P., Hanson, R. K., and Kruger, C. H., *Proceedings Seventeenth Symposium (International) on Combustion*, 1979.
5 Rubins, P. M., and Marchionna, N. R., AIAA Paper No. 76-612, 1976.
6 Kretschmer, D., and Odgers, J., ASME Paper No. 73-WA/GT-6, 1973.
7 Lewis, G. D., ASME Paper No. 81-GT-119, 1981.
8 Touchton, G. L., ASME Paper No. 84-GT-152, 1984.
9 Shaw, H., ASME Paper No. 73-WA/GT-1, 1973.
10 Blazwoski, W. S., et al., *Journal of Aircraft*, Vol. 12, No. 2, Feb. 1975, pp. 110–115.
11 Tuttle, J. H., et al., *Proceedings Sixteenth Symposium (International) on Combustion*, 1977.
12 Mellor, A. M., *Progress in Energy and Combustion Science*, Vol. 6, 1980, pp. 347–358.
13 Mellor, A. M., and Washam, R. A., ASME Paper No. 79-GT-194, 1979.
14 Appleton, J. P., and Heywood, J. B., *Proceedings Fourteenth Symposium (International) on Combustion*, 1973.
15 Fletcher, R. S., and Heywood, J. B., AIAA Paper No. 71-123, 1971.
16 Hung, W. S. Y., ASME JOURNAL OF ENGINEERING FOR POWER, July 1976, pp. 320–326.
17 Hammond, D. C., and Mellor, A. M., AIAA Paper No. 71-711, 1971.
18 Mosier, S. A., and Roberts, R., AFAPL-TR-73-36, 1974.
19 Pratt, D. T., *Gas Turbine Combustor Design Problems*, edited by A. H. Lefebvre, Hemisphere Publishing Corporation, Washington, D.C., 1980.
20 Edelman, R., and Economos, C., AIAA Paper No. 71-714, 1971.
21 Mongia, H., et al., USARTL-TR-78-55A, B, C, 1979.
22 Turan, A., et al., ASME Paper No. 83-GT-191, 1983.
23 Fenimore, C. P., *Proceedings Sixteenth Symposium (International) on Combustion*, 1977.
24 Zeldovich, Ya.B., *Acta Physicochimica* (U.S.S.R.), Vol. 21, 1946, p. 577.
25 Westenberg, A. A., *Combustion Science and Technology*, Vol. 4, 1971, p. 59.
26 Laurendeau, N. M., *Combustion Science and Technology*, Vol. 11, 1975.
27 Campbell, I. M., and Thrush, B. A., *Transactions of the Faraday Society*, Vol. 64, 1968, pp. 1265–1274.
28 Lenze, B., *Proceedings Nineteenth Symposium (International) on Combustion*, 1982.
29 Fenimore, C. P., *Proceedings Thirteenth Symposium (International) on Combustion*, 1971.
30 Bowman, C. T., and Seery, D. J., *Emissions from Continuous Combustion Systems*, edited by W. Cornelius and W. Agnew, Plenum, New York, 1972.
31 Bowman, C. T., *Proceedings Fourteenth Symposium (International) on Combustion*, 1973.
32 Sarofim, A. H., and Pohl, J. H., *Proceedings Fourteenth Symposium (International) on Combustion*, 1973.
33 Malte, P. C., et al., *Proceedings Sixteenth Symposium (International) on Combustion*, 1977.
34 Moore, J., *Combustion and Flame*, Vol. 17, 1971, pp. 265–267.
35 Haynes, B. S., *Combustion and Flame*, Vol. 28, 1977, pp. 81–91.
36 Fenimore, C. P., *Combustion and Flame*, Vol. 19, 1972, pp. 289–296.
37 DeSoete, G. G., *Proceedings Fifteenth Symposium (International) on Combustion*, 1975.
38 Sarofim, A. F., et al., AIChE 66th Annual Meeting, Philadelphia, PA, Nov. 1973.
39 Ambrose, M. J., et al., EPRI AP-3670, Dec. 1984.

New Integration Techniques for Chemical Kinetic Rate Equations: Part II—Accuracy Comparison

K. Radhakrishnan[1]
National Aeronautics and Space Administration, Lewis Research Center, Cleveland, Ohio 44135

A comparison of the accuracy of several techniques recently developed for solving stiff differential equations is presented. The techniques examined include two general-purpose codes EPISODE and LSODE developed for an arbitrary system of ordinary differential equations, and three specialized codes CHEMEQ, CREK1D, and GCKP84 developed specifically to solve chemical kinetic rate equations. The accuracy comparisons are made by applying these solution procedures to two practical combustion kinetics problems. Both problems describe adiabatic, homogeneous, gas-phase chemical reactions at constant pressure, and include all three combustion regimes: induction, heat release, and equilibration. The comparisons show that LSODE is the most efficient code – in the sense that it requires the least computational work to attain a specified accuracy level – currently available for chemical kinetic rate equations. An important finding is that an iterative solution of the algebraic enthalpy conservation equation for the temperature can be more accurate and efficient than computing the temperature by integrating its time derivative.

Introduction

Many practical chemical reaction flow problems require the simultaneous solution of systems of coupled, first-order ordinary differential equations (ode's). These ode's describe the time rate of change of species concentration and temperature. For species i ($i = 1, NS$) the governing ode can be written as

$$\frac{dn_i}{dt} = f_i(n_k, T); \quad i,k = 1, NS$$
$$n_i(t=0) = \text{given} \tag{1}$$
$$T(t=0) = \text{given}$$

where n_i is the mole number of species i (kmole i/kg mixture); t is the time (s); T is the temperature (K); f_i is the net rate of formation of species i (kmole i/kg mixture/s) due to all forward and reverse reactions in which species i participates; and NS is the total number of distinct chemical species in the gas mixture.

The initial value problem is to solve the system of equations (1) for the chemical composition (i.e., n_i, $i = 1, NS$) and temperature at the end of a specified time interval, given the initial conditions and the reaction mechanism. Classical methods such as the popular explicit Runge-Kutta method require prohibitive amounts of computer time to solve large sets of chemical kinetic rate equations [1-4]. This is due to the extremely small steplengths that classical methods have to use to satisfy stability requirements. Stable differential equations that impose severe steplength limitations on numerical integration routines are classified as stiff differential equations (e.g., [5, 6]).

Several solution techniques have been proposed and developed for stiff systems of ode's. In Part I of this effort and other recent publications [1-4], the computational work required by several recently developed routines in solving chemical kinetic rate equations has been examined in detail. In the present paper we compare their accuracy. The techniques examined in these studies include the general-purpose packages EPISODE and LSODE [7-9], developed as multipurpose stiff differential equation solvers, and the specialized methods CHEMEQ [10], CREK1D [11, 12] and GCKP84 [13, 14], all of which have been developed specifically for chemical kinetics applications. These solution procedures are summarized in Table 1 and discussed in more detail in [3].

All of the foregoing numerical methods are step-by-step methods (i.e., they compute approximations to the exact solutions of the ode's at discrete points in time). They limit

Table 1 Summary of solution procedures examined

Method	Description
GCKP84	Details not yet available.
CREK1D	Variable-step, predictor-corrector method based on an exponentially fitted trapezoidal rule; includes filtering of ill-posed initial conditions and automatic selection of functional iteration or Newton iteration.
LSODE EPISODE	Variable-step, variable-order backward differentiation method with a generalized Newton iteration[a].
CHEMEQ	Variable-step, second-order predictor-corrector method with an asymptotic integration formula for stiff equations.

[a]Other options are included in these packages but this option was found to be the fastest for both problems, and is the only one considered in this work.

[1]NRC-NASA Research Associate.

Contributed by the Gas Turbine Division of THE AMERICAN SOCIETY OF MECHANICAL ENGINEERS and presented at the 30th International Gas Turbine Conference and Exhibit, Houston, Texas, March 18-21, 1985. Manuscript received at ASME Headquarters December 18, 1984. Paper No. 85-GT-30.

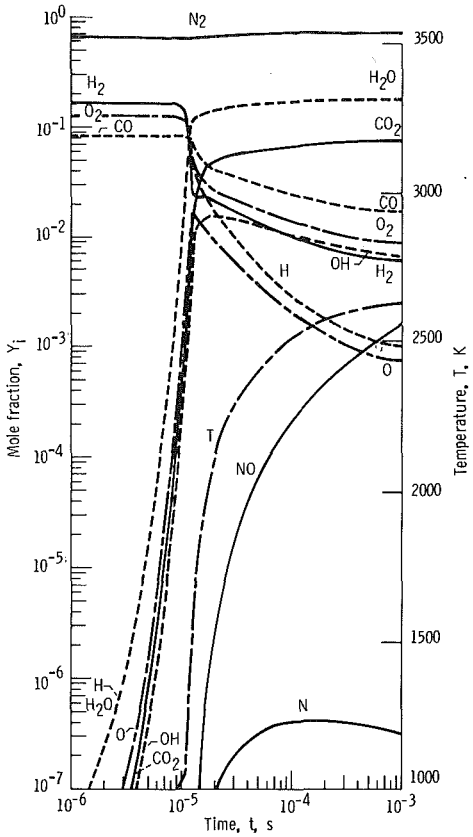

Fig. 1 Variation of temperature and species mole fractions with time for test problem 1. Solution generated using LSODE-B with EPS = 10^{-5}.

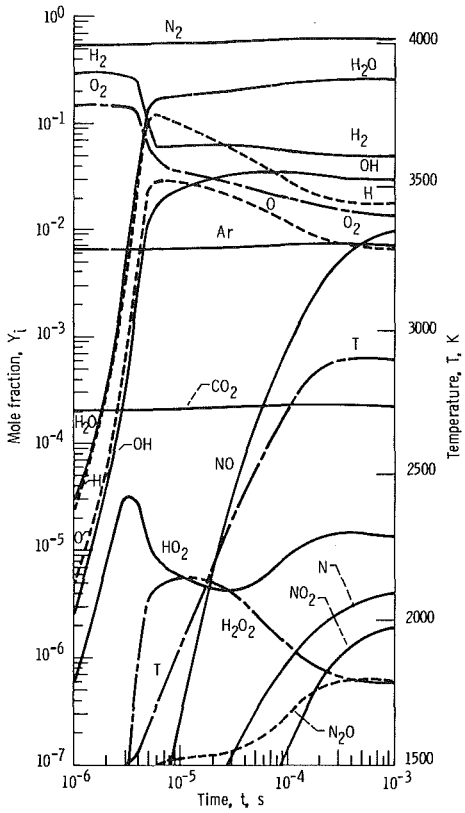

Fig. 2 Variation of temperature and species mole fractions with time for test problem 2. Solution generated using LSODE-B with EPS = 10^{-5}.

the estimated local truncation error (i.e., estimates of the error incurred over one time step) to be less than a user-supplied local error tolerance. However, the quantity that is of interest to the user is the global (i.e., actual) error incurred by a technique in solving the problem. In the present paper, which is based on a recent critical analysis of the accuracy of the foregoing techniques [15], we provide an estimate of the mean global error and examine its variation with the user-supplied local error tolerance (EPS) for two practical combustion kinetics problems. We also study the computational cost (expressed as the computer time required) associated with attaining desired accuracy levels.

The motivation for this work is the increasing interest in both multidimensional modeling of chemically reacting flows and in developing detailed reaction mechanisms for the combustion of fuels and pollutant formation and destruction. Computational speed is of primary concern in the former application and moderate accuracy is adequate [10–12]. However, for developing and validating reaction mechanisms, accuracy is of critical importance.

Evaluation of Temperature

The routines GCKP84 and CREK1D have been developed specifically for nonisothermal combustion rate equations and therefore include calculation procedures for the temperature. For the other techniques, however, the temperature had to be solved for along with the composition. This was done using one of two different methods (A and B) described below.

Nomenclature

ATOL = absolute error tolerance for species mole numbers
CPU = total computer time required on IBM 370/3033 computer, s
$c_{p,i}$ = constant-pressure, molar-specific heat of species i, J/kmol K
E_{rms} = mean integrated global root-mean-square error (equation (7))
EPS = for all methods, except EPISODE, local relative error tolerance; for EPISODE: local relative error tolerance for species with initially nonzero mole numbers and for the temperature, and local absolute error tolerance for species with initially zero mole numbers
ERMAX = relative error tolerance for Newton–Raphson iteration for temperature
e_i = error in ith species mole fraction (equation (4))
e_{rms} = root-mean-square error in species mole fractions and temperature (equation (6))
e_T = error in temperature (equation (5))
f_i = net rate of formation of species i (equation (1)), kmole i/kg mixture/s
HO = initial steplength to be attempted by integrator, s
h_i = molar-specific enthalpy of species i, J/kmol
h_o = mass-specific enthalpy of mixture, J/kg
NS = total number of distinct chemical species in mixture
n_i = mole number of species i, kmole i/kg mixture
T = temperature, K
T_{ST} = standard solution for temperature, K
t = time, s
Y_i = mole fraction of species i
$Y_{i,ST}$ = standard solution for the mole fraction of species i

In the present work, as in Part I, attention is restricted to adiabatic, homogeneous, gas-phase chemical reactions at constant pressure. For such reactions, the following enthalpy conservation equation

$$\sum_{i=1}^{NS} n_i h_i = h_o = \text{constant} \tag{2}$$

is an algebraic constraint on the species rate equations. In equation (2), h_i is the molar-specific enthalpy of species i (J/kmol i) and h_o is the mass-specific enthalpy of the gas mixture (J/kg). In method A, the temperature was calculated from the solution for the species mole numbers, $n_i (i = 1, NS)$ using the initial mixture mass-specific enthalpy, equation (2), and a Newton-Raphson iteration technique with a user-supplied local relative error tolerance, ERMAX. The temperature was therefore not an explicit dependent variable, and the integrator tracked only the solution for species mole numbers.

In method B, the temperature was evaluated by solving its time-derivative obtained by differentiating equation (2) with respect to time, t

$$\frac{dT}{dt} = \frac{\sum_{i=1}^{NS} f_i h_i}{\sum_{i=1}^{NS} n_i c_{p,i}} \tag{3}$$

where $c_{p,j}$ is the constant-pressure molar specific-heat of species i (J/kmol K). In this method, the temperature was an explicit dependent variable, and the integrator tracked the solutions for both the species mole numbers and the temperature.

Test Problems

The accuracy of the techniques summarized in Table 1 was examined by application to two practical combustion kinetics problems. Both problems describe adiabatic, homogeneous, constant-pressure, transient, batch chemical reaction and include all three combustion regimes: induction, heat release, and equilibration.

Test problem 1 describes the ignition and subsequent combustion of a mixture of 33 percent carbon monoxide and 67 percent hydrogen with 100 percent theoretical air at 10 atm and 1000 K initial temperature. It involves 12 reactions among 11 species. Test problem 2, involving 30 reactions and 15 species, describes the ignition and subsequent combustion of a stoichiometric hydrogen-air mixture at 2 atm and 1500 K initial temperature. The reaction mechanisms and rate constants for the two problems are given in [3].

Figures 1 and 2 present the variation of the species mole fractions and temperature with time for test problems 1 and 2, respectively. Both problems were integrated up to time $t = 1$ ms to obtain near-equilibration of all chemical species and temperature.

Computational Procedure

The aim of the present work was to compare the accuracy of currently available techniques in solving chemical kinetic rate equations. In the absence of exact solutions to the test problems, the only way to assess the accuracy of a technique is by comparing solutions generated with a particular value for the local error tolerance (EPS) with those generated with a reduced EPS, using either the same technique or a different one. To prevent any bias in favor of one technique, global errors for each technique were estimated by comparing its solutions with those generated by itself using a reduced EPS. For each technique and test problem, the solution used as a basis of comparison was the most accurate generated and is referred to as its standard solution. For example, for CREK1D standard solutions were generated with CREK1D and EPS = 10^{-5}. These standard solutions were compared with runs using CREK1D and EPS = 10^{-2}, 10^{-3}, and 10^{-4} to assess the global errors incurred by the latter.

A typical computational run consisted of initializing the time (t, set equal to zero), the species mole numbers, and the temperature. The integrator was called with values for the necessary input parameters including the local error tolerance (EPS) and the time at which the integration was to be terminated (= 1 ms for both problems). The values used for the other input parameters, obtained in a previous study [3] by a trial-and-error procedure, resulted in the least CPU time for each technique and value of EPS. After each step successfully executed by the code, values for the time reached by the integrator and the species mole fractions and temperature computed at that time were saved. The values saved for the time served as input data for the output stations at which the standard solution was to be generated. The global errors in the solutions for the species mole fractions and temperature were estimated by comparisons with the standard solution values for these quantities as follows

$$e_i(t) = \frac{Y_i(t)}{Y_{i,ST}(t)} - 1 \tag{4}$$

$$e_T(t) = \frac{T(t)}{T_{ST}(t)} - 1 \tag{5}$$

In equations (4) and (5) $e_i(t)$ and $e_T(t)$ are, respectively, the global errors at time t, in the mole fraction $Y_i(t)$ of species i and the temperature $T(t)$; $Y_{i,ST}(t)$ and $T_{ST}(t)$ are, respectively, the standard solution values for the mole fraction of species i and the temperature at time t. Detailed plots of $e_i(t)$ and $e_T(t)$ are presented in [15]. These plots show that CHEMEO is the most accurate code during induction and early heat release; during late heat release and equilibration, however, the other codes are more accurate.

Standard Solutions. For consistency, standard solutions were generated with the same value of EPS ($=10^{-5}$) for all methods, except EPISODE. In contrast to the other routines for which EPS is the local relative error tolerance, a mixed error tolerance is used for EPISODE – relative for species with initially nonzero mole numbers (i.e., reactants) and for the temperature; and absolute for species with initially zero mole numbers (i.e., all intermediate species and products) [15]. EPISODE is therefore inferior to the other codes – i.e., for a given value of EPS, it produces less accurate solutions [3, 15]. With EPISODE, we have therefore used the smallest value of EPS ($=10^{-6}$) that the single-precision version allowed.

All the techniques examined here required the specification of several input parameters, in addition to the local error tolerance EPS. In generating standard solutions for each technique, the values used for the input parameters were those that resulted in the most accurate solution – see [15] for details. For GCKP84, however, since details of the integration technique are not yet known, default values were used for all parameters except the initial steplength (HO) to be attempted by the ode solver. In our previous work [1–3] with GCKP84, a default value of $HO = 10^{-6}$ s had been used. However, Bittker and Scullin [14] have since then set the default value for HO at 5×10^{-8} s. We have, nevertheless, used $HO = 10^{-6}$ s because it produced more accurate results, while requiring comparable amounts of CPU time for all values of EPS used in this study.

Results and Discussion

The procedure outlined in the section Computational Procedure was used to examine the global errors incurred by all techniques in solving the two problems described in the

Table 2 Maximum percent rms errors and minimum CPU times required for test problem 1

Method	EPS	ATOL	HO, sec	Max rms error, percent	CPU, sec
GCKP84	[a] 10^{-2}	-----	[b] 10^{-6}	467.9	(a)
	5×10^{-3}	-----	[b] 10^{-6}	467.9	.86
	10^{-3}	-----	[b] 10^{-6}	258.6	.98
	10^{-4}	-----	[b] 10^{-6}	115.0	1.13
CREK1D	10^{-2}	-----	-----	30.79	.27
	10^{-3}	-----	-----	7.218	.33
	10^{-4}	-----	-----	2.311	.67
LSODE-A	10^{-2}	10^{-12}	-----	10.52	.37
	10^{-3}	10^{-11}	-----	8.596	.46
	10^{-4}	10^{-11}	-----	4.786	.63
LSODE-B	10^{-2}	10^{-12}	-----	10.57	.40
	10^{-3}	10^{-11}	-----	8.167	.44
	10^{-4}	10^{-11}	-----	6.366	.59
EPISODE-A	5×10^{-6}	-----	10^{-7}	825.7	.034
EPISODE-B	5×10^{-6}	-----	10^{-7}	825.9	.035
CHEMEQ-A	10^{-2}	-----	-----	34.47	15.1
	10^{-3}	-----	-----	6.580	28.4
	10^{-4}	-----	-----	.868	39.8
CHEMEQ-B	10^{-2}	-----	-----	57.61	15.5
	10^{-3}	-----	-----	19.48	22.7
	10^{-4}	-----	-----	2.219	36.5

[a]Terminated at $t \simeq 3.7\times10^{-5}$ sec because of problems with serious instability.
[b]Default value.

Table 3 Maximum percent rms errors and minimum CPU times required for test problem 2

Method	EPS	ATOL	HO, sec	Max rms error, percent	CPU, sec
GCKP84	10^{-2}	-----	[a] 10^{-6}	227.2	1.85
	10^{-3}	-----	[a] 10^{-6}	98.65	1.91
	10^{-4}	-----	[a] 10^{-6}	21.76	2.44
CREK1D	10^{-2}	-----	-----	3.959	1.18
	10^{-3}	-----	-----	2.148	1.07
	10^{-4}	-----	-----	0.612	2.32
LSODE-A	10^{-2}	10^{-8}	-----	29.38	.54
	10^{-3}	10^{-8}	-----	27.37	.78
	10^{-4}	10^{-8}	-----	29.44	.94
LSODE-B	10^{-2}	10^{-8}	-----	30.53	.52
	10^{-3}	10^{-9}	-----	3.484	.94
	10^{-4}	10^{-8}	-----	1.528×10^{3}	1.49
	10^{-4}	10^{-12}	-----	8.641	1.46
EPISODE-A	5×10^{-4}	-----	10^{-7}	290.4	.065
	10^{-4}	-----	10^{-7}	121.8	.59
	10^{-5}	-----	10^{-6}	54.08	.78
EPISODE-B	5×10^{-4}	-----	10^{-10}	280.1	2.38
	10^{-4}	-----	10^{-11}	131.6	.91
	10^{-5}	-----	10^{-9}	78.31	.88
CHEMEQ-A	10^{-2}	-----	-----	26.97	37.7
	10^{-3}	-----	-----	2.133	47.3
	10^{-4}	-----	-----	.207	76.1
CHEMEQ-B	10^{-2}	-----	-----	23.80	36.3
	10^{-3}	-----	-----	4.631	43.0
	10^{-4}	-----	-----	2.341	87.6

[a]Default value.

section Test Problems. All results presented herein were obtained on the NASA Lewis Research Center's IBM 370/3033 computer using single-precision accuracy, except GCKP84, which was in double precision.

With LSODE, EPISODE, and CHEMEQ, both temperature methods A and B were attempted. The following naming convention was used. Techniques using temperature method A were given the suffix A (LSODE-A, EPISODE-A, and CHEMEQ-A) and those using temperature method B were given the suffix B (LSODE-B, EPISODE-B, and CHEMEQ-B). For consistency between the two methods, ERMAX (the maximum local relative error allowed in the temperature in method A) was set equal to EPS, which is approximately the maximum local relative error allowed in the temperature in method B.

To facilitate accuracy comparisons, at each value of the time where global errors had been evaluated (and saved), the root-mean-square (rms) error $e_{\text{rms}}(t)$ was computed using

$$e_{\text{rms}}(t)=\sqrt{\frac{\sum_{i=1}^{NS} e_i^2(t)+e_T^2(t)}{NS+1}} \tag{6}$$

To prevent the possibility of requiring accuracy from species with immeasurably small concentrations, the summation in equation (6) does not include species whose standard solution mole fractions were less than 0.1 ppm; for such species, $e_i(t)$ was set equal to zero.

The maximum percent root-mean-square errors incurred by all techniques are given in Tables 2 and 3, respectively, for test problems 1 and 2. Also given in these tables are the values used for the input parameters required by each method. These values, taken from Radhakrishnan [3], resulted in the least CPU time (CPU in Tables 2 and 3) to solve the problem with the given value of EPS. In these tables, *HO* is the user-supplied value for the initial steplength to be attempted by the integrator, and ATOL is the absolute error tolerance for all species mole numbers – a value of zero was used for the absolute error tolerance for the temperature (required by LSODE-B).

For test problem 1, the run with GCKP84 and EPS = 10^{-2} displayed serious instability and so was terminated. For values of EPS $\geq 5\times10^{-6}$, EPISODE-A and -B predicted little or no change from the initial composition or temperature after an elapsed time of 1 ms. Similar remarks apply to test problem 2 and the runs with EPISODE-A and EPS $\geq 5\times10^{-4}$ and those with EPISODE-B and EPS $\geq 5\times10^{-3}$. Although the runs with EPISODE-B and EPS = 10^{-3} and 5×10^{-4} were successfully completed in that correct solutions were returned at $t = 1$ ms, they were significantly inaccurate during heat release. For example, the run with EPS = 5×10^{-4} predicted little or no change from the initial conditions until $t \simeq 40$ μs when heat release was predicted to start. In contrast, for the standard solution heat release is almost over by this time (Fig. 2).

Tables 2 and 3 show large variations in the maximum root-mean-square error incurred by the different techniques. GCKP84 and EPISODE experienced the greatest difficulty in tracking their standard solutions and maximum root-mean-square errors of over 100 percent were obtained with these codes. In contrast, the maximum errors incurred by CHEMEQ, CREK1D, and LSODE were significantly smaller. Comparisons of the runs with the largest values of *EPS* show that LSODE was the most accurate code for test problem 1, and CREK1D for test problem 2.

The accuracy obtained with LSODE was strongly influenced by the value selected for ATOL (the absolute error tolerance for the species mole numbers). For problem 2, LSODE-A showed little sensitivity to changes in EPS, because all runs used the same ATOL (Table 3). In contrast, the runs with LSODE-B showed decreased errors with reductions in EPS because of the use of smaller values of ATOL. Note the significant reduction in the maximum root-mean-square error obtained by decreasing ATOL from 10^{-8} to 10^{-12} for LSODE-B and EPS = 10^{-4} (Table 3). This decrease in the

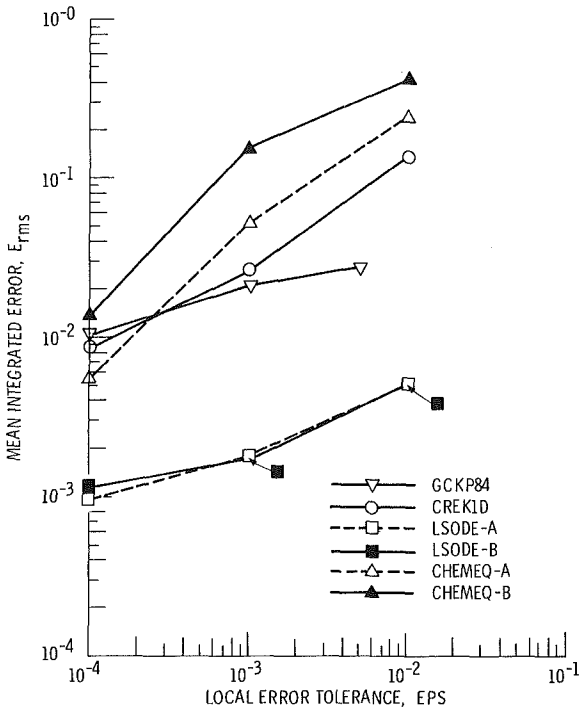

Fig. 3 Variation of the mean integrated global error (E_{rms}) with the local error tolerance (EPS) for test problem 1

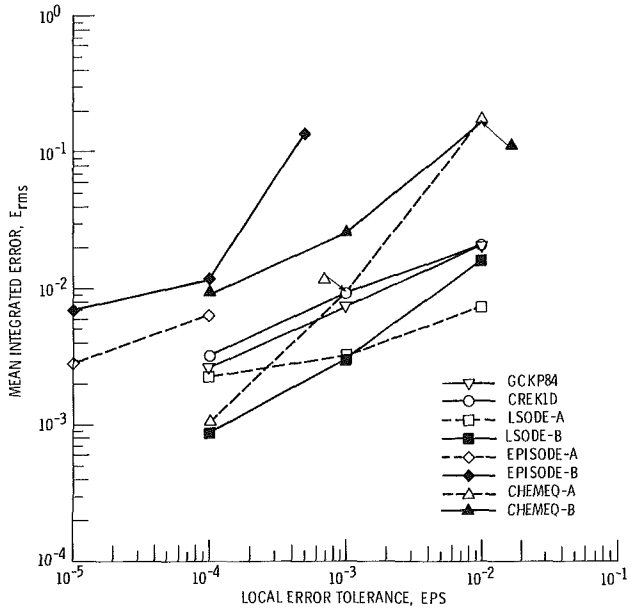

Fig. 4 Variation of the mean integrated global error (E_{rms}) with the local error tolerance (EPS) for test problem 2

maximum error with a reduction in ATOL is further illustrated for problem 2 by the results presented in Table 4 for LSODE-B and EPS = 10^{-5}. These results show that great care must be exercised in specifying values for ATOL. A poor guess for ATOL can result in significantly inaccurate solutions. The CPU time required by LSODE was also affected by ATOL. In general, a trial-and-error procedure was necessary to obtain the optimum value for ATOL (defined as that value which results in the least CPU time while satisfying prescribed accuracy requirements). This trial-and-error search – which can be time consuming, especially for large systems of ode's – for the optimum value for ATOL is the main difficulty associated with using LSODE for solving chemical kinetic rate equations. The use of extremely low values for ATOL to ensure accuracy can result in excessively large CPU

Table 4 Effects of absolute error tolerance for species mole numbers (ATOL) on maximum percent root-mean-square error, mean integrated root-mean-square (E_{rms}), and CPU time

[All results obtained with LSODE-B and EPS=10^{-5} for problem 2.]

ATOL	Max rms error, (percent)	E_{rms}	CPU, (sec)
10^{-8}	1.112×10^{4}	2.792×10^{-1}	4.17
10^{-9}	2.022×10^{3}	4.011×10^{-2}	3.24
10^{-10}	20.25	9.421×10^{-4}	2.52

times. For example, for test problem 2 the run using LSODE-B with EPS = 10^{-5} and ATOL = 10^{-11} required about 3.4 s CPU time; in contrast, the run with ATOL = 10^{-15} required almost 20 s although the solution was not significantly different. In addition, as discussed in Part I (4), the solution can be adversely affected by a poor choice for the output stations at which the solution is desired.

Tables 2 and 3 show also that the use of temperature method A does not result in significantly larger errors than those incurred by temperature method B. On the contrary, method A can be more accurate than method B – this difference in accuracy is most marked for CHEMEQ.

To provide a more comprehensive measure of the accuracy than the maximum root-mean-square error, we have adopted the following procedure. For each run a mean integrated root-mean-square error, E_{rms}, was calculated as follows

$$E_{rms} = \frac{1}{t_{end}} \int_0^{t_{end}} e_{rms}(t)dt \tag{7}$$

where t_{end} is the end of the prescribed time interval.

Equation (7) provides a single quantity that is a measure of the average error incurred in solving the complete problem. The integral was evaluated numerically using Simpson's rule modified for unequal step sizes.

Figures 3 and 4 present the variation of E_{rms} with the user-supplied local error tolerance EPS. In addition, Table 4 gives values of E_{rms} incurred by the different runs with LSODE-B and EPS = 10^{-5} for test problem 2. These results illustrate the increasing accuracy obtained with reductions in ATOL and the significant errors that can be incurred by a poor guess for ATOL. Figures 3 and 4 show that all methods used in the present study are tolerance-effective (i.e., decreasing EPS results in reduced error). For both problems, temperature method A is as accurate as method B – in many cases, it is significantly more accurate. For problem 2 and EPS = 10^{-4}, LSODE-B is more accurate than LSODE-A because of the smaller ATOL used.

Figures 3 and 4 illustrate the significant discrepancies between the values specified for EPS and the errors actually obtained. For example, for problem 1 a value of EPS = 10^{-2} (1 percent) has resulted in an average error of almost 50 percent error for CHEMEQ-B. These plots show that for a given value of EPS, LSODE is the most accurate code currently available for solving chemical kinetic rate equations. However, GCKP84, CREK1D, and CHEMEQ-A compare very favorably with LSODE for small values of EPS. EPISODE is significantly less accurate than the other codes because the error control used in it is inappropriate for chemical kinetics applications [3].

Figures 5 and 6 present the variation of the computational work (expressed as the CPU time in seconds required on the NASA Lewis Research Center's IBM 370/3033 computer) with the mean integrated error for test problems 1 and 2, respectively. For both problems the CPU times required by temperature method A are less than, or compare favorably with, those required by method B to attain the same accuracy

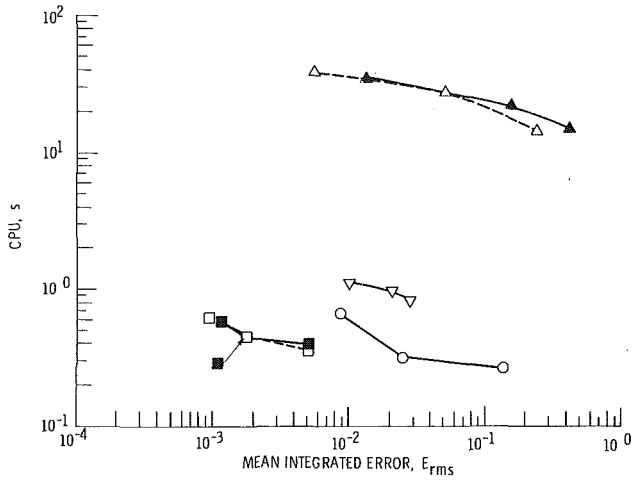

Fig. 5 Variation of the CPU time (s) with the mean integrated global error (E_{rms}) for test problem 1. All runs on the IBM 370/3033 computer. For symbol key, see Fig. 3.

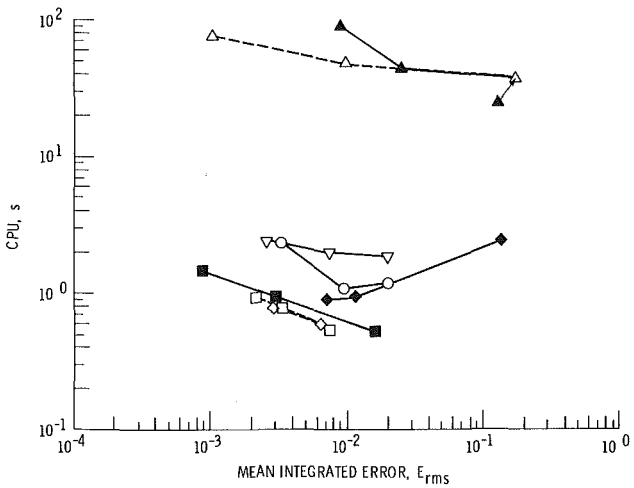

Fig. 6 Variation of the CPU time (s) with the mean integrated global error (E_{rms}) for test problem 2. All runs on the IBM 370/3033 computer. For symbol key, see Fig. 4.

levels. This difference is most pronounced for CHEMEQ and EPISODE. Note that for EPISODE-B the computational work increases with increasing error.

Figures 5 and 6 illustrate the large differences in the computational work required by the different techniques to attain comparable accuracy levels. For problem 1 and a one-half percent mean global error, the CPU time varies from about 0.37 s for LSODE-A to over 40 s for CHEMEQ-A. For problem 2, this difference is even greater. For both test problems LSODE is the most efficient code in the sense that it requires the least CPU time to attain a specified accuracy level.

For test problem 2, EPISODE-A compares very favorably with LSODE (Fig. 6). However, the solution generated by EPISODE was found to strongly depend on the value selected by the user for the initial steplength (*HO*) to be attempted by the integrator. A poor guess for *HO* can result in inaccurate and unstable solutions [1–4]. It can also result in excessive CPU times. For example, the run using EPISODE-A with EPS = 10^{-4} and *HO* = 10^{-8} s required almost 129 s for problem 2; in contrast, the run with *HO* = 10^{-7} s required only about 0.6 s.

To attain the same accuracy level, CREK1D requires more CPU time than LSODE for both test problems. CREK1D is, however, attractive for the following reason. It is intended primarily for performing multidimensional calculations of chemically reacting flows by coupling it with a hydrodynamic equation solver. Currently available hydrodynamic codes are at best accurate to within a few percent, so generation of highly accurate chemical kinetic solutions is wasteful [10]. For problem 1, CREK1D requires approximately 0.3 s to produce a solution with a mean global error of about 5 percent, which is sufficiently accurate for multipoint calculations of reacting flows. This CPU time compares favorably with the 0.37 s required by LSODE-A.

Conclusions

A comparison of the accuracy of several recently developed numerical techniques (GCKP84, CREK1D, LSODE, EPISODE, and CHEMEQ) in solving chemical kinetic rate equations has been made. This study has shown that LSODE is the most efficient code – in the sense that it requires the least CPU time to attain a specific accuracy level – currently available for solving chemical kinetic rate equations. The major difficulty associated with its use is the trial-and-error procedure necessary to obtain optimum values for the absolute error tolerances for the variables. A poor guess for the absolute error tolerance can result in excessive CPU times or in seriously inaccurate solutions. When accuracy is not of primary concern, as in multidimensional chemically reacting flow calculations, CREK1D is an attractive alternative to LSODE.

An important conclusion is that the use of an algebraic enthalpy conservation equation for calculating the temperature can be more accurate and efficient than evaluating the temperature by integrating its time derivative.

References

1 Radhakrishnan, K., "A Comparison of the Efficiency of Numerical Methods for Integrating Chemical Kinetic Rate Equations," NASA TM-83590, 1984.

2 Radhakrishnan, K., "Fast Algorithms for Combustion Kinetics Calculations: A Comparison," *Combustion Fundamentals Research*, NASA CP-2309, 1984, pp. 257–267.

3 Radhakrishnan, K., "Comparison of Numerical Techniques for Integration of Stiff Ordinary Differential Equations Arising in Combustion Chemistry," NASA TP-2372, 1984.

4 Radhakrishnan, K., "New Integration Techniques for Chemical Kinetic Rate Equations. I. Efficiency Comparison," *Combustion Science and Technology*, Vol. 46, No. 1, 1985, pp. 59–81.

5 Gelinas, R. J., "Stiff Systems of Kinetic Equations—A Practitioner's View," *Journal of Computational Physics*, Vol. 9, No. 4, Apr. 1972, pp. 222–236.

6 Pratt, D. T., and Radhakrishnan, K., "Physical and Numerical Sources of Computational Inefficiency in the Integration of Chemical Kinetic Rate Equations: Etiology, Treatment and Prognosis," NASA TP, 1986.

7 Hindmarsh, A. C., and Byrne, G. D., "EPISODE: An Effective Package for the Integration of Systems of Ordinary Differential Equations," UCID-30112-Rev. 1, Lawrence Livermore Laboratory, 1977.

8 Hindmarsh, A. C., "LSODE and LSODI, Two New Initial Value Ordinary Differential Equation Solvers," *SIGNUM Newsletter*, Vol. 15, No. 4, Dec. 1980, pp. 10–11.

9 Hindmarsh, A. C., "ODEPACK, A Systematized Collection of ODE Solvers," UCRL-88007, Lawrence Livermore Laboratory, 1982.

10 Young, T. R., and Boris, J. P., "A Numerical Technique for Solving Stiff Ordinary Differential Equations Associated with the Chemical Kinetics of Reactive-Flow Problems," *Journal of Physical Chemistry*, Vol. 81, No. 25, Dec. 15, 1977, pp. 2424–2427.

11 Pratt, D. T., "CREK-1D: A Computer Code for Transient, Gas-Phase Combustion Kinetics," Paper WSCI 83-21, *Proceedings, Spring Meeting of the Western States Section of the Combustion Institute*, Apr. 1983.

12 Pratt, D. T., and Radhakrishnan, K., "CREK1D: A Computer Code for Transient, Gas-Phase Combustion Kinetics," NASA TM-83806, 1984.

13 Zeleznik, F. J., and McBride, B. J., "Modelling the Internal Combustion Engine," NASA RP-1094, 1984.

14 Bittker, D. A., and Scullin, V. J., "GCKP84—General Chemical Kinetics Code for Gas-Phase Flow and Batch Processes Including Heat Transfer," NASA TP-2320, 1984.

15 Radhakrishnan, K., "A Critical Analysis of the Accuracy of Several Numerical Techniques for Chemical Kinetic Rate Equations," NASA TP, 1986.

Design of Combustor Cooling Slots for High Film Effectiveness: Part I—Film General Development

G. J. Sturgess
Senior Research Engineer,
Engineering Division,
Pratt & Whitney,
United Technologies Corporation,
East Hartford, Conn. 06108

The metal liners of gas turbine engine combustors usually have to be provided with some form of thermal protection from the high temperatures of the reacting mixture of gases contained therein. For aircraft gas turbines, where weight is a factor, the protective medium is air. The air is most usually introduced by tangential injection as a discrete film at a number of axial stations along the combustor liner so that as the cooling potential of one film is depleted it is periodically renewed by another. Although invariably referred to as film cooling, the most important function of the film air is to act as a relatively cool barrier between the vulnerable liner and the reacting gases. The design margin for error is very small. Failure to design a cooling slot that provides a high film effectiveness can result in thermal damage to the liner. Manufacturing considerations almost always determine how a real slot design is reduced to practice. The resulting liners (inner and outer in the case of an annular combustor) contain no two slots that are exactly alike in aerodynamic behavior and, therefore, in film effectiveness performance. Phenomenological models of the film cooling process are invariably based on considerations of two-dimensional shear mixing. Empirical factors may be introduced to account for the differences in performance existing between two-dimensional film slots and real slots. However, such methods are not of much help in designing a slot configuration that will deliver good performance, for making comparative evaluations of competing designs, or in establishing the performance penalties associated with compromises made for manufacturing reasons. Heuristic arguments are used to derive a dimensionless grouping of internal geometric parameters that describe the lateral aerodynamic uniformity of the films produced by practical slots. It is assumed that the average film effectiveness is uniquely related to the film lateral uniformity. Experimental data from a number of different practical slot designs are examined in terms of this geometric mixing parameter, and film effectiveness is shown to depend on it over a wide range of axial distances and film blowing ratios. It is concluded that the geometric mixing parameter provides a means to differentiate good film cooling slot designs from poor ones.

Introduction

Thermal protection of high-temperature components through injection of a coolant along the outer surface of the component is an established technique in many areas of engineering. It is usually described as film cooling and is used frequently in the gas turbine engine for protecting turbine disks, vanes and blades, in afterburner liners, and in main combustion chambers; its inverse, film heating, can be used for anti-icing of spinners and inlets, and to prevent loss of visibility through windscreens during adverse weather.

In the main combustion chamber of the gas turbine engine the metal liners forming the combustor have to be provided with some form of thermal protection from the high temperatures of the reacting mixture contained therein. This protection may be ceramic, ceramic (as a thermal barrier coating) with air cooling, or just air cooling. For aircraft gas turbines where weight is a factor, the protective medium is air, although operating conditions are becoming such that relatively thin thermal barrier coatings are now a frequent additional feature of these liners. The air is most usually introduced by axial injection tangential to the surface as a discrete film at a number of axial stations along the liner so that as the cooling potential of one film is depleted it is periodically renewed by another.

Although invariably referred to as film cooling because the air film does remove some of the heat received by the liners from flame radiation, the most important function of the film is to act as a relatively cool barrier between the vulnerable liner and the reacting gases. The reacting gases can have average temperatures between 2473 K (4000° F) and 1700 K

Contributed by the Gas Turbine Division of THE AMERICAN SOCIETY OF MECHANICAL ENGINEERS and presented at the 30th International Gas Turbine Conference and Exhibit, Houston, Texas, March 18–21, 1985. Manuscript received at ASME Headquarters, December 18, 1984. Paper No. 85-GT-35.

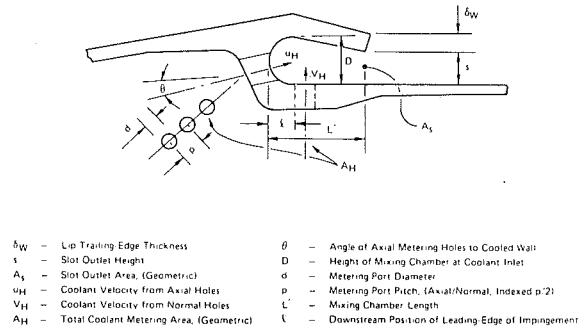

δ_W – Lip Trailing-Edge Thickness
s – Slot Outlet Height
A_s – Slot Outlet Area, (Geometric)
u_H – Coolant Velocity from Axial Holes
v_H – Coolant Velocity from Normal Holes
A_H – Total Coolant Metering Area, (Geometric)
θ – Angle of Axial Metering Holes to Cooled Wall
D – Height of Mixing Chamber at Coolant Inlet
d – Metering Port Diameter
p – Metering Port Pitch, (Axial/Normal, Indexed p/2)
L' – Mixing Chamber Length
ℓ – Downstream Position of Leading-Edge of Impingement

Fig. 1 Geometric description of practical slot

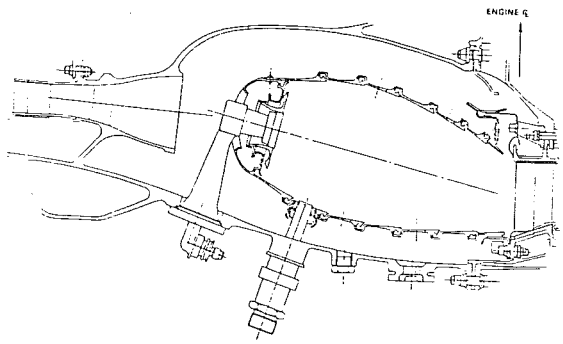

Fig. 2 Cross section of a typical modern annular combustion chamber

(2600° F) from front to rear of the combustor, while the cooling air temperature is typically around 813 K (1000° F) in modern high-pressure engines. The melting point of the liner material is in the range 1473–1593 K (2200–2400° F). The initial film thickness is normally less than 3 mm (0.1 in.). The quantity of air available for use as film cooling is between 20–50 percent of the total air passing through the combustor. Larger amounts cannot be provided without seriously compromising the operating requirements of the combustor. The distance between individual films is in the range 3–5 cm (1–2 in.). From these figures it can be appreciated that the design margin for error is very small. Failure to design a cooling slot that provides a high film effectiveness within these constraints can result in thermal damage to the liner. Such damage may be severe enough to lead to premature engine removal due to combustor failure, and can cause damage to expensive turbine components downstream of the combustor in the engine. The result of these shortcomings is increased maintenance costs for the engine, making it expensive to own.

The devices for introducing cooling air along the liner surface are called slots, and these may be fabricated from sheet stock or machined from forged or rolled stock. Figure 1 shows some of the features contained in a typical machined slot. Slots fabricated from sheet metal are similar, but contain a joint and tend to have less flexibility in design of specific features. Figure 2 shows a cross section of a modern combustion chamber and demonstrates advanced cooling devices in the liners.

Manufacturing considerations almost always determine how a real slot design is reduced to practice. In a given combustor design, slot heights tend to be standardized from front to rear of the liner, as are the distances along the cooled surface between individual slots (an odd-size length is sometimes used at the rear of the liner to meet overall length requirements). These fixed dimensions are to standardize on the manfacturing of the details that are assembled to form the liner, or to standardize on the tooling for machined liners. At this stage, this represents a disregarding of the hot gas temperature and velocity variations with position along the liner. Slot design modifications to locally optimize the film cooling to economize on air as has been proposed [1] are not usually made therefore. Cooling air is admitted to the slots through one or more lines of individual drilled or punched holes around the combustor circumference forming the slot. The diameter, pitch-to-diameter ratio, and angle of these holes depends on the amount of film air to be added at a particular location, the method of producing the holes, the type of slot blank into which they are introduced, and the pitch-circle diameter on which they are introduced. The shape and internal dimensions of the slot may also be established by the limitations of the manufacturing method used, i.e., rolling, machining, sheet-metal fabrication, etc. The resulting liners (inner and outer in the case of an annular combustor) contain

Nomenclature

D = internal height of slot mixing chamber
d = diameter of coolant metering ports
I = length of coolant jet from metering port discharge to impingement on an internal surface
L = slot lip internal length; internal flow path length
$\bar{M}$ = mean mass velocity ratio, or blowing ratio, $\rho_c \bar{u}_c / \rho_m u_m$
MIX = preliminary geometric parameter, $ps/(dL)$
MIX_N = revised geometric parameter, $p/d.s/D.I/L$
p = pitch between coolant metering ports
Re_s = coolant Reynolds number based on $\bar{u}_c$ and s
s = slot outlet height
T_c = coolant gas temperature
T_m = mainstream gas temperature
$T_{s,ad}$ = adiabatic wall temperature
$\bar{u}_c$ = mass-averaged coolant velocity at slot outlet
u_m = mainstream velocity outside any boundary layer at plane of slot outlet
$u_{\max}$ = maximum mean axial velocity in a representative run $(Z_2 - Z_1)$, of lateral or circumferential velocity profile at normal or radial position y
$u_{\min}$ = minimum mean axial velocity in a representative run $(Z_2 - Z_1)$ of lateral or circumferential velocity profile at normal or radial position y
$\bar{u}_y$ = average mean axial velocity over lateral distance $(Z_2 - Z_1)$ at normal position y, $\int u dz/(Z_2 - Z_1)$
x = downstream distance along cooled wall from slot outlet plane
x_p = thermal conditional potential core length from slot outlet plane
y = normal or radial distance from cooled wall
$(Z_2 - Z_1)$ = lateral extent of mean axial velocity lateral profile at normal distance y

Greek

η = film effectiveness, $(T_m - T_{s,\text{ad}})/(T_m - T_c)$
ρ_c = coolant density
ρ_m = mainstream density
Ψ = dimensionless peak-to-peak value of coolant mean axial velocity lateral profile at height y in slot outlet plane

no two slots that are exactly alike in aerodynamic behavior and therefore, in film effectiveness performance.

Problems of liner cooling and design development toward better film behavior are reviewed in [2] and [3]. Reference [3] also describes the effects of some slot geometry variations on film effectiveness. Experimental data in the literature also provide additional information on geometry effects, e.g., [4–7] inclusive. However, a calculation procedure is needed that relates film effectiveness to both injection conditions and slot geometry.

Phenomenological models of the film cooling process are invariably based on considerations of two-dimensional shear mixing. Empirical factors may be introduced, often in somewhat arbitrary fashion, to account for the differences in performance existing between two-dimensional film slots and real slots. A survey of such models is given in [8]. Some of the more sophisticated of these models can sometimes achieve rather satisfying predictions of film effectiveness measurements made for real slot geometries in simple rigs, and on occasion, in real combustors [9, 10]. However, they are not of much help in designing a slot that will ensure good performance, for making fast comparative evaluations of the relative worth of competing slot designs, or in establishing the performance penalties associated with design compromises made for ease of manufacture or cost reduction. For these purposes an account of internal slot geometry is required.

Scope

Heuristic arguments are used to derive a dimensionless grouping of internal geometric parameters that describe the lateral or circumferential uniformity of the films produced by practical slots. Experimental data from a number of different practical slot designs are examined in terms of this geometric mixing parameter, and film effectiveness is shown to depend on it over a wide range of axial distances and film blowing ratios.

Slot Geometry Effects

Geometry effects on film cooling performance were reviewed in [3] and [11]. In [11], it was argued that decay of the film from a practical slot is due to two effects: small-scale, turbulence-induced entrainment of the hot mainstream gases into the cooler film, and large-scale momentum-induced entrainment. These two effects arise as follows:

1 Turbulence generated by the shear between the film and the mainstream, turbulence inherent in the mainstream, and turbulence generated in the film by the coolant metering

2 Large-scale entrainment due to the bluff-body represented by the slot lip and by lateral nonuniformities existing in the film from incomplete mixing-out of the individual coolant jets formed inside the slot by the metering

Mainstream turbulence effects were quantitatively described by Sturgess and Lenertz [12]. Film turbulence generation was attributed to the coolant metering ports, related to grid-turbulence, and quantitatively described by Sturgess [11]. Large-scale entrainment due to the slot lip having finite thickness and boundary layers was assumed by Sturgess [13] to be accounted for through calculation of a conditional potential core length, defined as a region of unity film effectiveness for the developing film. In [11], a geometric grouping was argued to describe the influence of slot geometry on performance, and measured film effectiveness data apeared to support this group. The group, however, was not general, or widely tested.

Development of Slot Geometry Characterization

A promising description of the slot internal geometry was developed by generalizing the MIX grouping of [11]. The original definition used for characterization of conventional slot (like Fig. 1) mixing chambers with single-row coolant metering was

$$\mathrm{MIX} = \frac{ps}{dL} \tag{1}$$

where

p = pitch between metering ports
d = metering port diameter
s = slot outlet height
L = slot lip internal length

The following postulates were made:

1 Film decay is by entrainment-induced mixing and by turbulence-induced mixing.

2 Entrainment-induced mixing is due to lateral nonuniformities in the film, and these originate from the coolant metering, but are influenced by the internal design of the slot.

3 "Well-designed" slots have good performance by reducing entrainment-induced mixing to a minimum. Clean slots, having remote coolant metering, no internal obstructions, and smooth convergence to discharge (two-dimensional), have the absolute minimum of entrainment-induced mixing. Well-designed slots will attempt to reproduce clean slots with performance asymptotically approaching that of the clean slot.

4 "Poorly designed" slots have large entrainment-induced mixing. A step in the cooled wall with widely spaced coolant metering holes arranged in a row along the step represents a maximum of entrainment-induced mixing; poorly designed slots will have a performance asymptotically approaching that of the lipless-step "slot."

The very reasonable assumption is made that in the film, the downstream distribution of normalized adiabatic wall temperatures $(T_m - T_{s,ad})/(T_m - T_c)$ or film effectiveness η is uniquely related to the lateral or circumferential profile of axial velocity at the slot exit. This is justified to some extent by Fig. 11 of [11]. The profile is determined by the internal mixing of the individual coolant jets admitted through the metering ports in the slot (see Fig. 1). Experimental results [14] for the mixing of a line of jets therefore serve as a guide for desirable features in a design. With the introduction of discrete jets, entrainment is inevitable. It is clearly desirable that the initial entrainment appetite of the jets be satisfied through self-entrainment rather than by the jets entraining hot mainstream gases directly. Thus it can be deduced that the following features represent "goodness":

- Long lip lengths (Fig. 7 of [3])
- Impingement of coolant jets on a solid surface prior to discharge (Fig. 7 of [3], Fig. 13 of [11])
- Metering ports being placed as close together as possible ([14, 15] and Fig. 11 of [11])

In addition to the postulates, it was assumed that:

(*a*) Mean radial or normal profiles of axial velocity at slot outlet will not change significantly with blowing ratio $\bar{M}$, or slot-to-slot with mixing chamber design.

(*b*) Where impingement of coolant metering jets is used the jet angle with the impingement surface has no first-order effect.

(*c*) Wholesale turning of the flow within the slot has no effect, either positive or negative, on internal mixing.

With the foregoing postulates and assumptions, dimensional and heuristic reasoning was applied and resulted in MIX being redefined as MIX_N, the subscript N signifying "new," where

$$\mathrm{MIX}_N = \frac{psI}{dDL} \tag{2}$$

and

s,p,d = have their original meanings
D = internal height of slot mixing chamber where the coolant is admitted
I = length of coolant jet from metering to impingement on an internal surface
L = internal flow path length

Therefore, if the lateral or circumferential uniformity of the emerging film at the slot exit is described [11] by

$$\Psi = \frac{u_{\max} - u_{\min}}{\bar{u}_y} \tag{3}$$

where

$u_{\max}$ = film axial velocity crest
$u_{\min}$ = film axial velocity trough
{in a circumferential or
{lateral section of profile at height y

$$\bar{u}_y = \left[\frac{\int_{z_1}^{z_2} u dz}{(z_2 - z_1)} \right]_y$$

y = radial or normal position in slot outlet at which the considered circumferential or lateral profile exists
$(z_2 - z_1)$ = circumferential or lateral distance at radial or normal position y to encompass a representative number of velocity crests and troughs in the profile

then

$$\Psi = f_a(\mathrm{MIX}_N) \tag{4}$$

where f_a is an unknown function. The term Ψ has values falling between zero and unity from its definition.

Postulates 3 and 4 define reasonable limiting values for examining the sense of equation (4). Therefore, using the definition of MIX_N from equation (2), and equation (4),

(*a*) Clean Slot
$p = 0$, $d = <s$, $D >> s$, $I = 0$, $L >> s$
Hence, $\mathrm{MIX}_N = 0$, and as a consequence, $\Psi = 0$.
For $\Psi = 0$, $u_{\max} = u_{\min}$, i.e., uniform profile.

(*b*) Lipless Slot
$D = s$, $L = 0$
Hence, $\mathrm{MIX}_N = \infty$, and as a consequence, $\Psi = 1.0$, i.e., zero mixing before "film" is exposed to the mainstream

In the limit therefore, equation (4) satisfies postulates 3 and 4.

Investigation of Mix

Ideally, the unknown function f_a of equation (4) should be determined directly from experimental data. Unfortunately, it represents a difficult piece of modeling, adequate velocity profile information is not available and would be expensive to acquire, and it would be a large task to collate and reduce such data. However, film effectivenes data from a variety of conventional and indirectly metered slots are readily available from many sources. The validity of MIX_N can be inferred from a study of this data base.

In order to investigate MIX_N from adiabatic-wall effectiveness data, it is necessary to introduce some further assumptions. These assumptions are as follows

1 Entrainment-induced mixing will be determined by MIX_N alone.

2 Turbulence-induced mixing is adequately described by the three-zone film model described in [11, 12, 13, 16].

3 A quantitative prediction of film effectiveness for any given slot design is not immediately required.

Although the three-zone model is far from perfect, the second assumption is a reasonable one for the present purposes, and is necessary to separate effects. The third assumption allows a number of convenient simplifications to be introduced into the three-zone model.

Use of the three-zone model enables the important effects of slot lip thickness, as shown in Fig. 8 of [3] for all types of slot, to be accounted for in the conditional potential core region of the film. As a further consequence of adopting this model, the simplification of neglecting slot Reynolds number and film to mainstream viscosity ratio effects can be made since film effectiveness outside the potential core is only weakly dependent on them.

Two further simplifications may be made to the three-zone model. First, the experimental data were all taken in wind tunnels of similar and low, mainstream turbulence intensities. This effect may therefore be neglected. Also, to first order, the film turbulences generated by the metering will be similar for all practical slots, and they are all greater than the mainstream turbulences used in the experiments. The area ratio terms used to describe film turbulence [11] can therefore be neglected.

Therefore, for the present purposes, the film effectiveness downstream of the potential core can be described in terms of the simplified three-zone model and MIX_N as

$$\eta = f_b\left[\frac{(x - x_p)}{\bar{M}s}, \mathrm{MIX}_N \right] \tag{5}$$

where

f_b = unknown function
x = distance downstream from slot exit
x_p = conditional potential core length
$\bar{M}$ = mean mass velocity ratio (blowing ratio) of coolant to mainstream

The most convenient way to use equation (5) is to examine the variation of η with MIX_N at fixed values of $(x - x_p)/(\bar{M}s)$ for a wide range of slot geometries and blowing conditions. The result provides information on film behavior downstream of the potential core.

Experimental Data

Experimental data were available from a number of slots tested over the years. Geometrically, these slot designs could be divided into eight distinct classes. These classes were delineated as follows:

(*a*) Clean slot with realistically thick lip ($\mathrm{MIX}_N = 0$)
(*b*) Lipless, stepped "slot" ($\mathrm{MIX}_N = \infty$)
(*c*) Conventional (directly metered) with single row of ports
(*d*) Conventional with double row of ports
(*e*) Conventional with convergence (both single and double row of ports)
(*f*) Indirectly metered with single 90 deg turning
(*g*) Indirectly metered with double 90 deg turning
(*h*) Indirectly metered with multiple 90 deg turning

A directly metered slot is one where the line of coolant metering ports is directly visible when viewed from the slot exit. In an indirectly metered slot, these ports cannot be seen from the slot exit, due either to the presence of an intermediate impingement wall, or because they are placed out of plane and some flow turning is involved.

In most of the slot classes slots with more than one combination of dimensions were tested. Information was available for a total of 18 geometrically different slots. Classes (*a*) and (*b*) represented the limiting cases referred to above. Class (*c*) included slots with both machined and fabricated sheet metal form. Figure 1 represents a slot that falls into class (*e*), the slots just visible in Fig. 2 are of class (*h*). Slots in classes (*c*), (*d*), (*e*), (*g*), and (*h*) have all seen

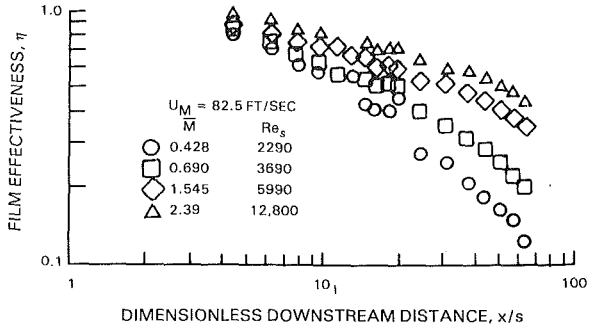

Fig. 3 Example of raw effectiveness data

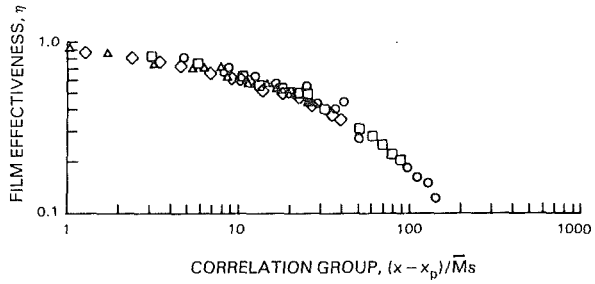

Fig. 4 Example of correlated effectiveness data for a class (e) slot

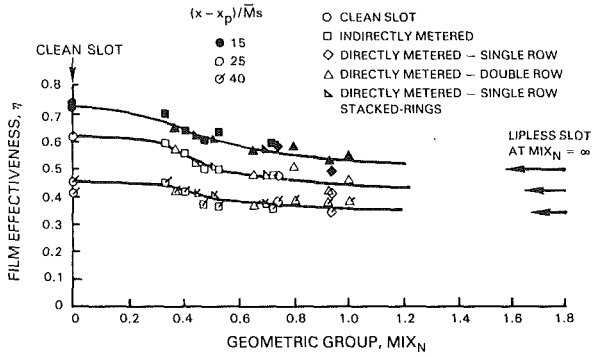

Fig. 5 Effect of mixing chamber design on downstream film

engine service, other slots in these and the remaining classes were experimental. Values of MIX_N for all the real slots ranged from a value of 0.34 to one of 1.0. The slot classes listed here do not form a definitive list; other classes can be described and are used in some engines.

The film effectivenesses used were the lateral averages of several lines of axial measurement at several lateral stations. These lines were removed from the tunnel sidewalls. This averaging supposes that the overall wind tunnel performance was a good approximation to two-dimensional flow, and this was so. With use of an average effectiveness it is the impact of slot mixing chamber characteristics on mean film performance that is being studied.

Data Reduction

An example of the raw laterally averaged, film effectiveness data from one of the slots (class (*e*)) examined is given in Fig. 3. The data in this case were for a fixed mainstream velocity and cover a range of blowing ratio, and by this means, a range of slot Reynolds number also. Slot heights varied slot-to-slot so a variation in slot Reynolds number was obtained by this means too. For some of the runs of other slots mainstream velocity was also a variable. In these cases, mainstream boundary layer effects were taken to be accounted for in the potential cores. From the raw data the thermal potential core lengths were extracted in the manner illustrated in [13], by plotting effectiveness against the natural logarithm of dimensionless distance x/s and extrapolating a straight line through the data representing the transition region of the three-zone model (see [12, 13, 16]) to unity effectiveness. This is discussed in more detail in the second part of this paper. The data for each slot were correlated against the group $(x-x_p)/(\bar{M}s)$ from equation (5). Such a correlation for the raw data from the class (*e*) slot of Fig. 3 is shown in Fig. 4. The majority of the data spread in the correlation plot can be seen to be associated with the uncertainty in the raw data. It is only fair to add that Fig. 4 is one of the better correlations.

From correlation plots like Fig. 4 the values of effectiveness pertaining at values of $(x-x_p)/(\bar{M}s)$ of 15, 25, and 40, respectively, were picked off and were plotted against the calculated values of MIX_N appropriate for each different slot. The values of effectiveness were taken for the middle of the scatter in the correlated data at each $(x-x_p)/(\bar{M}s)$. Values of $(x-x_p)/(\bar{M}s)$ of greater than 25 are appropriate for the dilution zone of the combustor, values for the primary zone are typically in the range of 6 to 10. Values of $\bar{M}$ are generally 2 or greater in primary zones and 0.5–1.5 in dilution zones.

To apply the expression for MIX_N (equation (2)) to double-row metering ports, the pitch used for staggered jets was the effective pitch for both rows, taken as one-half the geometric pitch for a single row of the ports. The port diameter used was a mass-weighted mean to account for those slot designs that split the total coolant flow unequally between the rows of metering. The fact that the two rows could be at essentially right angles (see Fig. 1) was ignored. The length of the jet to impingement (I) was estimated by projecting the metering port centerline until a solid surface was encountered. For those slots having the metering port centerlines parallel to the cooled surface (see Fig. $1-\Theta=0$) (rig models only as difficult to manufacture in production), I was taken as equal to L. For double-row metering I was a mass-weighted mean obtained from independent estimates for each individual row of ports. For those indirectly metered slots involving wholesale turning of the flow, the length L was based on the centerline distance for the slot passage total length from coolant inlet to discharge.

Results

The plots of average effectiveness η against the values of MIX_N at each value of $(x-x_p)/(\bar{M}s)$ are shown in Fig. 5. The lines shown are drawn through the data points. The values of η for the lipless design, being for a slot having a MIX_N value of infinity, are shown as asymptotes. Figure 6 shows a crossplot of η against $(x-x_p)/(\bar{M}s)$ made from Fig. 5, for the limiting geometries and for two imaginary practical slots described arbitrarily as "good" and "poor" designs respectively. In this figure the zero value of the abscissa represents the end of the thermal potential core where by definition, effectiveness is unity for all slots.

Considering the extensive nature of the data manipulation required to produce the plot, Fig. 5 shows excellent correlation of data for all values of $(x-x_p)/(\bar{M}s)$. No effect of slot Reynolds number is significant despite the order of magnitude variation that exists in the data. At each value of $(x-x_p)/(\bar{M}s)$ the mean line through the correlated data points clearly shows the asymptotic end behavior, as was postulated and as revealed in the limit analysis. The effect of real slot geometry, as represented by MIX_N, on effectiveness decreases as $(x-x_p)/(\bar{M}s)$ is increased. This is more clearly evident in Fig. 6 where the cross-plotted lines representing the clean slot and the lipless slot limits tend to converge at large $(x-x_p)/(\bar{M}s)$. At given $(x-x_p)/(\bar{M}s)$, effectiveness is not much affected by mixing chamber geometry until MIX_N reaches a value about 0.3, at which point there is a sharp decline. For

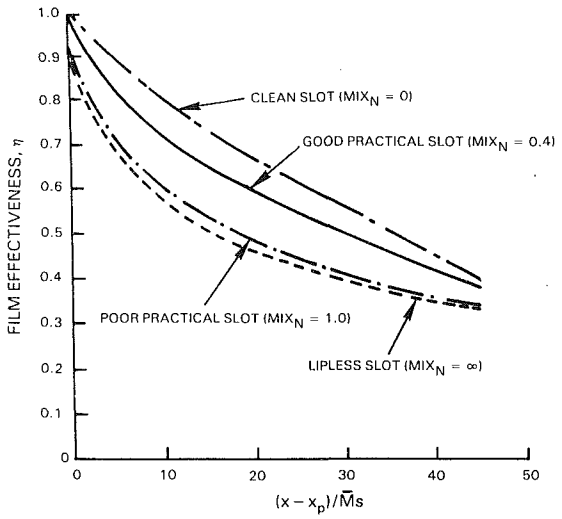

Fig. 6 Demonstration of dependence of film downstream performance on slot design

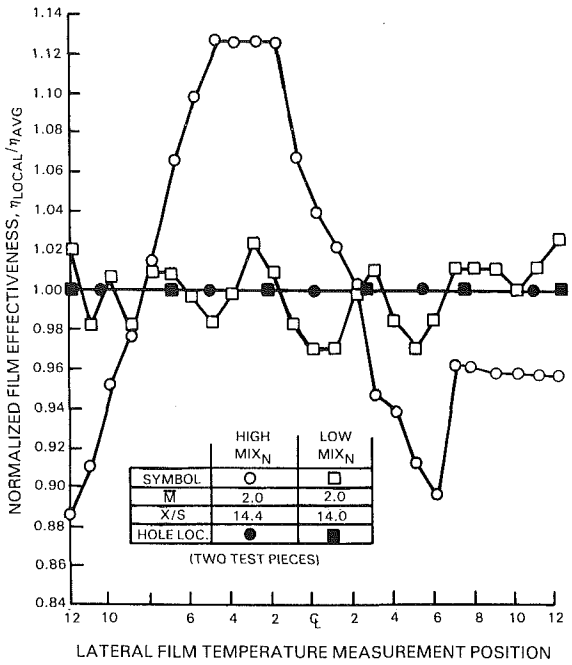

Fig. 7 Illustration of influence of MIX$_N$ on film uniformity

MIX$_N$ greater than about 0.9, there is not much further decline in effectiveness.

Discussion

The satisfactory correlation of the data achieved in Fig. 5 together with the correct asymptotic behavior at both high and low MIX$_N$ values indicates the essential correctness of equation (5) and demonstrates the success of the simple MIX$_N$ parameter for characterizing the mixing chamber geometry for a wide variety of practical and experimental film cooling slots. The data correlated were for 17 different slots falling into 7 distinct classes, one of the original classes being eliminated for proprietary reasons. The ranges of the major variables (excluding the limiting geometries) were as follows

s, mm	:	3–8
p/d (effective)	:	1.3–3.1
L/s	:	2.4–5.9
$\bar{M}$	:	0.2–4.5
Re$_s$	:	1,300–24,000
u_m, m/s	:	8.6–41

The postulates and assumptions used to arrive at the formulation of equation (5) and resulting in Figs. 5 and 6 appear to be justified by the success of Fig. 5; in particular, that, all else being equal, film development is dictated by large-scale film entrainment processes associated with the initially highly three-dimensional character of the film. When the slot internal geometry results in low values of MIX$_N$, the performance of idealized, clean slots can be approached. This is due to improved lateral or circumferential film uniformity, as Fig. 7 illustrates. The lateral effectiveness variation shown parallels the lateral "saw-tooth" variation in mean axial velocity measurements shown in Fig. 10 of [11]. However, it is surprising that:

1 The unaccounted-for radial mean velocity profile at slot outlet does not appear to exert much influence with either blowing condition, slot Reynolds number, internal passage turning, or mixing chamber design. This might be because radial velocity profile changes are more important in the initial regions of the film, i.e., in the conditional potential core region and are not so important in the downstream regions of the film due to rapid profile rearrangement. If this is so, the effects would not be detected in the present study.

2 The double-row metering, lines of jets essentially at right angles to each other, apparently acts only to halve the effective pitch of the metering. Any effect of jet turning through 90 deg in the mixing chamber, for a significant portion of the total coolant flow entering, seems not to be felt downstream of the potential core.

These two observations above might also be taken as support of one of the major assumptions made, that wholesale turning of the flow within the slot has no effect on internal mixing. However, turning a flow in a duct is usually understood to generate secondary flows [17], which certainly can influence mixing. The implication of the apparent lack of effect is that another, dominant, effect could be present.

At the levels of effectiveness required in the aircraft gas turbine engine combustor (0.5–0.6 minimum) the difference in performance between a "good" slot and a "poor" slot in Fig. 6 (0.1–0.15 in effectiveness within the working range of $(x-x_p)/(\bar{M}s)$), although small, is enough to make the difference between successful liner cooling and complete liner failure. Really good indirectly metered slot designs can approach clean slots (albeit with thick lips) in cooling performance. However, poorly designed, indirectly metered slots can be inferior to a well-designed conventional slot. A poorly designed conventional slot can be as low in performance as a machined lipless slot design, with the lipless design having better durability, since it has no unsupported lip overhang (Fig. 1) to overheat and fail by buckling or creeping closed [3]. The designer's problem is that he does not have complete freedom to select slot lip length, metering port pitch-to-diameter ratio, and other geometric parameters independently of either structural analysis and/or manufacturing technique and cost.

Figure 5 shows the usefulness of the MIX$_N$ parameter in characterizing the internal geometry of film cooling slots. MIX$_N$ can be used to decide the merits of competing slot designs and to assess the possible relative impacts of manufacturing tolerances on performance.

It should be recognized that although Fig. 5 does illustrate the usefulness of MIX$_N$ as a means of geometry characterization and to indicate trends, it does not represent through Fig. 5 the whole story with respect to performance. This is because the potential core region is not considered, and potential core has been demonstrated [18] as forming a significant portion of the panel length that can be cooled adequately by a single, well-designed slot. The potential core

region emerges again here as being extremely important, not only as part of the three-zone model upon which this study is based, but also because of the foregoing observations with respect to possible radial velocity profile effects and the apparent unimportance of bulk flow turning. The potential core is explored further in the second part of this paper.

Conclusions

Heuristic arguments have been used to formulate a geometric description of the internal features of practical film cooling slot designs. This description is simple and appears to be fairly general; it is easy to estimate. It covers features used in conventional and established slot designs, features used in the latest generation of slot designs, and features used in unconventional experimental designs. An existing model of film cooling was used to characterize operating conditions so that measured values of film effectiveness obtained from numerous tests of many slot geometries could be analyzed in terms of the slot internal geometry. The following conclusions were drawn:

1 The simplified three-zone model of film cooling does provide a suitable performance group for examining the efficacy of the geometric grouping MIX_N as a parameter for describing the effects of slot internal geometry on downstream film development.

2 For operating group values typical of the aircraft gas turbine combustor, the MIX_N parameter satisfactorily correlates laterally averaged values of measured film effectiveness.

3 The success of the geometric group MIX_N as a correlation parameter for a range of nonsimilar slots over a wide range of operating conditions supports the postulate that film development for practical slots over axial distances of current interest is dominated by large-scale mass-entrainment processes.

4 When characterized through MIX_N, film effectiveness for practical slot geometries falls between the two asymptotic conditions represented respectively by thick-lipped, idealized, two-dimensional slots and lipless slots. Low values of MIX_N result in film performances that approach the ideal slot, while high values of MIX_N give lower effectivenesses approaching those of the lipless slot.

5 MIX_N can be used to rank the likely performance of competing slot configurations. A superior configuration will have a low value of MIX_N. MIX_N can also be used to some extent for assessing potential performance penalties associated with manufacturing tolerances applied to a given design.

6 The initial region of the film, conditionally described as a potential core, is a critical part of film development and must be described before MIX_N can be used in a predictive capacity.

Acknowledgments

The author wishes to thank the Pratt and Whitney organization of United Technologies Corporation for permission to publish this paper. The opinions expressed are those of the author alone.

References

1 Sturgess, G. J., "Film Cooling Optimization for Minimum Cooling Airflow in Aircraft Gas Turbines," *Proc. Symp. Combustion in Advanced Gas Turbine Systems*, Edited by I.E. Smith, Pergamon Press, 1968, pp. 347–376.

2 Sturgess, G. J., "Gas Turbine Combustor Liner Durability—The Hot-Streak Problem," *Proc. Project SQUID Workshop Gas Turbine Design Problems*, Edited by A. H. Lefebvre, Hemisphere Publishing, 1980, pp. 133–150.

3 Sturgess, G. J., "Gas Turbine Combustor Design Challenges for 1980's," Paper No. AIAA-80-1285, AIAA/SAE/ASME 16th Joint Propulsion Conference, Hartford, Connecticut, June 30–July 2, 1980.

4 Sivasegarem, S., and Whitelaw, J. H., "Film-Cooling Slots: The Importance of Lip Thickness and Injection Angle," Imperial College Report EHT/TN/6, Oct. 1967.

5 Nina, M. N. R., and Whitelaw, J. H., "The Effectiveness of Film-Cooling with Three-Dimensional Slot Geometries," Imperial College Report EHT/TN/A/24, July 1970.

6 Rastogi, A. K., and Whitelaw, J. H., "The Effectiveness of Three-Dimensional Film-Cooling Slots—I: Measurements," *International Journal of Heat and Mass Transfer*, Vol. 16, 1973, pp. 1665–1681.

7 Folayan, C. O., and Whitelaw, J. H., "The Effectiveness of Combined Tangential and Normal Film-Cooling Slots with Finite Lip," ASME Paper 76-HT-30, presented at ASME–AIChE Heat Transfer Conference, St. Louis, Mo., Aug. 1976.

8 Lefebvre, A. H., *Gas Turbine Combustion*, McGraw-Hill, 1983.

9 Bayley, F. J., "Heat Transfer Problems in the Cooled Gas Turbine," AIAA Paper No. 72-10, presented at AIAA 10th Aerospace Sciences Meeting, San Diego, California, Jan. 17–19, 1972.

10 Ballal, D. R., and Lefebvre, A. H., "A Proposed Method for Calculating Film-Cooled Wall Temperatures in Gas Turbine Combustion Chambers," ASME Paper 72-WA/HT-24, 1972.

11 Sturgess, G. J., "Account of Film Turbulence for Predicting Film Cooling Effectiveness in Gas Turbine Combustors," ASME JOURNAL OF ENGINEERING FOR POWER, Vol. 102, July 1980, pp. 524–534.

12 Sturgess, G. J., and Lenertz, J. E., "Account of Mainstream Turbulence for Predicting Film Cooling Effectiveness of Gas Turbine Combustors," ASME Paper No. 77-HT-10, ASME–AIChE Heat Transfer Conference, Salt Lake City, Utah, Aug. 1977.

13 Sturgess, G. J., "Wall Cooling by Gaseous Injection for a High Performance Combustion System," Ph.D. thesis, Loughborough University, Loughborough, England, 1970.

14 Krystantas, R., "The Turbulent Jet from a Series of Holes in Line," *Aeronautical Quarterly*, Vol. 15, 1964, pp. 1–28.

15 Schlichting, H., *Boundary Layer Theory* (4th. ed.), McGraw-Hill, 1960, pp. 604–605.

16 Sturgess, G. J., "Correlation of Data and Prediction of Effectiveness from Film Cooling Injection Geometries of a Practical Nature," *Proc. Cranfield International Symposium Series*, Vol. 11, *Combustion and Heat Transfer in Gas Turbine Systems*, Edited by E. R. Norster, Pergamon Press, 1971, pp. 229–250.

17 Chang, S. M., Humphrey, J. A. C., and Modavi, A., "Turbulent Flow in a Strongly Curved U-Bend and Downstream Tangent of Square Cross-Section," University of California at Berkeley, Report No. FM-82-1, Nov. 1982.

18 Sturgess, G. J., "Application of Film Cooling Theory to the Cooling of Aircraft Gas Turbine Chambers," *J. Royal Aeronautical Society*, Vol. 71, June 1967, pp. 430–434.

G. J. Sturgess
Senior Research Engineer.

G. D. Pfeifer
Research Engineer.

Engineering Division,
Pratt & Whitney,
United Technologies Corporation,
East Hartford, Conn. 06108

Design of Combustor Cooling Slots for High Film Effectiveness: Part II—Film Initial Region

A heuristically based geometric grouping has been used to relate the geometry of practical film cooling slots of gas turbine engine combustors to the circumferential uniformity of axial velocity in the film and the average film effectiveness. To be satisfactory, the cooling performance of a slot has been shown to require a low value of this group. A study of film development has been extended to the initial region of the film where cooling performance is at its maximum. It is demonstrated that such a region exists for both practical slots and idealized two-dimensional slots, but that the character of the initial region flow is completely different for practical slots and cannot be described by the same methods as can be used for two-dimensional slots.

Introduction

Film cooling is a successful and essential technique to protect the liners of combustors for aircraft gas turbine engines. The thermal environment is particularly severe in modern, high-performance engines, so that the margin for design error in cooling is quite small. With the amount of air available for cooling being strictly limited, cooling slot designs must have high performance. However, they must also be structurally sound and inexpensive to manufacture. A compromise among these three, usually conflicting, demands commonly has to be made. In order to reach such a compromise, a link has to be established between the film cooling performance of a slot design and the geometrical features embodied in that design.

A summary of film cooling performance and general descriptions of the effects of some slot geometrical parameters are given in [1] and [2]. These studies have been extended in the first part of this paper to include a heuristically based geometric grouping of slot internal dimensions MIX_N [3] that describes the lateral uniformity of the films produced by practical slots, where

$$MIX_N = \frac{psI}{dDL} \tag{1}$$

where

- s = slot outlet height
- p = effective pitch of metering ports admitting coolant
- d = metering port effective diameter
- L = slot internal passage length
- D = internal height of the slot mixing chamber where coolant is admitted
- I = length of coolant jet from metering to impingement on an internal surface

The normalized adiabatic wall temperature distribution η is functionally related to MIX_N and the injection parameters through a simplification of the three-zone model [4, 5] by

$$\eta = f\left[\frac{(x-x_p)}{\bar{M}s}, MIX_N\right] \tag{2}$$

where

- x = distance downstream from slot exit
- x_p = conditional thermal potential core length
- $\bar{M}$ = mean mass velocity ratio (blowing ratio) of coolant to mainstream

Experimental data over a wide range of blowing ratios from 17 different slots of 7 distinct classes of slot design were used to show the utility of MIX_N for describing the slot performance in the film downstream of the conditional potential core (representation in the three-zone model). A high value for MIX_N indicates poor slot performance through low effectiveness. The so-called potential core region emerges as a parameter of importance for further clarification and investigation.

Scope

Experimental data are used to establish that the geometric grouping of slot internal geometric parameters MIX_N does characterize some aspects of the conditional potential core region in practical film cooling systems. However, while MIX_N does permit the relative merits of different slot designs to be compared in quantitative fashion, it does not provide a complete description of the potential core. Computational fluid dynamic calculations are used to substantiate limited flow visualization that the films from practical slots contain some degree of vortical motion in the conditional potential core.

Contributed by the Gas Turbine Division of THE AMERICAN SOCIETY OF MECHANICAL ENGINEERS and presented at the 30th International Gas Turbine Conference and Exhibit, Houston, Texas, March 18–21, 1985. Manuscript received at ASME Headquarters, December 18, 1984. Paper No. 85-GT-36.

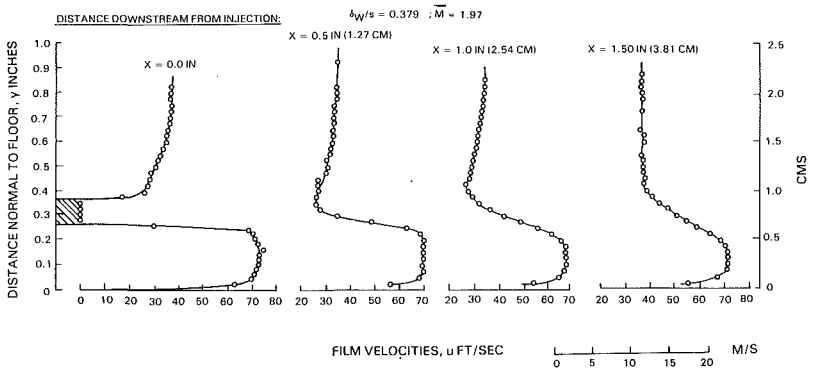

Fig. 1(a) Velocity profile development for intermediate – lipped slots, jetlike flow

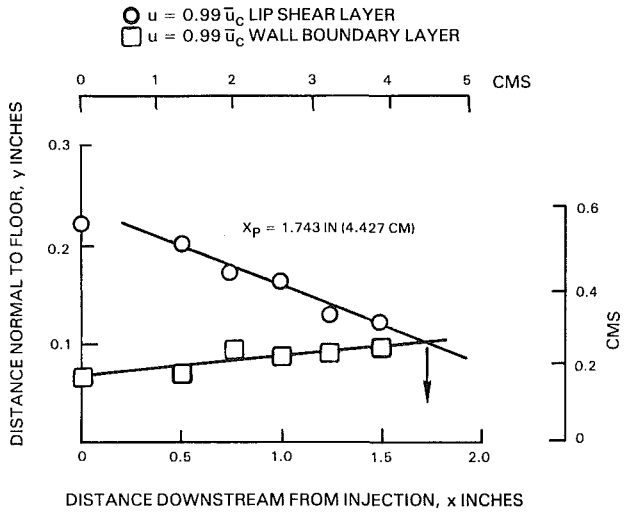

Fig. 1(*b*) Measurement of potential core from velocity profiles

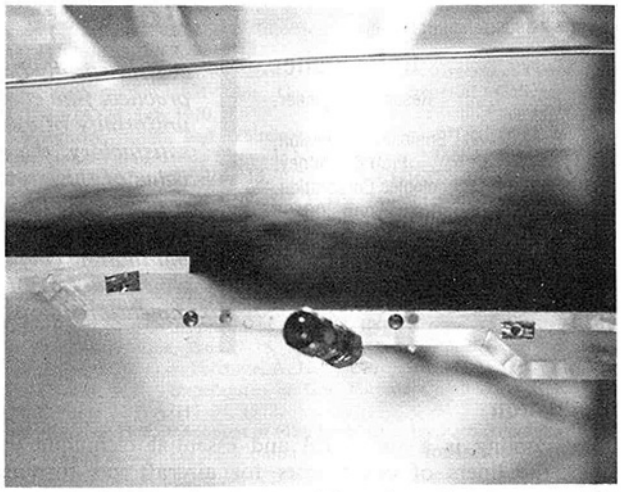

Fig. 2 Dye injection in water tunnel flow of practical sheet metal film cooling slot showing potential core development

Conditional Potential Core

For two-dimensional, ideal geometry slots a conditional hydrodynamic potential core is simply identified [4] as the region of comparatively low turbulence between the edge of the boundary layer growing on the cooled wall, and the inner-edge of the growing shear layer established off the slot lip between the coolant flow and the mainstream flow. The boundary layer and the shear layer will both have higher turbulence levels than the flow between them. The potential core length is defined as the downstream distance from the slot lip to where the wall boundary layer and the lip shear layer grow into each other. The appropriate "edges" of the layers are defined as the position in the axial velocity profiles where the local velocity reaches 99 percent of the coolant mean velocity. Figures 1(*a*, *b*) show such velocity profile development and measurement of the potential core length [4].

The thermal potential core can be obtained from the hydrodynamic value through assumption of either Reynolds analogy, or a Prandtl–Taylor flow where the Prandtl number is based on a suitable film mean temperature. Alternatively, the thermal potential core can be measured directly through the normalized adiabatic wall temperature distribution or film effectiveness η and is defined as the downstream distance for which η has a value of unity. For equivalency of hydrodynamic and thermal cores, a thermal boundary layer is presupposed on the cooled wall in the initial region.

When the three-dimensional character of the flow from real film cooling slots is realized [1], it is reasonable to question the existence of a definable potential core in this context.

Flow visualizaton in a water tunnel by means of time-averaged photographs of tracer-dye introduced into the

Nomenclature

D = slot internal height at coolant metering
d = diameter of coolant metering ports
I = distance from metering to coolant jet impingement on internal surface
K = specific kinetic energy of turbulence
L = slot internal flow path length
$\bar{M}$ = mean blowing ratio, or mass velocity ratio of coolant to mainstream
MIX_N = geometric correlation group defined by equation (1)
p = pitch between coolant metering ports
s = slot height at outlet
u = local axial velocity in film
$\bar{u}_c$ = mean coolant velocity at slot outlet
x = distance downstream from slot outlet
x_p = conditional potential core length
y = distance normal from cooled wall
z = lateral distance

Greek Symbols

δ_w = lip trailing-edge thickness
ϵ = dissipation rate of K
η = normalized adiabatic wall temperature distribution, or film effectiveness

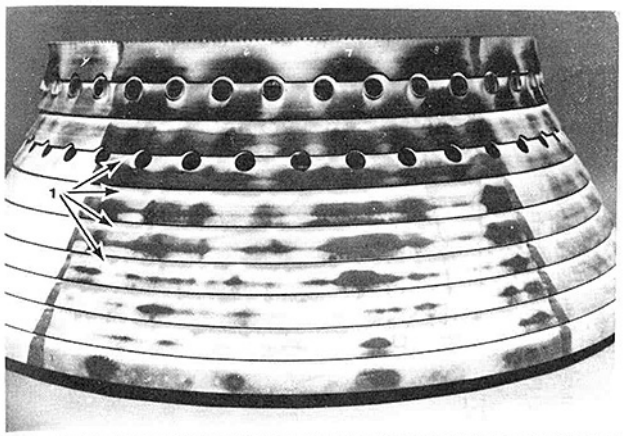

Fig. 3 Indications of initial region through temperature-sensitive paint on combustor liner after engine test

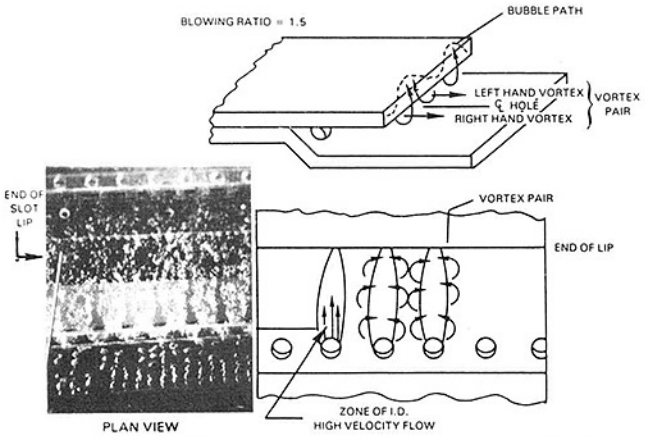

Fig. 4 Bubble injection in water tunnel flow model of practical sheet metal film cooling slot showing vortex formation in film

mainstream suggests that the potential core concept is reasonable as described, Fig. 2. Similarly, post-engine test inspection of temperature sensitive paints on actual combustor liners shows a region immediately downstream of slot lips, Fig. 3, (region marked "1") that represents temperatures close to unmixed cooling air temperatures, and therefore, good cooling. This appears supportive of the existence of something that might be described as a potential core. However, flow visualization by means of air bubbles introduced into the upstream coolant-side of a practical slot in the water tunnel shows the formation of vortical flow within the slot due to mutual self-entrainment by adjacent jets of coolant and impingement on slot internal surfaces. The vortex pairs are discharged from the slot and persist in the developing film. This is shown in Fig. 4. The motion is clearly completely different from the conditional hydrodynamic potential core described for classical clean slot geometries. It is not amenable to simple shear flow analysis as developed in [4] and proposed in [6].

Figure 5 is an infrared photograph of practical slot flow with heated coolant over an adiabatic flat plate (film heating, the inverse of film cooling). It shows at any axial station the lateral variation in adiabatic wall temperature arising from coolant film nonuniformities. Of course, it cannot provide any information on the nature of these nonuniformities. This particular slot had a fairly low value of MIX_N. For the purposes of investigating MIX_N in [3], lateral averages of film effectiveness were used. When the average film effectiveness is plotted against the natural logarithm of dimensionless distance x/s, a straight-line extrapolation through the data (representing the transition region of the three-zone model) is possible to ascertain a distance of implied unity effectiveness. This could be done for the practical slots. It satisfies the definition of thermal potential core length given above. Figure 6 illustrates the process for a slot of class (*c*) geometry, as described in [3].

Therefore, although it appears proper to talk about thermal potential cores for slots of both classical, clean design, and practical designs, it should be recognized that hydrodynamically, these "potential cores" may be quite different in character.

Relationship of Thermal Potential Core to MIX_N

The present objective is to show that the internal geometry of practical film cooling slots is adequately described by the MIX_N parameter. In Part I [3], this was established for film development downstream of a critical initial region. The critical initial region has been designated as a thermal potential core, and it has been shown above that such a region exists for practical slot geometries. If the flow visualization of

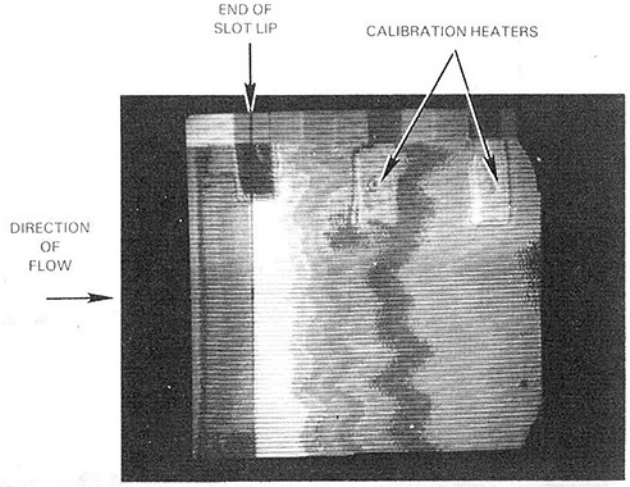

Fig. 5 Thermogram of film heating of an adiabatic flat plate showing lateral variations in surface temperature due to incomplete film mixing

Fig. 2 for a class (*c*) slot is compared with that of Fig. 7 for a class (*h*) slot (for slot classifications, see [3]) at the same blowing ratio, it is immediately apparent that different designs of slot do have different dimensionless potential core lengths. Therefore, some relationship between x_p/s and MIX_N might be expected.

It is reasonable to anticipate that some relationship would also exist between potential core length and blowing ratio $\bar{M}$. For those slots that do a good job of mixing out individual coolant jets before the coolant is exposed to the mainstream, mixing of the resultant film with the mainstream should be shear dominated, and a local maximum of potential core length at some value of $\bar{M}$ (dependent on the radial or normal profile of axial velocities) is to be expected.

Figure 8 shows the measured dependency of dimensionless thermal potential core length x_p/s on the average blowing ratio $\bar{M}$ for practical slots of different MIX_N, all having dimensionless lip thicknesses δ_w/s, in the range 0.4–0.8. All slots show a local maximum in potential core, with the optimum values of $\bar{M}$ being slightly different. The sharpness of the potential core peak becomes less as the value of MIX_N for the slot increases. This suggests the dominance of shear-mixing decays as MIX_N increases, as would be anticipated. The potential core length is reduced as MIX_N increases both at the optimum blowing peak, and at the subsequent plateau that exists for $\bar{M}$'s out to 4–5.

Figure 9 shows that the maximum dimensionless potential core length (at optimum blowing) decreases linearly with increasing MIX_N. The slots shown all have lip thicknesses in

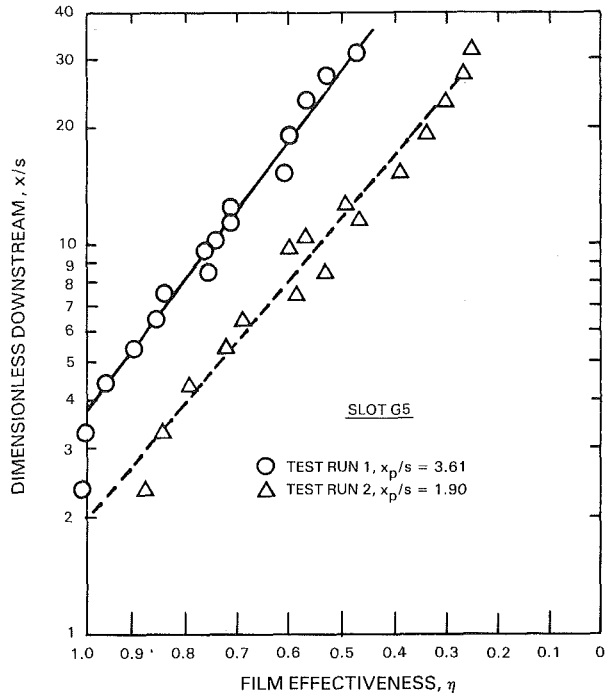

Fig. 6 Measurement of thermal potential core length

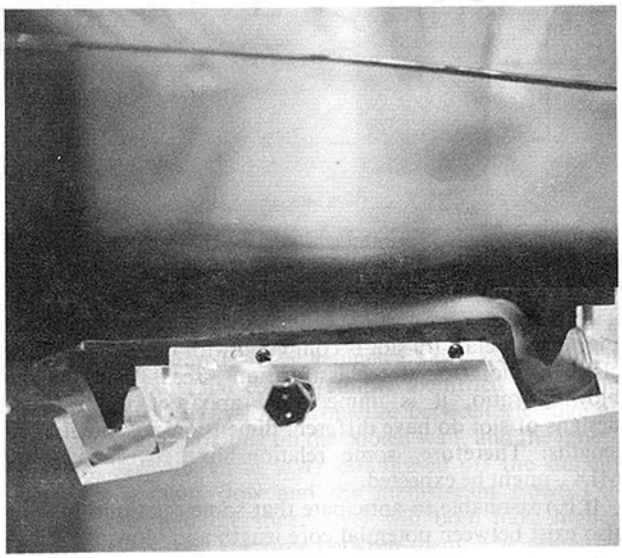

Fig. 7 Demonstration of a longer potential core for a low MIX_N slot

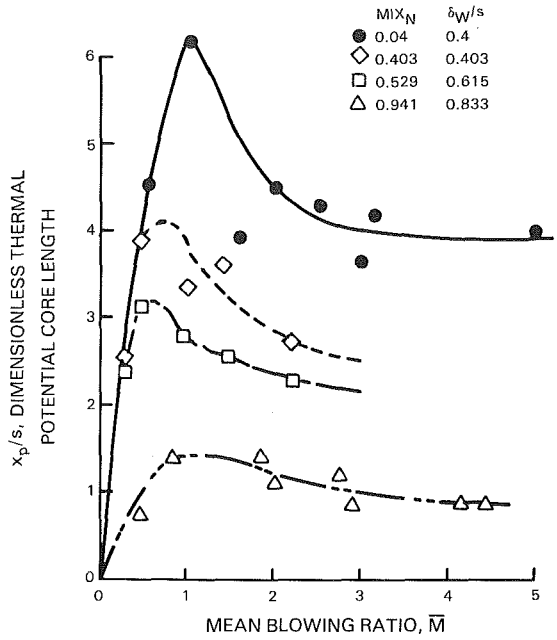

Fig. 8 Optimum blowing ratio and plateau thermal potential cores for practical slots

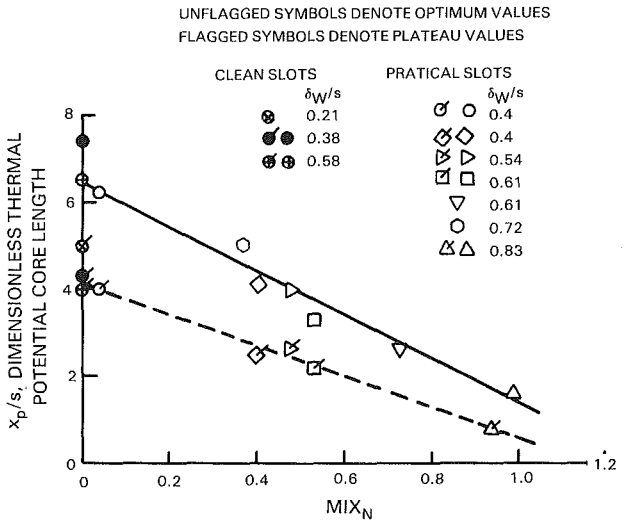

Fig. 9 Dependence of optimum and plateau values of thermal potential core on MIX_N

the range 0.4–0.8 slot heights. Data for a classical clean slot with δ_W/s's of 0.38 and 0.58 are included [4], and that for the slot with δ_w/s of 0.58 (approximately midway between 0.4 and 0.8) lines up nicely with the practical slot data. (An idea of the effect of lip thickness can be obtained from Fig. 8 of [2]). Also shown on Fig. 9 is a similar plot of the plateau values of x_p/s, for the same slots. (Not all of these slots had test-points at sufficiently high $\bar{M}$-values for their plateaux to be adequately defined.) Again, the relation with MIX_N is linear, and the clean slot data agree well with the practical slot results.

When the value of optimum blowing M_{opt} (value of M at which x_p/s reaches a maximum) is plotted against MIX_N, no relationship exists between them at all.

Character of Flow in the Potential Core

To obtain a comprehension of the character of the flow from a practical slot, computational fluid dynamics (CFD) was used. A numerical simulation was made of the slot shown in Figs. 2 and 4.

Numerical Simulation. The numerical simulations were made using a viscous flow code for turbulent, recirculating flows, which was a derivation of the so-called TEACH-code originated at Imperial College, London, England, as a teaching aid [7]. The approach used stays within the framework of continuum mechanics and uses a statistical description of turbulence coupled with the accepted Eulerian flow description offered by the Navier-Stokes equations of motion. Closure to the resulting time-mean equations is provided by turbulence modeling of the eddy-viscosity type. The modeled partial differential equations are manipulated into a general form that permits a single solution algorithm to be used for a numerical procedure. A compound finite differencing scheme is used to discretize the equations. More details of this type of code can be found in the results of a recent National Aeronautics and Space Administration (NASA) study of such methods [8].

The calculations were made using a three-dimensional

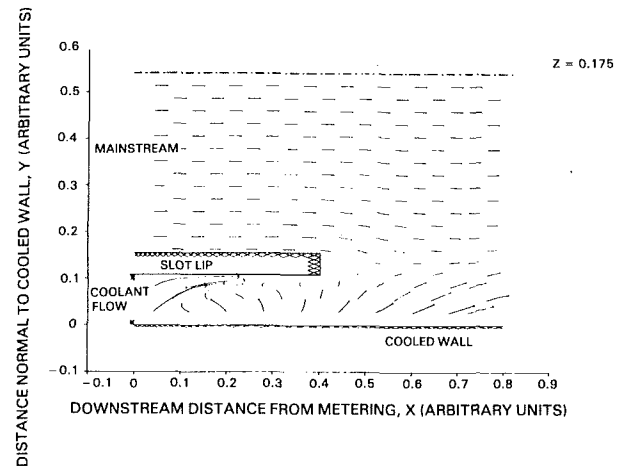

Fig. 10 Longitudinal section through a high MIX_N slot of conventional design with calculated streaklines

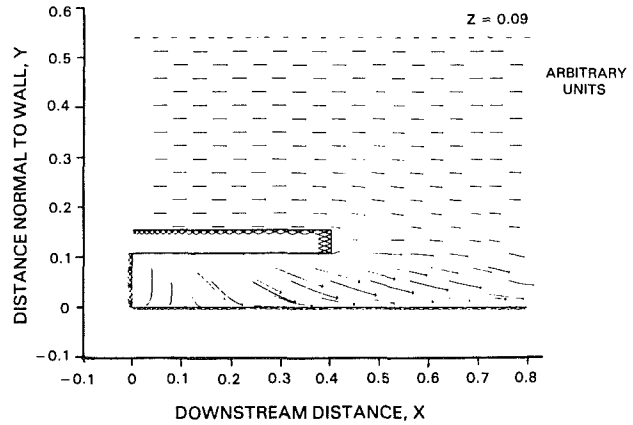

Fig. 11 Longitudinal section midway between cooling ports showing *three-dimensional flow inside slot*

version of the code. The finite differencing scheme was an improved-accuracy compound blend of central, upwind, and bounded skewed upwind differencing, which was developed under NASA sponsorship [9]. The turbulence model was the two-equation, or K − ϵ, model. There were some other slight differences from the standard TEACH-code.

Three-dimensional calculations were made on a 22 × 18 × 11 grid. The calculation domain extended between the centerlines of a pair of adjacent coolant metering ports, where symmetry was used as a boundary condition. Axially, it extended 8 slot heights downstream of the slot exit. Based on Fig. 8, this distance should be more than sufficient to cover the potential core region. The flow was isothermal, constant density, with a blowing ratio $\bar{M}$ of 1.5 and had a mainstream that was uniform in the plane of the coolant ports. The complete boundaries of the circular metering ports were represented in "stair-step" fashion by 20 nodes formed by the orthogonal grid. The coolant jets entered the slot mixing chamber with an angle of 40 deg to the slot lip. All dimensions shown on the figures are in arbitrary units. From a computational point of view, this is immaterial since the relevant turbulence quantities are expressed in terms of these dimensions. The dimensions do have the correct relationships to each other for practical cooling slots. The flow parameters are also correct for the application. The lip thickness to slot height ratio was 0.435, and the MIX_N value of the slot was 0.792.

Flow visualization was provided by a technique known as streaklines. Streaklines are the computational analogue of fine aluminum tracer-powder particles momentarily

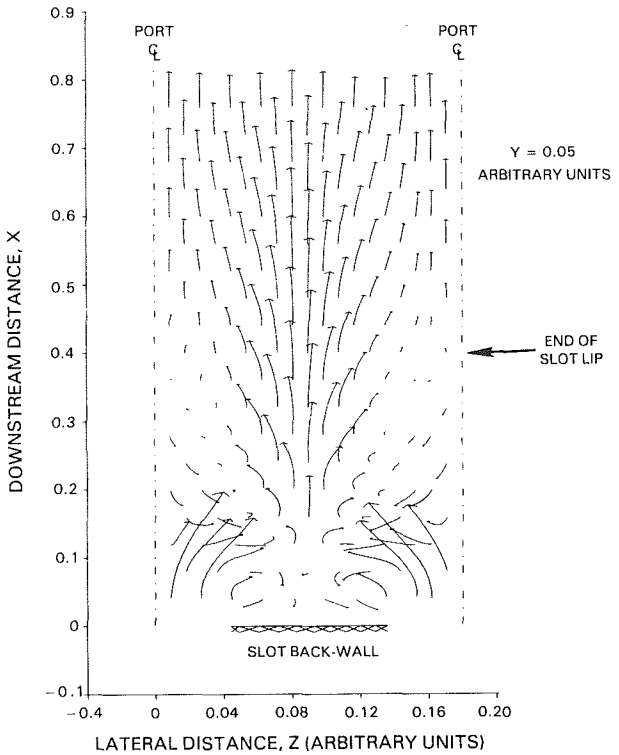

Fig. 12 Lateral section at midslot height showing flow buildup between port centerlines

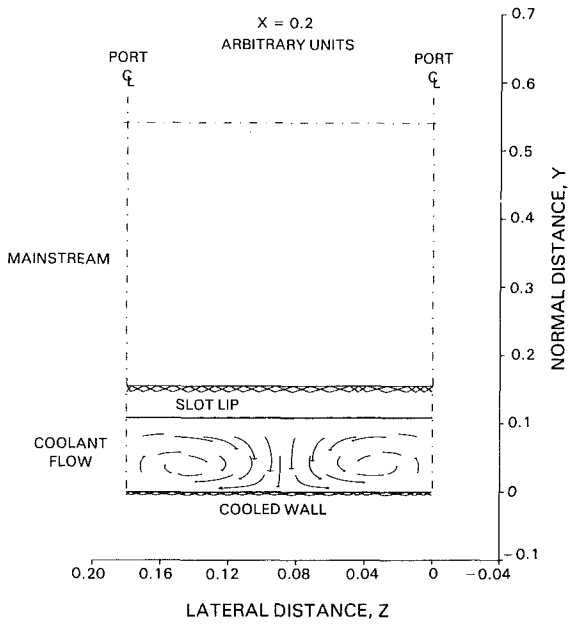

Fig. 13 Vortex development midway down slot

illuminated as they are carried by the flow through a finite-thickness thin sheet of laser light, as used for example, in water tunnels. Streaklines are not streamlines, nor are they vectors, although they have some characteristics of both. The code can generate either random streaklines or uniform lines of origin, in this case the uniform mode is used.

Flow Visualization. It is difficult to mass display three-dimensional flows in monochrome on a two-dimensional medium such as a sheet of paper. This is compounded if the flow to be represented is complex because the streaklines are frozen in time. In an actual water tunnel or on a computer terminal, the streaklines are dynamic, many realizations may

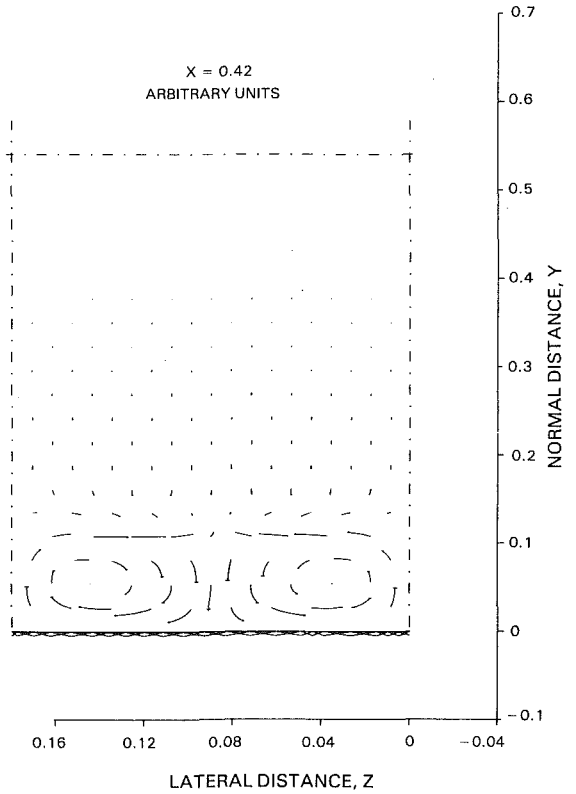

Fig. 14 Demonstration that all of slot flow is involved in vortices at exit from slot

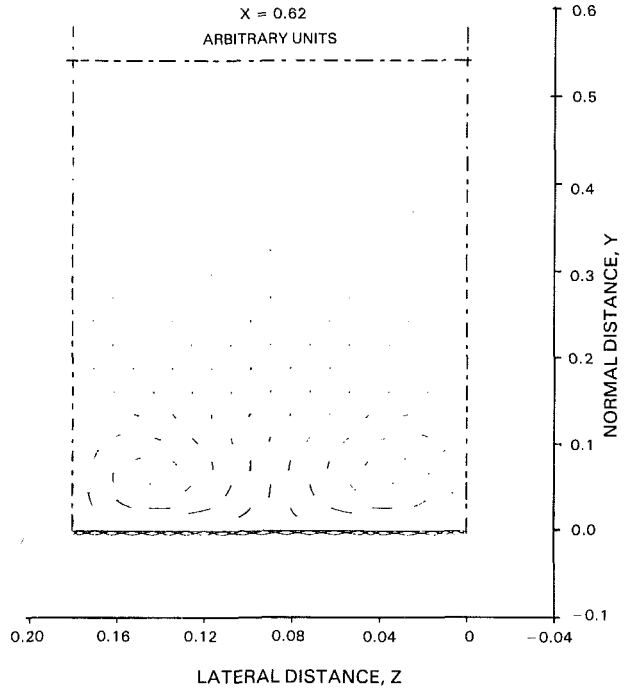

Fig. 15 Calculated vortices are shown to persist well out into initial region of film (1.5 slot heights here)

be viewed, and the field of view may be easily changed in position or rotated at a fixed position to enhance comprehension. In order to build up a complete mental picture of the flow, it therefore becomes necessary to display a number of sections through various planes in the flow.

Figure 10 shows a longitudinal section through the center of a coolant metering port. Coolant can be seen entering the mixing chamber through the port and impinging on the inner surface of the slot lip. However, most of the flow visible in the slot and just downstream of it in the initial region of the film is entering the field from out of this plane. Mainstream flow round the lip and into the film can be seen. A longitudinal section midway between coolant ports is shown in Fig. 11. As is to be expected in this case, all the slot flow is entering from out of plane, demonstrating the three-dimensional nature of the slot flow.

Figure 12 shows a plan view taken at the midslot height; the slot lip ends at an x value of 0.40, and the adjacent pair of coolant half-jets can be seen. Clearly, the flow is complex and the coolant jets do not simply expand like an unconfined single jet. At this plane the concentration of flow is between port centerlines rather than on them, as might have been anticipated. Planes taken very close to the cooled wall and to the lip wall exhibit flow patterns that are very different from this, and which are different from each other. This is a reflection of the coolant impingement on ths slot lip and the crossflows this sets up. Crossing of the streaklines in regions of high activity may be seen, and this is because of the finite thickness of the computational light sheet.

A cross section about halfway down the slot is displayed by Fig. 13. If further explanation of the slot flow revealed by Figs. 10–12 is needed, this figure provides it. The coolant flow within the slot is vortical, with each coolant jet forming a pair of counterrotating vortices. Note that the mainstream flow in this view is normal to the plane of the paper. Figure 14 gives a similar cross section just downstream of the slot lip. The vortices can be seen engaging the flow in the wake off the slot lip, and the mainstream flow is being drawn into the film.

Figure 15 is a further cross section about 1 1/2 slot heights downstream of the lip in the initial region of the film. The vortex motion persists, and about half of the mainstream flow now has a velocity component drawing it into the film. The entrained mainstream flow is directed down to the cooled wall between coolant port centerlines.

Summary of the Flow. The flow inside the slot quickly develops a counterrotating vortex pair from each port admitting coolant into the mixing chamber. The vortices are well developed at the end of the slot lip and persist out into the initial region of the film. Mainstream flow is entrained into the film by the vortex pairs and initially reaches the cooled wall between metering port centerlines. The calculated vortices reproduce the water tunnel observations of Fig. 4.

Figure 16 presents the calculated profiles of axial velocity at the slot outlet, showing the lateral variation at midslot height and, the normal profiles on coolant port centerlines and midway between ports. The velocities are nondimensionalized by the mean coolant velocity $\bar{u}_c$. The lateral distance z is normalized by the port pitch, and the height above the cooled wall y by slot height. In theory, the lateral profile should be symmetrical about z/p of 0.5, and the radial profiles at z/p of 0.0 and 1.0 should be identical. They are not. This is because the grid upon which the calculations were made was not symmetrical about z/p of 0.5, and this is of significance for grids as coarse as the one used presently.

Laterally, the axial velocity is extremely nonuniform, with a peak over twice that of the mean and occurring between the coolant ports. In-line with the metering ports the axial velocity peaks towards the cooled wall, whereas midway between ports the normal profile is fairly flat, with a slight tendency to peak towards the slot lip. These results might not have been entirely anticipated from phenomenological arguments. The profiles are the way they are through the action of the vortices formed.

Slot with Low MIX_N. It is desirable to ascertain if there are any changes in the character of the film initial region as the value of MIX_N is changed. To this end, a test geometry was devised to produce a very low value of MIX_N. The geometry

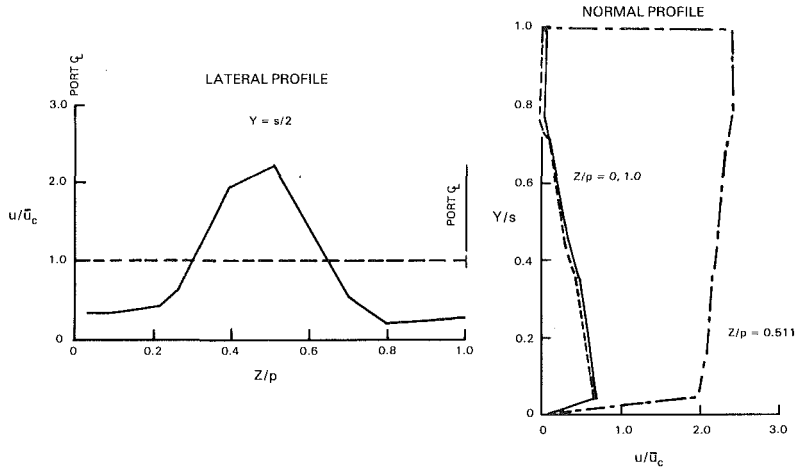

Fig. 16 Calculated profiles of axial velocity at slot outlet

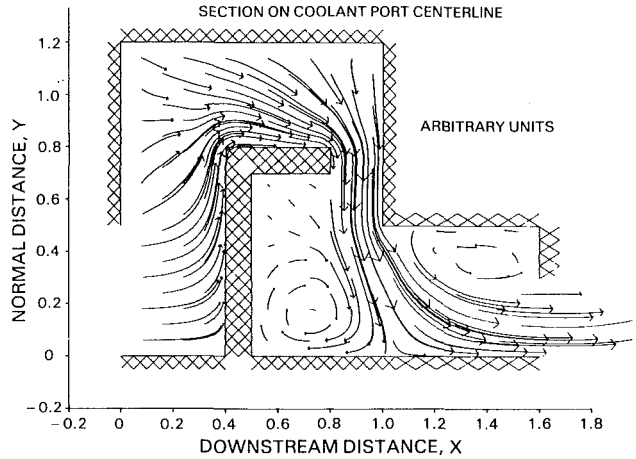

Fig. 17 Longitudinal section through low MIX_N test geometry with streaklines showing flow field

was chosen to include impingement of the coolant jets, a folded configuration to give an extended flow path, an intermediate expansion, and an overall convergence. These features should have been helpful in mixing out the individual jets. The folded flow path also turns the coolant through a full 360 deg rotation during its travel. The value of MIX_N that resulted for this configuration was 0.17, such that the cooling performance of this "slot" if it could have been made, should be good [3].

The calculations were performed on a 14 × 12 × 6 grid, which is a very coarse grid although the rectilinear form of the slot was helpful in this respect. Only the flow in the slot was calculated, i.e., no mainstream.

Flow visualization in this case was by random streaklines. Figure 17 shows the geometry and the general flow characteristics, and is a longitudinal section through the center of a rectangular coolant port. At the first flow turn following impingement the streaklines reveal the highly three-dimensional flow. A lateral section at about midheight of the coolant port is given in Fig. 18. It shows that impingement of the coolant jet and its confinement by adjacent jets on either side generates a vortex pair, much as for the high MIX_N slot. The vortex pair is carried around the first series of turns, and is responsible for the three-dimensionalities evident in Fig. 17. The vortex pair can be detected in the recirculating flow formed on the downstream side of the center partition (impingement wall). Figure 19 is a cross section taken in the outlet. Significant vortex motion persists even in the outlet, although the v and w velocity components have been reduced by a factor of 3–5 from their formation values at the jet inlet.

The lateral profile of axial velocity at midheight in the outlet is rather flat with a maximum $u/\bar{u}_c$ of 1.22 occurring on the slot centerline position, and a minimum of 1.02 midway between port centerlines. These values can be compared with those for the high MIX_N slot. The profiles of axial velocity normal to the cooled wall at the outlet peaked towards the cooled wall. This peaking persists across the outlet but is much more pronounced in-line with the jet inlet where the maximum $u/\bar{u}_c$ was 1.52.

Discussion

The intent was to determine if the slot geometric parameter MIX_N described the initial region of cooling film development. The initial region of the film was conditionally described as a potential core. The existence of a distinct initial region was demonstrated for practical slots in Figs. 2, 3, 6, and 7. However, the bubble tracers introduced inside a slot suggested in Fig. 4 that the hydrodynamics of this initial region were not the same as those described in Fig. 1 for a two-dimensional slot. This was not immediately evident when the (dye) tracer was introduced on the mainstream side of the mixing flow, Figs. 2 and 7. However, these two figures did demonstrate the existence of some kind of initial region and that different practical slots could have different dimensionless "potential core" lengths.

It was shown in Fig. 8 that the thermal potential core length (defined as in Fig. 6) varied with the mean blowing ratio. The nature of this variation suggested a degree of dependency on shear mixing of the mainstream with the growing film, the local peaks suggesting a "matching" condition. However, the peaks in dimensionless thermal potential core indicated this became less pronounced as the values of MIX_N for the slots increased. This is consistent with the postulates made in the first part of this paper concerning the relative parts played by turbulence-induced (shear generated) mixing and entrainment-induced mixing in film decay. The implication is that shear mixing becomes less important in the initial region as MIX_N increases and entrainment-induced mixing dominates.

Shown in Fig. 9 are the maximum values of dimensionless potential core length at optimum blowing ratio, and the plateau values reached at high blowing ratio, plotted against MIX_N for each slot. The relationship between potential core length and MIX_N is linear in each case for the range of data. Potential core length should be zero at infinite MIX_N. It should be remembered that there is an effect of slot lip thickness (see Fig. 8 of [2]), so that the results only apply for the ranges stated. MIX_N does, therefore, describe the initial region, at least in terms of the best performance possible.

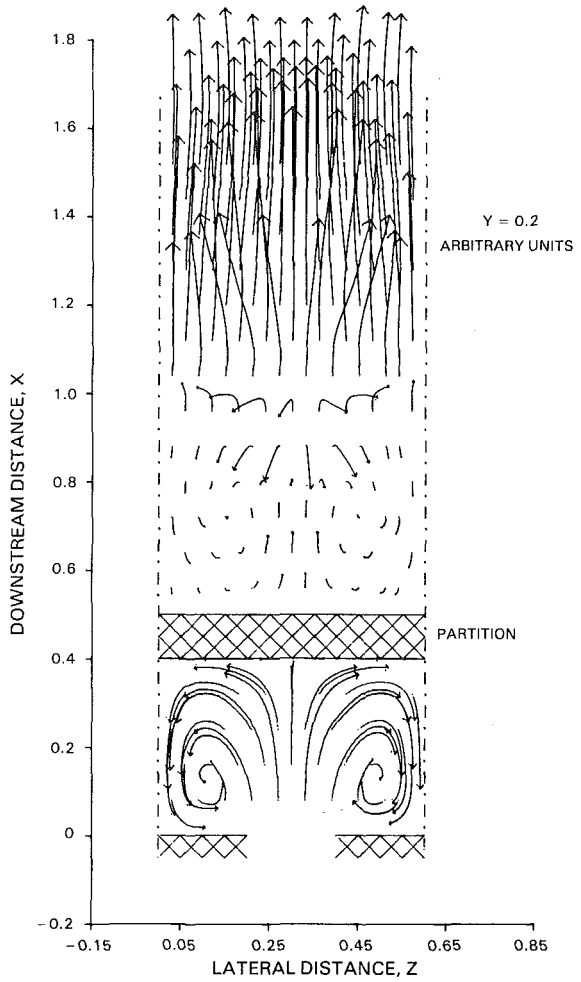

Fig. 18 Lateral section through coolant port showing calculated vortex formation and persistence in recirculated flow behind partition

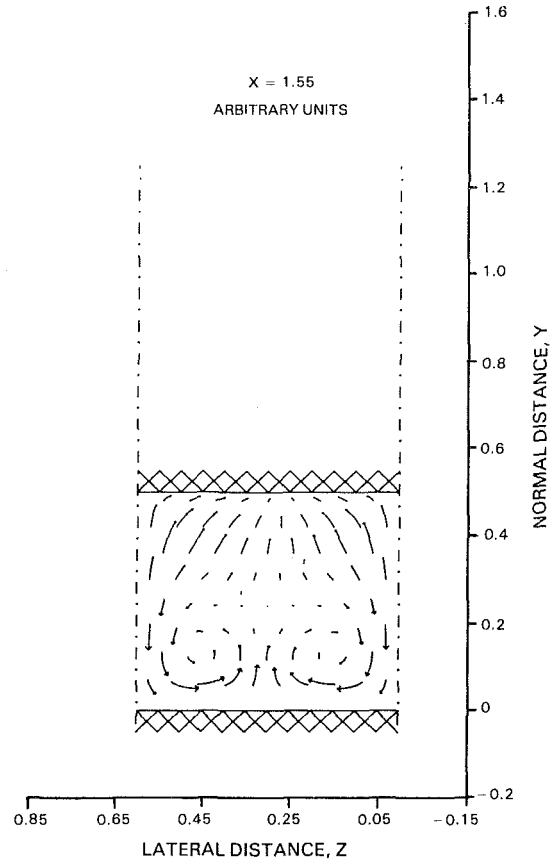

Fig. 19 Transverse cross section at outlet showing vortices despite low MIX_N geometry

With a linear extrapolation beyond the available data the curves of optimum x_p/s and plateau x_p/s do not cross at positive x_p/s. However, within the uncertainty of x_p determination, a crossing at zero x_p/s takes place for MIX_N about 1.2. If this value of MIX_N is entered into Fig. 5 of the first part [3] of this paper, the lines through those data for all $(x - x_p)/(\bar{M}\, s)$ indicate at MIX_N of 1.2 almost perfect agreement with the lipless slot asymptotes. By definition, the lipless slot has zero potential core length. There is consistency, therefore, between the two sets of correlated data. Figure 9 also shows that for MIX_N greater than unity it should be impossible to detect an optimum blowing ratio. Figure 8 supports this. Thus, for MIX_N greater than unity, shear mixing is insignificant.

MIX_N does not define either the value of optimum blowing $\bar{M}_{opt}$ or, the value of $\bar{M}$ at which the plateau is reached. For simple shear mixing with a thin slot lip and plug flows on either side of it, the optimum potential core length in isothermal flow occurs for a velocity ratio of unity. Deviations from unity velocity ratio as an optimum occur with temperature ratio, thickness of lip, and development of nonuniform velocity profiles normal to the cooled wall (see Fig. 9 of [1], for example). MIX_N is not set up to account for these factors. Pure shear mixing in the initial region of the film is only applicable for two-dimensional slots. Since the highest values of potential core lengths at the potential core lengths at the optimum and plateau blowing are observed for MIX_N of zero, i.e., two-dimensional slots, shear mixing gives the minimum entrainment of mainstream into the film. This is the expected behavior.

The CFD studies proved most useful in explaining the details of the behavior of the three-dimensional flows within practical slots. Figures 14–16 in particular, show the formation of persistent vortices within the high-MIX_N slot, and confirm the water tunnel observations of Fig. 4. The calculated profiles of axial velocity in Figs. 16 and 17 bear interesting comparison with Figs. 9 and 10 of [1]. They also may be related to the lateral variation of film effectiveness in Fig. 7 of the first part of this paper [3] and to the isotherms of Fig. 5 of this part.

The most important finding is that slots with a high value of MIX_N have an initial region that consists entirely of vortices (Fig. 15) rather than simple shear layers as had previously been supposed. Calculation methods for potential core length that are based on considerations of shear mixing [4] are seen to be inappropriate. The successes achieved by such methods [4, 5, 1] are more apparent than real. The adequate comparisons with measurements (e.g., [1]) arise through the incorporation of empirical factors that were supposed to account for normal and radial profile variations, the limited range of injection variables covered, and the severely restricted range of MIX_N investigated. Careful consideration of the calculations shown in [1] reveals too much sensitivity of potential core length to blowing ratio. This is a failing that the present work would explain.

Any system of metering ports discharging coolant into a confined mixing chamber will generate vortices. Once formed, these vortices appear to be remarkably persistent, as Fig. 19 indicates. A low value of MIX_N will reduce the lateral nonuniformities in coolant distribution very significantly but does not entirely eliminate the vortices formed. Wholesale turning of the flow within the slot can assist in maintaining these vortices. It may be said therefore, that all three-dimensional practical slots will most likely have an initial

region consisting to some degree of vortex flow. Further investigation is required into the conditions governing the relative dominances of shear mixing and vortex entrainment into the initial region of the film. The success of the simplified three-zone model of film cooling demonstrated in the first part of this paper suggests that the vortices are not important in the main region of the film. It would appear therefore, that treatment of the thermal potential core lengths measured for practical slots as being the distance required for the vortices to undergo a significant decrease in strength, would be a reasonable working hypothesis for future study.

Conclusions

An examination of flow visualization information and measured data, in conjunction with computational fluid dynamic investigations, has been used to study the flow development inside practical film cooling slots and in the initial regions of the films produced by such slots. These studies have been linked to the parameter MIX_N used to characterize the geometry of the slot mixing chamber. The following conclusions were drawn.

1 MIX_N successfully correlates the maximum possible values for the dimensionless distances representing the film initial regions.

2 MIX_N, overall, is a suitable parameter for characterizing cooling slot geometry. It may be used to compare the merit of one design to another, and to evaluate the impacts of manufacturing tolerances on the performance of a given design. A high value MIX_N will result in low film cooling effectiveness. A MIX_N value of zero corresponds to an ideal, two-dimensional slot.

3 The success of the MIX_N grouping for correlating slot performance indicates the following are good design features: long lips, close spacing of metering ports, and impingement of the coolant jets on a solid surface. It does not follow that these are good features from either a structural or cost point of view. Wholesale turning of the flow within the slot is probably not a desirable fluid dynamic feature.

4 When MIX_N is high the lateral variation in axial velocity of coolant at the slot exit is high; when the value of MIX_N is low the exit flow is much more uniform. Peaks in lateral axial velocity profile can be either in plane with the coolant metering ports, or between them, depending on the mixing chamber geometry. The lateral variation in axial velocity corresponds to a lateral variation in film effectiveness.

5 The initial region of the film produced by practical slots will consist of a line of pairs of counterrotating vortices, generated by the coolant metering at slot inlet. This is true for all values of MIX_N investigated but is more intense if MIX_N is large. Once formed, these vortices can be persistent.

6 When MIX_N is large, the length of the initial region and its sensitivity to mean blowing ratio $\bar{M}$ are reduced. Shear-control of the mainstream mixing with the initial region is at a minimum and entrainment dominates. It is incorrect to view the film initial region produced by practical slots as being like the potential core system of two-dimensional slots.

7 Downstream of the initial region, film models based on shear mixing appear to be adequate. The initial region therefore probably represents the distance required for the vortices to undergo a significant decrease in strength. Further study is required however.

8 CFD calculations of the film development from practical slots should start inside the slots at the coolant metering. Starting the calculations at the slot lip, even with realistic normal and lateral profiles of axial velocity, will not yield the correct flow picture. All calculations should be three-dimensional.

Acknowledgments

The authors wish to thank the Pratt & Whitney organization of the United Technologies Corporation for permission to publish this paper. Special thanks are given to the authors' colleagues Jim Dierberger for making available the photographs of Figs. 2, 4, and 7, Dr. V. J. Sarli who took the I.R. photograph of Fig. 5, and to Dr. S. A. Syed for assistance with Figs. 17–19 inclusive. Finally, the authors wish it to be known that the opinions expressed are personal and are not necessarily held by any of the organizations or persons referred to in this paper.

References

1 Sturgess, G. J., "Account of Film Turbulence for Predicting Film Cooling Effectiveness in Gas Turbine Combustors," ASME JOURNAL OF ENGINEERING FOR POWER, Vol. 102, July 1980, pp. 524–534.

2 Sturgess, G. J., "Gas Turbine Combustor Design Challenges for 1980's," Paper No. AIAA-80-1285, AIAA/SAE/ASME 16th, Joint Propulsion Conference, Hartford, Connecticut, June 30–July 2, 1980.

3 Sturgess, G. J., "Design of Combustor Cooling Slots for High Film Effectiveness: Part I—Film General Development," ASME JOURNAL OF ENGINEERING FOR GAS TURBINES AND POWER, this issue.

4 Sturgess, G. J., "Wall Cooling by Gaseous Injection for a High Performance Combustion System," Ph.D. thesis, University of Technology, Loughborough, England, 1970.

5 Sturgess, G. J., and Lenertz, J. E., "Account of Mainstream Turbulence for Predicting Film Cooling Effectiveness of Gas Turbine Combustors," ASME Paper No. 77-HT-10, ASME-AIChE Heat Transfer Conference, Salt Lake City, Utah, Aug. 1977.

6 Sturgess, G. J., "Correlation of Data and Prediction of Effectiveness from Film Cooling Injection Geometries of a Practical Nature," *Proc. Symp. Combustion and Heat Transfer in Gas Turbine Systems*, edited by E. R. Norster, Pergamon Press, 1971, pp. 229–250.

7 Gosman, A. D., and Ideriah, F. T. K., "TEACH-2E: A General Computer Program for Two-Dimensional, Turbulent, Recirculating Flows," Imperial College, London, England, Mech. Engng. Rept. (unnumbered), June 1976.

8 Sturgess, G. J., "Aerothermal Modeling, Phase I—Final Report," NASA Report CR 168202, May 27, 1983.

9 "Error Reduction," NASA Contract NAS3-23686, Dec. 1982.

Cold Flow and Combustion Experiments With a New Burner Air Distribution Concept

B. V. Johnson
Supervisor.
Heat Transfer Technology,
United Technologies Research Center,
E. Hartford, CT 06108

S. J. Markowski
Senior Staff Project Engineer,
Combustion Fuels and Emissions.

H. M. Craig
Development Engineer,
Combustion Technology.

Pratt & Whitney Aircraft Group,
E. Hartford, CT 06108

Experiments were conducted with a JT8D-engine sized can combustor modified such that all the combustion and dilution air entered through the burner front face from a single plenum through counter-rotating annular swirlers. Cold flow experiments were conducted to visualize and to develop a mixing and recirculation flow pattern within the combustor which contained annular and central recirculation cells and featured rapid mixing in the downstream section of the combustor. Laser velocimeter measurements, downstream of the air inlet configuration used in the combustion experiments, showed the largest velocity gradients in the radial direction were in the tangential velocity profile. Low-pressure combustion experiments were conducted with three flat spray fuel nozzle orientations and three air inlet geometries to determine the general air inlet and fuel injection characteristics required to produce acceptable combustion characteristics with the selected swirler configuration. The combustion experiments included emission, total pressure and total temperature measurements at the burner exit plane. Low emission levels and temperature pattern factors with relatively low burner pressure losses were demonstrated.

Introduction

The perennial goals for aircraft gas turbine combustion systems are (1) to increase burner durability, (2) reduce and tailor the temperature pattern distribution, (3) decrease the combustor pressure loss, (4) increase combustion stability and relight capability, and (5) decrease combustor length. More recent environmental and economical pressures are adding additional goals such as (6) reducing undesirable emissions, and (7) being able to burn a broad spectrum of fuels. Although the gas turbine combustor can be arranged in a can, annular, or cannular configuration, most combustor designs have similar characteristics, namely, the fuel and primary air are introduced in the upstream section of the burner and dilution air is injected through the holes in the downstream section of the burner walls (e.g., [1]). The technology for this type of combustor is mature and performance improvements are difficult to obtain. Therefore, new combustor design concepts are sought to obtain significantly improved performance in the combustor goals.

An innovative combustor air distribution concept, which shows promise of improving some of the aforementioned design factors without hindering the others, has been evolving at Pratt & Whitney (e.g., [2–5]). A sketch of the components for a can combustor employing this front-feed air management concept is shown in Fig. 1. The largest amount of air, 40–60% of the total, enters through the center tube as secondary combustion/dilution air. Lesser amounts, 15–20% of the total, enter through the primary combustion air duct; the remaining cooling air enters through cooling louvers in the burner walls. The primary air and most of the secondary/dilution air enters the combustor with swirl. As a result, the combustion flow patterns and dilution processes differ significantly from conventional practice.

This burner air distribution concept requires a toroidal recirculation cell for the primary combustion zone that surrounds the secondary combustion/dilution air pipe. The secondary fuel system utilizes a filming/air blast concept. A new primary fuel injection system was required to inject fuel into the primary toroidal recirculation zone for vaporization and combustion. Turbulent shear at the interface between the primary and secondary air stream is desired to produce high-rate diffusion burning in both combustion zones. Large-scale

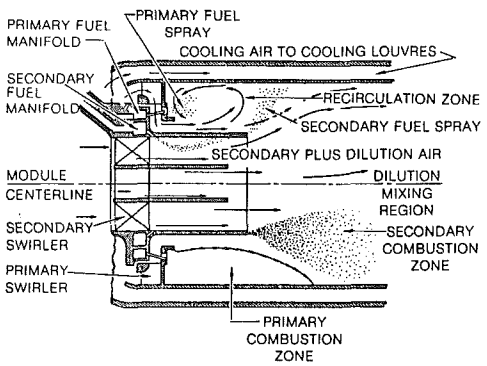

Fig. 1 Sketch of burner components and flow zones

Contributed by the Gas Turbine Division of THE AMERICAN SOCIETY OF MECHANICAL ENGINEERS and presented at the 30th International Gas Turbine Conference and Exhibit, Houston, Texas, March 18–21, 1985. Manuscript received at ASME Headquarters, December 18, 1984. Paper No. 85-GT-40.

mixing across the burner at an axial location a short distance downstream of the combustion zone is required to dilute the combustion products and make the exit temperature profile fairly uniform. These internal flow characteristics will be obtained by correct selection of the air inlet conditions and utilization of a compatible fuel injection/atomization system. Although the present research was conducted with a can burner, this innovative air distribution concept also appears applicable to annular or cannular burner designs.

The objectives of the research described herein were to develop air inlet configurations which are compatible with the new air distribution concept for a can combustor and to determine the fuel injection requirements for the resulting air flow and mixing patterns. The total research program was comprised of cold flow tests and combustion tests with a JT8D-engine sized burner fed from a single plenum. These experiments were a followup to previous experiments [5] which used multiple plenums for the primary combustion, secondary combustion/dilution and cooling air. Prior to the combustion experiments described herein, cold flow tests were conducted to develop primary combustion zone and dilution mixing zone characteristics compatible with the concept. Because the highest unburned hydrocarbon emissions usually occur at low power, the combustion tests were conducted with inlet air pressure, temperature and flow rates near the JT8D engine idle condition. Results from this research showed that attractive emission levels and temperature pattern factors could be obtained with low burner pressure losses. These results imply that the innovative burner air distribution concept described has good potential for use in future gas turbines.

Cold Flow Experiments

The cold flow experiments were conducted (1) to develop an air injection configuration which produces the flow pattern shown in Fig. 1 with low burner liner pressure losses and (2) to evaluate methods of simulating fuel injection configurations which would provide an annular fuel cloud in the annular recirculation cell. The parameters varied in the flow visualization experiments were the primary and secondary air swirl angles, the secondary air inlet length, and loss mechanisms in the primary air passages. Based on initial design studies which included consideration of pressure drop constraints and the desire to use JT8D-sized hardware, the secondary air inlet diameter was fixed at 76. mm (3.0 in.) and the burner maximum diameter was fixed at 165. mm (6.5 in.). The maximum axial Mach number envisioned for this configuration was 0.15.

Flow Visualization Apparatus and Conditions. The cold flow visualization experiments to develop acceptable flow patterns were conducted with water as the working fluid and dye or small air bubbles as flow tracers. These experiments were conducted in a 6.5 in. inside diameter lucite tube with the primary and secondary "air" injectors fed from a single plenum. The flow in the front portion of the burner was simulated in these experiments and no cooling flow was injected through wall cooling louvers in the downstream portion of the model. Previous flow visualization experiments (prior to the combustion experiments reported in [5]) with and without the downstream wall louvers showed that flow in the upstream end of the burner can with a convectively cooled upstream wall was generally unaffected by the injection of coolant through the downstream louvers.

The tests were conducted with flow rates of 4.88 L/s (76 gal/min) which produced a Reynolds number based on average velocity and chamber diameter of 40,000. This is about a factor of 10 less than the Reynolds number for the engine idle flow, based on the inlet temperature. However, the Reynolds number is well into the turbulent range where the major characteristics of the flow patterns have been shown to be independent of flow rate.

Flow Pattern Visualization Results. Several combinations of primary and secondary air swirl angles and secondary air injector lengths were evaluated before acceptable flow characteristics were obtained. The initial flow visualization experiments were conducted with a configuration similar to that used in [5] using corotating swirlers, i.e., θ_s = 30 deg and θ_p = 45 deg. The resulting flow pattern (Fig. 2*a*) had no centerline recirculation cell and had an annular recirculation cell which extended about 75. mm (3 in.) downstream of the inlet. Based on our previous work [5], this flow pattern was deemed unacceptable because (1) the mixing between the primary and secondary streams was inadequate at the equivalent burner exit plane location; and (2) the annular recirculation cell contained multiple recirculation cells and did not have the rapid mixing with the injected flow and entrainment of fresh air believed necessary for a good pilot flame region. The criteria used to determine an acceptable candidate combustor flow pattern for this combustor concept were based on the studies conducted in [5]. The significant change in flow patterns between the present study and [5] for similar primary and secondary swirl angles was attributed to (*a*) an increase in the ratios of swirler diameters to burner can diameter, (*b*) a decrease in shear between the primary and secondary flows and the annular recirculation zone, and (*c*) an increased effectiveness of the jet inside the secondary swirler to prevent the center recirculation cell from forming. Item (*a*) was viewed as a constraint for these experiments (to obtain the required flow rates at low Mach numbers) and therefore effort was directed toward lessening the effects of items (*b*) and (*c*).

Geometric configurations with the variations shown in Table 1 were evaluated. Although the 45-deg secondary swirler produced the type of flow pattern desired, this swirler was judged unacceptable because higher pressure losses were measured in concurrent air tests than with the 30-deg swirler. Therefore, the primary swirl angle was varied until most of the desired flow characteristics were obtained. A flow pattern

Nomenclature

EI_i = emission index of species i (equation (1))
L = combustor length, mm (in.)
f/a = fuel air ratio, W_f/W_a
M_s = average axial Mach number of secondary flow at inlet
M_{Wi} = molecular weight of species i
M_{Wp} = molecular weight of combustion products, 28
P_t = total pressure, kp (psia)
PPM_i = concentration of species i, parts per million
T = local gas temperature, K
T_{ave} = average gas temperature at exit plane, K
T_{in} = inlet gas temperature, K
T_{max} = maximum gas temperature at exit plane, K
U = local axial velocity, m/s
U_{ref} = average axial velocity at maximum burner diameter, m/s
V = local tangential velocity, m/s
W_a = total air flow rate, kg/s
W_f = fuel flow rate, kg/s
η_e = combustion efficiency (equation (2))
Θ_p = primary air swirl angle, deg
Θ_s = secondary air swirl angle, deg

Table 1 Parameters varied in flow pattern visualization tests

Secondary air swirl angle	+30, +45 deg mean angle free vortex
Primary air swirl angle	+60, +45, +30−, +20, 0, −30, −45, −60 deg
Secondary air swirler center tube	Configurations which produced center tube blockage and/or spillage at vane ID downstream of center tube
Primary air flow rate	Various degrees of blockage of primary air inlet passage upstream of swirler
Secondary air induct duct length	13 mm (0.5 in.), 32 mm (1.25 in.) and 64 mm (2.5 in.)

with the annular and centerline recirculation cells deemed desirable for this combustor concept was obtained with the secondary swirler angle of 30 deg and for a range of primary swirler angles: -30 deg > Θ_p > -60 deg. The flow pattern obtained for Θ_s = 30 deg and Θ_p = -45 deg with full flow through the primary vanes and some modification to the center tube through the secondary flow swirler is shown in Fig. 2(*b*).

Laser Velocimeter Measurements. Axial and tangential velocity profiles were obtained 13 mm (0.5 in.) downstream of the secondary flow inlet for selected combinations of the primary and secondary swirler angles to assist in assessing the cause-effect relationships in the production of vortex breakdown and the establishment of the annular and centerline recirculation cells. The inlet velocity profiles for the configuration producing the flow patterns shown in Fig. 2(*b*) are presented in Fig. 3. Note the magnitude of the peak tangential velocities in the positive and negative directions are approximately equal. Note also that the axial velocities along the entire swirler face are positive (axially downstream) ensuring that hot gases from the center recirculation cell will not burn the swirler. Note that relatively little shear occurs in the axial velocity profile between the flows from the primary and secondary swirler. With lower axial velocities than the secondary flow, the primary flow acts as a buffer layer and decreases large-scale mixing between the secondary flow and the annular recirculation cell. The turbulent shear that was observed probably occurred because of the sharp tangential velocity gradient between the flow from the secondary and primary swirlers.

Combustion Experiments

A series of combustion experiments was conducted to assess the combustion, dilution and pressure drop characteristics associated with this combustor in a "real combustor" environment. These experiments were conducted with previously used JT8D development cases and instrumentation. However, the burner length was shortened to approximately 60% of the conventional JT8D size in accordance with one of the the project goals to demonstrate that this new air management concept results in a more compact combustor. The experiments were conducted with the air flow rate, pressure, and temperature typical of advanced JT8D engines at the idle flow condition.

Test Apparatus. A photograph of the air and fuel injector module is shown in Fig. 4. This injector has secondary and primary air swirl angles (Θ_s = 30 deg and Θ_p = -45 deg) employed in the previously described cold flow test and a 13-mm (0.5-in.) secondary air inlet length. Twelve Spraying Systems Co. stainless steel flat spray nozzles were mounted equally spaced on the OD of the secondary air inlet duct. Extensions of 19 and 51 mm (0.75 and 2.00 in.) were bolted to the injector configuration shown to obtain the secondary air inlet lengths used in the experiments. The fuel injection nozzles used in the primary airstream for these exploratory

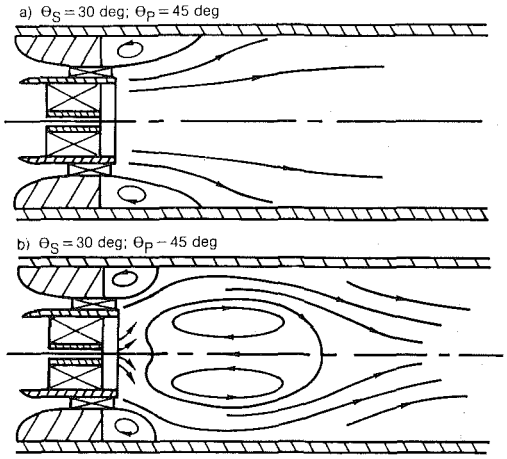

Fig. 2 Flow visualization patterns with initial configuration and combustion experiments configuration

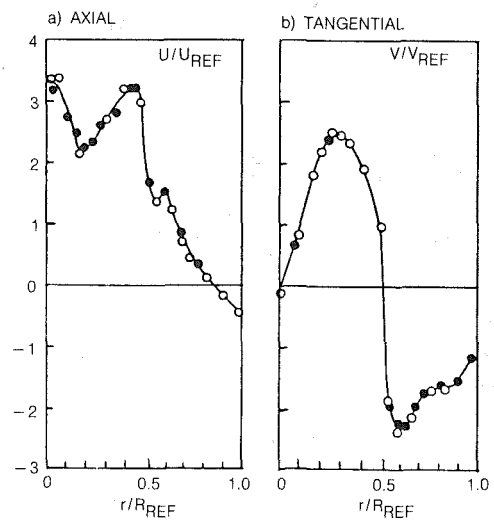

Fig. 3 Velocity profiles 13 mm (0.5 in.) downstream of secondary flow inlet plane for 13 mm (0.5 in.) inlet length

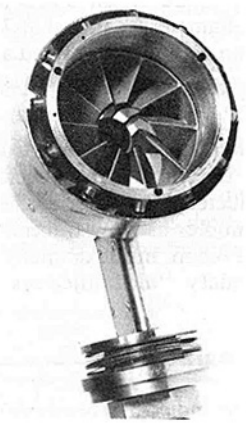

Fig. 4 Photograph of air and fuel injector

experiments were commercially available Spraying Systems Co. flat spray nozzles (Fig. 5). Four equally spaced nozzles produced a fuel droplet cloud that approximated the annular fuel spray desired for this combustion concept. The nozzles were arranged such that the angles between the fuel spray and the combustor centerline were 15, 30, and 45 deg. Each of the spray nozzles was fed with an individual supply tube con-

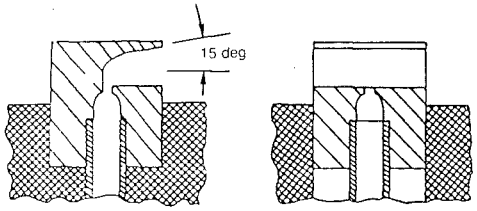

Fig. 5 Cross-sectional sketches of flat spray fuel injection nozzles

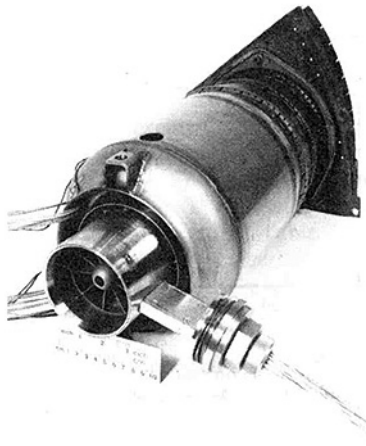

Fig. 6 Photograph of assembled injector, combustor can, and 1/9th sector transition duct

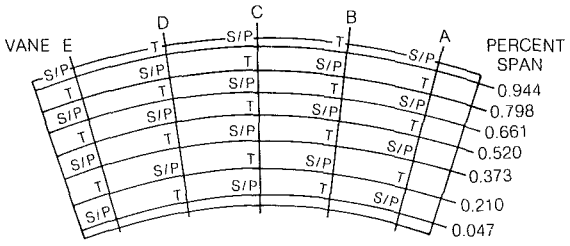

Fig. 7 Instrumentation map for combustion experiments; S/P = combined emission sampling and total pressure probe, T = total temperature probe

nected to a manifold outside the burner case. This fuel injection configuration provided the range of fuel spray locations required for these assessment experiments without requiring the development of a flight type fuel injector configuration.

The air and fuel injector module was mounted in the burner can and attached to the transition duct as shown in Fig. 6. A sketch of the instrumentation probe arrangement mounted on straight vanes at the transition duct exit is shown in Fig. 7.

Instrumentation. The instrumentation employed conformed to ASME and industry standards. The airflow rate was measured with a venturi nozzle. The fuel flow rate was measured by a calibrated turbine flowmeter. Metal-sheathed chromel-alumel thermocouples were employed for temperature measurements. Electrical pressure transducers were used to measure the gas stream pressures. Total pressure, gas sampling, and total temperature probes utilized Kiel heads to provide ± 30 deg of air angle incidence insensitivity. Gas samples were routed through heated lines to an array of solenoid valves by means of which the samples could either be combined or extracted individually. The emissions sampling and analysis system was capable of continuously monitoring the emission of carbon monoxide, oxygen, carbon dioxide,

Table 2 Parameters varied and results from combustion emission experiments

Run No.	Fuel injection angle	Secondary air duct length, mm (in.)	Standard conditions EI_{CO}	EI_{UHC}	$\Delta\eta\%$
5	45	13 (0.5)	200	100	85
7	45	64 (2.5)	25	16	97.6
8	15	64 (2.5)	26*	5*	98.4*
9	30	64 (2.5)	23	1.5	99.4
11	30	32 (1.25)	35	4	98.8

*Data obtained at f/a = 0.0128—lowest f/a ratio for which stationary experiments could be conducted.

unburned hydrocarbons, and oxides of nitrogen. The instruments employed were: CO-Nondispersive Infrared, Beckman Model 315B; CO_2-Nondispersive Infrared, Beckman Model 315B; O_2-Paramagnetic Analyzer, Scott Model 150; UHC-Flame Ionization Detector, and NO_x-Chemiluminescence Detector, TECO Model 10A.

The emission index was determined from

$$EI_i = \frac{PPM_i}{M_{Wp} \times 1000.0} \frac{1 + f/a}{f/a} M_{Wi} \tag{1}$$

The reported combustion efficiency was derived from the CO and UHC emission levels. For 100% efficiency, the CO emission level would be the equilibrium level and the UHC level would be zero. Assigning appropriate heating values to these constituents (assuming UHC can be represented by CH_4) the value of the combustion efficiency was calculated from

$$\eta_e = 100\left[1 - \frac{4.3(EI_{CO} - EI_{CO,equil}) + 21.6\ EI_{UHC}}{18.6 \times 10^3}\right] \tag{2}$$

Emission Measurements. Combustion tests were conducted for the five combinations of fuel injector angle and secondary air inlet length shown in Table 2 over a range of fuel air ratios limited at the high f/a ratios by the maximum measured temperature (2000° F) and at the low f/a ratios by the spatial and temporal stability of the flame. The flame characteristics were monitored visually with the aid of a TV camera viewed from the exhaust end through the straight vanes at the transition duct exit.

A series of tests was conducted with the longest secondary air inlet and the three fuel injection angles, i.e., Tests 7, 8, and 9. The unburned hydrocarbon (UHC) and carbon monoxide (CO) emission results and the overall efficiencies for these tests are shown in Figs. 8(*a*), (*b*), and (*c*). The CO results for these configurations (Fig. 8*b*) are essentially independent of fuel injection angle and a function of fuel/air ratio. At the standard condition (JT8D idle with f/a = 0.012) the EI_{CO} values range from 23 to 26 with an accompanying decrease in combustion efficiency of approximately 0.6%. The unburned hydrocarbon emission results, EI_{UHC} (Fig. 8*a*), show significant variations throughout the range of fuel/air ratios tested. The configuration with the fuel injection angle of 30 deg had the lowest hydrocarbon emissions with the values of EI_{UHC} = 1.5 ($\Delta\eta$ = 0.1%) at the standard fuel flow condition. The emission results obtained with a fuel injection angle of 15 deg are grouped between EI_{UHC} = 2 and 10. However, stable operation of the combustor could not be obtained at the standard f/a ratio, f/a = 0.012. The values of EI_{UHC} measured with a fuel injection angle of 45 deg were approximately 10 times those obtained for a fuel injection angle of 30 deg. The conclusion from these experiments is that the combustion characteristics are very sensitive to fuel droplet location. Injection at 30 deg caused the largest droplets to impinge on the burner wall just upstream of the annular recirculation cell stagnation line. This droplet

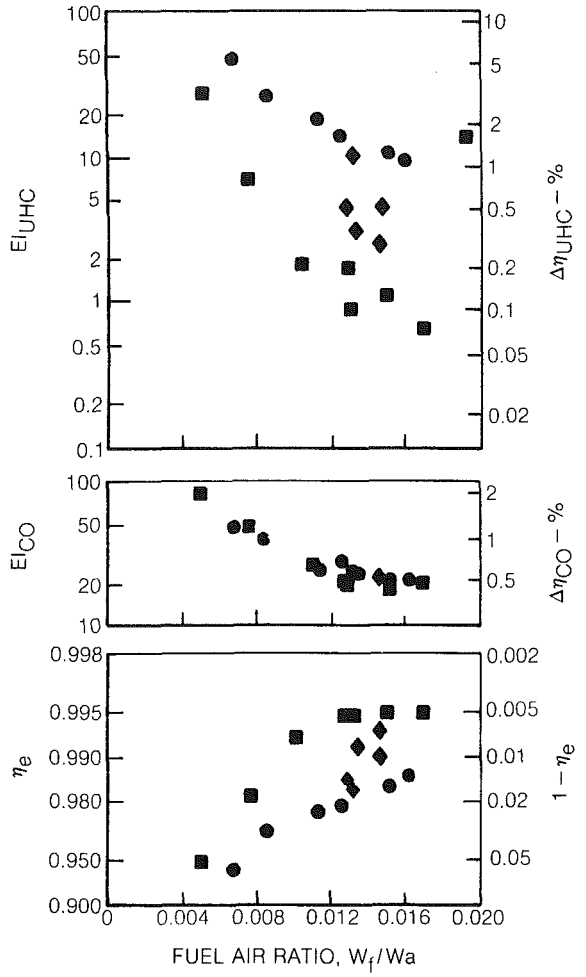

Fig. 8 Effects of fuel/air ratio on emissions and efficiency for three fuel injection angles with 64-mm (2.5-in.) secondary air inlet; • 45 deg – run 7, ■ 30 deg – run 9, ♦ 15 deg – run 8

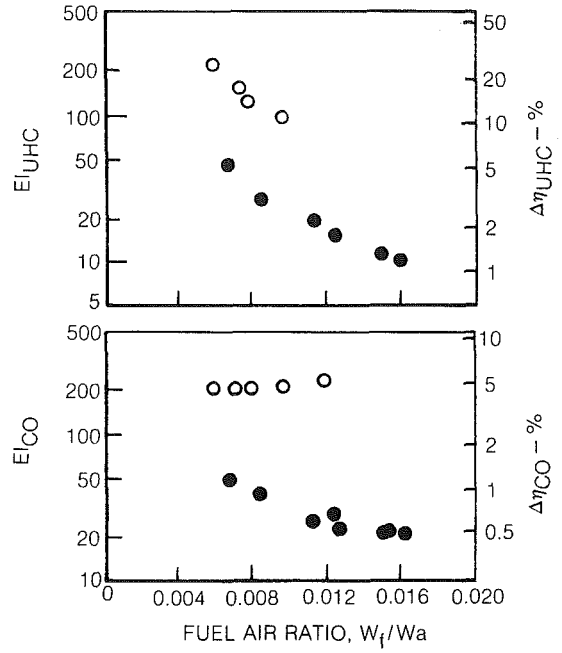

Fig. 9 Comparison of emission results with 13-mm (0.5-in.) and 64-mm (2.5-in.) secondary air inlet for 45-deg fuel injection angle; ○ 13 mm, • 64 mm

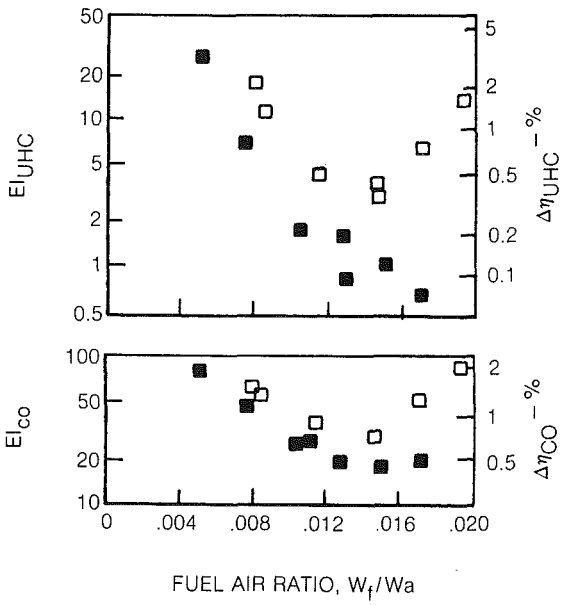

Fig. 10 Comparison of emission results with 32-mm (1.25-in.) and 64-mm (2.50-in.) secondary air inlet for 30-deg fuel injection angle; □ 32 mm, ■ 64 mm

trajectory probably causes the fuel to be contained in the annular recirculation region until vaporized and burned. The 45-deg fuel injection angle probably resulted in fuel being mixed with the fresh air before vaporization and combustion were complete. The 15-deg fuel injection angle resulted in better performance at the higher f/a ratios than the 45-deg injector. At these fuel flow rates the droplets must have penetrated the recirculation cell shear layers as a sheet. At the lower f/a ratios for which a consistent set of data could not be obtained, the fuel was probably swept directly into the mixing regions between the recirculation cell, the primary air and the secondary air stream.

The effects of secondary air inlet length on the combustion characteristics are presented in Figs. 9 and 10. For the 45-deg fuel injection configuration the values of EI_{UHC} and EI_{CO} increased by factors of 5 and 8, respectively, when the secondary air inlet length was shortened from 64 mm (2.5 in.) to 13 mm (0.5 in.). This caused the overall combustion efficiency to drop from 97.6 to about 85% at the standard flow condition. The conclusion from this comparison was that the annular recirculation cell required some protection from premature mixing with the secondary air stream, i.e., injecting the secondary air at the upstream end of the combustor caused the unburned fuel to be diluted by the secondary air. The second comparison (Fig. 10) shows the effects of shortening the secondary air inlet length from 64 mm (2.5 in.) to 32 mm (1.25) for the 30-deg fuel injector. For this fuel injection configuration, decreasing the secondary air injection length caused the EI_{UHC} and EI_{CO} to increase by factors of 3 and 1.5, respectively, at the standard air and fuel-flow conditions. The net result was a decrease of overall combustion efficiency from 99.4 to 98.8% at the standard-flow condition. The configuration with a 32-mm (1.25-in.) secondary air inlet shows minimum values of both EI_{UHC} and EI_{CO} at a f/a ratio of 0.0145 which probably indicates a strong sensitivity of the flow to the fuel-spray patterns for this configuration. The conclusion from this comparison was that reasonable combustion efficiencies could be obtained with both secondary air inlet lengths.

The overall conclusions from these emission measurements were that (1) fuel injectors which produce droplet spray patterns contained within the annular recirculation cell and

Table 3 Pressure drop ratio across burner at standard condition

Run No.	Secondary air inlet length, mm (in.)	$\Delta P/P$
5	13 (0.5)	0.029
7	64 (2.5)	0.024
8	64 (2.5)	0.023
9	64 (2.5)	0.025
11	32 (1.25)	0.021
Average		0.024

(2) a moderate length annular recirculation cell are required to produce good low-power emission characteristics with the subject combustor air management concept.

Pressure Drop Measurements. The total pressure drop between the inlet plenum and the gas-sample rakes mounted on the straight vanes (Fig. 7) at the transition duct exit was measured for each test point. The pressure drop ratios, $\Delta P/P$, across the burner are presented in Table 3 for each of the configurations evaluated. The uncertainty in the pressure difference measurements and the pressure drop ratio were approximately 0.1 psi and 0.004, respectively. Note the total average pressure drop ratio across the burner liner is 2.4%, a value somewhat less than current gas turbine design practice.

Pattern Factor Measurements. The total temperature was measured at each "T" location on Fig. 7 for each data point. The data were analyzed and reduced to determine a temperature pattern factor using the relationship: $PF = (T_{max} - T_{in})/(T_{ref} - T_{in})$. The pattern factors were calculated using $T_{ref} = T_{ideal}$ and $T_{ref} = T_{ave,center}$. The pattern factors determined for run 9 are shown in Fig. 11 as a function of the fuel/air ratio. The pattern factors determined using $T_{ref} = T_{ideal}$ are approximately 0.05 higher than those obtained in [5]. The differences are attributed to the use of a standard transition duct with cooling air in the present experiments. The pattern factor determined using the average of the temperatures measured between 20% and 80% span, i.e., $T_{ave,\ center} = T_{ref}$, produced the same range of temperature pattern factors as that obtained in [5]. The conclusion from these exit temperature measurements is that the temperature pattern factors obtained with them are satisfactory and indicate rather uniformly diluted combustion products. This is an especially remarkable result considering the liner pressure loss was less than 2.5%.

Low Blowout. The low blowout and ignition characteristics of this combustor are as good or better than reported in [5]. The low blowout fuel/air ratio for run 9 (with the lowest UHC and CO emissions) was 0.0024. The range of low blowout and ignition fuel/air ratios obtained was acceptable, i.e., $f/a(\text{min.}) < 0.0035$, for all the configurations except with the fuel nozzles at 15 deg from axial where a value of $f/a(\text{min.}) = 0.005$ was obtained.

Concluding Remarks

The results obtained from the present cold flow and combustion experiments with this novel combustor air management concept were generally favorable. The liner pressure drop and exhaust temperature pattern factors were both low ($\Delta P/P < 2.5\%$ and $PF \approx 0.10$ to 0.16) and are desirable combustor features.

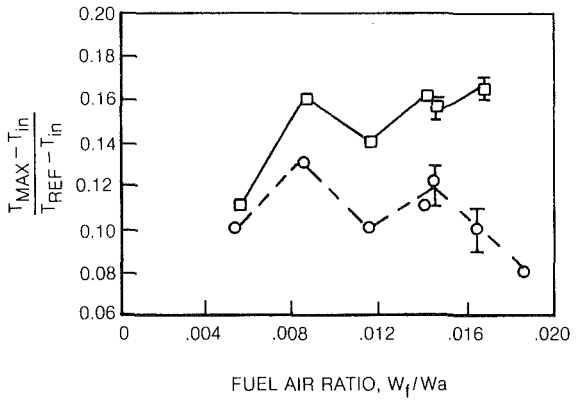

Fig. 11 *Pattern factor results for run 9;* ○ $T_{ref} = T_{ave,center}$, □ $T_{ref} = T_{ideal}$

The most unexpected difficulty in transferring the air-management technology from the laboratory combustor used in [5] to the present combustor configuration (operating from a single plenum) was in obtaining satisfactory centerline and annular recirculation cells. In retrospect, these flow-pattern problems can be attributed to the significant increase in swirler size and the change to a single plenum air supply.

The general burner-air-distribution concept, described in this paper, has been incorporated into annular burner conceptual designs and multimodule research burner configurations. Evaluations of selected air and fuel injection configurations in multiple-module combustion experiments for annular burners are currently planned and results will be reported by other researchers at a later date.

Acknowledgments

The authors gratefully acknowledge the efforts of the following UTRC staff for their assistance in obtaining the results reported herein: J. L. Kettle for the mechanical design of the combustion rig, Dr. J. C. Bennett (now at the University of Connecticut) for the emissions measurements, Mr. G. Gagnon for the laser velocimeter measurements and flow visualization photographs, and Ms. S. Orr for data reduction.

References

1 Henderson, R. E., and Blazowski, W. S., *Turbopropulsion Combustion Technology*. Chapter 20, the Aerothermodynamics of Aircraft Gas Turbine Engines (Ed. G. C. Oates). Air Force Aero Propulsion Laboratory Report AFAPL, TR 78-52, July 1978.

2 Markowski, S. J., Lohmann, R. P., and Reilly, R. S., "The VORBIX Burner—A New Approach to Gas Turbine Combustors," ASME JOURNAL OF ENGINEERING FOR POWER, Jan. 1976, pp. 123-129.

3 Roberts, R., Fiorentino, A., and Green, W., Experimental Clean Combustor Programs, Phase III—Final Report. NASA CR-135253, Oct. 1977.

4 Reilly, R. S., and Markowski, S. J., Vortex Burning and Mixing (VORBIX) Augmentation System. AIAA Paper No. 76-678 prepared for AIAA/ASME 12th Propulsion Conference, July 1976.

5 Markowski, S. J., Johnson, B. V., and Marshall, R. L., "Combustion Experiments with a New Burner Air Distribution Concept," ASME Preprint No. 83-GT-31, 28th International Gas Turbine Conference, Mar. 27-31, 1983.

Flame Temperature Estimation of Conventional and Future Jet Fuels

Ö. L. Gülder
National Research Council of Canada,
Division of Mechanical Engineering,
Ottawa, Ontario K1A OR6, Canada

An approximate formula is presented by means of which the adiabatic flame temperature of jet fuel-air systems can be calculated as functions of pressure, temperature, equivalence ratio, and hydrogen to carbon atomic ratio of the fuel. The formula has been developed by fitting of the data from a detailed chemical equilibrium code to a functional expression. Comparisons of the results from the proposed formula with the results obtained from a chemical equilibrium code have shown that the average error in estimated temperatures is around 0.4 percent, the maximum error being less than 0.8 percent. This formula provides a very fast and easy means of predicting flame temperatures as compared to thermodynamic equilibrium calculations, and it is also applicable to diesel fuels, gasolines, pure alkanes, and aromatics as well as jet fuels.

Introduction

Flame temperature is one of the most important properties in combustion. It has a controlling effect on the rate of chemical reaction, and it plays an important role in the design and performance of the jet engine hot sections. Combustor liner temperature, distribution of the species in combustion products and turbine inlet temperature are dependent on flame temperature. Critical parameters in design and optimization of the hot sections are the maximum liner temperature and maximum turbine inlet temperature, which are determined by the maximum flame temperature and flame emissivity.

The maximum attainable flame temperature for any given initial conditions is the adiabatic flame temperature. The adiabatic flame temperature is a function of fuel type (characterized by enthalpy of formation or enthalpy of combustion or hydrogen to carbon ratio H/C), fuel-air equivalence ratio ϕ, temperatures of the fuel T_f and air T_a, and pressure P. The adiabatic flame temperature can be calculated by assuming chemical equilibrium of the species. Then for a given fuel, temperature, and pressure, the mass action equations can be solved directly for species concentrations, from which the temperature and other thermodynamic properties can be derived. An alternative approach is to calculate the species concentrations that minimize the Gibbs free energy of the system. Unfortunately, either approach involves long iteration procedures resulting in time-consuming and expensive calculations.

Approximate but much simpler methods of estimating the flame temperature can provide appreciable advantages in routine calculations and simulation studies. Glassman and Clark [1] presented universal graphs for adiabatic flame temperature of hydrocarbon-air systems as a function of enthalpy of formation of the fuel, equivalence ratio, and hydrogen to carbon ratio for atmospheric initial conditions. Chang and Rhee [2] reported functional expressions for the adiabatic flame temperature of pure hydrocarbons in terms of equivalence ratio, combustion pressure, and the number of carbon atoms in the fuel molecule. Fuel-air equivalence ratio is limited to $0.5 \leq \phi \leq 1.0$ and the initial mixture temperature to 298 K. These limitations restrict the use of the equations to very special circumstances and prevent their application to real life fuels whose molecular carbon number or enthalpy of formation cannot be easily estimated.

In this paper, a simple equation that predicts the adiabatic

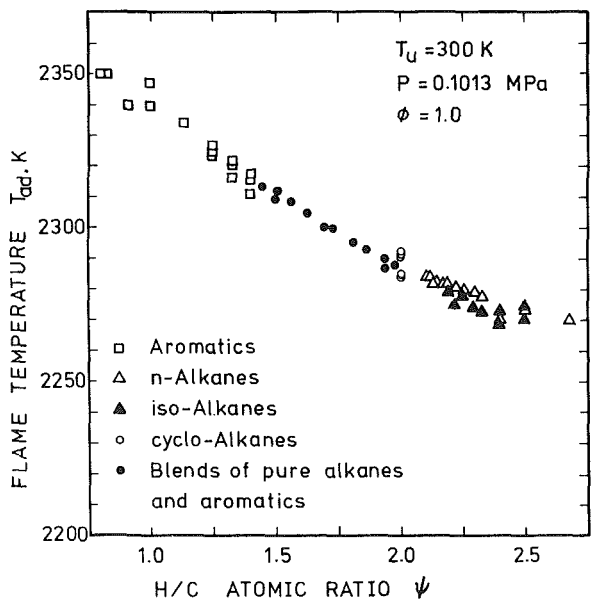

Fig. 1 Variation of the flame temperature of pure hydrocarbons and pure hydrocarbon blends with H/C atomic ratio

Contributed by the Gas Turbine Division of THE AMERICAN SOCIETY OF MECHANICAL ENGINEERS and presented at the 30th International Gas Turbine Conference and Exhibit, Houston, Texas, March 18-21, 1985. Manuscript received at ASME Headquarters, December 18, 1984. Paper No. 85-GT-31.

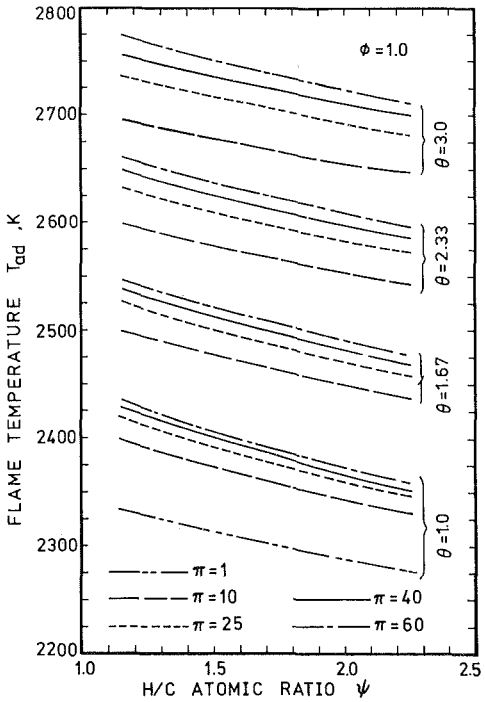

Fig. 2 Variation of the flame temperature with H/C atomic ratio at different initial temperatures and pressures

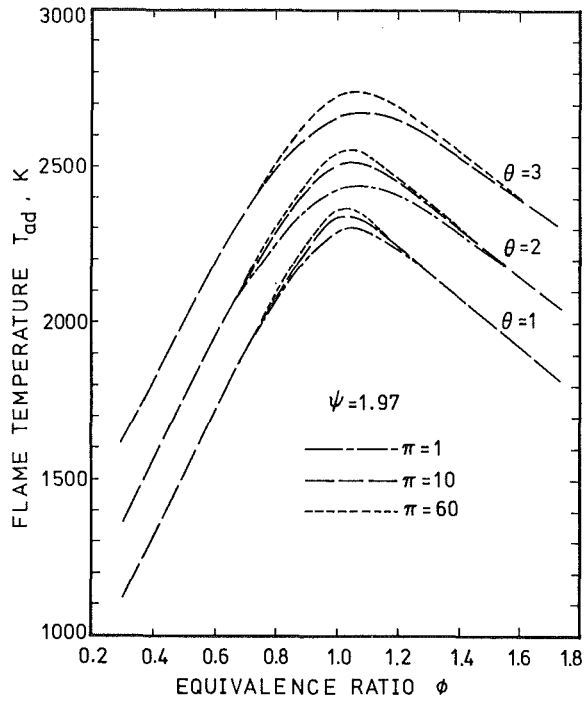

Fig. 3 Dependence of the flame temperature on fuel-air equivalence ratio at various pressures and temperatures

flame temperature as a function of atomic hydrogen to carbon ratio of the fuel, equivalence ratio, reactant temperature and pressure, will be presented and its accuracy will be evaluated. The equation has been developed by curve fitting of data obtained from a detailed chemical equilibrium code. The proposed equation is applicable in the following ranges: $0.3 \leq \phi \leq 1.6$, 0.1 MPa $\leq P \leq$ 7.5 MPa, 275 K $\leq T_u \leq$ 950 K, and $0.8 \leq$ H/C ≤ 2.5. These ranges cover the conditions of interest in gas turbines and the properties of conventional and future liquid jet fuels.

Background

The relationship between the flame temperature and the fuel properties is expressed in terms of enthalpy of formation and H/C atomic ratio of the fuel by Glassman and Clark [1]. Chang and Rhee [2] have utilized the number of carbon atoms in the fuel molecule and derived different sets of constants for each hydrocarbon group (paraffins, aromatics, etc.) for their proposed equation. In Fig. 1, the adiabatic flame temperature of 59 pure hydrocarbons (iso-, normal- and cyclo-alkanes, and aromatics) and 12 of their different blends are plotted as a function of H/C atomic ratio. It is obvious that fuel effects on the adiabatic flame temperature can be accurately predicted by considering only H/C atomic ratio for nonolefinic fuels (olefins less than 10 percent by volume). Similar relationships have been obtained for other equivalence ratios.

The variation of the adiabatic flame temperature with H/C atomic ratio is illustrated in Fig. 2 for different initial mixture temperatures and combustion pressures. The degree of effect of pressure on adiabatic flame temperature decreases with an increase in pressure. An increase in the initial mixture temperature will cause an increase in the flame temperature; however, only approximately half of an increase in initial temperature is translated into an increase in flame temperature, Fig. 2.

The variation of the adiabatic flame temperature with equivalence ratio is shown in Fig. 3. Due to dissociation effects, the peak flame temperature occurs at a slightly rich equivalence ratio independent of the initial temperature and pressure. For equivalence ratios leaner than $\phi = 0.65$ pressure does not affect the flame temperature. The same phenomenon is observed also on the rich side, Fig. 3; however, the equivalence ratio at which the pressure effect becomes nil varies with the initial temperature.

Results presented in Figs. 2 and 3 are for model fuels consisting of different proportions of pure hydrocarbons. The adiabatic flame temperatures were computed by using a chemical equilibrium code that considers 14 species in the products, namely H_2, H, O_2, N_2, N, OH, H_2O, O, NO, NO_2,

Nomenclature

A = constant, equation (1)
A/F = air to fuel mass ratio
a_i = constants, equations (2-4)
b_i = constants, equations (2-4)
C_p = specific heat at constant pressure, kJ/kgK
c_i = constants, equations (2-4)
ΔH = enthalpy of evaporation, kJ/kg
P = pressure, MPa
P_o = reference pressure, 0.1013 MPa (= 1 atm.)
T = temperature, K
T_o = reference temperature, 300 K
x = pressure exponent, equation (2)
y = temperature exponent, equation (3)
z = exponent for ψ, equation (4)

Greek Letters

α = constant, equation (1)
β = constant, equation (1)
θ = T_u/T_o dimensionless temperature
λ = constant, equation (1)
π = P/P_o dimensionless pressure
ρ = density
ϕ = fuel-air equivalence ratio; actual (A/F)/stoichiometric (A/F)
ψ = H/C atomic ratio

Subscripts

a = air
ad = adiabatic flame
f = fuel
mb = midboiling point
u = initial mixture

Table 1 Constants for equation (1)

	$0.3 \le \phi \le 1.0$		$1.0 < \phi \le 1.6$	
Constants	$0.92 \le \theta < 2$	$2 \le \theta \le 3.2$	$0.92 \le \theta < 2$	$2 \le \theta \le 3.2$
A	2361.7644	2315.7520	916.8261	1246.1778
α	0.1157	−0.0493	0.2885	0.3819
β	−0.9489	−1.1141	0.1456	0.3479
λ	−1.0976	−1.1807	−3.2771	−2.0365
a_1	0.0143	0.0106	0.0311	0.0361
b_1	−0.0553	−0.0450	−0.0780	−0.0850
c_1	0.0526	0.0482	0.0497	0.0517
a_2	0.3955	0.5688	0.0254	0.0097
b_2	−0.4417	−0.5500	0.2602	0.5020
c_2	0.1410	0.1319	−0.1318	−0.2471
a_3	0.0052	0.0108	0.0042	0.0170
b_3	−0.1289	−0.1291	−0.1781	−0.1894
c_3	0.0827	0.0848	0.0980	0.1037

N_2O, CO, CO_2, and Ar. Thermochemical data were taken from standard tables [3, 4]. The solution procedure of the code is similar to that described by Benson et al. [5]. The accuracy of the program was checked against NASA-Lewis program [6], and other published codes [7, 8] for various fuels and conditions, and good agreement has been obtained.

Approximate Flame Temperature Equation

An expression of the following form has been adopted to predict the adiabatic flame temperature of jet fuels

$$T_{ad} = A\sigma^{\alpha} \cdot \exp\left[\beta(\sigma+\lambda)^2\right] \cdot \pi^x \theta^y \psi^z \quad (1)$$

where

$$x = a_1 + b_1\sigma + c_1\sigma^2 \quad (2)$$

$$y = a_2 + b_2\sigma + c_2\sigma^2 \quad (3)$$

and

$$z = a_3 + b_3\sigma + c_2\sigma^2 \quad (4)$$

π is the dimensionless pressure P/P_o where $P_o = 0.1013$ MPa, θ the dimensionless initial mixture temperature T_u/T_o where $T_o = 300$K, ψ the H/C atomic ratio, $\sigma = \phi$ for $\phi \le 1.0$ where ϕ is the fuel-air equivalence ratio and $\sigma = \phi - 0.7$ for $\phi > 1.0$, and A, α, β, λ, a_i, b_i, and c_i are constants. In order to have an accurate prediction equation four sets of constants have been determined for the following ranges:

$$0.3 \le \phi \le 1.0 \text{ and } 0.92 \le \theta \le 2.0 \quad (5)$$

$$0.3 \le \phi \le 1.0 \text{ and } 2.0 \le \theta \le 3.2 \quad (6)$$

$$1.0 < \phi \le 1.6 \text{ and } 0.92 \le \theta < 2.0 \quad (7)$$

$$1.0 < \phi \le 1.6 \text{ and } 2.0 \le \theta \le 3.2 \quad (8)$$

The values of constants for each range classification are listed in Table 1.

It should be noted that equation (1) assumes that the fuel is in vapor form and is at the same temperature as that of the air, i.e.,

$$T_u = T_a = T_f \quad (9)$$

However, for the cases where the fuel is in liquid form, a correction should be applied to θ so that the enthalpy of evaporation of the fuel and the temperature difference between air and fuel can be accounted for. The enthalpy of evaporation of jet fuels can be estimated from the following equation [9], in terms of fuel density and temperature

$$\Delta H = \frac{360 - 0.39T_f}{\rho_f} (\text{kJ/kg}) \quad (10)$$

where ρ_f is the relative density of the liquid fuel. For more accurate estimation methods of the enthalpies of evaporation, the techniques proposed in [4, 10] can be used.

For the liquid fuel temperature T_f and the air temperature T_a, the equivalent T_u can be computed as follows

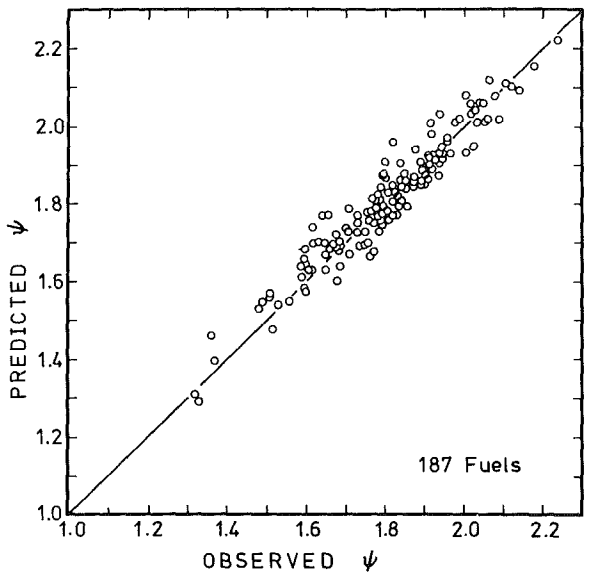

Fig. 4 Correlation between H/C atomic ratio and the relative density and midboiling point of the fuel

$$T_u = \frac{C_{pf}T_f + (A/F)C_{pa}T_a - \Delta H}{C_{pf} + (A/F)C_{pa}} \quad (11)$$

where C_{pf} and C_{pa} are the mean specific heats of the fuel vapor and air, respectively, and (A/F) is the air to fuel mass ratio. C_{pf} can be calculated as a function of temperature as follows [11]:

$$C_{pf} = (0.363 + 0.000467\ T)(5 - 0.001\ \rho_{fo})\ \text{kJ/kg•K} \quad (12)$$

where ρ_{fo} is the density of the fuel at 288.6 K. C_{pa} can be obtained from standard tables.

The H/C atomic ratio ψ for the jet fuels can be determined experimentally [12] with a high accuracy. It is also possible to estimate the hydrogen content using the density, averaged midboiling point and aromatic content of the fuel [13]. For quick and easy estimates of ψ, the following correlation, in terms of relative density and midboiling point, is proposed

$$\psi = 0.9479[T_{mb}/100]^{0.2527}[\rho_f]^{-2.4063} \quad (13)$$

where T_{mb} is the midboiling point and ρ_f is the relative density of the fuel at 20°C. Equation (13) has been derived using 187 jet and diesel fuels (both conventional and future fuels). Predicted H/C atomic ratios are plotted against observed values in Fig. 4. The accuracy of the correlation is acceptable for most practical cases of interest.

Accuracy of Approximate Equation

To evaluate the accuracy of the proposed equation, a set of comparisons of results obtained from equation (1) and those

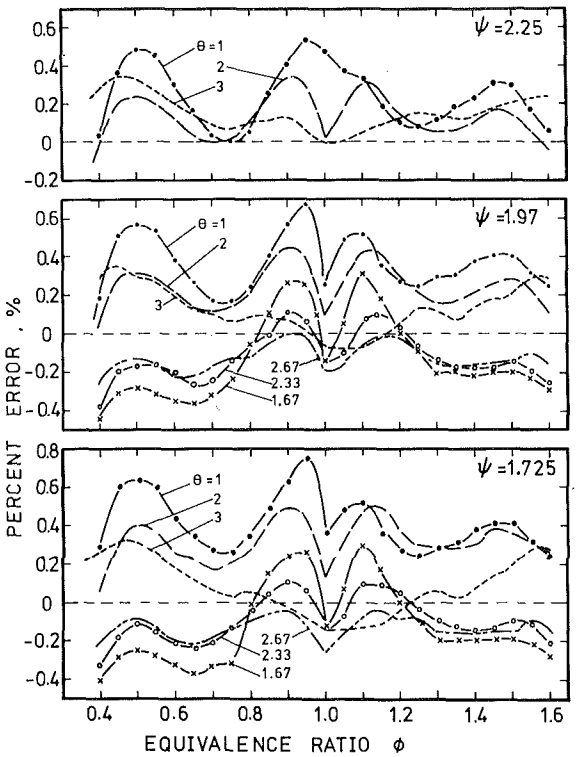

Fig. 5 Error of approximate temperature prediction versus equivalence ratio for various fuels and temperatures at $\pi = 10$

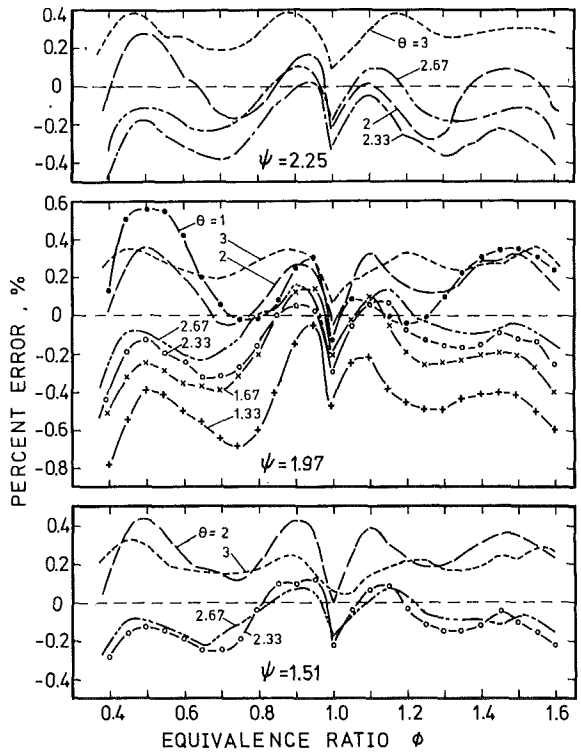

Fig. 6 Error of approximate temperature prediction versus equivalence ratio for various fuels and temperatures at $\pi = 25$

obtained from a detailed thermodynamic equilibrium code has been made. Results are compared for all possible combinations of the following values of pressure, temperature, equivalence ratio, and H/C atomic ratio

ψ = 2.25, 1.97, 1.725, 1.508, 1.316, 1.143

θ = 1, 1.33, 1.67, 2, 2.33, 2.67, 3

π = 1, 10, 25, 40, 60

ϕ = 0.3 to 1.6 with 0.05 increments

Comparisons made at $\pi = 10$ and $\pi = 25$ are shown in Figs. 5 and 6, respectively. Percent error is defined as $(T_{ad} - T'_{ad})/T_{ad}$, where T'_{ad} is the predicted flame temperature. The average error is around 0.4 percent and maximum error is less than 0.8 percent. Percentage errors similar to those of Figs. 5 and 6 have been observed at other conditions considered.

It should be noted here that the proposed equation is valid for the following ranges

$$0.3 \le \phi \le 1.6$$

$$0.8 \le \psi \le 2.5$$

$$0.92 \le \theta \le 3.2$$

$$1.0 \le \pi \le 75.0$$

But the applicability of the equation is not limited to only jet fuels; it is also valid for nonolefinic (less than 10 percent olefins) diesel fuels and gasolines as well as pure alkanes and aromatics within the specified limits.

Concluding Remarks

A functional expression is presented by means of which the adiabatic flame temperature of jet fuel–air systems can be calculated as functions of pressure, temperature, equivalence ratio, and H/C atomic ratio of the fuel. This equation provides a very fast means of predicting flame temperature as compared to thermodynamic equilibrium calculations. Results of the predictions using the proposed equation are compared with the results obtained from a detailed chemical equilibrium code incorporating 14 species in the combustion products, and it is shown that the accuracy of the approximate equation is acceptable over the conditions of interest for a wide range of fuel characteristics.

A procedure is outlined to determine the equivalent initial reactant's temperature for cases where the fuel is in liquid form. Also a correlation is presented for approximate estimates of the fuel's H/C atomic ratio using the midboiling point and relative density of the fuel. This correlation is applicable for jet and diesel fuels.

The proposed equation is expected to reduce the computation time considerably in gas turbine thermal calculations. Especially, for the development of simulation models and heat transfer calculations requiring multiple determinations of flame temperature as a function of time and space coordinates for varying equivalence ratios, the approximate equation provides distinct advantages over the chemical equilibrium codes. Another usage of the proposed equation is that for cases where exact adiabatic flame temperature is required equation (1) can be used to advantage as generator of good initial guesses (usually within 0.5 percent of the exact solution), to speed convergence of iterative calculations of chemical equilibrium codes.

References

1 Glassman, I., and Clark, G., "Universal Hydrocarbon-Air Temperature Graphs," Paper No. 12, Combustion Institute, Eastern Section, 1983 Fall Technical Meeting, Providence, RI, Nov. 8–10, 1983.

2 Chang, S. L., and Rhee, K. T., "Adiabatic Flame Temperature Estimates of Lean Fuel/Air Mixtures," *Combustion Science and Technology*, Vol. 35, 1983, pp. 203–206.

3 Stull, D. R., and Prophet, H. (Eds.), *JANAF Thermochemical Tables*, U.S. National Bureau of Standards Publications, NSRD-NBS 37 and supplement, 1971.

4 Reid, R. C., Prausnitz, J. M., and Sherwood, T. K., *The Properties of Gases and Liquids* (3rd ed.), McGraw-Hill, New York, 1977.

5 Benson, R. S., Annand, W. J. D., and Baruah, P. C., "A Simulation

Model Including Intake and Exhaust Systems for a Single Cylinder Four-Stoke Cycle Spark Ignition Engine," *International Journal of Mechanical Engineering Science*, Vol. 17, 1975, pp. 97–124.

6 Gordon, S., and McBride, B. J., "Complex Chemical Equilibrium Calculation," NASA SP-273, 1971.

7 Olikara, C., and Borman, S. L., "A Computer Program for Calculating Properties of Equilibrium Combustion Products with Some Application to I.C. Engines," SAE Paper 750463, 1975.

8 Agrawal, D. D., and Gupta, C. P., "Computer Program for Constant Pressure or Constant Volume Combustion Calculations in Hydrocarbon-Air Systems," ASME JOURNAL OF ENGINEERING FOR POWER, Vol. 99, 1977, pp. 246–254.

9 Lefebvre, A. W., *Gas Turbine Combustion*, ch. 9, McGraw-Hill, New York, 1983.

10 American Petroleum Institute, *Technical Data Book - Petroleum Refining* (4th ed.), Vols. 1 and 2, American Petroleum Institute, PA, 1983.

11 Chin, J. S., and Lefebvre, A. W., "Steady-State Evaporation Characteristics of Hydrocarbon Fuel Drops," *AIAA Journal*, Vol. 21, No. 10, Oct. 1983, pp. 1437–1443.

12 "Hydrogen Content of Aviation Turbine Fuels by Low Resolution Nuclear Magnetic Resonance Spectrometry," Institute of Petroleum, IP 338/78, 1978.

13 ASTM, "Standard Method for Estimation of Hydrogen Content of Aviation Fuels," ASTM D 3343-74 (reapproved 1979), 1979.

The Quantification and Improvement of the Thermal Stability of Aviation Turbine Fuel

J. S. Mills

D. R. Kendall

Shell Research Limited,
Thornton Research Centre,
P.O. Box 1, Chester, England

Studies of the propensity of aviation turbine fuels to lacquer engine oil-coolers that were described in an earlier paper have been extended to cover a wider range of fuels. Fuel performance was found to vary widely; some fuels were liable to lacquer oil-coolers to the extent of producing significant losses in efficiency at the most severe operating conditions currently encountered. Oxidation studies conducted in parallel with the rig investigations indicate that a fuel's performance is strongly dependent on its tendency to initiate radical oxidation reactions. The relatively high initiation rate of less stable fuels is believed to be due in part to their trace content of metals that catalyze oxidation reactions. Accordingly, an approved metal deactivating additive has been examined as a means of improving the performance of such fuels.

Introduction

Modern aircraft subject aviation turbine fuel to a range of thermal stresses. This results from the use of fuel as a sink for waste heat and the fact that certain components of the fuel system are located in regions of high ambient temperature. The heat thus acquired by the fuel stimulates oxidation reactions that lead to the formation of insoluble material. This is clearly undesirable and potentially harmful if, for example, lacquers form on heat exchanger and control surfaces, thereby reducing their efficiency.

The continuing trend toward higher engine operating temperatures means that there is an increasing likelihood of problems being encountered as a result of thermally induced deposit formation. Consequently, Shell Research Ltd. is engaged in a fuel thermal stability research and development program whose principal objectives are to define the performance limits of current generation fuels and to identify ways of improving fuel performance.

A major element of this work comprises tests on rigs that realistically simulate critical components of aircraft fuel systems. An earlier paper [1] described the results of tests to study the lacquering of engine oil-coolers; these studies indicated that there is only a small margin between current operational limits and the lower limits of fuel performance. This work has now been extended to cover a wider range of fuels and the test procedure has been modified to enable fuel performance limits to be more realistically defined.

In parallel with the rig studies, tests were conducted to identify some of the factors that influence fuel performance. Although numerous studies [2–8] have already been performed with the object of elucidating the fuel thermal degradation process, many questions remain unanswered; in particular, the roles played by different fuel constituents and the kinetics of the process are not understood in detail. Hitherto, this has not been of great consequence. But, as the operating temperatures of engines become higher, the risk of problems being encountered increases, and it becomes increasingly important to obtain a better understanding of the factors that influence fuel performance.

The work reported here was concentrated on the oxidation phase of the degradation process. Since it was found that there is a strong link between fuel oxidative stability and rig performance, this led to a further examination of the ability of metal deactivating additive to improve fuel performance by chelating metals that catalyze oxidation reactions.

Description of Test Rig and Experimental Procedure

Only a very brief description of the test rig will be given here; [1, 9] provide more detailed accounts. The essential features of the rig are its three heating stages, which comprise:

- A 20-L heated glass vessel where the fuel resides for about an hour. This simulates the wing tank of a supersonic aircraft, in which the fuel is subjected to aerodynamic heating, or the collector tank of a military aircraft that has some form of recirculatory fuel system.
- A preheater that simulates the avionics, hydraulic oil, and cabin air-coolers.
- The test heat exchanger that represents the engine oil-cooler.

Fuel attains its highest temperature in the test heat exchanger. This is comprised of a thin-walled stainless steel tube that simulates one element of a multielement engine oil-cooler; fuel is pumped through it at a realistic rate. The tube is heated electrically and is instrumented with thermocouples that enable its fuel-side heat transfer coefficient to be determined.

Contributed by the Gas Turbine Division of THE AMERICAN SOCIETY OF MECHANICAL ENGINEERS and presented at the 30th International Gas Turbine Conference and Exhibit, Houston, Texas, March 18–21, 1985. Manuscript received at ASME Headquarters, December 18, 1984. Paper No. 85-GT-33.

To assess the performance of a fuel, the rig is successively operated at several, increasingly severe test conditions; these are listed in Table 1 together with other test details.

At each condition the power supplied to the test element is kept constant. Lacquering of the inside of the tube is manifested by a rise in its surface temperature, since the lacquer imposes a thermal barrier between the hot tube and the relatively cool fuel flowing through it. The degree of lacquering is assessed via the rate of change of the tube's heat transfer coefficient.

Hitherto, the performance of a fuel in the rig was characterized by its temperature at the outlet of the test heat exchanger at which a deterioration in the element's efficiency could just be resolved [1]. This did not provide a realistic measure of a fuel's performance limit because the deterioration of the heat exchanger's efficiency usually had to exceed 0.05 percent per hour before it could be detected; from the standpoint of operational requirements this represents an unacceptably large deterioration, being equivalent to a 50 percent loss in oil-cooler efficiency after only 1000 hr service.

For the recent studies, therefore, the test and data analysis procedures were modified. At conditions where heat exchanger fouling was expected to be slight, the test duration was increased to a period in excess of 50 hr; this improved the test's resolution. Also, the results from a test sequence were used to construct an Arrhenius-type plot that enabled deterioration rates at lower, more realistic temperatures to be extrapolated from those measured at relatively high temperatures in the rig.

Eleven different fuels were utilized for the work reported here; their properties are listed in Table 2. The fuels were intended to be representative of current Jet A-1 production and covered a range of feedstocks and treatment processes. None of the fuels contained metal deactivator.

Table 1 Dimensions of test heat exchanger: length: 241 mm, i.d.: 2.78 mm, wall thickness: 0.18 mm. Fuel flow rate: 3.78 g/s.

Condition no.	Fuel temp. in heated tank, °C	Fuel temp. at preheater outlet, °C	Fuel temp. at test heat exchanger outlet, °C	Typical Reynolds no. of flow in test heat exchanger
1	85	149	171.5	5230
2	95	165	190.0	5750
3	105	180	207.5	6250
4	115	195	225.0	7220
5	125	210	242.5	8100

Results and Discussion

Results from tests on three fuels that exemplify the variations in performance observed are plotted in Fig. 1.

It will be evident that the degree of heat exchanger fouling was very dependent upon temperature; similar observations have been reported by other investigators of this phenomenon [10, 11]. It will also be apparent that the results are well fitted by Arrhenius-type relationships, which vindicates the use of these to extrapolate to more realistic temperatures.

The envelope shown in Fig. 2 covers the results obtained

Table 2 Properties of test fuels

Property	Fuel A	B	C	D	E	F	G	H	I	J	K
Acidity, total, mgKOH/g	0.012	0.003	0.005	0.006	0.004	0.003	0.002	0.002	0.001	0.002	0.0015
Aromatics, %v	20.2	9.8	15.2	19.9	21.1	20.0	18.0	19.0	16.5	18.7	19.5
Olefins, %v	0.6	0.5	<0.1	0.1	1.45	<0.5	0.5	0.2	0.5	0.4	0.8
Sulphur, total, %w	0.006	0.01	0.003	0.016	0.008	0.17	0.07	0.03	0.11	0.15	0.11
Sulphur, Mercaptan, %w	-	-	-	0.0004	0.0005	0.0003	0.0005	0.0001	0.0005	0.002	0.0001
Distillation											
10% recovered, °C	174	173	175	178	185	173	168	174	166	142	182
20% recovered, °C	183	180	186	187	191	185	177	182	175	165	186
50% recovered, °C	205	197	203	209	204	207	200	204	198	172	201
90% recovered, °C	237	224	235	245	230	235	236	238	238	194	225
F.B.P., °C	250	236	257	267	244	252	254	256	256	242	261
Flash point, °C	45.0	44.0	47.0	46.0	58.9	43.0	42.0	43.0	42.0	39.0	53.3
Density @ 15°C, kg/l	0.8057	0.7920	0.7987	0.8089	0.8048	0.8055	0.8030	0.8030	0.8020	0.7892	0.8035
Freezing point, °C	-48.0	-48.5	-49.0	-49.0	-48.0	-48.0	-48.5	-48.0	-47.5	-49.0	-50.0
Smoke point, mm	23.0	26.9	26.0	23.0	23.0	22.0	23.0	23.0	23.0	23.0	26.0
Napthalenes, %v	1.14	-	-	3.0	1.39	2.76	2.6	2.43	2.71	1.4	2.35
Thermal stability											
JFTOT pressure rise, mmHg	0	0	0	0	0	0	0	0	0	0	0
Tube colour code	0	0	<2	0	0	1	1	1	1	1	0
Existent gum, mg/100 ml	0	0	0	0	0	0	0	0	0	0.9	1.3
Additives											
Antioxidant, mg/l	20.0	22.0	20.0	19.1	0	0	0	0	0	0	0
Antistatic, mg/l	1.0	0.3	1.0	0.47	0	0.8	0.8	1.0	2.3	1.0	0.8
Metals											
Copper, µg/l	4	<2	<2	<2	<2	20	10	2	2	2	10
Iron, µg/l	-	<5	<5	<5	<5	-	5	10	-	-	-

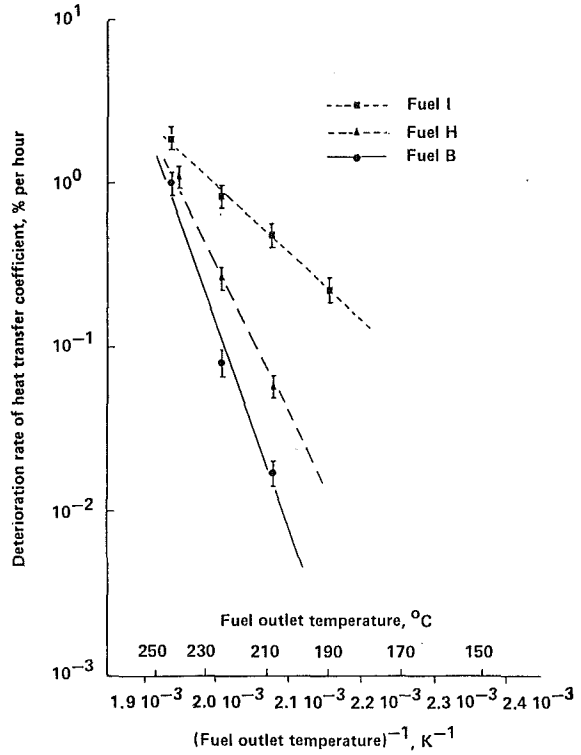

Fig. 1 Arrhenius plots of test results

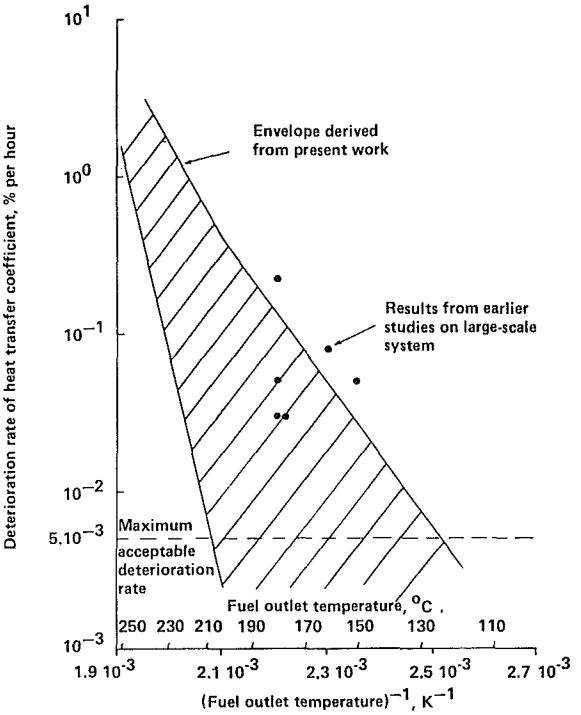

Fig. 2 Fuel performance limits

with all 11 fuels. To enable the implications of these results to be explored, it is necessary to define the maximum deterioration of oil-cooler efficiency that can be tolerated in practice. This parameter cannot be uniquely defined; it will be a function of both the engine system and the requisite service life. As a general upper limit, 0.005 percent per hour has been chosen, this being equivalent to a 5 percent loss in efficiency after 1000 hr service.

Applying this criterion to the results in Fig. 2 shows that fuel performance limits vary widely, from about 125 to 210°C. The highest temperature fuels currently sustain in engine oil-coolers for any reasonable period is believed to be about 150°C. Thus, some of the fuels examined were capable of performing satisfactorily up to relatively high temperatures. However, a proportion (about a third) were liable to produce significant losses in efficiency at the most severe operating conditions currently encountered, i.e., there is no margin between current operational limits and the lower limits of fuel stability.

The validity of this conclusion is supported by the results of earlier studies of heat exchanger fouling conducted on large-scale fuel system simulators by Shell Research Ltd. and by workers in the US with the object of defining fuel performance requirements for supersonic aircraft. The Shell work was similar to that reported here except that the test heat exchanger comprised a complete tubular engine oil-cooler and tests were of long duration, usually 100 hr [12]. A range of fuels were studied [13–17] at outlet temperatures between 150 and 180°C, i.e., similar to those currently encountered.

The results of these tests are also shown in Fig. 2. Fuel performance was found to vary widely and some of the fuels examined produced oil-cooler fouling rates that exceeded those extrapolated from the results of the present work.

The studies conducted in the US utilized a rig developed for the CRC by North American Aviation, Inc.; this simulated the whole of the engine fuel system and employed cyclic test conditions [18]. In studies oriented toward supersonic transport aircraft [19], deposits were observed to form under conditions representing Mach 2½ flight in which the fuel outlet temperature from the oil-cooler was varied between 70 and 200°C. Significantly more deposition occurred under Mach 3 conditions. Work conducted at about the same time on the smaller-scale Minex rig confirmed that significant heat exchanger fouling could occur at fuel outlet temperatures below 200°C [20]. Latterly, the large-scale simulator has been used for more general studies of fuel stability problems associated with supersonic flight. In one particular exercise with five different fuels [21], one fuel was observed to foul the oil-cooler under cyclic conditions in which its outlet temperature peaked at about 160°C.

It is pertinent to consider, therefore, why there have not been widespread reports by aircraft operators of problems relating to oil-cooler fouling. Several reasons can be identified: In particular, most aircraft utilize a range of fuels, only a proportion of which will be liable to lacquer oil-coolers, and fuel outlet temperatures of 150°C are only sustained during part of an advanced aircraft's flight cycle.

Despite these mitigating factors, the results shown in Fig. 2 demonstrate that a modest increase in operating temperatures would increase the likelihood of operational difficulties with some current fuels. For example, if maximum fuel outlet temperatures were to be increased from 150 to 160°C, certain fuels would lacquer oil-coolers to the extent of reducing their efficiency by 40 percent after 1000 hr of operation at that temperature.

Flask Oxidation Test Procedure

For conventional fuels, the principal driving force behind the degradation process has been shown to be oxidation of the fuel by the dissolved oxygen; deoxygenation improves fuel stability and limits the extent of oxidation [5, 7]. Oxidation products subsequently react with each other and with minor fuel constituents to generate the insoluble materials that deposit on fuel system surfaces. Although the route by which insolubles are formed is poorly characterized, the oxidation process is relatively well understood [22] and amenable to examination. Therefore, techniques were developed to characterize the oxidation behavior of fuels and thus facilitate

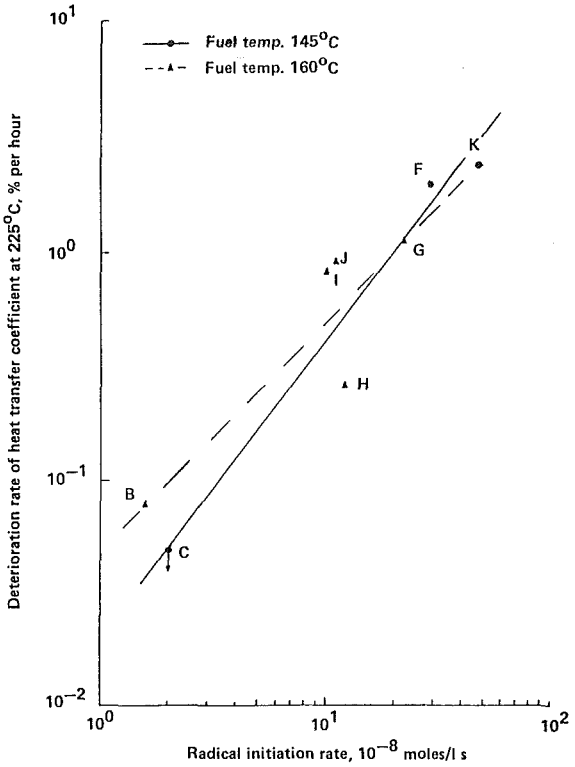

Fig. 3 Effect of radical initiation rate on fuel performance

an examination of the link between their oxidation stability and rig performance.

As the oxidation studies were complex, their methodology and the results arising from them will be dealt with in detail in future publications. Briefly, the inhibited kinetics encountered in the fuels studied enabled their propensity to initiate and scavenge radicals to be determined by measuring the change in fuel oxidation rate on adding a known radical initiator or scavenger to the fuel. Oxidations were performed by aerating fuel in a flask at selected temperatures in the region of 145 to 190°C, and the oxidation rate itself was determined by measuring the depletion of oxygen in the effluent air from the flask.

Results of Oxidation Tests

The most significant finding that emerged from the oxidation studies is that a fuel's rig performance is strongly dependent upon its propensity to initiate oxidation reactions. Evidence for this is presented in Fig. 3 that summarizes the results obtained with eight of the fuels utilized for the rig studies; the oxidation behavior of the other three was such that their initiation rates could not be determined.

The rig performance of each fuel has been characterized by the deterioration rate of the test element's efficiency at a fuel outlet temperature of 225°C; all fuels but one gave measurable deterioration rates at this condition. Although there is some scatter in the data, the dependence of rig performance on initiation rate is beyond question.

But the scatter inherent to the results in Fig. 3 is significant, since it demonstrates that a fuel's rig performance is a function of parameters in addition to its tendency to initiate oxidation reactions. Other workers have demonstrated that sulphur compounds can have a deleterious effect on fuel stability [6, 23] by reacting with oxidation products to generate deposit precursors. This is confirmed by the present work: Fig. 4 shows that there is a strong correlation between the rig performance and total sulphur content of the fuels examined.

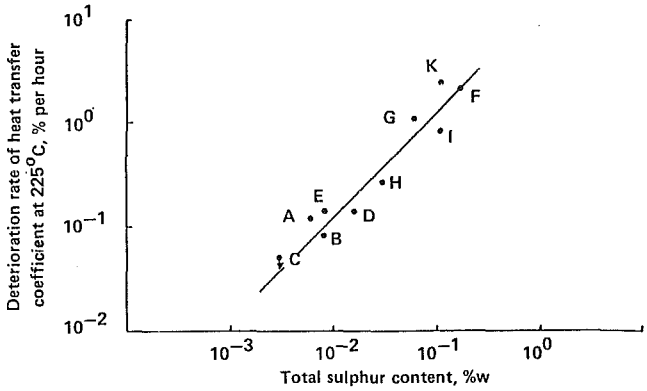

Fig. 4 Effect of sulphur compounds on rig performance

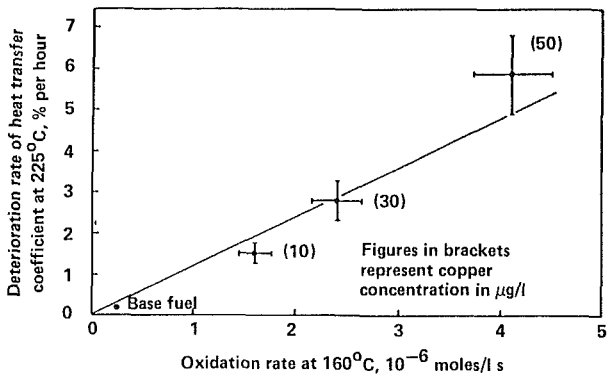

Fig. 5 Effect of copper on rig and oxidation performance of fuel H

It might be expected that fuels with very low sulphur contents would be of poor stability, since it is well known that certain sulphur compounds and their oxidation products inhibit oxidation [24–27]. However, most of the low sulphur content fuels utilized for this work were doped with synthetic antioxidant for storage stability purposes. The oxidation tests confirmed that this was also effective at elevated temperatures and it will therefore have compensated for the deficiency of natural antioxidant. Thus, overall, a low fuel sulphur content was beneficial.

To summarize, some of the factors that influence fuel performance have been identified. In particular, a fuel's performance appears to be strongly dependent upon both its tendency to initiate radical oxidation reactions and its sulphur content.

The Improvement of Fuel Stability

The relatively high initiation rate of less stable fuels is believed to be due in part to their trace content of metals, such as copper and iron, that catalyze oxidation reactions [28–30]. The deleterious effect of small amounts of catalytic metal was confirmed by doping fuel H, which had an average rig performance, with small concentrations of copper (as naphthenate). The results of rig and oxidation tests are compared in Fig. 5.

At concentrations in excess of 30 μg/L, copper produced a fuel that was worse in performance than any of the production fuels examined. The direct dependence of rig performance on oxidation rate shows that this can be attributed directly to the metal catalyzing the oxidation of fuel components. These results also show that the effect of copper was very similar at the different temperatures used in the rig and oxidation tests.

One way in which the catalytic effect of metals can be reduced is to dope fuel with metal deactivating additive

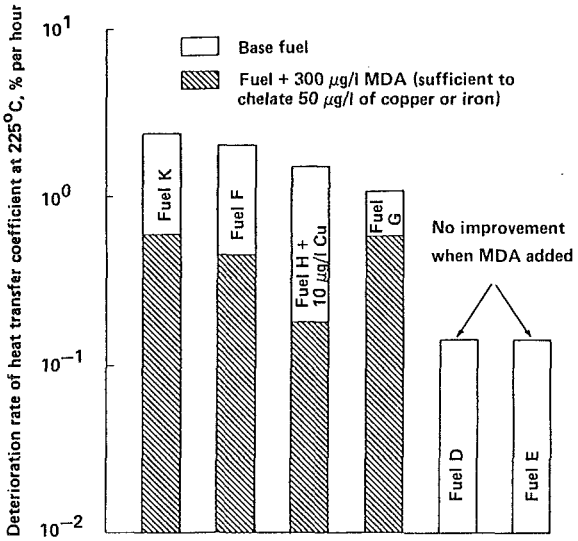

Fig. 6 The ability of MDA to improve fuel stability

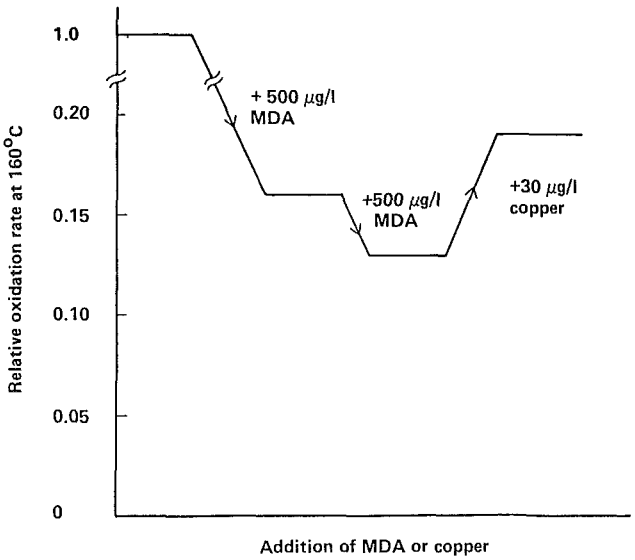

Fig. 7 The change in relative oxidation rate on successive additions of MDA or copper to fuel F doped with 30 μg/l of copper to give a total of 50 μg/l

(MDA), and jet fuel specifications permit the use of one such material [31]. Earlier studies indicated that MDA has a variable effect on fuel performance [1], and the additive was therefore subjected to a more detailed examination. This work had two aspects: rig studies with fuels having a range of metal contents and oxidation tests.

The results of the rig tests are shown in Fig. 6. The fuel that was most responsive to MDA was the sample of fuel H that had been doped with 10 μg/L of copper to give a total copper and iron content of 22 μg/L. Fuels F, G, and K, which contained 10–20 μg/L of these metals, also responded to additive treatment. But the performance of fuels D and E, which had very low metal contents, was not improved by doping them with MDA. Thus it would appear that a fuel's response to MDA is largely governed by the extent to which metals catalyze its oxidation.

But the results in Fig. 6 have another interesting feature: The performance of fuels F, G, and K when doped with MDA was still poorer than those of the two fuels with intrinsically low metal contents. This can be attributed in part to the metal/MDA chelates having some residual catalytic activity, as was demonstrated by the following oxidation test, the results of which are shown schematically in Fig. 7. Fuel F was doped with 30 μg/L of copper to give a total of 50 μg/L. Adding 500 μg/L of MDA, sufficient to chelate all the metal present, reduced the oxidation rate by 84 percent of the initial rate ν_o. A second addition of MDA produced only 3 percent ν_o reduction, indicating that all the metal was complexed and suggesting that an excess of MDA may begin to act as an antioxidant. Adding 30 μg/L of copper then produced a 6 percent ν_o increase in the oxidation rate, despite the fact that the fuel contained an excess of MDA, more than sufficient to fully chelate this additional metal.

This demonstrates that the copper/MDA chelates had some catalytic activity, since these observations cannot be interpreted as an equilibrium between free metal and MDA.

Thus the deleterious effect of metals on fuel stability has been confirmed and some insight gained both into MDA's mode of action and its limitations as a means of improving fuel performance.

Conclusions

The propensity of aviation turbine fuels to foul engine oil-coolers has been studied using a rig that employs realistic flow conditions. From tests conducted on a range of fuels the following conclusions can be drawn:

- The thermal degradation of aviation turbine fuel in an engine oil-cooler can significantly reduce the cooler's efficiency; it has been shown that there is little margin between current operating temperatures and the thermal stability limits of some current fuels.
- A modest increase in engine operating temperatures would increase the likelihood of operational difficulties with some current fuels.
- Oxidation studies have identified some of the factors that influence fuel performance. The poorer performance of certain fuels is believed to result from their relatively high propensity to initiate radical oxidation reactions and their high sulphur content.
- Metals can have a deleterious effect on fuel performance by catalyzing oxidation reactions. The effect of metals can be reduced by doping fuel with a metal deactivating additive. However, the chelates formed have some residual catalytic activity.

Thus thermally induced deposit formation poses a significant threat to the satisfactory operation of future aircraft whose fuel systems may have to contend with thermal stresses that exceed those currently experienced. Two ways of minimizing the likelihood of problems can be identified: The thermal stability of all future fuels will either have to equal that of the best fuels currently produced or closer attention will have to be paid to fuel stability limits when designing fuel system components.

In order to produce fuels with improved performance, it is necessary to understand the factors that govern fuel stability. The work reported here expands our knowledge in this respect by quantifying the role played by metals and by highlighting the deleterious effect of sulphur compounds. Furthermore, by realistically defining fuel thermal stability limits in a critical component of a fuel system the studies have provided hardware manufacturers with some of the information they require to design fuel systems that will operate satisfactorily with all current generation fuels.

References

1 Mills, J. S., and Edwards, F. R., "The Thermal Stability of Aviation Fuel," Paper No. 84-GT-69, presented at the 29th International Gas Turbine Conference, Amsterdam, June 1984.

2 CRC, "Literature Survey on the Thermal Oxidation Stability of Jet Fuel," Report No. 509, Apr. 1979.

3 Mayo, F. R., Kirshen, N., Richardson, H., and Stringham, R., "The Chemistry of Fuel Deposits and Their Precursors," Final Report NASC contract N00019-72-C-0161, Dec. 1972.

4 Mayo, F. R., Lan, B., Cotts, D. D., Butterill, S. E., and St. John, G. A., "Oxidation and Formation of Deposit Precursors in Hydrocarbons," NASC Contractor Report 168121, Mar. 1983.

5 Hazlett, R. N., Hall, J. M., and Matson, M., "Reactions of Aerated N-Dodecane Liquid Flowing Over Heated Metal Tubes," *Ind. Eng. Chem. Prod. Res. Dev.*, Vol. 16, 1977, p. 171.

6 Taylor, W. F., and Wallace, T. J., "Kinetics of Deposit Formation From Hydrocarbons: Effect of Trace Sulphur Compounds," *Ind. Eng. Chem. Prod. Res. Dev.*, Vol. 7, 1963, p. 198.

7 Taylor, W. F., "Deposit Formation From Deoxygenated Hydrocarbons. 1. General features," *Ind. Eng. Chem. Prod. Res. Dev.*, Vol. 13, 1974, p. 133.

8 Frankenfeld, J. W., and Taylor, W. F., "Deposit Formation From Deoxygenated Hydrocarbons. 4. Studies in Pure Compound Systems," *Ind. Eng. Chem. Prod. Res. Dev.*, Vol. 19, 1980, p. 65.

9 Smith, J. D., "Fuel for the Supersonic Transport: The Effects of Deposits on Heat Transfer to Aviation Kerosine," *I and EC Process Design and Development*, Vol. 8, No. 3, July 1969.

10 CRC, "Small-Scale Tests in the Esso Heat Transfer Unit," Report No. LD-149, Feb. 1965.

11 CRC, "Small-Scale Tests in the Minex Rig," Report No. LD-150, Feb. 1965.

12 Strawson, H., and Grant, W. J., "The Behaviour of Fuels in a High Temperature Aircraft Fuel System Rig—Part I," Shell Research Limited, Report K.171, Nov. 1966.

13 Grant, W. J., "The Behaviour of Fuels in a High Temperature Aircraft Fuel System Rig—Part III," Shell Research Limited, Report K.176, Apr. 1968.

14 Grant, W. J., "The Behaviour of Fuels in a High Temperature Aircraft Fuel System Rig—Part VI," Shell Research Limited, Report K.190, Aug. 1971.

15 Grant, W. J., "The Behaviour of Fuels in a High Temperature Aircraft Fuel System Rig—Part VII," Shell Research Limited, Report K.193, Dec. 1971.

16 Grant, W. J., "The Behaviour of Fuels in a High Temperature Aircraft Fuel System Rig—Part VIII," Shell Research Limited, Report K.201, Aug. 1975.

17 Grant, W. J., "The Behaviour of Fuels in a High Temperature Aircraft Fuel System Rig—Part XIII," Shell Research Limited, Report K.223, Nov. 1980.

18 CRC, "Development of Supersonic Transport Fuel System Test Rig," Report No. LD-127, June 1963.

19 CRC, "An Investigation of the Performance of Jet Engine Fuels for Supersonic Transport Aircraft: Summary Report," Report No. 393, July 1965.

20 Lander, H. R., and Zengel, A. E., "Relationship Between the Minex and the Helium-Driven Modified Coker in the Measurement of Jet Fuel Thermal Stability," AFAPL-TR-67-17, Feb. 1967.

21 Goodman, H., and Bradley, R., "High Temperature Hydrocarbon Fuels Research in an Advanced Aircraft Fuel System Simulator—Final Report," AFAPL-TR-70-13, Mar. 1970.

22 Mill, T., and Hendry, D. G., "Kinetics and Mechanisms of Free Radical Oxidation of Alkanes and Olefins in the Liquid Phase," *Comprehensive Chemical Kinetics*, Vol. 16, ed. by C. H. Bamford and C. F. H. Tipper, Elsevier, Amsterdam, 1980.

23 Daniel, S. R., and Heneman, F. C., "Deposit Formation in Liquid Fuels. 4. Effect of Selected Organosulphur Compounds on the Stability of Jet A Fuel," *Fuel*, Vol. 62, 1983, p. 1265.

24 Scott, G., "Mechanisms of Action of Sulphur Compounds in Autoxidation," *Mechanism of Reactions of Sulphur Compounds*, Vol. 4, 1969, p. 99.

25 Ingold, K. U., "Inhibition of the Autoxidation of Organic Substances in the Liquid Phase," *Chem. Rev.*, Vol. 61, 1961, p. 563.

26 Bridgewater, A. J., and Sexton, M. D., "Mechanism of Antioxidant Action: Reactions of Alkyl and Aryl Sulphides with Hydroperoxides," *J.C.S.* Perkin II, 1978, p. 530.

27 Koelewijn, P., and Berger, H., "Mechanism of the Antioxidant Action of Dialkyl Sulphoxides II. Aspects of the Antioxidant and Pro-Oxidant Actions of Sulphoxides," *Recl. Trav. Chim. Pays-Bas*, Vol. 93, 1974, p. 63.

28 Droegemueller, F. A., "Fuel Requirements for Supersonic Transport," 6th World Petroleum Congress, Frankfurt, June 1963.

29 Snitserov, Yu. V., "The Effects of Additives on the Formation of Deposits in Fuel T-1 at High Temperatures," *Khim. Tekhnol. Topliv Mazel*, Vol. 11, 1961.

30 Smith, J. D., "The Effects of Metals and Alloys on the Thermal Stability of Avtur 50," *Aircraft Engineering*, Vol. 39, 1967, p. 19.

31 Manual of ASTM Standards, ASTM D1655, Vol.05.01, 1983.

USAF Toxicology Research on Petroleum and Shale-Derived Aviation Gas Turbine Fuels[1]

J. A. Martone
Major, ASAF,
Deputy Director,
Toxic Hazards Division,
Air Force Aerospace Medical
Research Laboratory,
Wright-Patterson Air Force Base,
Ohio 45433

As one of the nation's largest users of aircraft turbine fuels, the USAF has interest in assuring the safe use of these hydrocarbons by its military and civilian workers. This concern stimulated research to define potential adverse health effects and develop criteria for safe exposure limits for military aviation fuels. The first inhalation exposure to JP-4, the primary fuel used in USAF aircraft, was conducted in 1973. Since this initial subchronic study, the USAF has conducted numerous subchronic and one-year oncogenic inhalation studies to establish health criteria for aviation fuels. This paper summarizes the status of studies to define the toxicity of petroleum and shale-derived aircraft turbine engine fuels and discusses the preliminary findings of toxic nephropathy and primary renal tumors observed in male Fischer 344 rats.

Introduction

The determination of accurate, up-to-date human tolerance criteria for chemicals and fuels used in Air Force work environments is a cornerstone of the Air Force Occupational Safety and Health Program. These standards are particularly critical since exposure situations in the Air Force are often different from those in the civilian industrial community due to the specific uses of the chemical; the type, level, or duration of exposure; and possible operational restraints on the use of protective equipment. When no national consensus standards exist or the standards are not applicable for Air Force use, the Toxic Hazards Division (TH) of the Air Force Aerospace Medical Research Laboratory (AFAMRL) develops human tolerance criteria for new chemicals, fuels, and structural materials being introduced into the Air Force inventory.

As one of the nation's largest users of aircraft turbine fuels, the Air Force has interest in assuring the safe use of these hydrocarbons by its military and civilian workers. This concern stimulated research to define potential adverse health effects and develop criteria for safe exposure limits for military aviation fuels. This paper focuses on proposed inhalation exposure criteria and the status of AFAMRL toxicology research on petroleum and shale JP-4. JP-4 was selected for attention because it is the primary fuel used in USAF aircraft. The paper is intended to have crossover interest to nontoxicologists.

Exposure Criteria Terminology. Workplace chemical exposure criteria for Air Force applications are given in Air Force Occupational Safety and Health (AFOSH) standards. Relatively few chemicals, such as vinyl chloride, asbestos, and hydrazine, have specific AFOSH standards. The majority of regulated chemicals are included in the generalized AFOSH Standard 161-8 [1]. This standard directs Air Force use of current chemical exposure limits listed [2] by the American Conference of Governmental Industrial Hygienists (ACGIH).

The most frequently used ACGIH limit is the Threshold Limit Value–Time-Weighted Average (TLV®–TWA). This is the time-weighted average concentration for a normal 8-hr workday and a 40-hr workweek, to which nearly all workers may be repeatedly exposed, day-after-day, without adverse effect. Another ACGIH guideline is the Threshold Limit Value–Short-term Exposure Limit (TLV–STEL). This is the concentration to which workers can be exposed continuously for a short period of time without ill effects. The STEL is defined as a 15-min, time-weighted average exposure which should not be exceeded at any time during a workday.

Some substances are given a "skin" notation by the ACGIH. This designation refers to the potential contribution to the overall exposure by the cutaneous route. Since little quantitative data are available describing absorption of vapors and gases through the skin, the "skin" notation is mostly an attention-calling designation intended to suggest appropriate measures for the prevention of cutaneous absorption.

The ACGIH limit definitions given above are abbreviated; complete discussion of these limits is given in [2]. Two important considerations are that the limits should be used as guides and not fine lines between safe and dangerous concentations, and are intended for application and interpretation by people trained in the practice of industrial hygiene.

Two other exposure limits – the emergency exposure limit or EEL and the continuous exposure limit or CEL – are somewhat unique to the military. EELs and CELs are established by the National Research Council's Committee on

[1] This article is also identified as AFAMRL-SR-85-505.

Contributed by the Gas Turbine Division of THE AMERICAN SOCIETY OF MECHANICAL ENGINEERS and presented at the 30th International Gas Turbine Conference and Exhibit, Houston, Texas, March 18–21, 1985. Manuscript received at ASME Headquarters, December 18, 1984. Paper No. 85-GT-34.

Table 1 General characteristics of selected petroleum products

PRODUCT	JP-4[1]	JP-5[1]	GASOLINE	KEROSENE[2]	PAINTERS' NAPHTHA[2]
Carbon Range	C_4 - C_{16}	C_8 - C_{16}	C_3 - C_{12}	C_9 - C_{16}	C_7 - C_{11}
Flash Point (°C)	-23 to 1	35 to 36	-40	38 to 74	-7 to 13
Vapor Pressure (20°C) mm Hg	78	1	200	1	2 - 20
Molecular Weight (Liquid)	125	160	90	170	100
Specific Gravity	0.75	0.81	0.68	0.80	0.74

1 Reference (4)
2 Reference (5)

Table 2 Description of fuel inhalation exposures

FUEL	EXPOSURE (months)	CONCENTRATION (mg/m^3)	SPECIES[1]	END DATE
SYNTHETIC				
JP-10	12, int[2]	560	D,R,Mi,H	Completed
RJ-5	6, cont[3]	155	D,R,Mi,M	Completed
RJ-5	12, int	30, 150	D,R,Mi,H	Jul 85
MCH	12, int	400, 2000	D,R,Mi	Completed
MIXED DISTILLATE				
JP-4	8, int	2500, 5000	D,R,M,Mi	Completed
JP-4	3, cont	500, 1000	D,R,Mi	Apr 85
JP-4	12, int	500, 1000	R,Mi	Dec 85
JP-5	3, cont	150, 750	D,R,Mi	Completed
JP-5(S)[4]	3, cont	150, 750	D,R,Mi	Completed
JP-4(S)	3, cont	500, 1000	R,Mi(M/F)	Dec 86
JP-7	12, int	150, 750	R,Mi	Jan 86
JP-8	3, cont	500, 1000	R,Mi	Jul 86
JP-TS	12, int	200, 1000	R,Mi	Jan 86
DFM	3, cont	50, 300	R,Mi	Completed
DFM(S)	3, cont	50, 300	R,Mi	Completed

1 D (dogs); R (rats); M (monkeys); Mi (mice, female); H (hamsters); Mi(M/F) (mice, male and female)
2 Intermittent
3 Continuous
4 Shale

Toxicology (NRC-COT) in response to specific requests from its military sponsors (U.S. Army, Navy, and Air Force).

The EEL is defined as a ceiling limit for an unpredictable single exposure – an occurrence expected to be rare in the lifetime of any person. It is designed to avoid substantial decrements in performance during emergencies. The CEL is recommended in specific situations where there may be exposure to a chemical continuously for up to 90 days. The EELs and CELs have been used as design criteria in considering the suitability of materials for particular missions (as in a submarine or spacecraft) and in assessing the habitability of particular enclosed environments. The TLV-TWAs or STELs and the EELs and CELs are usually expressed in concentration units of parts per million (ppm) by volume or as milligrams per cubic meter (mg/m^3). There are no occupational health limits for JP-4 established or recommended by the ACGIH, NRC-COT, Occupational Safety and Health Administration, or National Institute for Occupational Safety and Health.

USAF Proposed Limits for JP-4. JP-4 is a complex blend of up to 300 different hydrocarbon compounds. Other petroleum products such as gasoline, kerosene, JP-5 (a Navy aviation fuel), and naphtha also have complex chemical compositions. Because many hydrocarbons in these products have comparable health effects, proposed workplace exposure limits are frequently expressed as "total hydrocarbon vapors." The specific hydrocarbons that contribute to the total are defined by the vapor sampling and analysis technique. Presumably the sampling and analysis method gives results that reflect the true total hydrocarbon vapor concentration in the workplace. The practical advantage of a "total vapor" health limit is that only one analysis per workplace air sample is required. Initial samples may also require analysis of special interest substances such as benzene to verify that a "total vapor" limit is appropriate. Analysis of several individual hydrocarbon components per air sample would cost much more than a single "total vapor" analysis. Table 1 compares selected chemical and physical properties for JP-4, JP-5, gasoline, kerosene, and painters' naphtha.

The USAF has submitted rationale for JP-4 exposure limits to the ACGIH [6]. The proposal includes a TLV of 700 mg/m^3 (200 ppm) and a STEL of 1050 mg/m^3 (300 ppm) as n-hexane with a "skin" notation. The rationale is based on gas chromatograms of JP-4 headspace vapor at 25°C and proportional additivity of health effects for the identified components [6]. This same approach is the basis of the gasoline TLV (900 mg/m^3), which was adopted by the ACGIH in 1982 [3] after two years as an intended value. The "skin" notation was recommended because JP-4 is a defatting agent and can cause dermatitis, which may lead to increased skin absorption. The additivity of health effects approach for JP-4 requires established TLVs for the identified headspace components. The mathematics of this procedure is given in [6].

JP-4 is primarily aliphatic hydrocarbons (paraffins) with an average concentration of 10–11 percent aromatics and 1 percent unsaturated hydrocarbons [7]. As a class, paraffins are generally considered to be central nervous system (CNS) depressants with the exceptions of the first three members of the series, methane, ethane, and propane, which are simple asphyxiants, and n-hexane, which is a peripheral neuropathic agent. The vapors of the paraffins are generally considered to be irritating to the mucous membranes, but direct liquid contact with the lungs will cause pneumonitis [8]. Aromatics are also generally considered to be CNS depressants.

Benzene deserves special mention since it has toxic properties thought to be unique among hydrocarbon compounds. Benzene exerts a toxic effect on the blood-forming organs in the bone marrow [8] and is a suspect carcinogen [6]. Benzene has the lowest TLV (i.e., 30 mg/m^3) of any headspace component used in calculating the proposed "total vapor" TLV for JP-4.

Inhalation Toxicology Research on Petroleum and Shale JP-4

The USAF proposed exposure limits for JP-4 did not consider on-going hydrocarbon toxicology research at AFAMRL because the current research is not conclusively complete. The first inhalation exposure to JP-4 was conducted in 1973. Since this initial subchronic study, the USAF has conducted numerous subchronic and one-year oncogenic inhalation studies on petroleum and shale-derived aviation fuels and high-energy synthetic hydrocarbon fuels developed for missile applications (see Table 2). Reference [9] is a comprehensive summary of results for all mixed distillate and synthetic fuels studied at AMRL/TH.

Experimental Methods.

Exposure Chambers and Exposure Schedule. All inhalation exposures were conducted in the Thomas Domes located in the Toxic Hazards Research Unit (THRU), Wright-Patterson AFB, Ohio. The Thomas Domes are unique, 23.4 m^3 exposure chambers designed to provide long-term, continuous exposure of up to 400 rodents. Exposures were continued 24 hr per day during 90-day continuous studies and 6 hr per day, excluding weekends and holidays, for intermittent (occupational exposure schedule) studies (see Table 2).

Experimental Animals. The experimental animals used in these studies were randomized from main groups after quality control procedures and quarantine periods were completed. Each exposure chamber contained as few species as possible to reduce the risk of cross infection. Enough rodents were used to permit a statistically valid number of each species to reach the required age for tumor induction with natural and toxicologic attrition.

Generation of Test Atmospheres. The exposure chambers were operated from a single master generator to assure equivalent exposures at the desired concentrations. Concentrated fuel vapors were produced by passing fuel through dual constant temperature evaporator towers operated between 50°C and 57°C. The concentrated vapor was mixed with air to establish the desired atmospheric concentrations in the respective chambers. Fuel not vaporized was collected in a waste drum for disposal. Vapor concentrations were measured continuously using a Beckman Model 400 Hydrocarbon Analyzer and compared with measured fuel consumption and air flows. The absence of aerosols was documented using a Royco Aerosol Particle Counter. Quality control on the test fuels and analysis of the chamber atmospheres were performed using gas chromatography and mass spectrometry.

JP-4 Toxicity. The initial experiment was an intermittent eight-month exposure to 2500 mg/m^3 and 5000 mg/m^3 JP-4. An exposure concentration of 5000 mg/m^3 was chosen to produce a benzene vapor concentration of 80 mg/m^3, which was the TLV at that time. Benzene was selected as the critical vapor, since there were concerns that it might be the most toxicologically significant fuel component. Hematologic measurements and bone marrow analyses in JP-4 or benzene-exposed animals failed to show any statistically significant differences from controls. Histopathologic findings failed to show any treatment-related effects.

Ninety-day continuous exposures to 500 mg/m^3 and 1000 mg/m^3 were begun in 1979. Both concentrations of JP-4 caused reduced weight gain in male and female rats during the exposure; however, this difference disappeared during the 19-month post-exposure observation. Histopathology of animals sacrificed immediately following exposure indicated there were significant exposure-related tissue lesions in both rodent species. In male rats, for example, 100 percent of the kidneys in the high- and low-dose groups exhibited hyaline droplet formation in the proximal tubular epithelium. Furthermore, in 96 percent and 100 percent of the low- and high-dose male rats, respectively, focal dilatation of the renal tubules was present near the corticomedullary junction, and these dilated segments were plugged with necrotic cell debris. All lesions found in exposed and control dogs were common infectious/degenerative changes consistent with aging in all canine species.

A one-year intermittent exposure to 500 mg/m^3 and 1000 mg/m^3 was begun in February 1980 to allow comparison of the tumorigenic potential of petroleum-derived and JP-4 refined from shale oil as part of the USAF alternate fuels program. A 90-day exposure to shale JP-4 also at concentrations of 500 mg/m^3 and 1000 mg/m^3 was completed in March 1984. Examination of tissues collected for histopathologic evaluation from these studies is incomplete.

Discussion. The results for other fuel vapor exposures are consistent with those given for JP-4. A generalized picture of the toxic response to long-term exposure to hydrocarbon vapors is beginning to evolve. In male rats, continuous exposure for 90 days reduces body weight gain and increases kidney/body weight ratios. Hyaline droplets in the proximal tubule epithelium and multifocal dilatation near the corticomedullary junction present in 80 to 90 percent of exposed animals is absent in control animals.

In completed one-year intermittent exposures, there is only a slight weight depression in exposed rats, hyaline droplet formation in the proximal tubules, and a slight increase in mineralization in the loop of Henle. The most significant finding is the presence of renal carcinomas in male rats sacrificed at 24 months. Histopathologic evaluation of tissues collected during the one-year JP-4 exposure is also expected to demonstrate increased evidence of renal carcinomas in exposed male rats.

The etiology of this toxic nephropathy and renal tumors is unknown, leaving unanswered the question whether this effect is significant in humans. The effects appear generic and not related to any unique characteristics of aviation fuels. For example, the American Petroleum Institute recently reported similar results for unleaded gasoline [10].

As indicated in Table 2, results for many of the long-term inhalation studies on other hydrocarbon fuels conducted in the THRU will not be available for a number of years. The histopathology of the animals in these studies should provide additional data on this particular lesion and provide evidence to evaluate whether this is a generic effect of many hydrocarbons. There is a critical need for further definitive research to elucidate the mechanism of this hydrocarbon-induced renal effect to understand why this nephrotoxicity is specific to male rats.

Summary

The primary fuel used in USAF aircraft, JP-4, has a 25-year history of safe use. Based on this experience and on analogy with the rationale for adopted occupational exposure limits for gasoline, the USAF has submitted JP-4 exposure limits for consideration by the ACGIH. The USAF has an on-going hydrocarbon fuel toxicology research program. Completed studies show that extended exposure to fuel vapors causes significant numbers of tumors in male rat kidneys. The human significance of hydrocarbon-induced toxic nephropathy and renal cancer in male rats is unknown but is under study by the Air Force Aerospace Medical Research Laboratory.

Acknowledgments

The rationale for a JP-4 TLV was developed jointly by AFAMRL and the Air Force Occupational and Environmental Health Laboratory, Brooks AFB, Texas. The inhalation research studies were performed in the THRU which is operated for the Air Force Aerospace Medical Research Laboratory by the University of California under contract F33615-80-C-0512. The conduct of these studies by the University of California was under the direction of Dr. J. D. MacEwen, THRU Laboratory Director. The Navy shares support of the THRU operation and has a strong complementary hydrocarbon fuel toxicology research program. The Naval Medical Research Institute/Toxicology Detachment is located at Wright-Patterson AFB and is under the direction of Capt. D. E. Uddin. Pathology was performed by the Pathology Branch, Toxic Hazards Division, under the supervision of Lt. Col. R. H. Bruner. The opinions expressed herein are the opinions of the author and are not to be construed as official or reflecting those of the USAF, the U.S. Navy, or U.S. Army.

References

1 "Permissible Exposure Limits for Chemical Subtances," AFOSH Std 161-8, 20 June 1978.

2 *Threshold Limit Values for Chemical Substances and Physical Agents in the Work Environment and Biological Exposure Indices with Intended Changes for 1984-85*, American Conference of Governmental Industrial Hygienists, 1984.

3 *Threshold Limit Values for Chemical Substances and Physical Agents in the Work Environment and Biological Exposure Indices with Intended Changes for 1984-85*, American Conference of Governmental Industrial Hygienists, 1982.

4 "Military Specification, Turbine Fuel, Aviation, Grades JP-4 and JP-5," MIL-T-5264K, 1 April 1976, USAF.

5 "Criteria for a Recommended Standard, Occupational Exposure to Refined Petroleum Solvents," National Institute for Occupational Safety and Health, U.S. Department of Health, Education and Welfare, NIOSH 77-192, July 1977.

6 Bishop, E. C., MacNaughton, M. G., deTreville, R. T. P., and Drawbaugh, R. B., "Rationale for a Threshold Limit Value $(TLV)^R$ for JP-4/Jet B Wide Cut Aviation Turbine Fuel," OEHL-TR-83-128 EH111DGA, USAF Occupational and Environmental Health Laboratory, Brooks AFB TX, Apr. 1983.

7 Harrison, W. E., "The Chemical and Physical Properties of JP-4 for 1980-1981," AFWAL-TR-80-2052, Aero Propulsion Laboratory, Air Force Wright Aeronautical Laboratories, Wright-Patterson AFB, Ohio, 1982.

8 Gerrarde, H. W., "Aromatic Hydrocarbons," *Industrial Hygiene and Toxicology* (2d ed.), Vol. II, edited by F. A. Patty, Interscience, New York, 1962, pp. 1219-1240.

9 MacNaughton, M. G., and Uddin, D. E., "Toxicology of Mixed Distillate and High Energy Synthetic Fuels," Advances in Modern Environmental Toxicology series, Vol. VII, *Renal Effects of Petroleum Hydrocarbons*, edited by M. A. Mehlman, ch. 9, Princeton Scientific Publishers, Princeton, N.J., 1984, pp. 121-132.

10 Kitchen, D. N., "Neoplastic Renal Effects of Unleaded Gasoline in Fischer F344 Rats," Advances in Modern Environmental Toxicology series, Vol. VII, *Renal Effects of Petroleum Hydrocarbons*, edited by M. A. Mehlman, ch. 5, Princeton Scientific Publishers, Princeton, N.J., 1984, pp. 65-71.

Evaluation of Fuel Preparation Systems for Lean Premixing-Prevaporizing Combustors

W. J. Dodds

E. E. Ekstedt

General Electric Company,
Aircraft Engine Business Group,
Cincinnati, OH

A series of tests was conducted to provide data for the design of premixing-prevaporizing fuel–air mixture preparation systems for aircraft gas turbine engine combustors. Fifteen configurations of four different fuel–air mixture preparation system design concepts were evaluated to determine fuel–air mixture uniformity at the system exit over a range of conditions representative of cruise operation for a modern commercial turbofan engine. Operating conditions, including pressure, temperature, fuel–air ratio, and velocity had no clear effect on mixture uniformity in systems which used low-pressure fuel injectors. However, performance of systems using pressure atomizing fuel nozzles and large-scale mixing devices was shown to be sensitive to operating conditions. Variations in system design variables were also evaluated and correlated. Mixture uniformity improved with increased system length, pressure drop, and number of fuel injection points per unit area. A premixing system compatible with the combustor envelope of a typical combustion system and capable of providing mixture nonuniformity (standard deviation/mean) below 15% over a typical range of cruise operating conditions was demonstrated.

Introduction

The use of lean premixing-prevaporizing (LPP) combustors can provide ultra-low pollutant emissions as well as potential for improved performance, durability, and fuel flexibility in gas turbine engines. All of these advantages depend on complete prevaporization of the fuel and uniform premixing of the fuel and air prior to introduction of the mixture into the combustion chamber. A lean fuel–air mixture has a lower peak flame temperature than a conventional diffusion flame, where locally stoichiometric flame temperatures are obtained. This reduction in flame temperature decreases NO_x formation. By eliminating locally rich regions, premixing also largely prevents soot formation, thereby reducing flame radiation. This results in lower liner temperatures and improved fuel flexibility. Reduced soot formation also leads to lower smoke emission. Another potential benefit of premixing is improved turbine life because of reduced hot streaking and improved control of combustor exit temperature profiles.

All of the benefits of LPP combustion depend on complete evaporation and uniform mixing of the fuel and air. Locally unevaporated or rich mixtures lead to increased NO_x and soot formation.

The major challenge in designing a premixing system for a practical aircraft-type gas turbine combustor is to obtain complete premixing within the short combustion system envelope and within the time limitations imposed by autoignition of the fuel–air mixture. An example of a LPP combustion system designed for full-range operation in an aircraft gas turbine is depicted in Fig. 1 (from [1]). The system shown was sized and designed for the envelope and operating conditions of the General Electric CF6-50 engine. A conventional pilot stage is used for lightoff and low-power operation, while the LPP main stage is used for high-power operation. Premixing system design criteria for this combustor are a maximum premixing system length of only 15 cm, a maximum residence time of 2 ms (based on autoignition delay at takeoff operating conditions), and a total combined pressure drop in the premixing system and flow splitter of less than 5% of combustor inlet pressure.

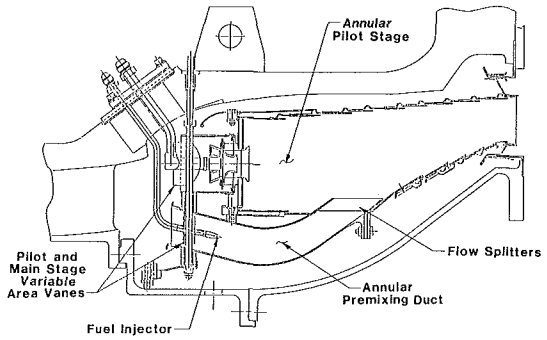

Fig. 1 Lean premixing-prevaporizing combustor

Analytical techniques are available (see, for example, [2]) to estimate fuel spray penetration, evaporation, and fuel–air mixing, but these estimates have not been experimentally verified for systems and operating conditions typical of the

Contributed by the Gas Turbine Division of THE AMERICAN SOCIETY OF MECHANICAL ENGINEERS and presented at the 30th International Gas Turbine Conference and Exhibit, Houston, Texas, March 18–21, 1985. Manuscript received at ASME Headquarters, January 7, 1985. Paper No. 85-GT-137.

Table 1 Test configurations

Concept	Configuration	Description
Vortex generator	A-1	Vane length = 0.64 cm, 45 deg angle of attack
	A-2	No vanes
	A-3	Vane length = 1.02 cm, 30 deg angle of attack
Multitube	B-1	Baseline
	B-2	Primary tubes removed[a]
	B-3	Reduced pressure drop[a]
	B-4	Twenty-five percent duct length reduction
	B-5	Fifty percent duct length reduction
	B-6	Annular duct adaptation
Perforated plate	C-1	Eighteen fuel tubes (Fig. 3)
	C-2	Six fuel tubes
	C-3	One fuel tube
Annular duct	D-1	One-tip injectors (Fig. 4)
	D-2	Four-tip injectors
	D-3	Six-tip injectors

[a]Modification incorporated in all subsequent configurations of Concept B

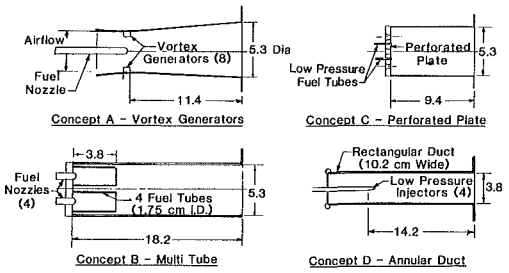

Fig. 2 Premixing duct design concepts (dimensions in cm)

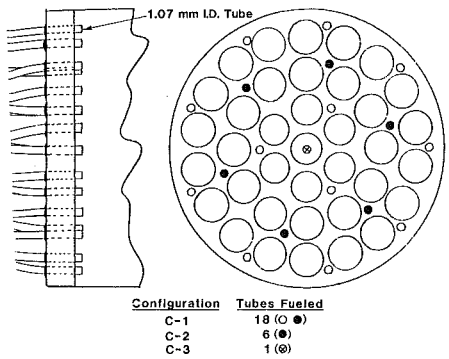

Fig. 3 Concept C fueling patterns

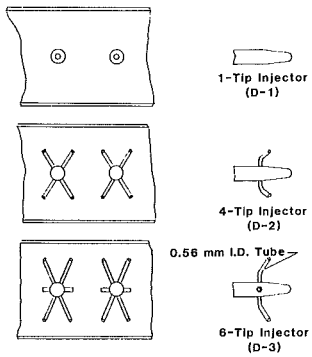

Fig. 4 Annular duct (concept D) fuel injector configurations

one shown in Fig. 1. The purpose of the experimental study described in this paper was to evaluate several premixing system design concepts applicable to aircraft-type LPP combustion systems at conditions typical of engine operation in order to develop a reliable test data bank for evaluation of analytical models, and to derive design correlation procedures for LPP combustion systems currently under consideration. Variations in operating conditions and critical design parameters were evaluated to provide data for correlation of these effects. Test evaluations were conducted on full-scale premixing systems at conditions typical of cruise operating conditions in a high-pressure ratio turbofan engine.

Test Configurations

Four different premixing system concepts were evaluated, as illustrated in Fig. 2. Several variations of each concept were evaluated, as described in Table 1.

Concept A uses a pressure atomizing nozzle to inject fuel into the throat of a converging/diverging tube. Eight flat vanes, or vortex generators, are mounted at the throat of the duct. These vanes generate trailing vortices within the duct. The objective of these vortices is to promote large-scale mixing of the fuel and air in the duct. Four of the vortex generators are oriented so as to swirl the air in a clockwise direction, and the other four are oriented to swirl the air in a counterclockwise direction. The swirl direction is alternated so that there is no net swirl in the duct. The size and strength of the vortices is determined by the angle of attack, length, and width of the vortex generators. The length and angle of attack of the vortex generators were varied in this test series, as described in Table 1.

Concept B uses four pressure atomizing fuel nozzles mounted at the throat of four cylindrical primary air tubes. The function of these primary air tubes is to ensure that an appropriate amount of air is mixed with the fuel flow from each nozzle. Eighty percent of the airflow enters through these primary tubes, while the remaining 20% is introduced between the primary tubes to prevent recirculation of the fuel–air mixture at the primary tube exit. Six variations of this concept were evaluated. Modifications included elimination of the primary tubes, increase in duct area to reduce pressure drop, and reduction in duct length. The first five variations utilized cylindrical ducts, while the sixth was the same concept applied to an annular duct. This sixth system simulated an array of 45 injectors mounted in 45 primary tubes equally spaced about the annular duct inlet. This annular system was simulated with a rectangular duct having three fuel injector/primary tube assemblies spaced as in the actual duct system (representing a 24 deg sector of the annular duct).

Concept C uses a perforated plate at the inlet to the duct to meter the inlet air and to position the fuel tubes. The number and position of fuel tubes can be varied to trim the fuel distribution. Three modifications of this concept were evaluated, containing one, six, and eighteen fuel tubes, respectively, as shown in Fig. 3. Equal length fuel tubes were used, and flow calibration tests were conducted prior to

Table 2 Test conditions

Conditions	Typical cruise range[a]	Experimental values
Inlet temperature, K	600–725	533, 644,[c] 756
Pressure, MPa	0.6–1.1	0.45,[c] 0.69, 1.03
Premixing duct velocity,[b] ms	60	45, 60,[c] 75
Premixing duct equivalence ratio	0.6	0.45, 0.6[c]

[a] CF6 engine.
[b] Varies with configuration.
[c] Baseline operating condition.

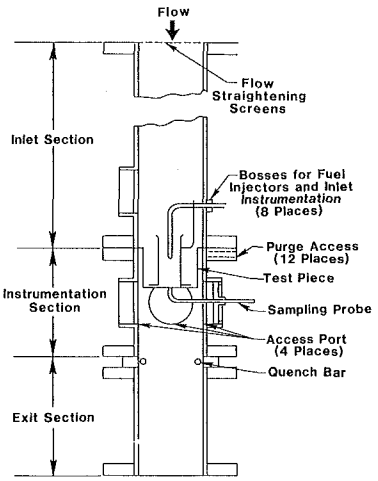

Fig. 5 Premixing duct test rig

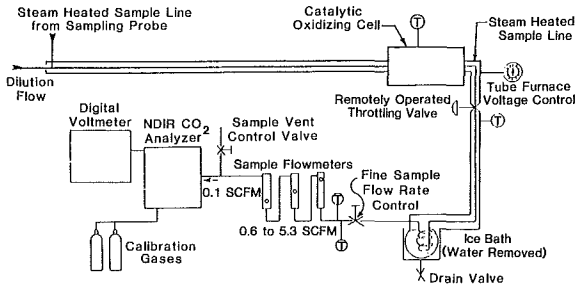

Fig. 6 Fuel-air ratio analysis system diagram

evaluation of this concept to ensure that fuel was equally distributed among the tubes.

Concept D is an annular duct system consisting of an array of 60 fuel injectors mounted at the inlet to an annular duct. This system was simulated with a rectangular test piece containing four injectors. This test piece represented a full scale, 24 deg sector of the actual duct. Three different variations of this concept were evaluated in which three different injector-tip configurations were used. The three injector-tip configurations were comprised of one, four, and six-point low-pressure injection tubes, respectively, as shown in Fig. 4.

Experimental Setup and Procedures

The fuel-air mixing tests were conducted using the high-pressure test rig shown schematically in Fig. 5. This test rig is mounted vertically to avoid gravitational effects, and is designed to operate at pressures up to 1.4 MPa and temperatures up to 800K.

The test rig is fabricated from stainless steel pipe having a nominal internal diameter of 15 cm. Screens are mounted in the rig inlet section to provide a uniform velocity profile at the inlet to the test piece. The test piece is mounted in an instrumentation section which contains four 10 cm access panels which can be adapted for visual/optical access or for mounting sample, pressure, or thermocouple probes.

Table 3 Premixing test summary

Configuration	Test results[a] $\frac{f_{max}}{f_{avg}}$	$\frac{\sigma_f}{f_{avg}}$	$\Delta P/P$,%[b]
A-1	2.48	1.06	4.3
A-2	1.88	0.74	1.2
A-3	1.76	0.74	14.7
B-1	1.09	0.05	7.8
B-2	1.04	0.03	8.9
B-3	1.17	0.14	4.7
B-4	1.22	0.15	5.1
B-5	1.18	0.14	4.1
B-6	2.15	0.77	2.0
C-1	1.45	0.40	3.8
C-2	1.91	0.59	3.8
C-3	2.53	0.96	3.8
D-1	9.33	2.42	1.8
D-2	2.04	0.45	2.1
D-3	1.37	0.25	1.2

[a] At baseline conditions indicated in Table 2.
[b] Percent of inlet pressure (corrected for rapid expansion loss at duct exit).

For the current test series, a traversing, single-element gas sampling probe was used to evaluate the time average fuel-air ratio distribution at the premixing duct exit plane. A water-cooled probe design was employed to prevent autoignition and stabilization of a flame in the wake of the probe. For the conditions and configurations tested, fuel evaporation was predicted to be essentially complete at the duct exit [3]. Also, for the configurations evaluated, axial flow was expected at the duct exit. Therefore, isokinetic sampling was not required to obtain representative results. In early tests, the effect of sub- and super-isokinetic sampling rates was evaluated and found to have a negligible effect on fuel-air ratio measurements.

The test rig exit section is a straight pipe containing a water injection ring to protect against autoignition of the fuel-air mixture. Pressure within the test rig is controlled using a pressure regulating valve in the facility exit ducting. The facility also contains a filter/separator system to remove the fuel vapor from the exhaust.

In addition to the gas sampling probe, instrumentation included total airflow (ASME thin plate orifice), inlet air temperature (two chromel/alumel thermocouple probes at the test piece inlet), inlet total pressure (single impact probe on the duct centerline), fuel flow (turbine flowmeters), fuel pressure and temperature, and test piece pressure drop.

Gas samples were analyzed with the fuel-air ratio measurement system shown in Fig. 6. This system contains a catalytic oxidizing cell which completely oxidizes the fuel so that the fuel-air ratio can be determined from the CO_2 concentration. CO and hydrocarbon analyzers were also used to verify that oxidation was complete. A metered dilution air source is also used to allow analysis of rich fuel-air mixtures.

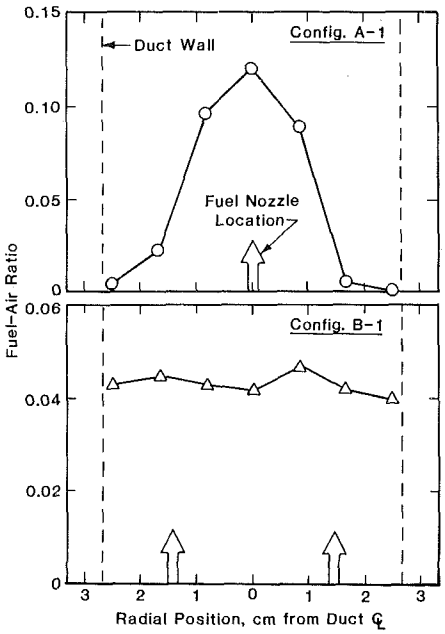

Fig. 7 Typical fuel-air ratio profiles (average fuel-air ratio = 0.042)

Each test configuration was typically evaluated over a range of inlet temperatures, velocities, pressures, and fuel-air ratios as described in Table 2. The test conditions were selected to overlap typical cruise operating conditions for a modern turbofan engine. At each condition, a seven-point gas sample traverse was generally conducted. A more detailed traverse was obtained to more thoroughly characterize the fuel-air ratio patterns produced by each configuration at the baseline operating condition indicated in Table 2.

Results and Discussion

A summary of test results obtained with the fifteen test configurations is presented in Table 3. For each configuration, pressure drop and two different measures of fuel-air mixture uniformity at the baseline test point are presented. The first uniformity parameter is the peak local measured fuel-air ratio divided by the average of the locally measured fuel-air ratios. The second parameter is the sample standard deviation of the local measurements divided by the average of the measured values. Detailed fuel-air ratio measurements for each of the test configurations at each test condition are presented in [4].

Fuel-air ratio profiles for two different premixing duct configurations are shown in Fig. 7. Peak fuel-air ratio values in most cases were measured in-line with the fuel injection points. Agreement between average gas sample fuel-air ratios and the overall fuel-air ratio calculated from metered fuel and air flows was generally good.

Effect of Operating Conditions. The effect of variations in inlet temperature, velocity, pressure, and fuel-air ratio varied from configuration to configuration. Operating conditions affected mixture uniformity to varying degrees in concepts A and B, while concepts C and D were virtually unaffected.

Premixing system concepts A and B were both sensitive to variations in operating conditions, but the trends observed with variation in operating conditions were quite different. Mixture uniformity with concept A became slightly worse when temperature and pressure were increased, and better when fuel-air ratio was increased. With concept B, fuel-air mixing was improved with increasing temperature and velocity, while fuel-air ratio and pressure effects were weak, as shown in Fig. 8.

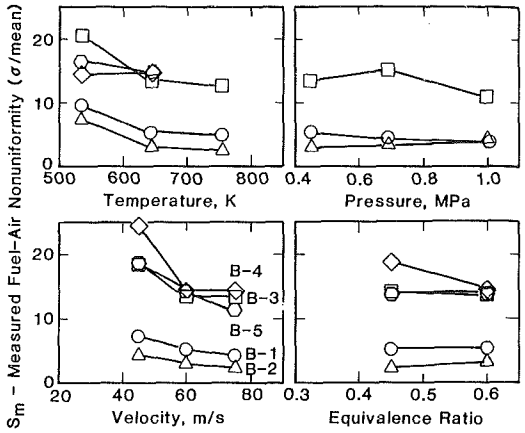

Fig. 8 Effect of operating conditions on premixing performance (multitube injector)

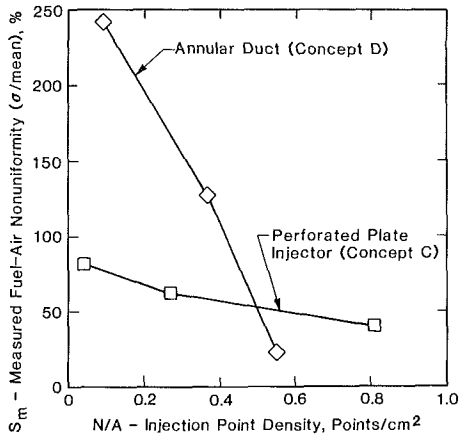

Fig. 9 Effect of fuel injection point density on premixing performance

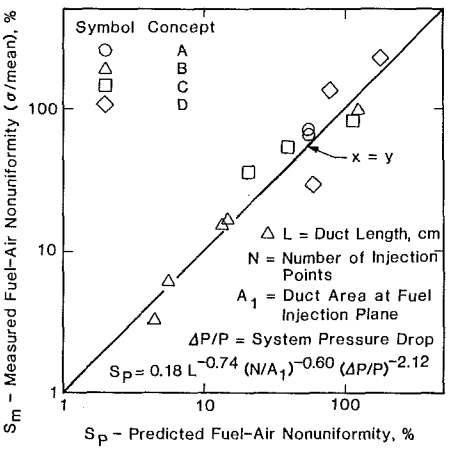

Fig. 10 Effect of design variables on premixing performance

The common design features of concepts A and B are the use of pressure atomizing fuel nozzles and the presence of devices to promote large-scale mixing. In the case of concept A, large-scale mixing is promoted by the use of vortex generators. In concept B the rapid expansion as the flow exits the primary tubes promotes large-scale mixing.

The effects of operating conditions on concepts A and B can be rationalized by considering spray atomization and penetration. Increased pressure [5], temperature [5], air velocity, and fuel-air ratio all improve atomization and reduce droplet penetration [6] with a pressure atomizing injector under the conditions studied (note that for the

conditions tested, fuel flow increases with pressure, velocity, and fuel-air ratio). For concept A, the reduced penetration is apparently detrimental, probably because the fuel droplets do not reach the location of the trailing vortices behind the vortex generators. On the other hand, in concept B the improved atomization apparently improves the turbulent dispersion characteristics of the droplets, thereby improving fuel-air mixing. Since four fuel injectors are used in concept B, fuel penetration is not as critical as in concept A.

Mixture uniformity with concepts C and D was virtually unaffected by operating conditions. Both of these concepts depend on airblast atomization of the fuel, using low-pressure fuel tubes in which low-velocity fuel jets are injected into a high-velocity airstream. These concepts also depend on smaller-scale turbulent dispersion and diffusion for fuel-air mixing.

Modification Effects. As described in Table 2, fuel-air mixture nonuniformity levels obtained with concept A were close to 1.0 (100%) for all three configurations tested. Of the concepts evaluated, concept A generally had the least favorable mixing characteristics. There was no consistent effect of variation in vortex generator vane length on mixture uniformity. As expected, pressure drop did increase with vane length.

Concept B produced the most uniform fuel-air mixtures of the systems tested, with nonuniformity in the 0.03 to 0.15 (3 to 15%) range for configurations B-1 through B-5. Mixture uniformity improved rapidly with increased pressure drop. Surprisingly, there was little change in mixture uniformity when the duct length was reduced. Removal of the primary tubes had little effect on mixture uniformity.

In both concepts C and D, mixture uniformity was found to be a strong function of the density of fuel injection points (points per unit area), as shown in Fig. 9. Nonuniformity levels with concept C were generally more than twice the levels obtained with concept B. However, it is thought that much improved uniformity could be obtained by adjusting the location of the fuel injectors. The best configuration of concept D provided satisfactory uniformity.

A linear regression analysis was run to correlate the effects of pressure drop, duct length, and density of fuel injection points on mixture uniformity. The objective of this analysis was to provide a means of estimating the uniformity obtainable with a given system. The resulting correlation is shown in Fig. 10.

In the design of a fuel-air premixing system for an actual LPP combustor, the primary design variables are duct length, airflow velocity, pressure drop, and the number of fuel injection points. Duct length, velocity, and pressure drop are limited by allowable combustion system pressure drop, autoignition delay time, and combustion system envelope. Once the length, velocity, and pressure drop have been defined based on these considerations, the required number of fuel injection points needed to meet a given fuel-air mixture uniformity goal can be estimated from Fig. 10.

Conclusions

A series of tests was run to evaluate four different fuel-air premixing system concepts. Based on this test series, the following conclusions have been drawn:

1 Time-average fuel-air nonuniformity values below 15% (standard deviation/mean) can be obtained with a premixing system meeting the envelope and autoignition requirements of a modern aircraft gas turbine engine at typical cruise operating conditions.

2 Effects of operating conditions on mixture uniformity depend on features of the premixing system design. Observed performance of systems using pressure atomizing fuel nozzles and large-scale mixing devices was sensitive to operating pressure, temperature, velocity, and/or fuel-air ratio.

3 An approximate correlation of the effects of premixing system fuel-injection-point density, pressure drop, and mixing length on fuel-air mixing performance has been derived. This correlation can be used to estimate the system size and required number of fuel injection points to obtain a specified level of fuel-air mixture uniformity.

Acknowledgments

The work reported in this paper was sponsored by the United States National Aeronautics and Space Administration under Contract NAS3-22006. Mr. James S. Fear is the NASA Project Manager.

References

1 Goyal, A., and Ekstedt, E. E., "NASA Advanced Low Emissions Combustor Program," ASME Paper No. 83-JPGC-GT-10, 1983.

2 Anderson, O. L., Chiappetta, L. M., Edwards, D. E., and McVey, J. B., "Analytical Modeling of Operating Characteristics of Premixing-Prevaporizing Fuel-Air Mixing Passages," NASA CR-167990, 1982.

3 Dickman, R. A., Dodds, W. J., and Ekstedt, E. E., "Lean, Premixing-Prevaporized (LPP) Combustor Conceptual Design Study," NASA CR-159629, 1979.

4 Dodds, W. J., and Ekstedt, E. E., "Advanced Low Emissions Combustor Program—Premixing Test Final Report," NASA Contractor Report, Contract NAS3-22006, in publication.

5 Abou-Ellail, M. M. M., Elkotb, M. M., and Rafat, N. M., "Effect of Fuel Pressure, Air Pressure, and Air Temperature on Droplet Size Distribution in Hollow Cone Kerosene Sprays," *First International Conference on Liquid Atomization and Spray Systems*, 1978, pp. 85-92.

6 Lefebvre, A. H., *Gas Turbine Combustion*, 1983, pp. 401-402.

Thermal Mechanical Crack Growth Rate of a High Strength Nickel Base Alloy

D. A. Wilson
Assistant Professor.
Dept. of Mechanical Engineering,
Tennessee Technological University,
Cookeville, TN
Mem. ASME

J. R. Warren
Assistant Materials Project Engineer.
Pratt & Whitney Aircraft Group,
Engineering Division—Florida Operations,
West Palm Beach, FL

An understanding of thermal mechanical fatigue (TMF) crack propagation is fundamental to the application of fracture mechanics to gas turbine components. Typical operating conditions for a cooled turbine disk rim consist of a complex mechanical history and an associated variable amplitude thermal history. While thermally induced stress gradients are commonly incorporated in the mechanical history, the effects of thermal cycling on crack growth must be addressed in an appropriate fatigue model. A current computer-based empirical crack propagation modeling system has demonstrated effectiveness under isothermal conditions and can be readily expanded to include thermal-mechanical effects. The existing isothermal models were developed from an extensive data base and describe crack growth over a broad range of temperature and loading conditions. Building on this established system, a model of thermal-mechanical crack growth is being developed.

Introduction and Background

Historically, methods used for predicting the life of gas turbine engine components have resulted in a conservative estimation of useful life. For example, most rotor disks are limited by low cycle fatigue (LCF), generally expressed in terms of mission equivalency cycles. When some predetermined cyclic life limit is reached, disks are retired from service. These limits evolve from a statistical analysis of laboratory specimen data, which indicates the cyclic life at which one in 1000 parts, such as disks, will have a fatigue-induced crack of approximately 0.030 in. in length. The life limits are based on test specimen data, but are subsequently verified and adjusted based on laboratory and engine component test results. By definition, only one part in 1000 will have a detectable crack of the predicted length after one service life; the remaining 999 parts will have less damage. Many of these parts are usable for one or more additional service lives.

Economic pressures resulting from reduced availability of strategic materials, the high cost of engine components, and the resulting effect of increased lead time on force readiness have made this conservative approach untenable. As a result, a new methodology has evolved that would use the available safe life in each part. This methodology, referred to as retirement for cause (RFC), is not intended to extend the life of a component, but rather to use safely the life capacity inherent in each individual part [1]. A program jointly sponsored by the Air Force Wright Aeronautical Laboratories (AFWAL) and the Defense Advanced Research Projects Agency (DARPA) entitled "Engine Component Retirement for Cause" (F33615-80-C-5160) was established to reduce this concept to practice. Work is in progress to develop the probabilistic life analyses and integrated logistics/economic methodology to support this implementation.

A key area of concern in the crack growth analyses of gas turbine engine disks is the impact that simultaneous variation in temperature and stress has on the crack growth predictions. Traditionally, these crack growth predictions are made using isothermal crack growth data at the temperature corresponding to the maximum stress and have produced predictions considered, in general, to be accurate, or at least conservative.

A limited number of thermal mechanical crack growth experiments were performed to assess the adequacy of using isothermal data to predict TMF behavior.

Material

Two high-strength nickel-base turbine disk alloys were investigated: IN100 and Astroloy. For brevity, only the IN100 results are presented.

Nominal composition is presented in Table 1. This alloy has been used extensively for high-pressure compressor and turbine disks and spacers in the Air Force F100 engine since its initial production in 1972. The material is produced under all-inert conditions. Powder, made by gas atomization, is hot compacted and extruded to forging billets. The material is then forged to near net component shape using the Gatorizing® superplastic, isothermal forging process, and then fully heat treated. Resultant grain size is typically ASTM 11.5 to 13 for current production hardware.

Contributed by the Gas Turbine Division of THE AMERICAN SOCIETY OF MECHANICAL ENGINEERS and presented at the 30th International Gas Turbine Conference and Exhibit, Houston, Texas, March 18–21, 1985. Manuscript received at ASME Headquarters, December 17, 1984. Paper No. 85-GT-12.

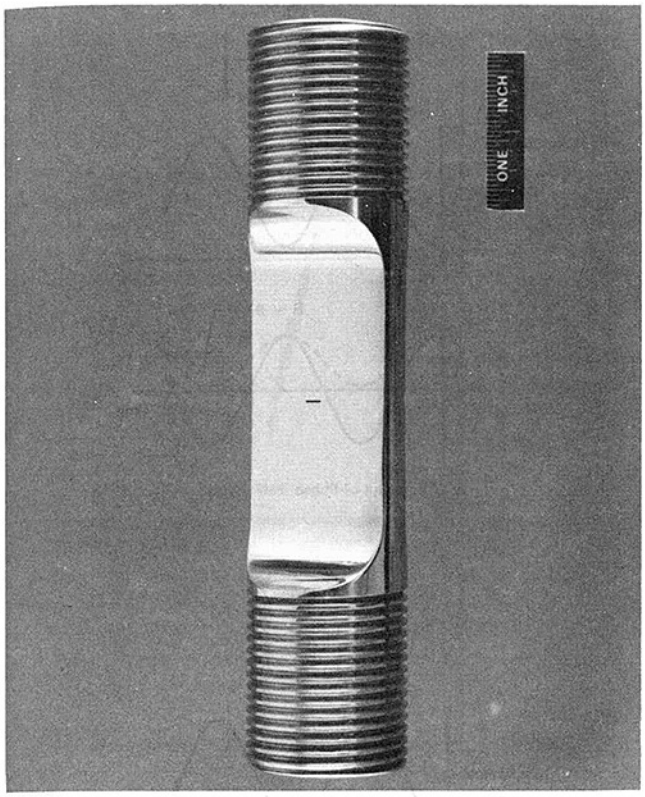

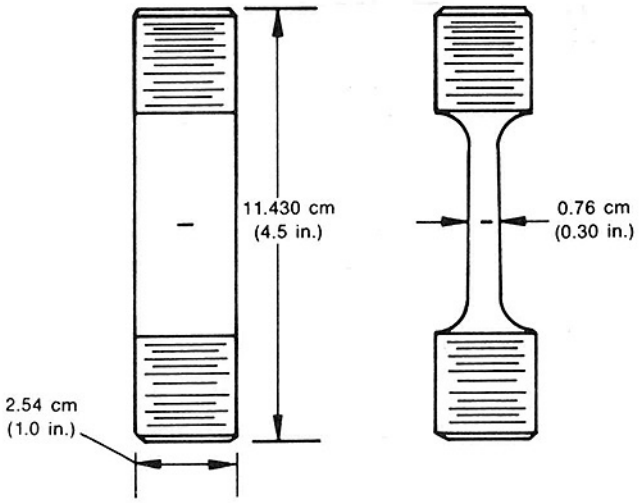

Fig. 1 ASTM standard center-crack-tension specimen

Experimental Program

The objective of this work was to assess the capability of an existing empirical model to accurately (or conservatively) predict crack growth in F100 engine components subject to thermal mechanical fatigue (TMF). The experimental TMF crack growth testing is summarized in Table 2. ASTM standard center-crack-tension (CCT) specimens as shown in Fig. 1 were used.

Table 1 Chemical composition of IN100

Carbon	0.07
Manganese	0.020 max
Sulfur	0.010 max
Phosphorus	0.010 max
Silicon	0.10 max
Chromium	12.40
Cobalt	18.50
Molybdenum	3.20-3.32
Titanium	4.32
Aluminum	4.97
Boron	0.02
Zirconium	0.06
Tungsten	0.05 max
Iron	0.30 max
Copper	0.07 max
Lead	0.0002 max
Tantalum and Columbium	0.04 max
Vanadium	0.78
Oxygen	0.010 max
Nickel	Balance

Nominal composition - percent by weight

Table 2 Thermal mechanical fracture mechanics test matrix

Specimen Number	*Temperature Range*	*Stress Ratio*	*Cycle Type*
2227	500°F to 1000°F	−1.0	In-Phase
2228	500°F to 1000°F	−1.0	In-Phase
2229	300°F to 1000°F	−1.0	In-Phase
2230	300°F to 1000°F	−1.0	In-Phase
2231	500°F to 1000°F	−1.0	Out-of-Phase
2232	500°F to 1000°F	−1.0	Out-of-Phase
2233	300°F to 1000°F	−1.0	Out-of-Phase
2234	300°F to 1000°F	−1.0	Out-of-Phase
2235	300°F to 1000°F	0.1	Out-of-Phase
2236	300°F to 1000°F	0.1	Out-of-Phase

Fig. 2 TMF test system

Nomenclature

a = crack length, in. (mm)
C_1, C_2, C_3, C_4 = crack growth model coefficients
N = cycles
R = stress ratio (min. stress/max stress)
T = temperature
ΔK = stress intensity range, lb/in.$^{3/2}$
ν = frequency, cycles/s

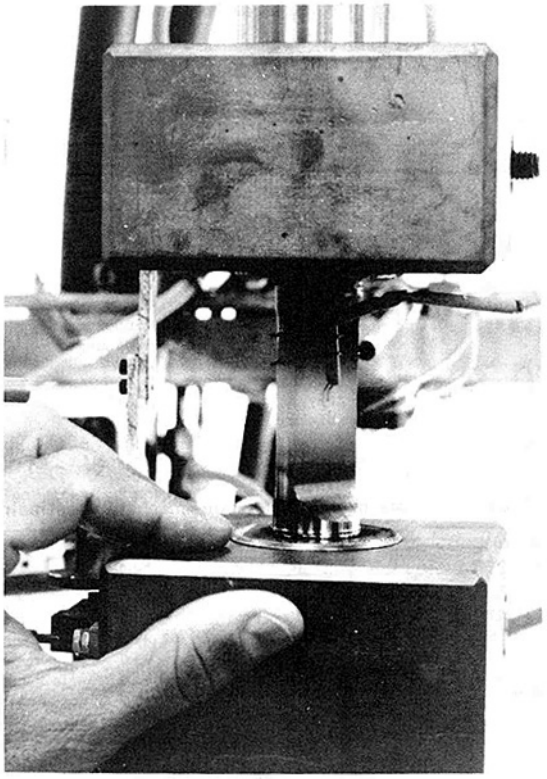

Fig. 3 TMF crack growth specimen on test

Test Method

The TMF test system (Fig. 2) is a conventional servo-hydraulic test machine which has been modified to simultaneously ramp and control temperature and stress. The machine contains two electronically controlled servo-systems: One is a hydraulic system for closed-loop control of load, strain, or displacement; the other is used concurrently for closed-loop control of specimen temperature. Command waveforms for each parameter are independent and can be programmed to conduct any TMF test cycle within the ramp rate capacity of the servo-systems.

Temperature control is accomplished using direct resistance heating from a low voltage–high current transformer and external air cooling. The transformer primary is driven by a variable-voltage, phase angle fired power control circuit. Current from the transformer is passed through the insulated load fixturing to the specimen and back to the transformer. The high current (0 to 1200 A at 0 to 3 V a-c) passing through the minimum cross section of the specimen supplies the thermal energy for rapid heating. Controlled closed-loop heating rates of 100°F (56°C) per second or less are generally used for TMF testing. For the cooldown portion of the waveform, the servo-system applies only the quantity of air required to maintain the temperature ramp. With the addition of water-cooled heat sinks to the specimen fixturing (Fig. 3), sufficient cooling (approximately 50°F/s, 28°C/s) can be obtained by conduction through the fixturing to reduce the through-thickness temperature gradient. The cooling is so efficient that the fixture is only warm to the touch at the maximum specimen temperature. A surface temperature profile around the crack using pyrometry showed no localized surface crack tip temperature differential. This test method has been successfully used previously for screening and alloy/coating system development [2].

All the precracking and testing were performed generally in accordance with procedures outlined in ASTM E647-83 except

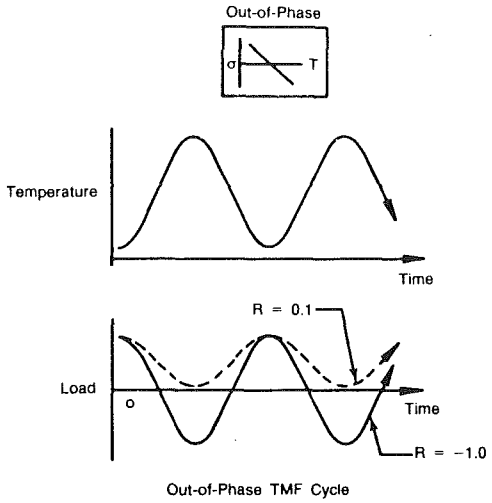

Out-of-Phase TMF Cycle

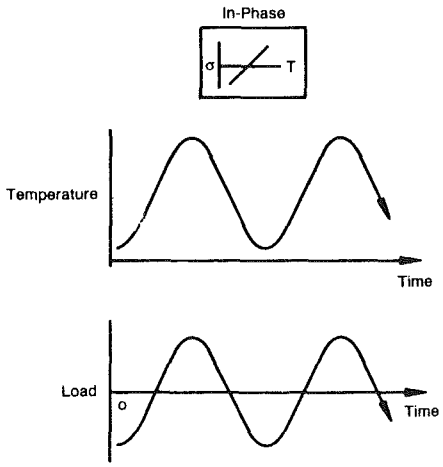

In-Phase TMF Cycle

Fig. 4 Typical temperature and load waveforms

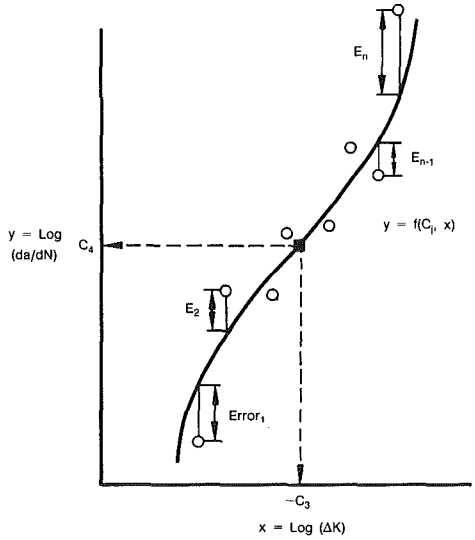

Fig. 5 Model development using method of least squares

for the variation in test temperature. The crack lengths were measured on both sides of the notch and on front and back surfaces directly with a traveling microscope. Typical TMF temperature/load waveforms are shown in Fig. 4. TMF

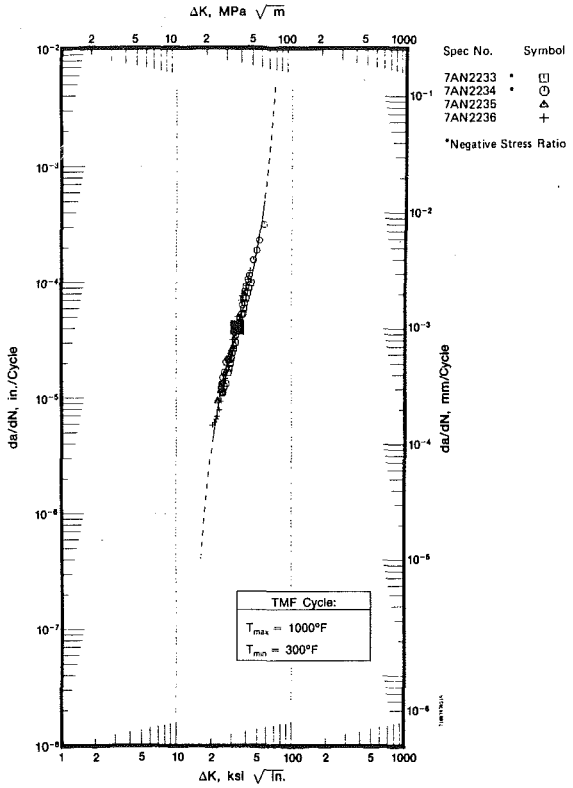

Fig. 6 Negative stress ratio has no effect

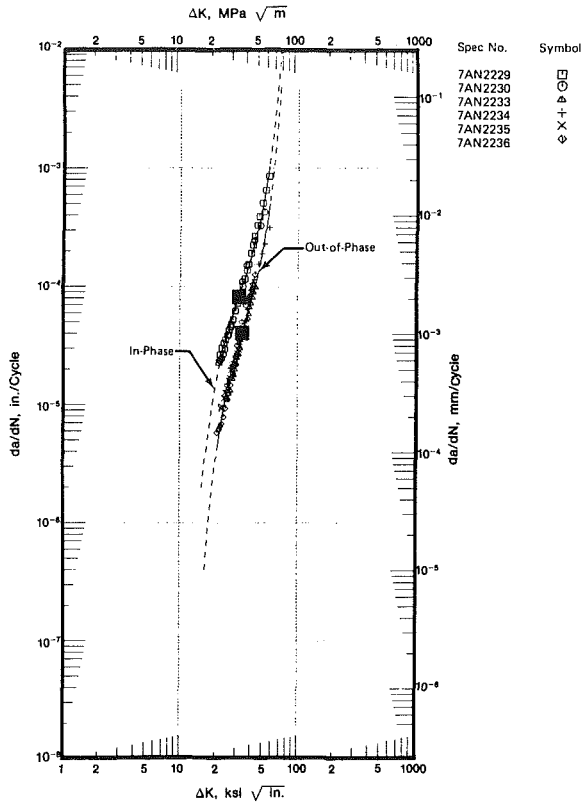

Fig. 7 Effect of TMF cycle with T_{min} = 300°F (149°C)

testing with an in-phase cycle shape has the maximum load occurring at the maximum temperature. In the out-of-phase cycle, maximum load occurs at the minimum temperature. Two stress ratios ($R = -1.0$ and 0.1) were used for the out-of-phase testing. Maximum cyclic temperature was 1000°F (538°C) with minimum cyclic temperatures of 500°F and 300°F (260 and 149°C). The test frequency was established at 0.5 cpm to permit sufficient time for cooling the test specimen thereby minimizing the amount of air cooling required.

Data Analysis Technique

The fundamental analytical tool used in assessing TMF crack growth is the SINH model. This computer-based interpolative crack propagation modeling system has demonstrated effectiveness under isothermal conditions and may be readily expanded to include thermal mechanical effects. The existing isothermal models were developed from an extensive data base and describe crack growth over a broad range of temperature and loading conditions for several alloy systems. Based on this established system, development of a thermal mechanical crack growth model required minimal additional testing and analysis.

The interpolative hyperbolic sine model (SINH) is in the form of computer software capable of describing crack propagation at various stress ratios, temperatures, and frequencies representative of gas turbine engine operation. The model is based on the hyperbolic sine equation,

$$\log(da/dN) = C_1 \sinh(C_2(\log\Delta K + C_3)) + C_4$$

where the coefficients have been shown [3, 4, and 5] to be functions of test frequency (ν), stress ratio (R), and temperature (T):

$$C_1 = \text{material constant}$$
$$C_2 = f_2(\nu, R, T)$$
$$C_3 = f_3(\nu, R, T)$$
$$C_4 = f_4(\nu, R, T)$$

Because of the simple relationships observed between the coefficients of the SINH model and the fundamental

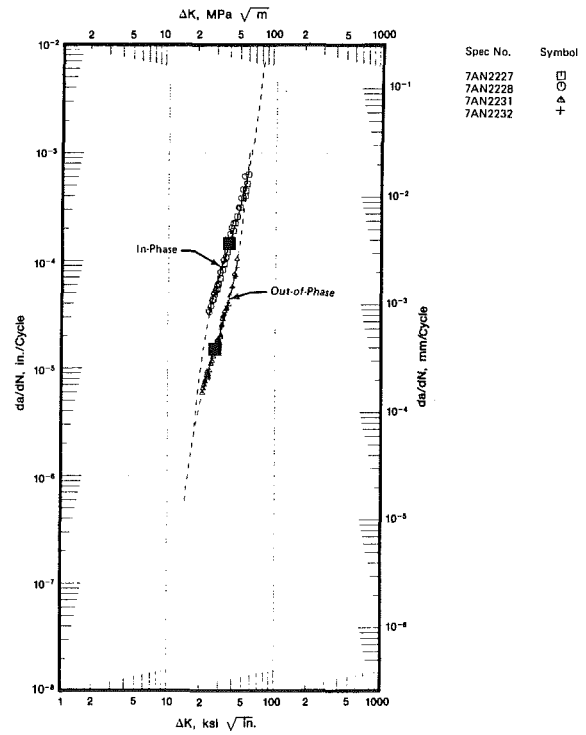

Fig. 8 Effect of TMF cycle with T_{min} = 500°F (260°C)

propagation controlling parameters, interpolations are straightforward. It is here the model demonstrates its great usefulness: The hyperbolic sine model provides descriptions of crack propagation characteristics where data are unavailable.

The goal of this procedure is to determine model coefficients for which the resulting curve through the data will

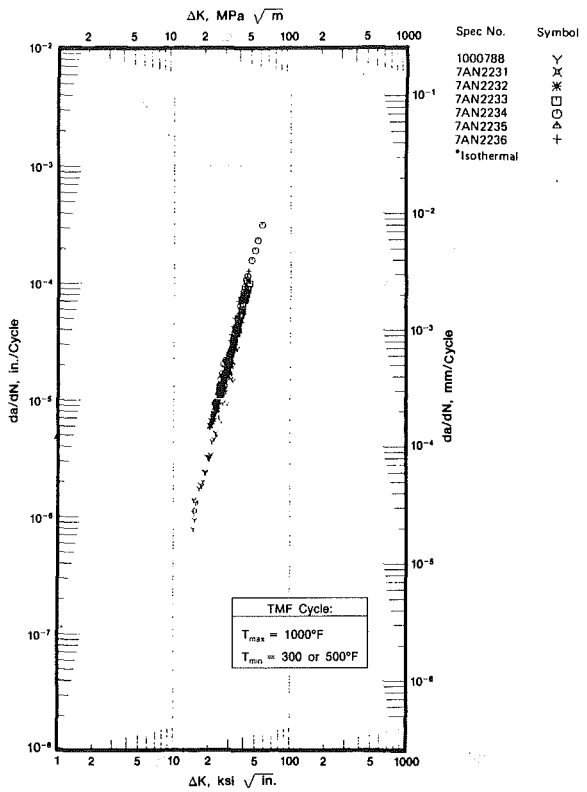

Fig. 9 Comparison of out-of-phase TMF with 300°F (149°C) 10 cpm isothermal crack growth data

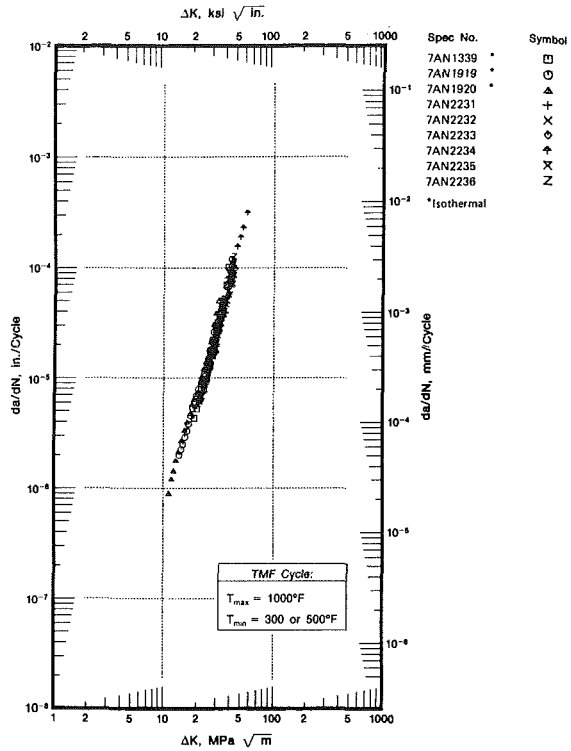

Fig. 10 Comparison of out-of-phase TMF with 500°F (260°C) 10 cpm isothermal crack growth data

have the least (minimum) summed squared error between calculated and observed values for the dependent variable (see Fig. 5). In this instance, the independent and dependent variables, x and y, are $\log(\Delta K)$ and $\log(da/dN)$, respectively.

Results

No significant difference in crack growth rate was observed for IN100 subjected to an out-of-phase thermal cycle at stress ratios of -1.0 and 0.1 as illustrated in Fig. 6. This indicated that no discernible damage (creep or slip) occurred during the high-temperature compressive portion of the cycle.

Comparisons of TMF in-phase and out-of-phase crack growth rate data at comparable temperature ranges for IN100 are plotted in Figs. 7 and 8. The in-phase specimen tests exhibit more rapid crack growth (approximately three times faster) than the out-of-phase tests.

No discernible difference was observed for IN100 out-of-phase TMF (T_{min} = 300 or 500°F, 149 or 260°C) when compared to 300°F (149°C) and 500°F (260°C), 10 cpm isothermal data (Figs. 9 and 10, respectively). A comparison of IN100 TMF in-phase data with 1000°F (538°C), 10 cpm isothermal data (Fig. 11) showed the crack growth rate isothermally to be slightly slower than for TMF. This effect is due to the higher frequency of the isothermal data (10 cpm versus 0.5 cpm for TMF tests) at a temperature where oxidation is significant.

A comparison of all TMF crack growth rate data is presented in Fig. 12, with the corresponding hyperbolic sine model coefficients given in Table 3. The data can generally be divided into in-phase and out-of-phase cycle types with no significant crack growth rate effect from negative stress ratio and minimum cycle temperature.

Integration of the crack growth model equation from the starting flaw size to the critical crack length results in the predicted life for a given set of test conditions. Comparison of predicted versus actual (P/A) lives indicates the model can fit the TMF crack growth data quite well, and where no TMF

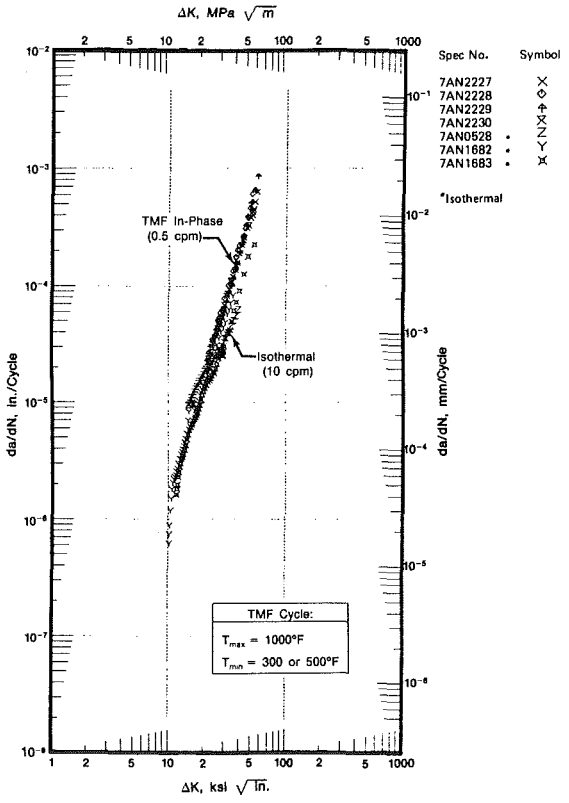

Fig. 11 Comparison of in-phase TMF with 1000°F (538°C) 10 cpm isothermal crack growth data

data are available, a reasonable life prediction should be expected using isothermal data at the appropriate temperature.

All crack growth rate data conformed to standards outlined in ASTM E-647 for constant load amplitude fatigue testing except the results for the out-of-phase TMF testing. The out-

Table 3 Model coefficients for TMF crack growth data

$$Y = C_1 \times \text{SINH}\ (C_2 \times (X \times C_3)) + C_4$$

Where $Y = \log(da/dN)$ and $X = \log(\Delta K)$

Curve	C_1	C_2	C_3	C_4	ΔK Range (min, max)	Number of Points	Correlation Factor (R^2)	Standard Error of Estimate
1	0.5000	6.0424	−1.5262	−3.9805	(21.39, 56.29)	78	0.9858	0.0513
2	0.5000	6.5882	−1.5034	−4.5224	(20.55, 56.85)	132	0.9620	0.0752

Total RSQRD = 0.9820 Std Error Est = 0.0674

Curve	Spec No.	Temp, °F	Freq.	Stress Ratio	Thickness, in.	Remarks	Predicted/ Actual
1	7AN2227	500-1000	0.5 cpm	−1.0	0.300	In-Phase	0.960
1	7AN2228	500-1000	0.5 cpm	−1.0	0.300	In-Phase	0.960
1	7AN2229	300-1000	0.5 cpm	−1.0	0.300	In-Phase	0.991
1	7AN2230	300-1000	0.5 cpm	−1.0	0.299	In-Phase	0.966
2	7AN2231	500-1000	0.5 cpm	−1.0	0.297	Out-of-Phase	0.941
2	7AN2232	500-1000	0.5 cpm	−1.0	0.299	Out-of-Phase	0.828
2	7AN2233	300-1000	0.5 cpm	−1.0	0.299	Out-of-Phase	0.916
2	7AN2234	300-1000	0.5 cpm	−1.0	0.298	Out-of-Phase	1.092
2	7AN2235	300-1000	0.5 cpm	1.0	0.298	Out-of-Phase	1.137
2	7AN2236	300-1000	0.5 cpm	1.0	0.300	Out-of-Phase	1.021

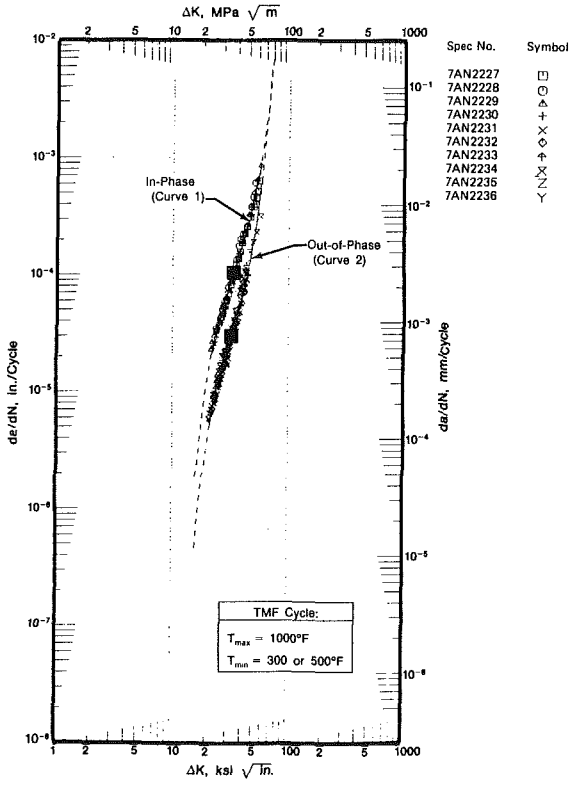

Fig. 12 Effect of TMF cycle on crack growth (all data)

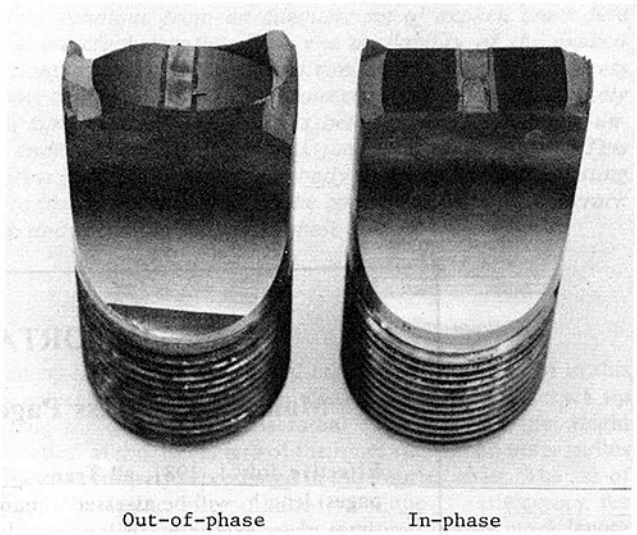

Fig. 13 Comparison of fracture surface morphologies

of-phase testing resulted in the development of large shear planes (Fig. 13) which departed by more than 5 deg from the plane of symmetry. Initially, the shear was thought to result from the component of crack growth or damage that occurred during the compressive portion of the cycle. However, as testing progressed, similar shear planes developed in specimens with a stress ratio (R) of 0.1 (i.e., no compressive loading during the cycle).

Observations with regard to the out-of-phase TMF fracture mechanism and results from previous testing provided the following:

1 No shear planes have been observed in the fracture of isothermal specimens tested previously with either negative or positive stress ratios at 300, 800, and 1200°F (149, 427, and 650°C).

2 No shear planes were observed on isothermal specimens tested in an inert environment. This condition is similar to the out-of-phase TMF tests where minimum oxidation would occur as a result of the crack tip being opened only at the lower temperature.

Other hypotheses were tested with no satisfactory explanation for the appearance of the out-of-plane fractures.

Conclusions

The objective of this investigation was to assess the capability of the existing hyperbolic sine model to predict accurately or conservatively the crack growth in gas turbine engine disks subject to thermal mechanical fatigue (TMF). The results are summarized as follows:

1 Using the lowest temperature of the out-of-phase TMF cycle, the existing isothermal model will accurately predict crack growth in engine disks subject to thermal mechanical fatigue.

2 Using the highest temperature of the in-phase TMF cycle, the model again should accurately predict crack growth.
3 Crack growth rates under compressive loading ($R = -1$) did not differ from all tensile loading ($R = +0.1$) for out-of-phase TMF cycling.
4 Out-of-phase TMF testing resulted in the development of large shear planes which had no noticeable influence on crack propagation rates measured normal to the loading axis, and for which no satisfactory explanation has been found.

Caution must be used in extending these results to other materials and conditions (e.g., creep range stress/temperatures, coated systems, etc.).

References

1 Harris, J., Jr., Sims, D. L., and Annis, C. G., Jr., "Concept Definition: Retirement for Cause of F100 Rotor Components," AFWAL-TR-800-4188, Sept. 1980.

2 Warren, J. R., and Cowles, B. A., "Thermal Mechanical Fatigue Screening Method for Gas Turbine Engine Applications," AMMRC MS 82-4, presented at "Army Symposium on Solid Mechanics, 1982 Critical Mechanics Problems in Systems Design," Bass River, Cape Cod, Mass., Sept. 22, 1982.

3 Annis, C. G., Wallace, R. M., and Sims, D. L., "An Interpolative Model for Elevated Temperature Fatigue Crack Propagation," AFML-TR-76-176, Part I, Nov. 1976.

4 Wallace, R. M., Annis, C. G., and Sims, D. L., "Application of Fracture Mechanics at Elevated Temperature," AFML-TR-76-176, Part II, Nov. 1976.

5 Sims, D. L., Annis, C. G., and Wallace, R. M., "Cumulative Damage Fracture Mechanics at Elevated Temperature," AFML-TR-76-176, Part III, Nov. 1976.

Weight Functions of Radial Cracks in Hollow Disks

George T. Sha

Chien-Tung Yang

Allison Gas Turbine Division,
General Motors Corporation,
P.O. Box 420,
Indianapolis, Indiana 46206-0420

Explicit nodal weight functions for both bore and rim radial cracks in a hollow disk are presented with special emphasis on the load independent characteristics of the weight functions that can eliminate the repeated finite element computations of the Mode I stress intensity factors (K_I) *for a given crack geometry under different loading conditions. An analytical expression, which relates the explicit crack-face weight functions to the radial distance* (r_s) *from the crack tip along the crack face, is also provided for wide range ratios of crack length* (a) *to the difference between outer disk radius* (R_o) *and inner disk radius* (R_i) [$0.01 \leq a/(R_o - R_i) \leq 0.8$]. *The accurate explicit weight functions of any crack length can be obtained easily with a cubic spline interpolation technique from an adequate set of explicit crack-face weight functions of discrete crack lengths. With the availability of the explicit crack-face weight functions for both the bore and rim cracks, the Mode I stress intensity factors under any complex loading conditions can be calculated accurately and inexpensively by a sum of worklike products between the equivalent "uncracked" stress field and the interpolated crack-face weight functions. This equivalent uncracked stress field could include the body force loading of a rotating disk, thermal loading, complex residual stresses, the applied tractions at the crack face and other locations, and any combinations of these loading conditions.*

Introduction

An efficient finite evaluation of the explicit weight functions [1] has been established recently at all locations within the structure of interest. This needed computational efficiency is achieved by combining the virtual crack extension technique [2 and 3] with the singular elements [4 and 5]. The weight function concept [6 and 7] is in fact the Green's function for the stress intensity factors of a cracked body. In other words, the weight function is a universal function that depends only on geometry and not on loading conditions [7]. In the practical application of linear elastic fracture mechanics, the determination of the explicit weight function is often more advantageous than the calculation of the Mode I stress intensity factor (K_I) alone. The use of weight function can obviate the unnecessary repeated finite element calculations of K_I values under different loading conditions of a given crack geometry. The virtual crack extension technique has also been extended recently to mixed mode crack problems by Sha et al. [8 and 9] with the symmetric mesh in the crack-tip neighborhood.

The primary purposes of this paper are to present the characteristics of the explicit weight functions along the crack face, and inner and outer perimeter locations for both bore and rim cracks in a hollow disk having an external radius (R_o) twice the size of an internal radius (R_i). An analytical expression for the crackface weight function for both bore (inner) and rim (outer) radial cracks is also presented in this paper as a function of radial distance (r_s) from the crack tip along the crack face. The radial component of the weight function at the perimeters of the inner radius and outer radius can be accurately represented in the Fourier series. The use of the cubic spline interpolation technique is satisfactory for obtaining the crack-face weight functions of any crack length from an adequate set of crack-face weight functions of different crack lengths.

According to Rice's displacement derivative representation, the weight function vector at the (x_i, y_i) location with crack length (a) is defined as

$$h_{1i}(x_i,y_i,a) = \frac{H}{2K_1(a)^*} \frac{\partial u_i(x_i,y_i,a)^*}{\partial a} \tag{1}$$

where

H = the effective modulus
$K_1(a)^*$ = the Mode I stress intensity factor under * loading system with crack length (a)

and

$\frac{\partial u(x_i,y_i,a)^*}{\partial a}$ = the partial displacement derivative with respect to the virtual crack extension Δa under * loading system

The Mode I weight function vector, h_{1i} (x_i, y_i, a), at all (x_i, y_i) locations consists of h_{1x} (x_i, y_i, a) and h_{1y} (x_i, y_i, a) components, which are defined as

$$h_{1x}(x_i,y_i,a) = \frac{H}{2K_1(a)^*} \cdot \frac{\partial u_x(x_i,y_i,a)^*}{\partial a} \tag{2a}$$

Contributed by the Gas Turbine Division of THE AMERICAN SOCIETY OF MECHANICAL ENGINEERS and presented at the 30th International Gas Turbine Conference and Exhibit, Houston, Texas, March 18-21, 1985. Manuscript received at ASME Headquarters, December 17, 1984. Paper No. 85-GT-14.

$$h_{1y}(x_i,y_i,a) = \frac{H}{2K_I(a)^*} \cdot \frac{\partial u_y(x_i,y_i,a)^*}{\partial a} \quad (2b)$$

where u_x and u_y are the displacement component along the x and y axes, respectively, under * loading system.

Following Rice [6], the Mode I stress intensity factor (K_I) is expressed as a sum of worklike products between the applied traction and the explicit weight functions (h_I) at their points of application for two-dimensional crack geometry as

$$K_I = \int_S t \cdot h_I dS + \int_A f^b \cdot h_I dA \quad (3)$$

where

S = the boundary with surface traction (t) applied
f^b = body force within area A

Without body-force loading, only the line integral is involved in the K_I calculation, as shown in equation (3) for two-dimensional crack problems. However, by applying the linear superposition principle, the K_I calculation for a given crack geomtetry can be evaluated from the line integral alone even with body-force loading by combining the resultant uncracked stress field $\sigma(r_s)$ with the crack-face weight function, $h_{1r_s}(r_s, a)$, at the crack-face location as

$$K_I = \int_0^a \sigma(r_s) \cdot h_{1r_s}(r_s,a)\, dr_s = \sum f_i(r_s) \cdot h_{1r_s}(r_s,a) \quad (4)$$

where

r_s = the radial distance from the crack tip along the crack face
$h_{1r_s}(r_s,a)$ = the crack-face weight function component for Mode I deformation with crack length (a)
$f_i(r_s)$ = consistent nodal forces equivalent to $\sigma(r_s)$ applied uncracked stress

The resultant uncracked stress field, $\sigma(r_s)$, can include body force loading for the rotating disk, thermal loading, applied tractions at the crack face and any other locations, complex residual stresses of a partially autofrettaged thick-wall cylinder, and any of their loading combinations.

The crack-face weight function component, $h_{1r_s}(r_s, a)$, for both bore and rim radial cracks in a hollow disk can be accurately represented by

$$h_{1r_s}(r_s,a) = \sum_{n=1}^{N} C_n(a) r_s^{(\frac{n}{2}-1)} \quad (5)$$

where

N = the maximum number of terms needed for accurate representation of $h_{1r}(r_s, a)$
$C_n(a)$ = the least-square regressed coefficients that are a function of crack length (a) only

The crack-face weight function for any crack length (a) can be accurately obtained with the cubic spline interpolatory technique from an adequate set of crack-face weight functions of discrete crack lengths.

The needed stress intensity factors at any crack length for life calculation can be evaluated economically and accurately from equation 4 by combining the uncracked stress field and the interpolated crack-face weight function. With this approach of evaluating K_I for bore and rim radial cracks, the total loss of K_I accuracy is found to be less than 1%.

The implied weight function approach with Rice's displacement derivative representation has been used by Besuner [10], Grandt [11], Andrasic et al. [12], and Pu [13] for calculating stress intensity factors of a given crack geometry under different loading conditions. It can be divided into two categories depending on whether the partial displacement derivative with respect to crack length ($\partial u/\partial a$) at the crack-face location is approximated. The former group is represented by Grandt [11] and Andrasic et al. [12] with $\partial u/\partial a$ approximation, which is made either from the conic section given by Orange [14] or from the numerical approximation of crack-face displacement data of different crack lengths. The latter group is typified by Pu [13], with no assumptions on u and $\partial u/\partial a$, using the finite element method to compute stress intensity factors associated with different simple loading systems. The present work on explicit weight function vectors differs from these previously mentioned implied weight function publications [10–13] in that both nodal weight function vectors h_{1i} (x_i, y_i, a) and partial displacement derivatives for the entire structure of interest are determined explicitly and efficiently with the finite element virtual crack extension technique. This is done through the following two-step process:

1 Obtain the displacement derivative with respect to the crack extension du/da at the perturbed locations for the entire structure of interest from the perturbations of elemental stiffness and nodal forces of a few elements as a result of virtual crack extension.
2 Convert the displacement derivatives from the perturbed locations to the unperturbed locations. Mathematically, this is equivalent to changing the total displacement derivatives du/da to partial displacement derivatives $\partial u/\partial a$.

Mathematically rigorous procedures are adopted in carrying out this two-step process within the framework of finite element methodology.

By coupling the virtual crack extension technique with the singular elements, an efficient finite element methodology for evaluating stress intensity factors and explicit nodal weight functions for the entire structure of interest has been established [1]. The application of this efficient finite element methodology to bore and rim radial cracks of a hollow disk is exercised in this paper. Once the explicit nodal weight functions for a given crack geometry are predetermined, the application of these predetermined weight functions to other loading conditions can be made efficiently and economically for calculating the needed stress intensity factors for life evaluation of a disk component. An excellent agreement in numerically determined K_I values for disk geometry is demonstrated in this paper between the results obtained from explicit weight functions and the literature data obtained from other numerical techniques.

Explicit Weight Functions

As indicated in equation 1 of Rice's displacement derivative representation of weight function, the determination of explicit weight function requires both Mode I stress intensity factor (K_I) and partial displacement derivatives with respect to crack length ($\partial u/\partial a$). The details for finite element evaluation of explicit weight functions with the virtual crack extension technique coupled with singular elements can be found in a recent paper by Sha [1] with special emphasis on computational efficiency. A brief outline of the finite element evaluation of explicit weight function will be followed for the sake of completeness.

The degenerated quarter-point quadratic elements with $\sqrt{r}$ displacement variation were assembled in the crack-tip vicinity. These singular crack-tip elements were surrounded by the standard eight-noded quadratic elements for the remainder of the two-dimensional crack model. The virtual crack extension of an amount Δa was simulated by advancing the crack-tip node by Δa in the direction colinear with the Mode I crack. The surrounding quarter-point nodes were also shifted to the new quarter node locations for the proposed mode of virtual crack extension technique used in the numerical calculation of stress intensity factor and explicit weight functions for two-dimensional Mode I cracks.

The determination of K_I value with the energy method is normally made from the energy release rate (G), which is the potential energy difference ($\Delta\pi$) between two successive crack-tip positions, with respect to crack extension, under a given loading condition. In the virtual crack extension technique, the G evaluation is made only by one complete finite element computation of original crack geometry and partial analysis of new crack geometry with a few elements, as contrasted with two complete finite element runs of slight difference in crack length for the regular energy method under the identical loading condition. Therefore, the virtual crack extension technique is certainly preferred, from a computational efficiency viewpoint. In terms of finite element language, the calculation of G with the virtual crack extension technique is obtained from the displacement field $\{u\}$ of original crack geometry and the perturbation in elemental stiffness ($\partial[K]/\partial a$) and in prescribed load vector ($\partial\{f\}/\partial a$) with respect to crack extension of a few elements, indicated by Parks [2] as

$$G = -\frac{\partial\pi}{\partial a} = -\frac{1}{2}\{u\}^T\frac{\partial[K]}{\partial a}\{u\} + \{u\}^T\frac{\partial\{f\}}{\partial a} \tag{6}$$

since the Mode I stress intensity factor, K_I, is related to G by

$$GH = K_I^2 \tag{7}$$

where

H = effective modulus width
$H = E$ for generalized plane stress and
$H = E/(1 - \nu^2)$ for plane strain

and

ν = Poisson's ratio

In the proposed method of virtual crack extension, the degenerated crack-tip elements are the only elements experiencing the changes in elemental stiffness (k_i). Thus, the evaluation of $\partial[K]/\partial a$ in equation (5) can be made as follows:

$$\frac{\partial[K]}{\partial a} = \sum_{i=1}^{N_a}\frac{\partial[k_i]}{\partial a} \tag{8}$$

where

N_a = number of crack-tip elements with nodal location changes resulting from virtual crack extension

With relatively small virtual crack extension (Δa), the $\partial[k_i]/\partial a$ can be accurately approximated by simple finite differences as

$$\frac{\partial[k_i]}{\partial a} \simeq \frac{[k_i]|_{a+\Delta a} - [k_i]|_a}{\Delta a} \tag{9}$$

where

$[k_i]|_{a+\Delta a}$ = elemental stiffness of i's element after virtual crack extension
$[k_i]|_a$ = elemental stiffness of i's element before virtual crack extension

Similarly, $\partial\{f\}/\partial a$ can be approximated by the following:

$$\frac{\partial\{f\}}{\partial a} \simeq \sum_{i=1}^{N_c}\frac{\{f_i\}|_{a+\Delta a} - \{f_i\}|_a}{\Delta a} \tag{10}$$

where

N_c = number of crack-tip elements with nodal location perturbation
$\{f_i\}|_{a+\Delta a}$ = consistent nodal force at i's element along crack face after virtual crack extension

and

$\{f_i\}|_a$ = consistent nodal force at i's element along crack face before virtual crack extension

Note that $N_c = 1$ for the virtual crack extension used in the finite element evaluation for crack-face loading. In general, $\partial\{f\}/\partial a$ is equal to zero unless the body force, thermal loading, and crack-face loading are applied. With the numerical approximation of equations (9) and (10) for G calculation, the stress intensity factor (K_I) can be accurately obtained from equation (7).

The displacement derivatives at the unperturbed locations needed for weight function calculations as shown in equation (1) can be obtained efficiently through the following two-step process:

1 Obtain the displacement derivatives for the entire structure at the perturbed location ($d\{u\}/da$).
2 Convert displacement derivatives at the perturbed locations to unperturbed locations. This is equivalent to changing the total derivatives ($d\{u\}/da$) to partial derivatives with respect to crack extension ($\partial\{u\}/\partial a$) mathematically.

The displacement derivatives at the perturbed locations ($d\{u\}/da$) at all locations of the entire structure of interest can be obtained efficiently. This is achieved through the changes in elemental stiffness of a few elements and the perturbation of nodal force for a single crack-face element undergoing crack-face loading with the proposed virtual crack extension mode by using the global stiffness equation as the starting point as

$$[K]\{u\} = \{f\} \tag{11}$$

Differentiating equation (11) with respect to crack length (a) yields the following equation after rearrangement:

$$\frac{d\{u\}}{da} = [K]^{-1}\left[\frac{d\{f\}}{da} - \frac{d[K]}{da}\{u\}\right] \tag{12}$$

Equation (12) provides an efficient analytical methodology for evaluating the displacement derivatives at the perturbed locations for the entire structure of interest from the stiffness perturbation of a few singular elements and the changes in nodal force of a single crack-face element with the proposed virtual crack extension technique. The evaluation of $d\{u\}/da$ according to equation (12) without account $d\{f\}/da$ term has been made by Gallagher [15] and Parks et al. [16]. The $d\{f\}/da$ term of equation (12) must be accounted for in dealing with crack-face loading, thermal loading, body-force loading, and their combinations.

The numerical corrections resulting from changing the perturbed displacement derivatives ($d\{u\}/da$) to the unperturbed displacement derivatives ($\partial\{u\}/\partial a$) can be carried out as suggested by Vanderglas [17] as follows. The displacement vector can be expressed as

$$\{u\} = \{u(x,y,a)\} \tag{13}$$

Applying the chain rule of differentiation of equation (13) with respect to crack length (a) produces the following equation after rearrangement:

$$\frac{\partial\{u\}}{\partial a} = \frac{d\{u\}}{da} - \frac{\partial\{u\}}{\partial x}\cdot\frac{dx}{da} - \frac{\partial\{u\}}{\partial y}\cdot\frac{dy}{da} \tag{14}$$

The last two terms of equation (14) serve as correction factors of changing the total displacement derivatives to partial displacement derivatives with respect to crack length (a). These correction factors are null for nodes without geometric changes in nodal location as a result of virtual crack extension. For Mode I, cracks with colinear virtual crack extension give results of $dx/da = 1.0$ and $dy/da = 0$ for a crack lying on the x axis. The finite element evaluation of $\partial\{u\}/\partial x$ and $\partial\{u\}/\partial y$ of equation (14) resulting from virtual crack extension can be obtained from the Jacobian matrix [J], which provides a differential relationship between local coordinates (ξ, η) and global coordinates (x, y) for isoparametric elements, as in the following:

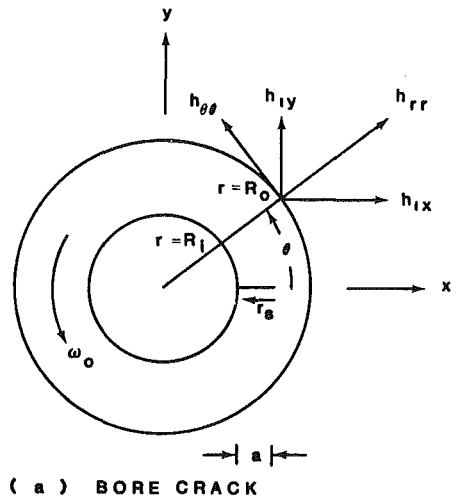

(a) BORE CRACK

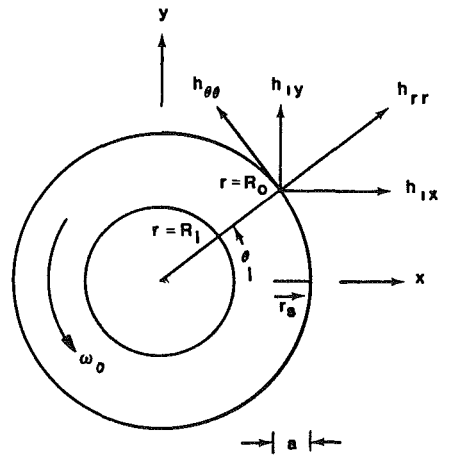

(b) RIM CRACK

Fig. 1 Nomenclature used in a hollow disk with a single radial crack

$$\frac{\partial\{u\}}{\partial x} = \frac{1}{\det[J]}\left\{\frac{\partial[N_i u_i]}{\partial\xi}\cdot\frac{\partial y}{\partial\eta} - \frac{\partial[N_i u_i]}{\partial\eta}\frac{\partial y}{\partial\xi}\right\} \tag{15a}$$

$$\frac{\partial\{u\}}{\partial y} = \frac{1}{\det[J]}\left\{\frac{\partial[N_i u_i]}{\partial\eta}\cdot\frac{\partial x}{\partial\xi} - \frac{\partial[N_i u_i]}{f\partial\xi}\frac{\partial x}{\partial\eta}\right\} \tag{15b}$$

where

u_i = nodal displacement
N_i = shape function
$\det[J]$ = determinant of the Jacobian matrix

By substituting equation (15) into equation (14), the weight function for Mode I crack geometry at all (x_i, y_i) locations can be expressed as the following:

$$h_I(x_i,y_i,a) = \frac{H}{2K_I(a)}\left[\frac{d\{u\}}{da} - \frac{1}{\det[J]}\left\{\frac{\partial[N_i u_i]}{\partial\xi}\cdot\frac{\partial y}{\partial\eta} - \frac{\partial[N_i u_i]}{\partial\eta}\cdot\frac{\partial y}{\partial\xi}\right\}\right] \tag{16}$$

The $1/\sqrt{r}$ singular behavior of the explicit crack-face nodal weight functions in the crack-tip neighborhood is duly restored with the corrections as indicated in equation (16) for the coordinate transformation. Also note that the load independent characteristics of a given crack geometry under different loading conditions are confirmed numerically with different loading conditions in this investigation. By using the linear superposition principle, the calculation of both K_I and explicit weight functions under remote loading can be replaced with equivalent crack-face loading, which requires the proper account for $d\{f\}/da$ term as shown in equations (6) and (12), respectively. It is concluded that the efficient finite element evaluation of Mode I stress intensity factors and explicit weight functions for the entire structure of interest is achieved by coupling the virtual crack extension technique with singular elements in the immediate crack-tip vicinity.

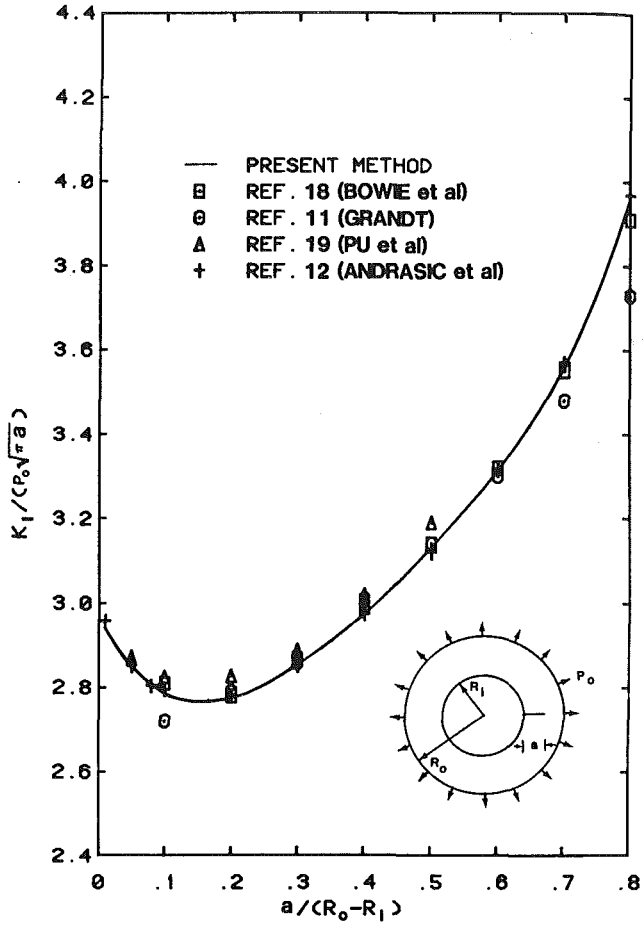

Fig. 2 Normalized stress intensity factors as a function of $a/(R_o-R_i)$ ratio for a bore crack in a hollow disk with $R_o/R_i = 2$ under uniform external pressure loading

Results and Discussions

Mode I stress intensity factors (K_I) and explicit weight functions (h_I) for bore and rim radial cracks of a hollow disk, as shown in Fig. 1, with outer radius (R_o) twice the inner radius (R_i), are investigated in this paper with the virtual crack extension technique coupled with singular crack-tip elements. The purposes of this paper are to present the characteristics of explicit weight functions along the crack face, inner perimeter, and outer perimeter with different $a/(R_o-R_i)$ ratios and to illustrate the ability of obviating the repeated finite element calculation of K_I values for a given crack geometry under different loading conditions with Bueckner's weight function concept. An analytical expression, which relates the explicit crack-free weight function component for Mode I deformation to the radial distance (r_s) from the crack tip along the crack face as shown in equation (5), is also provided to facilitate the K_I calculation by combining the uncracked stress field and the explicit crack-face weight function.

A wide range of crack lengths for both bore and rim cracks with $0.01 \le a/(R_o - R_i) \le 0.80$ and $R_o/R_i = 2$ is used for the numerical evaluation of K_I and h_I values under Mode I loading of the hollow disk geometries. The normalized stress intensity factors for a bore crack of different crack lengths

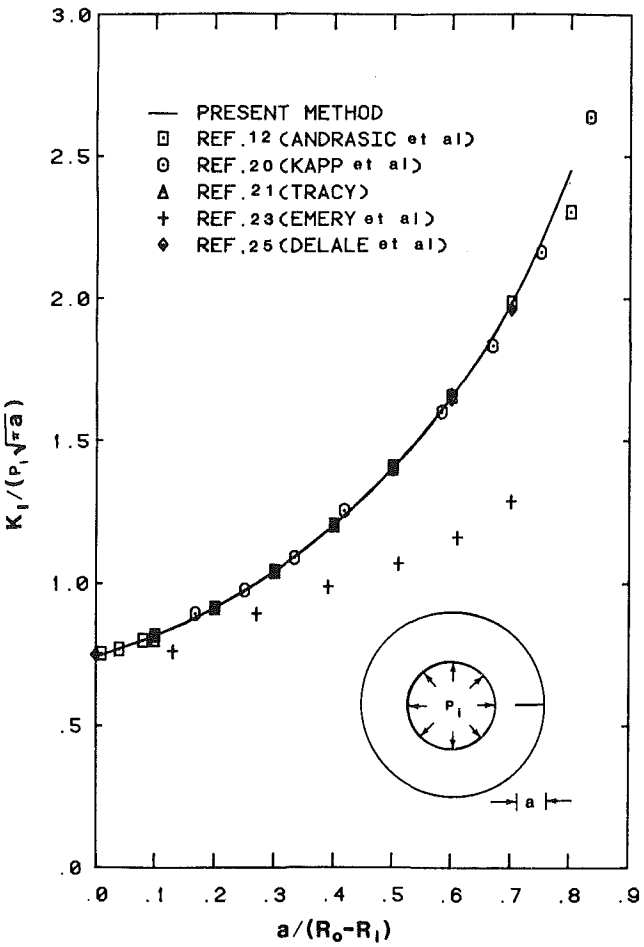

Fig. 3 Normalized stress intensity factors as a function of $a/(R_o-R_i)$ ratio for a rim crack in a hollow disk with $R_o/R_i = 2$ under the uniform internal pressure loading condition

under uniform tension loading at the outer radius, as shown in Fig. 2, compare well with those of Bowie et al. [18], Grandt [11], Andrasic et al. [12], and Pu et al. [19]. The normalized stress intensity factors for a rim radial crack of different crack lengths under uniform pressure at the inner radius, as shown in Fig. 3, are in good agreement with those of Andrasic et al. [12], Kapp et al. [20], Tracy [21], and Delale et al. [22] but not with the finite difference results of Emery et al. [23]. The typical finite element mesh for either a bore radial crack or a rim radial crack in a hollow disk is shown in Fig. 4 with $R_o/R_i = 2$. The normalized stress intensity factor from the weight function concept, as shown in equation (4), can be expressed in terms of dimensionless crack-face weight function component $[\sqrt{a} \cdot h_{1y}(r_s/a, a)]$ and dimensionless crack-face radial distance (r_s/a) through the change of variable by letting $X = r_s/a$ at a given $a/(R_o-R_i)$ ratio as

$$\frac{K_I}{\sigma\sqrt{\pi a}} = \frac{1}{\sigma\sqrt{\pi a}} \int_0^1 \sigma(aX) \cdot h_1(aX,a)\, a \cdot dX \qquad (17a)$$

$$= \frac{1}{\sigma\sqrt{\pi}} \int_0^1 \hat{\sigma}(X) \cdot \sqrt{a}\hat{h}_1(X,a)\, dX \qquad (17b)$$

This dimensionless form of equation (17) can facilitate the normalized K_I calculation from the crack-face weight function of the similar disk geometry regardless of its actual size. The normalized crack-face weight function, $\sqrt{a} \cdot \hat{h}_{1y}$ $[r_s/a, a/(R_o-R_i)]$, as a function of r_s/a for bore radial crack and rim radial crack of different $a/(R_o-R_i)$ ratios with $R_o/R_i = 2$, is shown in Figs. 5 and 6, respectively. By using the invariant characteristics of the explicit weight functions with respect to the loading conditions for a given geometry and constraint

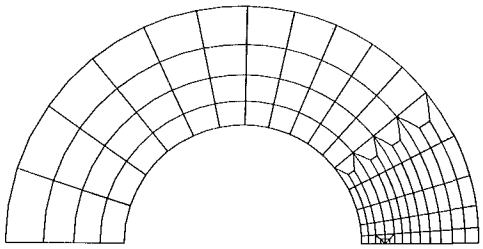

Fig. 4 A typical finite element mesh for either a bore crack or a rim crack in a hollow disk with $R_o/R_i = 2$

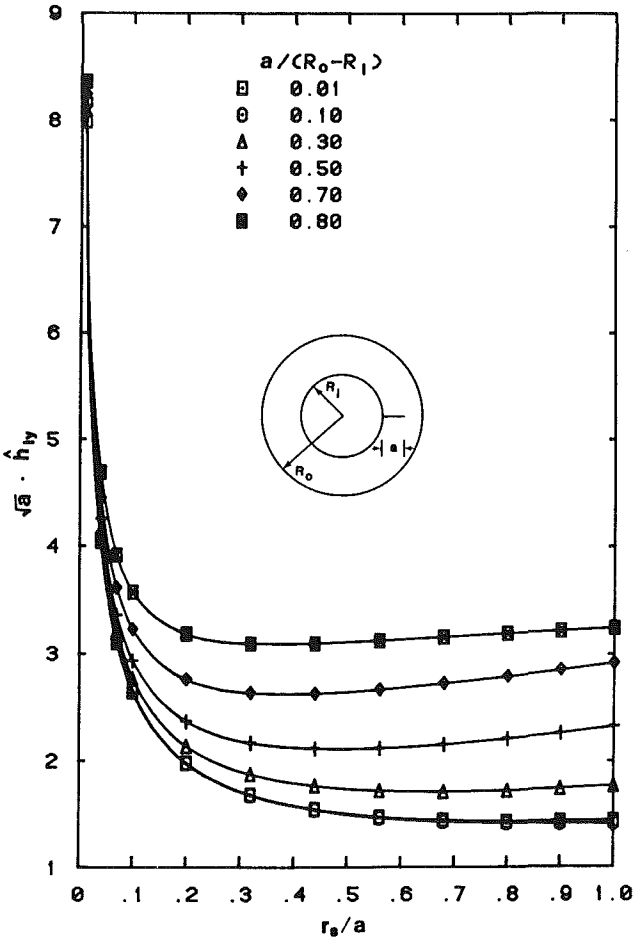

Fig. 5 Dimensionless explicit crack-face weight functions $(\sqrt{a} \cdot \hat{h}_{1y})$ as a function of normalized crack-face radial distance (r_s/a) of different $[a/(R_o-R_i)]$ ratios for a bore crack in a hollow disk with $R_o/R_i = 2$

condition, one can easily obtain the accurate stress intensity factor solutions and the stress intensity ranges for life prediction purposes for any loading condition from the predetermined explicit weight functions. For instance, the stress intensity factors can be easily obtained for a rotating disk at any angular velocity if the explicit crack-face weight functions are obtained in advance. By applying the linear superposition principle to the weight function concept, the needed stress intensity can be evaluated by combining the uncracked hoop stress field $(\sigma_{\theta\theta})$ for a radial crack with the predetermined Mode I crack-face weight functions $h_{\theta\theta}(r_s, a)$. The uncracked stress field of a rotating disk under generalized plane stress is well established [24] as follows:

$$\sigma_{rr} = \left(\frac{3+\nu}{8}\right)\rho\omega_o^2\left(R_o^2 + R_i^2 - \frac{R_o^2 R_i^2}{r^2} - r^2\right) \qquad (18a)$$

$$\sigma_{\theta\theta} = \left(\frac{3+\nu}{8}\right)\rho\omega_o^2\left(R_o^2 + R_i^2 + \frac{R_o^2 R_i^2}{r^2} - \frac{1+3\nu}{3+\nu}r^2\right) \qquad (18b)$$

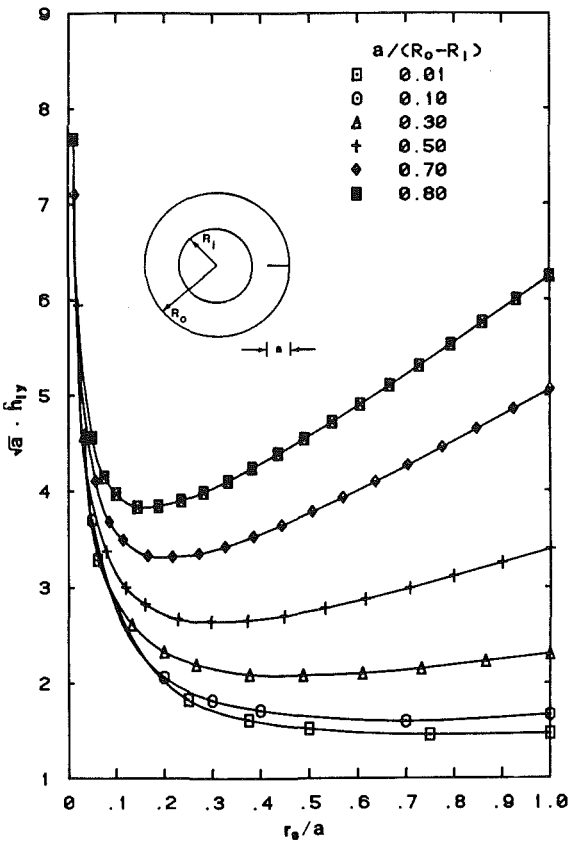

Fig. 6 Dimensionless explicit crack-face weight functions ($\sqrt{a} \cdot \hat{h}_{1y}$) as a function of normalized crack-face radial distance (r_s/a) of different [$a/(R_o - R_i)$] ratios for a rim crack in a hollow disk with $R_o/R_i = 2$

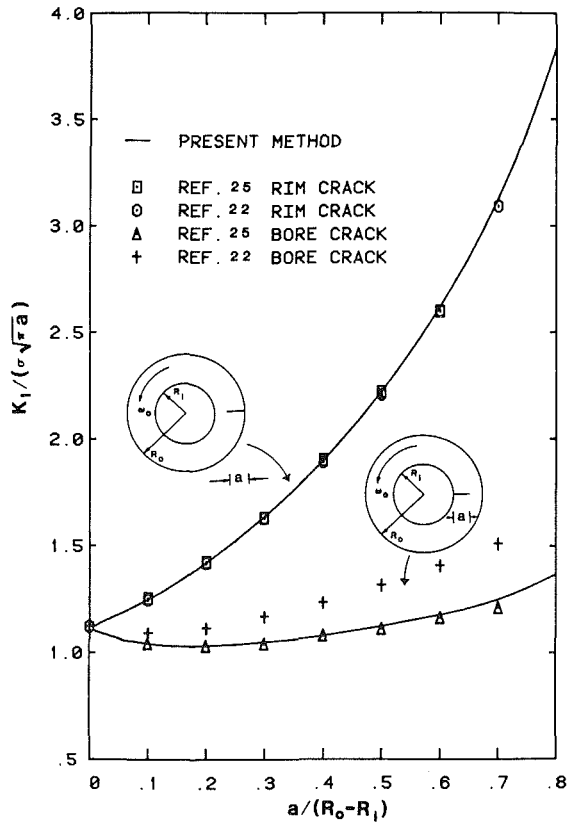

Fig. 7 Normalized stress intensity factors as a function of [$a/R_o - R_i$)] ratio for a bore crack and a rim crack in a rotating hollow disk with $R_o/R_i = 2$

Table 1 Least square fitted coefficients of equation (19) for a single bore crack in a hollow disk with $R_o/R_i = 2$ and $0.01 \le a/(R_o - R_i) \le 0.8$

$\frac{a}{R_o-R_i}$	B_1	B_2	B_3	B_4
0.01	0.7966D+00	-0.7721D-02	0.2935D+00	0.3620D+00
0.02	0.7976D+00	-0.6980D-02	0.2840D+00	0.3608D+00
0.03	0.8130D+00	-0.7176D-01	0.3711D+00	0.3134D+00
0.05	0.8008D+00	-0.5811D-02	0.2649D+00	0.3551D+00
0.06	0.8335D+00	-0.1714D+00	0.4942D+00	0.2421D+00
0.08	0.8051D+00	-0.2789D-01	0.3116D+00	0.3270D+00
0.10	0.8286D+00	-0.1818D+00	0.6119D+00	0.1554D+00
0.20	0.8132D+00	-0.8254D-01	0.5769D+00	0.2414D+00
0.30	0.8026D+00	0.1409D-02	0.5881D+00	0.3756D+00
0.40	0.7981D+00	0.4661D-01	0.6908D+00	0.4935D+00
0.50	0.7956D+00	0.7236D-01	0.9065D+00	0.5437D+00
0.60	0.7990D+00	0.4395D-01	0.1361D+01	0.4059D+00
0.70	0.8004D+00	0.2255D-01	0.2130D+01	-0.3915D-01
0.80	0.7976D+00	0.4388D-01	0.3537D+01	-0.1131D+01

Table 2 Least square fitted coefficients of equation (19) for a single rim crack in a hollow disk with $R_o/R_i = 2$ and $0.01 \le a/(R_o - R_i) \le 0.8$

$\frac{a}{R_o-R_i}$	B_1	B_2	B_3	B_4
0.01	0.8092D+00	-0.8840D-01	0.4417D+00	0.3106D+00
0.02	0.8286D+00	-0.1582D+00	0.5527D+00	0.2719D+00
0.04	0.8135D+00	-0.8503D-01	0.4789D+00	0.3231D+00
0.06	0.8146D+00	-0.8191D-01	0.4979D+00	0.3361D+00
0.08	0.8109D+00	-0.6491D-01	0.5082D+00	0.3531D+00
0.10	0.7872D+00	0.1061D+00	0.1969D+00	0.5759D+00
0.20	0.8148D+00	-0.9375D-01	0.8573D+00	0.3456D+00
0.30	0.8033D+00	-0.2914D-02	0.9497D+00	0.5551D+00
0.40	0.7984D+00	0.5222D-01	0.1125D+01	0.8152D+00
0.50	0.7941D+00	0.1112D+00	0.1318D+01	0.1171D+01
0.60	0.7894D+00	0.1828D+00	0.1549D+01	0.1614D+01
0.70	0.7832D+00	0.2763D+00	0.1915D+01	0.2072D+01
0.80	0.7716D+00	0.4404D+00	0.2672D+01	0.2334D+01

where

ρ = density
ω_0 = angular velocity
r = radial distance, $R_i \le r \le R_o$

The results of the normalized stress intensity factors for both the radial bore crack and rim crack of different crack lengths that were obtained, according to equation (17), by coupling the uncracked stress field ($\sigma_{\theta\theta}$) with the dimensionless crack-face weight functions, $\sqrt{a} \cdot h_{\theta\theta}(r_s/a,\ a/(R_o - R_i))$, are compared with Tracy's results [25], which were obtained by the modified mapping-collocation method and Delale et al.'s results [22] with integral equation technique. As shown in Fig. 7, an excellent agreement with the exception of Delale et al.'s bore radial crack solutions has been achieved. $\nu = 0.3$ is used in our numerical computations. Note that the $h_{\theta\theta}$ weight function concept at the crack-face location for the Mode I crack, as shown in Fig. 1, is identical to the h_{1y} crack-face weight function component. The normalization made with the uncracked reference stress field, which is normal to the crack face in the absence of a radial crack emanating either from the inner radius for a bore crack or from the outer radius for a rim crack, can be obtained from equation (18*b*) by letting $r = R_i$ for bore crack or $r = R_o$ for rim crack. Similar to equation (5), the dimensionless explicit crack-face weight function component, $\sqrt{a} \cdot \hat{h}_1(X)$ at a given $a/(R_o - R_i)$ ratio can be expressed as function X by

$$\sqrt{a} \cdot \hat{h}(X) = \sum_{n=1}^{N} B_n X^{\left(\frac{n}{2}-1\right)} \tag{19}$$

where

N = maximum number of terms needed for accurate representation of $h_{\theta\theta}(r_s, a)$
B_n = least square regressed coefficients, which are related to coefficient C_n of equation (5) as $C_n = B_n a^{-(n-1)/2}$

$N = 4$ of equation (19) is found to represent accurately the dimensionless explicit crack-face weight functions for both bore and rim radial cracks in a hollow disk. The regressed least square coefficients, B_n, of different r_s/a ratios for the

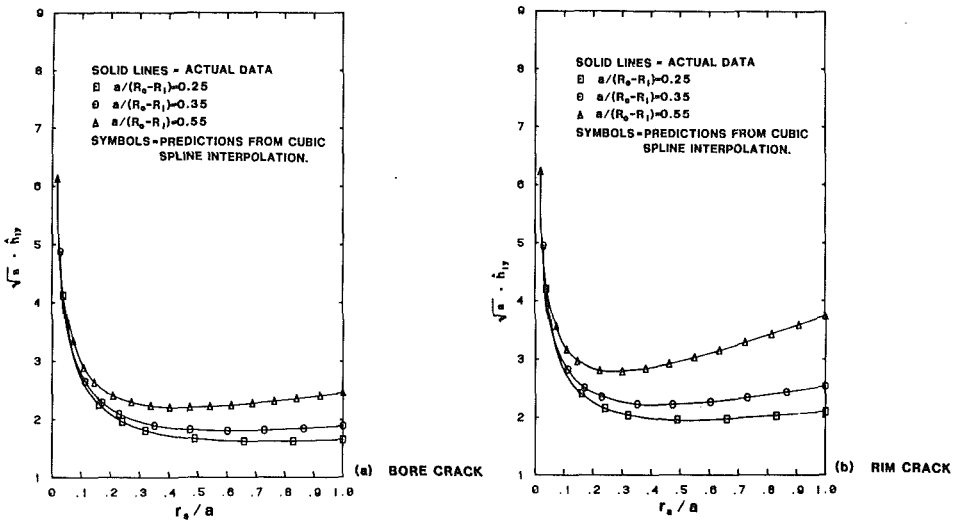

Fig. 8 Comparison between calculated and predicted dimensionless explicit crack-free weight functions as a function of (r_s/a) ratios

bore radial crack and rim radial crack of a hollow disk with $R_o/R_i = 2$ and $X = r_s/a$ are shown in Tables 1 and 2, respectively. It is noted that for symmetry, only half of the total geometry is modeled in finite element analyses. The dimensionless explicit crack-face weight functions, as tabulated in Tables 1 and 2, contain a factor 2 in order to facilitate directly the K_I calculation according to equation (17*b*). The cubic spline interpolation technique has been successfully used to obtain the explicit crack-face weight functions of any crack length from an adequate set of crack-face weight functions of discrete crack lengths. The following procedures are adopted for applying the cubic spline interpolation technique to obtain explicit crack-face weight functions of an arbitrary crack length for a given hollow disk geometry:

1 Obtain the least-square fitted coefficients B_n according to equation (19) from the finite element results of dimensionless explicit crack-face weight functions for each crack length of an adequate set of different crack lengths ($0.01 \le a/(R_o - R_i) \le 0.80$).
2 Evaluate $\sqrt{a} \cdot h\ (r_s/a,\ a/(R_o - R_i))$ values from the predetermined coefficients at the equally spaced $M + 1$ knot locations with M = integer within the range of $r_s/a = 0$ and $r_s/a = 1.0$ for each of the involved crack lengths, with the exception of $r_s/a = 0$, which is the crack-tip location.
3 The cubic interpolation subroutines ICSCCU and ICSEVU of the IMSL mathematic library [26] are used for the interpolatory approximation at the new $a/(R_o - R_i)$ location for each of the M knot locations with $0 < r_s/a \le 1$.
4 The end conditions are determined automatically by the ICSCCU subroutine with the continuous third derivative of the spline at the second and penultimate knots.

The comparisons are made as shown in Fig. 8 for $a/(R_o - R_i) = 0.25$, 0.35, and 0.55 with good agreement between the predicted explicit crack-face weight function component (h_{1y}), obtained from the cubic spline interpolation procedures, and the actual explicit crack-face weight functions, obtained from the finite element runs of the selected crack length conducted afterward. Consequently, the stress intensity factor K_I and ΔK_I at any crack length and loading can be obtained economically and accurately for life prediction purposes through equation (17) with the interpolated crack-face weight functions and with the equivalent uncracked stress field based on the superposition principle. This approach of evaluation K_I for radial bore and rim cracks in a hollow disk resulted in a total loss of accuracy of less than 1%.

The implicit weight function approach takes advantage of the load independent characteristics of weight function for K_I evaluation without involving explicit determination of the partial displacement derivative with respect to crack length ($\partial u/\partial a$) and weight functions (h_I). This approach was adopted primarily by Grandt [11] and Andrasic et al. [12] with the uncracked stress field $P(x)$ and stress intensity factor, respectively, as

$$P(x) = \sum_{n=0}^{6} A_n \left(\frac{x}{R_o - R_i}\right)^n = \sum_{n=0}^{6} A_n \left(\frac{a - r_s}{R_o - R_i}\right)^n = P(r_s) \tag{20}$$

$$K_I = \sum_{n=0}^{6} K_n = \sqrt{\pi a} \sum_{n=0}^{6} \frac{K_n}{A_n \sqrt{\pi a}} \cdot A_n \tag{21}$$

Comparing equation (21) with equation (4) of the explicit weight functions shows that

$$K_n = \frac{A_n}{(R_o - R_i)^n} \int_0^a (a - r_s)^n \cdot h(r_s, a)\, dr_s \tag{22}$$

Substituting $h_I(r_s, a) = \Sigma_{n=1}^{4} C_n\, r_s^{(n/2 - 1)}$ of the crack-face weight function expression for bore and rim radial cracks into equation (22) produces the following equation, which relates the explicit weight functions to the implicit weight functions as

$$K_n = \frac{A_n}{(R_o - R_i)^n} \left[\frac{2^{2n+1}(n!)^2}{(2n)!} \cdot \frac{1}{2n+1} C_1 a^{\frac{2n+1}{2}} + \frac{1}{(n+1)} C_2 a^{n+1} + \frac{2^{2n+1}(n!)^2}{(2n)!} \cdot \frac{1}{(2n+1)(2n+3)} \cdot C_3 a^{\frac{2n+3}{2}} + \frac{1}{(n+1)(n+2)} C_4 a^{n+3} \right] \tag{23}$$

The calculation of the dimensionless stress intensity factors for a single bore radial crack and rim crack in a hollow disk of $R_o/R_i = 2$ with the uncracked crack-face pressure $P(r_s) = A_n\ [(a - r_s)/(R_o - R_i)]^n$ from the explicit weight function expression of equation (4) for different crack lengths is evaluated according to equation (23) with results as shown in Tables 3 and 4, respectively. There is excellent agreement in the implicit weight functions between the results obtained by Andrasic et al. [12] with the modified mapping-collocation method and the results obtained with the finite element calculation of explicit weight functions. (The starting position

Table 3 Dimensionless stress intensity factors evaluated from explicit crack-face weight functions for a single bore crack in a hollow disk ($R_o/R_i = 2.0$) loaded with a crack-face pressure $p(x) = A_n[x/(R_o - R_i)]^n$

$Kn/(A_n \sqrt{\pi a})$ n

$a/(R_o-R_i)$	0	1	2	3	4	5	6
0.01	0.1107E+01	0.6753E-02	0.5202E-04	0.4368E-06	0.3834E-08	0.3456E-10	0.3171E-12
0.02	0.1105E+01	0.1349E-01	0.2080E-03	0.3495E-05	0.6137E-07	0.1106E-08	0.2030E-10
0.03	0.1105E+01	0.2030E-01	0.4702E-03	0.1186E-04	0.3127E-06	0.8462E-08	0.2331E-09
0.05	0.1100E+01	0.3370E-01	0.1301E-02	0.5468E-04	0.2401E-05	0.1083E-06	0.4969E-08
0.06	0.1098E+01	0.4054E-01	0.1884E-02	0.9524E-04	0.5028E-05	0.2725E-06	0.1502E-07
0.08	0.1102E+01	0.5403E-01	0.3337E-02	0.2245E-03	0.1578E-04	0.1138E-05	0.8357E-07
0.10	0.1106E+01	0.6787E-01	0.5244E-02	0.4412E-03	0.3878E-04	0.3500E-05	0.3214E-06
0.20	0.1156E+01	0.1396E+00	0.2139E-01	0.3582E-02	0.6274E-03	0.1129E-03	0.2070E-04
0.30	0.1234E+01	0.2184E+00	0.4963E-01	0.1238E-01	0.3238E-02	0.8713E-03	0.2390E-03
0.40	0.1326E+01	0.3055E+00	0.9146E-01	0.3019E-01	0.1048E-01	0.3746E-02	0.1366E-02
0.50	0.1433E+01	0.4032E+00	0.1490E+00	0.6099E-01	0.2631E-01	0.1171E-01	0.5323E-02
0.60	0.1553E+01	0.5138E+00	0.2251E+00	0.1097E+00	0.5646E-01	0.3004E-01	0.1633E-01
0.70	0.1706E+01	0.6477E+00	0.3269E+00	0.1842E+00	0.1099E+00	0.6782E-01	0.4283E-01
0.80	0.1936E+01	0.8305E+00	0.4730E+00	0.3013E+00	0.2035E+00	0.1425E+00	0.1022E+00

Table 4 Dimensionless stress intensity factors evaluated from explicit crack-face weight functions for a single rim crack in a hollow disk ($R_o/R_i = 2.0$) loaded with a crack face pressure $p(x) = A_n[x/(R_o - R_i)]^n$

$Kn/(A_n \sqrt{\pi a})$ n

$a/(R_o-R_i)$	0	1	2	3	4	5	6
0.01	0.1117E+01	0.6795E-02	0.5229E-04	0.4390E-06	0.3853E-08	0.3473E-10	0.3187E-12
0.02	0.1130E+01	0.1375E-01	0.2117E-03	0.3556E-05	0.6244E-07	0.1126E-08	0.2067E-10
0.04	0.1141E+01	0.2762E-01	0.8479E-03	0.2843E-04	0.9970E-06	0.3592E-07	0.1318E-08
0.06	0.1155E+01	0.4177E-01	0.1920E-02	0.9648E-04	0.5072E-05	0.2740E-06	0.1507E-07
0.08	0.1169E+01	0.5611E-01	0.3431E-02	0.2295E-03	0.1607E-04	0.1157E-05	0.8477E-07
0.10	0.1185E+01	0.7059E-01	0.5377E-02	0.4486E-03	0.3920E-04	0.3522E-05	0.3223E-06
0.20	0.1286E+01	0.1496E+00	0.2251E-01	0.3728E-02	0.6484E-03	0.1161E-03	0.2121E-04
0.30	0.1419E+01	0.2396E+00	0.5315E-01	0.1307E-01	0.3386E-02	0.9051E-03	0.2470E-03
0.40	0.1584E+01	0.3445E+00	0.1001E+00	0.3243E-01	0.1112E-01	0.3940E-02	0.1427E-02
0.50	0.1785E+01	0.4686E+00	0.1668E+00	0.6674E-01	0.2835E-01	0.1248E-01	0.5627E-02
0.60	0.2032E+01	0.6182E+00	0.2587E+00	0.1225E+00	0.6188E-01	0.3247E-01	0.1747E-01
0.70	0.2345E+01	0.8051E+00	0.3848E+00	0.2096E+00	0.1222E+00	0.7424E-01	0.4631E-01
0.80	0.2783E+01	0.1061E+01	0.5675E+00	0.3477E+00	0.2289E+00	0.1573E+00	0.1113E+00

of numerical deviation is underlined as shown in Table 3 for the bore crack and Table 4 for the rim crack.)

The explicit weight functions at load application locations other than the crack face can also facilitate K_I evaluation under complex loading conditions, as demonstrated recently by Sha et al. [27] for a radial crack emanating from a circular hole in a plate. The radial weight function along the inner and outer perimeters of a hollow disk for bore and rim radial cracks can be obtained with the coordinate transformation from h_{Ix} and h_{Iy} components as

$$h_{Ir}(r,\theta,a) = h_{Ix}(x,y,a)\cos\theta + h_{Iy}(x,y,a)\sin\theta \qquad (24)$$

The plots of the dimensionless explicit radial component weight function ($\pi R_i/\sqrt{a} \cdot h_{Ir}$) for a bore radial crack as a function of normalized angular position (θ/π) along the perimeters of the inner and outer radius of a hollow disk with $R_o/R_i = 2$ and $0.01 \le a/(R_o - R_i) \le 0.8$ are shown in Figs. 9 and 10, respectively. The similar plots for a rim radial crack in a hollow disk with $R_o/R_i = 2$ are shown in Figs. 11 and 12, respectively, for the inner radius perimeter and outer radius perimeter, respectively. These radial weight functions can be represented by the Fourier series as:

$$h_{Ir}(r,\theta,a) = \sum_{n=0}^{6} (a_n \sin n\,\theta + b_n \cos n\,\theta) \qquad (25)$$

The Fourier coefficients a_n and b_n are shown in Tables 5*a* and 5*b* for the radial bore crack of different crack lengths at the outer radius perimeters of a hollow disk.

There is excellent agreement in the normalized K_I values, which are obtained from the combination of radial weight function components of equation (25) with the applied uniform pressure at the inner perimeters for the rim crack or with the outer tension for the bore crack, with direct finite element virtual crack extension results of different $a/(R_o - R_i)$ ratios. The normalized stress intensity factors for a cracked ring with a bore crack, which is aligned with compressive tractions, of different crack lengths loaded in compression are calculated with the radial weight function component according to equation (4). These normalized K_I values with the weight function concept are in good agreement with those of Grandt [28] and Jones [29] as shown in Fig. 13.

The application of the explicit weight function of different crack lengths to the calculation of the normalzed stress intensity factors is made, according to equation (4), under the compressive load with the rim crack normal to the compress loading axes. Again, the K_I results obtained from the weight function concepts are in good agreement with those of Kapp et al. [20], as shown in Fig. 14. The stress intensity factors become negative as $a/(R_o - R_i) \ge 0.75$ for a deep rim crack in a hollow disk under compressive loading, as shown in Fig. 14, with $R_o/R_i = 2$. This implies specifically that a rim crack of $a/(R_o - R_i) \ge 0.75$ with concentrated compressive point

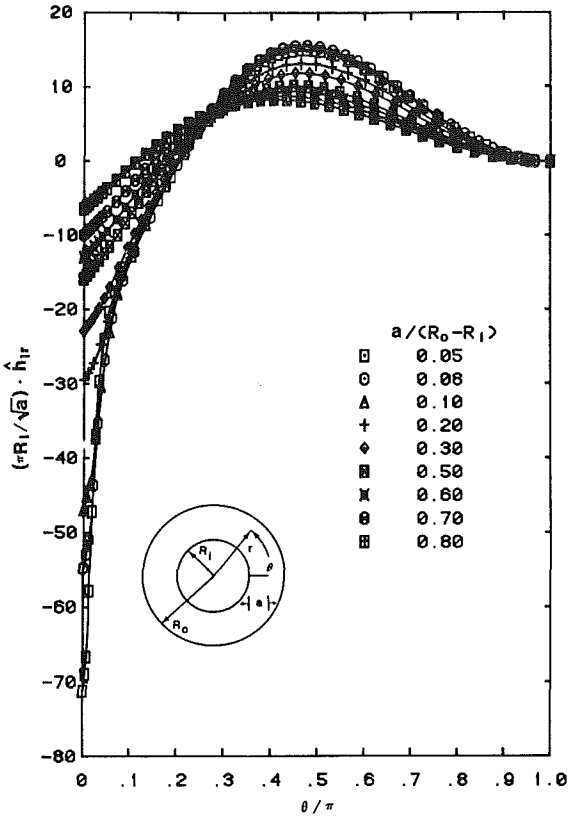

Fig. 9 The dimensionless radial explicit weight function component ($\pi R_i/\sqrt{a} \cdot h_{Ir}$) as a function of normalized angular position (θ/π) along the inner perimeter for a bore crack in a hollow disk with various crack lengths

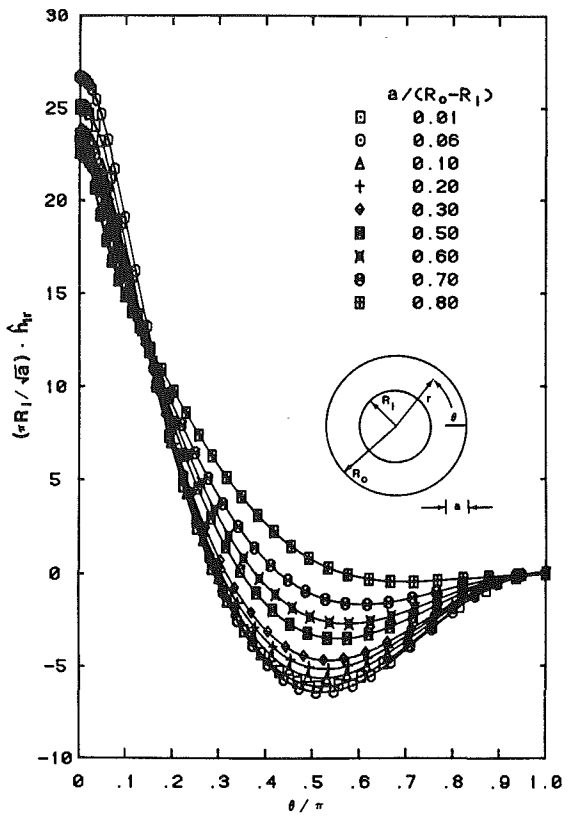

Fig. 11 The dimensionless radial explicit weight function component ($\pi R_i/\sqrt{a} \cdot h_{Ir}$) as a function of normalized angular position (θ/π) along the inner perimeter for a rim crack in a hollow disk with various crack lengths

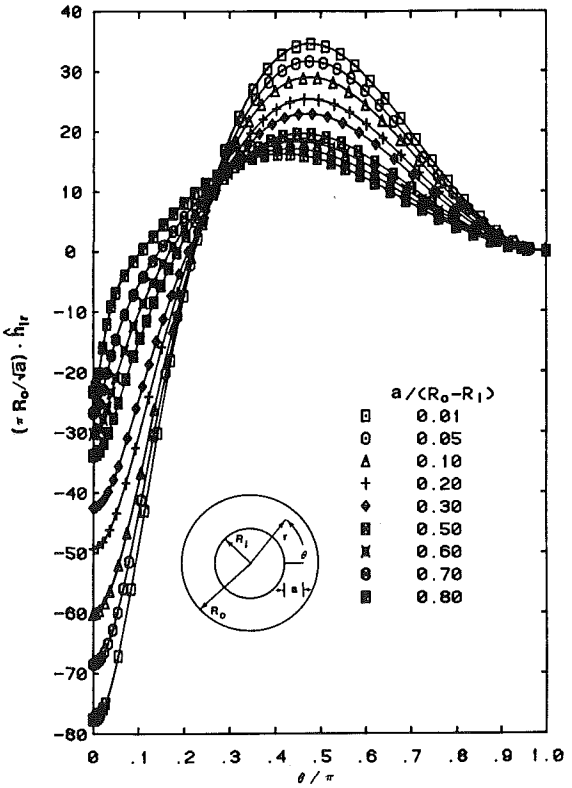

Fig. 10 The dimensionless radial explicit weight function component ($\pi R_o\sqrt{a} \cdot h_{Ir}$) as a function of normalized angular position (θ/π) along the outer perimeter for a bore crack in a hollow disk with various crack lengths

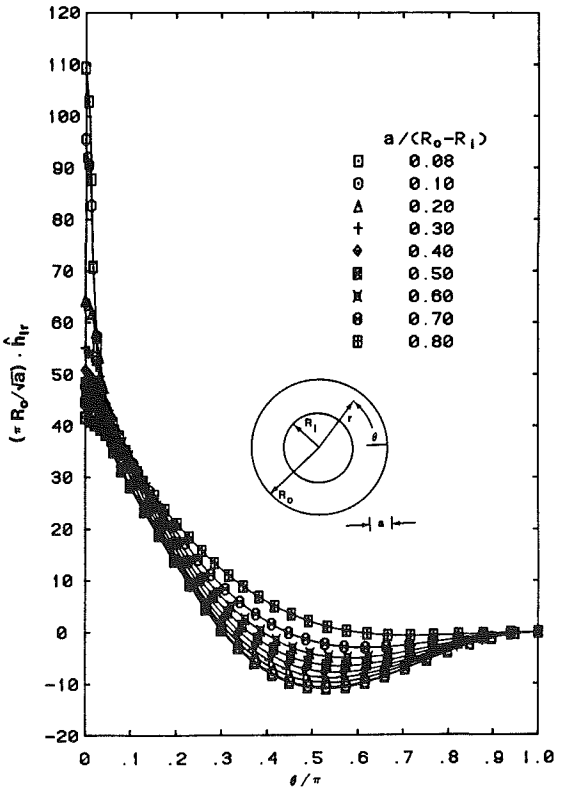

Fig. 12 The dimensionless radial explicit weight function component ($\pi R_o/\sqrt{a} \cdot h_{Ir}$) as a function of normalized angular position (θ/π) along the outer perimeter for a rim crack in a hollow disk with various crack lengths

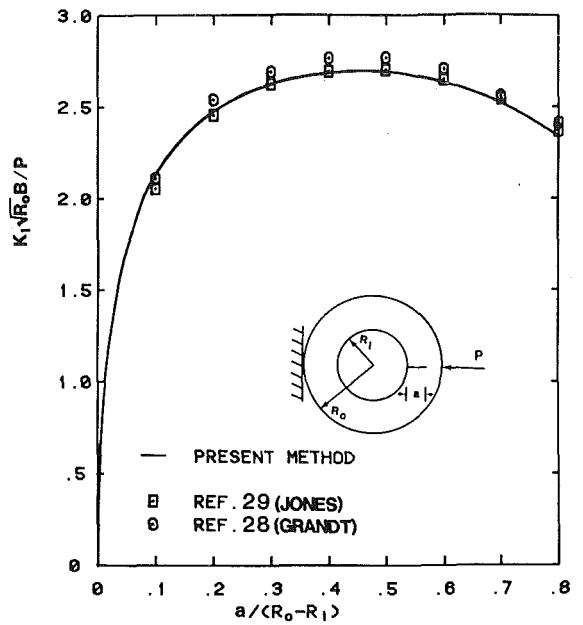

Fig. 13 Normalized Mode I stress intensity factors as a function of $a/(R_o - R_i)$ for a bore crack in a hollow disk under compressive concentrated point force

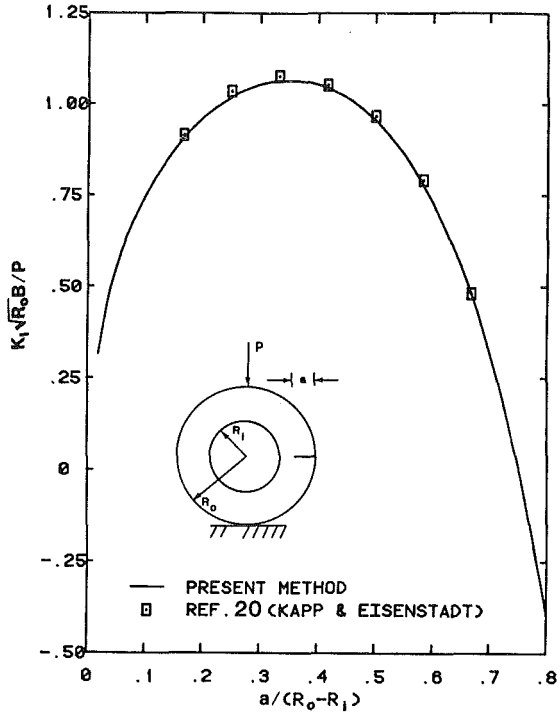

Fig. 14 Normalized Mode I stress intensity factors as a function of $a/(R_o - R_i)$ for a rim crack in a hollow disk under compressive concentrated point force

Table 5*a* Sine Fourier coefficients of equation (25) at outer periphery location for a bore crack of a hollow disk with $R_o - R_i = 2$, and $0.01 \le a/(R_o - R_i) \le 0.8$

$a/(R_o-R_i)$	a_1	a_2	a_3	a_4	a_5	a_6
0.01	0.1041D+01	-0.5653D+00	-0.6351D+00	0.2831D+00	0.1719D+00	-0.4846D-02
0.03	0.1292D+01	-0.8871D+00	-0.8537D+00	0.4422D+00	0.2504D+00	-0.7240D-02
0.05	0.1619D+01	-0.1040D+01	-0.1049D+01	0.5169D+00	0.3012D+00	-0.7866D-02
0.08	0.9652D+00	-0.1193D+01	-0.8182D+00	0.5942D+00	0.2915D+00	-0.9714D-02
0.10	0.1947D+01	-0.1381D+01	-0.1252D+01	0.6934D+00	0.3583D+00	-0.1567D-01
0.20	-0.2069D+01	-0.2054D+01	0.3373D+00	0.1062D+01	0.2025D+00	-0.3866D-01
0.30	-0.1430D+02	-0.3241D+01	0.5383D+01	0.1730D+01	-0.3934D+00	-0.8810D-01
0.40	-0.3647D+02	-0.4557D+01	0.1467D+02	0.2506D+01	-0.1549D+01	-0.1499D+00
0.50	-0.7175D+02	-0.5489D+01	0.2966D+02	0.3142D+01	-0.3500D+01	-0.2105D+00
0.60	-0.9796D+02	-0.6249D+01	0.4126D+02	0.3786D+01	-0.5130D+01	-0.2900D+00
0.70	-0.1104D+03	-0.2513D+01	0.4780D+02	0.2170D+01	-0.6324D+01	-0.2148D+00
0.80	-0.2200D+02	0.9644D+01	0.1299D+02	-0.3764D+01	-0.2450D+01	0.1728D+00

Table 5*b* Cosine Fourier coefficients of equation (25) at outer periphery location for a bore crack of a hollow disk with $R_o/R_i = 2$, and $0.01 \le a/(R_o - R_i) \le 0.8$

$a/(R_o-R_i)$	b_o	b_1	b_2	b_3	b_4	b_5	b_6
0.01	-0.5126D+00	0.2406D+00	0.6317D+00	-0.5849D+00	-0.4273D+00	0.6820D-01	0.3211D-01
0.03	-0.6102D+00	0.3692D+00	0.7254D+00	-0.9219D+00	-0.6098D+00	0.1050D+00	0.4688D-01
0.05	-0.7663D+00	0.4220D+00	0.9065D+00	-0.1087D+01	-0.7404D+00	0.1207D+00	0.5598D-01
0.08	-0.3778D+00	0.4778D+00	0.3662D+00	-0.1252D+01	-0.6779D+00	0.1396D+00	0.5514D-01
0.10	-0.9082D+00	0.5829D+00	0.1051D+01	-0.1432D+01	-0.8852D+00	0.1734D+00	0.6625D-01
0.20	0.1377D+01	0.9872D+00	-0.1941D+01	-0.2077D+01	-0.2683D+00	0.3048D+00	0.4737D-01
0.30	0.8209D+01	0.1781D+01	-0.1086D+02	-0.3174D+01	0.1856D+01	0.5642D+00	-0.3715D-01
0.40	0.2054D+02	0.2675D+01	-0.2703D+02	-0.4401D+01	0.5848D+01	0.8765D+00	-0.2090D+00
0.50	0.4011D+02	0.3314D+01	-0.5285D+02	-0.5324D+01	0.1241D+02	0.1157D+01	-0.5112D+00
0.60	0.5458D+02	0.3830D+01	-0.7231D+02	-0.6150D+01	0.1766D+02	0.1478D+01	-0.7757D+00
0.70	0.6134D+02	0.1290D+01	-0.8219D+02	-0.3073D+01	0.2103D+02	0.9643D+00	-0.9986D+00
0.80	0.1201D+02	-0.6959D+01	-0.1914D+02	0.7358D+01	0.6813D+01	-0.1180D+01	-0.4604D+00

loads becomes a nonpropagating crack unless residual tension stress results in positive K_I and ΔK_I under cyclic fatigue loading conditions. This trend of having a negative stress intensity factor for a deep rim crack, which is normal to the compressive loading axis, is somewhat indicated in the results of Kapp et al. [20]. By incorporating the singular elements into the stiffness derivative technique, the accuracy enhancement of both the stress intensity factors and explicit weight

functions is achieved as indicated in this paper for a radial crack in a hollow disk.

Conclusions

The virtual crack extension technique coupled with singular elements can provide an efficient finite element evaluation of the stress intensity factor and explicit weight functions, which are obtained for the entire structure of interest. The weight functions at the locations of the crack-face inner radius circumference and outer radius perimeter are provided in this paper for different $a/(R_o - R_i)$ ratios of a bore radial crack or a rim crack in a hollow disk with $R_o/R_i = 2$. The explicit weight function approach as indicated in this publication is more attractive than the implicit weight function approach as shown in the work of Grandt [11], Andrasic et al. [12], Besuner [10], and Pu [13] because of its ability to provide efficient calculation of K_I and ΔK_I values with improved accuracy under complex loading conditions, including the residual stress effect.

An analytical expression for the crack-face weight function component for Mode I deformation is provided in this paper as a function of radial distance (r_s) from the crack tip along the crack face for both bore and rim cracks in a hollow disk. This crack-face explicit weight function expression can facilitate the K_I calculation according to equation (4) by combining the uncracked stress field with the predetermined crack-face explicit weight functions. The explicit crack-face weight function of any crack face can be obtained from a cubic spline interpolation procedure, as indicated in this paper, from an adequate set of explicit crack-face weight functions of different crack lengths for the same hollow disk geometry. The calculated K_I value, which is obtained by combining the uncracked stress field with the interpolated explicit crack-face weight functions, led to a total loss of accuracy of less than 1%. Therefore, the cycle-by-cycle life analysis is economically feasible with the proposed weight function procedures for improving prediction accuracy.

The weight function is a vector that has x and y weight function components at any given location within the structure of interest. By using the coordinate transformation, as shown in equation (24), the radial component of weight functions can be obtained at both inner and outer perimeters of a hollow disk. These radial weight functions associated with a bore crack or rim crack can be accurately represented by a Fourier series. With the availability of the radial weight function component at the inner and outer perimeter location, the calculation of K_I with any pressure distributions (uniform or nonuniform) at these locations is greatly facilitated.

The explicit weight functions of a hollow disk, as presented in this paper, are confined to $R_o/R_i = 2$. The cubic spline interpolation procedures have been successfully applied to obtain the accurate crack-face weight functions for any crack length. It is anticipated that the interpolatory approximation of h_{1r} $(r_s/a, a/(R_o - R_i), R_o/R_i)$ can be obtained from the bicubic spline interpolation technique with adequate sets of weight function runs with varying $a/(R_o - R_i)$ and R_o/R_i as dependent variables. This suggested bicubic spline interpolation procedure is not verified yet for obtaining the crack-face weight functions of arbitrary $a/(R_o - R_i)$ and R_o/R_i values.

The application of the compressive loading condition to a rim crack, which is normal to the compressive loading axes, is assessed with explicit radial weight functions of different rim crack lengths. These results for $R_o/R_i = 2$ indicate that for a deep rim crack with $a/(R_o - R_i) \geq 0.75$, the crack becomes a nonpropagating crack unless there is an excessive residual tensile stress effect.

It is concluded that an efficient finite element methodology has been achieved for calculating K_I and explicit weight functions at all locations of the entire structure of interest. This paper deals primarily with the explicit weight functions for both rim and bore radial cracks in a hollow disk of $R_o/R_i = 2$ geometrically.

References

1 Sha, G. T., "Stiffness Derivative Finite Element Technique to Determine Nodal Weight Functions with Singularity Elements," *Engineering Fracture Mechanics*, Vol. 19, No. 4, 1984, pp. 685-699.

2 Parks, D. M., "A Stiffness Derivative Finite Element Technique for Determination of Crack Tip Stress Intensity Factors," *Int. J. Fracture*, Vol. 10, 1974, pp. 487-501.

3 Hellen, T. K., "On the Method of Virtual Crack Extensions," *Int. J. Numerical Methods in Engng.*, Vol. 9, 1975, pp. 187-207.

4 Henshell, R. D., and Shaw, K. G., "Crack Tip Elements are Unnecessary," *Int. J. Numerical Methods in Engng.*, Vol. 9, 1975, p. 495-507.

5 Barsoum, R. S., "On the Use of Isoparametric Finite Elements in Linear Fracture Mechanics," *Int. J. Numerical Methods in Engng.*, Vol. 10, 1976, pp. 25-37.

6 Rice, J. R., "Some Remarks on Elastic Crack-Tip Stress Fields," *International Journal Solids Structures*, Vol. 8, 1972, pp. 751-758.

7 Bueckner, H. F., "Field Singularities and Related Integral Representations," *Mechanics of Fracture I, Method of Analysis and Solutions of Crack Problems* (Ed. by G. C. Sih), Noordhoff, The Netherlands, 1972.

8 Sha, G. T., and Chien-Tung Yang, "Weight Function Calculations for Mixed Mode Fracture Problems with the Virtual Crack Extension Technique," *Engineering Fracture Mechanics* (in press).

9 Sha, G. T., "On the Virtual Crack Extension Technique for Stress Intensity Factors and Energy Release Rate Calculations for Mixed Fracture Mode," *Int. J. Fracture*, Vol. 25, 1984, pp. R33-R42.

10 Besuner, P. M., "The Influence Function Method for Fracture Mechanics and Residual Fatigue Life Analysis of Cracked Components Under Complex Stress Fields," *Nuclear Engng. and Design*, Vol. 43, 1977, pp. 115-154.

11 Grandt, A. F., Jr., "Stress Intensity Factors for Cracked Holes and Rings Loaded with Polynomial Crack Face Pressure Distributions," *Int. J. Fracture*, Vol. 14, 1978, pp. R221-R229.

12 Andrasic, C. P., and Parker, A. P., "Dimensionless Stress Intensity Factors for Cracked Thick Cylinders under Polynomial Crack Face Loadings," *Engineering Fracture Mechanics*, Vol. 19, No. 1, 1984, pp. 187-193.

13 Pu, S. L., "A Functional Stress Intensity Approach to Multiply Cracked, Partially Autofrettaged Cylinders," *Transactions of the 28th Conference of Army Mathematicians*, ARO Report 83-1, 1983, pp. 263-283.

14 Orange, T. W., "Crack Shapes and Stress Intensity Factors for Edge-Cracked Specimens," *Stress Analysis and Growth of Cracks*, ASTM STP 513, American Society for Testing and Materials, 1972, pp. 71-78.

15 Gallagher, R. H., "A Review of Finite Element Techniques in Fracture Mechanics," *Proceedings of the First International Conference on Numerical Methods in Fracture Mechanics*, 1978, pp. 1-25.

16 Parks, D. M., and Kamentzky, E. M., "Weight Functions from Virtual Crack Extension," *Int. J. Numerical Methods in Engng.*, Vol. 14, 1979, pp. 1693-1706.

17 Vanderglas, M. L., "A Stiffness Derivative Finite Element Technique for Determination of Influence Functions," *Int. J. Fracture*, Vol. 14, 1978, pp. 291-295.

18 Bowie, O. L., and Freese, C. E., "Elastic Analysis for a Radial Crack in a Circular Ring," *Engineering Fracture Mechanics*, Vol. 4, 1972, pp. 315-321.

19 Pu, S. L., and Hussain, M. A., "Stress-Intensity Factors for Radial Cracks in a Partially Autofrettaged Thick-Walled Cylinder," *Fracture Mechanics*, ASTM STP 791, American Society for Testing and Materials, 1983, pp. I194-I215.

20 Kapp, J. A., and Eisenstadt, R., "Crack Growth in Externally Flawed, Autofrettaged Thick-Walled Cylinders and Rings," *Fracture Mechanics*, ASTM STP 677, 1979, pp. 746-756.

21 Tracy, P. G., "Elastic Analysis of Radial Cracks Emanating from the Outer and Inner Surfaces of a Circular Ring," *Engineering Fracture Mechanics*, Vol. 11, 1979, pp. 291-300.

22 Delale, F., and Erdogan, F., "Stress Intensity Factors in a Hollow Cylinder Containing a Radial Crack," *Int. J. Fracture*, Vol. 20, 1982, pp. 251-265.

23 Emery, A. F., and Segedin, C. M., "The Evaluation of the Stress Intensity Factors for Cracks Subjected to Tension, Torsion and Flexure by an Efficient Numerical Technique," *J. Basic Engineering*, Vol. 94, 1972, pp. 387-393.

24 Timoshenko, S. P., and Goodier, J. N., *Theory of Elasticity*, Third Edition, McGraw-Hill, 1970, p. 82.

25 Tracy, P., "Stress Intensity Factors for Multiple Edge Cracks in Rotating Hollow Discs," *Int. J. Fracture*, Vol. 16, 1980, pp. 85-93.

26 IMSL reference manuals, Vol. 1-4, IMSL Library, Edition 9.

27 Sha, G. T., and Yang, C. T., "Weight Functions of Radial Cracks Emanating from a Circular Hole," presented at the 17th National Symposium on Fracture Mechanics, Albany, New York, 7-9 August 1984.

28 Grandt, A. F., Jr., "Two Dimensional Stress Intensity Factor Solutions for Radially Cracked Rings," Technical Report AFML-TR-75-121, 1975.

29 Jones, A. T., "A Radially Cracked, Cylindrical Fracture Toughness Specimen," *Engineering Fracture Mechanics*, Vol. 6, No. 3, 1974, pp. 435-446.

T. Sato
Manager,
Aerodynamic Research Laboratory.

K. Takeishi
Senior Research Engineer,
Combustion & Heat Transfer
Research Laboratory.

T. Sakon
Senior Research Engineer,
Material & Strength
Research Laboratory.

Takasago Technical Institute,
Mitsubishi Heavy Industries, Ltd.,
Takasago, Japan

Thermal Fatigue Life Prediction of Air-Cooled Gas Turbine Vanes

Introduction

The demand for high efficiency in industrial gas turbine engines is being satisfied by raising the turbine inlet temperature. Increasing the turbine inlet temperature subjects the hot parts exposed to the mainstream of gas, such as the first stationary vane, to severe conditions. With the raising of the turbine inlet temperature, an effective air-cooling structure for the vanes must be adopted.

The worldwide growing demand for energy saving means that large-scale combined plants are attracting attention in Japan. These combined plants consist of the latest high-temperature gas turbine for the topping cycle, to be operated under base load conditions for many hours, and a conventional gas turbine for daily peak load start/stop purposes. It is important, therefore, to secure a high degree of reliability for the first stationary vane in such high-temperature gas turbines. A sufficiently accurate life prediction technique for the first stationary vane is indispensable when deciding both the operating mode and the maintenance and repair program.

The first stationary vane in a high-temperature gas turbine has a complicated cooling structure and is subjected to high thermal stress because of the cooling. The temperature distribution in the air-cooled vane is influenced by the aerodynamic and heat transfer boundary conditions, and the thermal stress by the temperature distribution and structure. So, to increase the reliability of the air-cooled vane, it is essential to comprehensively analyze and study the aerodynamics, heat transfer, and stress as well as the strength of the material.

The present paper describes the life prediction method as applied to an air-cooled turbine vane on the basis of an integrated study of those factors and compares the results with the data on the life of the actual machine.

Contributed by the Gas Turbine Division of THE AMERICAN SOCIETY OF MECHANICAL ENGINEERS and presented at the 30th International Gas Turbine Conference and Exhibit, Houston, Texas, March 18–21, 1985. Manuscript received at ASME Headquarters, December 17, 1984. Paper No. 85-GT-17.

The First Stationary Vane on an MW-701B$_2$ Gas Turbine Engine

In answer to the call for energy saving, there is a strong trend toward increasing the turbine inlet temperature of industrial gas turbines. Figure 1 shows the relationship between the output power and inlet temperature in Mitsubishi's industrial gas turbines.

MW-701B$_2$ engines have been operated for a long time in the field. The MW-701B$_2$ engines referred to in this paper were unintentionally operated under unusually severe conditions and suffered cracks on the first stationary vanes. It is considered that these were good examples for testing the usefulness of life prediction. A sectional view of the gas turbine is shown in Fig. 2.

The first stationary vane segment is made up of three blades (cobalt base super alloy by integrated casting) and an internal air-cooling structure is adopted. The cooling structure of the first stationary vane is illustrated in Fig. 3. The vane is provided with a single insert and designed so that the cooling air is supplied from the outer shroud. The leading edge of the

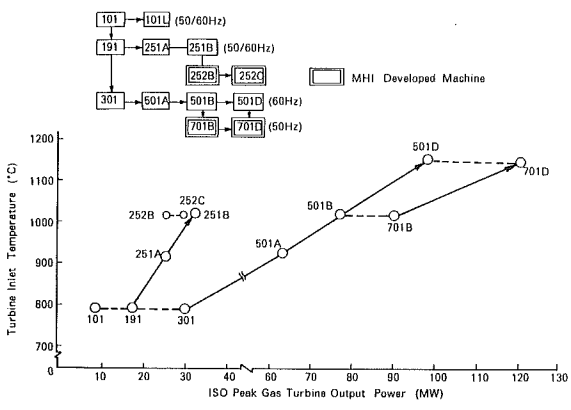

Fig. 1 Evolution of power generation of Mitsubishi's gas turbine

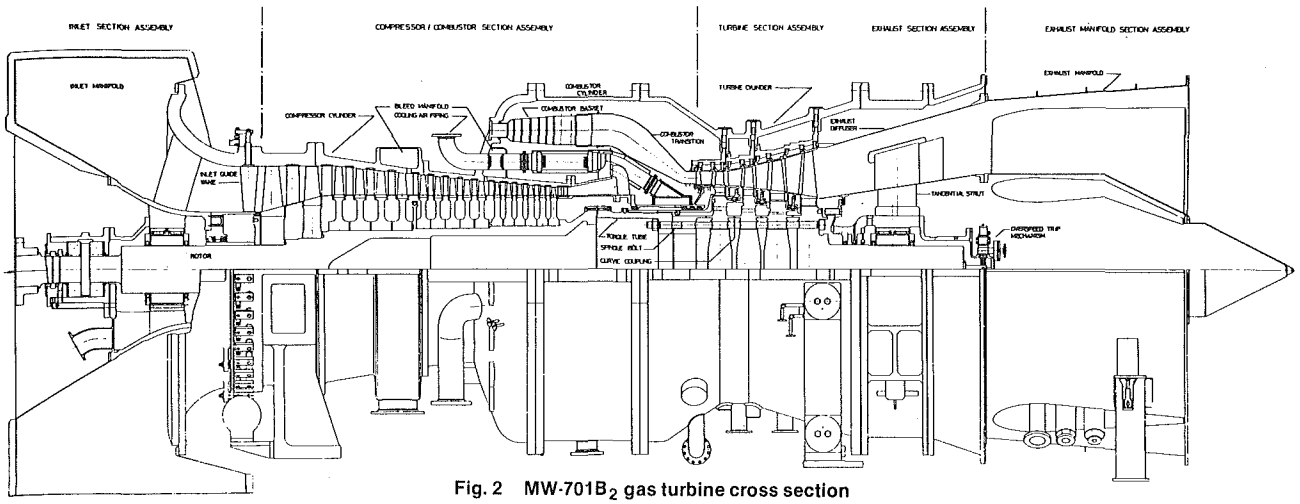

Fig. 2 MW-701B_2 gas turbine cross section

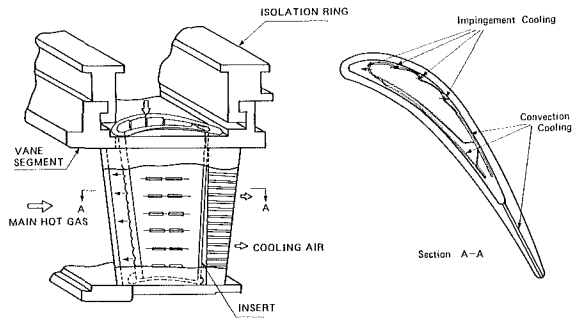

Fig. 3 Cooling structure of MW-701B_2 first vane

vane, which is subjected to the highest heat load, is impingement cooled from the inner side. After cooling the leading edge, the air separates and flows along the blade suction and pressure side, proceeding to a narrow gap between the insert and the vane. There are three lines of angled impingement cooling holes on the suction side of the vane where the heat transfer coefficient of the gas surface is high. The vane trailing edge area is cooled by convection with the cooled air flowing through electric discharge-machined cooling holes. With these cooling arrangements, the metal temperature of the vane is kept below the critical temperature of the vane material.

Life Prediction Procedure for a Stationary Vane

The life of a stationary vane can be estimated by analyzing the local elastic-plastic behavior and comparing it with the creep-fatigue material data. However, a three-dimensional, elastic-plastic stress analysis is not possible because it requires too much CPU time and there is a lack of material data. So we devised the schematic life prediction procedure that is presented in this paper and shown in Fig. 4.

Each block diagram in Fig. 4 shows a step in predicting the fatigue life of a first stationary vane. Firstly, prediction of the local metal temperature distribution is important, so this was calculated by the "TACOOL" program, which consisted of basic experimental results from aerodynamics and heat transfer tests. This computer program was verified by cascade tests under normal engine operating conditions.

Next, three-dimensional elastic stress was analyzed by the finite element method using the "MARC" program. Thirdly, the local inelastic strain was estimated from the elastic stress using Neuber's law and the thermal fatigue life of the vane by using the local metal temperature and creep-fatigue material data. Finally, the predicted life was confirmed through a comparison with the field data.

Analysis of Metal Temperature Distribution

To improve the accuracy of metal temperature prediction, heat transfer tests were carried out inside and outside the vane. With the data thus obtained, a calculation program, "TACOOL," was developed. This improved prediction accuracy was confirmed by measuring the metal temperature during a cascade test under conditions equivalent to actual operation. The metal temperature of the cooled vane of the actual engine in operation was predicted on the basis of this program.

Nomenclature

D = leading edge diameter
d = diameter of impingement cooling hole
h = heat transfer coefficient
M = blowing mass flow ratio, $\rho_a U_a / \rho_\infty U_\infty$
Nc = number of cycles to crack initiation
Nf = number of cycles to failure
Nu = Nusselt number
Pr = Prandtl number
P = pressure
P = pitch of impingement cooling holes
Re = Reynolds number
S = two-dimensional film cooling slot width
S = elastically calculated stress
T = temperature
t_H = strain hold time per cycle
U = velocity
X = surface distance from leading edge
X = distance from the film cooling slot
Xo = distance from the boundary layer starting point to the film cooling slot
Z = number of impingement cooling holes
α = coefficient of thermal expansion
ϵ = strain
$\Delta\epsilon$ = strain range
η = film cooling effectiveness
θ = injection angle of film cooling
μ = viscosity
ν = frequency
ρ = density
σ = stress
τ = turbulence intensity
τ = periodic time, $1/\nu$

Subscripts

a = cooling air
aw = adiabatic wall
ax = axial chord of an airfoil
e = elastic
M = metal
P = plastic
t = total
∞ = main flow

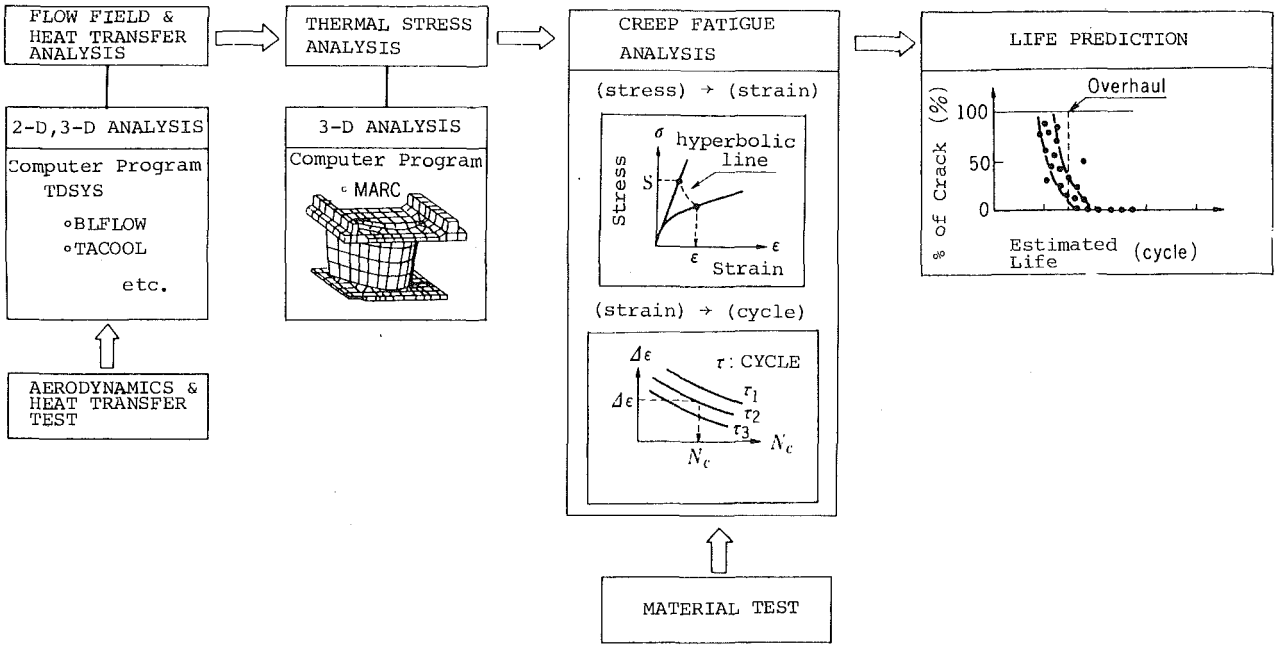

Fig. 4 Diagram of thermal fatigue life prediction

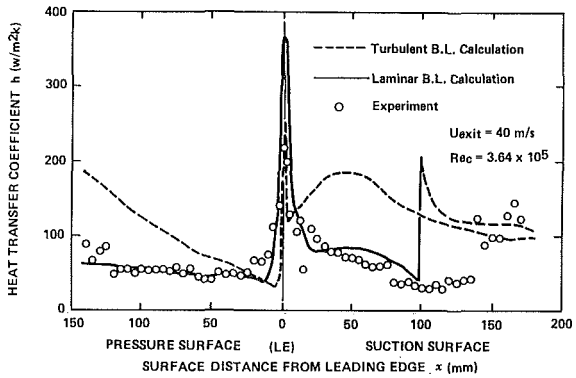

Fig. 5 Heat transfer coeffcient around the airfoil

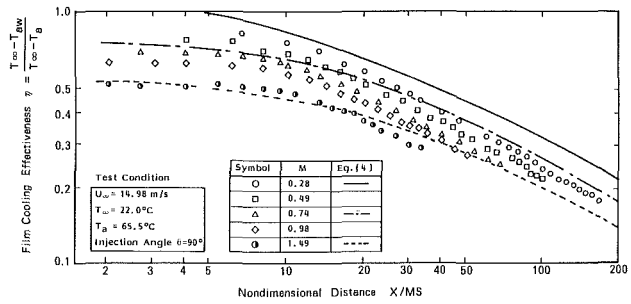

Fig. 6 Typical result of film cooling test

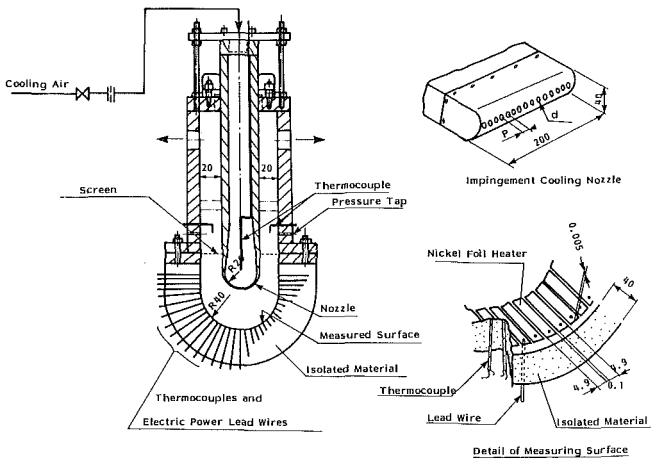

Fig. 7 Leading edge impingement cooling test apparatus

Following is a discussion of the boundary conditions used for the temperature analysis of an MW-701B_2 first stationary vane. The heat transfer coefficient around the vane, except for the leading edge, is calculated by the boundary layer program [1]. The program is confirmed by a basic low-speed cascade test. The vane under test was made from a heat insulating material. Five-micrometer-thick nickel foil resistors were pasted on the test vane to effect the electric heating. The heat transfer coefficient around the vane and the shroud was obtained by measuring the electric power and the temperature difference between the wall and the mainstream, keeping the wall temperature constant. A comparison between typical measurements and the analytical results is shown in Fig. 5 [2].

To calculate the heat transfer coefficient of the vane leading edge, the heat transfer coefficient of the laminar flow around a cylinder placed perpendicular to the flow as represented by Schmidt's empirical formula [1] was used. The influence of the mainflow turbulence intensity τ on the heat transfer coefficient is estimated by equation (2) [3, 4].

$$\mathrm{Nu}_D = 1.14\left\{1-\left(\frac{\phi}{90}\right)^3\right\}\mathrm{Re}_D{}^{0.5}\mathrm{Pr}^{0.4} \tag{1}$$

$$\mathrm{Nu}_{D'} = \xi(\mathrm{Re}_D,\tau)\mathrm{Nu}_D \tag{2}$$

where

$$\xi = \left\{0.945+3.48\left(\frac{\tau\sqrt{\mathrm{Re}}}{100}\right)-3.99\left(\frac{\tau\sqrt{\mathrm{Re}}}{100}\right)^2\right\}/1.022 \tag{3}$$

The heat transfer coefficient on the shroud surface is predicted from the laminar and turbulent flow over a flat plate and by measuring the distance along the stream line from the joint between the transition piece of the combustor and the first stationary vane. Meanwhile, the air leaking through the narrow gap between the transition piece and the vane film cools the shroud surface. To determine the film cooling effectiveness, a basic cooling experiment was carried out. The film cooling test was undertaken employing a low-speed, induced-flow wind tunnel keeping the mainstream at

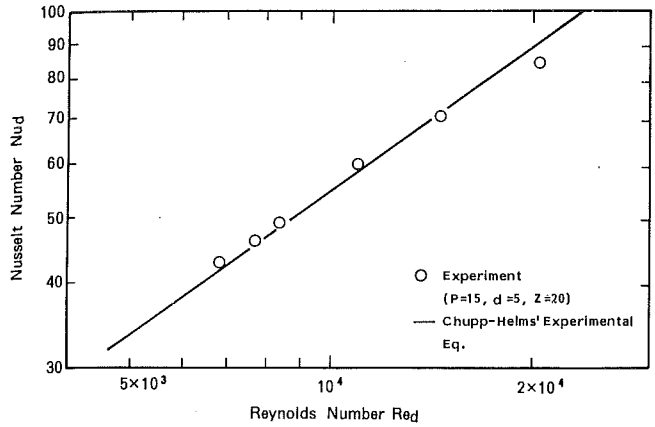

Fig. 8 Typical result of leading edge impingement cooling test

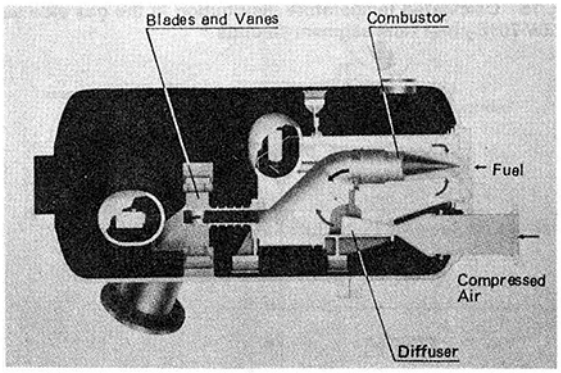

Fig. 9 High-temperature and high-pressure combustion and cooled vane test facility

room temperature. Heated air was blown in through a two-dimensional, 90-deg slot, width 10 mm.

A semi-theoretical equation (4) was obtained.

$$\eta = \frac{T_\infty - T_{aw}}{T_\infty - T_a} = 3.97\left(\frac{\rho_a U_a S}{\mu a}\right)^{0.2}\left(\frac{X+X_o}{MS}\right)^{-0.8}\left\{1-\left(1-2.3Ho^{-15/7}\right)\times\left(\frac{Xo}{X+Xo}\right)^{3/2}\right\}^{-8/15} \quad (4)$$

where

$$Ho = 0.376Xo\mathrm{Re}_{Xo}{}^{-0.2}(1+0.5M\sin\theta)/1.4MS\sin\theta$$

This equation (4) was utilized in our evaluation. Shown in Fig. 6 is a comparison between equation (4) and typical blowing mass flow ratio experimental results with M as the parameter.

The leading edge of the vane is impingement cooled by a row of round holes. Very few data on the impingement heat transfer coefficient of concave surfaces, such as leading edge, have been reported. To find the heat transfer coefficient in the area, an experiment was carried out using a model as shown in Fig. 7. The heat transfer coefficient was determined in the same way as the heat transfer coefficient around the vane. Figure 8 illustrates a comparison between the measurements and Chupp-Helms's empirical formula [5]. For convection cooling of the trailing edge the heat transfer coefficient of a fully developed turbulent pipe flow was used.

$$\mathrm{Nu}_D = 0.023\mathrm{Re}_D{}^{0.8}\mathrm{Pr}^{0.333} \quad (5)$$

TACOOL was formulated on the basis of the heat transfer coefficient, the film cooling effectiveness, the resistance

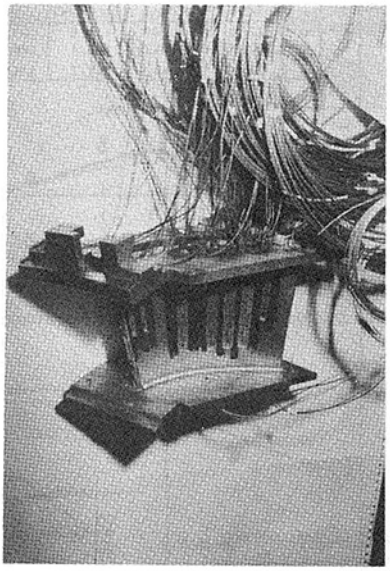

Fig. 10 View of test vane with instrumentation thermocouples (before plasma spray coating)

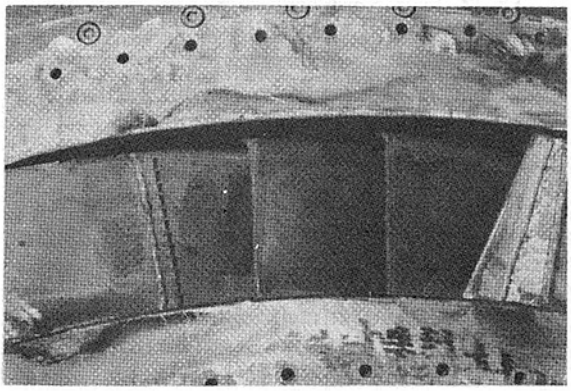

Fig. 11 Instrumented cascade test segment assembly

coefficient of the cooling passage, and other factors. TDSYS was the name of a gas turbine interactive design system developed to accelerate design improvements [6]. TDSYS is composed of several subsystems, each subsystem containing several programs. For our analysis, BLFLOW and TACOOL computer programs were used. BLFLOW is a program to calculate airfoil surface velocity distribution.

Cascade Heat Transfer Test

It is difficult to measure the hot parts of the actual engine in operation, and furthermore, measuring points are limited. To confirm the accuracy of the program, a cascade test was carried out under conditions as close to actual use as possible.

A cascade test in sector form was conducted using an MW-701B_2 gas turbine five-bladed first stationary vane and its four passages. For the cascade test, a high-temperature and high-pressure combustion and cooled blade test facility as shown in Fig. 9 was used. The main specifications of the facility were maximum air flow rate (50 kg/s), maximum pressure (15 ata), maximum temperature of the combustion gas (1500°C).

The cascade test was carried out using an MW-701B_2 combustor under simulated normal operating conditions. Gas temperature distribution at the cascade inlet was measured with seven temperature probes mounted in the section connecting the combustor transition piece and the first vane. Each temperature probe was vertical and measured tem-

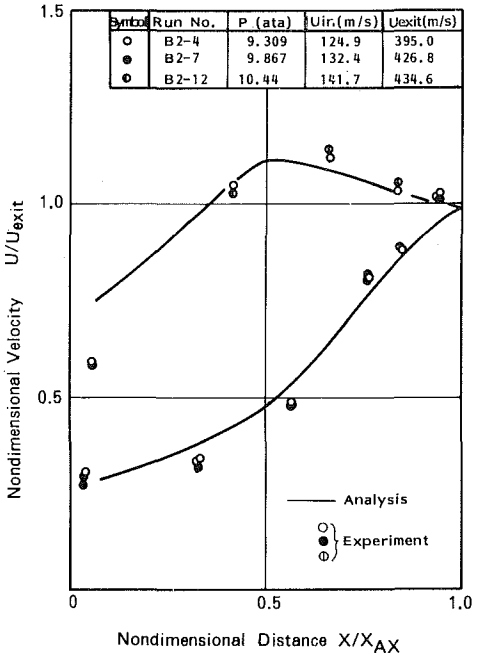

Fig. 12 Velocity distribution of the MW-701B_2 first vane

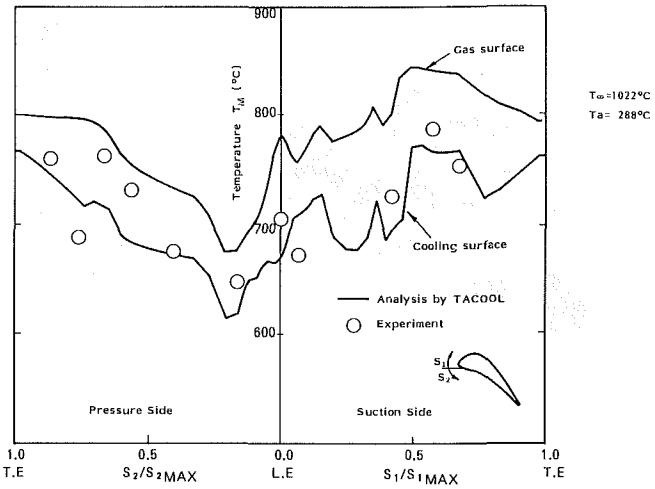

Fig. 13 Metal temperature distribution of MW-701B_2 first vane (mean section)

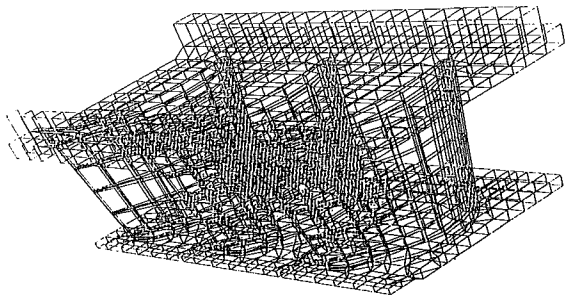

Fig. 14 Finite element model of MW-701B_2 first vane segment

peratures at five different points. The metal temperature of central vane No. 3 was measured by grooving it by electric discharge machining and then embedding Chromel-Alumel thermocouples with inconel sheaths of 1.0ϕ o.d. in nickel-based plasma coating material. Inlet gas temperature distribution just before the vane was measured by thermocouples installed on the leading edge. The thermocouples mounted on the vane are shown in Fig. 10. The cascade is

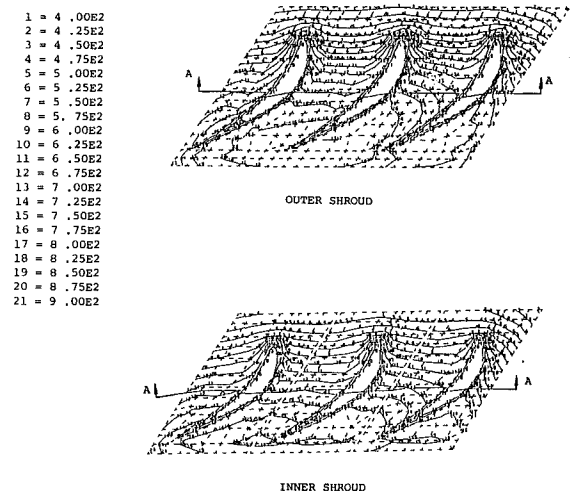

Fig. 15 Calculated temperature distribution in the gas side surfaces of MW-701B_2 first vane segment shrouds

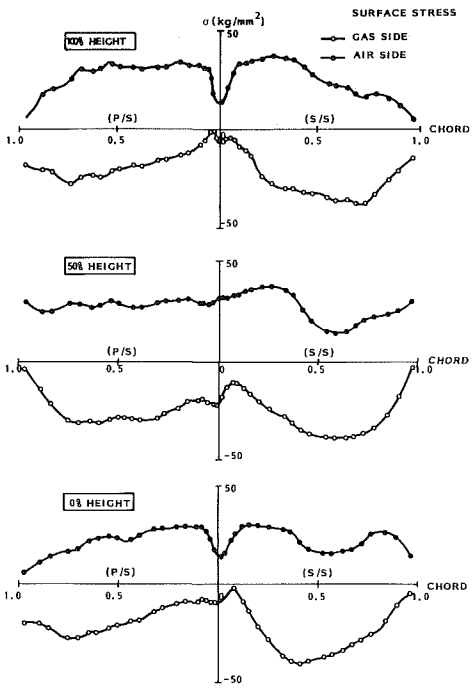

Fig. 16 Calculated thermal stress distribution of the center vane of MW-701B_2 first vane segment

shown in Fig. 11. Static pressure distribution on the surface of the stationary vane was measured by static pressure taps on vanes No. 2 and No. 4 on the sides facing vane No. 3. The amount of cooling air supplied to each vane was adjusted by valves. The cooling air temperature was measured just before the vane inlet and in the cavity at the trailing edge slot inlet inside the vane. The velocity distribution obtained by the static pressure distribution thus measured in mean section is illustrated in Fig. 12. Using the velocity distribution around the vane, a boundary layer analysis was made and the metal temperature analyzed using the aforementioned boundary conditions. Figure 13 shows a comparison between the measured metal temperatures and the temperatures of the TACOOL computer program analysis. Figure 13 shows that the measured values are in overall agreement with the analytical values, except for the fact that the measured metal temperatures are lower than those of the analysis near the inlet region of the trailing edge cooling holes.

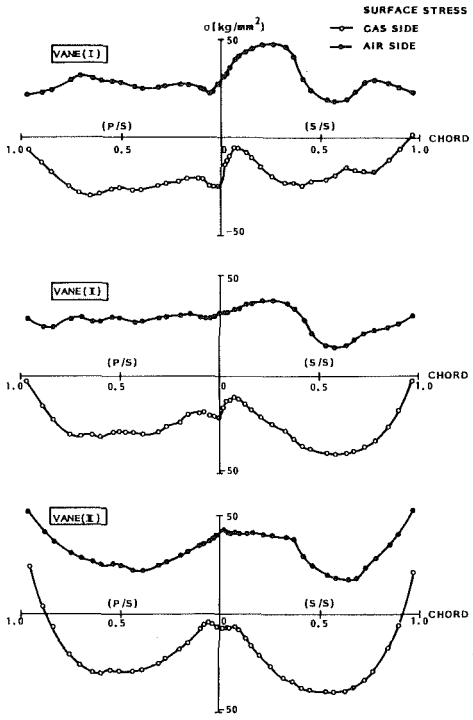

Fig. 17 Calculated thermal stress distribution in the mean sections of three vanes of MW-701B_2 segment

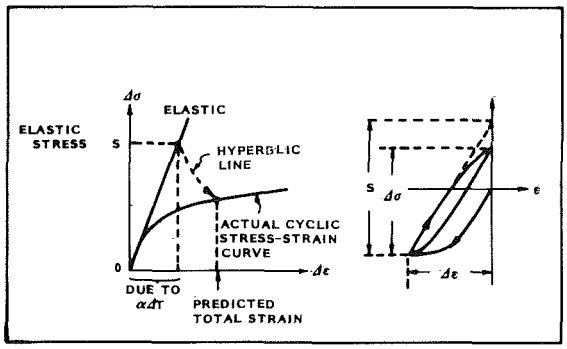

Fig. 18 Estimation of the inelastic behavior from elastic analysis

Thermal Stress Analysis

Stress distribution in air-cooled vanes is difficult to predict with accuracy by a simple calculation method because the thermal boundary conditions are complicated and the effect of the vane as a three-dimensional structure is also involved. Therefore, stress has to be analyzed by a three-dimensional finite element method. The first stationary vane of an MW-701B_2 gas turbine was analyzed by the structural analysis computer program known as "MARC." Shown in Fig. 14 is the model used for the analysis. It is a three-dimensional model with 948 elements and 2,112 nodal points for the analysis of temperature and thermal stress. The heat transfer coefficient, cooling air, gas temperature distribution, and static pressure distribution were given as the boundary conditions.

In the air-cooled vane of an industrial gas turbine, the thermal stress occurring in the steady state is higher than that in the transient state. Therefore, thermal stress in the steady state was analyzed. The analysis was conducted by elastic calculation. A typical example of calculated temperature distribution in the shroud area for the steady state is shown in Fig. 15. Typical calculation results of thermal stress in the airfoil portion are given in Fig. 16 and Fig. 17. Figure 16

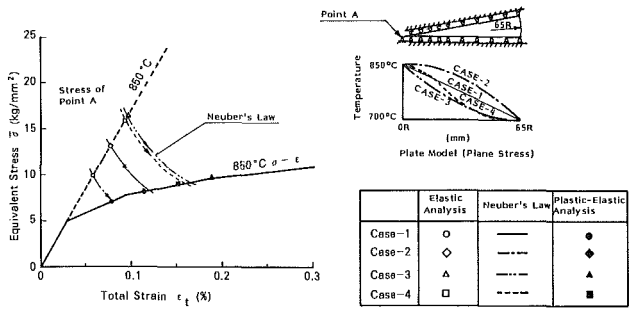

Fig. 19 Comparison of simple estimation method and plastic-elastic analysis

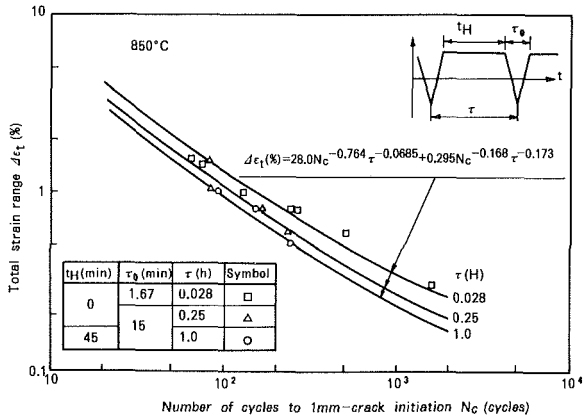

Fig. 20 Data of creep-fatigue interaction test on Co base material

shows that high compression stress appeared in the region of the blade root of the shroud on the suction side. The metal temperature of the outer shroud is higher than that of the inner shroud, as shown in Fig. 15. The life of the outer shroud was estimated to be shorter than that of the inner shroud. Figure 17 shows that the thermal stress of each vane is the same though it is estimated that the middle vane undergoes higher stress because it is restricted by No. 1 and No. 3 vanes.

Prediction of Inelastic Behavior

The thermal stress in the cooled vane where the temperature gradient is largest usually exceeds the yield stress, and for accuracy, an inelastic stress analysis is required. However, elastic-plastic stress analysis of such a three-dimensional structure requires quite a lot of calculation time, so it is not practical. For this reason, a three-dimensional analysis was carried out by the elastic finite element method, and on the basis of the results, inelastic behavior was predicted having regard to the strain concentration and the elastic follow-up behavior. For the simple prediction of inelastic strain from elastic thermal stress, Neuber's law was applied, a technique shown in Fig. 18.

The method was checked by a simple model as shown in Fig. 19, which showed overall agreement with the elastic-plastic stress analysis. Although Neuber's law is a method of estimating stress/strain concentration at notch root, it is also considered applicable to local temperature distribution problems, such as in cooled vanes.

Creep-Fatigue of Vane Material

The metal temperature of the first stationary vane is very high and, as previously mentioned, temperature distribution is most severe in the steady state.

Therefore, in the steady state, a high thermal strain is maintained and creep occurs, so creep-fatigue is the most

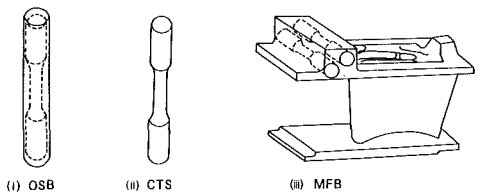

Fig. 21 Examples of test segment materials

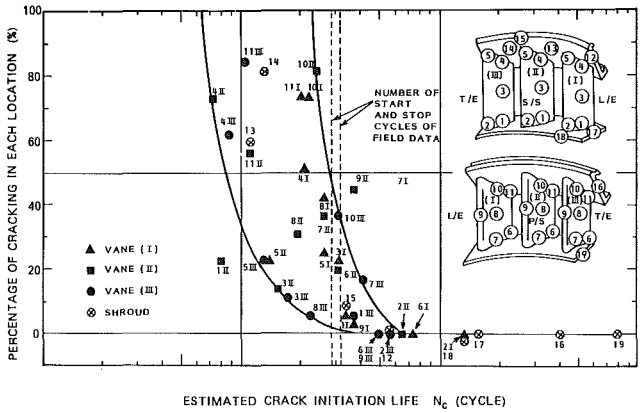

Fig. 22 Relationship between actual cracking trends in MW-701B$_2$ first vanes and the estimated crack initiation lives at corresponding locations

important fracture mode. The material and strength test must be undertaken with combined creep and fatigue data.

An example of experimental data on a cobalt base superalloy under such condition is illustrated in Fig. 20. Based on such experimental material test data, the crack initiation life of actual vanes, which have long continuous operating periods, was predicted by the frequency modified fatigue life equation proposed by L. F. Coffin [7].

$$\Delta\epsilon_t = \Delta\epsilon_p + \Delta\epsilon_e$$
$$= C_1 N_f^{-\beta_1 \nu K_1} + C_2 N_f^{-\beta_2 \nu K_2} \quad (6)$$

where C_1, β_1, K_1, C_2, β_2, and K_2 are material constants.

Such tests have also been carried out with temperature cycling and long operation periods on the compression side under the conditions closest to the actual operation of the vanes. It is noted that in Fig. 20, the time it takes for a crack 1 mm long to be generated on the surface of the test piece is taken as the end of its life. Meanwhile, properties of precision cast alloys often vary greatly with casting conditions. For this reason, test pieces manufactured under different conditions from those indicated in Fig. 21 are used to enhance the accuracy of life prediction of the actual vane.

Verification of Life Prediction Procedure

As verification of the life prediction procedure, the predicted crack initiation was compared with field data obtained from two MW-701B$_2$ machines. The prediction procedure was applied to estimate the life of the stationary vanes of those engines.

Figure 22 shows the relation between the actual cracking frequencies and the predicted lives for the various parts of the vane segments. The dotted line in Fig. 22 indicates the number of start/stop cycles prior to inspection of the machine. Shorter lives than indicated by the dotted line were predicted for areas showing high cracking frequencies such as points 4, 10 and 11. On the other hand, tiny cracks were found in the areas predicted to have longer lives, such as points 17 and 18. The accuracy of the prediction of temperature, stress, inelastic strain, material data, etc., have effects on the accuracy of the life prediction, but it can be said that it is possible to predict the thermal creep-fatigue life of air-cooled gas turbine vanes by the procedure advanced in the present study.

Conclusions

A technique for evaluating the life of turbine stationary vane has been described. The life prediction method presented concerned air-cooled vanes and involved the calculation of metal temperature, thermal stress, and creep-fatigue material data simulating the engine operation cycle. The conclusions of this paper are as follows:

- Temperature distribution analysis by the "TACOOL" computer program is in general agreement with the high-temperature and high-pressure cascade test performed on full-scale segment blades.
- Predicting the inelastic strain from elastic thermal stress analysis by Neuber's law is considered applicable when temperature distribution is local, as in a cooled vane.
- According to this proposed life prediction method, a short-term fatigue life equation based upon a simulated creep-fatigue material test is of practical use.
- The comparison between the predicted life and our field experience shows an acceptable relationship between the figures. It is considered that the proposed procedure is useful for predicting the life of air-cooled vanes.

References

1 McNally, W. D., "Fortran Program for Calculating Compressible Laminar and Turbulent Boundary Layers in Arbitrary Pressure Gradients," NASA TND-5681, 1970.

2 Nakahara, T., Aoki, S., and Takeishi, K., "Effect of Surface Pressure Distribution of Gas Turbine Vane on Film Cooling," Paper No. GT-16, 14th International Congress on Combustion Engines (CIMAC), Helsinki, 1981.

3 Kestin, J., "The Effect of Free-Stream Turbulence on Heat Transfer Rates," *Advances in Heat Transfer*, Vol. 3, Academic Press, New York, 1966, pp. 1-32.

4 Tobery, E. W., and Bunce, R. H., "Cascade Heat Transfer Tests of the Air Cooled W501D First Stage Vane," ASME Paper Number 84-GT-114, 1984.

5 Chupp, R. E., and Helms, H. E., "Evaluation of Internal Heat Transfer Coefficients for Impingement-Cooled Turbine Airfoils," *Journal of Aircraft*, Vol. 6, 1969, pp. 203-208.

6 Aoki, S., Mase, M., and Murai, T., "Gas Turbine Interactive Design System (TDSYS)," Mitsubishi Technical Review, June 1981.

7 Coffin, L. F., Jr., "Life Prediction of Metals Subjected to High Temperature Fatigue," *Proceedings of the Int. Conf. on Mechanical Behavior of Metals*, Vol. 2, 1972, pp. 516-529.

Low-Temperature Hot Corrosion in Gas Turbines: a Review of Causes and Coatings Therefor

G. W. Goward
Turbine Components Corp.,
Branford, CT 06405

In about 1975 an apparently new form of hot corrosion attack of gas turbine airfoils was identified during low-power, low-metal-temperature operation of a marine gas turbine. The rate of this corrosion was substantially greater at about 700°C than that usually observed for sulfate-induced hot corrosion at 800° to 1000°C. The same type of hot corrosion has been subsequently reported to occur in ground-based gas turbines, and is similar in principle to fireside corrosion of boiler tubes. This paper presents a review of probable mechanisms of this so-called low-temperature hot corrosion, of test methods for its laboratory and rig simulation, and of coatings in use or in advanced development for protection of gas turbine airfoils operating in this corrosion regime.

Introduction

In about 1975 an apparently new form of hot corrosion attack of gas turbine airfoil materials was identified during low-power, low-metal temperature operation of a marine gas turbine [1]. The first-stage blades of the turbine were coated with a cobalt-chromium-aluminum-yttrium (CoCrAlY) coating which had exhibited satisfactory hot corrosion resistance in the temperature range of 800° to 1000°C in this and similar applications. Analysis of temperature profiles and corrosion rates on the first-stage blades indicated that corrosion rates were greater than anticipated in the range of 600° to 730°C metal temperature.

In the same time period, Taylor et al. [2] at the U.K. Admiralty Materials Laboratory reported higher corrosion rates in rig testing at 750°C than at 830°C for several alloys and coatings.

Several years later Spengler [3] presented evidence of similar low-temperature corrosion on airfoils from ground-based turbines. Corrosion microstructures similar to those observed for field turbines were also observed during low-temperature rig testing.

In 1982 Wood et al. [4] reported the occurrence of low-temperature corrosion on first-stage blades of ground-based turbines fueled with sour natural gas and in locations where ingestion of salt-contaminated sand was inevitable. It is now generally accepted that the phenomenon can be encountered in both marine and ground-based gas turbines. No public documentation of occurrence of low-temperature corrosion in aircraft gas turbines has appeared to date but there is no doubt that conditions conducive to such corrosion are possible.

For several years after these early observations there was some confusion over the nomenclature of this abnormal corrosion mode. It is now common practice to refer to it as low-temperature hot corrosion. Alternatively, the use of the term Type 2 corrosion, in contrast to high-temperature (800° to 1000°C) Type 1 corrosion is widely accepted.

The potential economic and logistical impact of the abnormally high corrosion rates prompted intensive studies to identify the mechanism of the process and to provide coatings and alloys with more satisfactory durability in the critical temperature range involved. It was necessary to achieve the latter without compromising corrosion properties in higher temperature ranges.

This paper will provide a brief review of the current state of knowledge of the corrosion mechanism, its relation to previously observed fireside corrosion and of progress in the development of coatings with improved resistance to this form of hot corrosion. Sources of information for the review are open technical literature, patent publications, and contacts with investigators working on nonproprietary and unclassified aspects of the problem.

The review is not intended to be technically complete but is intended to provide those involved in applied areas of gas turbine technology with a working knowledge of the problem. This should aid in achieving more effective design and materials selection for gas turbines and other heat engines functioning in this critical corrosion regime.

Characterization of Low-Temperature Hot Corrosion

The major characteristics of so-called low-temperature hot corrosion are as follows [1-3, 5-7]:

- Under conditions where sodium salts ingested into the gas turbine cause deposition of sodium sulfate (Na_2SO_4) on hot section airfoils, hot corrosion of coatings and alloys with moderate (10-20%) chromium contents occurs at rates significantly greater at about 700°C than at 800° to 1000°C.

Contributed by the Gas Turbine Division of THE AMERICAN SOCIETY OF MECHANICAL ENGINEERS and presented at the 30th International Gas Turbine Conference and Exhibit, Houston, Texas, March 18-21, 1985. Manuscript received at ASME Headquarters, December 21, 1984. Paper No. 85-GT-60.

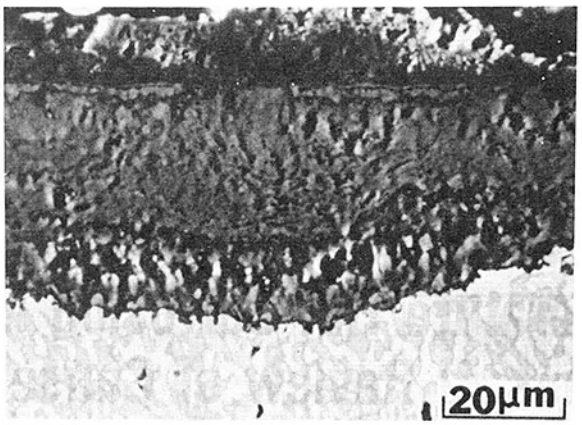

Fig. 1 Typical microstructure of low-temperature corrosion of a CoCrAlY coating

Some appreciable level of sulfur in the fuel used is also required but is not yet quantitatively defined. The phenomenon is not exclusive to sodium sulfate, but can occur with potassium sulfate and more complex mixtures of other sulfate salts, including sodium sulfate–magnesium sulfate.

- Leaching of the corroded surfaces with water and analysis of the leachate indicates the presence of significant amounts of water-soluble sulfates, cobalt sulfate ($CoSO_4$) from CoCrAlY coatings, and nickel sulfate ($NiSO_4$) from nickel base alloys. The leachate is invariably acidic (pH 1 to 4).
- The microstructure of the corroded coating or alloy is characteristically similar to that shown in Fig. 1. Unaffected coating alloy or superalloy is covered with a voluminous scale. In contrast to structures obtained at high temperatures, for example 1000°C, there is no zone of denudation of substructure containing chromium or other sulfides. In CoCrAlY coatings, there can be an indication of attack favoring the phase richer in aluminum, that is, the CoAl or β phase. Electron-beam microprobe analysis invariably indicates the presence of a sulfur-rich phase adjacent to the unaffected alloy, and for CoCrAlY coatings, a cap of oxide rich in cobalt oxide.

Transition microstructures between that described above and areas of high-temperature corrosion have been observed [1] but need not be described in detail for the purposes of this review.

Laboratory Reproduction of Microstructures

Up until the observation of the low-temperature corrosion described above, most laboratory methods for studying hot corrosion involved application of sodium-sulfate layers, sometimes doped with sodium chloride, to specimens, and heating these in the range of 800° to 1000°C. With few exceptions, the cover gas was air or oxygen. Lower temperatures were not used because corrosion of "resistant" materials was considered to be negligible below 750° to 800°C. Immersion in mixtures of sodium sulfate–sodium chloride with air as the cover gas was another widely used test. Some burner rig tests, "simulating" gas turbine conditions by combustion of appropriate fuels combined with sea-salt injection, were also run in the same higher temperature range because significant corrosion of "resistant" materials was not expected or observed in the range of 650° to 750°C.

Re-evaluation of CoCrAlY coatings with these types of test methods, including those with intentionally added sodium chloride [5], failed to reproduce the rates and/or characteristic microstructures found on airfoils from the above-described field service.

More or less simultaneously in several laboratories [5, 7, 8] it was found that the abnormally high corrosion rates and microstructures could be reproduced by application of Na_2SO_4 to CoCrAlY and heating in the range of 650° to 750°C in the presence of finite and known partial pressures of SO_3 in air or oxygen. Similar results were also achieved with burner rigs [9, 10] where partial pressures of SO_2–SO_3 were maintained at finite and controlled values in the vicinity of test specimens. It was thus established that two conditions are necessary for accelerated corrosion of, e.g., CoCrAlY, in the range of 600° to 750°C:

- a molten sulfate salt on the surface of the alloy, and
- a cover gas of air or oxygen containing SO_3 at partial pressures of at least 10^{-5} to 10^{-4} atm.

Mechanisms of Low-Temperature Hot Corrosion

Extensive studies to elucidate the mechanism of this unusual form of hot corrosion were undertaken at laboratories of General Electric, Pratt & Whitney, and government laboratories of the United States and United Kingdom. This review cannot describe these studies in complete detail. Briefly, and with the risk of minimizing several details which are still controversial and unresolved, the corrosion process proceeds approximately as follows [7, 11, 12]:

- Sulfate salts, typified by sodium sulfate, deposit on the coating (alloy) surface.
- Sulfur trioxide (oxidation of SO_2 to SO_3 is perhaps catalytically aided by oxides on the alloy surface) reacts with, for example, cobalt oxide, to form cobalt sulfate ($CoSO_4$) which lowers the melting point of sodium sulfate. Other extraneous materials, for example magnesium sulfate ($MgSO_4$) [3] and potassium sulfate (K_2SO_4), can also contribute to melting-point suppression of the sodium sulfate.
- Sulfur trioxide (SO_3) absorbed from the gas phase into the melt, most likely as pyrosulfate ion ($S_2O_7^=$), acts as the principal oxidant to rapidly convert the surface of the alloy to nonprotective oxides.
- The details of mass transport and rapid conversion of alloy to oxide in the complex molten phase–oxide mixture remain somewhat controversial although a number of plausible mechanisms have been formulated [7, 11, 12].

Several studies [13–15] of the solubilities of relevant oxides in sodium sulfate as a function of partial pressure of SO_3 (analogous to pH in aqueous solutions) have aided studies of the complex mechanism, and in formulation of alloys and coatings more resistant to this form of hot corrosion. It is noteworthy that most relevant oxides exhibit amphoteric behavior; that is, solubility minima characteristic for each oxide are observed. The major exception to this behavior is silicon dioxide (SiO_2), which remains virtually insoluble in highly acidic (high partial pressures of SO_3) sodium sulfate.

It is also interesting to note that Pettit and co-workers [16] identified sites of corrosion initiation to be associated with localized high concentrations of yttrium oxide (Y_2O_3) in alumina scales on CoCrAlY. This oxide is more soluble than Al_2O_3 in Na_2SO_4 acidified with SO_3.

Related Hot-Corrosion Phenomena

Review of the literature on hot corrosion from 1945 to 1970 reveals that there are striking similarities between the newly discovered low-temperature hot corrosion and so-called fireside corrosion of boiler tubes. Several similarities are as follows:

- Surface coverage with a molten sulfate salt is necessary in both cases, for example Na_2SO_4–$CoSO_4$ in the gas turbine and Na_2SO_4 or K_2SO_4–$Fe_2(SO_4)_3$ in fireside corrosion.

• The presence of sulfur trioxide (SO_3), the formation of which may be catalytically aided by surface oxides, is necessary in both cases. Sulfur trioxide in solution in the molten salt is thought to exist as the pyrosulfate ion ($S_2O_7^=$).

• Microstructures of corroded alloys and/or coatings are similar; that is, voluminous oxide over unaffected alloy.

• Corrosion rates increase from about 540°C up to about 675°C and then rapidly decrease with increasing temperature [17].

• Resistance to corrosion increases with increasing chromium content of relevant alloy steels.

Study of some of the higher-quality work on fireside corrosion mechanisms, for example that of Cutler [18] and Rahmel [19] on electrochemistry of molten sulfates as related to hot corrosion, and that of Reid [17] has greatly aided in formulating practical working models useful for gas turbine technology.

Related studies on materials and/or coatings to lower the rates of boiler-tube wastage by fireside corrosion have continued into the 1980s. Test methods for evaluation of improved materials and coatings are similar to those used for testing improved coatings and alloys for gas turbine low-temperature hot corrosion. For example, Rehn [20] simulated fireside corrosion by coating samples with a K_2SO_4–Na_2SO_4–Fe_2O_3 mixture and heating these at 677°C in an apparatus which caused a synthetic flue gas containing SO_2 and SO_3 to pass over the "slag-coated" samples. This convergence of technology related to boiler fireside corrosion and turbine airfoil corrosion holds promise for accelerated development of solutions to both problems.

Empirically Important Aspects of Mechanism Studies

Several major design considerations emerge from the marine gas turbine experience with low-temperature hot corrosion and mechanism studies thereof.

• For turbines operating on most fuels, and in any environment from which sodium and similar salts can be ingested, accelerated corrosion can be anticipated in locations on the turbine where metal temperatures are in the range of 600° to 750°C.

• The rate of such corrosion will increase with increasing sulfur content of the fuel. Quantitative calculations of the relationships involved are not yet dependable.

• There is probably a threshold value of salt concentration above which this type of corrosion occurs and an upper limit beyond which the corrosion does not increase in rate. Quantitative calculations of these parameters are also not yet dependable.

• Rates of low-temperature corrosion of alloys and coatings decrease with increasing chromium contents but achieving properties balanced to resist corrosion over the useful metal-temperature range of 600° to 1000°C is proving to be somewhat difficult. Currently available information on this subject is summarized in the following section.

Perhaps the most difficult problem involves the presence of both low and high-temperature corrosion on the same airfoil with corrosion on the low-temperature area taking place at a rate several times that occurring on hotter locations. To unequivocally substantiate conclusions drawn from laboratory experiments on this problem, Davis and Grinnell at Rolls-Royce [21] varied the cooling air supply, and thus the temperature profiles of three blades in the same rotor of a Tyne engine run in a hot-corrosion environment. With no exception, it was demonstrated that the areas of low-temperature corrosion on the airfoils decreased in size with increasing metal temperature. It was thereby suggested that by the judicious balance of design temperatures for creep and corrosion, more effective use of superalloy properties could be achieved.

Development of More Durable Coatings

Since the discovery of low-temperature hot corrosion on gas turbine airfoils in the mid-1970s, development programs, including actual engine trials, have provided several coating systems with improved durability in the critical temperature range. Brief descriptions of unclassified developments follow.

Several organizations evaluated platinum-modified aluminide coatings for resistance to the low-temperature (600°–700°C) mode of corrosion. Rahmel et al. [22] used an electrochemical method to test a platinum-containing coating designated as LCD-2 for resistance to acidic and basic fluxing which characterize the mode of attack of low-temperature and high-temperature corrosion, respectively. It was concluded that the addition of platinum to aluminide coatings effects significant improvement to the resistance to neutral and basic fluxing occurring during high-temperature corrosion, but offers little improvement in resistance to acidic fluxing which occurs during low-temperature corrosion.

Barkalow and Pettit [5] demonstrated, however, that if the critical platinum–aluminum phase (possibly $PtAl_2$) is continuous at the surface of a platinum-modified aluminum coating, the coating is very resistant to acidic (Na_2SO_4 + SO_3) fluxing at 650°C.

Davis and Grinnell [21] described a comprehensive program of engine testing of several coatings under conditions of both low and high-temperature hot corrosion. It was concluded, in general, that platinum-modified aluminides were satisfactory for protection against both types of corrosion. Some variations in properties were noted, however, for variants in microstructure obtained from different vendors.

Wood et al. [4] report generally favorable results of engine service tests of Pt–Al coatings, but poorer corrosion properties, similar to unmodified aluminides, for platinum–rhodium–aluminum coatings.

Aprigliano and Wacker [23] described field-service testing, in a marine engine, of several coatings, including a platinum–rhodium–modified aluminide. This coating was moderately superior to standard CoCrAlY in the low-temperature hot corrosion regime, but it was pointed out that the life of all systems was unsatisfactory, with corrosion penetration to the substrate in less than 4800 hours. Thus, some platinum-modified aluminide coatings appear to have somewhat superior resistance to both types of corrosion but tests under more controlled laboratory conditions and additional well-documented engine tests are still necessary to resolve remaining questions. Grisik et al. [24] chose to combine the properties of CoCrAl type coatings with those of platinum and/or aluminum–hafnium modifications. Thus, electron beam vapor deposited Co–Cr–Al was modified by the addition of more aluminum along with some hafnium to provide a nominal Co–Cr–Al–Hf coating with about 20% Al and 10% Hf in the outer surface. A second coating system was made by the same addition of aluminum and hafnium followed by application of a thin layer of platinum on the outer surface. Engine testing showed that the Co–Cr–Al–Hf–Pt coating on first-stage blades had a factor of more than two lifetime advantage over the standard CoCrAlY coating then in use. The Co–Cr–Al–Hf coating showed a factor of greater than two lifetime advantage over a diffusion aluminide coating on cobalt-base first-stage vanes. A rhodium-modified aluminide tested at the same time on first vanes was better than the simple diffusion aluminide but not as good as the Co–Cr–Al–Hf system.

Taylor and co-workers [2] at the U.K. Admiralty Materials Laboratory were perhaps the first to note that increased

chromium content in both superalloys and coatings provided significant increases in low-temperature (750°C) hot corrosion resistance of gas turbine material systems. The effect was noted for IN-939, an alloy with 23% chromium, and a NiCrAlY coating with about 39% chromium. Condé et al. [25] provided a more detailed evaluation of this effect by 750°C testing of NiCrAlY with 26, 34, and 42% chromium; only the latter two compositions showed significant resistance to low-temperature hot corrosion.

This beneficial effect of chromium has been repeatedly confirmed in several independent laboratories, and a number of medium to large-scale coating development programs have been initiated to exploit the effect.

Goebel [26] has rig tested a number of high (30 to 35%) chromium MCrAlY (M = Co and/or Ni) coatings, all of which showed improved resistance to low-temperature (704°C) hot corrosion compared to CoCrAlY with 20% chromium. A 35% chromium CoCrAlY and a 35% chromium NiCoCrAlY were selected for field-service engine testing, which is still in process.

Luthra [27] has described laboratory and rig tests of cobalt-base coatings which show that a critical chromium content of no less than 37% is required to provide improved cobalt-base coatings with balanced resistance to low and high-temperature hot corrosion. Minor additions of reactive metals such as yttrium and hafnium, and also silicon, apparently do not impart further improvements to the coatings.

McCarron and Brobst [28], in reporting initial results on testing various alloys and coatings in a pressurized fluidized bed coal-combustion facility, noted that low-temperature hot corrosion occurs in this medium and is further accelerated by deposition of potassium sulfate derived from coal combustion. Of several coatings tested, Co-30% Cr-5% Al appeared to have the best corrosion resistance across the temperature range of 593° to 816°C. Noble metal (platinum, rhodium) modified aluminides showed reasonable resistance in the higher-temperature regime but were not quite as good as the above CoCrAl coating at 593° to 704°C.

In Europe there has been a consistent and apparently successful effort over the past decade to use silicon as an additive element to coatings used in land-based turbines [29-32]. Grünling and Bauer [33] provide a sound rationale for the use of silicon in coatings based on the known resistance of SiO_2 to acidic fluxing ($Na_2SO_4 + SO_3$) and much of the laboratory testing used to substantiate hot corrosion properties of these coatings gives proper attention to the use and control of SO_2-SO_3 in the test media. Condé et al. [25] at the U.K. Admiralty Marine Technology Establishment have tested Elcoat 360, a titanium-silicon diffusion coating developed by vanAmerongen [34] in Holland. In a well-calibrated low-temperature (700°C) rig test, the coating was found to have significantly improved properties over pack aluminizing and additional testing across a higher temperature range was promised.

In agreement with Grünling and Bauer [33] that SiO_2-forming systems should be quite resistant to low-temperature acidic sulfate media, Goebel [35] has evaluated siliconized MCrAlY (M = Co and NiCo) coatings in low-temperature (732°C) corrosion and at a higher temperature of 899°C. Corrosion resistance at 732°C was markedly superior to the unmodified coatings. At 899°C however, coating performance was inferior to unmodified MCrAlY systems apparently because of unsatisfactory diffusional stability. Further development of this concept and field service evaluation are anticipated.

Summary

An accelerated form of sulfate-induced hot corrosion has been identified during low-power operation of marine gas turbines. Under appropriate conditions higher rates of hot corrosion occur at 600°-750°C than at 800°-1000°C.

The corrosion mechanism involves acidic fluxing of protective oxides by sulfur trioxide (SO_3) dissolved in molten sulfates in the presence of air. The corrosion rate is proportional to the partial pressure of SO_3 and is therefore proportional to sulfur content of the fuel burned. The mechanism of this low-temperature corrosion is similar, if not identical, to fireside corrosion of boiler tubes.

Similar low-temperature hot corrosion has been observed in ground-based engines and while not yet reported in the open literature, it is anticipated that it can occur in aircraft gas turbines.

Certain types of platinum-modified diffusion aluminide coatings provide moderate protection against this form of hot corrosion. Coatings and alloys exhibit increasing resistance to low-temperature hot corrosion with increasing chromium content. Cobalt-based coatings with about 35% chromium provide good protection against both low and high-temperature corrosion. Coatings containing silicon are particularly resistant to low-temperature hot corrosion but are less resistant to corrosion at higher temperatures (900°C).

References

1 Wortman, D. J., Fryxell, R. E., and Bessen, I. I., "A Theory for Accelerated Turbine Corrosion at Intermediate Temperatures," *Proceedings of the Third Conference on Gas Turbine Materials in a Marine Environment*, Session V, Paper No. 11, Bath, England, 1976.

2 Taylor, A. R., Wareham, B. A., Booth, G. C., and Condé, J. F., "Low and High Pressure Rig Evaluation of Materials and Coatings," Ibid., Session III, Paper No. 3.

3 Spengler, C. J., "Characterization of Corrosion Attack of Superalloys in Combustion Turbines in the Temperature Range 1110-1400°F," *Proceedings of Symposium Superalloys 1980*, American Society for Metals, 1980, pp. 395-404.

4 Wood, J. H., Schilling, W. F., and Aeshbacher, H. J., "Evaluation of Gas Turbine Bucket Corrosion Protection Systems Following Long-Time Service in Saudi Arabia," ASME Paper No. 82-GT-99.

5 Barkalow, R. H., and Pettit, F. S., "Degradation of Coating Alloys in Simulated Marine Environments," Report No. FR-10225, U.S. Navy Contract N-00173-75-C0146, June 1978.

6 Barkalow, R. H., and Goward, G. W., "Microstructural Features of Low Temperature Hot Corrosion in Nickel and Cobalt Base MCrAlY Coating Alloys," *Proceedings of Symposium on High Temperature Corrosion*, National Association of Corrosion Engineers, San Diego, CA, 1981, pp. 502-506.

7 Luthra, K. L., "Mechanism of Low Temperature Hot Corrosion," Ibid., pp. 507-512.

8 Jones, R. L., "Cobalt Oxide-SO_2/SO_3 Reactions in Cobalt-Sodium Mixed Sulfate Formation and Low Temperature Hot Corrosion," Ibid., pp. 513-518.

9 Aprigliano, L. F., "Burner Rig Simulation of Hot Corrosion," Report MAT-77-68, Nov. 1977, David W. Taylor Ship Research and Development Center, Bethesda, MD.

10 Wortman, D. J., Fryxell, R. E., Luthra, K. L., and Bergman, P. A., "Mechanism of Low Temperature Corrosion: Burner Rig Studies," *Metallurgical Coatings 1979, Proceedings of International Conference*, Volume II, American Vacuum Society, 1979, pp. 281-288.

11 Chiang, K. T., Pettit, F. S., and Meier, G. H., "Low Temperature Hot Corrosion," *Proceedings of Symposium on High Temperature Corrosion*, National Association of Corrosion Engineers, San Diego, CA, 1981, pp. 519-530.

12 Luthra, K. L., "Low Temperature Hot Corrosion of Cobalt-Base Alloys: Part II, Reaction Mechanism," *Metallurgical Transactions A*, Vol. 13A, Oct. 1982, pp. 1853-1864.

13 Liang, W. W., and Elliott, J. F., "Reaction Between Cr_2O_3 and Liquid Sodium Sulfate at 1200K," *Proceedings of Meeting on Properties of High Temperature Alloys*, The Electrochemical Society, 1976, p. 557.

14 Gupta, D. K., and Rapp, R. A., "The Solubilities of NiO, Co_3O_4, and Ternary Oxides in Fused Na_2SO_4 at 1200K," *J. Electrochem Soc.*, Vol. 127, No. 10, Oct. 1980, pp. 2194-2202.

15 Stern, K. H., "Metal Oxide Solubility and Molten Salt Corrosion," NRL Memorandum Report 4772, Mar. 1982.

16 Hwang, S. Y., Meier, G. H., Pettit, F. S., Johnston, G. R., Provenzano, V., and Smidt, F. A., "The Initial Stages of Hot Corrosion Attack of CoCrAlY Alloys at 700°C," *Proceedings of Conference on High Temperature Protective Coatings*, The Metallurgical Society, Atlanta, 1983, pp. 121-134.

17 Reid, W. T., *External Corrosion and Deposits, Boilers and Gas Turbines*, Elsevier, New York, 1971, p. 131.

18 Cutler, A. J. B., "The Effect of Oxygen and SO_3 on Corrosion of Steels in Molten Sulfates," *Journal of Applied Electrochemistry*, Vol. 1, 1971, pp. 19-26.

19 Rahmel, A., "Thermodynamic Aspects of Corrosion in Molten Sulfates. The Construction and Application of E/log P_{SO_3} Diagrams," *Electochim. Acta*, Vol. 13, No. 3, 1968, pp. 495-505.

20 Rehn, I. M., "Laboratory Fireside Corrosion. Evaluation of Superheater Tube Alloys and Coatings," EPRI CS 3134, June 1983, Electric Power Research Institute, Palo Alto, CA.

21 Davis, F. N., and Grinnell, C. E., "Engine Experience of Turbine Rotor Blade Materials and Coatings," ASME Paper 82-GT-244.

22 Wu, W. T., Rahmel, A., and Schorr, M., "Role of Platinum in the Na_2SO_4-Induced Hot Corrosion Resistance of Aluminum Diffusion Coatings," *Oxidation of Metals*, Vol. 22, Nos. 1/2, 1984, pp. 59-81.

23 Aprigliano, L., and Wacker, G., "Laboratory and Service Evaluation of the Hot Corrosion Resistance of Precious Metal Duplex Coatings," *Proceedings of the Third Conference on Gas Turbine Materials in a Marine Environment*, Session III, Paper 4, Bath, England, 1976.

24 Grisik, J. J., Miner, R. G., and Wortman, D. J., "Performance of Second Generation Airfoil Coatings in Marine Service," *Metallurgical Coatings, 1980, Proceedings of the International Conference*, Vol. II, The American Vacuum Society, 1980, pp. 397-406.

25 Condé, J. F. G., Booth, G. C., Taylor, A. F., and McGreath, C. G., "Hot Corrosion in Marine Gas Turbines," *Proceedings of Conference on High Temperature Alloys for Gas Turbines*, COST 50, 1982, pp. 237-247.

26 Goebel, J. A., "Advanced Coating Development for Industrial/Utility Gas Turbine Engines," *Proceedings of The First Conference on Advanced Materials for Alternative Fuel Capable Directly Fired Heat Engines*, DOE-EPRI, Castine, ME, 1979, pp. 473-488.

27 Luthra, K. L., and Wood, J. H., "High Chromium Cobalt-Base Coatings for Low Temperature Hot Corrosion," *Thin Solid Films*, Vol. 119, 1984, pp. 271-280.

28 McCarron, R. L., and Brobst, R. P., "1100-1500°F Corrosion of Turbine Materials Following Long Term Exposure to the Effluent from an Experimental PFBC," *Corrosion 84*, National Association of Corrosion Engineers, Paper No. 92, New Orleans, LA, Apr. 1984.

29 Fitzer, F., and Schlichting, J., "Coatings Containing Chromium, Aluminum, and Silicon for High Temperature Alloys," *Proceedings of Symposium on High Temperature Corrosion*, National Association of Corrosion Engineers, San Diego, CA, 1981, pp. 604-614.

30 Malik, M., Morbioli, R., and Huber, P., "The Corrosion Resistance of Protective Coatings," *Proceedings of Conference on High Temperature Alloys for Gas Turbines*, COST-50, 1982, pp. 237-247.

31 Felix, P. C., and Villat, M., "Plasma Sprayed Protective Coatings for Blades of Industrial Gas Turbines," *Proceedings of Twelfth International Congress on Combustion Engines*, Japan Internal Combustion Engine Federation, Tokyo, May 1977, pp. 2565-2589.

32 Bauer, R., Grünling, H. W., and Schneider, K., "Silicon and Chrome Base Coatings for Stationary Gas Turbines," *Proceedings of the First Conference on Advanced Materials for Alternative Fuel Capable Directly Fired Heat Engines*, Castine, ME, DOE-EPRI, 1979, pp. 505-521.

33 Grünling, J. W., and Bauer, R., "The Role of Silicon in Corrosion Resistant High Temperature Coatings," *Metallurgical Coatings 1982, Proceedings of the International Conference*, Vol. 1, 1982, pp. 3-20.

34 vanAmerongen, H., "Structure and Properties of Silicide-Based Diffusion Coatings," *High Temperature Alloys for Gas Turbines*, Applied Science, London, 1978.

35 Goebel, J. A., Giggins, C. S., Krasij, M., and Stringer, J., "Protective Coatings for Electric Utility Gas Turbines," *Proceedings of the Second Conference on Advanced Materials for Alternative-Fuel-Capable Heat Engines*, DOE-EPRI, Monterey, CA, 1981, pp. 7-1 to 7-16.

Journal of Engineering for Gas Turbines and Power
Formerly Journal of Engineering for Power

Technical Briefs

Effects of Tip Endwall Contouring on the Three-Dimensional Flow Field in an Annular Turbine Nozzle Guide Vane: Part 2 – Numerical Investigation

T. Arts[1]

Introduction

Most of the methods attempting the modeling of three-dimensional flows, including secondary and viscous effects, are based on the solution of either the full Reynolds averaged Navier–Stokes equations (e.g., [1, 2]) or the full Navier–Stokes equations (e.g., [3, 4]). However, a fully three-dimensional, inviscid approach also allows the computation of the main secondary flows, providing the resolution of the discretization grid is high enough in the secondary flow region in order to introduce with a sufficient accuracy the total pressure gradient simulating an endwall boundary layer. An inviscid three-dimensional code has been developed at VKI and was successively applied to subsonic [5, 6] and transonic [7] flows in single fixed blade rows and to steady transonic flows in axial turbine stages [8]. The aim of this contribution is to present a numerical investigation of the three-dimensional rotational flow through a low-speed, low-aspect-ratio, high turning annular turbine nozzle guide vane with meridional tip endwall contouring and to compare these results with detailed measurements obtained at VKI [9].

Numerical Approach

The computational method is based on a time marching method (corrected viscosity scheme) and a finite volume discretization, allowing to solve the three-dimensional Euler equations written in a cylindrical coordinate system. A detailed description of the discretization procedure, numerical scheme, boundary conditions, consistency requirements, and overall accuracy of the code is given in [5, 10].

Results and Discussion

Geometry, test conditions, and measurement results are completely documented in [9]. The flow field is discretized by 31 streamwise surfaces (including hub and tip endwalls), 21 bladewise surfaces (including suction and pressure sides), and 65 spanwise surfaces (Fig. 1). The inlet conditions are purely axial flow, a uniform total temperature distribution and a spanwise total pressure profile determined from the measured upstream loss distribution [9]. The measured and numerical inlet boundary layer profiles are fully similar with respect to a nondimensional total pressure coefficient $CP_0 = (p_{0,FS} - p_{0,\text{local}})/(p_{0,FS} - \bar{p}_2)$; six and nine points were respectively used to model the hub and tip endwall boundary layers. Downstream of the blade row, the static pressure is fixed at the hub, corresponding to a value of the outlet Mach number equal to 0.3. Its spanwise distribution is determined from a simple radial equilibrium and compared with the measurements in Fig. 2, under the form of a static pressure coefficient $CP_s = (p_{01,FS} - p)/(p_{01,FS} - \bar{p}_2)$.

The blade velocity distributions at hub and tip are presented in Fig. 3. As expected from endwall contouring, an important unloading of the first 60 percent of the vane is observed in the tip region. The agreement between measured and computed

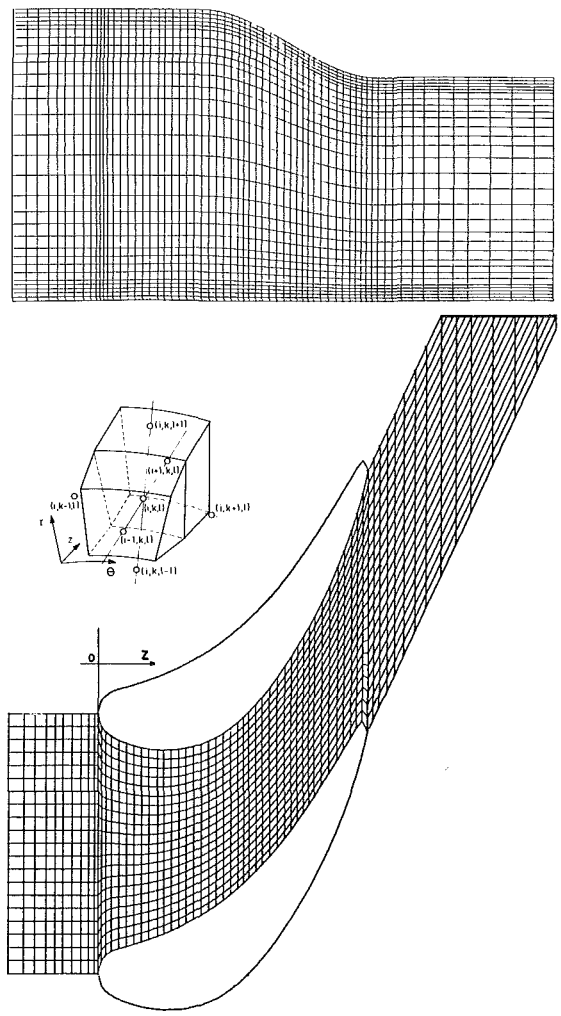

Fig. 1

[1]von Karman Institute for Fluid Dynamics, B-1640 Rhode Saint Genèse, Belgium.

Contributed by the Gas Turbine Division for publication in the JOURNAL OF ENGINEERING FOR GAS TURBINES AND POWER. Manuscript received at ASME Headquarters May 29, 1985.

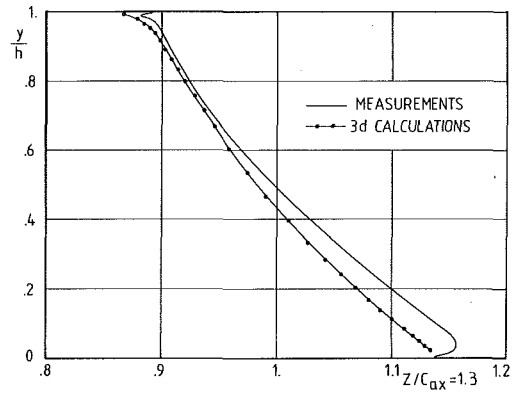

Fig. 2

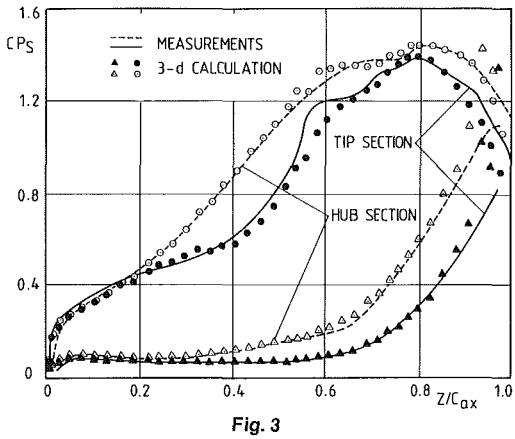

Fig. 3

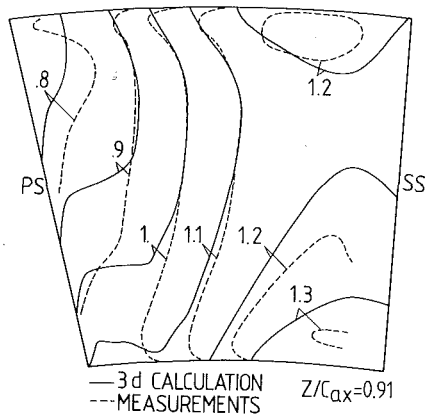

Fig. 4(a)

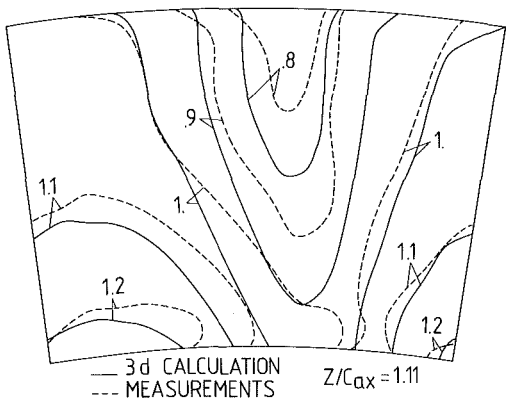

Fig. 4(b)

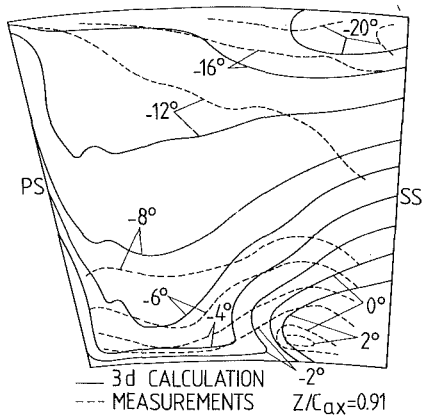

Fig. 5

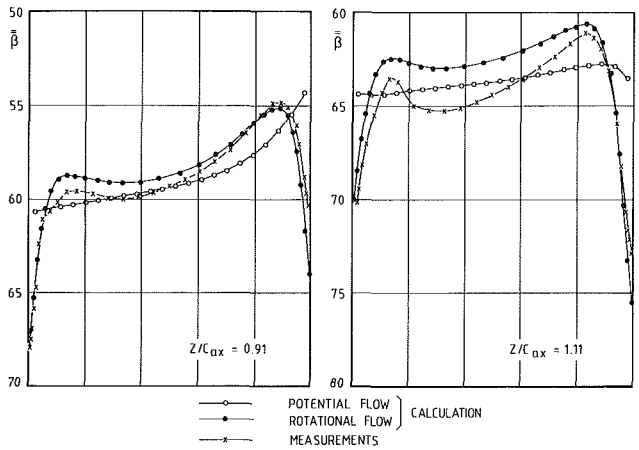

Fig. 6

values is quite good. It is also noticeable that a rather important low-velocity region ($M \cong 0.035$) along the pressure side has been handled without difficulty by the code.

The comparison between lines of constant CP_s coefficient is shown in Fig. 4. At $z/C_{ax} = 0.91$, the reduction in radial pressure gradient is well predicted. Downstream of the passage ($z/C_{ax} = 1.1$), the agreement is still impressive in spite of the fact that only a purely inviscid periodicity condition and a pitchwise uniform outlet static pressure condition at $z/C_{ax} = 1.7$ are enforced.

Measured and computed lines of meridional flow angle are compared in Fig. 5 ($z/C_{ax} = 0.91$). The overall gradients as well as the important inward flow regions are also correctly modeled.

The calculated spanwise distributions of the pitchwise mass-averaged blade-to-blade flow angle are compared with the measurements and with results obtained from a potential flow calculation in Fig. 6 ($z/C_{ax} = 0.9$, 1.1). The potential results were obtained using the same code but enforcing a uniform total pressure profile as inlet boundary condition. Inside the passage, the under- and overturning of the flow are quite well predicted. Downstream of the channel, however, a uniformization of the calculated flow field takes place, affecting mostly the underturning; it is most probably due to the enforcement of a purely inviscid periodicity condition.

An extensive and detailed description of all the computed results is presented in [10].

Conclusions

Inside the passage, the agreement between computed and measured static pressure and angle distributions is fairly

good. The influence of an inviscid periodicity condition is felt downstream of the channel, especially with respect to the underturning of the flow, whereas the static pressure distributions remain quite well predicted. The results obtained in the present contribution as well as in [5, 6] tend to confirm the hypothesis that the main secondary flows are mainly an inviscid phenomenon due to the rotational character of the incoming flow although the origin of this character is due to the viscous inlet endwall boundary layers.

References

1 Moore, J., and Moore, J. G., "Viscous Flow Calculations in Turbomachinery," in: *Computational Methods in Turbomachinery*, VKI LS 1982-05.

2 Lawerenz, M., "Calculation of the Three-Dimensional Viscous Flow in Annular Cascades Using Parabolized Navier-Stokes Equations," in: *Secondary Flows and Endwall Boundary Layers in Axial Turbomachines*, VKI LS 1984-05.

3 Moore, J., and Moore, J. G., "Calculation of Horseshoe Vortex Flow Without Numerical Mixing," ASME Paper No. 84-GT-241.

4 Hah, C., "A Navier-Stokes Analysis of Three-Dimensional Turbulent Flows Inside Turbine Blade Rows at Design and Off-Design Conditions," ASME JOURNAL OF ENGINEERING FOR GAS TURBINES AND POWER, Vol. 106, No. 2, Apr. 1984, pp. 421-429.

5 van Hove, W., "Calculation of Three-Dimensional, Inviscid, Rotational Flow in Axial Turbine Blade Rows," ASME JOURNAL OF ENGINEERING FOR GAS TURBINES AND POWER, Vol. 106, No. 2, Apr. 1984, pp. 430-436.

6 Arts, T., "Effects of Tip Endwall Contouring on the Three-Dimensional Flow Field in an Annular Turbine Nozzle Guide Vane: Part 2—Numerical Investigation," ASME Paper No. 85-GT-108; also VKI Preprint 1984-31.

7 Arts, T., "Calculation of the Three Dimensional Flow in the Ultimate Stator of a Large Steam Turbine Using a Time Marching Method and a Finite Volume Approach," 38th A.T.I. Congress, Bari, Italy, 1983; also VKI Preprint 1983-23.

8 Arts, T., "Calculation of the Three-Dimensional, Steady, Inviscid Flow in a Transonic Axial Turbine Stage," ASME JOURNAL OF ENGINEERING FOR GAS TURBINES AND POWER, Vol. 107, 1985, pp. 286-292; also VKI Preprint 1984-24.

9 Boletis, E., "Effects of Tip Endwall Contouring on the Three Dimensional Flow Field in an Annular Turbine Nozzle Guide Vane: Part 1—Experimental Investigation," ASME JOURNAL OF ENGINEERING FOR GAS TURBINES AND POWER, Vol. 107, 1985, pp. 983-990; also VKI Preprint 1984-30.

10 Arts, T., "Three-Dimensional Rotational Inviscid Flow Calculation," in: *Secondary Flows and Endwall Boundary Layers in Axial Turbomachines*, VKI LS 1984-05.

Journal of Engineering for Gas Turbines and Power

Discussion

Authors' Closure[1]

We are grateful for the meaningful discussion to our paper presented by Dr. Starken. When we said our method "provided accurate detailed information about the flow through the cascade," our emphasis was first on the "detailed information," such as those along the mean streamline. The "accuracy" is of course limited by the inviscid model.

In the comparison between the theoretical calculation and experimental data, it is important that, first of all, the effect of the axial velocity density ratio be taken into account. The theoretical calculations given in our paper were all made for this ratio equal to unity, i.e., a true plane cascade. However, it was recently shown that the axial velocity density ratio in the DFVLR cascade test data is 1.05. When the theoretical calculation is made for this axial velocity density ratio the pressure distribution around the blade is much closer to the test data than that previously calculated for this ratio equal to unity (see Fig. 15). It is to be noted that instead of Mach number, pressure is used here for comparison, because the decreasing stagnation pressure downstream of the passage shock is not available from the test data and Mach numbers calculated from the pressures measured at the blade surface and an undecreased value of stagnation pressure would give values of the Mach number higher than the actual values, such as in the case of the comparison given by Dr. Starken (Fig. 14). Furthermore, due to the very strong viscous effect in the region downstream of the passage shock, in order that the result of inviscid calculation would still be comparable to the test result, it is necessary to account, in some way, for the large viscous effect. A simple approximate way is to compute the entropy increase from the passage shock station to the blade exit station according to the stagnation pressure measured there. Assuming a linear variation of this entropy increase along the stream line downstream of the passage shock and using an overall "axial velocity density ratio" of 1.18 in order to include the effect of reduction in effective flow area in the calculation, the result of theoretical calculation is now much closer to the test data (see Fig. 15). It seems that when a suitable "overall" axial velocity density ratio and entropy increase downstream of the passage shock are included, the simple inviscid calculation is still capable of giving some useful information. Of course, for high inlet Mach number, a viscous solution is more desirable and is eagerly sought. It is also desirable to have more detailed measurement of flow along surfaces of revolution in turbomachines so that the three-dimensional effects can be fully included and the serious effect of side walls in a cascade can be avoided in assessing the accuracy of theoretical inviscid transonic flow calculations.

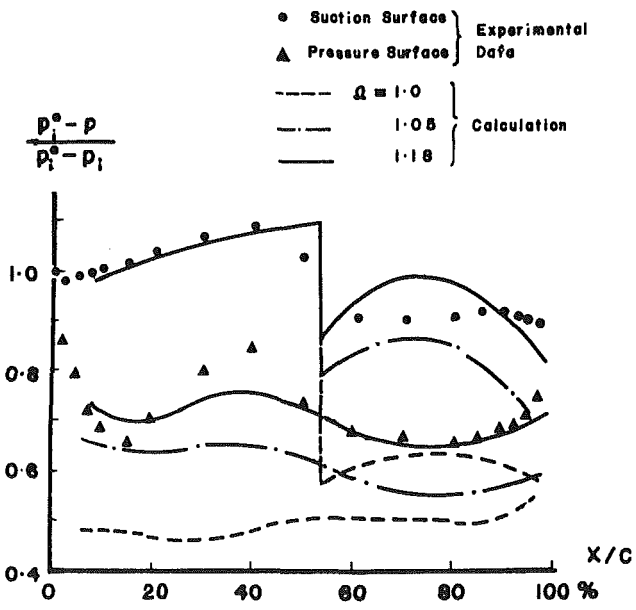

Fig. 15 Comparison between theoretical calculation and experimental data

[1] To the discussion by Dr. H. Starken of the paper "Transonic Cascade Flow Solved by Separate Supersonic and Subsonic Computations With Stock Fitting," by Wu Wenquan, Wu Chung-Hua, and Yu Dabang, JOURNAL OF ENGINEERING FOR GAS TURBINES AND POWER, Vol. 107, No. 2, April 1985, pp. 329–336.